

Frame, Fill, Finish



HydroFrame[®]
HydroCoil[®] Embolic System



HydroFill[®]
HydroCoil[®] Embolic System



HydroSoft[®]
HydroCoil[®] Embolic System

- CLINICALLY STUDIED HYDROGEL
- EFFECTIVE^{1,2,3}
- ESTABLISHED SAFETY PROFILE⁴
- SOFTER DESIGN⁵

For more information or a product demonstration,
contact your local MicroVention representative:



MicroVention, Inc.

Worldwide Headquarters

1311 Valencia Avenue
Tustin, CA 92780 USA

MicroVention UK Limited

MicroVention Europe, S.A.R.L.

MicroVention Deutschland GmbH

microvention.com

PH +1.714.247.8000

PH +44 (0) 191 258 6777

PH +33 (1) 39 21 77 46

PH +49 211 210 798-0

References

1. Speirs, Burke, Lee, and Ala. The next generation HydroCoil: initial clinical experience with the HydroFill embolic coil. J NeuroIntervent Surg, 2013.
2. Brinjikiji et al. Abstract 112. Presented at: International Stroke Conference 2015, Nashville, Tennessee, February 11-13, 2015.
3. Lee, Seo, Less, Cho, Kang and Han. Mid-term outcome of intracranial aneurysms treated with HydroSoft coils compared to historical controls treated with bare platinum coils: a single-center experience. Acta Neurochir, 156:1687-1694, 2014.
4. Laymond et al. Patients prone to recurrence after endovascular treatment: periprocedural results of the PRET randomized trial on large and recurrent aneurysms, AJNR AM J Neuroradiol, 2014.
5. Data on file at MicroVention, Inc.



BARRICADE™ COIL SYSTEM

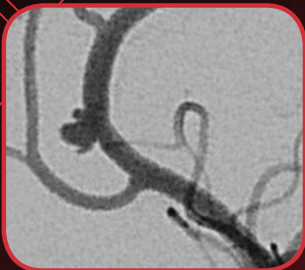
COILS THAT PERFORM

Cost Analysis of Cerebral Aneurysms Treated with the Barricade Coil System, A Retrospective Review

22 Patients Treated ♦ 114 Total Barricade Coils Used ♦ 8.2mm Mean Aneurysm Size

RIGHT PERICALLOSAL ANEURYSM

LEFT ICA TERMINUS ANEURYSM



PRE-TREATMENT

POST-TREATMENT

PRE-TREATMENT

POST-TREATMENT

“ I have successfully treated a wide range of aneurysms with the Barricade Coil System. I am impressed with the overall performance of the coils and the realized cost savings.”

-Yince Loh, M.D.

COILS THAT SAVE \$

\$110,000*
SAVED

Images and data courtesy of Yince Loh, M.D., Seattle, WA

* Estimated savings in this case, data on file.

The Barricade Coil System is intended for the endovascular embolization of intracranial aneurysms and other neurovascular abnormalities such as arteriovenous malformations and arteriovenous fistulae. The System is also intended for vascular occlusion of blood vessels within the neurovascular system to permanently obstruct blood flow to an aneurysm or other vascular malformation and for arterial and venous embolizations in the peripheral vasculature. Refer to the instructions for use for complete product information.

18 TECHNOLOGY DRIVE #169, IRVINE CA 92618 | p: 949.788.1443 | f: 949.788.1444
WWW.BLOCKADEMEDICAL.COM

MKTG-050 Rev. A





Smooth and stable.

Target Detachable Coils deliver consistently smooth deployment and exceptional microcatheter stability. Designed to work seamlessly together for framing, filling and finishing. Target Coils deliver the high performance you demand.

For more information, please visit www.strykerneurovascular.com/Target or contact your local Stryker Neurovascular sales representative.



Target®
DETACHABLE COILS

The Foundation of the ASNR Symposium 2017: *Discovery and Didactics* April 22-23, 2017

ASNR 55th Annual Meeting: *Diagnosis and Delivery* April 24-27, 2017



Long Beach Convention & Entertainment Center © Long Beach Convention & Visitors Bureau

Jacqueline A. Bello, MD, FACR
ASNR 2017 Program Chair/President-Elect

Programming developed in cooperation with and appreciation of the...

American Society of Functional Neuroradiology (ASFNR)
Kirk M. Welker, MD

American Society of Head and Neck Radiology (ASHNR)
Rebecca S. Cornelius, MD, FACR

American Society of Pediatric Neuroradiology (ASPNR)
Susan Palasis, MD

American Society of Spine Radiology (ASSR)
Joshua A. Hirsch, MD, FACR, FSIR

Society of NeuroInterventional Surgery (SNIS)
Blaise W. Baxter, MD

American Society of Neuroradiology (ASNR)
Health Policy Committee
Robert M. Barr, MD, FACR

Computer Sciences & Informatics (CSI) Committee
John L. Go, MD, FACR

Research Scientist Committee
Dikoma C. Shungu, PhD and Timothy, P.L. Roberts, PhD

The International Hydrocephalus Imaging Working Group (IHIWG)/CSF Flow Group
William G. Bradley, Jr., MD, PhD, Harold L. Rekate, MD and Bryn A. Martin, PhD



ASNR 55th Annual Meeting

c/o American Society of Neuroradiology
800 Enterprise Drive, Suite 205 • Oak Brook, Illinois 60523-4216
Phone: 630-574-0220 • Fax: 630 574-0661 • www.asnr.org/2017



ASFNR ASHNR ASPNR ASSR SNIS

THE FOUNDATION OF THE ASNR



Come to the beach! Please join us in Long Beach, California, April 22-27, 2017, for the 55th Annual Meeting of the ASNR. Known for its 5.5 miles of Pacific Ocean waterfront, this southern California beach resort boasts a blend of city sophistication and seaside serenity. ASNR is delighted to provide a “4D” focus for this meeting, as depicted by our meeting logo: **Discovery and Didactics** for The Foundation of the ASNR Symposium 2017: **Diagnosis and Delivery** for the ensuing Annual Meeting Program.

Centered on Discovery and Didactics, the symposium will feature sessions on “What’s New?” in the role neuroimaging plays defining CNS disease mechanisms and how to best prepare for “What’s Next?” for our subspecialty in terms of training, teaching, and leading the process of lifelong learning. The annual meeting programming will address best practices in Diagnosis and Delivery, as we strive to provide value, promote quality in better health and care and consider cost. Our discussions will consider how to navigate the changing landscape of healthcare reform and reimbursement as subspecialists in a field that is changing at an equally “fast forward” pace!



Hyatt Regency Long Beach
© Hyatt Regency Long Beach



Westin Long Beach
© The Westin Long Beach



American Society of Head & Neck Radiology

Comprehensive Head and Neck Imaging: 50 Years of Progress

September 7 - 11, 2016

Hyatt Regency Washington on Capitol Hill
Washington, D.C.

29.25 AMA PRA Category 1 Credit(s)TM

Four sessions of the meeting program will be submitted for SAM qualification.

**Hands-on US and US-Guided Biopsy Seminar
Saturday, September 10, 2016**

Separate Registration Required
Registration is Limited to 20 Attendees Per Session.

Not accredited for AMA PRA Category 1 Credit(s)TM

Please contact Educational Symposia at 813-806-1000 or ASHNR@edusymp.com or visit www.ASHNR.org for additional information.



AMA Preferred Provider Offers and Services



AMA Preferred Provider Offers and Services

Special offers that fit you and your practice's needs.

Which savings would benefit you the most? Discounts on pharmaceuticals, medical supplies and equipment? Or on travel, practice financing, and financial and insurance services? Now physicians can save in all of these professional and personal categories and more through the AMA Preferred Provider Offers and Services program.

Please activate your 2016 AMA membership by calling **(800) 262-3211** or visit **ama-assn.org/go/join**.



* Subsidiary of the American Medical Association.

Target® Detachable Coil

See package insert for complete indications, contraindications, warnings and instructions for use.

INTENDED USE/ INDICATIONS FOR USE

Target Detachable Coils are intended to endovascularly obstruct or occlude blood flow in vascular abnormalities of the neurovascular and peripheral vessels.

Target Detachable Coils are indicated for endovascular embolization of:

- Intracranial aneurysms
- Other neurovascular abnormalities such as arteriovenous malformations and arteriovenous fistulae
- Arterial and venous embolizations in the peripheral vasculature

CONTRAINDICATIONS

None known.

POTENTIAL ADVERSE EVENTS

Potential complications include, but are not limited to: allergic reaction, aneurysm perforation and rupture, arrhythmia, death, edema, embolus, headache, hemorrhage, infection, ischemia, neurological/intracranial sequelae, post-embolization syndrome (fever, increased white blood cell count, discomfort), TIA/stroke, vasospasm, vessel occlusion or closure, vessel perforation, dissection, trauma or damage, vessel rupture, vessel thrombosis. Other procedural complications including but not limited to: anesthetic and contrast media risks, hypotension, hypertension, access site complications.

WARNINGS

- Contents supplied STERILE using an ethylene oxide (EO) process. Do not use if sterile barrier is damaged. If damage is found, call your Stryker Neurovascular representative.
- For single use only. Do not reuse, reprocess or resterilize. Reuse, reprocessing or resterilization may compromise the structural integrity of the device and/or lead to device failure which, in turn, may result in patient injury, illness or death. Reuse, reprocessing or resterilization may also create a risk of contamination of the device and/or cause patient infection or cross-infection, including, but not limited to, the transmission of infectious disease(s) from one patient to another. Contamination of the device may lead to injury, illness or death of the patient.

- After use, dispose of product and packaging in accordance with hospital, administrative and/or local government policy.
- **This device should only be used by physicians who have received appropriate training in interventional neuroradiology or interventional radiology and preclinical training on the use of this device as established by Stryker Neurovascular.**
- Patients with hypersensitivity to 316LVM stainless steel may suffer an allergic reaction to this implant.
- MR temperature testing was not conducted in peripheral vasculature, arteriovenous malformations or fistulae models.
- The safety and performance characteristics of the Target Detachable Coil System (Target Detachable Coils, InZone Detachment Systems, delivery systems and accessories) have not been demonstrated with other manufacturer's devices (whether coils, coil delivery devices, coil detachment systems, catheters, guidewires, and/or other accessories). Due to the potential incompatibility of non Stryker Neurovascular devices with the Target Detachable Coil System, the use of other manufacturer's device(s) with the Target Detachable Coil System is not recommended.
- To reduce risk of coil migration, the diameter of the first and second coil should never be less than the width of the ostium.
- In order to achieve optimal performance of the Target Detachable Coil System and to reduce the risk of thromboembolic complications, it is critical that a continuous infusion of appropriate flush solution be maintained between a) the femoral sheath and guiding catheter, b) the 2-tip microcatheter and guiding catheters, and c) the 2-tip microcatheter and Stryker Neurovascular guidewire and delivery wire. Continuous flush also reduces the potential for thrombus formation on, and crystallization of infusate around, the detachment zone of the Target Detachable Coil.
- Do not use the product after the "Use By" date specified on the package.
- Reuse of the flush port/dispenser coil or use with any coil other than the original coil may result in contamination of, or damage to, the coil.
- Utilization of damaged coils may affect coil delivery to, and stability inside, the vessel or aneurysm, possibly resulting in coil migration and/or stretching.

- The fluoro-saver marker is designed for use with a Rotating Hemostatic Valve (RHV). If used without an RHV, the distal end of the coil may be beyond the alignment marker when the fluoro-saver marker reaches the microcatheter hub.
 - If the fluoro-saver marker is not visible, do not advance the coil without fluoroscopy.
 - Do not rotate delivery wire during or after delivery of the coil. Rotating the Target Detachable Coil delivery wire may result in a stretched coil or premature detachment of the coil from the delivery wire, which could result in coil migration.
 - Verify there is no coil loop protrusion into the parent vessel after coil placement and prior to coil detachment. Coil loop protrusion after coil placement may result in thromboembolic events if the coil is detached.
 - Verify there is no movement of the coil after coil placement and prior to coil detachment. Movement of the coil after coil placement may indicate that the coil could migrate once it is detached.
 - Failure to properly close the RHV compression fitting over the delivery wire before attaching the InZone® Detachment System could result in coil movement, aneurysm rupture or vessel perforation.
 - Verify repeatedly that the distal shaft of the catheter is not under stress before detaching the Target Detachable Coil. Axial compression or tension forces could be stored in the 2-tip microcatheter causing the tip to move during coil delivery. Microcatheter tip movement could cause the aneurysm or vessel to rupture.
 - Advancing the delivery wire beyond the microcatheter tip once the coil has been detached involves risk of aneurysm or vessel perforation.
 - The long term effect of this product on extravascular tissues has not been established so care should be taken to retain this device in the intravascular space.
- Damaged delivery wires may cause detachment failures, vessel injury or unpredictable distal tip response during coil deployment. If a delivery wire is damaged at any point during the procedure, do not attempt to straighten or otherwise repair it. Do not proceed with deployment or detachment. Remove the entire coil and replace with undamaged product.
- After use, dispose of product and packaging in accordance with hospital, administrative and/or local government policy.

CAUTIONS / PRECAUTIONS

- Federal Law (USA) restricts this device to sale by or on the order of a physician.
- Besides the number of InZone Detachment System units needed to complete the case, there must be an extra InZone Detachment System unit as back up.
- Removing the delivery wire without grasping the introducer sheath and delivery wire together may result in the detachable coil sliding out of the introducer sheath.
- Failure to remove the introducer sheath after inserting the delivery wire into the RHV of the microcatheter will interrupt normal infusion of flush solution and allow back flow of blood into the microcatheter.
- Some low level overhead light near or adjacent to the patient is required to visualize the fluoro-saver marker; monitor light alone will not allow sufficient visualization of the fluoro-saver marker.
- Advance and retract the Target Detachable Coil carefully and smoothly without excessive force. If unusual friction is noticed, slowly withdraw the Target Detachable Coil and examine for damage. If damage is present, remove and use a new Target Detachable Coil. If friction or resistance is still noted, carefully remove the Target Detachable Coil and microcatheter and examine the microcatheter for damage.
- If it is necessary to reposition the Target Detachable Coil, verify under fluoroscopy that the coil moves with a one-to-one motion. If the coil does not move with a one-to-one motion or movement is difficult, the coil may have stretched and could possibly migrate or break. Gently remove both the coil and microcatheter and replace with new devices.
- Increased detachment times may occur when:
 - Other embolic agents are present.
 - Delivery wire and microcatheter markers are not properly aligned.
 - Thrombus is present on the coil detachment zone.
- Do not use detachment systems other than the InZone Detachment System.
- Increased detachment times may occur when delivery wire and microcatheter markers are not properly aligned.
- Do not use detachment systems other than the InZone Detachment System.



Stryker Neurovascular
47900 Bayside Parkway
Fremont, CA 94538

strykerneurovascular.com

Date of Release: MAR/2016

EX_EN_US

Copyright © 2016 Stryker
NV00018669.AA

AXS Catalyst™ 6 Distal Access Catheter

See package insert for complete indications, complications, warnings, and instructions for use.

INTENDED USE/INDICATIONS FOR USE

The AXS Catalyst Distal Access Catheter is indicated for use in facilitating the insertion and guidance of appropriately sized interventional devices into a selected blood vessel in the peripheral and neurovascular systems. The AXS Catalyst Distal Access Catheter is also indicated for use as a conduit for retrieval devices.

CONTRAINDICATIONS

None known.

ADVERSE EVENTS

Potential adverse events associated with the use of catheters or with the endovascular procedures include, but are not limited to: access site complications, allergic reaction, aneurysm perforation, aneurysm rupture, death, embolism (air, foreign body, plaque, thrombus), hematoma, hemorrhage, infection, ischemia, neurological deficits, pseudoaneurysm, stroke, transient ischemic attack, vasospasm, vessel dissection, vessel occlusion, vessel perforation, vessel rupture, and vessel thrombosis.

WARNING

Contents supplied sterile using an ethylene oxide (EO) process. Do not use if sterile barrier is damaged. If damage is found, call your Stryker Neurovascular representative. For single use only. Do not reuse, reprocess or resterilize. Reuse, reprocessing or resterilization may compromise the structural integrity of the device and/or lead to device failure which, in turn, may result in patient injury, illness or death. Reuse, reprocessing or resterilization may also create a risk of contamination of the device and/or cause patient infection or cross-infection, including, but not limited to, the transmission of infectious disease(s) from one patient to another.

Contamination of the device may lead to injury, illness or death of the patient. After use, dispose of product and packaging in accordance with hospital, administrative and/or local government policy.

- Limited testing has been performed with solutions such as contrast media, and saline. The use of these catheters for delivery of solutions other than the types that have been tested for compatibility is not recommended.
- Not intended for use with power injectors.
- If flow through catheter becomes restricted, do not attempt to clear catheter lumen by infusion. Doing so may cause catheter damage or patient injury. Remove and replace catheter.

- Never advance or withdraw an intravascular device against resistance until the cause of the resistance is determined by fluoroscopy. Movement of the device against resistance could dislodge a clot, perforate a vessel wall, or damage the device.

PRECAUTIONS

- Carefully inspect all devices prior to use. Verify size, length, and condition are suitable for the specific procedure. Do not use a device that has been damaged in any way. Damaged device may cause complications.
- To control the proper introduction, movement, positioning and removal of the catheter within the vascular system, users should employ standard clinical angiographic and fluoroscopic practices and techniques throughout the interventional procedure.
- Use the product prior to the "Use By" date printed on the label.
- To prevent thrombus formation and contrast media crystal formation, maintain a constant infusion of appropriate flush solution through catheter lumen.
- Torquing the catheter may cause damage which could result in kinking or separation of the catheter shaft.

Copyright © 2016 Stryker
NV00018756.AA



Stryker Neurovascular
47900 Bayside Parkway
Fremont, CA 94538

strykerneurovascular.com

Date of Release: MAR/2016

EX_EN_US

Engineered

by MicroVention®



HYDROGEL ADVANCED COILS

The clinical benefits of **hydrogel** NOW engineered with the softness of bare platinum on the **V-Trak® Advanced Coil System**.

INDICATIONS FOR USE:

The HydroCoil® Embolic System (HES) is intended for the endovascular embolization of intracranial aneurysms and other neurovascular abnormalities such as arteriovenous malformations and arteriovenous fistulae. The HES is also intended for vascular occlusion of blood vessels within the neurovascular system to permanently obstruct blood flow to an aneurysm or other vascular malformation and for arterial and venous embolizations in the peripheral vasculature. The device should only be used by physicians who have undergone pre-clinical training in all aspects of HES procedures as prescribed by MicroVention.

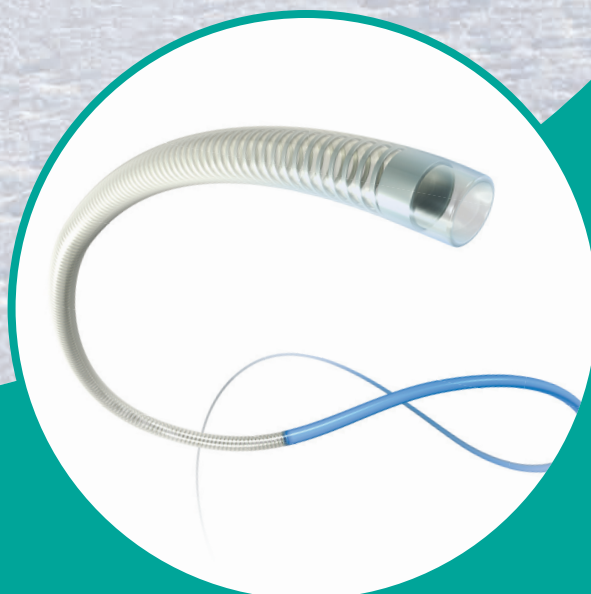
MICROVENTION, V-Trak, HydroCoil, HydroFrame, HydroFill and HydroSoft are registered trademarks of MicroVention, Inc. Refer to Instructions for Use, contraindications and warnings for additional information. Federal (USA) law restricts this device for sale by or on the order of a physician. © 2015 MicroVention, Inc. 6/15

CE
0297

Success accelerated.

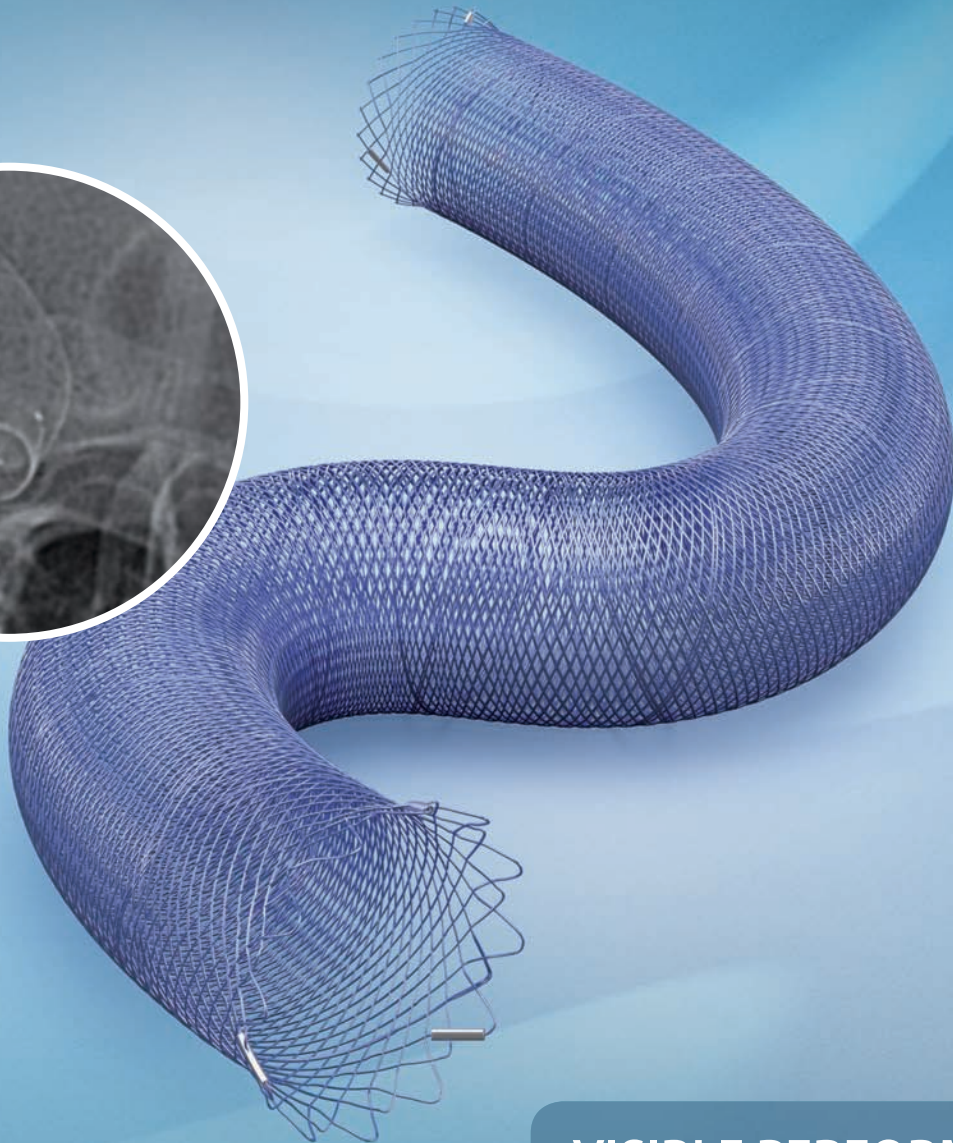
With superior trackability, resilient design and strong aspiration force, the AXS Catalyst™ 6 Distal Access Catheter is designed for fast access and rapid revascularization with Trevo® XP Retrievers.*†

*To facilitate revascularization with Trevo XP ProVue Retrievers.
†Bench test results. n=3 trackability, aspiration. n=1 kink resistance.
Bench test results may not necessarily be indicative of clinical performance.



AXS Catalyst™ 6
DISTAL ACCESS CATHETER

DERIVO[®] Embolisation Device



VISIBLE PERFORMANCE

- New visibility concept
- Unique BlueXide[®] surface

AJNR

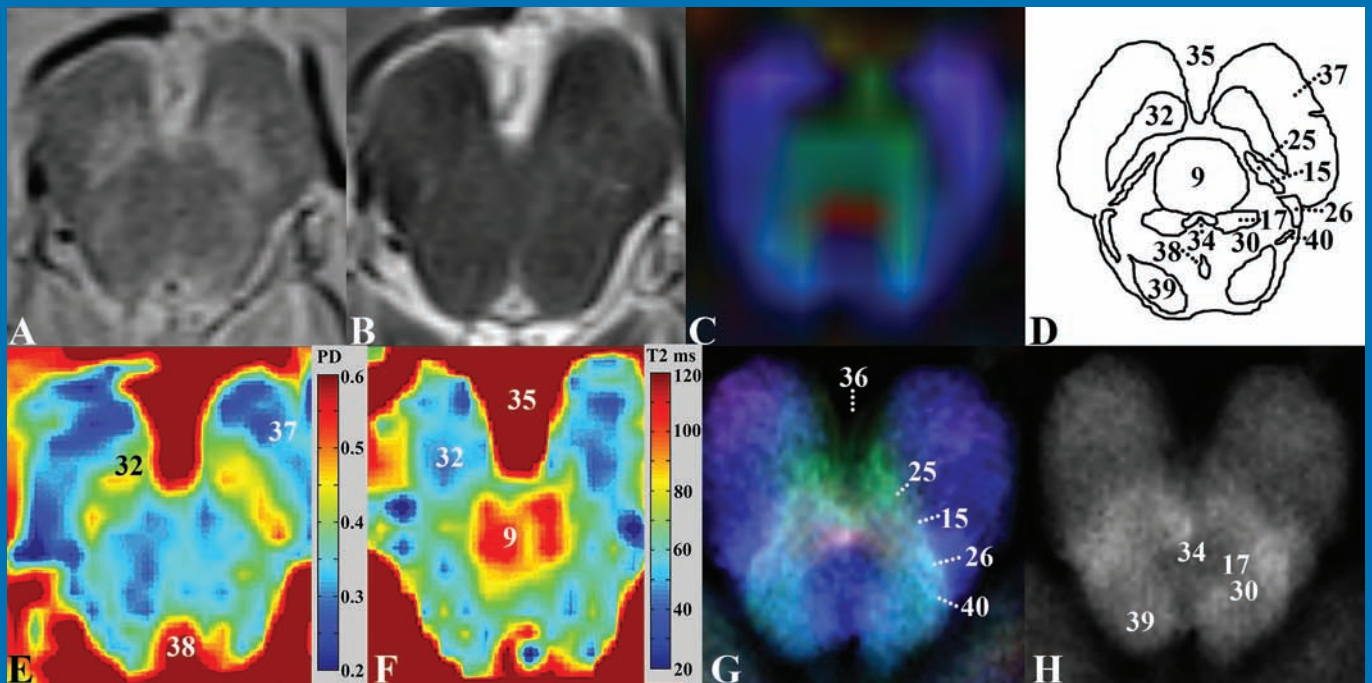
AMERICAN JOURNAL OF NEURORADIOLOGY

JUNE 2016
VOLUME 37
NUMBER 6
WWW.AJNR.ORG

THE JOURNAL OF DIAGNOSTIC AND
INTERVENTIONAL NEURORADIOLOGY

3T brain stem anatomy
Functional correlates of intracranial stenosis collateralization
Workflow in acute ischemic stroke

Official Journal ASNR • ASFNR • ASHNR • ASPNR • ASSR



AJNR

AMERICAN JOURNAL OF NEURORADIOLOGY

JUNE 2016
VOLUME 37
NUMBER 6
WWW.AJNR.ORG

Publication Preview at www.ajnr.org features articles released in advance of print. Visit www.ajnrblog.org to comment on AJNR content and chat with colleagues and AJNR's News Digest at <http://ajnrndigest.org> to read the stories behind the latest research in neuroimaging.

977 **PERSPECTIVES** *B. Thomas*

REVIEW ARTICLE

  978 **Imaging, Intervention, and Workflow in Acute Ischemic Stroke: The Calgary Approach** *C. Zerna, et al.*

INTERVENTIONAL

PATIENT SAFETY

 985 **Radiation Dose Reduction by Indication-Directed Focused z-Direction Coverage for Neck CT** *A.K. Parikh, et al.*

**HEAD & NECK
PEDIATRICS**

  990 **How to Reduce Head CT Orders in Children with Hydrocephalus Using the Lean Six Sigma Methodology: Experience at a Major Quaternary Care Academic Children's Center** *A. Tekes, et al.*

PEDIATRICS

PRACTICE PERSPECTIVES

997 **Myelography CPT Coding Updates: Effects of 4 New Codes and Unintended Consequences** *F.H. Chokshi, et al.*

**SPINE
INTERVENTIONAL**

1000 **Same-Day Sinus and Brain CT Imaging in the Medicare Population: Are Practice Patterns Changing in Association with Medicare Policy Initiatives?** *H. Kroll, et al.*

**HEAD & NECK
ADULT BRAIN**

FUNCTIONAL VIGNETTE

1005 **Nonmotor Functions of the Cerebellum: An Introduction** *A.P. Klein, et al.*

GENERAL CONTENTS

 1010 **Autoimmune Comorbidities Are Associated with Brain Injury in Multiple Sclerosis** *R. Zivadinov, et al.*

ADULT BRAIN

  1017 **Incidence of Radiologically Isolated Syndrome: A Population-Based Study** *Y. Forslin, et al.*

ADULT BRAIN

    1023 **Clinical Feasibility of Synthetic MRI in Multiple Sclerosis: A Diagnostic and Volumetric Validation Study** *T. Granberg, et al.*

ADULT BRAIN

 1030 **White Matter Diffusion Changes during the First Year of Natalizumab Treatment in Relapsing-Remitting Multiple Sclerosis** *O.T. Wiebenga, et al.*

ADULT BRAIN

AJNR (Am J Neuroradiol ISSN 0195-6108) is a journal published monthly, owned and published by the American Society of Neuroradiology (ASNR), 800 Enterprise Drive, Suite 205, Oak Brook, IL 60523. Annual dues for the ASNR include \$170.00 for journal subscription. The journal is printed by Cadmus Journal Services, 5457 Twin Knolls Road, Suite 200, Columbia, MD 21045; Periodicals postage paid at Oak Brook, IL and additional mailing offices. Printed in the U.S.A. POSTMASTER: Please send address changes to American Journal of Neuroradiology, P.O. Box 3000, Denville, NJ 07834, U.S.A. Subscription rates: nonmember \$380 (\$450 foreign) print and online, \$305 online only; institutions \$440 (\$510 foreign) print and basic online, \$875 (\$940 foreign) print and extended online, \$365 online only (basic), extended online \$790; single copies are \$35 each (\$40 foreign). Indexed by PubMed/Medline, BIOSIS Previews, Current Contents (Clinical Medicine and Life Sciences), EMBASE, Google Scholar, HighWire Press, Q-Sensei, RefSeek, Science Citation Index, and SCI Expanded. Copyright © American Society of Neuroradiology.

-      1038 **Computer-Assisted Detection of Cerebral Aneurysms in MR Angiography in a Routine Image-Reading Environment: Effects on Diagnosis by Radiologists** *S. Miki, et al.* **ADULT BRAIN**
- 1044 **Brain MR Imaging Findings of Cardiac-Type Fabry Disease with an IVS4+919G>A Mutation** *H.-J. Lee, et al.* **ADULT BRAIN**
PEDIATRICS
-    1050 **Automated Hippocampal Subfield Segmentation at 7T MRI** *L.E.M. Wisse, et al.* **ADULT BRAIN**
-      1058 **New Clinically Feasible 3T MRI Protocol to Discriminate Internal Brain Stem Anatomy** *M.J. Hoch, et al.* **ADULT BRAIN**
- 1066 **Commentary**
Super-Resolution Track Density Imaging: Anatomic Detail versus Quantification *F. Calamante*
-    1068 **Endovascular Treatment versus Best Medical Treatment in Patients with Acute Ischemic Stroke: A Meta-Analysis of Randomized Controlled Trials** *A.I. Qureshi, et al.* **INTERVENTIONAL**
ADULT BRAIN
-   1074 **Clinical Impact of Ventilation Duration in Patients with Stroke Undergoing Interventional Treatment under General Anesthesia: The Shorter the Better?** *O. Nikoubashman, et al.* **INTERVENTIONAL**
ADULT BRAIN
- 1080 **Outcomes Are Not Different between Patients with Intermediate and High DWI-ASPECTS after Stent-Retriever Embolectomy for Acute Anterior Circulation Stroke** *S.K. Kim, et al.* **INTERVENTIONAL**
-  1086 **Angiographic Structural Differentiation between Native Arteriogenesis and Therapeutic Synangiosis in Intracranial Arterial Steno-Occlusive Disease** *Y.C. Ooi, et al.* **INTERVENTIONAL**
ADULT BRAIN
- 1092 **Occlusion of Posterior Fossa Dural Sinuses in Vein of Galen Malformation** *A. Berenstein, et al.* **INTERVENTIONAL**
PEDIATRICS
- 1099 **Association between Postprocedural Infarction and Antiplatelet Drug Resistance after Coiling for Unruptured Intracranial Aneurysms** *M.S. Kim, et al.* **INTERVENTIONAL**
ADULT BRAIN
-  1106 **Current Trends and Results of Endovascular Treatment of Unruptured Intracranial Aneurysms at a Single Institution in the Flow-Diverter Era** *O. Petr, et al.* **INTERVENTIONAL**
-   1114 **Differential Gene Expression in Coiled versus Flow-Diverter-Treated Aneurysms: RNA Sequencing Analysis in a Rabbit Aneurysm Model** *A. Rouchaud, et al.* **INTERVENTIONAL**
-  1122 **Smoking Does Not Affect Occlusion Rates and Morbidity-Mortality after Pipeline Embolization for Intracranial Aneurysms** *A. Rouchaud, et al.* **INTERVENTIONAL**
- 1127 **Pipeline Embolization Device with or without Adjunctive Coil Embolization: Analysis of Complications from the IntrePED Registry** *M.S. Park, et al.* **INTERVENTIONAL**
-    1132 **Interrogating the Functional Correlates of Collateralization in Patients with Intracranial Stenosis Using Multimodal Hemodynamic Imaging** *B.A. Roach, et al.* **FUNCTIONAL**
ADULT BRAIN
-  1139 **Abnormal Amygdala Resting-State Functional Connectivity in Irritable Bowel Syndrome** *R. Qi, et al.* **FUNCTIONAL**
-  1146 **Optimal MR Plaque Imaging for Cervical Carotid Artery Stenosis in Predicting the Development of Microembolic Signals during Exposure of Carotid Arteries in Endarterectomy: Comparison of 4 T1-Weighted Imaging Techniques** *Y. Sato, et al.* **EXTRACRANIAL**
VASCULAR
- 1155 **Modified Core Biopsy Technique to Increase Diagnostic Yields for Well-Circumscribed Indeterminate Thyroid Nodules: A Retrospective Analysis** *S. Han, et al.* **HEAD & NECK**
INTERVENTIONAL

Official Journal:

American Society of Neuroradiology
American Society of Functional Neuroradiology
American Society of Head and Neck Radiology
American Society of Pediatric Neuroradiology
American Society of Spine Radiology

EDITOR-IN-CHIEF

Jeffrey S. Ross, MD

Professor of Radiology, Department of Radiology,
Mayo Clinic College of Medicine, Phoenix, Arizona

SENIOR EDITORS

Harry J. Cloft, MD, PhD

Professor of Radiology and Neurosurgery,
Department of Radiology, Mayo Clinic College of
Medicine, Rochester, Minnesota

Thierry A.G.M. Huisman, MD

Professor of Radiology, Pediatrics, Neurology, and
Neurosurgery, Chairman, Department of Imaging
and Imaging Science, Johns Hopkins Bayview,
Director, Pediatric Radiology and Pediatric
Neuroradiology, Johns Hopkins Hospital,
Baltimore, Maryland

C.D. Phillips, MD, FACR

Professor of Radiology, Weill Cornell Medical
College, Director of Head and Neck Imaging,
New York-Presbyterian Hospital, New York,
New York

Pamela W. Schaefer, MD

Clinical Director of MRI and Associate Director of
Neuroradiology, Massachusetts General Hospital,
Boston, Massachusetts, Associate Professor,
Radiology, Harvard Medical School, Cambridge,
Massachusetts

Charles M. Strother, MD

Professor of Radiology, Emeritus, University of
Wisconsin, Madison, Wisconsin

Jody Tanabe, MD

Professor of Radiology and Psychiatry,
Chief of Neuroradiology,
University of Colorado, Denver, Colorado

STATISTICAL SENIOR EDITOR

Bryan A. Comstock, MS

Senior Biostatistician,
Department of Biostatistics,
University of Washington, Seattle, Washington

EDITORIAL BOARD

Ashley H. Aiken, *Atlanta, Georgia*
A. James Barkovich, *San Francisco, California*
Walter S. Bartynski, *Charleston, South Carolina*
Barton F. Branstetter IV, *Pittsburgh, Pennsylvania*
Jonathan L. Brisman, *Lake Success, New York*
Julie Bykowski, *San Diego, California*
Donald W. Chakeres, *Columbus, Ohio*
Asim F. Choudhri, *Memphis, Tennessee*
Alessandro Cianfoni, *Lugano, Switzerland*
Colin Derdeyn, *St. Louis, Missouri*
Rahul S. Desikan, *San Francisco, California*
Richard du Mesnil de Rochemont, *Frankfurt, Germany*
Clifford J. Eskey, *Hanover, New Hampshire*
Massimo Filippi, *Milan, Italy*
David Fiorella, *Cleveland, Ohio*
Allan J. Fox, *Toronto, Ontario, Canada*
Christine M. Glastonbury, *San Francisco, California*

John L. Go, *Los Angeles, California*
Wan-Yuo Guo, *Taipei, Taiwan*
Rakesh K. Gupta, *Lucknow, India*
Lotfi Hachein-Bey, *Sacramento, California*
David B. Hackney, *Boston, Massachusetts*
Christopher P. Hess, *San Francisco, California*
Andrei Holodny, *New York, New York*
Benjamin Huang, *Chapel Hill, North Carolina*
George J. Hunter, *Boston, Massachusetts*
Mahesh V. Jayaraman, *Providence, Rhode Island*
Valerie Jewells, *Chapel Hill, North Carolina*
Timothy J. Kaufmann, *Rochester, Minnesota*
Kenneth F. Layton, *Dallas, Texas*
Ting-Yim Lee, *London, Ontario, Canada*
Michael M. Lell, *Erlangen, Germany*
Michael Lev, *Boston, Massachusetts*
Karl-Olof Lovblad, *Geneva, Switzerland*
Franklin A. Marden, *Chicago, Illinois*
M. Gisele Matheus, *Charleston, South Carolina*
Joseph C. McGowan, *Merion Station, Pennsylvania*

Kevin R. Moore, *Salt Lake City, Utah*
Christopher J. Moran, *St. Louis, Missouri*
Takahisa Mori, *Kamakura City, Japan*
Suresh Mukherji, *Ann Arbor, Michigan*
Amanda Murphy, *Toronto, Ontario, Canada*
Alexander J. Nemeth, *Chicago, Illinois*
Laurent Pierot, *Reims, France*
Jay J. Pillai, *Baltimore, Maryland*
Whitney B. Pope, *Los Angeles, California*
M. Judith Donovan Post, *Miami, Florida*
Tina Young Poussaint, *Boston, Massachusetts*
Joana Ramalho, *Lisbon, Portugal*

Otto Rapalino, *Boston, Massachusetts*
Álex Rovira-Cañellas, *Barcelona, Spain*
Paul M. Ruggieri, *Cleveland, Ohio*
Zoran Rumboldt, *Rijeka, Croatia*
Amit M. Saindane, *Atlanta, Georgia*
Erin Simon Schwartz, *Philadelphia, Pennsylvania*
Aseem Sharma, *St. Louis, Missouri*
J. Keith Smith, *Chapel Hill, North Carolina*
Maria Vittoria Spampinato, *Charleston, South Carolina*
Gordon K. Sze, *New Haven, Connecticut*
Krishnamoorthy Thamburaj, *Hershey, Pennsylvania*
Kent R. Thielen, *Rochester, Minnesota*
Cheng Hong Toh, *Taipei, Taiwan*
Thomas A. Tomsick, *Cincinnati, Ohio*
Aquila S. Turk, *Charleston, South Carolina*
Willem Jan van Rooij, *Tilburg, Netherlands*
Arastoo Vossough, *Philadelphia, Pennsylvania*
Elysa Widjaja, *Toronto, Ontario, Canada*
Max Wintermark, *Charlottesville, Virginia*
Ronald L. Wolf, *Philadelphia, Pennsylvania*
Kei Yamada, *Kyoto, Japan*

EDITORIAL FELLOW

Hillary R. Kelly, *Boston, Massachusetts*

SPECIAL CONSULTANTS TO THE EDITOR

AJNR Blog Editor

Neil Lall, *Denver, Colorado*

Case of the Month Editor

Nicholas Stence, *Aurora, Colorado*

Case of the Week Editors

Juan Pablo Cruz, *Santiago, Chile*
Sapna Rawal, *Toronto, Ontario, Canada*

Classic Case Editor

Sandy Cheng-Yu Chen, *Taipei, Taiwan*

Facebook Editor

Peter Yi Shen, *Sacramento, California*

Health Care and Socioeconomics Editor

Pina C. Sanelli, *New York, New York*

Physics Editor

Greg Zaharchuk, *Stanford, California*

Podcast Editor

Yvonne Lui, *New York, New York*

Twitter Editor

Ryan Fitzgerald, *Little Rock, Arkansas*

YOUNG PROFESSIONALS

ADVISORY COMMITTEE

Asim K. Bag, *Birmingham, Alabama*
Anna E. Nidecker, *Sacramento, California*
Peter Yi Shen, *Sacramento, California*

Founding Editor

Juan M. Taveras

Editors Emeriti

Mauricio Castillo, Robert I. Grossman,
Michael S. Huckman, Robert M. Quencer

Managing Editor

Karen Halm

Electronic Publications Manager

Jason Gantenberg

Executive Director, ASNR

James B. Gantenberg

Director of Communications, ASNR

Angelo Artemakis



Title: Colors. Watercolor on handmade paper. This painting was inspired by the scene of my MBBS classmates enthusiastically taking their group photos (with all the female doctors in beautiful ethnic Indian dresses) at our 25th anniversary get-together.

Bejoy Thomas, MD, DNB, PDCC, Trivandrum, Kerala, India

Imaging, Intervention, and Workflow in Acute Ischemic Stroke: The Calgary Approach

 C. Zerna,  Z. Assis,  C.D. d'Este,  B.K. Menon, and  M. Goyal



ABSTRACT

SUMMARY: Five recently published clinical trials showed dramatically higher rates of favorable functional outcome and a satisfying safety profile of endovascular treatment compared with the previous standard of care in acute ischemic stroke with proximal anterior circulation artery occlusion. Eligibility criteria within these trials varied by age, stroke severity, imaging, treatment-time window, and endovascular treatment devices. This focused review provides an overview of the trial results and explores the heterogeneity in imaging techniques, workflow, and endovascular techniques used in these trials and the consequent impact on practice. Using evidence from these trials and following a case from start to finish, this review recommends strategies that will help the appropriate patient undergo a fast, focused clinical evaluation, imaging, and intervention.

ABBREVIATIONS: MR CLEAN = Multicenter Randomized Clinical trial of Endovascular treatment for Acute ischemic stroke in the Netherlands; EMS = Emergency Medical Services; ESCAPE = Endovascular Treatment for Small Core and Proximal Occlusion Ischemic Stroke; EXTEND-IA = Extending the Time for Thrombolysis in Emergency Neurological Deficits–Intra-Arterial; REVASCAT = Endovascular Revascularization With Solitaire Device Versus Best Medical Therapy in Anterior Circulation Stroke Within 8 Hours; SWIFT-PRIME Solitaire With the Intention for Thrombectomy as Primary Endovascular Treatment

Endovascular treatment of acute ischemic stroke in the anterior circulation due to large-vessel occlusion is now the new standard of care as a result of 5 recently published trials with positive outcomes. Each of the recently published clinical trials (MR CLEAN, ESCAPE, SWIFT-PRIME, EXTEND-IA and REVASCAT) enrolled 70–500 previously independent subjects with (proximal) anterior circulation occlusion.^{1–5} Eligibility varied by age, baseline stroke severity, treatment time window, IV rtPA treatment, and additional extracranial occlusions. A variety of imaging techniques were used to determine the site of occlusion and salvageable brain, including multiphase CTA, CT perfusion, and diffusion-weighted MR imaging. Results clearly favored emergency endovascular intervention in the management of large proximal vessel occlusions in eligible patients in addition to standard care. Endovascular intervention is safe and effective for achieving reperfusion and substantially reduces the degree of disability while increasing the proportion of patients with functional

independence 3 months after stroke (summarized in the On-line Table).^{1–5}

These recent endovascular trials led to 4 major conclusions, in our opinion: 1) Fast reperfusion is the key to good outcome (“time is brain”), 2) endovascular treatment by using stent retrievers is safe and effective, 3) imaging plays a critical role in patient selection for endovascular therapy, and 4) teamwork is the key to success.

Herein, we lead the reader along the management workflow of a patient with acute ischemic stroke treated within the ESCAPE trial, from the onset of stroke until the 90-day outcome assessment. We use this actual patient example to illustrate our current approach to acute ischemic stroke management and, more specifically, to endovascular therapy. We discuss this approach in the context of results from the recent endovascular trials.^{1–5}

From Acute Ischemic Stroke Onset to 90 Days: A Case Experience

Stroke treatment is a time-sensitive matter. A treatment goal for acute ischemic stroke is now 60 minutes from hospital arrival to the bolus of IV rtPA.⁶ Specialized stroke centers have successfully reduced their door-to-needle time for IV rtPA to 20 minutes; there is a call for a new benchmark door-to-needle time of <30 minutes.⁷ Because the recent endovascular trials demonstrate that fast reperfusion is the key to a good outcome, metrics such as onset-to-reperfusion time and imaging-to-reperfusion time will gain importance.

From the Calgary Stroke Program, Clinical Neurosciences, and Department of Radiology, University of Calgary, Calgary, Alberta, Canada.

Please address correspondence to Mayank Goyal, MD, FRCPC, Seaman Family MR Research Centre, Foothills Medical Centre, 1403 29th St NW, Calgary, AB T2N 2T9 Canada; e-mail: mgoyal@ucalgary.ca

 Indicates open access to non-subscribers at www.ajnr.org

 Indicates article with supplemental on-line table.

<http://dx.doi.org/10.3174/ajnr.A4610>

Workflow: Improving Preclinical Times

The success of endovascular treatment relies on timely access to hospitals with fully equipped angiography suites. Patient education will likely ensure fast recognition of stroke syndromes. Subsequent medical contact by phone should lead to priority Emergency Medical Services (EMS) dispatch and transport to the nearest facility for hyperacute treatment. Geographic access to such centers can be challenging. With the “drip and ship” paradigm, patients are initially assessed, imaged, and, if eligible, undergo thrombolysis at a nearby primary stroke center before being transferred to a tertiary stroke center with an angiography suite. In contrast, the “mothership” paradigm leads to direct patient transfer to a tertiary stroke center after field assessment by EMS. These paradigms are mainly influenced by the local health care infrastructure and possibilities for transport. Prior studies have shown that direct referral of patients with stroke from a community hospital without prior imaging before transport shortens the onset-to-treatment time.^{8,9} A centralized model of endovascular care with a high-volume dedicated hub hospital receiving patients could help maintaining case volumes, providing expertise and efficient in-hospital systems, and reducing door-to-recanalization times, thereby further improving patient outcomes.¹⁰ This needs to be balanced with quick access to a primary stroke center and thrombolysis. To achieve this balance, we will need to adapt triage rules and processes and train new and existing personnel.

Our case took place in a city with an angiography suite-equipped hospital.

14:00: Last Seen Healthy. A 71-year-old man with no remarkable medical history aside from being a past smoker was last seen healthy by his wife at 14:00 hours when she left the house to run some errands.

16:14. When she returned >2 hours later, she found her husband with right-sided weakness and unable to speak. She called Emergency Medical Services.

16:21. EMS arrived at the patient’s home and found the patient sitting in a chair, unable to follow commands or verbally interact. The right arm fell rapidly. The patient was able to walk with a 2-person assist to the ambulance but was dragging his right foot. They determined that he had a major stroke and decided to transport him directly to the comprehensive stroke center.

16:41. They called the triage desk at this hospital and described the patient’s symptoms. The triage nurse completed the Short Turn-Around Time stroke checklist. The patient fit the Short Turn-Around Time stroke criteria of speech disturbance and rapidly falling limbs within 4.5 hours from onset. A Short Turn-Around Time stroke page including expected time of hospital arrival went out to the stroke team, including the emergency department and neurointerventional team, and to the CT suite.

Workflow: Improving Door-to-Imaging Times

Hospital arrival to imaging time can be reduced under the following conditions: Prior patient information is available; the patient is transferred directly from door to scanner; and a quick, focused clinical assessment is performed in parallel. Local EMS personnel

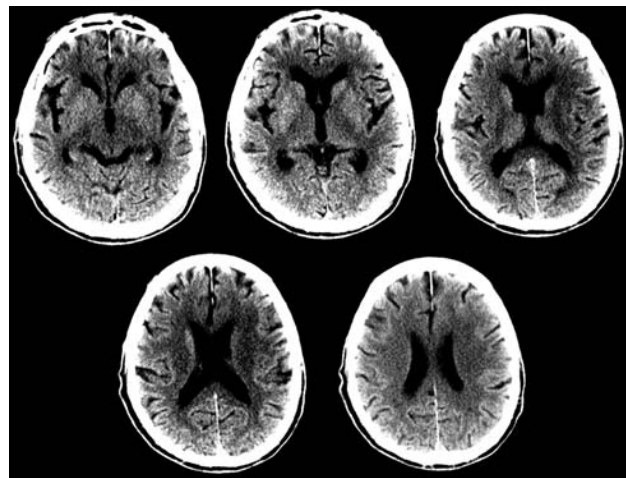


FIG 1. The unenhanced CT ASPECTS score is 7, with 1 point subtracted for early ischemic changes in the caudate nucleus, lentiform nucleus, and insula on the left.

need to be trained to recognize major strokes, and a centralized paging system can prepare emergency staff for patient arrival.¹¹

17:09. The patient arrived in the emergency department and was assigned an electronic number for subsequent diagnostic or treatment orders rather than taking all his demographics at the triage desk. In Calgary, we have developed a stretcher-to-CT protocol to minimize delays. The patient stayed on the EMS stretcher and was quickly assessed by the emergency physician. His vital parameters were recorded. The NIHSS score was approximately 29 points. While the patient was being positioned on the CT table, the stroke neurologist acquired additional information about the medical history, current medication, recent surgery, or trauma from the patient’s family. In this case, the patient history included no contraindications against IV rtPA or endovascular treatment. Routine blood work was drawn in parallel.

Neuroimaging: Ruling Out Intracranial Hemorrhage

Because of its fast and widely available acquisition, noncontrast CT remains the primary imaging technique for stroke syndrome presentations. It helps to quickly differentiate ischemic and hemorrhagic stroke and to measure the extent of early ischemic changes with ASPECTS. ASPECTS applies a 10-point scale at the basal ganglia and supraganglionic level of the MCA territory and subtracts 1 point for each subtle parenchymal hypoattenuation of tissue in 1 of the 10 regions. The details of ASPECTS interpretation are available at www.aspectsinstroke.com. All recent clinical trials used NCCT as a first-line imaging tool in most patients.¹⁻⁵

17:25. An NCCT scan for the patient was acquired. There was no sign of intracranial hemorrhage. The ASPECTS score was 7–8 with early ischemic changes in the caudate nucleus, lentiform nucleus, and insula (Fig 1). In Calgary, we have divided the ASPECTS score into 3 broad categories: 0–4, poor; 5–6, moderate; and 7–10, good. In our opinion, this scoring system is more practical for decision-making.

Immediately after the NCCT, a decision for IV tPA is made, and the bolus is administered to the patient on the CT table

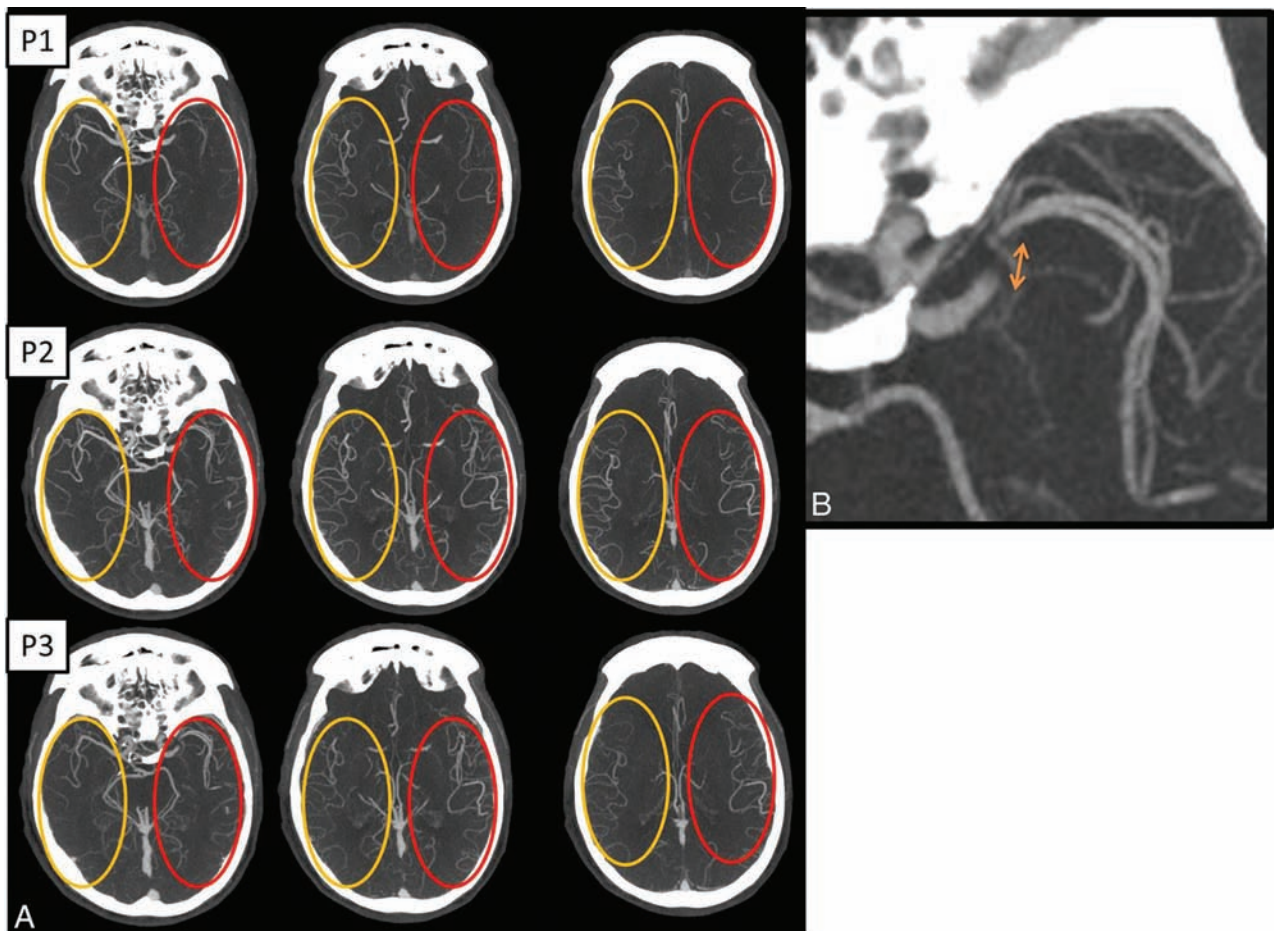


FIG 2. A, Axial multiphase CT angiography (3 phases) maximum-intensity-projection images (arterial, phase 1 [P1]; midvenous, phase 2 [P2]; and late venous, phase 3 [P3] from top to bottom) show left middle cerebral artery segment 1 occlusion. In addition, during phase 1, there is a delay in contrast opacification of the left middle cerebral artery branches compared with the contralateral normal side; however, during phase 2, the contrast opacification appears to be symmetric. This is labeled as “one phase delay.” There is also symmetric “extent” of collaterals (*red oval*) compared with the contralateral normal side (*yellow oval*). Overall, this gives an impression of fairly good collaterals. B, Magnified axial MIP image in the second delayed phase (P3) shows the possible clot length (*arrow*) calculated as the distance between the site of abrupt vessel cutoff (proximal end) and the site of distal vessel opacification, either through slow antegrade or retrograde collateral filling (distal end). This can help in preplanning the length of the stent retriever to be used.

(door-to-needle time of 16 minutes), while the CT technician is preparing the patient for the next set of imaging, including CTA (and CT perfusion, if necessary).

Neuroimaging: The Intracranial Occlusion and Collaterals

To provide images of cerebral blood vessels, a CTA is most commonly used. All recent clinical trials used a CTA technique to detect proximal intracranial occlusions.¹⁻⁵ Additionally, collateral status can be measured by assessing backfilling pial arteries distal to the intracranial occlusion compared with the unaffected contralateral hemisphere.¹² The quality of collateral assessment depends on the timing of the image acquisition in relation to the IV contrast bolus. If obtained accurately (eg, by using multiphase CTA), collateral status helps to corroborate the status of the brain parenchyma. We typically obtain 2 additional phases of CTA (a total of 3 phases). The ESCAPE trial used collateral imaging to increase the reliability of NCCT ASPECTS assessments. Furthermore, the anatomy of the aortic arch and tortuosity of extracranial vessels and the status of ipsilateral carotid bifurcation, circle of Willis collaterals, and site and size of the thrombus help the neu-

rointerventionalist choose the appropriate devices for endovascular treatment.¹³

17:27. The multiphase CTA of this patient showed an occlusion of the M1 segment of the left MCA with the presence of good collaterals (Fig 2A, -B). We additionally went back and looked at the NCCT in light of the findings on the collaterals. This step helps improve the accuracy of the NCCT ASPECTS assessment.

At this stage, because the patient had a proximal occlusion and good collaterals, a decision was made in the CT suite at 17:32 hours to take the patient for endovascular thrombectomy by using stent retrievers. The key components of decision-making available in the CT suite were the following:

- 1) Clinically severe ischemic stroke (NIHSS 29)
- 2) Relatively early from onset (212 minutes from last seen healthy)
- 3) Excellent premorbid status
- 4) Proximal vessel occlusion: M1
- 5) Small core/good collaterals on NCCT and multiphase CTA

6) No major access or technical challenges (eg, severe arch tortuosity).

Neuroimaging: Approximation of Infarct Core/Salvageable Brain Tissue

CT perfusion has been shown to provide information about tissue salvageability but still remains controversial and therefore not universally adopted. It has many limitations, including lack of standardization, effect of motion, potential for seriously slowing down of the decision-making process, and lack of uniform definitions of core and penumbra and so forth.¹⁴ Varying studies have used different CTP parameters and thresholds to define ischemic core and penumbra, yet we still do not know the exact threshold for total at-risk tissue and tissue that will die if reperfusion occurs within 20–60 minutes from CT, which is now possible in dedicated centers. There has been a recent move toward fully automated software that allows timely postprocessing of perfusion functional maps robust to common artifacts, allowing rapid clinician interpretation even after hours.¹⁵

Even in the best of circumstances, the acquisition of CT perfusion data (especially proper z-axis coverage for arterial input function selection), transferring for postprocessing, the postprocessing itself (including motion correction and so forth), and interpretation can consume time. The median time between head CT and successful postprocessing of CTP imaging in the SWIFT-PRIME and EXTEND-IA trials was approximately 22 minutes (M. Goyal, personal communication, August, 2015) and 6 minutes 30 seconds, respectively.¹⁵

17:33. CT perfusion imaging showed a time-to-maximum lesion to indicate ischemic core, while CBV was maintained throughout the area of hypoperfusion (the low CBV ASPECTS was 10). In Calgary, this study was performed as part of a research study. It was not examined acutely and was not used for decision-making.

Neuroimaging: A Decision-Making Paradigm

In general, the more complicated the imaging technique gets, the more time it takes. The pragmatic approach should be to get by with the minimum necessary information that is relevant for the decision-making process. The decision to pursue thrombectomy is an evolving process, with some factors pushing us toward intervening (moderate-to-severe stroke, age younger than 80 years, potential for independent living, large vessel occlusion, time from symptom onset <6 hours) and some arguing against it (an inability to obtain access due to vascular disease, serious comorbidities, patient views on life and disability, living will). These factors help a physician determine when he or she has enough confidence to proceed without the need for further studies (no further test threshold). During this decision-making process, the chance of a poor outcome with thrombectomy increases as time passes and with each additional test obtained.¹⁶ In Calgary, our decision-making approach is based on the following: 1) exclusion of patients with poor ASPECTS, 2) the presence of proximal vessel occlusion, and 3) the absence of poor collaterals on multiphase CTA. We do not typically use CT perfusion for decision-making.

Workflow: Improving Imaging-to-Puncture Time

In the ESCAPE trial, the key metrics of performance were head CT to groin puncture (target, <60 minutes) and head CT to first reperfusion (target, <90 minutes).² The start of the NCCT was used to measure this metric. This was deliberately chosen to encourage efficient image acquisition, interpretation, and decision-making. This time metric is influenced by the type of imaging technique used, the postprocessing and physician interpretation time, and the efficiency of the image arrival/retrieval system.¹⁷ During scanning, further information can be acquired from EMS personnel, family members, or electronic patient data bases, if available. The SWIFT-PRIME trial aimed for a qualifying imaging-to-puncture time target of ≤ 70 minutes, with a permitted maximum of 90 minutes.⁴ If patients are eligible, the workflow around IV rtPA administration can be time-consuming because it is usually administered in a dedicated space away from the angiography suite and sometimes patients are assessed for clinical improvement before being moved to the angiography suite and notification of the endovascular team.¹⁸ The recent trials proved that endovascular therapy is effective with or without IV rtPA. We do not wait for clinical improvement, and we move the patient as soon as possible to the angiography suite. A group-alert paging system for acute stroke, like we use in Calgary, enables all team members to be prepared and provide enough time to travel to the hospital. Cross-training x-ray and CT technicians to help in the angiography suite may speed up the process on weekends or during nights.

17:47. After obtaining surrogate consent from the patient's wife, the patient was brought to the endovascular suite. In Calgary, the angiography tray is always ready (Brisk Recanalization Ischemic Stroke Kit), and the patient was positioned on the angiography table.

Neurointervention: Use of Anesthesia

A growing body of evidence is against the use of general anesthesia in acute stroke intervention, with higher rates of poorer outcome and mortality in the general anesthesia group. Hypotension during general anesthesia is also considered a contributing factor toward a poorer outcome.¹⁹ The ESCAPE and REVASCAT trials recommended against the use of general anesthesia for endovascular intervention (only 9.1% in ESCAPE and 6.7% in REVASCAT).^{2,5} We believe that with the availability of newer generation stent retrievers and prior knowledge of vascular anatomy from CTA, it is possible to achieve successful recanalization despite some degree of patient motion. The stroke physician provides conscious sedation if necessary and helps the interventional team with all aspects of patient management.

Neurointervention: Initiating the Endovascular Procedure

It is ideal to have a prearranged stroke tray ready for use in the angiogram suite at all times so that the procedure can be initiated without delay. We also emphasize using standardized techniques and devices as much as possible.²⁰ Almost all our patients with anterior circulation stroke end up having an 8F femoral sheath with an 8F balloon-guide catheter (parked in the internal carotid artery; the level is decided on the basis of tortuosity and can usually be determined on the CTA), an appropriate coaxial selective

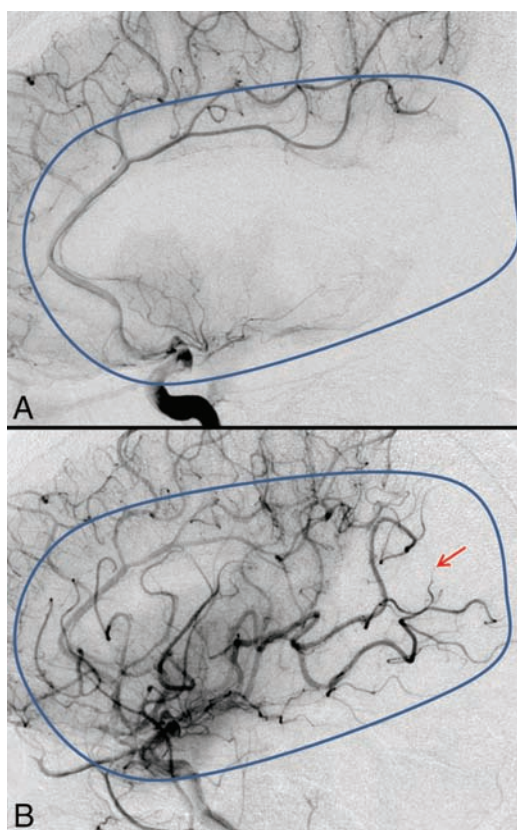


FIG 3. Measuring the extent of revascularization. Comparison between the TIC1 scoring before (TIC1 0, A) and after (TIC1 2b, B) mechanical thrombectomy in the late arterial phase. The *blue outline* depicts the normal extent of the MCA territory. Note, the region shown by the *red arrow* suggesting non-/slow filling of a few distal cortical branches.

inner catheter for arch access, and a stent retriever (4 × 40 mm for M1 occlusions) with an appropriate microcatheter (this may change with advances in technology). The angiography staff (technicians and nurses) is cross-trained to be capable of managing work-flow seamlessly, single-handed if such a situation arises. It is not advisable to delay the procedure for shaving the groin region or insertion of a Foley catheter.²¹

18:14. Groin puncture was achieved, and an 8F femoral sheath was inserted in the right common femoral artery. Meanwhile, the balloon-guided catheter was taken over a 5.5F inner catheter in a coaxial fashion (the shape of the coaxial catheter is decided on the basis of the coronal formats of the CT angiogram of the arch and neck vessel; no exchange wire is used) and was parked in the internal carotid artery. We do not recommend time-consuming anatomic and collateral assessment during angiography because this information is already available from the CTA.

18:19. The first intracranial angiography run confirmed the left MCA segment 1 occlusion with an initial TIC1 flow of zero (no perfusion, no antegrade flow beyond the point of occlusion) (Fig 3A).

Neurointervention: Deciding on Devices and Techniques

Many endovascular techniques are available for thrombus removal like intra-arterial thrombolysis, thrombus aspiration, stent

retrievers, wire disruption, and so forth. However, all the recently published endovascular trials used newer retrievable stents in most of their patients (81.5%, 86.1%, 89%, 100%, and 95.1% in MR CLEAN, ESCAPE, SWIFT-PRIME, EXTEND-IA, and REVASCAT, respectively). Newer stent retrievers like the Solitaire FR (Covidien, Irvine, California) and Trevo (Stryker, Kalamazoo, Michigan) have been proved superior in efficacy and safety compared with the first-generation Merci retrievers (Concentric Medical, Mountain View, California).²² ESCAPE and SWIFT-PRIME trialists also advocated for the use of negative suction through a balloon-guide catheter with proximal balloon occlusion during thrombus retrieval to avoid distal emboli.^{2,4}

18:23. A .021-inch microcatheter was taken over a .016-inch microguidewire (with the tip shaped to give a nontraumatic J configuration) into the occluded MCA and was carefully navigated distal to the site of the thrombus (proximal M2 segment). A check microcatheter injection with minimal contrast was performed to confirm the correct positioning of the distal end of the microcatheter and to rule out any iatrogenic microguidewire perforations. An appropriately sized stent retriever (4 × 40 mm as default) was then carefully deployed across the M1 segment. After the deployment of the stent retriever, an angiographic run was performed primarily to assess the immediate bypass effect after stent deployment. In case there is absolutely no bypass effect, the possibilities are the following: 1) The stent retriever is not in the correct position and is covering only part of the clot. The exact location of the clot/thrombus is relatively easy to determine on the source images of the multiphase CTA: The proximal end of the clot can be determined on the first phase while the distal end of the clot can be seen on the second or third phase. In this case, without waiting further, the stent retriever is repositioned. 2) There is complete capture of the clot: The clot has come through the interstices of the stent and is ready to be pulled out. 3) The clot is firm and the stent retriever has no impact on the clot. The differentiation between 2 and 3 is difficult and often the only way to differentiate is to actually remove the stent and see if the clot is captured. In case there is some degree of bypass effect, one can wait 2–3 minutes and repeat a run; as the clot starts to get incorporated into the stent retriever, the repeat run shows irregularity and narrowing of the lumen of the vessel. This is usually a sign that the thrombus has been incorporated and can be removed.

In addition, if there is excellent flow due to a temporary bypass effect, it is important to remember that at that time the brain is getting excellent blood flow and can theoretically “reset the clock” in case the vessel reoccludes after removal of the stent retriever.

18:25. After retrieval of the stent, a control left ICA angiogram demonstrated restoration of flow in both the M1 and both M2 branches with residual occlusion of the distal M2 branch (Fig 3B). The patient started improving clinically on the angiography table. The patient was assessed and the NIHSS was recorded. As soon as reperfusion was achieved, the stroke physician ensured that the blood pressure was lowered. The patient was transferred to the neurology critical care unit for further care.

Neurointervention: Assessing the Neuroangiographic Outcome

Success of endovascular therapy can be judged by measuring reperfusion by using the TIC1 or the modified TIC1 scoring system.²³ Generally speaking, a TIC1 score of 2b or 3 is considered good reperfusion. Recently, a revised TIC1 scale that includes a 2c designation has been advocated for better end-point assessment.²⁴ The reperfusion rates in the recent trials (TIC1 or modified TIC1) were 72.4%, 58.7%, 86.2%, 88%, and 65.7% in ESCAPE, MR CLEAN, SWIFT-PRIME, EXTEND-IA, and REVASCAT, respectively.¹⁻⁵ The reasons for this variability are currently not clear and may be related to lack of standardized methodology for scoring and patient selection.

Neurointervention: Deciding on Tandem Lesion Treatment

The implications of emergency treatment of additional proximal extracerebral artery disease on the outcome have yet to be studied; 12.7%, 32.2%, and 18.6% of patients in the intervention group in the ESCAPE, MR CLEAN, and REVASCAT trials, respectively, had documented ipsilateral cervical arterial occlusive disease on angiography; and 12.9% of patients in the MR CLEAN trial and 8.7% in the REVASCAT trial underwent cervical artery stent placement in the acute setting.^{1,2,5} In ESCAPE, the use of acute cervical carotid stent placement was discouraged. The best way of treating cervical carotid disease in acute stroke is still unclear, and further post hoc analysis of these major trials will hopefully give more answers.

In-Hospital Follow-Up. The next day following admission, the patient's NIHSS score was zero, and he was symptom-free. The follow-up DWI showed a small lesion in his caudate nucleus. His echocardiogram revealed severe dilative cardiomyopathy with presumed intracardiac thrombus as the source of his embolization. The patient was discharged home on warfarin (Coumadin).

Ninety-Day Clinic Follow-Up. After 3 months, the patient's NIHSS score was still zero; his Barthel-Index score of 100 and mRs score of zero indicated that he was fully functional and independent.

CONCLUSIONS

In patients with anterior circulation acute ischemic stroke due to large-vessel occlusion, endovascular treatment by using stent retrievers is now the standard of care. While the precise imaging paradigm was slightly variable across trials, there is clear evidence to support the use of CT/CTA as part of the work-up. We routinely use multiphase CTA to get additional information on collaterals and use it to further refine the ASPECTS reading. Additional imaging may be performed, such as CTP, as long as it does not introduce delays and does not falsely exclude patients from the benefit of endovascular therapy. Future focus should be on integrating such techniques into the stroke workflow. Several factors of endovascular workflow need to be addressed within the near future: The 3 most important, in our opinion, are geographic access to centers with angiography suites, prenotification, and parallel processing with a multispecialty team approach.

ACKNOWLEDGMENTS

We thank all the members of the Calgary Stroke Program who participated in the care of this patient.

Disclosures: Mayank Goyal—RELATED: Grant: Covidien,* Comments: partial funding of the ESCAPE trial; Consulting Fee or Honorarium: Covidien, Comments: for speaking engagements; for design and conduct of the SWIFT-PRIME trial; Other: GE Healthcare, Comments: licensing agreement for further development of systems of acute stroke diagnosis; Statement: M.G. was one of the Principal Investigators for the ESCAPE and SWIFT-PRIME trials; he was also the core lab lead for cross-sectional imaging within the REVASCAT study. He has a consulting agreement with Covidien for the conduct and design of SWIFT-PRIME and for teaching engagements. Covidien also provided part of the funding for the ESCAPE trial through a grant to the University of Calgary. M.G. has a licensing agreement with GE Healthcare for systems of stroke diagnosis. Bijoy K. Menon—Statement: B.K.M. was a member of the steering and executive committee of the ESCAPE trial and Principal Investigator for PReVOLT (Perfusion CT using the Aquilion One: Visual assessment of blood flow parameters in a clinical setting Enhances diagnostic and prognostic ability in patients with ischemic strokes when compared to NECT and CTA based Imaging Techniques) study testing the utility of multiphase CTA and other imaging modalities in the triage of patients with stroke. B.K.M. holds a Heart and Stroke Foundation/University of Calgary Professorship in Stroke Imaging and a Canadian Institutes of Health Research New Investigator Award. *Money paid to the institution.

REFERENCES

1. Berkhemer OA, Fransen PSS, Beumer D, et al; for the MR CLEAN Investigators. **A randomized trial of intraarterial treatment for acute ischemic stroke.** *N Engl J Med* 2015;372:11–20 CrossRef Medline
2. Goyal M, Demchuk AM, Menon BK, et al; for the ESCAPE Trial Investigators. **Randomized assessment of rapid endovascular treatment of ischemic stroke.** *N Engl J Med* 2015;372:1019–30 CrossRef Medline
3. Campbell BC, Mitchell PJ, Kleinig TJ, et al; for the EXTEND-IA Investigators. **Endovascular therapy for ischemic stroke with perfusion-imaging selection.** *N Engl J Med* 2015;372:1009–18 CrossRef Medline
4. Saver JL, Goyal M, Bonafe A, et al; for the SWIFT-PRIME Investigators. **Stent-retriever thrombectomy after intravenous t-PA vs. t-PA alone in stroke.** *N Engl J Med* 2015;372:2285–95 CrossRef Medline
5. Jovin TG, Chamorro A, Cobo E, et al; for the REVASCAT Trial Investigators. **Thrombectomy within 8 hours after symptom onset in ischemic stroke.** *N Engl J Med* 2015;372:2296–306 CrossRef Medline
6. National Institute of Neurological Disorders and Stroke. Proceedings of a National Symposium on Rapid Identification and Treatment of Acute Stroke. http://www.ninds.nih.gov/news_and_events/proceedings/strokeworkshop.htm. Accessed March 20, 2015
7. Kamal N, Benavente O, Boyle K, et al. **Good is not good enough: the benchmark stroke door-to-needle time should be 30 minutes.** *Can J Neurol Sci* 2014;41:694–96 CrossRef Medline
8. Prabhakaran S, Ward E, John S, et al. **Transfer delay is a major factor limiting the use of intra-arterial treatment in acute ischemic stroke.** *Stroke* 2011;42:1626–30 CrossRef Medline
9. El Khoury R, Jung R, Nanda A, et al. **Overview of key factors in improving access to acute stroke care.** *Neurology* 2012;79:S26–34 CrossRef Medline
10. Menon BK, Saver JL, Goyal M, et al. **Trends in endovascular therapy and clinical outcomes within the nationwide Get With The Guidelines-Stroke Registry.** *Stroke* 2015;46:989–95 CrossRef Medline
11. Goyal M, Menon BK, Hill MD, et al. **Consistently achieving computed tomography to endovascular recanalization <90 minutes: solutions and innovations.** *Stroke* 2014;45:e252–56 CrossRef Medline
12. Menon BK, d'Este CD, Qazi EM, et al. **Multiphase CT angiography: a new tool for the imaging triage of patients with acute ischemic stroke.** *Radiology* 2015;275:510–20 CrossRef Medline
13. Menon BK, Campbell BC, Levi C, et al. **Role of imaging in current acute ischemic stroke workflow for endovascular therapy.** *Stroke* 2015;46:1453–61 CrossRef Medline

14. Zussman B, Flanders A, Rosenwasswer MD, et al. **Behind the technology: CT perfusion in the setting of acute stroke management.** *JHN Journal* 2010;5. <http://jdc.jefferson.edu/jhnj/vol5/iss2/1>. Accessed September 20, 2015
15. Campbell BC, Yassi N, Ma H, et al. **Imaging selection in ischemic stroke: feasibility of automated CT-perfusion analysis.** *Int J Stroke* 2015;10:51–54 CrossRef Medline
16. Goyal M, Fargen KM, Menon BK. **Acute stroke: Bayes' theorem and the art and science of emergency decision-making.** *J Neurointerv Surg* 2014;6:256–59 CrossRef Medline
17. Almekhlafi MA, Eesa M, Menon BK, et al. **Ultrashort imaging to reperfusion time interval arrests core expansion in endovascular therapy for acute ischemic stroke.** *J Neurointerv Surg* 2013;5(suppl 1):i58–61 CrossRef Medline
18. Fonarow GC, Smith EE, Saver JL, et al. **Improving door-to-needle times in acute ischemic stroke: the design and rationale for the American Heart Association/American Stroke Association's target: stroke initiative.** *Stroke* 2011;42:2983–99 CrossRef Medline
19. Abou-Chebl A, Lin R, Shazam Hussain M, et al. **Conscious sedation versus general anesthesia during endovascular therapy for acute anterior circulation stroke: preliminary results from a retrospective, multicenter study.** *Stroke* 2010;41:1175–79 CrossRef Medline
20. Almekhlafi MA, Hockley A, Desai JA, et al. **Overcoming the evening/weekend effects on time delays and outcomes of endovascular stroke therapy: the Calgary Stroke Program experience.** *J Neurointerv Surg* 2014;6:729–32 CrossRef Medline
21. Nedeltchev K, Arnold M, Brekenfeld C, et al. **Pre- and in-hospital delays from stroke onset to intra-arterial thrombolysis.** *Stroke* 2003;34:1230–34 CrossRef Medline
22. Nogueira RG, Lutsep HM, Gupta R, et al; for the TREVO 2 Trialists. **Trevo versus Merci retrievers for thrombectomy revascularisation of large vessel occlusions in acute ischemic stroke (TREVO 2): a randomised trial.** *Lancet* 2012;380:1231–40 CrossRef Medline
23. Fugate JE, Klunder AM, Kallmes DF. **What is meant by "TICI"?** *AJNR Am J Neuroradiol* 2013;34:1792–97 CrossRef Medline
24. Goyal M, Fargen KM, Turk AS, et al. **2C or not 2C: defining an improved revascularization grading scale and the need for standardization of angiographic outcomes in stroke trials.** *J Neurointerv Surg* 2014;6:83–86 CrossRef Medline

Radiation Dose Reduction by Indication-Directed Focused z-Direction Coverage for Neck CT

A.K. Parikh and C.C. Shah



ABSTRACT

BACKGROUND AND PURPOSE: The American College of Radiology–American Society of Neuroradiology–Society for Pediatric Radiology Practice Parameter for a neck CT suggests that coverage should be from the sella to the aortic arch. It also recommends using CT scans judiciously to achieve the clinical objective. Our purpose was to analyze the potential dose reduction by decreasing the scan length of a neck CT and to assess for any clinically relevant information that might be missed from this modified approach.

MATERIALS AND METHODS: This retrospective study included 126 children who underwent a neck CT between August 1, 2013, and September 30, 2014. Alteration of the scan length for the modified CT was suggested on the topographic image on the basis of the indication of the study, with the reader blinded to the images and the report. The CT dose index volume of the original scan was multiplied by the new scan length to calculate the dose-length product of the modified study. The effective dose was calculated for the original and modified studies by using age-based conversion factors from the American Association of Physicists in Medicine Report No. 96.

RESULTS: Decreasing the scan length resulted in an average estimated dose reduction of 47%. The average reduction in scan length was 10.4 cm, decreasing the overall coverage by 48%. The change in scan length did not result in any missed findings that altered management. Of the 27 abscesses in this study, none extended to the mediastinum. All of the lesions in question were completely covered.

CONCLUSIONS: Decreasing the scan length of a neck CT according to the indication provides a significant savings in radiation dose, while not altering diagnostic ability or management.

ABBREVIATIONS: AAPM = American Association of Physicists in Medicine; ACR-ASNR-SPR = American College of Radiology–American Society of Neuroradiology–Society for Pediatric Radiology; CTDI_{vol} = CT dose index volume; DLP = dose-length product

Numerous conditions can occur within the pediatric neck prompting an imaging request, commonly a CT scan. These include, but are not limited to, tonsillar disease, odontogenic infection, congenital anomalies, and neoplastic conditions. The history and physical examination in the symptomatic child can be difficult and limited, rendering the use of imaging pivotal.¹ CT is vital in teasing out the many varying conditions of the pediatric extracranial head and neck that will often present in an acute care setting.¹ The American College of Radiology–American Society of

Neuroradiology–Society for Pediatric Radiology (ACR-ASNR-SPR) practice parameter for the performance of CT of the extracranial head and neck suggests that coverage should be through the area of interest, specifically from the skull base (sella floor) to the top of the aortic arch.²

While providing simplicity, a neck CT with “blanket” coverage irrespective of indication is contrary to the principles of as low as reasonably achievable in reducing or optimizing the radiation dose.³ The principle of as low as reasonably achievable is paramount because recent studies have demonstrated a small but significant increase in cancer incidence among children exposed to ionizing radiation.⁴ Furthermore, it is well-documented that infants and children are much more vulnerable to the effects of radiation exposure, given their longer life span and increased sensitivity to radiation-induced cancers than their adult counterparts.⁵ Given that approximately 7 million CT scans are performed annually in children in the United States, any attempts at dose reduction can have a positive impact.⁶

By decreasing the scan length (z-axis) to the clinical indication, unnecessary radiation exposure can be eliminated. Our purpose was

Received August 24, 2015; accepted after revision November 24.

From the Department of Radiology (A.K.P.), Mayo Clinic, Jacksonville, Florida; and Department of Radiology (C.C.S.), Nemours Children’s Specialty Care, Wolfson’s Children’s Hospital, Jacksonville, Florida.

Paper previously presented at: Society for Pediatric Radiology Annual Meeting, April 27 to May 1, 2015; Bellevue, Washington. The first and corresponding author was given the John Kirkpatrick Young Investigator Award for research in the above project.

Please address correspondence to Ashishkumar K. Parikh, MD, 807 Children’s Way, Jacksonville, FL 32207; e-mail: ashishckt@gmail.com; @ashishckt

Indicates article with supplemental on-line table.

<http://dx.doi.org/10.3174/ajnr.A4672>

Table 1: Demographics

	Mean	Median	Range	SD
Age (mo)	99.4	85.0	2–216	66.6
Age (yr)	8.3	7.1	0–18	5.5
Height (cm)	125.7	125.0	55–190	35.6
Weight (kg)	36.7	25.5	5–128	27.9

Table 2: Technique

Parameters	Setting
Kilovolt	100–140
Milliamperere (min)	79
Milliamperere (max)	300
Detector	0.625 mm
CT scanner	64 section
Section thickness	2.5 mm
Gantry rotation time	0.5 seconds
Pitch	0.96875

Note:—Min indicates minimum; Max, maximum.

to analyze the potential dose reduction by decreasing the z-axis length of neck CT scans and to assess for any clinically relevant information that might be missed from this modified approach.

MATERIALS AND METHODS

This retrospective study included 126 children 18 years of age or younger who underwent a neck CT on a 64-section CT scanner (LightSpeed VCT; GE Healthcare, Milwaukee, Wisconsin) at a tertiary care children’s hospital between August 1, 2013, and September 30, 2014. Wolfson’s Children’s Hospital/Nemours Children’s Speciality Care institutional review board approval was obtained, and informed consent was waived for this Health Insurance Portability and Accountability Act–compliant retrospective study. The cohort studied comprised 60 girls and 66 boys, with age ranges from 2 months to 18 years, with a mean age of 8.3 years. The average weight and height within the cohort analyzed were 37 kg (range, 5–128 kg) and 126 cm (range, 55–190 cm), respectively (Table 1). No children were included who had a combined neck, chest, abdomen, and pelvis CT for an oncologic diagnosis or surveillance. In the oncologic setting, altering the length in the craniocaudal dimension would not be indicated, given the need for complete coverage to assess sites of disease spread. Two children for whom the dose information was not available were excluded.

Helical acquisitions were obtained. Imaging parameters were as follows: 100–140 kV; Automatic Exposure Control; 64 × 0.625 mm detector; gantry rotation time, 0.5 seconds; pitch, 0.96875; and a soft-tissue reconstruction algorithm (Table 2). Iterative reconstruction was available on our CT scanner. The range in kilovolts was due to variations in weight, with heavier patients scanned with 140 kV and lighter patients scanned with 100 kV. For instance, 6 patients were on the lighter side, weighing <22.5 kg with a set kilovolt of 100. Two patients were scanned with a kilovolt of 140 because they weighed 89 kg and 128 kg, respectively. The remaining 118 patients were scanned with the standard set kilovolt of 120 (Table 3). With Automatic Exposure Control, the maximum milliamperere was 350 and varied with patient weight (Table 3). The minimum milliamperere was 79 for all the patients. In children weighing <22.5 kg, the maximum milliamperere was 200. From 22.5 to 31.5 kg, the maximum milliamperere was 250. The maximum milliamperere was 300 for children weigh-

Table 3: Weight-adjusted tube current and kilovolt

Weight (kg)	Min	Max	Kilovolt
	Milliamperere	Milliamperere	
<22.5	79	200	100
22.5–31.5	79	250	120
31.5–40.5	79	300	120
≥40.5	79	350	140

Note:—Min indicates minimum; Max, maximum.

ing between 31.5 and 40.5 kg. In children weighing greater than 40.5 kg, the maximum milliamperere was 350.

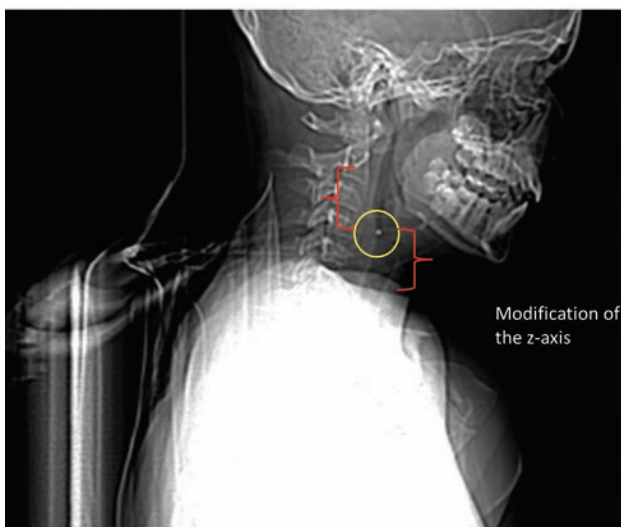
Among all the included patients, we analyzed the following data points: indication, z-start of the scan (beginning or cranial extent), z-end of the scan (terminal or caudal extent), CT dose index volume (CTDI_{vol}) (milligray), dose-length product (DLP) (milligray × centimeter, based on a 16-cm phantom), modified z-start of the scan, modified z-end of the scan, kilovolt, minimum milliamperere, maximum milliamperere, milliseconds, patient weight (kilograms), patient height (centimeters), amount of iodinated contrast (milliliter), sex, finding/diagnosis, any findings that would have been missed due to modification of the z-axis, clinical relevance of the missed finding, follow-up method of the main/diagnostic finding, follow-up imaging/pathology of the main finding (if any), age in years and months, total scan length (centimeter), modified scan length (centimeter), modified DLP (milligray × centimeter), weighting factor, effective dose (millisievert), modified effective dose (millisievert), percentage reduction in craniocaudal length (centimeter) for the modified scans, and percentage reduction in dose from the z-axis modification. Please refer to the Appendix for an explanation of the terminology used in this article.

The investigator (A.K.P., 3 years’ experience) was initially presented with the indication of the study and the topographic (scout) image while blinded to the cross-sectional and reformatted CT images and the CT report. On the basis of this information, the investigator suggested an alteration of the z-axis for the modified CT scan (Figure). The z-start/end level and modified z-start/end level were based on the topographic image (eg, beginning at C4 instead of the sella). Each modification of the z-axis length was individualized to the examination indication in its cranial and caudal extent. However, in cases of a suspected abscess, the z-axis length was modified to begin at the temporomandibular joint and end at the sternoclavicular junction. In cases of “lumps and bumps,” the scan length covered several centimeters above and below the lesion in question. For instance, for a palpable lesion of <2 cm, the marker would be placed at the epicenter of the abnormality and the scan would be performed 3 cm above and below the marker. For lesions of >2 cm, the marker would be placed at the cranial and caudal margins of the lesions and the scan would be performed 3 cm above and below the marker.

“Missed” findings were abnormalities noted on the original CT scan that would no longer be seen due to the reduced z-axis coverage (ie, if the z-axis were modified according to the indication). The clinical relevance of this missed finding was determined by examining the patient’s chart to determine whether the initial management would have been altered on the basis of the missed finding. The follow-up method of the diagnostic finding was either clinical or surgical. If the follow-up method was surgical treatment of the offending lesion, the pathology report was reviewed.



A



B

FIGURE. Two topographic images of the same patient demonstrate a radiopaque marker at the epicenter of a lesion (yellow circle). The modification of the z-axis is then performed on the basis of the initial clinical indication of a palpable abnormality in the second image (red brackets).

Dose-length product for the modified study was extrapolated from the DLP of the original examination by factoring for the scan length. The modified DLP was calculated by multiplying the modified scan length (centimeters) by the $CTDI_{vol}$.

$$\text{Modified DLP (mGy)} = CTDI_{vol} (\text{mGy} \cdot \text{cm}) \times \text{modified z-axis length (cm)}.$$

The effective dose was calculated from the DLP for the original examination and for the modified study by using the conversion factors (Table 4) for various age groups provided in the American Association of Physicists in Medicine (AAPM) Report No. 96 (2008).⁷ These conversion factors were multiplied by the DLP to get the effective dose for the original and modified DLP. The Mann-Whitney *U* test was used to determine statistically significant differences between the 2 groups (modified and original scans).

Table 4: Age-specific conversion factors [$\mu\text{Sv} \times \text{mGy}^{-1} \times \text{cm}^{-1}$]]^a

	0 Years	1 Year	5 Years	10 Years	Adult
Neck	0.017	0.012	0.011	0.0079	0.0059

^a AAPM No. 96 (2008).

Table 5: Radiation dose

	Mean	Median	Range	SD
Z-length (cm)	20.18	20.13	5.2–34.0	52.2
DLP (mGy × cm)	111.5	69.2	20–656	97.6
Modified z-length (cm)	10.43	10.00	1.8–20.8	5.16
Modified DLP (mGy × cm)	59.2	35.1	5–363	60.0
Effective dose (mSv)	1.02	0.78	0.25–5.18	0.71
Modified effective dose (mSv)	0.54	0.42	0.05–2.86	0.45
Dose reduction (%)	47	43	15–93	20

RESULTS

Data comparing the DLP and the effective dose for the original and modified examinations are described in Table 5. Briefly, the mean DLP for the original examinations was 111.5 ± 97.6 mGy × cm (range, 20–656 mGy × cm; median, 69.2 mGy × cm). The mean DLP for the modified examinations was 59.2 ± 60.0 mGy × cm (range, 5.0–362.5 mGy × cm; median, 35.1 mGy × cm). The mean effective dose for the original examinations was 1.02 ± 0.71 mSv (range, 0.25–5.18 mSv; median, 0.78 mSv). In contrast, the mean effective dose for modified examinations was 0.54 ± 0.45 mSv (range, 0.05–2.86 mSv; median, 0.42 mSv). Decreasing the longitudinal scan length along the z-direction resulted in an average estimated dose reduction of 47% (range, 1.02–0.54 mSv) and a median dose reduction of 43% (range, 0.78–0.42 mSv). The Mann-Whitney *U* test demonstrated the differences between the original and modified examinations to be statistically significant with a *P* value < .0001.

The estimated mean effective dose reduction was 53% in children younger than 1 year of age and 46% for children between 10 and 18 years of age. Furthermore, there was an average reduction in scan length from the original to the modified examinations of approximately 10.4 cm, which decreased the overall coverage by an average of 48% in the modified scans. Additional data regarding dose reduction among different age groups in our study are listed in detail in Table 6.

There were no clinically relevant “missed” findings by using the modified CT approach (On-line Table). Most of the abnormalities that would not have been identified with the modified z-length were various congenital anomalies (often vascular) that were not relevant for the clinical indication. One patient had multiple abnormalities involving the head and neck, but none were new findings to the clinicians, confirmed with a search of the patient’s electronic medical records. None of the 27 abscesses encountered extended to or involved the mediastinum.

DISCUSSION

As mentioned previously, the current guidelines adopted by the ACR-ASNR-SPR for the performance of CT of the extracranial head and neck suggest that coverage should be through the area of interest, specifically from the floor of the sella to the top of the aortic arch. This coverage can extend to involve the aortopulmonary window if left recurrent laryngeal nerve pathology is sus-

Table 6: Radiation dose and scan length by age

	Younger Than 1 Year	1 Year to Younger Than 5 Years	5 Years to Younger Than 10 Years	10 Years to Younger Than 18 Years	All Children
No. of children	7	42	27	50	126
Mean original z-length (cm)	13.91	15.93	19.94	24.77	20.18
Mean modified z-length (cm)	6.63	8.04	10.32	13.04	10.43
% Decrease in mean z-length for modified CT	52	50	48	47	48
Mean effective dose for original CT (mSv)	0.86	0.63	0.73	1.53	1.02
Mean effective dose for modified CT (mSv)	0.41	0.32	0.38	0.83	0.54
% Decrease in mean effective dose for modified CT	53	49	48	46	47

pected.² However, the ACR-ASNR-SPR guidelines also recommend using CT scans judiciously to achieve the clinical objective.

Standard neck CT protocols in adults and children often extend to the aortic arch, imaging the superior mediastinum. Although not specifically mentioned with the ACR-ASNR-SPR practice guidelines, the mediastinal coverage is presumed to evaluate mediastinal pathology, often to determine the mediastinal extent of retropharyngeal abscesses. In children, mediastinal abscesses are very rare, especially with the advent of widespread antibiotic treatment.⁸ When mediastinal abscesses do occur, they are most often following iatrogenic or traumatic causes (ie, following thoracic surgery or esophageal perforation).⁸ According to a publication by Tercier et al,⁸ there have been only 8 reported cases in the literature of nontraumatic mediastinal abscesses in children within the 15 years preceding the publication of the article (1989–2004). The rarity of nontraumatic mediastinal abscesses is reinforced by Kumar et al⁹ as being “extremely uncommon in childhood, especially since the advent of widespread antibiotic treatment.” Kumar et al reported approximately 13 cases in the past 2 decades.

This study has demonstrated that the change in scan length would not have resulted in missed findings that could alter patient management. This is important, particularly in situations in which a neck CT is performed for the evaluation of a suspected abscess, a common scenario. With the modified approach, the scan length was changed from the sella to the sternoclavicular junction, rather than extending to the mediastinum. This approach is contrary to the widespread belief that the mediastinum must be included in all neck CT examinations when evaluating a suspected abscess to exclude mediastinal extension. Of the 27 abscesses seen in this study, none extended to the mediastinum.

An average estimated dose reduction of 47% supports the hypothesis of this study that decreasing the z-axis length will achieve significant dose savings. This finding is in concordance with the principles of as low as reasonably achievable. Furthermore, children are much more susceptible to the deleterious effects of ionizing radiation than their adult counterparts. In addition, the smaller size of a child leads to a greater amount of energy being imparted to the center of their body than in an adult, consequently increasing organ and effective doses.¹⁰ This outcome is because the absorbed dose is defined as the energy absorbed per unit mass (measured in grays). The smaller size of a child will impart a greater absorbed dose compared with adults. Therefore, it is important to alter scanning parameters when performing CT scans in children to optimize the radiation dose. Parameters that can be changed to optimize the radiation dose in children are the

kilovolt and milliamperere. For instance, in our study, the milliamperere was increased for heavier patients weighing >40.5 kg (350 mA), and concordantly, it was decreased in children weighing <22.5 kg (200 mA) (Table 3).

Decreasing the scan length is another widely accepted method of reducing the radiation dose, but standardized protocols are often an obstacle to this approach. However, the use of standardized protocols is beneficial in many ways. Creating simpler, easy-to-use protocols allows more interoperator independence and provides a consistent presentation of images.¹¹ Particularly within the emergency department setting, standardized protocols provide an efficient, often physician-independent method of imaging patients.

The inference of results from our study could lead one to surmise that basic knowledge of the anatomy from the initial topographic image is necessary to appropriately adjust the scan length to the clinical indication. This inference is correct. However, CT technologists perform this task every day on each scan length that is chosen for every routine CT. Furthermore, if alteration of the protocol were to occur, the CT technologist should be able to correctly identify the relevant anatomy on the topographic image to appropriately modify the scan length. According to the American Registry of Radiologic Technologists, the certifying board for CT technologists in the United States, sectional anatomic knowledge is required of CT technologists to successfully pass the required certifying examination. This includes knowledge of the anatomy of the soft-tissue structures in the neck.¹²

The communication between the CT technologist and radiologist should increase before the examination to select the region of interest to be scanned. This would increase the involvement of the technologist and radiologist when performing the examination, thereby decreasing the throughput of the CT scanner, which may be particularly troublesome in busy emergency departments. Furthermore, the need for a radiologist to constantly communicate with the technologist to tailor the protocols after hours could be a burden to many practices and could be impractical in certain circumstances. Therefore, additional investigation would need to analyze the practicality of tailoring the z-axis scan length to the specified indication.

Certain guidelines may alleviate some anxiety by tailoring protocols according to the examination indication:

1) When evaluating an abscess of a nontraumatic etiology, termination of the examination at the sternoclavicular junction would not only reduce the radiation dose, but in teenage girls, it would eliminate direct radiation exposure to breast tissue. Of the 27 neck abscesses, 18 were in teenage girls. If one applied this recommendation to this study, all 18 teenage girls would have

been saved from having direct radiation exposure to their breast tissue. Furthermore, under Automatic Exposure Control, the milliamperes would increase when scanning thicker body parts due to their increased attenuation of x-rays. Eliminating the thicker regions of a standard neck CT (ie, the upper chest/breast/shoulders) would eliminate the higher milliamperes sections. Therefore, the modified DLP would be in the conservative range of the actual DLP because the original $CTDI_{vol}$ was used in the calculation of the modified DLP. Additionally, in cases of suspected neck abscesses, the cephalad extent of the scan would be to the temporomandibular joint. This was chosen due to the anatomic ease of finding it on the initial prescan topographic image, and at the level of the temporomandibular joint, the entire oropharynx would be included.

2) For evaluation of specific “lumps and bumps,” a radiopaque marker at the area of interest can be placed, with the scan performed a few centimeters above and below the marker, as described above. Again, for a palpable lesion <2 cm, the marker would be placed at the epicenter of the abnormality and the scan would be performed 3 cm above and below the marker. For lesions >2 cm, the marker would be placed at the cranial and caudal margins of the lesions, and the scan would be performed 3 cm above and below the marker. These numbers were chosen due to convenience. They may need to be varied depending on the characteristics of the palpable finding.

A few potential limitations for this new modified approach for obtaining neck CT scans in children are as follows:

- 1) If a patient moves between the scout image and the scan acquisition, the relevant anatomy may not be fully covered. Although this possibility exists for any CT study, the extra few minutes needed to plan the coverage increases the chance that the child may move, and limited coverage reduces the margin for error.
- 2) Z-axis-length modification relies on the clinician to specify the purpose of the examination. At times, this can be difficult to elicit, given the complexity of clinical presentations. The retrospective analysis limits assessment of the practicality of modifying z-axis length to the specified indication. A multi-institutional randomized, prospective trial may be helpful for further analysis in this regard.

CONCLUSIONS

Decreasing the z-axis length of a neck CT targeted to the clinical indication provides a significant savings in radiation dose while not altering diagnostic ability or management. Using standardized protocols regardless of the indication on neck CTs subjects children to substantially more radiation exposure than necessary.

APPENDIX

Explanation of Terminology

Z-axis-directional coordinate oriented along the length in a craniocaudal fashion with respect to the patient.

Effective dose—biologic effect of radiation exposure is expressed in millisieverts, which incorporates exposure of various organs to ionizing radiation and the susceptibility of organs to this exposure.¹³

$CTDI_{vol}$ -calculated absorbed dose is based on a phantom expressed in milligrays. It is effective for comparing radiation doses for scans of varying techniques (eg, CT chest versus CT head).¹³

Dose-length product is expressed in mGy × cm and is the $CTDI_{vol}$ (mGy) × z-axis length (cm).¹³

Automatic Exposure Control manages the radiation dose and image quality in a reproducible manner by modification of the tube current (milliamperes) to the patient’s shape, size, and density.

Minimum milliamperes is the minimum setting of the tube current used for milliamperes modulation during Automatic Exposure Control.

Maximum milliamperes is the maximum setting of the tube current used for milliamperes modulation during Automatic Exposure Control.¹⁴

Kilovolt or kilovolt(peak) is the maximum voltage applied across an x-ray tube. Unlike with milliamperes, the radiation dose relationship with kilovolt is nonlinear (eg, increasing the kilovolt from 120 to 140 increases the dose by 40%).

REFERENCES

1. Ludwig B, Foster B, Saito N, et al. **Diagnostic imaging in nontraumatic pediatric head and neck emergencies.** *Radiographics* 2010;30:781–99 CrossRef Medline
2. ACR–ASNR–SPR Practice Parameter for the Performance of Computed Tomography (CT) of the Extracranial Head and Neck. http://www.acr.org/%7E/media/ACR/Documents/PGTS/guidelines/CT_Head_Neck.pdf. Accessed December 15, 2015
3. Huda W. **Radiation risks: what is to be done?** *AJR Am J Roentgenol* 2015;204:124–27 CrossRef Medline
4. Pearce MS, Salotti JA, Little MP, et al. **Radiation exposure from CT scans in childhood and subsequent risk of leukaemia and brain tumours: a retrospective cohort study.** *Lancet* 2012;380:499–505 CrossRef Medline
5. Meulepas JM, Ronckers CM, Smets AM, et al. **Leukemia and brain tumors among children after radiation exposure from CT scans: design and methodological opportunities of the Dutch Pediatric CT Study.** *Eur J Epidemiol* 2014;29:293–301 CrossRef Medline
6. Shah NB, Platt SL. **ALARA: is there a cause for alarm? Reducing radiation risks from computed tomography scanning in children.** *Curr Opin Pediatr* 2008;20:243–47 CrossRef Medline
7. Report of AAPM Task Group 23 of the Diagnostic Imaging Council Committee. The Measurement, Reporting, and Management of Radiation Dose in CT. http://www.aapm.org/pubs/reports/rpt_96.pdf. Accessed December 11, 2014
8. Tercier S, Meier R, Vasseur-Maurer S, et al. **Huge mediastinal abscess in a 12-month-old child: case report and review of the literature.** *Internet J Thoracic Cardiovascular Surg* 2004;7. <http://ispub.com/IJTCVS/7/2/3121>. Accessed February 12, 2015
9. Kumar S, Kumar V, Bishnoi A, et al. **Non-traumatic anterior mediastinal abscess in childhood.** *J Indian Assoc Pediatr Surg* 2011;16:75–77 CrossRef Medline
10. Thomas KE, Wang B. **Age-specific effective doses for pediatric MSCT examinations at a large children’s hospital using DLP conversion coefficients: a simple estimation method.** *Pediatr Radiol* 2008;38:645–56 CrossRef Medline
11. Haggett S, Van Hoorn W. Working with Protocols. <http://www.nuclear-medicine.gr/home/viewFile/4>. Accessed March 11, 2015
12. ARRT Structured Education Requirements: CT. <https://www.arrt.org/pdfs/Structured-Education-Requirements/CT-Structured-Education-Requirements.pdf>. Accessed September 26, 2015
13. Saini S. **Multi-detector row CT: principles and practice for abdominal applications.** *Radiology* 2004;233:323–27 CrossRef Medline
14. Brueswitz, MR, Yu L, Vrieze TJ, et al. **Smart mA-Automatic Exposure Control (AEC): physics principles and practical hints.** In: *Proceedings of the Radiological Society of North America 94th Scientific Assembly and Annual Meeting*, Chicago, Illinois. November 30 to December 5, 2008

How to Reduce Head CT Orders in Children with Hydrocephalus Using the Lean Six Sigma Methodology: Experience at a Major Quaternary Care Academic Children's Center

 A. Tekes,  E.M. Jackson,  J. Ogborn,  S. Liang,  M. Bledsoe,  D.J. Durand,  G. Jallo, and  T.A.G.M. Huisman



ABSTRACT

BACKGROUND AND PURPOSE: Lean Six Sigma methodology is increasingly used to drive improvement in patient safety, quality of care, and cost-effectiveness throughout the US health care delivery system. To demonstrate our value as specialists, radiologists can combine lean methodologies along with imaging expertise to optimize imaging elements-of-care pathways. In this article, we describe a Lean Six Sigma project with the goal of reducing the relative use of pediatric head CTs in our population of patients with hydrocephalus by 50% within 6 months.

MATERIALS AND METHODS: We applied a Lean Six Sigma methodology using a multidisciplinary team at a quaternary care academic children's center. The existing baseline imaging practice for hydrocephalus was outlined in a Kaizen session, and potential interventions were discussed. An improved radiation-free workflow with ultrafast MR imaging was created. Baseline data were collected for 3 months by using the departmental radiology information system. Data collection continued postintervention and during the control phase (each for 3 months). The percentage of neuroimaging per technique (head CT, head ultrasound, ultrafast brain MR imaging, and routine brain MR imaging) was recorded during each phase.

RESULTS: The improved workflow resulted in a 75% relative reduction in the percentage of hydrocephalus imaging performed by CT between the pre- and postintervention/control phases (Z-test, $P = .0001$).

CONCLUSIONS: Our lean interventions in the pediatric hydrocephalus care pathway resulted in a significant reduction in head CT orders and increased use of ultrafast brain MR imaging.

ABBREVIATIONS: DMAIC = Define, Measure, Analyze, Improve, and Control; LSS = Lean Six Sigma; PED = pediatric emergency department; UF-MRI = ultrafast brain MRI; US = ultrasonography

Lean and Six Sigma are 2 prominent quality-improvement methodologies that have been successfully applied in health care since 1998, with increasing use during the past decade related to the increased emphasis on patient safety and cost-effectiveness in medicine.^{1,2} “Six Sigma” is a process initially developed by the Motorola Corporation in 1986, which aims to improve quality by identifying and correcting the causes of errors to reduce the error rate to a six sigma level, (ie, 3.4 defects per million opportunities).

“Lean” is another quality-improvement methodology that evolved from the Toyota Production system in 1990, which uses improvements to eliminate waste and preserve steps that incrementally optimize the “value” created by the process in question. Combined as Lean Six Sigma (LSS), a 5-stage powerful methodology, Define, Measure, Analyze, Improve, and Control (DMAIC), has evolved.

Approximately 39,000 children with hydrocephalus require inpatient admissions annually in the United States.^{3,4} Most or all of these children will require cross-sectional imaging to diagnose and follow their condition. Because CT is currently the mainstay of hydrocephalus imaging at most centers, patients with hydrocephalus have a cumulative radiation exposure much higher than that of the average population. Patients exposed to higher cumulative radiation doses have an increased risk of cancer (especially children), with the brain being the most sensitive to radiation-induced cancers on the basis of recent empiric studies.⁵⁻¹⁰ Disease-specific imaging protocols and pathways to help mitigate unnecessary radiation

Received September 15, 2015; accepted after revision November 12.

From the Division of Pediatric Radiology and Pediatric Neuroradiology (A.T., D.J.D., T.A.G.M.H.), Department of Radiology (S.L., M.B.), Russell H. Morgan Department of Radiology and Radiological Science; Division of Pediatric Neurosurgery, Department of Neurosurgery (E.M.J., G.J.); and Department of Pediatrics (J.O.), The Johns Hopkins Medical Institutions, Baltimore, Maryland.

Please address correspondence to Aylin Tekes, MD, Division of Pediatric Radiology and Pediatric Neuroradiology, The Russell H. Morgan Department of Radiology and Radiological Science, The Johns Hopkins School of Medicine, Charlotte R. Bloomberg Children's Center, Sheikh Zayed Tower, Room 4155, 1800 Orleans St, Baltimore, MD 21287-0842; e-mail: atekes1@jhmi.edu

<http://dx.doi.org/10.3174/ajnr.A4658>

exposure in high-risk/vulnerable populations have been discussed in various medical/scientific forums.

Despite these considerations, radiation-free imaging modalities, such as brain MR imaging and head ultrasonography (US), are often underused due to logistic barriers and/or resource constraints such as lack of a 24/7 in-house MR imaging technologist, the longer examination times of MR imaging compared with CT, MR imaging often requiring sedation/anesthesia in the youngest patients, the higher unit cost of MR imaging, and so forth. Some authors have advocated the use of rapid-sequence MR imaging/rapid brain MR imaging/quick brain MR imaging (different terminologies have been used; in this article, we will use the term “ultrafast brain MR imaging”) in patients with hydrocephalus in the past decade. Ultrafast brain MR imaging (UF-MR imaging) offers reliable visualization of the ventricular catheter and superior anatomic detail of the ventricular system; therefore, diagnostic accuracy of the test is not reduced as the child benefits from radiation-free imaging.¹¹⁻¹⁵ However, in our experience, these MR imaging protocols are limited to relatively few centers or are performed only during certain hours of the day.

Because the barriers to using radiation-free imaging more effectively in pediatric hydrocephalus are so frequently logistic and involve complex, multidisciplinary workflows, we took an LSS approach for process improvement. The purpose of this study was to determine whether a multidisciplinary LSS approach could successfully reduce our reliance on head CT in the pediatric hydrocephalus population by 50% within 6 months, 24/7, from all referring units.

MATERIALS AND METHODS

In accordance with the Health Insurance Portability and Accountability Act, our institutional review board reviewed the protocol for this prospective study and waived the requirement for informed consent. The Division of Pediatric Radiology and Pediatric Neuroradiology convened a working team with representation from all key stakeholder groups involved in the care of children with hydrocephalus. Our team involved pediatric neuro-radiologists, pediatric neurosurgeons, pediatric emergency department (PED) physicians; chief technologists of CT, US, and MR imaging; scheduling staff; a department administrator; and a data analyst. A project leader (a pediatric neuroradiologist) and a physician champion (a pediatric neuroradiologist) were identified. Weekly/bimonthly team meetings were held. We deployed the following 5-step LSS methodology (DMAIC):

- 1) Define. All team members gathered around the table under the leadership of the project leader and physician champion. After hearing each group member’s input, a decision was made on the project title, problem statement, and scope of the work; the project goal was aligned with institutional and departmental priorities (Table 1).
- 2) Measure. Benchmark data were requested from 2 major national children’s hospitals because they had comparable patient profiles, inpatient/outpatient distributions, practitioners, and scanner capabilities compared with our children’s center. Both hospitals used a charge modifier to reduce the patient cost for UF-MR imaging by approximately 20%. The benchmark data were used to better understand the perfor-

Table 1: Project charter

Project Name: Reduce Head CT Studies in Children with Hydrocephalus
Green Belt: Champion: Master Black Belt: Problem Statement: Radiation is dangerous especially in children. There is an increasing rate of head CT orders in children with hydrocephalus. Many children with hydrocephalus need repeat imaging, adding additional risk for cumulative radiation, which may lead to cancer.
Project Goal: Reduce the percentage of head CT orders for hydrocephalus by 50 percent in 6 months (project start date: January 24, 2014)
Project Y: Percentage of each modality (head CT, ultrafast brain MRI, head US) per ordering department, time of the day, ordering physician rank
Scope: All children with known or suspected hydrocephalus, 0–18 years of age, presenting to emergency department, inpatient, and outpatient services
Team Members: Project leader, pediatric radiology and pediatric neuroradiology Physician champion, pediatric radiology and pediatric neuroradiology Member, pediatric emergency department Member, pediatric neurosurgery Member, radiology administrator Member, radiology department, financial analyst Member, pediatric radiology manager Member, chief CT technologists Member, chief US technologists Member, radiology patient care coordinator Member, chief pediatric MRI technologists
Benefits: 1) Eliminate radiation in evaluation of hydrocephalus 2) Reduce MRI time in the evaluation of hydrocephalus 3) Reduce cost with limited charge 4) Reduce shunt survey orders
Timeline: Define/Measure: January 24–February 1, 2014 Analyze/Improve: March 10–May 30, 2014 Control: July 1–September 1, 2014

mance with regard to UF-MR imaging. Optimal and practical metrics for defining and measuring the process using institutional/departmental resources were discussed. The departmental radiology information system was searched for the following criteria/key words: hydrocephalus; 0–18 years of age; and type of imaging performed being head CT, head US, routine brain MR imaging, and UF-MR imaging (with respective examination codes), with date and time of examination and ordering physician rank. Exclusion criteria included acuity of the medical condition requiring an immediate need for transfer to pediatric intensive care unit; the presence of a cochlear implant, lumbar implants/drain, or a Codman device (Codman/Johnson & Johnson, Raynham, Massachusetts) requiring adjustment after MR imaging; and extreme claustrophobia. Baseline data were collected retrospectively for 3 months on a monthly basis and continued to be collected prospectively

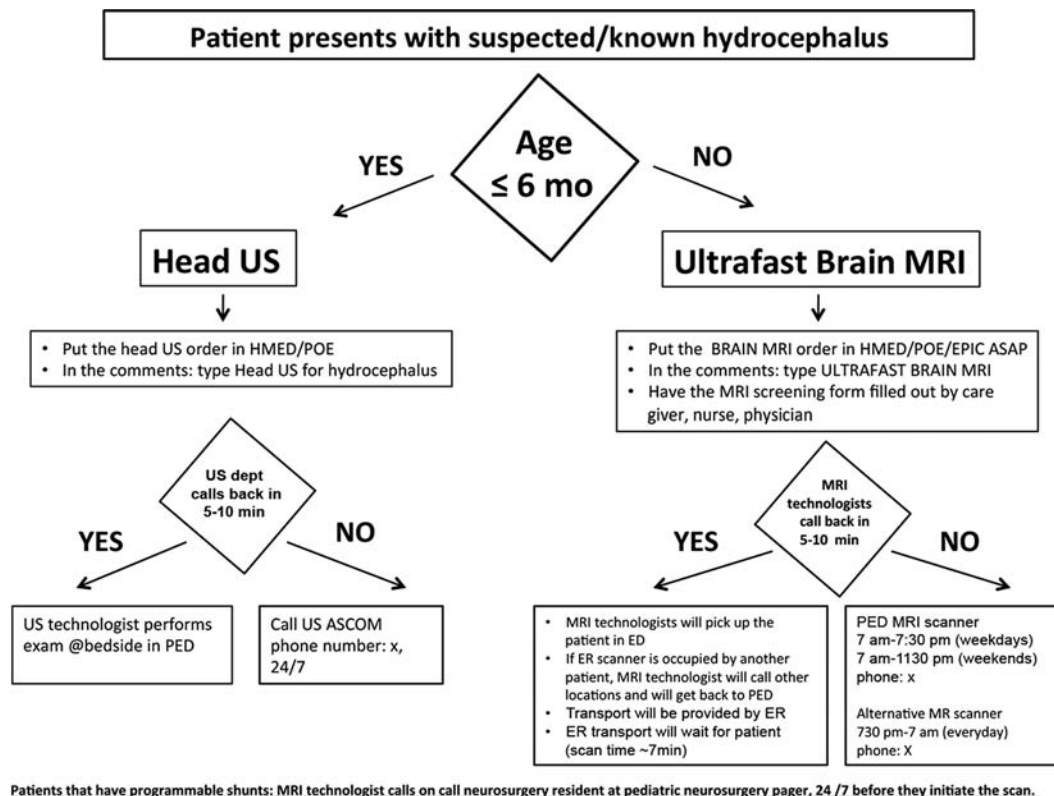


FIG 1. Improved workflow for the hydrocephalus imaging pathway. Imaging technologists are required to respond in a timely fashion. In case they could not respond on time, their phone numbers are outlined so that the ordering units can follow-up on their orders. HMED indicates HealthMatics Emergency Department (Allscripts, Chicago, Illinois); POE, Physician Order Entry; EPIC, Epic Systems (Madison, Wisconsin); ASCOM, tel.

during the postintervention/improvement phase and control phase in a similar fashion.

- 3) Analyze. The percentages of head CT, head US, routine brain MR imaging, and UF-MR imaging examinations were calculated during the baseline, improvement, and control phases. The percentage of the above-mentioned orders was analyzed per ordering unit (PED, inpatient, outpatient), per time of practice (routine day time, after hours, and weekends), and per rank of ordering physician (resident/fellow versus attending), to identify the target areas for improvement.
- 4) Improve. A visual flow chart for improved hydrocephalus imaging workflow was created (Fig 1) by the team and was implemented during the postintervention phase. Gemba was visited. Four major interventions were identified. Data collection continued for 3 months.
- 5) Control. Existing interventions were consistently pursued, and data were recorded. The electronic ordering systems were revisited during the control phase.

Lean Interventions

Lean interventions were categorized as follows: workflow changes and communication, technology improvement, equipment/process improvement, and reducing patient charges for UF-MR imaging.

Workflow Changes and Communication. Education of all units with the new workflow was performed via an in-person visit to the PED, inpatient, and outpatient units during their internal departmental meetings by the project leader. The radiologic value of

UF-MR imaging in pediatric hydrocephalus was explained in detail. Limitations of UF-MR imaging in clinical presentations other than hydrocephalus were explained in detail, such as but not limited to assessment of hemorrhage or ischemia, postoperative tumor assessment, and developmental milestone evaluations. In addition an electronic e-mail alert was sent to all residents, fellows, and attending physicians summarizing the new workflow (Fig 1). The new workflow was printed and placed over each ordering station for easy visual display of information. The electronic ordering system was revisited by the PED physician and pediatric neuroradiologist prioritizing head US and UF-MR imaging in the list of examination choices in the hydrocephalus imaging ordering package with a “pop-up” information box summarizing the improved imaging workflow.

Technology Improvements. Optimization of the existing UF-MR imaging protocol was undertaken to reduce the total MR imaging time to <5 minutes while improving image quality using a triplanar T2-weighted HASTE sequence (Fig 2). Due to the short acquisition time, no sedation or anesthesia was used. This process was led by the project leader, physician champion, and the chief MR imaging technologist. The chief MR imaging technologist updated all MR imaging scanners with the optimized protocol and trained/informed all technologists.

Equipment/Process Improvements. A separate shunt programmer was provided to the PED by pediatric neurosurgery. In-service training to the PED staff was given by the manufacturer of the shunt

programmer. The imaging technologists were required to respond within 5–10 minutes of placement of imaging orders in our radiology information system. MR imaging technologists were required to page the pediatric neurosurgery resident before initiating the MR imaging. All UF-MR images were obtained in the dedicated pediatric MR imaging scanner except when the scanner was occupied by other medical emergencies. In such cases, MR imaging technologists were responsible for identifying alternative available scanners and directing patient care. The process did not require new staff hiring or new job creation. Diagnostic image quality was obtained in all UF-MR imaging studies. No patient required a head CT after undergoing UF-MR imaging (ie, UF-MR images were diagnostically adequate in all patients in this study).

Reduce Patient Charges for UF-MR Imaging. The cost of UF-MR imaging was initially equal to that of routine brain MR imaging. A “charge modifier” was created by the administrator of Billing, Coding, and Compliance to reduce the technical fee.

Statistical significance in the percentage change of head CTs from baseline to improvement and control phases was calculated by using Z-test. Attribute capability analysis was performed to predict the long-term effects of the improved results (Minitab Statistical Software; Minitab, State College, Pennsylvania).

RESULTS

We had 794 patients, of whom 25 were excluded due to following reasons: claustrophobia ($n = 6$), medical emergency to evaluate the ventricular size and shunt positioning in which MR imaging

scanner availability could not meet the medical acuity ($n = 4$), concern for intracranial hemorrhage ($n = 10$), seizures ($n = 3$), and the presence of a lumbar drain for which the provider was uncomfortable with drain settings ($n = 2$). Of the 769 patients, the mean age was 5.3 ± 6 years.

Benchmark data were received from 2 major national children’s hospitals, where the distribution of head CTs was less and UF-MR imaging was more than our existing baseline data (we are not allowed to share the actual numbers or percentages), indicating the timeliness of improvement in our pediatric hydrocephalus imaging pathway. One hospital reported that most of the UF-MRs were obtained on outpatients, whereas the other hospital reported that UF-MRs were predominantly done on patients in the emergency department.

In our children’s center during baseline, the PED was the unit with the highest percentage of head CT orders (86.6%); 62% of all baseline orders including all neuroimaging modalities came from residents or fellows (Table 2). Most imaging (67%) was performed during regular work hours (7 AM to 5 PM) (Table 3); however, when we focused on the PED, most the studies were performed after hours (5:01 PM to 6:59 AM) and on weekends (Saturday and Sunday).

There was a statistically highly significant 75% relative decrease in the total head CT examinations from baseline to the control phase, surpassing our goal of 50% reduction (Z-test, $P < .0001$) (Table 4). The goal was achieved at 3 months from deployment of the project. UF-MR imaging examinations increased from 18% during baseline to 50% during improvement and control phases, showing a nearly 3-fold increase. Although there was a minimal increase in head CT and a minimal decrease in UF-MR

imaging orders during the first 2 months of the control phase, similar percentages to the improvement phase were reached at the third month of the control phase.

There was a decreasing trend in head US studies, with favored use of UF-MR imaging. The weekly changes in head CT orders from baseline to control phases are summarized in a p-chart in Fig 3. Attribute capability analysis showed that the head CT examination reduction at the final control phase almost reached the 95%

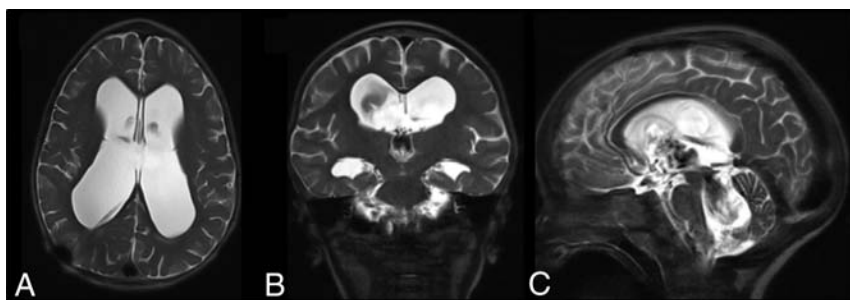


FIG 2. Ultrafast brain MR imaging protocol: axial (A), coronal (B), and sagittal (C) T2-weighted HASTE of the brain. Note the clear visualization of the ventricular system and catheter tip.

Table 2: Number and percentage of each modality per rank of ordering physician from baseline to control phases^a

	Baseline		I-Phase I		I-Phase II		I-Phase III		C-Phase I		C-Phase II		C-Phase III	
	No.	%	No.	%	No.	%	No.	%	No.	%	No.	%	No.	%
Attending														
RB-MRI	16	20.3	4	26.7	5	18.5	3	10.0	14	20.9	6	8.8	9	12.7
UF-MRI	18	22.8	4	26.7	16	59.3	10	33.3	31	46.3	34	50.0	38	53.5
Head CT	16	20.3	2	13.3	0	0.0	1	3.3	4	6.0	6	8.8	3	4.2
Head US	29	36.7	5	33.3	6	22.2	16	53.3	18	26.9	22	32.4	21	29.6
Attending total	79	38.5	15	24.2	27	31.4	30	32.6	67	70.5	68	58.1	71	63.4
Resident														
RB-MRI	22	17.5	5	10.6	5	8.5	5	8.1	4	14.3	5	10.2	7	17.1
UF-MRI	19	15.1	27	57.4	33	55.9	35	56.5	11	39.3	22	44.9	16	39.0
Head CT	46	36.5	3	6.4	6	10.2	6	9.7	6	21.4	8	16.3	6	14.6
Head US	39	31.0	12	25.5	15	25.4	16	25.8	7	25.0	14	28.6	12	29.3
Resident total	126	61.5	47	75.8	59	68.6	62	67.4	28	29.5	49	41.9	41	36.6
Grand total	205	100.0	62	100.0	86	100.0	92	100.0	95	100.0	117	100.0	112	100.0

Note:—I-Phase indicates improvement phase; C-phase, control phase; RB-MRI, routine brain MRI.

^a Duration of baseline was 3 months, followed by 3 months of improvement (each phase for 1 month), and 3 months of control phases (each phase for 1 month).

Table 3: Number and percentage of each modality during different hours of the day from baseline to control phases^a

	Baseline		I-Phase I		I-Phase II		I-Phase III		C-Phase I		C-Phase II		C-Phase III	
	No.	%	No.	%	No.	%	No.	%	No.	%	No.	%	No.	%
Work hours														
RB-MRI	27	19.7	6	14.3	6	9.4	6	9.8	12	16.4	6	8.6	11	12.5
UF-MRI	34	24.8	21	50.0	40	62.5	26	42.6	34	46.6	38	54.3	44	50.0
Head CT	28	20.4	2	4.8	1	1.6	1	1.6	8	11.0	1	1.4	6	6.8
Head US	48	35.0	13	31.0	17	26.6	28	45.9	19	26.0	25	35.7	27	30.7
Work hour total	137	66.8	42	67.7	64	74.4	61	66.3	73	76.8	70	59.8	88	78.6
After hours														
RB-MRI	7	20.6	2	14.3	3	25.0	2	13.3	3	23.1	3	13.6	4	25.0
UF-MRI	2	5.9	8	57.1	5	41.7	9	60.0	6	46.2	9	40.9	8	50.0
Head CT	19	55.9	2	14.3	3	25.0	3	20.0	1	7.7	6	27.3	2	12.5
Head US	6	17.6	2	14.3	1	8.3	1	6.7	3	23.1	4	18.2	2	12.5
After hours total	34	16.6	14	22.6	12	14.0	15	16.3	13	13.7	22	18.8	16	14.3
Weekend														
RB-MRI	4	11.8	1	16.7	1	10.0		0.0	3	33.3	2	8.0	1	12.5
UF-MRI	1	2.9	2	33.3	4	40.0	10	62.5	2	22.2	9	36.0	2	25.0
Head CT	15	44.1	1	16.7	2	20.0	3	18.8	1	11.1	7	28.0	1	12.5
Head US	14	41.2	2	33.3	3	30.0	3	18.8	3	33.3	7	28.0	4	50.0
Weekend total	34	16.6	6	9.7	10	11.6	16	17.4	9	9.5	25	21.4	8	7.1
Grand total	205	100.0	62	100.0	86	100.0	92	100.0	95	100.0	117	100.0	112	100.0

Note:—I-Phase indicates improvement phase; C-phase, control phase; RB-MRI, routine brain MRI.

^a Duration of baseline was 3 months, followed by 3 months of improvement (each phase for 1 month), and 3 months of control phases (each phase for 1 month).

Table 4: Number and percentage of each modality from baseline to control phases^a

	Baseline		I-Phase I		I-Phase II		I-Phase III		C-Phase I		C-Phase II		C-Phase III	
	No.	%	No.	%	No.	%	No.	%	No.	%	No.	%	No.	%
RB-MRI	38	18.5	9	14.5	10	11.6	8	8.7	18	18.9	11	9.4	16	14.3
UF-MRI	37	18.0	31	50.0	49	57.0	45	48.9	42	44.2	56	47.9	54	48.2
Head CT	62	30.2	5	8.1	6	7.0	7	7.6	10	10.5	14	12.0	9	8.0
Head US	68	33.2	17	27.4	21	24.4	32	34.8	25	26.3	36	30.8	33	29.5

Note:—I-Phase indicates improvement phase; C-phase, control phase; RB-MRI, routine brain MRI.

^a Duration of baseline was 3 months, followed by 3 months of improvement (each phase for 1 month), and 3 months of control phases (each phase for 1 month).

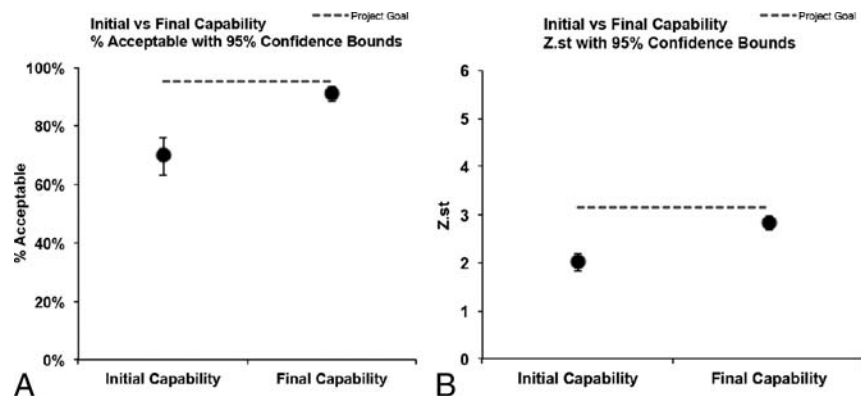


FIG 3. Attribute capability analysis demonstrates that our control data are almost at the 95% confidence bounds.

confidence bounds. Z St. analysis showed that the final control phase data almost reached 2 SDs, which was the 95% confidence bound, indicating a sustainable long-term stability of the process (Fig 4).

DISCUSSION

We reduced head CT orders by 75% within 3 months from deploying the LSS project, surpassing our goal of reducing head CT orders by 50% in 6 months in children with hydrocephalus. More important, subsequent data collection/analysis during postintervention and control phases demonstrated that these changes were sustainable.

Head CT has been the mainstay of hydrocephalus imaging pathways to assess the ventricular size because it is easily accessible in most hospitals and provides quick information with a reasonably low total charge. Long-term survival has significantly improved in children with hydrocephalus with the use of modern CSF diversion techniques and advances in the care of shunts. Low-dose CT protocols have been used in some hospitals, including our own, following the principle of as low as reasonably achievable¹⁶; however, children with hydrocephalus will have multiple neuroimaging studies throughout their lives, increasing their total lifetime radiation exposure and consequently having a greater lifetime risk of radiation-induced brain cancers.⁵⁻¹⁰ Therefore, elimination of radiation-based imaging techniques whenever possible is critical to ensure the long-term health of this population. Highlighting this belief, Koral et al⁷ recently found that there is an increased risk of developing fatal cancer if children with hydrocephalus undergo neuroimaging surveillance with head CTs. These and similar results have repeatedly been reported in the lay press, and as a result, both providers and patients' families are routinely demanding that radiation-free protocols be used whenever possible.

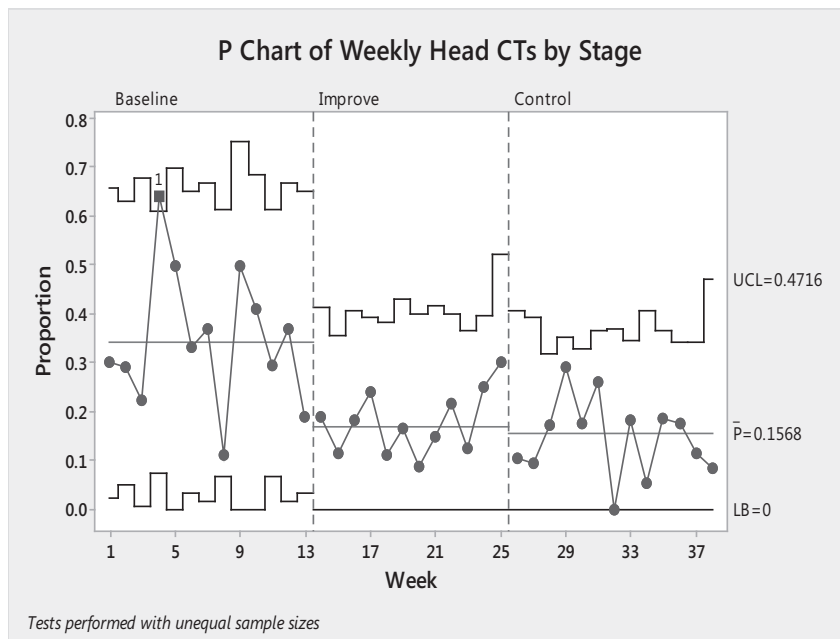


FIG 4. P-chart demonstrating weekly changes in head CT orders from baseline to control phases. Note the reduced fluctuations during improvement and control phases. UCL indicates upper control limit; LB, lower boundary.

Use of UF-MR imaging was first published in 2005 as a radiation-free alternative for neuroimaging in children with hydrocephalus and has been applied by the principal author since the late 1990s.¹¹ Since then, UF-MR imaging has been validated with similar test characteristics for the evaluation of possible shunt failure (assessment of ventricular size and catheter visualization) compared with head CT.¹⁷⁻¹⁹ Diagnostic image quality and the short image-acquisition time of UF-MR imaging have also been reported.¹¹⁻¹⁵ Despite the aforementioned publications, consistent nationwide use of this radiation-free neuroimaging technique has been somewhat limited. The palpable growing demand to improve quality and safety in imaging is now requiring radiologists to take leadership responsibilities, beyond simply reading a timely accurate radiology examination.²⁰

Health care delivery systems are complex, and each institution has its unique resources, qualities, and challenges. In our study, we deployed an LSS methodology for solving our problem. In this article, we summarize and present our results in the framework of “how to do” this methodology. Lean methodology focuses on elimination of waste, which can be defective products, overproduction beyond demand, increased inventories, unnecessary motion/transport, and wait times as typically described in the manufacturing industry. In this study, the “defect” we sought to eliminate was the clinically unnecessary use of head CT. We reduced the overall radiation exposure to children significantly by using radiation-free imaging techniques. We completely eliminated the use of sedation/anesthesia by optimizing/shortening the UF-MR imaging protocol and educating technologists.

Unnecessary motion of the patient and transport staff was effectively eliminated by use of the emergency department MR imaging scanner and having our MR imaging technologists pick up and return the patients to their beds in the PED. We further reduced the patient’s postimaging wait times by paging the neuro-

surgery resident as soon as the patients were transferred into the MR imaging scanner. The purchase of an additional shunt programmer for the PED enabled the pediatric neurosurgery staff to immediately check the shunt settings for patients on completion of imaging. We placed printed improved workflow charts at the ordering workstations of each unit to provide visual display.

Although there was some increase in head CTs and reduction in UF-MR imaging in the early control phase, the percentage of decrease in the head CTs did not fall below 50%. The early control phase coincided with the new academic year, with influx of new residents and fellows, which, in part, may explain a temporary change. The electronic ordering system of our hospital was renewed during the course of this project. Therefore, before implementation of the new electronic ordering system, which coincided with the beginning of the control phase and the beginning of the new

academic year, the revision of the hydrocephalus imaging package with the pop-up information box was not accomplished. This likely explains the brief, transient relative increase in head CTs during this period. After implementation of the changes in the new electronic ordering system, the head CT and UF-MR imaging orders returned to a level similar to that seen during the early improvement phase. This difference highlights the importance/value of the use of electronic health care systems for a successful execution of interventions that related to imaging appropriateness. Attribute capability analysis demonstrated that the control phase data almost reached the 95% confidence bounds.

Our study has several limitations. We identified our patients by using radiology information systems with the search term “hydrocephalus,” which resulted in the inclusion of all patients with hydrocephalus regardless of whether they were shunted. We offered a timely service 24/7 to all providing units; however, we did not measure the total cycle time or throughput of the patients. Although we did not collect such data, the fact that the services have been used well in excess of our initial goal suggests that UF-MR imaging scans are being obtained in fashion timely enough for referring providers to effectively change their ordering patterns. We did not aim for 100% elimination of head CT, keeping in mind the potential need for head CT for medical reasons in select cases. We did not calculate the radiation savings for our patients, though this is a goal of our team for future.

CONCLUSIONS

We surpassed our goal of a 50% reduction in head CT orders, achieving a sustained 75% reduction by effectively replacing most head CTs within a radiation- and sedation-/anesthesia-free UF-MR imaging protocol. Building a multidisciplinary team, having a tightly scoped project outline with clear goals aligned

with our institutional and departmental priorities, and adhering closely to the DMAIC framework of LSS were all crucial in achieving our goal. Although factors may vary by hospital, similar LSS methodology could yield positive results for other indications such as adult hydrocephalus or other health care delivery systems.

ACKNOWLEDGMENTS

We acknowledge the contributions and support of each team member that we could not include in the authors list: Diane Novak (MR Imaging Manager), Bina Patel (Chief Pediatric MR Imaging Technologist and Manager), Beatrice Mudge (CT Manager), Robert DeJong (US Manager), Elyce Wolfgang (Pediatric Radiology Manager), and Allison Greene (medical student) from the Johns Hopkins Hospital; and Rich Hill from the Armstrong Institute for Patient Safety and Quality.

Disclosures: Eric M. Jackson—UNRELATED: *Expert Testimony*: I was an expert for a case of a neurosurgical patient with a diagnosis unrelated to this project. I have not been paid as of yet; *Grants/Grants Pending*: I had a grant from the institution for shunt development and have currently submitted requests for additional grants. I did not receive any money directly.* Martin Bledsoe—UNRELATED: *Expert Testimony*: West Virginia University; ninety-minute case review. Daniel J. Durand—UNRELATED: *Employment*: Evolent Health, *Comments*: For 2 years I worked as a health care consultant, helping to improve the value delivered by imaging to patient populations. None of the pediatric MRI work described here overlaps any of my work at Evolent, however; *Other*: National Decision Support Company, *Comments*: unpaid advisor to a maker of clinical decision-support software designed to help ensure that the appropriate test is ordered for the right patient at the right time. They do not make a product for pediatric patients, and this work has no overlap with their Clinical Decision Support solution. George Jallo—UNRELATED: *Expert Testimony*: defense work for a law firm. Thierry A.G. Huisman—UNRELATED: *Board Membership*: Senior Editor for the *American Journal of Neuroradiology*. *Money paid to the institution.

REFERENCES

- DelliFraine JL, Langabeer JR 2nd, Nembhard IM. **Assessing the evidence of Six Sigma and Lean in the health care industry.** *Qual Manag Health Care* 2010;19:211–25 CrossRef Medline
- Vest JR, Gamm LD. **A critical review of the research literature on Six Sigma, Lean and StuderGroup's Hardwiring Excellence in the United States: the need to demonstrate and communicate the effectiveness of transformation strategies in healthcare.** *Implement Sci* 2009;4:35 CrossRef Medline
- Simon TD, Riva-Cambrin J, Srivastava R, et al; Hydrocephalus Clinical Research Network. **Hospital care for children with hydrocephalus in the United States: utilization, charges, comorbidities, and deaths.** *J Neurosurg Pediatr* 2008;1:131–37 CrossRef Medline
- Stein SC, Guo W. **The prevalence of shunt-treated hydrocephalus: a mathematical model.** *Surg Neurol* 2009;72:131–37 CrossRef Medline
- Brenner D, Elliston C, Hall E, et al. **Estimated risks of radiation-induced fatal cancer from pediatric CT.** *AJR Am J Roentgenol* 2001;176:289–96 CrossRef Medline
- Brenner DJ, Hall EJ. **Computed tomography: an increasing source of radiation exposure.** *N Engl J Med* 2007;357:2277–84 CrossRef Medline
- Koral K, Blackburn T, Bailey AA, et al. **Strengthening the argument for rapid brain MR imaging: estimation of reduction in lifetime attributable risk of developing fatal cancer in children with shunted hydrocephalus by instituting a rapid brain MR imaging protocol in lieu of head CT.** *AJNR Am J Neuroradiol* 2012;33:1851–54 CrossRef Medline
- Durand DJ. **A rational approach to the clinical use of cumulative effective dose estimates.** *AJR Am J Roentgenol* 2011;197:160–62 CrossRef Medline
- Pearce MS, Salotti JA, Little MP, et al. **Radiation exposure from CT scans in childhood and subsequent risk of leukaemia and brain tumours: a retrospective cohort study.** *Lancet* 2012;380:499–505 CrossRef Medline
- Mathews JD, Forsythe AV, Brady Z, et al. **Cancer risk in 680,000 people exposed to computed tomography scans in childhood or adolescence: data linkage study of 11 million Australians.** *BMJ* 2013;346:f2360 CrossRef Medline
- Ashley WW Jr, McKinsty RC, Leonard JR, et al. **Use of rapid-sequence magnetic resonance imaging for evaluation of hydrocephalus in children.** *J Neurosurg* 2005;103(2 suppl):124–30 Medline
- Iskandar BJ, Sansone JM, Medow J, et al. **The use of quick-brain magnetic resonance imaging in the evaluation of shunt-treated hydrocephalus.** *J Neurosurg* 2004;101:147–51 Medline
- Niederhauser BD, McDonald RJ, Eckel LJ, et al. **Retrospective review of rapid pediatric brain MR imaging at an academic institution including practice trends and factors affecting scan times.** *AJNR Am J Neuroradiol* 2013;34:1836–40 CrossRef Medline
- O'Neill BR, Pruthi S, Bains H, et al. **Rapid sequence magnetic resonance imaging in the assessment of children with hydrocephalus.** *World Neurosurg* 2013;80:e307–312 CrossRef Medline
- Rozovsky K, Ventureyra EC, Miller E. **Fast-brain MRI in children is quick, without sedation, and radiation-free, but beware of limitations.** *J Clin Neurosci* 2013;20:400–05 CrossRef Medline
- Pindrik J, Huisman TA, Mahesh M, et al. **Analysis of limited-sequence head computed tomography for children with shunted hydrocephalus: potential to reduce diagnostic radiation exposure.** *J Neurosurg Pediatr* 2013;12:491–500 CrossRef Medline
- Yue EL, Meckler GD, Fleischman RJ, et al. **Test characteristics of quick brain MRI for shunt evaluation in children: an alternative modality to avoid radiation.** *J Neurosurg Pediatr* 2015;15:420–26 CrossRef Medline
- Mater A, Shroff M, Al-Farsi S, et al. **Test characteristics of neuroimaging in the emergency department evaluation of children for cerebrospinal fluid shunt malfunction.** *CJEM* 2008;10:131–35 Medline
- Lehnert BE, Rahbar H, Relyea-Chew A, et al. **Detection of ventricular shunt malfunction in the ED: relative utility of radiography, CT, and nuclear imaging.** *Emerg Radiol* 2011;18:299–305 CrossRef Medline
- Durand DJ, Kohli MD. **Advanced practice quality improvement project: how to influence physician radiologic imaging ordering behavior.** *J Am Coll Radiol* 2014;11:1155–59 CrossRef Medline

Myelography CPT Coding Updates: Effects of 4 New Codes and Unintended Consequences

 F.H. Chokshi,  R.K. Tu,  G.N. Nicola, and  J.A. Hirsch

ABSTRACT

SUMMARY: The Current Procedural Terminology of the American Medical Association has recently introduced coding changes for myelography with the introduction of new bundled codes. The aim of this review was to help neuroradiologists understand these code changes and their unintended consequences and to discuss various scenarios in which permutations of various codes could occur in clinical practice.

ABBREVIATIONS: AMA = American Medical Association; CPT = Current Procedural Terminology

The Current Procedural Terminology (CPT) system has been the national medical coding standard in the United States¹ since 2000. CPT, owned and trademarked by the American Medical Association (AMA), provides physicians, including neuroradiologists, an opportunity to directly participate in the creation of procedural codes. The work of the CPT Editorial Panel and advisors is published in the CPT manual and educational materials in an effort to provide coding clarity and preserve the intended coding integrity of medical procedures. The effects of this recent bundling,^{2,3} including the interplay among radiologic modalities, are important for neuroradiologists. The authors illustrate these complexities with recent updates to the differentiation of x-ray and CT with intrathecal contrast media and the unintended consequences of reevaluation of the original codes. This review will provide clarity for physicians and coders who wish to enhance their familiarity with these changes. Of note, we intentionally

used “providers” instead of “physicians” because allied health professionals or other qualified health care providers (eg, nurse practitioners) can also perform and increasingly code these procedures,^{4,5} especially because diagnostic imaging volume has increased with time.⁶

Definition of Myelography

Myelography is a comprehensive radiographic examination of the spine following intrathecal injection of iodinated contrast media, involving assessment of static structures such as the spinal canal and each exit foramen, and dynamic, real-time assessment of contrast injection and its flow dynamics under direct visualization.⁷ Fluoroscopic gastrointestinal studies require maneuvers to move contrast; so too are patient and table maneuvers often used as tools to evaluate canal stenosis, leaks, complications of surgery, and spinal instrumentation. A myelogram is not a single image documenting needle placement but a comprehensive evaluation of the contrast-enhanced thecal sac with assessment of each exit foramen for pathology. Specialized techniques such as flexion, rotation, and hyperextension to show spinal stenosis and lateral recess stenosis are tools chosen by the provider as trouble-shooting techniques of assessment as contrast disperses in the thecal sac. Perhaps, the single most important message of this article is that one should not code for a myelogram when one is using x-ray imaging simply to document the intrathecal location of the needle placement and contrast injection.

Bundling of Myelography CPT Codes

The CPT 2015 Professional Edition⁸ introduced 4 new bundled codes, increasing the total number to 8. The new codes combined intrathecal contrast administration via lumbar injection, fluoroscopic guidance, and x-ray myelographic radiologic supervision

Received November 17, 2015; accepted November 20.

From the Division of Neuroradiology (F.H.C.), Department of Radiology and Imaging Sciences, Emory University School of Medicine, Atlanta, Georgia; Department of Radiology (R.K.T.), Progressive Radiology, NFPHC/United Medical Center, Washington, DC; Department of Radiology (R.K.T.), BridgePoint Hospital Hadley, BridgePoint Subacute and Rehabilitation Hadley, BridgePoint Hospital Capitol Hill, Washington, DC; Department of Radiology (R.K.T.), George Washington University, Washington, DC; Hackensack Radiology Group (G.N.N.), Hackensack University Medical Center, River Edge, New Jersey; and Neuroendovascular Division (J.A.H.), Massachusetts General Hospital, Harvard Medical School, Boston, Massachusetts.

Falgun H. Chokshi, MD, MS, is an Association of University Radiologists GE Radiology Research Academic Fellow (2015–2017). This investigation was supported, in part, by the Association of University Radiologists GE Radiology Research Academic Fellowship Award.

Please address correspondence to Falgun H. Chokshi, MD, MS, Division of Neuroradiology, Department of Radiology and Imaging Sciences, Emory University School of Medicine, 1364 Clifton Rd NE, Atlanta, GA 30068; e-mail: falgun.chokshi@emory.edu; @FalgunChokshiMD

<http://dx.doi.org/10.3174/ajnr.A4666>

Table 1: CPT codes for myelography

Myelographic Region	Nonbundled Code	Bundled Code
	(2 Separate Providers: 1 Doing Injection and Other Doing Myelogram Interpretation)	(1 Provider Doing Both Injection and Myelogram Interpretation)
Cervical	72240	62302
Thoracic	72255	62303
Lumbar	72265	62304
±2 Regions	72270	62305
Intrathecal injection only and fluoroscopic guidance code	62284 + 77003 ^a	Not Applicable

^aNo myelography at all; injection and CT spine with contrast only.

Table 2: CPT codes for CT spine with contrast^a

Spine Level	CPT Code
Cervical	72126
Thoracic	72129
Lumbar	72132

^aAdd Modifier 59 if x-ray myelography is performed on the same day on the same patient by the same provider.

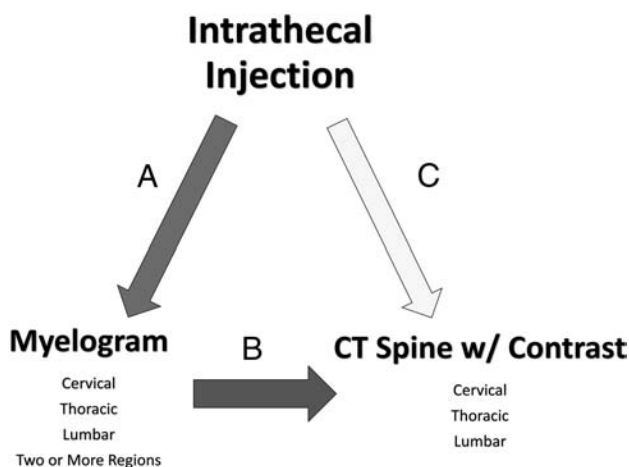


FIG 1. Permutations of myelography coding. A, B, and C denote paths of coding.

and interpretation into codes used only when the same provider performs both injection and myelography on the same day on the same patient. Bundling occurred following recommendations by the Relativity Assessment workgroup screen. The Relativity Assessment workgroup, one of many committees of the Relative Value Scale Update Committee of the AMA, screens for procedures occurring together 75% of the time. Existing codes were not replaced because there are scenarios in which one provider injects the lumbar spine with contrast media and another provider interprets the study.^{2,3} Table 1 shows both nonbundled and bundled CPT codes for myelography.

Modifier 59

Distinct from the Relativity Assessment workgroup screen of the AMA, the National Correct Coding Initiative of the Centers for Medicaid and Medicare Services reviews codes for potential misuse. The National Correct Coding Initiative flagged myelography and contrast-enhanced CT of the spine and submitted a query to the AMA requesting clarification. Because myelography and contrast-enhanced CT of the lumbar spine occurred in the same patients, the National Correct Coding Initiative was concerned

that these concurrent procedures may be unnecessary and duplicative. Sub-specialty societies including the American Society of Neuroradiology replied and provided detailed explanations clarifying myelography and contrast-enhanced CT as distinct procedures. Accepting the explanation, the National Correct Coding Initiative recommended that Modifier 59, Distinct Procedural Service, be added to CPT codes if the CT examination is performed following myelography on the same patient on the same day for the reason described above.

Table 2 provides CPT codes for CT of the spine with contrast, which have been used since July 1, 2014. Modifier 59 flags and clarifies procedures that may be mistaken as duplicative. Again, this modifier is not applied if x-ray images were merely obtained to check intrathecal spinal needle placement (code 62284). Only in this latter situation can code 62284 be combined with billing code 77003, the code for fluoroscopic guidance.

Coding Permutations for Myelography

To help radiologists and coders understand these coding changes further, we have included a set of scenarios to show various permutations of myelography coding.

Scenario 1 involves intrathecal lumbar injection only (code 62284) followed by CT of the spine with contrast (codes 72126–73132) (Fig 1, path C). This scenario does not include x-ray myelography at all; therefore, neither bundled codes nor Modifier 59 is used. Scenario 1 can include a single provider injecting and interpreting the CT or a single provider injecting (eg, nurse practitioner) and another provider interpreting the CT (eg, neuroradiologist). Again, scenario 1 also allows billing of code 77003, a separate code for fluoroscopic guidance. Code 77003 can only be billed with 62284 if none of the new bundled codes are used (62302–62305), which already account for fluoroscopic guidance. For example, a patient undergoing an intrathecal lumbar injection only followed by CT lumbar spine with contrast would be coded as 62284 + 77003 + 72132. For C1–C2 injection only, use code 61055 instead of 62284.

Scenario 2 would include both x-ray myelography and CT spine interpretation by a single provider performing both parts (Fig 1, paths A and B). Most important, this scenario warrants the new bundled myelography codes in the last column of Table 1 and the CT spine codes in Table 2 plus Modifier 59. In this scenario, do not bill for fluoroscopic guidance, code 77003. Therefore, a patient receiving intrathecal lumbar injection + lumbar x-ray myelography + CT lumbar spine with contrast would be coded as 62304 (bundled) + 72132 + Modifier 59.

Scenario 3, albeit presumably rare, would involve one provider doing the intrathecal lumbar injection and a second provider performing myelography and interpreting the CT of the spine with contrast (Fig 1, paths A and B). In this scenario, provider 1 performs the intrathecal lumbar injection, which is coded as 62284 + 77003. Provider 2 performs the x-ray myelography, which is coded with an old (unbundled) x-ray myelography code

(72240–72270). In addition, provider 2 interprets the CT spine with contrast, which is coded with a CT with contrast code (72126–72132) plus Modifier 59. If no myelography is performed, then provider 1 performs intrathecal injection only (62284 + 77003) and provider 2 interprets the CT spine with contrast, which is coded 72126–73132 without Modifier 59 (scenario 1).

CONCLUSIONS

Myelography is a procedure that predates cross-sectional imaging and provides unique radiographic information as dynamic, real-time imaging. These studies are commonly obtained and interpreted by neuroradiologists. During the past several years, as other imaging modalities became available to evaluate the spine, interest in these modalities by the AMA and Centers for Medicaid and Medicare Services increased. The screens⁹ of the AMA for codes reported together above a certain predefined threshold were bundled as a result of being identified by the Relativity Assessment Workgroup, thereby adding 8 codes for myelography. The Centers for Medicaid and Medicare Services introduced Modifier 59 for CT. In addition to new codes, there were new valuations of the bundled and pre-existing nonbundled codes, an unintended consequence. It is very important that neuroradiologists and their coders understand the nuances of myelography coding based on changes in 2015 to maintain coding integrity of the procedures that are performed and to avoid Recovery Audit Contractor audits. Proper coding ensures appropriate reimbursement and accurate retrospective use of physician work.

ACKNOWLEDGMENTS

The authors acknowledge Rahul Bhala, MBA, MPH (Managing Director–Economics and Health Policy, American Society of Neuroradiology), and Jacqueline A. Bello, MD, FACR (Professor of Clinical Radiology and Neurosurgery, Director of Neuroradi-

ology, Albert Einstein College of Medicine, Montefiore Medical Center), for their assistance.

Disclosures: Joshua A. Hirsch—UNRELATED: Consultancy: Medtronic (ongoing, related to the spine), CareFusion (taught single course in last 36 months, not ongoing).

REFERENCES

1. Hirsch JA, Leslie-Mazwi TM, Nicola GN, et al. **Current procedural terminology; a primer.** *J Neurointerv Surg* 2015;7:309–12 CrossRef Medline
2. Hirsch JA, Donovan WD, Leslie-Mazwi TM, et al. **Component coding and the neurointerventionalist: a tale with an end.** *J Neurointerv Surg* 2013;5:615–19 CrossRef Medline
3. Hirsch JA, Silva E 3rd, Nicola GN, et al. **The RUC: a primer for neurointerventionalists.** *J Neurointerv Surg* 2014;6:61–64 CrossRef Medline
4. Hawkins CM, Bowen MA, Gilliland CA, et al. **The impact of nonphysician providers on diagnostic and interventional radiology practices: operational and educational implications.** *J Am Coll Radiol* 2015;12:898–904 CrossRef Medline
5. Chittle MD, Vanderboom T, Borsody-Lotti J, et al. **An overview of clinical associate roles in the neurointerventional specialty.** *J Neurointerv Surg* 2015 Jan 5. [Epub ahead of print] CrossRef Medline
6. Chokshi FH, Hughes DR, Wang JM, et al. **Diagnostic radiology resident and fellow workloads: a 12-year longitudinal trend analysis using national Medicare aggregate claims data.** *J Am Coll Radiol* 2015;12:664–69 CrossRef Medline
7. Myelography. RadiologyInfo. Org; 2015. <http://www.radiologyinfo.org/en/info.cfm?pg=myelography>. Accessed November 11, 2015
8. CPT 2015 Professional Edition. American Medical Association; 2015. https://commerce.ama-assn.org/store/catalog/productDetail.jsp?product_id=prod2480008&navAction=push. Accessed November 11, 2015
9. Donovan WD, Leslie-Mazwi TM, Silva E 3rd, et al. **Diagnostic carotid and cerebral angiography: a historical summary of the evolving changes in coding and reimbursement in a complex procedure family.** *J Neurointerv Surg* 2014;6:712–17 CrossRef Medline

Same-Day Sinus and Brain CT Imaging in the Medicare Population: Are Practice Patterns Changing in Association with Medicare Policy Initiatives?

H. Kroll, R. Duszak Jr, J. Hemingway, D. Hughes, and M. Wintermark

ABSTRACT

BACKGROUND AND PURPOSE: Monitoring the frequency of same-day sinus and brain CT (Outpatient Measure 14, “OP-14”) is part of a recent large Centers for Medicare and Medicaid Services hospital outpatient quality initiative to improve imaging efficiency. This study investigates patient-level claims data in the Medicare population focusing on where same-day sinus and brain CT imaging is performed and how the frequency of same-day studies changed with time before and during OP-14 measure program implementation.

MATERIALS AND METHODS: Research Identifiable Files were used to identify all sinus and brain CT examinations from 2004 through 2012 for a 5% random patient sample of Medicare fee-for-service beneficiaries. Overall and site of service use rates were calculated for same- and non-same-day examinations. Changes were mapped to policy initiative timetables.

RESULTS: The number of same-day sinus and brain CT studies from 2004 to 2012 increased 67% from 1.85 (95% CI, 1.78–1.91) per 1000 Medicare beneficiaries in 2004 to 3.08 (95% CI, 3.00–3.15) in 2012. The biggest driver of increased same-day studies was the emergency department setting, from 0.56 (95% CI, 0.53–0.60) per 1000 to 1.78 (95% CI, 1.72–1.84; +215.7%). Overall use of brain CT from 146.0 (95% CI, 145.1–146.9) per 1000 to 176.3 (95% CI, 175.4–177.2; +21%) and sinus CT from 12.6 (95% CI, 12.4–12.8) per 1000 to 15.4 (95% CI, 15.2–15.6; +22%) increased until 2009 and remained stable through 2012.

CONCLUSIONS: Previously increasing same-day sinus and brain CT in Medicare beneficiaries plateaued in 2009, coinciding with the implementation of targeted measures by the Centers for Medicare and Medicaid Services. Same-day imaging continues to increase in the emergency department setting.

ABBREVIATIONS: CMS = Centers for Medicare and Medicaid Services; ED = emergency department; ICD-9 = International Classification of Diseases, Ninth Revision; OP-14 = Outpatient Measure 14 (simultaneous use of brain CT and sinus CT) of the Hospital Outpatient Quality Reporting Program; RIF = Research Identifiable Files

Rising health care costs in the United States have resulted in a number of policy initiatives and professional society campaigns¹ to use limited resources more judiciously. The rapid increase in spending on medical imaging during the early part of the past decade,^{2,3} along with an increased societal awareness of radiation dose,⁴ has focused those initiatives and campaigns on imaging services. The injudicious use of sinus CT imaging, for example, received considerable attention as part of the multispecialty “Choosing Wisely” initiative.¹ In response to Congressional leg-

islation in 2006,⁵ the Centers for Medicare and Medicaid Services (CMS) also focused on potentially inappropriate sinus CT imaging as part of its outpatient imaging efficiency program. With the rationale that except in specific and narrow circumstances, same-day sinus and brain CT imaging is rarely indicated, CMS established metric Outpatient Measure 14 (OP-14) to track the use by facilities of such same-day imaging.⁶ The goals of the initiative were to improve transparency through public reporting and potentially serve as the basis for value-based payments. Although the overall program was announced in 2006, testing did not begin until 2010 and was not officially implemented until 2012. Nonetheless, even before that official implementation, it received widespread media coverage.⁷

Using just 2 years of CMS Web site data, Rosenkrantz and Doshi⁸ recently reported a relatively low incidence of same-day sinus and brain CT imaging but did not examine how that frequency changed during program rollout or expand their analysis beyond the specific target of the CMS initiative (ie, hospital out-

Received June 26, 2015; accepted after revision November 24.

From the Department of Radiology (H.K., M.W.), Neuroradiology Section, Stanford University, Stanford, California; Harvey L. Neiman Health Policy Institute (R.D., J.H., D.H.), Reston, Virginia; Department of Radiology and Imaging Sciences (R.D.), Emory University School of Medicine, Atlanta, Georgia; and Department of Health Administration and Policy (D.H.), George Mason University, Fairfax, Virginia.

Please address correspondence to Max Wintermark, MD, MAS, MBA, Stanford University, Department of Radiology, Neuroradiology Division, 300 Pasteur Dr, Room S047, Stanford, CA 94305-5105; e-mail: Max.Wintermark@gmail.com

<http://dx.doi.org/10.3174/ajnr.A4670>

patient setting). Thus, despite the attention this program has received in the media, little is known about how physician-testing behavior has changed in association with its implementation.

The aim of our investigation was to study patient-level claims data in the Medicare population, focusing on where same-day sinus and brain CT imaging is performed and how the frequency of same-day studies changed with time before and during the OP-14 measure program implementation.

MATERIALS AND METHODS

Data Source

Our methodology was modeled on that previously described for other imaging procedures.⁹ Under a data-use agreement from the Centers for Medicare and Medicaid Services, we acquired 5% carrier claims Research Identifiable Files (RIF) from 2004 through 2012, which contain all Medicare Part B fee-for-service claims for a 5% random sample of Medicare beneficiaries. These files contain detailed information, including date and place of service, procedures performed as identified by Current Procedural Terminology or the Healthcare Common Procedure Coding System code, and beneficiary diagnoses as identified by the International Classification of Diseases, Ninth Revision (ICD-9) code associated with each fee-for-service claim for the approximately 2.5 million beneficiaries present in each year of the data. We received an exemption from the institutional review board of the American College of Radiology for the use of the retrospective administrative data in this study.

Data Parameters

Sites of service are identified within the 5% RIF with provider self-reported site-of-service codes. For the purposes of this study, those with site-of-service codes for the physician's office, inpatient hospital, outpatient hospital, and emergency department (ED) settings were specifically identified; all considerably less common sites were grouped together in an "other" site category. All services reported with Current Procedural Terminology codes for sinus CT (70486, 70487, 70488) and for brain CT (70450, 70460, 70470) were identified annually from 2004 to 2012.

Analysis

Usage rates for sinus and brain CT in the 5% random Medicare fee-for-service patient sample were calculated for years 2004 until 2012. All ICD-9 codes associated with each examination were recorded. In concordance with CMS OP-14 methodology, studies performed for the indications of trauma (ICD-9 codes 800-839, 850-854, 860-869, 905-909, 926.11, 926.12, 929, 952, 958-959), infection (ICD-9 Clinical Modification code: 376.01), or known or suspected mass (ICD-9 codes: 140-239) were analyzed separately. These are hereafter termed "exclusion measures," because CMS deemed these diagnoses as ones in which same-day sinus and brain CT examinations may be more appropriate. In addition, the rate of same-day sinus and brain CT was calculated from 2004 until 2012 by using coincident date of service claims, again with and without applied exclusion measures. We classified a sinus and brain CT as "same-day services" if these services were recorded as occurring on the same date of service regardless of whether these were submitted on the same or separate claim

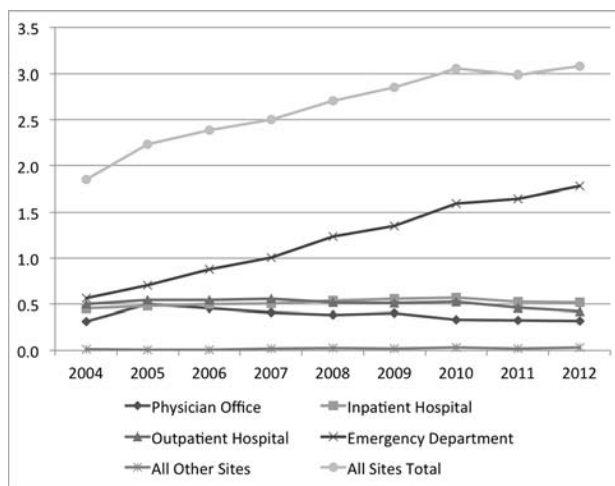


FIG 1. Overall same-day sinus and brain CTs by site of service per 1000 Medicare beneficiaries with exclusion measures applied (exclusion measures are studies performed for trauma, infection, or tumor that were not included in this analysis).

forms. Because physicians and facilities usually submit separate claims for their services, we excluded technical-only claims and included only professional-only and global claims.¹⁰

Use per 1000 beneficiaries was calculated by dividing the total number of services by the total number of beneficiaries in the 5% RIF claims files for each year. Data analysis was performed with SAS 9.3 (SAS Institute, Cary, North Carolina).

RESULTS

From 2004 to 2012, same-day sinus and brain CT examinations per 1000 Medicare beneficiaries were infrequent but increased moderately (+67%) with time from 1.85 (95% CI, 1.78–1.91) in 2004 to 3.08 (95% CI, 3.00–3.15) in 2012 (Fig 1). A peak in same-day examinations was reached in 2010, 3.05 (95% CI, 2.98–3.13) studies per 1000 beneficiaries, followed by a relative plateau through 2012, 2.99 (95% CI, 2.91–3.07) in 2011 and 3.08 (95% CI, 3.00–3.15) in 2012.

With regard to sites of service, small increases in same-day examinations were identified in the physician's office and inpatient hospital settings, from 0.31 (95% CI, 0.29–0.34) to 0.32 (95% CI, 0.3–0.35) (+2.4%) and from 0.45 (95% CI, 0.42–0.49) to 0.52 (95% CI, 0.49–0.55) (+14.3%), respectively. At the same time, the incidence of same-day examinations in the outpatient hospital setting declined moderately, from 0.50 (95% CI, 0.47–0.54) to 0.42 (95% CI, 0.39–0.45) (–16.1%). The biggest contributor to the overall increase in same-day studies was observed in the emergency department, with a cumulative increase of 215.7% from 2004 to 2012, from 0.56 (95% CI, 0.53–0.60) to 1.78 (95% CI, 1.72–1.84). In 2004, 31% of all same-day studies were performed in the ED; in 2012, the ED accounted for 58% of all same-day studies.

With respect to non-same-day services, there was an increase in the overall use of brain CT in the Medicare fee-for-service population from 2004 until 2012, from 146.0 (95% CI, 145.1–146.9) per 1000 beneficiaries in 2004 to 176.3 (95% CI, 175.4–177.2) in 2012 (+21%). However, a plateau was achieved in 2009, after which the number of studies stabilized (Fig 2A). A large percent-

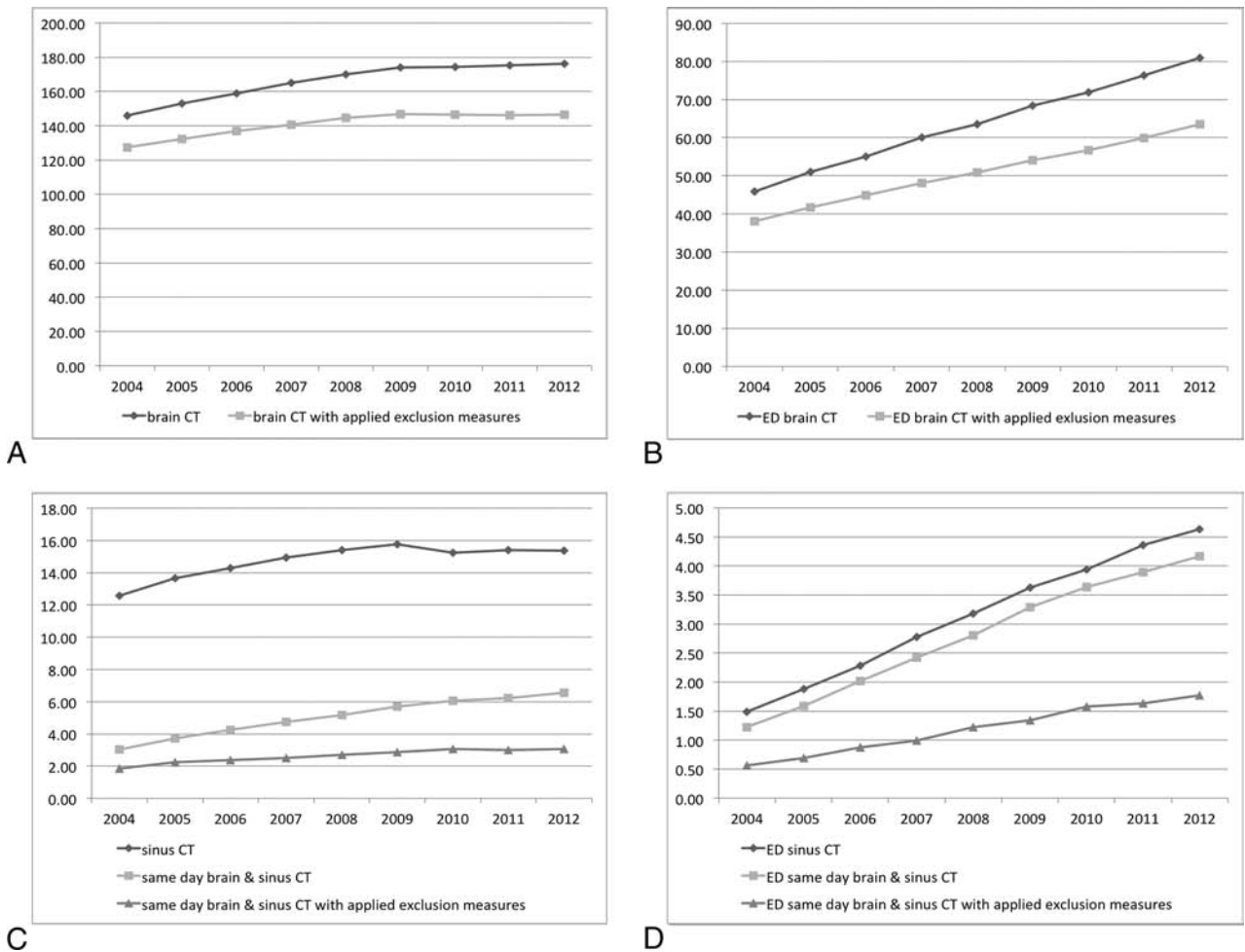


FIG 2. A, All brain CTs and all brain CTs (*dark gray line*) with applied exclusion measures (*light gray line*) per 1000 beneficiaries (A). Brain CTs (*dark gray line*) and brain CTs with applied exclusion criteria (*light gray line*) performed in the ED (B). Sinus CT (*dark gray with rhombs line*) and all same-day brain and sinus CT, without and with exclusion measures applied, totals are shown in C, and those performed in the ED in D. Exclusion measures are CTs that were performed for indications such as trauma, infection, or neoplasm.

age of those studies were performed for a diagnosis other than trauma, infection, or tumor (Fig 2A, 87% in 2004 versus 83% in 2012, -5%). Brain CTs performed in the ED showed a steady increase from 2004 to 2012, from 45.8 (95% CI, 45.5–46.2) per 1000 beneficiaries in 2004 to 80.9 (95% CI, 80.4–81.4) in 2012 (+76.5%). Similar to these findings, though slightly less pronounced, was the number of studies performed for diagnoses other than trauma, infection, or tumor, from 38.1 (95% CI, 37.7–38.4) per 1000 beneficiaries in 2004 to 63.6 (95% CI, 63.2–64.0) in 2012 (+67%), as illustrated in Fig 2B.

The growing use of sinus CT overall slowed in 2009, from 12.6 (95% CI, 12.4–12.8) per 1000 beneficiaries in 2004 to 15.4 (95% CI, 15.2–15.6) in 2012 (+22%); then, it plateaued until 2012 (Fig 2C). However, the frequency of sinus CT performed in the ED continued to increase, from 1.5 (95% CI, 1.4–1.6) per 1000 beneficiaries in 2004 to 4.6 (95% CI, 4.6–4.8) in 2012 (+211%; Fig 2D). Overall, only a minority of all sinus CTs were performed on the same day as brain CT. In the ED setting, in contrast, most sinus CTs were performed with a same-day brain CT (Fig 2C, -D). Although a number of these studies were performed for trauma, infection, or tumor (“exclusion measures” as designated by CMS), a substantial portion of same-day brain CTs and sinus CTs

were performed for other indications (gray line with triangles in Fig 2D) from 0.6 (95% CI, 0.5–0.6) per 1000 beneficiaries in 2004 to 1.8 (95% CI, 1.7–1.8) in 2012 (+216%).

DISCUSSION

Although the frequency of same-day sinus and brain CT imaging in the Medicare fee-for-service population is low, it did, in fact, increase in the years leading up to the early stages of implementation of a specific Medicare metric program designed to identify and curb such same-day examinations, supporting the rationale for such an initiative. In the 2 years from metric testing until actual implementation, the frequency of same-day studies plateaued. While we are unable to attribute causation to the OP-14 initiative, our results, nonetheless, suggest that gains are being made in achieving desired testing behavior in accordance with the goals of Medicare. This trend parallels the national stabilization in the use of sinus and brain CT examinations overall (ie, not necessarily on the same day), which began in 2009, suggesting a greater overall awareness of appropriateness in general, which may, in part, be related to concerns about rising costs.

Related to these trends is a new societal emphasis on patient radiation exposure. The effort of professional organizations to

reduce radiation doses, such as the Image Wisely campaign,¹¹ as well as public awareness and media attention¹² to the potentially harmful side effects of ionizing radiation, may also be impacting effort to reduce use and, therefore, overall population dose. While our study cannot directly link increased radiation awareness to the slowing of growth in medical imaging, it likely contributed to at least part of the decline in imaging studies.

When identifying potential reasons for the increase of same-day studies up to the rollout of the OP-14 policy initiative of Medicare, the most remarkable contributions to overall growth were those performed in the ED setting. Of note, OP-14 applies specifically to the hospital outpatient setting, but the changes in that setting parallel those in all other settings except for the ED. The reasons for this trend and the ED divergence are multifactorial and can only be partially explained by our work. Despite the stabilization in the overall use of sinus and brain CT imaging since 2009, volume in the ED for CT overall continues to rise.¹³ Our observations for sinus and brain imaging parallel this overall discordant trend, which may, in part, explain the continued increased same-day sinus and brain CT imaging in the ED setting. The national trends reported by Levin et al¹³ used aggregated (ie, no patient-specific information) claims data. Our use of more detailed claims-level data permitted us to examine reported indications for individual examinations, providing additional perspectives. Many simultaneous ED examinations, for example, were ordered in the setting of trauma, infection, or tumor. In such situations, same-day examinations are more appropriate because they include clinical scenarios other than generic headache, such as suspected or known masses involving the paranasal sinuses, face, nasopharynx, or skull base and suspected intracranial extension of infectious processes involving the sinuses.

Nonetheless, almost half of same-day sinus and brain CT scans were not ordered for these 3 specific recognized groups of indications. While our study was not designed to investigate other indications, we can propose several potential explanations.

In our study, we applied exclusion measures for patients with trauma, infection, or tumor on the basis of the ICD codes detailed in the OP-14 criteria, to exclude studies from our analysis that clearly warrant both a sinus and a head CT. Using exclusion criteria based on ICD codes, however, has limitations. While primary ICD codes incorporate the main diagnoses, many additional diagnoses may exist but not be captured through the ICD coding system because coders may focus on only key diagnoses necessary to establish medical necessity in the eyes of a payer. For example, a patient might have a syncopal event with a fall and present to the ED to evaluate presenting symptoms of dizziness. The ED provider may have ordered a sinus CT and brain CT as part of a minor trauma work-up. The traumatic event, however, may not have been captured by the ICD coding, which only included the syncope and/or altered mental status. An additional limitation is that by using administrative claims data, actual sites of service cannot be verified; we thus relied on self-reported sites of service. Because some patients in the ED are subsequently hospitalized, some ED claims could be erroneously reported by using the inpatient hospital setting as the site of service, thus underestimating ED volumes.

Another indication that may account for same-day sinus and

brain CT imaging outside the context of trauma, infection, and tumor is headache. Wang and You¹⁴ found that approximately one-quarter of patients without trauma who underwent brain CT in the ED presented with headaches. Because sinusitis is a frequent source of headaches, many same-day studies may have been performed to investigate both the sinuses and brain as causes of headaches, resulting in unnecessary duplicate examinations. Educating ordering physicians that portions of the paranasal sinuses could be covered on routine brain CT examinations or adjusting sinonasal coverage on brain CTs when sinusitis is of clinical concern could help decrease the frequency of duplicate examinations in the work-up of headache. On the other hand, increasing effort to limit the radiation dose to the lens on routine head CT examinations by patient positioning and gantry tilt leads to decreased paranasal sinus coverage, which further underpins the need to tailor the imaging protocols to the clinical and anatomic ROIs.

Independent of the clinical scenarios leading to the ordering of same-day sinus and brain CT examinations, our data clearly demonstrate that the ED is the setting most responsible for the recent increase in simultaneous sinus and brain CT imaging. Multiple studies have already demonstrated an increased use of brain CT in the ED for minor head trauma.¹⁵⁻¹⁸ Emergency physicians are exposed to growing pressure to address increasing patient loads despite ongoing demands for faster turnaround times and quicker ED and hospital discharges. This likely leads ED physicians to rely more heavily on imaging to achieve quicker diagnoses. While there is no easy solution for this problem, better communication between emergency physicians and radiologists with closer interaction through increasing physical proximity may help both specialties in collaborating to ensure the most appropriate use of imaging for the work-up of patients in the ED.¹⁹ Growing as well are clinical decision-support tools, which may help emergency physicians more effectively leverage finite imaging resources.^{20,21}

We acknowledge certain limitations to our study. First, the datasets included in our study are from 2004 to 2012 and do not include the recent years 2013 and 2014, which were not available to the authors for analysis at the time of publication. Omitting these data points clearly limits the ability of this study to report on the long-term effects of the OP-14 measure on the performance of same-day brain and sinus CTs. Second, the descriptive methodology of this publication limits the ability to attribute causation to the changes in same-day brain and sinus imaging. Further studies that include more longitudinal data points and incorporate regression-based models may be necessary to prove such causation.

CONCLUSIONS

Same-day brain and sinus CT scans in the Medicare population increased until the year 2009 when a plateau was reached, which coincided with the implementation of targeted measures by CMS to reduce imaging over-utilization. While no causal relationship between the CMS measure and the plateauing of same-day studies could be established, emergency departments were identified as the biggest driver of same-day examinations. Targeted strategies to reduce same-day orders out of the emergency room may have a significant impact for future appropriate imaging utilization.

REFERENCES

1. Cassel CK, Guest JA. **Choosing wisely: helping physicians and patients make smart decisions about their care.** *JAMA* 2012;307:1801–02 CrossRef Medline
2. Iglehart JK. **The new era of medical imaging—progress and pitfalls.** *N Engl J Med* 2006;354:2822–28 CrossRef Medline
3. Iglehart JK. **Health insurers and medical-imaging policy: a work in progress.** *N Engl J Med* 2009;360:1030–37 CrossRef Medline
4. Brenner DJ, Hall EJ. **Computed tomography: an increasing source of radiation exposure.** *N Engl J Med* 2007;357:2277–84 CrossRef Medline
5. Tax Relief and Health Care Act of 2006, Pub L No. 109-432 (2006)
6. Medicare.gov Hospital Compare. <http://www.medicare.gov/hospitalcompare/search.html>. Accessed January 5, 2015
7. Bogdanich W, McGinty JC. **Medicare claims show overuse of CT scanning.** *New York Times*. June 17, 2011. <http://www.nytimes.com/2011/06/18/health/18radiation.html>. Accessed January 5, 2015
8. Rosenkrantz AB, Doshi A. **Characterizing the performance of the nation's hospitals in the Hospital Outpatient Quality Reporting Program's imaging efficiency measures.** *J Am Coll Radiol* 2015;12:166–73 CrossRef Medline
9. Duszak R Jr, Allen B Jr, Hughes DR, et al. **Emergency department CT of the abdomen and pelvis: preferential utilization in higher complexity patient encounters.** *J Am Coll Radiol* 2012;9:409–13 CrossRef Medline
10. Levin DC, Rao VM, Parker L. **Physician orders contribute to high-tech imaging slowdown.** *Health Aff (Millwood)* 2010;29:189–95 CrossRef Medline
11. Brink JA, Amis ES Jr. **Image wisely: a campaign to increase awareness about adult radiation protection.** *Radiology* 2010;257:601–02 CrossRef Medline
12. Bogdanich W. **Radiation boom: newspaper series.** 2010–2015. *New York Times*. March 17, 2015. http://topics.nytimes.com/top/news/us/series/radiation_boom/index.html. Accessed January 5, 2015
13. Levin DC, Rao VM, Parker L, et al. **Continued growth in emergency department imaging is bucking the overall trends.** *J Am Coll Radiol* 2014;11:1044–47 CrossRef Medline
14. Wang X, You JJ. **Head CT for nontrauma patients in the emergency department: clinical predictors of abnormal findings.** *Radiology* 2013;266:783–90 CrossRef Medline
15. Haydel MJ, Preston CA, Mills TJ, et al. **Indications for computed tomography in patients with minor head injury.** *N Engl J Med* 2000;343:100–05 CrossRef Medline
16. Jagoda AS, Bazarian JJ, Bruns JJ Jr, et al; American College of Emergency Physicians, Centers for Disease Control and Prevention. **Clinical policy: neuroimaging and decision making in adult mild traumatic brain injury in the acute setting.** *Ann Emerg Med* 2008;52:714–48 CrossRef Medline
17. Smits M, Dippel DW, de Haan GG, et al. **External validation of the Canadian CT Head Rule and the New Orleans Criteria for CT scanning in patients with minor head injury.** *JAMA* 2005;294:1519–25 CrossRef Medline
18. Stiell IG, Clement CM, Rowe BH, et al. **Comparison of the Canadian CT Head Rule and the New Orleans Criteria in patients with minor head injury.** *JAMA* 2005;294:1511–18 CrossRef Medline
19. Tillack AA, Borgstede JP. **An evaluation of the impact of clinically embedded reading rooms on radiologist-referring clinician communication.** *J Am Coll Radiol* 2013;10:368–72 CrossRef Medline
20. Blackmore CC, Mecklenburg RS, Kaplan GS. **Effectiveness of clinical decision support in controlling inappropriate imaging.** *J Am Coll Radiol* 2011;8:19–25 CrossRef Medline
21. Zafar HM, Mills AM, Khorasani R, et al. **Clinical decision support for imaging in the era of the Patient Protection and Affordable Care Act.** *J Am Coll Radiol* 2012;9:907–18.e5 CrossRef Medline

Nonmotor Functions of the Cerebellum: An Introduction

A.P. Klein, J.L. Ulmer, S.A. Quinet, V. Mathews, and L.P. Mark

The concept of nonmotor functions of the cerebellum (little cerebrum)¹ is an intriguing proposal that has garnered little attention in the past but has become a relatively recent focal point for neuroscience investigators. The preponderance of anatomic and clinical evidence supporting the traditional view of the cerebellum as a motor mechanism has understandably overwhelmed the sporadic reports of behavioral and intellectual dysfunction associated with cerebellar pathology during the 19th and most of the 20th century.²⁻⁷ Developments during the past 25 years, coinciding with the development of functional MR imaging, however, have greatly increased our awareness and understanding of cerebellar cognitive functions. Neuroimaging in conjunction with anatomic and clinical investigations is helping to cultivate new ways of thinking about cerebellar organization and function. This vignette will introduce some of these major observations of nonmotor cerebellar functions from a neuroradiologic perspective.

The correlation of cerebellar function and morphology has been a long-standing mystery that raises interesting questions. Although the cerebellum accounts for only about 10% of the mass of the brain, why does it contain as many neurons as all the rest of the central nervous system combined?¹ Does this imply the existence of underappreciated functions beyond modulation of motor activities? Why did the lateral aspect of the human cerebellum, the cerebellar hemispheres, undergo enormous enlargement during the course of human evolution?⁸ Furthermore, why did this lateral cerebellar growth seem to parallel the evolutionary enlargement of the prefrontal cortex?^{9,10} Functional MR imaging combined with clinical observations provide a novel backdrop to frame the answers.

More recent concepts of cerebellar organization provide a more complete picture of the cerebellum. The traditional morphologic description of the cerebellum subdivides it into lobes, lobules, and zones (Fig 1). The phylogenetic description cate-

gorizes the cerebellum into the vestibulocerebellum (archicerebellum), spinocerebellum (paleocerebellum), and cerebrocerebellum (neocerebellum) (Fig 2).¹¹ The oldest portion, the vestibulocerebellum, primarily receives input fibers from the vestibular system. The phylogenetically intermediate component, the spinocerebellum, receives fiber input directly from the spinal cord. The newest part, the cerebrocerebellum, receives input from many different areas of the cerebral cortex. Interesting observations from fMRI studies, however, offer a different type of cerebellar organization based on function. Mapping of cognitive functions shows a lateral cerebellar distribution, while the sensorimotor cerebellar functions are more medially located (Fig 3).¹² This medial-to-lateral functional gradient also applies to the group of 3 deep cerebellar nuclei (fastigial; interposed, consisting of the globose and emboliform nuclei; and dentate). The cognitive functions of the cerebellum, therefore, are primarily distributed in the lateral aspect of the neocerebellum and ventral lateral aspect of the dentate nuclei.¹³ These same areas have shown an enormous increase in size during hominid evolutionary development, correlating with similar unusually large increases in prefrontal and association cortices during the same phylogenetic period.^{14,15} The mapping of associative learning with emotional, motor, and cognitive functions also reveals a medial-to-lateral cerebellar distribution (Fig 4).¹⁶

Asymmetry of cerebellar functions is another interesting feature exposed by lesion and fMRI investigations. Language, for instance, lateralizes to the right posterior cerebellar hemisphere (in individuals who are left cerebral hemisphere language dominant), and visuospatial function lateralizes to the left posterior hemisphere.^{17,18} Executive functions, however, seem to be bilateral, while affective functions are primarily midline in the so-called “limbic cerebellum” (Fig 5). In addition, recent resting-state functional connectivity studies that explored functional coupling showed asymmetrically organized cerebral cortical networks in which functional coupling is stronger on one side of the brain than the other. A fascinating corollary observation is the parallel-though-reversed asymmetry of that functional coupling in the cerebellum.¹⁹ In other words, the cerebellum not only reflects a homotopic map of the cerebral cortex but also the asymmetric functional organization of the cerebrum. These discoveries, therefore, not only demonstrate the novel

From the Medical College of Wisconsin, Department of Radiology, Neuroradiology Section, Froedtert Hospital, Milwaukee, Wisconsin.

Please address correspondence to Leighton P. Mark, MD, Department of Radiology, Neuroradiology Section, Froedtert Hospital, 9200 West Wisconsin Ave, Milwaukee, WI 53226; e-mail: lmark@mcw.edu

<http://dx.doi.org/10.3174/ajnr.A4720>

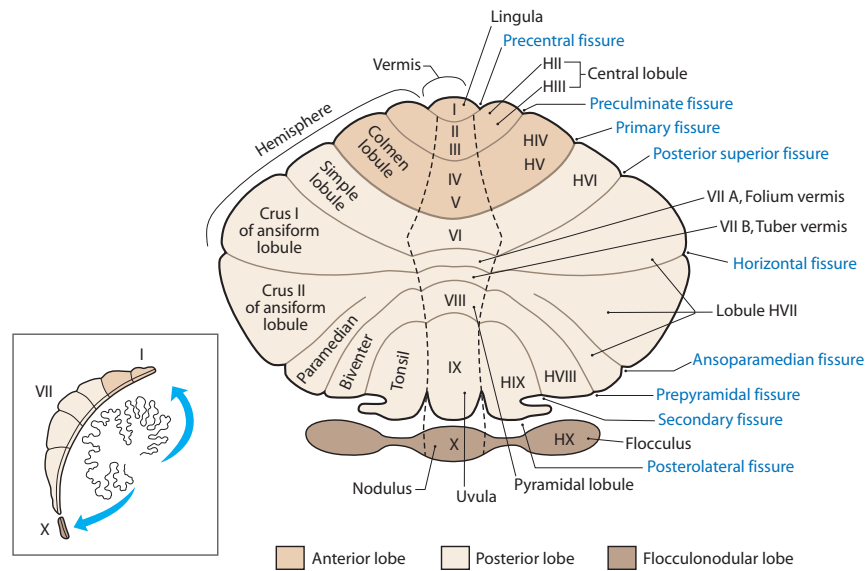


FIG 1. Unfolded view of the cerebellar cortex showing the lobes, lobules (by name on the right and number on the left), and main fissures (blue font). The hemispheric lobules are designated with the prefix H followed by the Roman numeral indicating their corresponding vermicular lobules. Adapted from Haines DE. *Fundamental Neuroscience for Basic and Clinical Applications*. 4th ed. Philadelphia: Elsevier/Saunders; 2013 with permission of Elsevier.³⁰

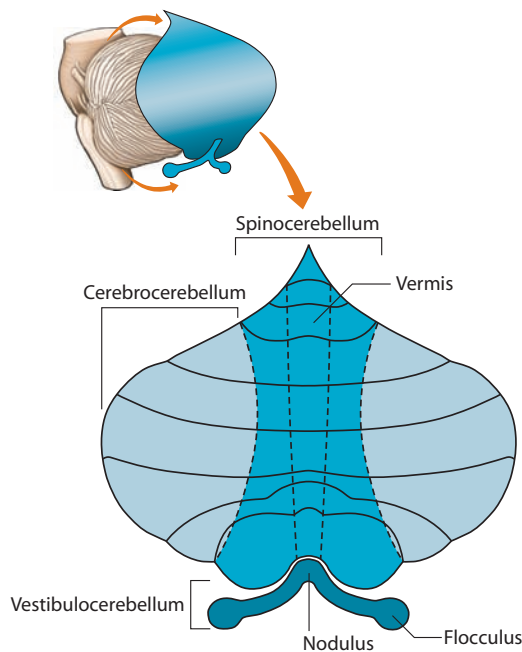


FIG 2. The cerebrocerebellum is the phylogenetically newest and largest portion of the cerebellum. It primarily receives input indirectly from many cerebral cortical areas. The spinocerebellum occupies the median and paramedian zone of the cerebellum and receives input directly from the spinal cord. The vestibulocerebellum is the phylogenetically oldest part of the cerebellum, and it receives input from the vestibular nuclei of the brain stem. Adapted with permission from Purves et al.¹¹

concept of nonmotor cerebellar functions but also a particular set pattern of organization of those functions within the cerebellum.

A closer examination of the functional maps of the cerebellum reveals even greater levels of detailed organization.²⁰ The motor tasks of the foot, hand, and face, for instance, demonstrate a somatotopic distribution predominantly at the medial aspect of the

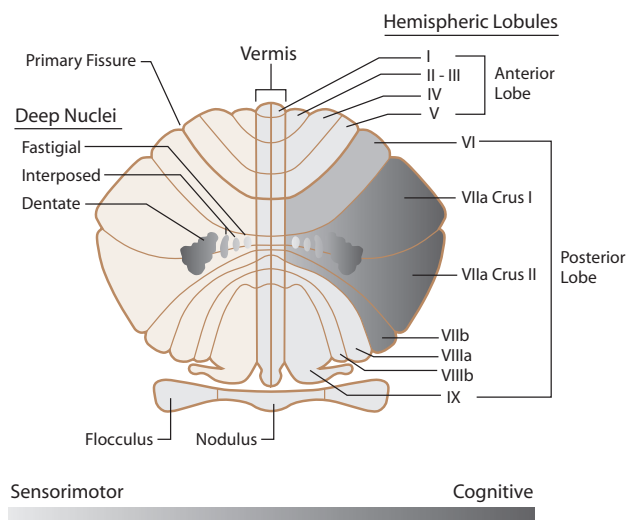


FIG 3. Unfolded view of the cerebellum illustrating sensorimotor-to-cognitive functions distributed in a gradient-like fashion from medial to lateral. The sensorimotor functions are distributed more toward the midline, while the cognitive functions are located more laterally in the cerebellar hemispheres. The same medial-to-lateral organization is seen in the corresponding cerebellar nuclei. Adapted with permission from Fatemi et al.¹²

anterior lobe of the cerebellum, but surprisingly, this same somatotopic relationship is also reflected in a mirror image fashion in the posterior lobe (Fig 6). When cerebellar maps of the cerebral association cortices are included on a sagittal view of the left cerebellar hemisphere, several broad organizing principles become evident (Fig 7). Most of the cerebellum between the anterior and posterior lobe motor areas maps to cerebral association areas.²⁰⁻²³ The amount of cerebellum dedicated to a particular cerebral network is proportional to the size of that cerebral network. In other words, large cerebral networks are coupled to correspondingly large cerebellar territories. The only exceptions are the primary visual and auditory cortices, which are not represented in the

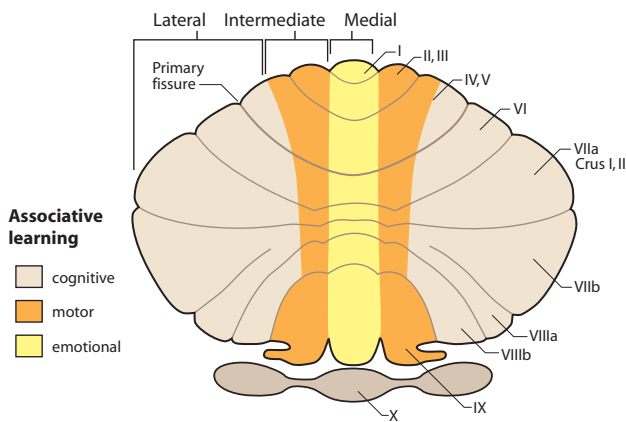


FIG 4. Unfolded view of the cerebellum demonstrating associative learning with emotional tasks located in the medial zone (yellow). Motor tasks locate to the intermediate zone (orange), and cognitive tasks occupy most of the cerebellar hemisphere in the lateral zone (beige). Adapted from Timmann D, Drepper J, Frings M, et al. The human cerebellum contributes to motor, emotional and cognitive associative learning: a review. *Cortex* 2010;46:845–57 with permission of Elsevier.¹⁶

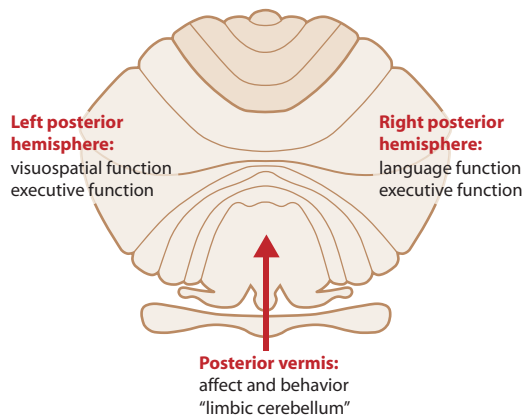


FIG 5. Unfolded view of the cerebellum showing the asymmetric distribution of some cerebellar functions. The right cerebellar hemisphere is associated with language, and the left cerebellar hemisphere, with visuospatial functions. Executive functions, including verbal working memory, are related to both hemispheres. Attention is also a neocerebellar function. The vermis or "limbic cerebellum" is involved in modulating affective behavior. Adapted from Konczak J, Timmann D. The effect of damage to the cerebellum on sensorimotor and cognitive function in children and adolescents. *Neurosci Biobehav Rev* 2007;31:1101–13 with permission of Elsevier.¹⁷

human cerebellum. Figure 7 shows the primary cerebellar map with motor functions in the anterior lobe followed by representations of premotor networks, executive control networks, and then limbic-association networks, sometimes also referred to as the default network. The secondary map continues around the cerebellum in reverse order with a flipped representation of the primary map. Crura I and II form the junction between the primary and secondary maps. A map of the entire cerebellum also provides an important overview (Fig 8). Most of the human cerebellum maps to association areas rather than the motor cortex. Those association areas also include executive control networks and the default network. This pattern of distribution of cerebellar functions implies that most of the cerebellum is coupled to nonmotor functions paralleling the evolutionary development of the large

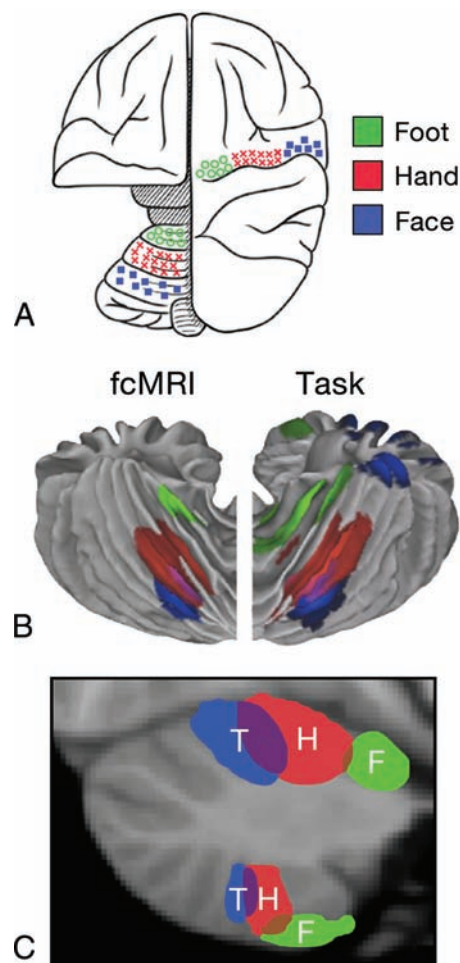


FIG 6. A, Schematic demonstration of the cerebral and cerebellar functional locations of the foot (green), hand (red), and face (blue) in the monkey. B, Cerebellar locations of the foot (green), hand (red), and tongue (blue) in humans measured by fMRI. "fcMRI" refers to results based on functional connectivity studies. "Task" refers to results from task-based fMRI studies. C, Cerebellar locations of foot (F, green), hand (H, red), and tongue (T, blue) representations in humans from fcMRI studies displayed on a parasagittal image. Note the mirror image representation of the somatomotor functions with the primary or dominant location in the anterior lobe of the cerebellum. Adapted from Buckner RL. The cerebellum and cognitive function: 25 years of insight from anatomy and neuroimaging. *Neuron* 2013;80:807–15 with permission of Elsevier.³¹

nonmotor portions of the cerebrum, prefrontal, and association cortices.

Perhaps the most challenging basic issue for neuroradiologists is accommodating to the novel and perhaps astonishing idea that the cerebellum has fundamental cognitive and emotional functions, let alone the equally astonishing proposal that most functions of the cerebellum may be cognitive rather than motor in nature. Considerable clinical evidence supports the concept of cerebellar pathology associated with cognitive and psychiatric illnesses. Schmahmann^{24,25} was the first to propose the idea of a "dysmetria of thought" due to cerebellar dysfunction. This concept refers to the significant role of the cerebellum in sensory, cognitive, and affective processing. The "cerebellar cognitive affective syndrome" proposed by Schmahmann²⁶ has proved to be clinically significant in disease recognition and understanding. The litany of other psychiatric disorders now associated with cer-

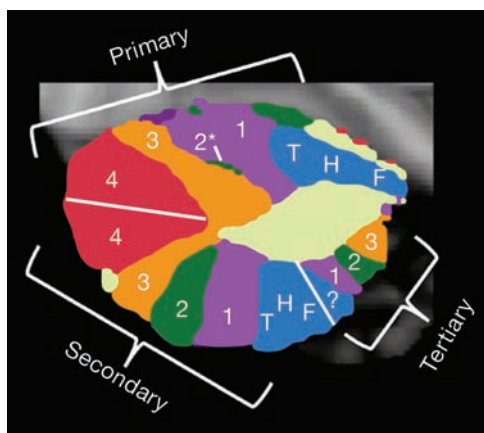


FIG 7. Topographic map of various cerebellar functions displayed on a parasagittal view of the left cerebellar hemisphere. The primary cerebellar distribution of cerebral functions is an orderly map of the somatomotor functions of the foot, hand, and tongue (blue) in the anterior lobe followed by a hierarchy of association cortices labeled 1–4 (magenta, green, orange, red) on the superior surface of the cerebellum. An inverted secondary representation in reverse order is seen on the inferior cerebellar surface. A small tertiary representative map is hypothesized to be present in the posterior lobe as well. Adapted from Buckner RL. The cerebellum and cognitive function: 25 years of insight from anatomy and neuroimaging. *Neuron* 2013;80:807–15 with permission of Elsevier.³¹

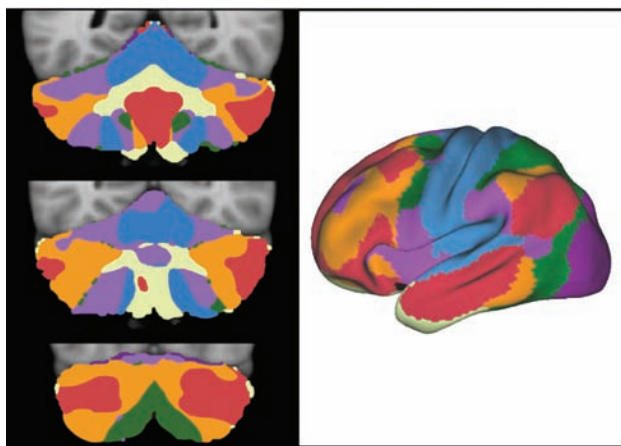


FIG 8. The 3 images on the left represent multiple coronal sections of the cerebellum with colors representing different cortical functions. The right-sided image is the cerebellum with the colors representing the different functional areas. The somatomotor cortex is blue. This cortex is represented at the more medial aspect of the cerebellum. Most of the human cerebellum, however, is linked to cerebral association networks, including executive networks (orange) and the default network (red). These association networks have multiple cerebellar representations. Adapted from Buckner RL. The cerebellum and cognitive function: 25 years of insight from anatomy and neuroimaging. *Neuron* 2013;80:807–15 with permission of Elsevier.³¹

ebellar pathology includes bipolar disorder, posttraumatic stress disorder, attention deficit autism spectrum disorders, and schizophrenia.^{12,27} Many physicians, however, remain skeptical about cognitive impairment due to cerebellar lesions. Part of this skepticism may be due to the lack of sensitivity of most traditional tests to evaluate cerebellar function because those tests were mostly designed to detect motor abnormalities.²⁸ Another part may be a lack of awareness/understanding of the precise nature of the more

nuanced functional abnormalities to look for on the clinical examination of cerebellar functions. Even so, not everyone is convinced of cerebellar cognitive functions, and some effectively express a healthy skepticism.²⁹ For most neuroradiologists engaged in fMRI studies, however, the cerebellar activation observed during functional testing that was once dismissed as an aberration or an exercise in technical rationalization should now be viewed with a more critical eye.

The next Functional Vignette will review some of the important anatomic pathways that correlate with the cognitive functions of the cerebellum.

Disclosures: Vincent Mathews—UNRELATED: Grants/Grants Pending: GE Clinical Trial,* National Institutes of Health,* Comments: both pending; Payment for Lectures (including service on Speakers Bureaus); Eli Lilly, Comments: Amyvid Speakers Bureau in 2013. *Money paid to the institution.

REFERENCES

- Nolte J. *The Human Brain: An Introduction to its Functional Anatomy*. 6th ed. Philadelphia: Mosby/Elsevier; 2009
- Combettes M. **Absence complète du cervelet, des pédoncules postérieurs et de la protubérance cérébrale chez une jeune fille morte dans sa onzième année.** *Bull Soc Anat Paris* 1831;5:10
- Holmes G. **A form of familial degeneration of the cerebellum.** *Brain* 1907;30:23
- Babinski J. *Expos des Travaux Scientifiques*. Paris: Masson; 1913
- Holmes G. **The symptoms of acute cerebellar injuries due to gunshot injuries.** *Brain* 1917;40:461–534
- Holmes G. **Clinical symptoms of cerebellar disease and their interpretation.** *Lancet* 1922;2:59–65
- Adrian ED. **Afferent areas in the cerebellum connected with the limbs.** *Brain* 1943;66:289–315 CrossRef
- Dow RS. **The evolution and anatomy of the cerebellum.** *Biol Rev Camb Philos Soc* 1942;17:179–220 CrossRef
- Passingham RE. **Changes in the size and organisation of the brain in man and his ancestors.** *Brain Behav Evol* 1975;11:73–90 CrossRef Medline
- Passingham RE, Wise S. *The Neurobiology of the Prefrontal Cortex. Anatomy, Evolution and the Origin of Insight*. London: Oxford University Press; 2012
- Purves D, Augustine GJ, Fitzpatrick D, et al. *Neuroscience*. 4th ed. Sunderland: Sinauer Associates; 2008
- Fatemi SH, Aldinger KA, Ashwood P, et al. **Consensus paper: pathological role of the cerebellum in autism.** *Cerebellum* 2012;11:777–807 CrossRef Medline
- Leiner HC, Leiner AL, Dow RS. **Cognitive and language functions of the human cerebellum.** *Trends Neurosci* 1993;16:445–47 Medline
- Matano S. **Brief communication: proportions of the ventral half of the cerebellar dentate nucleus in humans and great apes.** *Am J Phys Anthropol* 2001;114:163–65 Medline
- Schneider GE. *Brain Structure and Its Origins in Development and in Evolution of Behavior and the Mind*. Cambridge: MIT Press; 2014
- Timmann D, Drepper J, Frings M, et al. **The human cerebellum contributes to motor, emotional and cognitive associative learning: a review.** *Cortex* 2010;46:845–57 CrossRef Medline
- Konczak J, Timmann D. **The effect of damage to the cerebellum on sensorimotor and cognitive function in children and adolescents.** *Neurosci Biobehav Rev* 2007;31:1101–13 CrossRef Medline
- Murdoch BE. **The cerebellum and language: historical perspective and review.** *Cortex* 2010;46:858–68 CrossRef Medline
- Wang D, Buckner RL, Liu H. **Cerebellar asymmetry and its relation to cerebral asymmetry estimated by intrinsic functional connectivity.** *J Neurophysiol* 2013;109:46–57 CrossRef Medline
- Buckner RL, Krienen FM, Castellanos A, et al. **The organization of the human cerebellum estimated by intrinsic functional connectivity.** *J Neurophysiol* 2011;106:2322–45 CrossRef Medline

21. Habas C, Kamdar N, Nguyen D, et al. **Distinct cerebellar contributions to intrinsic connectivity networks.** *J Neurosci* 2009;29:8586–94 CrossRef Medline
22. Krienen FM, Buckner RL. **Segregated fronto-cerebellar circuits revealed by intrinsic functional connectivity.** *Cereb Cortex* 2009;19:2485–97 CrossRef Medline
23. O'Reilly JX, Beckmann CF, Tomassini V, et al. **Distinct and overlapping functional zones in the cerebellum defined by resting state functional connectivity.** *Cereb Cortex* 2010;20:953 CrossRef Medline
24. Schmahmann JD. **An emerging concept: the cerebellar contribution to higher function.** *Arch Neurol* 1991;48:1178–87 CrossRef Medline
25. Schmahmann JD. **Dysmetria of thought: clinical consequences of cerebellar dysfunction on cognition and affect.** *Trends Cog Sci* 1998;2:362–71 CrossRef
26. Schmahmann JD. **Disorders of the cerebellum: ataxia, dysmetria of thought, and the cerebellar cognitive affective syndrome.** *J Neuropsychiatry Clin Neurosci* 2004;16:367–78 CrossRef Medline
27. Shakiba A. **The role of the cerebellum in neurobiology of psychiatric disorders.** *Neurol Clin* 2014;32:1105–15 CrossRef Medline
28. Noroozian M. **The role of the cerebellum in cognition: beyond coordination in the central nervous system.** *Neurol Clin* 2014;32:1081–104 CrossRef Medline
29. Glickstein M. **What does the cerebellum really do?** *Curr Biol* 2007;17:R824–27 CrossRef Medline
30. Haines DE. *Fundamental Neuroscience for Basic and Clinical Applications*. 4th ed. Philadelphia: Elsevier/Saunders; 2013
31. Buckner RL. **The cerebellum and cognitive function: 25 years of insight from anatomy and neuroimaging.** *Neuron* 2013;80:807–15 CrossRef Medline

Autoimmune Comorbidities Are Associated with Brain Injury in Multiple Sclerosis

R. Zivadinov, B. Raj, M. Ramanathan, B. Teter, J. Durfee, M.G. Dwyer, N. Bergsland, C. Kolb, D. Hojnacki, R.H. Benedict, and B. Weinstock-Guttman



ABSTRACT

BACKGROUND AND PURPOSE: The effect of comorbidities on disease severity in MS has not been extensively characterized. We determined the association of comorbidities with MR imaging disease severity outcomes in MS.

MATERIALS AND METHODS: Demographic and clinical history of 9 autoimmune comorbidities confirmed by retrospective chart review and quantitative MR imaging data were obtained in 815 patients with MS. The patients were categorized on the basis of the presence/absence of total and specific comorbidities. We analyzed the MR imaging findings, adjusting for key covariates and correcting for multiple comparisons.

RESULTS: Two hundred forty-one (29.6%) study subjects presented with comorbidities. Thyroid disease had the highest frequency ($n = 97$, 11.9%), followed by asthma ($n = 41$, 5%), type 2 diabetes mellitus ($n = 40$, 4.9%), psoriasis ($n = 33$, 4%), and rheumatoid arthritis ($n = 22$, 2.7%). Patients with MS with comorbidities showed decreased whole-brain and cortical volumes ($P < .001$), gray matter volume and magnetization transfer ratio of normal-appearing brain tissue ($P < .01$), and magnetization transfer ratio of gray matter ($P < .05$). Psoriasis, thyroid disease, and type 2 diabetes mellitus comorbidities were associated with decreased whole-brain, cortical, and gray matter volumes ($P < .05$). Psoriasis was associated with a decreased magnetization transfer ratio of normal-appearing brain tissue ($P < .05$), while type 2 diabetes mellitus was associated with increased mean diffusivity ($P < .01$).

CONCLUSIONS: The presence of comorbidities in patients with MS is associated with brain injury on MR imaging. Psoriasis, thyroid disease, and type 2 diabetes mellitus comorbidities were associated with more severe nonconventional MR imaging outcomes.

ABBREVIATIONS: EDSS = Expanded Disability Status Scale; LV = lesion volume; MTR = magnetization transfer ratio; MD = mean diffusivity; NABT = normal-appearing brain tissue; PD = proton density

MS is a chronic immune-mediated disorder that affects the CNS and is characterized by specific clinical and MR imaging findings.¹ Studies have suggested genetic, environmental, and infectious agents as interacting factors influencing the risk for development of MS.^{2,3}

Epidemiologic evidence from the North American Research Committee on Multiple Sclerosis, the large registry containing patient self-reported data, suggests an increased risk for disability progression in individuals with MS who have additional comorbidities.⁴ An increased prevalence of autoimmune- and nonimmune-mediated comorbidities was reported in patients with MS compared with the general population.⁵⁻¹⁴ Examples of the most frequent comorbidities or secondary disorders that co-occur with MS include thyroid disease, rheumatoid arthritis, psoriasis, cardiovascular disorders, depression and anxiety, diabetes mellitus, chronic lung disease, and irritable bowel syndrome, among others.^{4-6,8-10,14,15} The pathogenesis of these associations with MS is unclear at this time but may be linked to a genetic predisposi-

Received October 2, 2015; accepted after revision November 25.

From the, Department of Neurology (R.Z., B.R., J.D., M.G.D., N.B.), Buffalo Neuroimaging Analysis Center, and Department of Neurology (B.T., C.K., D.H., R.H.B., B.W.-G.), Jacobs MS Center, University at Buffalo, State University of New York, Buffalo, New York; MR Imaging Clinical Translational Research Center (R.Z.) and Department of Pharmaceutical Sciences (M.R.), School of Medicine and Biomedical Sciences, State University of New York, Buffalo, New York; and Magnetic Resonance Laboratory (N.B.), IRCCS Don Gnocchi Foundation, Milan, Italy.

Robert Zivadinov, Brian Raj, Bianca Weinstock-Guttman and Murali Ramanathan substantially contributed to the concept and design of the study. Robert Zivadinov drafted the article, while all authors revised it critically for important intellectual content. Robert Zivadinov and Brian Raj performed statistical analysis. All authors had access to the data.

This study was funded by internal resources of the Buffalo Neuroimaging Analysis Center and Department of Neurology, University of Buffalo. In addition, we received support from the National Multiple Sclerosis Society (RG4836A5, RR2007A2) and Department of Defense (MS090122).

Please address correspondence to Robert Zivadinov, MD, PhD, Buffalo Neuroimaging Analysis Center, Department of Neurology, University at Buffalo, School of Medicine and Biomedical Sciences, 100 High St, Buffalo, NY 14203; e-mail: rzivadinov@bnac.net

Indicates open access to non-subscribers at www.ajnr.org

<http://dx.doi.org/10.3174/ajnr.A4681>

tion,^{5,16,17} the presence of a chronic inflammatory condition,¹⁰ environmental factors,¹⁸ and the use of disease-modifying therapy.¹⁹

It has been postulated that CD4+ T-cells of the Th1 phenotype, CD8+ T-cells, and B-cells play a key role in focal and diffuse destruction of the CNS in patients with MS.²⁰ The immune deviation of CD 4+ T-cells into Th1 and Th2 phenotypes has been the subject of many immunologic and epidemiologic studies in MS.^{21,22} In particular, it has been reported that Th1 responses associated with autoimmunity may be attenuated by a Th2 shift.¹³ Several studies reported a positive association of comorbidities in patients with MS when explored from the Th1/Th2 point of view.^{13,22,23} However, some other studies suggested that these associations were related more to a demographic selection bias than a true sharing of immunologic and pathologic processes.¹⁴

Conventional MR imaging examines visible focal inflammatory changes within the CNS. However, it does not capture the true extent of diffuse GM and WM pathology that is mostly undetected in patients with MS and responsible for long-term development of disability progression.²⁴ On the other hand, nonconventional MR imaging techniques are more sensitive biomarkers for measuring these nonfocal pathologic processes associated with tissue damage in the GM and WM and that are better associated with disease severity.²⁴ Some of these techniques include measures of brain atrophy, magnetization transfer imaging, DWI and DTI, MR spectroscopy, and functional MR imaging.

It has been shown that patients with MS with ≥ 1 cardiovascular risk factor have increased lesion burden and more advanced brain atrophy on MR imaging.^{25,26} However, it is not clear whether the presence of other comorbidities may also influence the severity of conventional and nonconventional MR imaging measures in patients with MS. Therefore, in this large-cohort MS study, we aimed to investigate the impact of autoimmune comorbidities on the severity of conventional and nonconventional MR imaging outcomes in patients with MS.

MATERIALS AND METHODS

Study Population

The study was approved by the institutional review board, and all subjects provided written informed consent.

Clinical, demographic, MR imaging, and comorbidity data were prospectively collected during the New York State Multiple Sclerosis Consortium annual follow-up visit at the Buffalo site. The inclusion criteria for this study were the following: MR imaging examination performed at the time of the clinical visit (± 30 days), 18–70 years of age, Expanded Disability Status Scale (EDSS) score of 0–8.5, diagnosis of MS according to the McDonald criteria,²⁷ and collection of comorbidity information. Exclusion criteria consisted of relapse and steroid treatment in the 30 days preceding study entry and insufficient quality of the MR image for quantitative analysis. Clinical data included the presence, type, and duration of disease-modifying treatment; MS clinical subtype; and disease duration and disability as measured by the EDSS score. Information on autoimmune comorbidities was collected from a questionnaire,²⁸ which was completed at the time of the clinical visit. We included information on the following autoimmune comorbidities: asthma, Crohn disease, type 1 and 2

diabetes mellitus, myasthenia gravis, psoriasis, rheumatoid arthritis, systemic lupus erythematosus, and thyroid disease. The self-report comorbidity information obtained from the questionnaire was cross-examined against the medical record chart review to determine the accuracy of the reported data. Only self-reported comorbidities confirmed by the retrospective chart review were used in the present analyses.

MR Imaging Acquisition

Patients underwent brain MR imaging by using a 1.5T Signa 4x/Lx scanner (GE Healthcare, Milwaukee, Wisconsin) with an 8-channel head and neck coil. Dual-echo proton density (PD)/T2WI, DWI, 3D spoiled gradient-recalled T1WI, spin-echo T1WI with and without gadolinium contrast, FLAIR, PD, and PD with magnetization transfer pulse images were obtained. All images were acquired axially. The PD/T2 sequence was acquired with the following parameters: TE, 30/90 ms; TR, 3000 ms; NEX, 1; echo-train length, 14; FOV, 24×18 cm²; matrix, 192×256 ; 5-mm section thickness with a total of 28 sections; no gap. The 3D T1WI sequence was acquired with the following parameters: FOV, 24×18 cm²; matrix, 192×256 ; 2.5-mm section thickness; 70 sections; no gap; TE, 7 ms; TR, 24 ms; NEX, 1; flip angle, 30°. Axial FLAIR was acquired with the following parameters: FOV, 24×24 cm²; matrix, 192×256 ; 28 sections; 5-mm section thickness; no gap; TE, 128 ms; TI, 2000 ms; TR, 8002 ms; echo-train length, 22; NEX, 1. PD was acquired with the following parameters: FOV, 24×24 cm²; matrix, 192×256 ; 28 sections; 5-mm section thickness; no gap; TE, 12 ms; TR, 1400 ms; NEX 1. A similar PD with magnetization transfer contrast had a 1200-Hz off-resonance pulse. Spin-echo T1WI was acquired with the following parameters: FOV, 24×18 cm²; matrix, 192×256 ; 28 sections; 5-mm section thickness; no gap; TE, 9 ms; TR, 600 ms; NEX, 2, while the gadolinium-enhanced spin-echo T1WI sequence was obtained after injection of a single-dose intravenous bolus (0.1 mmol/Kg of Gd-DTPA) 5 minutes after administration of the contrast agent. Echo-planar imaging was used to obtain T2WI ($b=0$ s/mm²) and DWI ($b=1000$ s/mm²) with the following parameters: FOV, 36×27 cm²; matrix, 128×128 ; 46 sections; 3-mm section thickness; no gap.

MR Imaging Analysis

The image analysis was blinded to patient clinical and sex characteristics. The patients were assessed for a number of conventional and nonconventional MR imaging measures.

Lesion Measures. The T1-, T2-, and gadolinium-lesion volumes (LVs) were calculated by using a highly reproducible, semi-automated local contour-thresholding technique for lesion segmentation.²⁹

Brain Volume Measures. For brain extraction and tissue segmentation, we used the SIENAX 2.6 cross-sectional brain atrophy analysis tool (<http://fsl.fmrib.ox.ac.uk/fsl/fslwiki/SIENAX>).³⁰ Global and tissue-specific normalized volumes were quantified for the whole brain, GM (normalized gray matter volume), WM (normalized white matter volume), cortex (normalized cortical volume), and lateral ventricle volume (normalized lateral ventricle volume).³¹ Images were preprocessed by using an in-house

Table 1: Demographic and clinical characteristics of patients with MS with and without comorbidities^a

	Total Patients with MS (N = 815)	Patients with MS with Comorbidities (n = 241)	Patients with MS without Comorbidities (n = 574)	P Value ^b
Females (No.) (%)	626 (76.8)	201 (83.4)	425 (74.0)	.300
Age (yr) (mean) (SD)	45.7 (10.3)	46.3 (10.4)	45 (10.2)	.082
Disease duration (yr) (mean) (SD)	13.1 (9.4)	13.3 (10)	12.8 (8.8)	.452
EDSS (median) (IQR)	2.5 (1.5–6.0)	2.5 (1.5–5.5)	2.5 (2.0–6.0)	.732
MS subtype (No.) (%)				
RR	554 (67.9)	157 (65.1)	397 (69.2)	.120
SP	227 (27.9)	77 (32.0)	150 (26.1)	
PP	34 (4.2)	7 (2.9)	27 (4.7)	
DMT use (No.) (%)	598 (73.4)	175 (72.6)	423 (73.7)	.900
DMT months (mean) (SD)	48.9 (35.2)	48.8 (35.2)	49 (39.2)	.942

Note:—RR indicates relapsing-remitting; SP, secondary-progressive; PP, primary-progressive; DMT, disease-modifying therapy; IQR, interquartile range.

^a Demographic and clinical characteristics were tested using the χ^2 , Student *t*, and Mann-Whitney rank sum tests.

^b *P* values refer to analyses between patients with MS with and without comorbidities.

developed lesion in-painting technique to minimize the effects of T1 hypointensities on tissue segmentation.

Magnetization Transfer Measures. FLAIR, 3D spoiled gradient-echo T1WI, and PD + magnetization transfer images were coregistered to the PD image. The FLAIR and T1WI lesion masks were used to nullify overt lesions, and the remaining PD was algebraically combined with the coregistered PD + magnetization transfer (MT) images with the following equation: Percentage Magnetization Transfer Ratio (MTR) = [PD – (PD + MT)]/PD × 100 to generate whole-brain (in case the lesions were not nullified), normal-appearing brain tissue (NABT), normal-appearing gray matter, normal-appearing white matter, or T2-LV maps. The mean MTR of the final image was calculated for each tissue class.

Diffusivity Measures. The whole-brain mean diffusivity (MD) was computed from the T2 and DWIs, which were combined to create an MD map by performing the following calculation on each voxel:

$$\bar{D} = (-b/3)\ln(DW/T2)$$

where *DW* represents the average diffusion signal intensity and *T2* represents the T2-weighted signal intensity without the diffusion weighting.

Statistical Analysis

Statistical analysis was performed by using the Statistical Package for the Social Sciences, Version 21.0 (IBM, Armonk, New York).

The comorbidity status of patients with MS was classified on the basis of the presence/absence of comorbidities. The comorbidity status variable (presence or absence) was created for total and specific comorbidities. Demographic and clinical characteristic differences between subjects with and without the presence of comorbidities were tested by using the χ^2 , Student *t*, or Mann-Whitney rank sum test.

To decrease the number of MR imaging variables and statistical tests used in the study, we predetermined primary and secondary MR imaging outcomes for both conventional and nonconventional MR imaging measures. T2-LV, T1-LV, and gadolinium-LV were chosen as primary conventional MR imaging measures because their increase represents accumulation of lesion burden in patients with MS, and normalized brain volume and MTR-NABT were selected as nonconventional MR imaging measures because a normalized brain volume decrease represents an

overall loss of brain tissue and an MTR-NABT decrease is a more specific indicator of severity of demyelination.²⁴ Secondary MR imaging outcomes were used for further characterization of tissue damage and included the following: 1) tissue-specific brain atrophy measures: normalized gray matter volume, normalized white matter volume, normalized cortical volume, and normalized lateral ventricle volume; 2) MTR measures: normal-appearing gray matter, normal-appearing white matter, and T2-LV; and 3) diffusivity measures: whole-brain MD. MR imaging analyses between patients with MS with and without comorbidities and between patients with MS with specific comorbidities and those without any comorbidities were performed by using ANCOVA, adjusted for age, sex, MS subtype, disability status, and the use and duration of disease-modifying treatment. Given the collinearity between age and disease duration, the latter was not used as a covariate.

The Benjamini-Hochberg correction was used to control the false discovery rate for the primary and secondary MR imaging outcome comparisons between patients with MS with and without comorbidities and between patients with MS with specific comorbidities and those without any comorbidities. Differences in secondary MR imaging outcomes were explored only if significant differences were shown among the primary MR imaging outcomes. False discovery rate–corrected *P* values < .05 were considered significant.³²

RESULTS

Demographic and Clinical Characteristics

The demographic and clinical characteristics of the total cohort of subjects with MS (*N* = 815) and those with (*n* = 241) and without (*n* = 574) comorbidities are summarized in Table 1. Of the 815 subjects in the study, 598 (73.4%) were on disease-modifying treatment for a mean of 48.9 months: 88 on glatiramer acetate, 445 on interferon- β , 31 on methotrexate, 25 on intravenous immunoglobulin, 5 on cyclophosphamide, and 4 on azathioprine.

Patients with MS with comorbidities showed a trend toward older age (*P* = .082). Comorbidities were present in 241 (29.6%) study subjects, and 199 of those (82.6%) had 1, whereas 42 (17.4%) had ≥ 2 comorbidities.

The demographic and clinical characteristics of patients with MS with specific comorbidities are shown in Table 2. Among specific comorbidities, thyroid disease showed the highest frequency (*n* = 97, 11.9%), followed by asthma (*n* = 41, 5%), type 2

Table 2: Demographic and clinical characteristics of patients with MS with comorbidities, according to their specific comorbidity type

Disease	Females (No.) (%)	Age (yr) (Mean) (SD)	DD (yr) (Mean) (SD)	EDSS (Median) (IQR)	MS Subtype (No.) (%)			DMT Use (No.) (%)	DMT Months (Mean) (SD)
					RR	SP	PP		
Asthma (<i>n</i> = 41)	38 (92.7)	45.2 (8.8)	12.4 (10.0)	2.5 (1.5–5.0)	32 (78)	7 (17.1)	2 (4.9)	32 (78.0)	51.7 (40.7)
Crohn disease (<i>n</i> = 1)	1 (100)	53	16	3.0	0 (0)	1 (100)	0 (0)	1 (100)	60
Diabetes mellitus type 1 (<i>n</i> = 3)	2 (66.6)	36.3 (4.7)	6.7 (4.2)	2.3 (1.5–2.5)	2 (66.7)	1 (33.3)	0 (0)	0 (0.0)	0 (0)
Diabetes mellitus type 2 (<i>n</i> = 40)	28 (70.0)	49.3 (8.7)	14.5 (9.9)	5.5 (2.0–5.0)	23 (57.5)	16 (40)	1 (2.5)	29 (72.5)	50.9 (40.7)
Myasthenia gravis (<i>n</i> = 1)	1 (100)	47	12	6.5	0 (0)	1 (100)	0 (0)	1 (100)	24
Psoriasis (<i>n</i> = 33)	23 (69.7)	50.4 (9.1)	15.9 (10)	3.0 (2.0–5.5)	21 (63.6)	11 (33.3)	1 (3.1)	24 (72.7)	63.7 (34.2)
Rheumatoid arthritis (<i>n</i> = 22)	17 (77.3)	51.8 (9.1)	16.4 (11.8)	3.0 (1.5–5.5)	13 (59.1)	8 (36.4)	1 (4.5)	17 (77.2)	58.4 (31.4)
SLE (<i>n</i> = 3)	2 (66.6)	50 (3)	15.7 (1.5)	4.0 (4.0–5.0)	0 (0)	3 (100)	0 (0)	3 (100)	50.3 (24.6)
Thyroid disease (<i>n</i> = 97)	89 (91.8)	46.6 (10.6)	14.6 (11.1)	2.5 (1.5–5.5)	66 (68.0)	29 (29.9)	2 (2.1)	68 (70.1)	46.5 (35.2)

Note:—SLE indicates systemic lupus erythematosus; DD, disease duration; RR, relapsing-remitting; SP, secondary-progressive; PP, primary-progressive; DMT, disease-modifying therapy; IQR, interquartile range.

Table 3: Primary and secondary MRI outcomes in patients with MS with and without comorbidities^a

	Patients with MS with Comorbidities (<i>n</i> = 241)	Patients with MS without Comorbidities (<i>n</i> = 574)	<i>P</i> Value
Primary MRI outcomes			
T2-LV	15.7 (15.5)	15.3 (18.2)	.943
T1-LV	2.8 (4.7)	2.6 (4.7)	.955
Gd-LV	0.08 (0.3)	0.1 (0.4)	.992
NBV	1451.1 (97.3)	1481 (86.4)	<.001 ^b
MTR-NABT	34.1 (5.1)	35.3 (5)	.01 ^b
Secondary MRI outcomes			
NGMV	722.8 (86.9)	747.9 (81.5)	.01 ^b
NWMV	728.3 (86.7)	732.6 (64)	.311
NCV	537.1 (67.3)	557.6 (62.8)	<.001 ^b
NLVV	47.5 (20.6)	45.3 (20.5)	.528
MTR-NAGM	31.1 (5.5)	32.3 (5.1)	.045 ^b
MTR-NAWM	37.1 (5.3)	38.1 (4.9)	.105
MTR-T2-LV	32.3 (4.8)	32.8 (5.1)	.650
MD × 10 ³	1.26 (0.29)	1.22 (0.22)	.136

Note:—Gd indicates gadolinium; NWMV, normalized white matter volume; NLVV, normalized lateral ventricle volume; NAGM, normal-appearing gray matter; NBV, normalized brain volume; NGMV, normalized gray matter volume; NCV, normalized cortical volume; NAWM, normal appearing-white matter.

^a The data are expressed as mean and SD. Volumes are expressed in milliliters. MTR values are expressed as percentage units. MD is expressed as mm²/s. Analysis of covariance, adjusted for age, sex, MS subtype, disability status, and use and duration of disease-modifying treatment, was used to explore the difference between patients with MS with and without comorbidities. The Benjamini-Hochberg correction was used to minimize the false discovery rate.

^b Corrected *P* value < .05 was significant.

diabetes mellitus (*n* = 40, 4.9%), psoriasis (*n* = 33, 4%), and rheumatoid arthritis (*n* = 22, 2.7%).

Comorbidities and MR Imaging Outcomes

Because there were only a few subjects with systemic lupus erythematosus (*n* = 3), type 1 diabetes mellitus (*n* = 3), Crohn disease (*n* = 1), and myasthenia gravis (*n* = 1), they were excluded from MR imaging analyses.

Table 3 shows primary and secondary MR imaging outcome differences in patients with MS with and without the presence of comorbidities. Patients with MS with comorbidities showed significantly decreased normalized brain volume and normalized cortical volume (both, *P* < .001), normalized gray matter volume and MTR-NABT (*P* < .01), and MTR-normal-appearing gray matter (*P* < .05).

Table 4 shows primary and secondary MR imaging outcome differences in patients with MS with specific comorbidities, compared with those without any at all. Patients with MS having psoriasis had significantly decreased normalized brain volume (*P* < .001), normalized gray matter volume and normalized cortical volume (both, *P* < .01), and normalized white matter volume and

MTR-NABT (both, *P* < .05). Patients with MS with type 2 diabetes mellitus had significantly decreased normalized cortical volume (*P* < .01) and normalized brain volume and normalized gray matter volume (both, *P* < .05). Patients with MS with thyroid disease had significantly decreased normalized brain volume, normalized gray matter volume, and normalized cortical volume (all, *P* < .05). Patients with MS presenting with rheumatoid arthritis and asthma showed no significant differences on primary MR imaging outcomes; therefore, analysis of secondary MR imaging outcomes was not conducted.

DISCUSSION

This study investigated the association of autoimmune comorbidities and conventional and nonconventional MR imaging outcomes in patients with MS. Our main finding was that the presence of comorbidities in patients with MS

was associated with more severe MR imaging outcomes of neurodegeneration and demyelination. The tissue injury of patients with MS with comorbidities was localized to the GM and particularly to the cortex. Psoriasis, thyroid disease, and type 2 diabetes mellitus comorbidities were associated with more severe MR imaging outcomes.

In general, patients with comorbidities compared with those without had more severe brain damage as evidenced by a number of nonconventional MR imaging measures, including brain atrophy, magnetization transfer imaging, and diffusivity. The findings were significant for psoriasis, type 2 diabetes mellitus, and thyroid disease, though a low occurrence of Crohn disease, type 1 diabetes mellitus, myasthenia gravis, and systemic lupus erythematosus prevented us from exploring the impact of these comorbidities on the MR imaging outcomes. The more severe MR imaging findings in patients with MS having psoriasis is of particular interest, considering that medications beneficial for the treatment of this disease are also effective for treatment of patients with MS.³³

In addition, we found that patients with MS with type 2 diabetes mellitus showed more severe nonconventional MR imaging

Table 4: Primary and secondary MRI outcomes in patients with MS with specific comorbidities^a

	Patients with MS without Comorbidities (n = 574)	Patients with MS with Asthma (n = 41)	Patients with MS with Diabetes Mellitus Type 2 (n = 40)	Patients with MS with Psoriasis (n = 33)	Patients with MS with Rheumatoid Arthritis (n = 22)	Patients with MS with Thyroid Disease (n = 97)
Primary MRI outcomes						
T2-LV	15.3 (18.2)	12.9 (14.2)	19.3 (17)	17.2 (18.1)	17.1 (19.1)	12.9 (14.2)
T1-LV	2.6 (4.7)	2.2 (2.7)	2.9 (3.5)	3.5 (5.2)	3.4 (5.9)	2.2 (4)
Gd-LV	0.1 (0.4)	0.08 (0.1)	0.1 (0.05)	0.04 (0.1)	0.1 (0.2)	0.08 (0.2)
NBV	1481 (86.4)	1490.6 (90.5)	1434.4 (89) ^b	1394.3 (105) ^c	1461.2 (91.9)	1454.3 (87.3) ^b
MTR-NABT	35.3 (5)	36.4 (3.7)	35.1 (4.5)	33.1 (4.7) ^b	33 (4.6)	33.8 (5.7)
Secondary MRI outcomes						
NGMV	747.9 (81.5)	NA	708.2 (58.9) ^b	694.4 (89) ^d	NA	722.9 (68.5) ^b
NWMV	732.6 (64)	NA	726.3 (58.9)	699.8 (84) ^b	NA	731.3 (52.9)
NCV	557.6 (62.8)	NA	522.8 ((53.7) ^d	516.2 (91) ^d	NA	537.9 (52.7) ^b
NLVV	45.3 (20.5)	NA	52.5 (21.5)	50.7 (20.8)	NA	45.5 (21.3)
MTR-NAGM	32.3 (5.1)	NA	32 (4.3)	30.1 (4.7)	NA	30.8 (6.2)
MTR-NAWM	38.1 (4.9)	NA	38.2 (4.3)	36.2 (5.6)	NA	36.7 (5.9)
MTR-T2-LV	32.8 (5.1)	NA	32.9 (4.6)	32.1 (4.4)	NA	32.7 (5.2)
MD × 10 ³	1.22 (0.22)	NA	1.32 (0.37) ^d	1.25 (0.13)	NA	1.23 (0.31)

Note:—NA indicates not available; NBV, normalized brain volume; Gd, gadolinium; NGMV, normalized gray matter volume; NWMV, normalized white matter volume; NCV, normalized cortical volume; NLVV, normalized lateral ventricle volume.

^a The data are expressed as mean and SD. Volumes are expressed in milliliters. MTR values are expressed as percentage units. MD is expressed as mm²/s. Because there were only a few subjects with systemic lupus erythematosus (n = 3), type 1 diabetes mellitus (n = 3), Crohn disease (n = 1), and myasthenia gravis (n = 1), they were excluded from MRI analyses. Because no significant MRI primary outcome differences in patients with MS with asthma and rheumatoid arthritis, compared with patients with MS without any comorbidities, were found, no comparison of secondary MRI outcomes was performed for these comorbidities (NA). Analysis of covariance, adjusted for age, sex, MS subtype, disability status, and use and duration of disease-modifying treatment, was used to explore the difference between patients with MS with specific comorbidities compared with patients with MS without any comorbidities. The Benjamini-Hochberg correction was used to minimize the false discovery rate, and corrected P values < .05 were considered significant.

^b P < .05 shows significant differences of specific comorbidities compared with patients with MS without any comorbidities.

^c P < .001.

^d P < .01.

outcomes compared with those without. In particular, patients with MS with type 2 diabetes mellitus showed more advanced whole-brain and cortical atrophy. While we observed that patients with MS having asthma had less severe damage on nonconventional MR imaging outcomes compared with those without, these differences did not reach significance after correction for multiple comparisons. Previous clinical studies suggested that having asthma may provide a potential benefit to MS.^{13,22,23}

MS is thought to be associated with Th1-mediated autoimmunity, along with diseases such as type 1 diabetes mellitus, rheumatoid arthritis, and psoriasis,^{22,23} though it is evident that MS is not an exclusively Th1 disease, given that humoral immunity is an important contributor to its pathogenesis.¹ Th2-mediated immunity is involved in the pathogenesis of atopic diseases, such as asthma, eczema, and some allergies.^{22,34} Whether autoimmunity and atopy reflect cytokine polarization and thus are mutually protective in patients with MS is unknown at this time.²¹⁻²³ For example, previous studies showed that ulcerative colitis is positively associated with MS,²³ while asthma may have positive^{22,23,34} or negative¹³ associations, which could be also related to medications.³⁵ Presence of Th1-immune-mediated comorbidities in patients with MS (psoriasis, thyroid disease, and rheumatoid arthritis) may reflect a common underlying pathobiology resulting in increased disease severity, while Th2-immune-mediated comorbidity in patients with MS (asthma) may contribute to shifting of a Th-1- to Th2-immune-mediated response.

The presence of autoimmune comorbidities among patients with MS is in agreement with previously published literature and supports the concept of a link between these disorders and MS.⁵

Marrie et al⁵ recently reported, in a meta-analysis study, summary rates of 6.4% for thyroid disease, 7.7% for psoriasis, and ranges of 0.3%–3.64% for rheumatoid arthritis among patients with MS. In the present study, 11.9% of patients with MS had thyroid disease, 4% had psoriasis, and 2.7% had rheumatoid arthritis. The increased rate of autoimmune thyroid disease in patients with MS with respect to a control population could be influenced by the higher frequencies of major histocompatibility antigens, such as HLA-DRB1*15 and HLA-DRB1*17,³⁶ or by MS treatment.¹⁹

While the presence of comorbidities was associated with more severe MR imaging outcomes in the present study, there were no clinical differences between patients with MS with and without comorbidities. Therefore, a better understanding of the genetic and/or epigenetic influences causing these differences can help in identifying patients with MS at risk of more aggressive disease. A temporal disassociation between the detection of more severe damage on MR imaging and its immediate translation to clinical disease severity has been reported previously.^{24,37-40} Different levels of functional reserve and plasticity mechanisms that may compensate for the damage are the most plausible explanations for this phenomenon.^{39,40} When these compensatory mechanisms are exhausted, patients with MS enter a progressive clinical stage more rapidly.^{24,37} Future longitudinal studies should determine whether the presence of autoimmune comorbidities is a contributing factor to an increased risk for clinical and radiologic progression in MS.

Limitations of our study include self-reporting of comorbidities, which was limited to the data-collection instrument. Although the retrospective chart review confirmed the presence of

self-reported comorbidities and potentially increased the accuracy of the collected data, it was unable to determine the onset time of these autoimmune comorbidities in most of the examined cases. Therefore, we did not include the relative disease duration of these comorbidities as a covariate in our analyses, which limited our analyses to explore only the effect of comorbidity presence/absence on the MR imaging outcomes. Furthermore, we did not define thyroid disease subtypes by laboratory data. There was no case-control group included in the study, which limits interpretation of the comorbidity frequency data; however, our aim was to explore the associations of comorbidities with MR imaging disease severity. The study design was cross-sectional; therefore, the relationship of the comorbidities to MR imaging outcomes should be interpreted with caution.

CONCLUSIONS

The presence of comorbidities in MS is associated with more severe brain injury on MR imaging. This effect may not be visualized by using lesion burden MR imaging measures.

ACKNOWLEDGMENTS

We acknowledge Jesper Hagemeyer for critical reviewing of the manuscript.

Disclosures: Robert Zivadinov—UNRELATED: Consultancy: Genzyme, EMD Serono, Novartis, IMS Health; Grants/Grants Pending: Genzyme,* EMD Serono,* Novartis,* IMS Health,* Biogen, Teva Pharmaceuticals,* Claret Medical,* InteKrin Therapeutics*; Payment for Lectures (including service on Speakers Bureaus): Genzyme, EMD Serono; OTHER: Robert Zivadinov received personal compensation from Biogen Idec, Teva Pharmaceuticals, EMD Serono, Novartis, Claret Medical, and Genzyme for speaking and consultant fees. He received financial support for research activities from Biogen Idec, Teva Pharmaceuticals, EMD Serono, Novartis, Claret Medical, and Genzyme. He serves on the editorial boards of *J Alzheimers Dis*, *BMC Med*, *BMC Neurol*, *Vein and Lymphatics*, and *Clinical CNS Drugs*. He is Treasurer of the International Society for Neurovascular Disease. Murali Ramanathan—UNRELATED: Royalties: self-published textbook; OTHER: Murali Ramanathan received research funding or consulting fees from EMD Serono, Biogen Idec, Pfizer, the National Multiple Sclerosis Society, the Department of Defense, the Jog for the Jake Foundation, the National Institutes of Health, and the National Science Foundation. He received compensation for serving as an Editor from the American Association of Pharmaceutical Scientists. Barbara Teter—UNRELATED: Grants/Grants Pending: EMD Serono,* Biogen Idec,* Novartis,* Genzyme,* Genentech, Teva Pharmaceuticals,* Comments: observational research study grants. Michael G. Dwyer—UNRELATED: Consultancy: EMD Serono, Claret Medical, Comments: Dr Dwyer has served on a scientific advisory board for EMD Serono and provided consulting services to Claret Medical; Grants/Grants Pending: Novartis,* Comments: investigator-initiated research grant support; OTHER: Michael G. Dwyer has received consultant fees from Claret Medical and EMD Serono. Channa Kolb—UNRELATED: Consultancy: Advisory Board for Teva Pharmaceuticals and Biogen; Payment for Lectures (including service on Speakers Bureaus): speaker's honoraria from Novartis, Teva Pharmaceuticals, Acorda Therapeutics, EMD Serono, and Biogen-Idec. David Hojnacki—UNRELATED: Consultancy: Teva Pharmaceuticals, Biogen, Genzyme, EMD Serono; Payment for Lectures (including service on Speakers Bureaus): Teva Pharmaceuticals, Biogen, Genzyme, EMD Serono; OTHER: David Hojnacki has received speaker's honoraria and consultant fees from Biogen Idec, Teva Pharmaceutical, EMD Serono, Pfizer, and Novartis. Ralph H. Benedict—UNRELATED: Consultancy: Biogen, Genzyme, Genentech, Novartis, Adamas Pharmaceuticals; Grants/Grants Pending: National MS Society, Biogen, Acorda Therapeutics, Novartis, Genzyme, Mallinckrodt; Royalties: Psychological Assessment Resources; OTHER: Ralph Benedict has acted as a consultant or scientific advisory board member for Bayer, Biogen Idec, Actelion Pharmaceuticals, and Novartis. He receives royalties from Psychological Assessment Resources. He has received financial support for research activities from Shire Pharmaceuticals, Acorda Therapeutics, and Biogen Idec. Bianca Weinstock-Guttman—UNRELATED: Board Membership: Novartis; Consultancy: Biogen Idec, Teva Neuroscience, EMD Serono, Novartis, Genzyme, Sanofi, Genentech; Grants/Grants Pending: Biogen Idec,* Teva Neuroscience,* EMD Serono,* Novartis,* Genzyme,* Sanofi*; Payment for Lectures (including service on Speakers Bureaus): Biogen Idec, Teva Neuroscience, EMD Serono, Novartis, Genzyme, Sanofi; OTHER: Bianca Weinstock-Guttman received honoraria as a

speaker and as a consultant for Biogen Idec, Teva Pharmaceuticals, EMD Serono, Genzyme&Sanofi, Novartis, and Acorda Therapeutics. Dr Weinstock-Guttman received research funds from Biogen Idec, Teva Pharmaceuticals, EMD Serono, Genzyme&Sanofi, Novartis, Acorda Therapeutics. *Money paid to the institution.

REFERENCES

1. Frohman EM, Racke MK, Raine CS. **Multiple sclerosis: the plaque and its pathogenesis.** *N Engl J Med* 2006;354:942–55 CrossRef Medline
2. Ascherio A, Munger K. **Multiple sclerosis.** In: Nelson LM, Tanner CM, Van Den Eeden SK, et al, eds. *Neuroepidemiology: From Principles to Practice.* New York: Oxford University Press; 2004:188–222
3. Ramagopalan SV, Dobson R, Meier UC, et al. **Multiple sclerosis: risk factors, prodromes, and potential causal pathways.** *Lancet Neurol* 2010;9:727–39 CrossRef Medline
4. Marrie R, Rudick R, Horwitz R, et al. **Vascular comorbidity is associated with more rapid disability progression in multiple sclerosis.** *Neurology* 2010;74:1041–47 CrossRef Medline
5. Marrie RA, Reider N, Cohen J, et al. **A systematic review of the incidence and prevalence of autoimmune disease in multiple sclerosis.** *Mult Scler* 2015;21:282–93 CrossRef Medline
6. Marrie RA, Reider N, Cohen J, et al. **A systematic review of the incidence and prevalence of cardiac, cerebrovascular, and peripheral vascular disease in multiple sclerosis.** *Mult Scler* 2015;21:318–31 CrossRef Medline
7. Marrie RA, Reider N, Cohen J, et al. **A systematic review of the incidence and prevalence of sleep disorders and seizure disorders in multiple sclerosis.** *Mult Scler* 2015;23:342–49 CrossRef Medline
8. Marrie RA, Reider N, Stuve O, et al. **The incidence and prevalence of comorbid gastrointestinal, musculoskeletal, ocular, pulmonary, and renal disorders in multiple sclerosis: a systematic review.** *Mult Scler* 2015;21:332–41 CrossRef Medline
9. Marrie RA, Reider N, Cohen J, et al. **The incidence and prevalence of psychiatric disorders in multiple sclerosis: a systematic review.** *Mult Scler* 2015;21:305–17 CrossRef Medline
10. Marrie RA, Yu BN, Leung S, et al; CIHR Team in Epidemiology and Impact of Comorbidity on Multiple Sclerosis. **Rising prevalence of vascular comorbidities in multiple sclerosis: validation of administrative definitions for diabetes, hypertension, and hyperlipidemia.** *Mult Scler* 2012;18:1310–19 CrossRef Medline
11. Marrosu MG, Cocco E, Lai M, et al. **Patients with multiple sclerosis and risk of type 1 diabetes mellitus in Sardinia, Italy: a cohort study.** *Lancet* 2002;359:1461–65 CrossRef Medline
12. Tettey P, Simpson S Jr, Taylor BV, et al. **Vascular comorbidities in the onset and progression of multiple sclerosis.** *J Neurol Sci* 2014; 347:23–33 CrossRef Medline
13. Tremlett HL, Evans J, Wiles CM, et al. **Asthma and multiple sclerosis: an inverse association in a case-control general practice population.** *QJM* 2002;95:753–56 CrossRef Medline
14. Ramagopalan SV, Dymont DA, Herrera BM, et al. **Clustering of autoimmune disease in families at high risk for multiple sclerosis?** *Lancet Neurol* 2007;6:206–07; author reply 207 Medline
15. Marrie RA. **Psychiatric comorbidity in multiple sclerosis: it's not the genes.** *Mult Scler* 2014;20:1803–05 CrossRef Medline
16. Ramagopalan SV, Dymont DA, Valdar W, et al; Canadian Collaborative Study Group. **Autoimmune disease in families with multiple sclerosis: a population-based study.** *Lancet Neurol* 2007;6:604–10 CrossRef Medline
17. Marrosu MG, Motzo C, Murru R, et al. **The co-inheritance of type 1 diabetes and multiple sclerosis in Sardinia cannot be explained by genotype variation in the HLA region alone.** *Hum Mol Genet* 2004; 13:2919–24 CrossRef Medline
18. Zorzon M, Zivadinov R, Nasuelli D, et al. **Risk factors of multiple sclerosis: a case-control study.** *Neurol Sci* 2003;24:242–47 CrossRef Medline
19. Daniels GH, Vladic A, Brinar V, et al. **Alemtuzumab-related thyroid dysfunction in a phase 2 trial of patients with relapsing-remitting**

- multiple sclerosis.** *J Clin Endocrinol Metab* 2014;99:80–89 CrossRef Medline
20. Gold R, Montalban X. **Multiple sclerosis: more pieces of the immunological puzzle.** *Lancet Neurol* 2012;11:9–10 CrossRef Medline
 21. Kozovska ME, Hong J, Zang YC, et al. **Interferon beta induces T-helper 2 immune deviation in MS.** *Neurology* 1999;53:1692–97 CrossRef Medline
 22. Simpson CR, Anderson WJ, Helms PJ, et al. **Coincidence of immune-mediated diseases driven by Th1 and Th2 subsets suggests a common aetiology: a population-based study using computerized general practice data.** *Clin Exp Allergy* 2002;32:37–42 CrossRef Medline
 23. Edwards LJ, Constantinescu CS. **A prospective study of conditions associated with multiple sclerosis in a cohort of 658 consecutive outpatients attending a multiple sclerosis clinic.** *Mult Scler* 2004;10:575–81 CrossRef Medline
 24. Zivadinov R, Cox JL. **Neuroimaging in multiple sclerosis.** *Int Rev Neurobiol* 2007;79:449–74 CrossRef Medline
 25. Weinstock-Guttman B, Zivadinov R, Horakova D, et al. **Lipid profiles are associated with lesion formation over 24 months in interferon- β treated patients following the first demyelinating event.** *J Neurol Neurosurg Psychiatry* 2013;84:1186–91 CrossRef Medline
 26. Zivadinov R, Weinstock-Guttman B, Hashmi K, et al. **Smoking is associated with increased lesion volumes and brain atrophy in multiple sclerosis.** *Neurology* 2009;73:504–10 CrossRef Medline
 27. Polman CH, Reingold SC, Edan G, et al. **Diagnostic criteria for multiple sclerosis: 2005 revisions to the “McDonald Criteria.”** *Ann Neurol* 2005;58:840–46 CrossRef Medline
 28. Weinstock-Guttman B, Jacobs LD, Brownschidle CM, et al; New York State Multiple Sclerosis Consortium. **Multiple sclerosis characteristics in African American patients in the New York State Multiple Sclerosis Consortium.** *Mult Scler* 2003;9:293–98 CrossRef Medline
 29. Zivadinov R, Rudick RA, De Masi R, et al. **Effects of IV methylprednisolone on brain atrophy in relapsing-remitting MS.** *Neurology* 2001;57:1239–47 CrossRef Medline
 30. Smith SM, Zhang Y, Jenkinson M, et al. **Accurate, robust, and automated longitudinal and cross-sectional brain change analysis.** *Neuroimage* 2002;17:479–89 CrossRef Medline
 31. Zivadinov R, Heininen-Brown M, Schirda CV, et al. **Abnormal subcortical deep-gray matter susceptibility-weighted imaging filtered phase measurements in patients with multiple sclerosis: a case-control study.** *Neuroimage* 2012;59:331–39 CrossRef Medline
 32. Benjamin Y, Drai D, Elmer G, et al. **Controlling the false discovery rate in behavior genetics research.** *Behav Brain Res* 2001;125:279–84 CrossRef Medline
 33. Fox RJ, Miller DH, Phillips JT, et al; CONFIRM Study Investigators. **Placebo-controlled phase 3 study of oral BG-12 or glatiramer in multiple sclerosis.** *N Engl J Med* 2012;367:1087–97 CrossRef Medline
 34. Ponsoby AL, Dwyer T, van der Mei I, et al. **Asthma onset prior to multiple sclerosis and the contribution of sibling exposure in early life.** *Clin Exp Immunol* 2006;146:463–70 CrossRef Medline
 35. Makhlof K, Weiner HL, and Khoury SJ. **Potential of beta2-adrenoceptor agonists as add-on therapy for multiple sclerosis: focus on salbutamol (albuterol).** *CNS Drugs* 2002;16:1–8 Medline
 36. Vaidya B, Kendall-Taylor P, Pearce SH. **The genetics of autoimmune thyroid disease.** *J Clin Endocrinol Metab* 2002;87:5385–97 CrossRef Medline
 37. Barkhof F, Calabresi PA, Miller DH, et al. **Imaging outcomes for neuroprotection and repair in multiple sclerosis trials.** *Nat Rev Neurol* 2009;5:256–66 CrossRef Medline
 38. Buckle GJ. **Functional magnetic resonance imaging and multiple sclerosis: the evidence for neuronal plasticity.** *J Neuroimaging* 2005;15:82S–93S CrossRef Medline
 39. Pelletier J, Audoin B, Reuter F, et al. **Plasticity in MS: from functional imaging to rehabilitation.** *Int MS J* 2009;16:26–31 Medline
 40. Strasser-Fuchs S, Enzinger C, Ropele S, et al. **Clinically benign multiple sclerosis despite large T2 lesion load: can we explain this paradox?** *Mult Scler* 2008;14:205–11 Medline

Incidence of Radiologically Isolated Syndrome: A Population-Based Study

Y. Forslin, T. Granberg, A. Antwan Jumah, S. Shams, P. Aspelin, M. Kristoffersen-Wiberg, J. Martola,
and S. Fredrikson



ABSTRACT

BACKGROUND AND PURPOSE: Incidental MR imaging findings resembling MS in asymptomatic individuals, fulfilling the Okuda criteria, are termed “radiologically isolated syndrome.” Those with radiologically isolated syndrome are at high risk of their condition converting to MS. The epidemiology of radiologically isolated syndrome remains largely unknown, and there are no population-based studies, to our knowledge. Our aim was to study the population-based incidence of radiologically isolated syndrome in a high-incidence region for MS and to evaluate the effect on radiologically isolated syndrome incidence when revising the original radiologically isolated syndrome criteria by using the latest radiologic classification for dissemination in space.

MATERIALS AND METHODS: All 2272 brain MR imaging scans in 1907 persons obtained during 2013 in the Swedish county of Västmanland, with a population of 259,000 inhabitants, were blindly evaluated by a senior radiologist and a senior neuroradiologist. The Okuda criteria for radiologically isolated syndrome were applied by using both the Barkhof and Swanton classifications for dissemination in space. Assessments of clinical data were performed by a radiology resident and a senior neurologist.

RESULTS: The cumulative incidence of radiologically isolated syndrome was 2 patients (0.1%), equaling an incidence rate of 0.8 cases per 100,000 person-years, in a region with an incidence rate of MS of 10.2 cases per 100,000 person-years. There was no difference in the radiologically isolated syndrome incidence rate when applying a modified version of the Okuda criteria by using the newer Swanton classification for dissemination in space.

CONCLUSIONS: Radiologically isolated syndrome is uncommon in a high-incidence region for MS. Adapting the Okuda criteria to use the dissemination in space–Swanton classification may be feasible. Future studies on radiologically isolated syndrome may benefit from a collaborative approach to ensure adequate numbers of participants.

ABBREVIATIONS: DIS = dissemination in space; RIS = radiologically isolated syndrome

Due to the increased sensitivity, availability, and use of MR imaging, incidental findings have increased during the past decade.^{1,2} Incidental MR imaging findings resembling MS, termed “radiologically isolated syndrome” (RIS), are 1 consequence of the increased use and sensitivity of MR imaging.³ RIS was introduced in 2009 by Okuda et al,³ to categorize incidental

WM lesions suggestive of demyelinating disease in patients without typical MS symptoms and no better explanation for the MR imaging anomalies.⁴ RIS has, since its emergence, been debated, and the risk of RIS evolving into MS has been investigated.⁵ Non-conventional MR imaging methods and neuropsychological testing have revealed similar findings in RIS and MS.^{6–10} One-third of patients with RIS develop MS in 5 years, implying that RIS, in some cases, constitutes a preclinical stage or subclinical form of MS. These results suggest that the McDonald criteria lack some degree of sensitivity in detecting MS in its earliest phases. This interpretation raises questions about the early pathophysiology of MS and motivates us to investigate to what extent it is possible to

Received October 14, 2015; accepted after revision November 20.

From the Departments of Clinical Science, Intervention and Technology (Y.F., T.G., S.S., P.A., M.K.-W., J.M.), Radiology (Y.F., T.G., S.S., P.A., M.K.-W., J.M.), Clinical Neuroscience (S.F.), and Neurology (S.F.), Karolinska University Hospital, Stockholm, Sweden; and Department of Radiology (Y.F., T.G., A.A.J.), Västmanland Hospital, Västerås, Sweden.

Contributions: T.G. conceived the study. Y.F., T.G., A.A.J., P.A., M.K.-W., J.M., and S.F. jointly initiated the study. Y.F., T.G., A.A.J., and J.M. designed the study. Y.F., A.A.J., and J.M. performed data acquisition. Y.F., T.G., S.S., M.K.-W., and S.F. analyzed the data. All authors contributed to the interpretation of the data and revised the manuscript. Y.F., T.G., and S.S. drafted the manuscript. Y.F. is a guarantor.

This work was funded by the Stockholm County Council and Karolinska Institutet through the regional agreement on medical training and clinical research (ALF grant 20120213).

Please address correspondence to Yngve Forslin, MD, Department of Clinical Science, Intervention and Technology, C1-46, Karolinska University Hospital, 141 86 Stockholm, Sweden; e-mail: yngve.forslin@ki.se

Indicates open access to non-subscribers at www.ajnr.org

Indicates article with supplemental on-line tables.

<http://dx.doi.org/10.3174/ajnr.A4660>

Table 1: Comparison of the 2 latest radiologic criteria for DIS in MS

DIS Barkhof Classification ⁴	DIS Swanton Classification ²⁶
At least 3 of ≥3 Periventricular lesion ≥1 Juxtacortical lesion ≥1 Infratentorial or spinal cord lesion ≥1 Contrast-enhancing or ≥9 T2 lesions	At least 2 of ≥1 Periventricular lesion ≥1 Juxtacortical lesion ≥1 Infratentorial lesion ≥1 Spinal cord lesion

detect MR imaging findings before the symptomatic onset of MS. It is therefore of further interest to determine the frequency of RIS in clinical practice.^{3,5,11-18}

However, despite the interest in RIS, its epidemiology remains largely unclear. Postmortem studies have shown a prevalence of incidental MS findings ranging from 0.06% to 0.7%.^{5,19-21} The hospital-based incidence has been estimated between 0.05% and 0.7%.^{17,22} Our aim was to study the population-based incidence of RIS in a country with a high incidence (10.2 per 100,000 person-years) and prevalence (189/100,000) of MS.^{23,24} This was done by retrospectively re-evaluating all MR imaging brain examinations performed during 2013 in the Swedish county of Västmanland, with approximately 259,000 inhabitants.²⁵ We secondarily aimed to evaluate how implementing the newer Swanton classification for dissemination in space (DIS), from the 2010 McDonald criteria for MS, would affect the incidence of RIS.^{3,4,26,27}

MATERIALS AND METHODS

Study Population

Ethics approval was obtained from the regional ethics review board in Stockholm, Sweden. All brain MR images obtained during 2013 in Västmanland County, Sweden, were anonymized and included in the study. Written informed consent was obtained for reviewing the clinical patient charts.

Criteria and Assessments

The Okuda criteria for RIS, summarized in On-line Table 1, were used.³ Similar to a previous study,²⁸ radiologic DIS was assessed according to both the original implementation with the Barkhof classification (DIS-Barkhof)⁴ and with the more recent Swanton classification (DIS-Swanton)^{26,27} to study the effect of the 2 different classifications on the RIS incidence. Table 1 compares the 2 DIS classifications.

The screening of all patients was conducted in several steps, illustrated in Fig 1. First, all brain MR imaging scans obtained in 2013 were anonymized and systematically evaluated by a senior radiologist (A.A.). The assessment was blinded to the original radiologic reading and all clinical information. The primary radiologic screening by A.A. focused strictly on the location, number, and presence of gadolinium enhancement of the WM lesions in regard to the Swanton and Barkhof criteria, respectively, to assess whether the DIS/Okuda A2 criterion was fulfilled and to preserve a high sensitivity for WM anomalies. Thus, no interpretation of the likely cause of the lesions was performed in the initial radiologic screening. Consistent with the study by Liu et al,²⁹ a more liberal definition of juxtacortical lesions “within 3 mm from the GM-WM border” was used in the initial screening by A.A., to

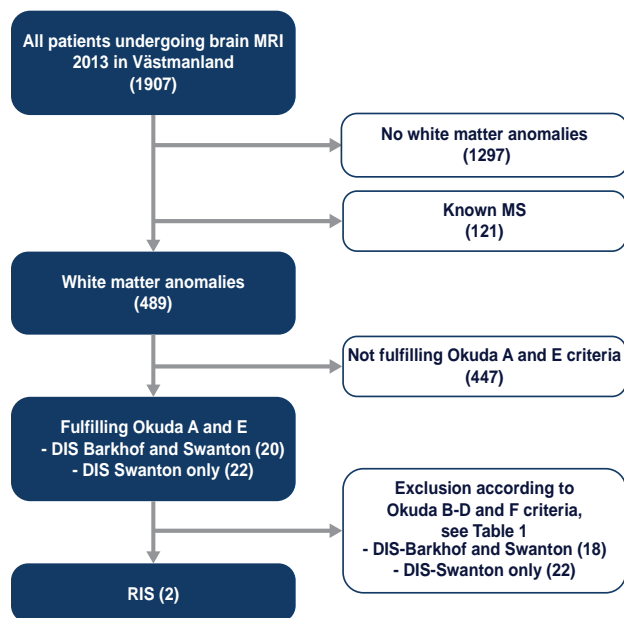


FIG 1. Flow chart of the screening process for identifying patients with RIS.

preserve a high sensitivity for WM anomalies. All patients with DIS were re-evaluated by a senior neuroradiologist (J.M.); for this evaluation, the definition “in direct contact with the cortex” was used when assessing juxtacortical lesions, for higher specificity. J.M. also assessed whether the lesions fulfilled the Okuda A and E criteria.

The clinical information for patients fulfilling the Okuda A and E criteria was reviewed by a resident in radiology (Y.F.). Exclusions from the study, according to the Okuda B–D and F criteria, were based on the clinical information in the referral notes and, when needed, clinical patient charts. Any uncertain cases and all included patients were discussed with a senior neurologist (S.F.), and final decisions on inclusion/exclusion were made by a consensus of Y.F. and S.F. On-line Table 1 summarizes the causes for exclusion.

MR Imaging Acquisition

There are 2 MR imaging centers in Västmanland county: the regional hospital in Västerås and Medicinsk Röntgen Eriksborg. Both centers participated in the study. There are 3 MR imaging scanners in Västmanland: one 1.5T Avanto (Siemens, Erlangen, Germany), one 1.5T Symphony (Siemens), and one 3T Ingenia scanner (Philips Healthcare, Best, the Netherlands). All brain MR imaging was performed according to standard clinical protocols based on the clinical query. The MR imaging protocols at the 2 centers and on the 3 scanners varied but always included conventional axial MR imaging sequences (such as T1- and T2-weighted images) with a section thickness of ≤5 mm. Naturally, all examinations were individualized for the patients’ clinical needs. However, most protocols included FLAIR sequences, and 42% of the MR images were acquired with the administration of gadolinium-based contrast media. The few protocols that did not include FLAIR were for the following clinical queries: control after intracranial bleeding or aneurysm coiling, arterial angiography, meningioma control,

Table 2: Overview of MRI scanners, sequences in standard brain protocol, and number of patients receiving gadolinium-based contrast media

MRI Scanner	Philips Ingenia	Siemens Symphony	Siemens Avanto
Field strength	3T	1.5T	1.5T
Standard MRI brain protocol	T1 tra, T1 sag, T2 tra, T2 cor, FLAIR tra, DWI tra	T1 tra, T1 sag, T2 tra, T2 cor, FLAIR tra, DWI tra	T1 sag, T2 tra, FLAIR cor, SWI tra, DWI tra
Largest section thickness in any protocol	5 mm	5 mm	5 mm
No. of scans with/without contrast media	790/924		169/389

Note:—Cor indicates coronal; sag, sagittal; tra, transversal.

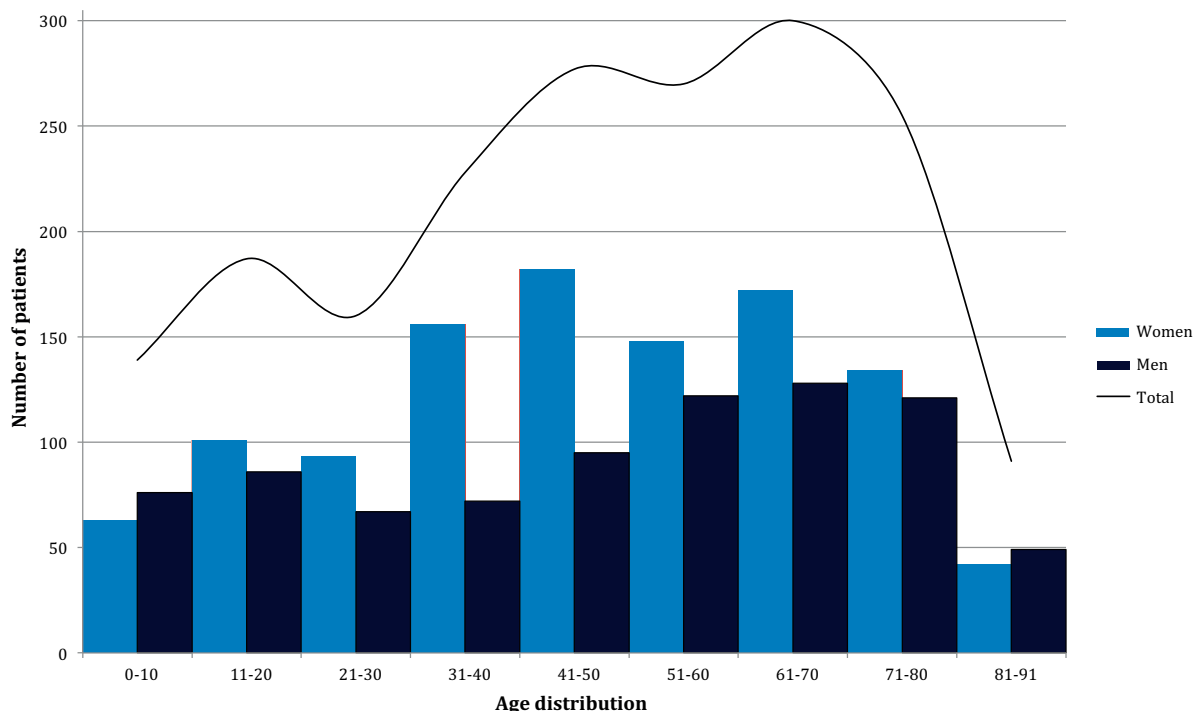


FIG 2. Demographics and distribution of the study population. The ages in the cohort ranged between 0 and 91 years, and the mean age was 47 years (the first and third quartiles were 30 and 66 years, respectively).

and tumor near the pons or a vestibular schwannoma. Table 2 shows the details of the most frequently used standard brain MR imaging protocols, the different MR imaging scanners, and the number of scans with contrast media.

Statistics

SPSS, Version 22.0 (IBM, Armonk, New York) was used for descriptive statistics, and Excel Mac 2011 14.4.8 (Microsoft, Redmond, Washington), for presenting demographics. The analyses were performed by a resident in radiology (Y.F.).

RESULTS

Cohort Characteristics

In 2013, 1907 individuals (1091 females, 816 males) each had between 1 and 6 brain MR imaging scans, with a total of 2272 brain MR imaging scans, equivalent to 877 scans per 100,000 person-years. Figure 2 shows the demography of the study population. An overview of the MR imaging findings is presented in On-line Table 2, which is based on the original radiologic reports (before the study) and, in some cases, complementary information from medical records to specify radiologic findings.

Incidence of RIS

Of the 1907 patients, 1297 did not have any WM anomalies and 121 were patients with MS with a known diagnosis before the MR imaging. As described in Fig 1, after the exclusion of 447 patients not fulfilling the A and E criteria, 20 patients remained fulfilling both DIS-Barkhof and DIS-Swanton criteria, and 22 patients, fulfilling only the DIS-Swanton criteria. Thus, twice as many patients fulfilled the radiologic criteria for DIS-Swanton ($n = 42$, 2.2%) in comparison with DIS-Barkhof ($n = 20$, 1.0%).

The main indications for the MR imaging of these patients fulfilling the Okuda A criterion are presented in On-line Table 3, and the causes for exclusion due to clinical reasons (ie, Okuda B–D and F) are presented in On-line Table 1. The most common reason for MR imaging among the 42 patients fulfilling the DIS criteria was headache. Patients with neurologic symptoms consistent with MS were excluded according to the B criterion. Patients with severe dementia were excluded due to the C criterion. Patients with a history of severe cardiovascular disease or other cardiovascular risk factors, which can lead to cerebral WM anomalies, were excluded according to the Okuda F criteria. CSF analysis had not been performed in most of the excluded patients because

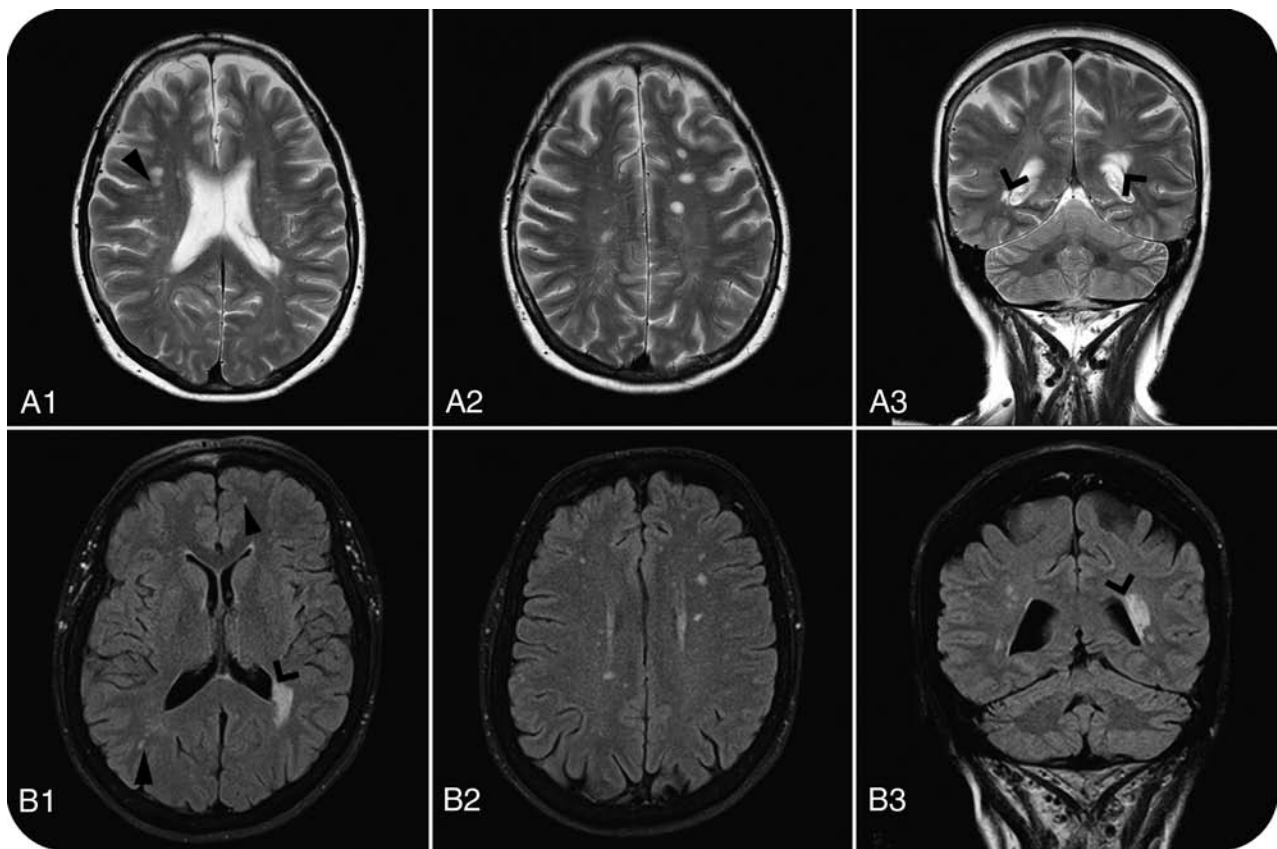


FIG 3. Brain MR imaging WM anomalies in 61-year-old (A1–A3: T2WI) and 66-year-old (B1–B3: FLAIR) women with RIS. *Open arrows* show periventricular lesions, and *closed arrows* show juxtacortical lesions, which, together with >9 lesions, made both patients fulfill the DIS-Barkhof and DIS-Swanton criteria. Columns 1 and 2 are axial sections; column 3 shows coronal sections.

no clinical indication existed. In those who had the analysis, 1 CSF sample was positive for oligoclonal bands.

After exclusion through the Okuda B–D and F criteria, 2 patients with RIS were identified fulfilling both classifications for DIS, while none of the patients fulfilling only the DIS-Swanton criteria remained. Thus, of the 1907 patients undergoing brain MR imaging in 2013, 2 patients fulfilled the criteria for RIS, equivalent to a cumulative incidence of 0.1% per year and a population-based incidence of 0.8 cases of RIS per 100,000 inhabitants per year.

Description of Individuals with RIS

The first individual with RIS was an otherwise healthy 61-year-old woman referred for brain MR imaging due to headache and mild unspecific vertigo. In our blinded neuroradiologic re-evaluation, we found 3 periventricular lesions, 2 juxtacortical lesions, and >9 T2 lesions in total, thus fulfilling both DIS classifications. There were no contrast-enhancing lesions. CSF analysis showed immunoglobulin G oligoclonal bands but normal values of the immunoglobulin G index. There were no abnormal neurologic findings, and the patient did not recall having any earlier signs consistent with MS.

The second individual with RIS was a 66-year-old woman with hypothyroidism and asthma. She was referred for brain MR imaging because of suspected epilepsy with 2 self-reported episodes of generalized tonic-clonic seizures. The findings of electroencephalography were normal, and the suspicion of epilepsy was not

confirmed. In the neuroradiologic assessment, 3 periventricular, 1 juxtacortical, and >9 T2 lesions were found, fulfilling both DIS classifications. Findings on CSF analysis were normal, and there was no history of remitting neurologic symptoms or any abnormalities in the neurologic examination. The imaging findings of both patients with RIS are shown in Fig 3. Conditions of both patients had, before the study, been detected in the clinical context; they were referred to a neurologist and informed about the MR imaging findings. The patients did not fulfill the McDonald criteria for MS clinically, and neither of the 2 patients received disease-modifying therapy. None of the patients had any signs or symptoms consistent with MS 1 year after the MR imaging.

DISCUSSION

Of 1907 patients undergoing MR imaging, 2 patients were found to have RIS (0.1%), regardless of using the Barkhof or Swanton classification for DIS. This finding equals an RIS incidence rate of 0.8 per 100,000 person-years. In comparison, the incidence rate of MS in Sweden is 10.2 per 100,000 person-years.²³

Studies on the epidemiology of RIS are scarce. The few studies conducted have been hospital-based or studied the prevalence of RIS in selected cohorts such as in MS relatives.^{17,22,28} In a study of unexpected MR imaging findings suggestive of MS in a tertiary hospital in Pakistan, a frequency of 0.7% was reported in the age group 15–40 years.²² In a hospital-based study performed by us at a tertiary hospital in Stockholm, Sweden, we found an RIS fre-

quency of 0.05% in all ages and 0.15% in the same age range as that in the study in Pakistan.¹⁷ Our studies do not overlap because they were performed with different sample years in different counties. The RIS frequency in the current study is in line with the reported hospital-based RIS frequency in our previous study. Meanwhile, the study from Pakistan showed a higher frequency of RIS, despite a lower incidence and prevalence of MS in the region.^{23,24,30,31} Gabelic et al²⁸ showed, in a smaller study in relatives of patients with MS, that 3% fulfilled the RIS criteria by using the DIS-Barkhof criteria, and 10%, with the DIS-Swanton criteria. In healthy volunteers, they found RIS in 2.4% according to the DIS-Barkhof and 3.7% by using DIS-Swanton criteria. In the current study, 2.2% fulfilled the DIS-Swanton, and 1.0%, the DIS-Barkhof criteria after neuroradiologic assessment (Okuda A and E), while no difference in RIS incidence (0.1%) remained after exclusion according to clinical data (the Okuda B–D and F).

Possible explanations for the differences in RIS frequencies include methodologic differences (prospective/retrospective design, selection, and ages of study samples), regional differences in MR imaging practices, and availability and technical differences (field strengths, MR imaging sequences and orientation, section thickness, frequency of using contrast media). In our study, 2D FLAIR sequences were used and only approximately half of the MR imaging scans were obtained with gadolinium contrast media, which might influence the number of patients fulfilling DIS according to the Barkhof classification, in which the presence of enhancing lesions can substitute for 9 T2-hyperintense lesions. Increased awareness of MS signs and symptoms, both in the general population and among physicians, in regions with a high incidence of MS is also likely to influence the rate of unexpected MS-like findings. An alternative interpretation could be that the RIS frequency may be higher in regions with lower MS incidence if differences in the genetic or environmental background reduce the risk of converting to manifest MS. If that interpretation is the case, studying the difference between patients with RIS and those with MS is of major importance, to understand the mechanisms that may constrain the development of MS.

The individuals with RIS in our study had a surprisingly older age, considering that the incidence for women with MS in Sweden peaks at 30 years of age.²³ These results suggest that RIS may reflect a more benign entity, but longitudinal data on the natural history of RIS are needed to better understand its prognosis.^{4,5,11,18} Whether individuals with RIS should receive MS treatment is debated,^{32,33} but a clinical treatment trial is already planned.³⁴ Due to the low incidence of RIS, conducting studies on patients with RIS may necessitate large nation-based cohorts or multicenter studies. Our results may be of importance when designing future treatment trials and longitudinal studies on the natural history of RIS.

The main strength of our study is the population-based perspective, being the first study of RIS with a known population size and an involvement of all MR imaging centers in the area. The design reduces the risk of selection bias, which has been considered the main limitation of previous hospital-based studies. The comprehensive inclusion of all performed MRIs in a region, such as in this study, can yield the incidence rate of RIS, because RIS is defined as an incidental MR imaging finding. Our results of RIS

incidence are representative of the clinical entity RIS, which causes clinical dilemmas in terms of management, but does not reflect an estimation of the prevalence of RIS in the general population, in which most had not undergone a brain MR imaging. The selection bias of the imaged individuals most likely yields a higher RIS incidence among the imaged than the nonimaged population. If the imaged population were representative of the nonimaged one, the frequency of RIS would be 105 cases per 100,000 person-years (based on the 2 cases of RIS per 1907 persons), which would be >10 times larger than the MS incidence (10.2 cases per 100,000 person-years).

An additional strength is the blinded radiologic readings performed by a senior radiologist and a senior neuroradiologist. The high accessibility of the clinical patient charts and clinical information was essential for the assessment regarding Okuda B–D and F and for not overestimating the RIS incidence.

A limitation is the use of different MR imaging scanners and MR imaging protocols, which may have different sensitivities for WM lesions. This variability is, however, a consequence of the natural variation of equipment used at different centers and increases the generalizability of the results because scanner variations are common in clinical practice. The main limitation of the study is its sample size, because the relative sparseness of RIS renders the incidence estimate to some degree uncertain. Future epidemiologic RIS studies would therefore benefit from longer study periods or a larger study population.

CONCLUSIONS

Our study shows that RIS is relatively uncommon in a high-incidence region for MS. Future studies on RIS may therefore benefit from a collaborative approach to ensure adequate numbers of participants. There was no difference in RIS incidence when applying the newer Swanton classification for DIS, suggesting that it may be feasible to adapt the Okuda criteria to harmonize with the 2010 MacDonald MS criteria, without affecting the incidence of RIS.

ACKNOWLEDGMENTS

We thank the Department of Radiology at Västmanland Hospital and Medicinsk Röntgen Eriksborg for participating in the study, and we especially thank Per Hammar and Arne Thorén, the directors of the respective clinics, for facilitating this study.

Disclosures: Yngve Forslin, Ayad Antwan Jumah—*RELATED: Grant:* This research was funded by Stockholm County Council and Karolinska Institutet through the regional agreement on medical training and clinical research (ALF grant 20120213). Sten Fredrikson—*UNRELATED: Board Membership:* Teva, Genzyme; *Payment for Lectures (including service on Speakers Bureaus):* Allergan, Bayer, Biogen Idec, Genzyme, Merck Serono, Novartis, Sanofi, Teva; *Payment for Development of Educational Presentations:* Teva; *Other:* received honoraria for lectures, educational activities, or consultancy from Allergan, Bayer, Biogen Idec, Genzyme, Merck Serono, Novartis, Sanofi, and Teva.

REFERENCES

1. OECDiLibrary. Magnetic resonance imaging (MRI) exams, total per 1000 population. www.oecd-ilibrary.org/content/table/mri-exam-total-table-2014-1-en. Accessed June 18, 2014
2. Morris Z, Whiteley WN, Longstreth WT, et al. **Incidental findings on brain magnetic resonance imaging: systematic review and meta-analysis.** *BMJ* 2009;339:b3016 CrossRef Medline

3. Okuda DT, Mowry EM, Beheshtian A, et al. **Incidental MRI anomalies suggestive of multiple sclerosis: the radiologically isolated syndrome.** *Neurology* 2009;72:800–05 CrossRef Medline
4. Barkhof F, Filippi M, Miller DH, et al. **Comparison of MRI criteria at first presentation to predict conversion to clinically definite multiple sclerosis.** *Brain* 1997;120(pt 11):2059–69 CrossRef Medline
5. Granberg T, Martola J, Kristoffersen-Wiberg M, et al. **Radiologically isolated syndrome: incidental magnetic resonance imaging findings suggestive of multiple sclerosis—a systematic review.** *Mult Scler* 2013;19:271–80 CrossRef Medline
6. Lebrun C, Blanc F, Brassat D, et al; CFSEP. **Cognitive function in radiologically isolated syndrome.** *Mult Scler* 2010;16:919–25 CrossRef Medline
7. De Stefano N, Stromillo ML, Rossi F, et al. **Improving the characterization of radiologically isolated syndrome suggestive of multiple sclerosis.** *PLoS One* 2011;6:e19452 CrossRef Medline
8. Giorgio A, Stromillo ML, Rossi F, et al. **Cortical lesions in radiologically isolated syndrome.** *Neurology* 2011;77:1896–99 CrossRef Medline
9. Amato MP, Hakiki B, Goretti B, et al; Italian RIS/MS Study Group. **Association of MRI metrics and cognitive impairment in radiologically isolated syndromes.** *Neurology* 2012;78:309–14 CrossRef Medline
10. Stromillo ML, Giorgio A, Rossi F, et al. **Brain metabolic changes suggestive of axonal damage in radiologically isolated syndrome.** *Neurology* 2013;80:2090–94 CrossRef Medline
11. Lebrun C, Bensa C, Debouverie M, et al; CFSEP. **Unexpected multiple sclerosis: follow-up of 30 patients with magnetic resonance imaging and clinical conversion profile.** *J Neurol Neurosurg Psychiatry* 2008;79:195–98 CrossRef Medline
12. Derwenskus Joy, Cohen B. **Clinically silent multiple sclerosis: description of a patient cohort without symptoms typical of MS but abnormal brain magnetic resonance imaging.** *Multiple Sclerosis (Houndmills, Basingstoke, England)* 2007;3:1226–27
13. Lebrun C, Bensa C, Debouverie M, et al; Club Francophone de la Sclérose en Plaques. **Association between clinical conversion to multiple sclerosis in radiologically isolated syndrome and magnetic resonance imaging, cerebrospinal fluid, and visual evoked potential: follow-up of 70 patients.** *Arch Neurol* 2009;66:841–46 CrossRef Medline
14. Siva A, Saip S, Altintas A, et al. **Multiple sclerosis risk in radiologically uncovered asymptomatic possible inflammatory-demyelinating disease.** *Mult Scler* 2009;15:918–27 CrossRef Medline
15. Okuda DT, Mowry EM, Cree BA, et al. **Asymptomatic spinal cord lesions predict disease progression in radiologically isolated syndrome.** *Neurology* 2011;76:686–92 CrossRef Medline
16. Maia AC Jr, Rocha AJ, Barros BR, et al. **Incidental demyelinating inflammatory lesions in asymptomatic patients: a Brazilian cohort with radiologically isolated syndrome and a critical review of current literature.** *Arq Neuropsiquiatr* 2012;70:5–11 CrossRef Medline
17. Granberg T, Martola J, Aspelin P, et al. **Radiologically isolated syndrome: an uncommon finding at a university clinic in a high-prevalence region for multiple sclerosis.** *BMJ Open* 2013;3:e003531 CrossRef Medline
18. Okuda DT, Siva A, Kantarci O, et al; Radiologically Isolated Syndrome Consortium (RISC), Club Francophone de la Sclérose en Plaques (CFSEP). **Radiologically isolated syndrome: 5-year risk for an initial clinical event.** *PLoS One* 2014;9:e90509 CrossRef Medline
19. Gilbert JJ, Sadler M. **Unsuspected multiple sclerosis.** *Arch Neurol* 1983;40:533–36 CrossRef Medline
20. Engell T. **A clinical patho-anatomical study of clinically silent multiple sclerosis.** *Acta Neurol Scand* 1989;79:428–30 CrossRef Medline
21. Johannsen LG, Stenager E, Jensen K. **Clinically unexpected multiple sclerosis in patients with mental disorders: a series of 7301 psychiatric autopsies.** *Acta Neurol Belg* 1996;96:62–65 Medline
22. Wasay M, Rizvi F, Azeemuddin M, et al. **Incidental MRI lesions suggestive of multiple sclerosis in asymptomatic patients in Karachi, Pakistan.** *J Neurol Neurosurg Psychiatry* 2011;82:83–85 CrossRef Medline
23. Ahlgren C, Odén A, Lycke J. **High nationwide incidence of multiple sclerosis in Sweden.** *PLoS One* 2014;9:e108599 CrossRef Medline
24. Ahlgren C, Odén A, Lycke J. **High nationwide prevalence of multiple sclerosis in Sweden.** *Mult Scler* 2011;17:901–08 CrossRef Medline
25. Statistics Sweden. **Population in the country, counties and municipalities by sex and age December 31, 2014.** <http://www.scb.se/en/Finding-statistics/Statistics-by-subject-area/Population/Population-composition/Population-statistics/Aktuell-Pong/25795/Yearly-statistics-Municipalities-Counties-and-the-whole-country/370301/>. Accessed January 27, 2015
26. Swanton JK, Rovira A, Tintore M, et al. **MRI criteria for multiple sclerosis in patients presenting with clinically isolated syndromes: a multicentre retrospective study.** *Lancet Neurol* 2007;6:677–86 CrossRef Medline
27. Polman CH, Reingold SC, Banwell B, et al. **Diagnostic criteria for multiple sclerosis: 2010 revisions to the McDonald criteria.** *Ann Neurol* 2011;69:292–302 CrossRef Medline
28. Gabelic T, Ramasamy DP, Weinstock-Guttman B, et al. **Prevalence of radiologically isolated syndrome and white matter signal abnormalities in healthy relatives of patients with multiple sclerosis.** *AJNR Am J Neuroradiol* 2014;35:106–12 CrossRef Medline
29. Liu S, Kullnat J, Bourdette D, et al. **Prevalence of brain magnetic resonance imaging meeting Barkhof and McDonald criteria for dissemination in space among headache patients.** *Mult Scler* 2013;19:1101–05 CrossRef Medline
30. Wasay M, Khatri IA, Khealani B, et al. **MS in Asian countries.** *Int MS J* 2006;13:58–65 Medline
31. Wasay M, Ali S, Khatri IA, et al. **Multiple sclerosis in Pakistan.** *Mult Scler* 2007;13:668–69 CrossRef Medline
32. Brassat D, Lebrun-Frenay C; Club Francophone de la SEP. **Treat patients with radiologically isolated syndrome when the MRI brain scan shows dissemination in time: yes.** *Mult Scler* 2012;18:1531–32 CrossRef Medline
33. Bourdette D, Yadav V. **Treat patients with radiologically isolated syndrome when the MRI brain scan shows dissemination in time: no.** *Mult Scler* 2012;18:1529–30 CrossRef Medline
34. Okuda D, Frenay CL, Siva A, et al. **Multi-center, randomized, double-blinded assessment of dimethyl fumarate in extending the time to a first attack in radiologically isolated syndrome (RIS) (ARISE Trial) (P7.207).** *Neurology* 2015;84(suppl):P7.207

Clinical Feasibility of Synthetic MRI in Multiple Sclerosis: A Diagnostic and Volumetric Validation Study

T. Granberg, M. Uppman, F. Hashim, C. Cananau, L.E. Nordin, S. Shams, J. Berglund, Y. Forslin, P. Aspelin, S. Fredrikson, and M. Kristoffersen-Wiberg



ABSTRACT

BACKGROUND AND PURPOSE: Quantitative MR imaging techniques are gaining interest as methods of reducing acquisition times while additionally providing robust measurements. This study aimed to implement a synthetic MR imaging method on a new scanner type and to compare its diagnostic accuracy and volumetry with conventional MR imaging in patients with MS and controls.

MATERIALS AND METHODS: Twenty patients with MS and 20 healthy controls were enrolled after ethics approval and written informed consent. Synthetic MR imaging was implemented on a Siemens 3T scanner. Comparable conventional and synthetic proton-density-, T1-, and T2-weighted, and FLAIR images were acquired. Diagnostic accuracy, lesion detection, and artifacts were assessed by blinded neuro-radiologic evaluation, and contrast-to-noise ratios, by manual tracing. Volumetry was performed with synthetic MR imaging, FreeSurfer, FMRIB Software Library, and Statistical Parametric Mapping. Repeatability was quantified by using the coefficient of variance.

RESULTS: Synthetic proton-density-, T1-, and T2-weighted images were of sufficient or good quality and were acquired in 7% less time than with conventional MR imaging. Synthetic FLAIR images were degraded by artifacts. Lesion counts and volumes were higher in synthetic MR imaging due to differences in the contrast of dirty-appearing WM but did not affect the radiologic diagnostic classification or lesion topography ($P = .50-.77$). Synthetic MR imaging provided segmentations with the shortest processing time (16 seconds) and the lowest repeatability error for brain volume (0.14%), intracranial volume (0.12%), brain parenchymal fraction (0.14%), and GM fraction (0.56%).

CONCLUSIONS: Synthetic MR imaging can be an alternative to conventional MR imaging for generating diagnostic proton-density-, T1-, and T2-weighted images in patients with MS and controls while additionally delivering fast and robust volumetric measurements suitable for MS studies.

ABBREVIATIONS: BPF = brain parenchymal fraction; BV = brain volume; CoV = coefficient of variance; GMF = gray matter fraction; ICV = intracranial volume; PD = proton density; SPM = statistical parametric mapping; SyMRI = synthetic MR imaging; WMF = white matter fraction

In conventional MR imaging, multiple sequences with different contrast weightings are obtained. This process is time-consuming with redundant data acquisition. Techniques such as MR fingerprinting and synthetic MR imaging can reduce acquisition times and thereby increase MR imaging availability for both clin-

ical applications and research.¹⁻³ SyMRI is a synthetic MR imaging method based on a quantitative approach in which a single saturation recovery TSE sequence is used to estimate absolute physical properties, the proton density (PD), longitudinal relaxation rate, and transverse relaxation rate, including correction for B₁-inhomogeneities. Rather than predetermining acquisition parameters such as TE, T1, and TR to maximize tissue contrast,³ synthetic MR imaging produces a free range of synthetic weightings based on a single sequence through mathematic inference.^{4,5} The quantitative nature of the method and its ability to probe multiple physical properties in a single sequence make it suitable for volumetric analysis.⁶⁻¹⁰ Synthetic MR imaging has shown

Received September 29, 2015; accepted after revision November 24.

From the Departments of Clinical Science, Intervention and Technology (T.G., M.U., F.H., L.E.N., S.S., J.B., Y.F., P.A., M.K.-W.) and Clinical Neuroscience (S.F.), Karolinska Institutet, Stockholm, Sweden; and Departments of Radiology (T.G., F.H., C.C., S.S., Y.F., P.A., M.K.-W.), Diagnostic Medical Physics (M.U., L.E.N., J.B.), and Neurology (S.F.), Karolinska University Hospital, Stockholm, Sweden.

This work was supported by Karolinska Institutet and Stockholm County Council through an ALF grant.

Paper previously presented at: Annual Meeting of the Radiological Society of North America, November 29–December 1, 2015; Chicago, Illinois.

Please address correspondence to Tobias Granberg, MD, PhD, Department of Clinical Science, Intervention and Technology, C1-46, Karolinska University Hospital, 141 86 Stockholm, Sweden; e-mail: tobias.granberg@ki.se

Indicates open access to non-subscribers at www.ajnr.org

Indicates article with supplemental on-line tables.

Indicates article with supplemental on-line photos.

<http://dx.doi.org/10.3174/ajnr.A4665>

Table 1: MRI acquisition parameters

Sequence Type	Synthetic MRI	TSE PD-/T2WI	FLAIR	TSE T1WI	3D MPRAGE	3D FLAIR
Acquisition plane	Axial	Axial	Axial	Axial	Axial	Sagittal
In-plane resolution (mm)	0.9 × 0.9	0.9 × 0.9	0.9 × 0.9	0.9 × 0.9	0.9 × 0.9	1.0 × 1.0
Sections (No.)	30	30	30	30	160	160
Section thickness (mm)	4.0	4.0	4.0	4.0	1.0	1.0
Distance factor, (%)	30	30	30	30	–	–
Flip angle	120 ^{oa}	120 ^{oa}	130 ^{oa}	120 ^{oa}	9°	120°
TR (ms)	4260 ^b	4120	9000	550	1900	6000
TE (ms)	22/100 ^b	15/92	90	8	3.48	388
TI (ms)	150/580/2000/4130 ^b	–	2500	–	900	2100
Turbo factor	5	7	12	2	–	–
Generalized partially parallel acquisition factor	2	0	2	0	2	2
Bandwidth (Hz/pixel)	154	250	283	283	180	781
No. of averages	1	1	1	2	1	1
Acquisition time	6:50	2:38	3:38	4:44	5:15	7:02

^a Flip angles denote the flip angles of the echo pulses; excitation flip angles, 90°.

^b Acquisition parameters. Synthetic images were generated using TRs, TIs, and TEs matching the conventional sequences.

promising initial results for use in MS and patients with an ischemic event.^{11,12} The technique is consequently gaining interest as a potentially time-efficient alternative to conventional MR imaging to visualize and quantify brain tissue properties.

MS is a chronic neuroinflammatory disorder affecting 2.5 million people globally.¹³ MS has a heterogeneous clinical expression, which complicates the choice of disease-modifying therapy.¹⁴ MR imaging is a cornerstone for the diagnosis and monitoring of MS, but qualitative MR imaging measurements are poorly correlated with the clinical outcome. Volumetric MR imaging measurements have an independent predictive value in MS but require laborious image postprocessing, limiting its clinical potential.^{15,16} Robust and fully automatic volumetry approved for clinical use would thus be important for clinical care and research purposes. The synthetic MR imaging technique has initially been developed for use on Philips (Best, the Netherlands) and GE Healthcare (Milwaukee, Wisconsin) MR imaging systems, but it is not available for other systems and independent evaluations of the method are scarce.^{5,6}

The purpose of this study was to implement the synthetic MR imaging technique for use on Siemens (Erlangen, Germany) MR imaging scanners and to compare the diagnostic accuracy of synthetic and conventional images in MS. A secondary aim was to test the repeatability of the volumetric synthetic MR imaging measurements and compare the volumetric results and practicality with other commonly used brain volumetric methods.

MATERIALS AND METHODS

Participants and Clinical Assessment

In this prospective study, 20 patients with MS were recruited from the MS center at Karolinska University Hospital. A senior consultant in neurology (S.F.) performed neurologic examinations and rated physical disability by using the Expanded Disability Status Scale, blinded to the radiologic evaluations. Characteristics for patients with MS were the following: 16 women, 4 men; mean age, 44 ± 14 years. MS subtypes were 9 relapsing-remitting, 10 secondary-progressive, and 1 primary-progressive. The mean disease duration was 17.4 ± 11 years; median Expanded Disability Status

Scale score, 2.5 (range, 1.0–8.5) with disease-modifying therapy in 12 patients (60%). A group of 20 age-matched neurologically healthy controls (11 women, 9 men; mean age, 41 ± 17 years) was also recruited. The ethics review board in Stockholm approved the study, and written informed consent was obtained from all participants.

Image Acquisition

Technical details for all MR imaging sequences are given in Table 1. Synthetic MR imaging was implemented as a saturation recovery TSE sequence with a saturation pulse flip angle of 120°, a multiecho readout including phase and magnitude data, with 4 repetitions on a Magnetom Trio 3T scanner (Siemens) on the VB17 software platform using a 12-channel head coil. The section acquisition order was altered for each repetition, resulting in 4 different effective saturation delays (150, 580, 2000, and 4130 ms) for each section. The resulting data formed a matrix of 8 complex images per section at different saturation delays and TEs. A least squares fit was performed on the signal intensity of these images as previously described,³ resulting in estimates of the longitudinal and transverse relaxation rates, PD, and B₁ field inhomogeneities. The synthetic MR imaging acquisition time was 6:50 minutes. Conventional PD-, T1-, and T2-weighted, and FLAIR images were acquired on the basis of the standard brain imaging protocol of the clinic, with section thickness and in-plane resolutions matching those of the synthetic MR imaging sequence. Total acquisition time was 11:00 minutes for all 4 2D conventional MR imaging sequences. Conventional 3D T1WI MPRAGE and 3D FLAIR sequences were additionally acquired (12:17 minutes) for gold standard radiologic and volumetric analyses. Synthetic PD-, T1-, and T2-weighted, and FLAIR images were obtained by using synthetic MR imaging (SyMRI) 7.2 RC software (Synthetic MR, Linköping, Sweden) with synthetic TE, TI, and TR matching the conventional images. To study the repeatability of the volumetric SyMRI measurements, we temporarily took each participant out of the scanner and repositioned them for a second synthetic MR imaging acquisition. Similarly, a second MPRAGE sequence was obtained after re-

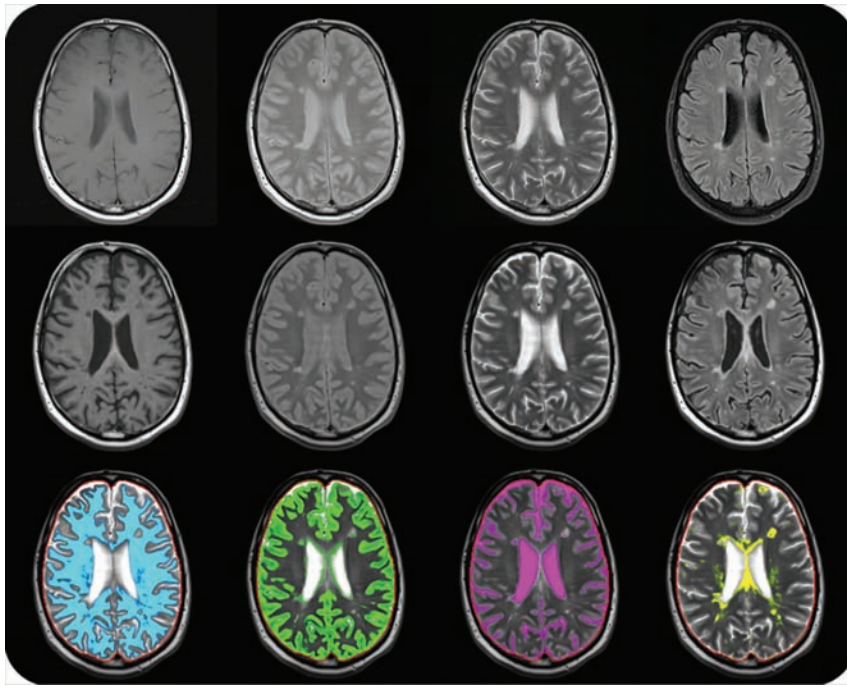


FIG 1. Conventional (*top row*) and synthetic (*middle row*) axial noncontrast MR imaging in a 49-year-old male patient with MS, from left to right: T1-, PD-, and T2-weighted, and FLAIR images. The *bottom row* shows brain tissue segmentations of the WM (cyan), GM (green), CSF (magenta), and other remaining brain tissues (yellow) from SyMRI.

positioning in 5 controls, to compare the repeatability of conventional and synthetic volumetrics.

Radiologic Assessment

All images were blindly and independently assessed by a neuroradiologist and a fellow in neuroradiology (F.H., C.C.) on standard radiologic workstations in the PACS in a random order in 2 sessions 2–4 weeks apart, in which each participant was only represented once per session with either the synthetic or conventional images. Image quality was rated on a 4-level scale: poor (artifacts or image-quality issues rendering the image quality insufficient for diagnostic purposes), sufficient (sufficient image quality for diagnostic purposes but noticeable artifacts or image-quality issues), good (only minor artifacts or image-quality issues), and excellent (no artifacts or image-quality issues). MS lesions were assessed by number and localization (periventricular, juxtacortical, infratentorial) and for the presence of black holes, defined as lesions with lower signal intensity than the normal-appearing white matter in T1WI (yes, no). Discrepancies were compared to the gold standard: the majority decision of the 2 original raters based on all available imaging data, including the 3D T1WI and FLAIR sequences, with any discrepancies resolved by a third rater, senior neuroradiologist (M.K.-W.). Due to the difficulty of quantifying and delineating confluent-versus-nonconfluent lesions for the lesion count, manual lesion segmentations were additionally performed on the 2D synthetic and conventional images by a resident in radiology (T.G.) in ITK-SNAP (www.itksnap.org).¹⁷

Contrast-to-noise ratio analyses were performed by manual tracing of 12 circular ROIs. Two were placed in the CSF (ante-

rior horns of the lateral ventricles bilaterally), 6 in the GM (thalami, frontal cortex, occipital cortex bilaterally), and 4 in the WM (centrum semiovale bilaterally, genu and splenium), and the measurements were averaged for each tissue type. For patients with MS, an additional ROI was placed in the largest MS lesion. Care was taken to avoid regions with artifacts and tissue borders. The contrast-to-noise ratios were calculated by dividing the intensity difference of the tissues by the median SD of all 12 ROIs.

Volumetry

Volumetric measurements from synthetic MR imaging were obtained by using the automatic segmentation in SyMRI, Version 7.2 RC. Conventional volumetric measurements were obtained by using MPRAGE in FreeSurfer (<http://surfer.nmr.mgh.harvard.edu>), Statistical Parametric Mapping (SPM; <http://www.fil.ion.ucl.ac.uk/spm/software/spm12>), and the FMRIB Software Library (FSL; [http://www.fmrib.](http://www.fmrib.ox.ac.uk/fsl)

<http://www.fil.ion.ucl.ac.uk/fsl>).^{18–20} Automatic lesion segmentation based on the conventional 3D images was performed in the Lesion Segmentation Toolbox (Technische Universität München, Munich, Germany) for SPM,²¹ and lesion filling and masking were performed in FSL and SPM to reduce the bias of MS lesions on GM segmentations.²² Segmentations were quality-controlled by a resident in radiology (T.G.), and segmentation parameters in FreeSurfer, FSL, SPM, and the Lesion Segmentation Toolbox were optimized to ensure accurate volumetric data. Initial FSL parameters were chosen on the basis of previous recommendations.²³ Software versions, input, parameters, and processing times can be found in On-line Table 1.

The volumetric measurements of interest were the brain volume (BV), the white matter volume, the gray matter volume, and the intracranial volume (ICV). In the SyMRI software, lesion volume is not estimated, but there is a segmentation of the remaining intracranial content that is not recognized as WM, GM, or CSF. This segmentation class is henceforth referred to as “non-WM/GM/CSF” and contains not only MS lesions but also flow voids in larger blood vessels. The brain tissue measurements were further normalized to the ICV, resulting in the brain parenchymal fraction (BPF), white matter fraction (WMF), gray matter fraction (GMF), and non-WM/GM/CSF fraction. Examples of the synthetic segmentation output can be seen in Fig 1.

Statistical Analysis

Statistical analysis was performed in SPSS Statistics 23 (IBM, Armonk, New York). The Shapiro-Wilk normality test was used to investigate the normality of distribution. Group differences were studied by using the Wilcoxon signed rank test for

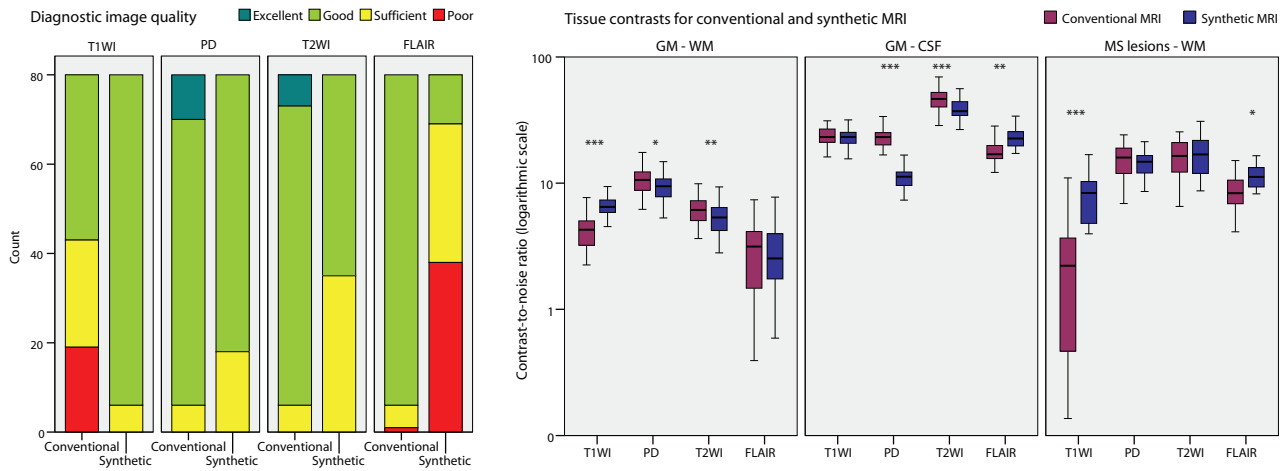


FIG 2. Comparison of the diagnostic image quality (A) and contrast-to-noise ratios (B) for conventional and synthetic MR imaging in patients with MS and controls. Wilcoxon signed rank test: single asterisk indicates $P < .05$; double asterisks, $P < .01$; triple asterisks, $P < .001$.

ordinal dependent data and the McNemar test for binary dependent data. The Spearman rank correlation coefficient was used for correlation analysis. Repeatability was quantified by using the intermeasurement coefficient of variance (CoV) according to the following equation (A and B being the first and second measurements per patient):

$$CoV = \frac{SD}{Mean} = \frac{\sqrt{\frac{\sum(A - B)^2}{2n}}}{\frac{\sum(A + B)}{2n}}$$

Statistical significance was an α level of 5% (2-tailed, equal variances not assumed).

RESULTS

Image Quality and Diagnostic Accuracy

A representative example of conventional and synthetic MR images is seen in Fig 1. The diagnostic image quality and contrast-to-noise ratio measurements are given in Fig 2. Synthetic images were of sufficient or good quality overall, except for FLAIR images, which were degraded by basilar artery and CSF pulsation artifacts in 48% of the scans. Other image artifacts encountered in the synthetic MR images were chemical-shift displacement, discrete Gibbs ringing phenomenon along the superior sagittal sinus, and a sinusoidal intensity difference in the CSF in PD-weighted and T2WI in the anteroposterior direction, which was more easily detected if the lateral ventricles were enlarged. Artifacts are exemplified in On-line Fig 1. A proportion (23%) of the conventional spin-echo T1WIs were considered of poor diagnostic quality, mainly due to pulsation artifacts and low tissue contrast. Meanwhile, none of the synthetic T1WIs were rated of poor diagnostic quality, and synthetic T1WIs were assessed as having better image quality overall for diagnostic purposes ($P < .001$). The difference in tissue contrast was independently corroborated by objective differences in contrast-to-noise ratios, also illustrated in Fig 2.

All 40 participants were correctly classified as patients/controls with both MR imaging techniques, and incidental findings were identical: unspecific white matter changes in healthy controls ($n = 3$), pineal cysts ($n = 3$), mucosal thickening in the

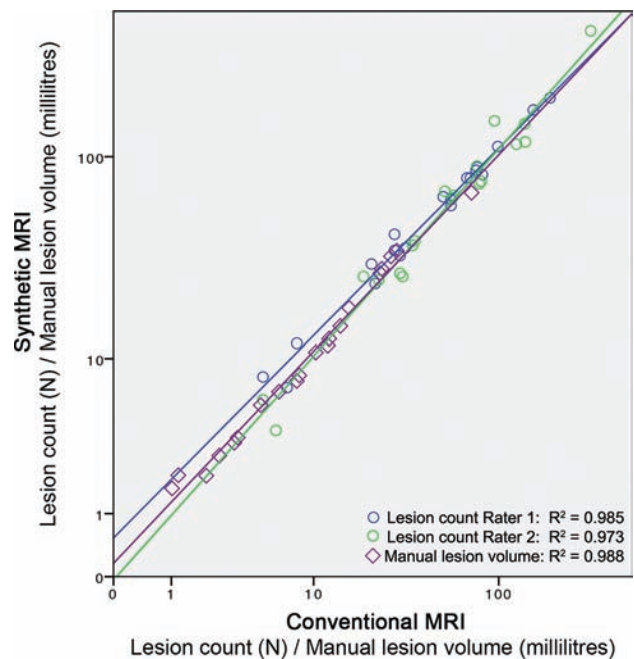


FIG 3. MS lesion counts and manual MS lesion volume segmentation in conventional and synthetic MR imaging with linear regression lines.

maxillary sinuses ($n = 2$), cerebrovascular lesions ($n = 1$), contusional injury ($n = 1$), choroid plexus cyst ($n = 1$), arachnoid cyst ($n = 1$), and abnormally shaped eye bulb ($n = 1$). The lesion count was higher in synthetic MR imaging compared with conventional MR imaging (median, 71 versus 64; interquartile range, 62 versus 56; $P < .001$), but this difference was on the same order of magnitude as the difference between the 2 raters (median, 74 versus 62; interquartile range, 68 versus 53), illustrated in Fig 3. Manual lesion segmentations corroborated this difference with higher manual lesion volumes in synthetic MR imaging (9.5 versus 9.3; interquartile range, 18 versus 16 mL; $P = .009$). The surplus in synthetic lesion volume was mainly due to inclusion of tissue considered “dirty-appearing” WM in the conventional images, exemplified by differences in manual lesion segmentations in On-line Fig 2. There was no statistical difference in the detec-

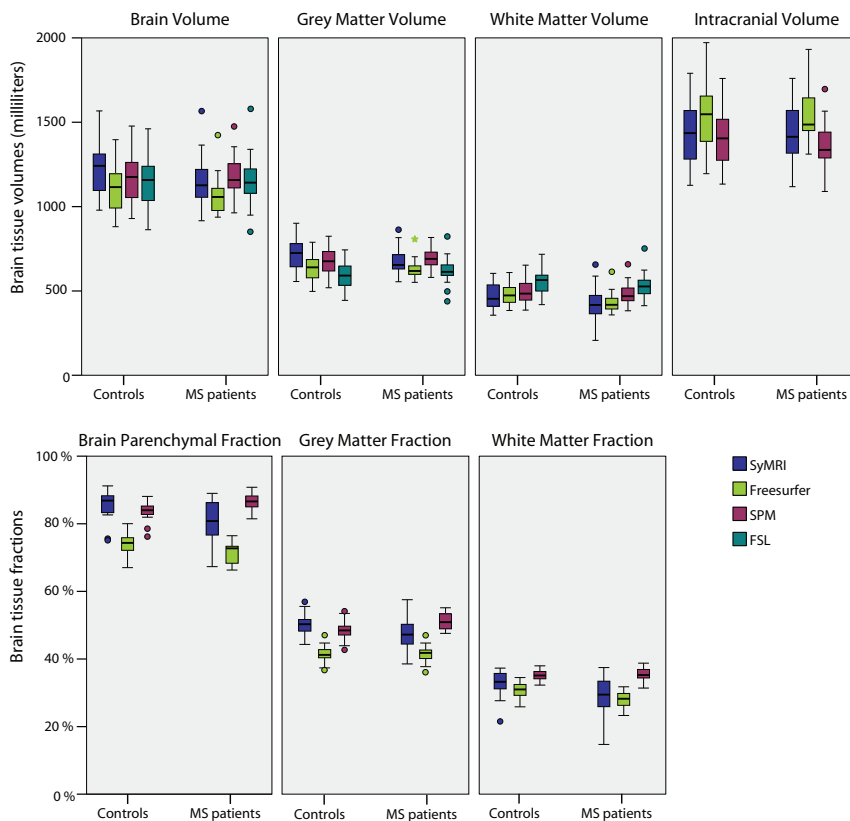


FIG 4. Comparison of conventional and synthetic MR imaging volumetry in patients with MS and controls.

tion of periventricular lesions ($P = .50$, 1 false-negative finding on synthetic MR imaging), juxtacortical lesions ($P = .50$, 1 false-negative finding on synthetic MR imaging), or infratentorial lesions ($P = .77$, 1 false-negative finding on conventional MR imaging, 1 false-positive finding on synthetic MR imaging). There was no statistical difference in the detection of black holes ($P = .50$); 2 additional black holes were detected with synthetic MR imaging (1 false-negative finding on conventional MR imaging, 1 false-positive finding on synthetic MR imaging).

Repeatability and Feasibility of Volumetry

The SyMRI software provided volumetric measurements in the same order of magnitude as 3 commonly used volumetric software programs, illustrated in Fig 4. SyMRI was also the fastest segmentation method by several orders of magnitude (16 seconds compared with 12–187 minutes), without manual intervention, as reported in On-line Table 1. The test-retest repeatability of all volumetric methods is reported in Table 2. SyMRI had a lower repeatability error than FreeSurfer, FSL, and SPM for BV, ICV, BPF, and GMF. However, SyMRI had a similar error compared with the other volumetry methods regarding the segmentation of GM, WM, and WMF.

The SyMRI CoV for all 40 participants was 0.30% for BV and 0.23% for BPF, while the CoV was higher for WM and GM segmentations (gray matter volume and GMF, both 1.4%; white matter volume, 1.8%; WMF, 1.9%). The largest repeatability errors in the SyMRI segmentations of patients with MS were for the smallest tissue volumes and fractions: the non-GM/WM/CSF vol-

ume (CoV, 6.5%) and fraction (CoV, 6.1%). The average absolute and relative measurement differences for patients with MS and controls are reported in On-line Table 2. In terms of the clinical significance, the Expanded Disability Status Scale score was correlated with SyMRI BPF ($r = -0.52$, $P = .02$) and GMF ($r = -0.53$, $P = .02$), but not with WMF ($r = -0.2$, $P = .42$) or non-GM/WM/CSF fraction ($r = 0.21$, $P = .37$).

DISCUSSION

This is the first implementation of synthetic MR imaging on a Siemens MR imaging system and, to the best of our knowledge, the first independent evaluation of the diagnostic accuracy of the technique in MS. In this initial study, we found that synthetic MR imaging may be feasible as an alternative or complement to conventional PD-, T1-, and T2WI in MS. Differences in the contrast of lesions and dirty-appearing WM caused discrepancies in the lesion count and volume, but these differences did not affect the diagnostic classification or lesion topography. However, pulsation artifacts in the synthetic FLAIR imaging must be addressed before it can substitute for conventional FLAIR. Similar

FLAIR artifacts have previously been reported in an implementation on a 1.5T scanner from another manufacturer.¹¹ Artifacts in the synthetic images could also be seen in the preprocessed DICOM files and were therefore not related to a postprocessing issue in the image reconstruction of the SyMRI software. Implementation of the sequence on the newer Siemens E11 software platform and on 1.5T scanners is underway, and we hope to re-evaluate these issues in the next implementation. Although incidental findings were identical with the 2 MR imaging techniques, future studies will have to evaluate the diagnostic accuracy of synthetic MR imaging in pathologies other than MS. The time-savings compared with conventional MR imaging was 7% for PD-, T1-, and T2WI (6:50 versus 7:22 minutes).

We have further shown that the volumetric measurements in the SyMRI are in agreement with those in other volumetric software and that SyMRI had the lowest repeat measurement errors for BV, ICV, BPF, and GMF among all tested volumetric methods. This finding is likely because the sequence inherently has information about PD, the longitudinal and transverse relaxation rates, and B_1 field inhomogeneities, which can render more precise delineations of the intracranial and brain surfaces compared with just using information from T1WI. The multiparametric acquisition is equivalent to a multichannel approach, but without the need for image coregistration because the synthetic volumetrics are based on a single sequence. Because patients with MS are followed longitudinally, normalized brain volumetrics are of special interest. BPF was measured in patients with MS with SyMRI with repeatability errors (CoV, 0.25%; average measurement difference, 0.06%) well below the reported annual brain atrophy rate

Table 2: Coefficients of variance of volumetric MRI measurements^a

	SyMRI (40 Participants)	SyMRI (20 Patients with MS)	SyMRI (20 Controls)	SyMRI (5 Controls)	SPM (5 Controls)	FreeSurfer (5 Controls)	FSL (5 Controls)
Brain volume	0.30	0.35	0.25	0.14	0.29	0.21	0.18
Gray matter volume	1.4	1.2	1.6	0.64	0.81	0.78	0.25
White matter volume	1.8	1.6	2.0	0.81	0.68	0.70	0.28
Intracranial volume	0.26	0.28	0.24	0.12	0.17	0.15	–
Brain parenchymal fraction	0.23	0.25	0.21	0.14	0.17	0.20	–
Gray matter fraction	1.4	1.2	1.6	0.56	0.78	0.64	–
White matter fraction	1.9	1.7	2.1	0.96	0.79	0.67	–

^a All values represent the CoV in percentages. Volume is expressed in milliliters.

(0.5%–1.3%).^{24–27} The variability in measurements was larger in WMF and GMF (CoV, 1.2% and 1.7%; average measurement difference, 0.4% and 0.5%), but still lower than or equal to reported atrophy rates. The segmentation of the non-GM/WM/CSF fraction, which is the smallest tissue compartment, had the largest test-retest variability (CoV, 6.1%; average measurement difference, 1.6%) but may be of clinical importance because it is expected to partly reflect the lesion burden in MS. For comparison, MS lesion volume increases by approximately 5%–10% annually in MS.^{28,29} These results imply that GM, WM, and non-GM/WM/CSF measurements should preferably be studied in perspectives longer than 1 year. From a clinical perspective, the SyMRI was the most practical segmentation method because it could be launched in the PACS and delivered robust volumetrics within a few tens of seconds. In radiologic practice, the feasibility of SyMRI volumetry lowers the threshold for being able to deliver quantitative biomarkers, which is becoming increasingly requested by our clinical colleagues.

This study has several strengths, such as the evaluation of both the diagnostic and volumetric output of SyMRI. The consecutive recruitment of the patients with MS is also advantageous because it reflects a typical panorama of patients with MS in a neurologic outpatient clinic, with all 3 subtypes of MS represented with a wide range of disease duration and Expanded Disability Status Scale scores, as well as the use of a control group. Limitations include a relatively small sample size and that repeat MPRAGE sequences could only be obtained in a subset of controls due to the length of the combined imaging protocol with reproducibility scans. In this study, we primarily harmonized settings in terms of voxel size and timing parameters, but unfortunately, the receiver bandwidth was not optimized in the same way. A lower bandwidth results in a higher signal-to-noise ratio and therefore hampers this comparison, but it also means that SyMRI was affected with chemical-shift displacement artifacts and theoretically longer minimum TEs and TRs, longer echo spacing, and increased susceptibility artifacts.

In terms of generalizability, the study is limited by the use of a 4-mm section thickness with a 30% gap, while a 3-mm section thickness is recommended for MS studies with 2D sequences.³⁰ Subsequently, we have been able to reduce this section thickness to 3 mm, but the gap remains to reduce cross-talk between sections. Future technical effort should try to eliminate the need for this gap in SyMRI and should try to make high-resolution 3D acquisitions possible, which is increasingly important in MS studies.^{30,31} Previous studies of the effects of intravenous gadolinium-based contrast media on the volumetric output of SyMRI indicate that it is important to consistently acquire synthetic MR imaging

either pre- or postcontrast for comparability³²; these findings are the reason we chose to focus on nonenhanced acquisitions in this study. Future studies will be able to clarify how synthetic MR imaging could be implemented as a postcontrast examination and in a longitudinal fashion in MS. Although the basic concepts of synthetic MR imaging implementation on other MR imaging systems are similar, a comparative study across 1.5 and 3T scanners from the 3 major MR imaging systems is warranted. Lastly, an advantage with SyMRI that remains to be studied is the possibility of being able to adjust the synthetic TR, TE, and TI parameters post hoc, which may potentially allow the user to optimize the contrast between normal and pathologic tissues.

CONCLUSIONS

This study shows that synthetic MR imaging can be implemented on Siemens MR imaging scanners and can be an alternative to conventional MR imaging for generating diagnostic PD-, T1-, and T2-weighted images, but not yet FLAIR images, in patients with MS and healthy controls. Volumetric segmentations can be obtained with a few tens of seconds of processing without any extra scanning time in SyMRI. The measurements of BV and BPF have an excellent repeatability and are thus feasible for longitudinal studies in MS.

ACKNOWLEDGMENTS

We would like to thank the participants of the study and the staff at the Karolinska University Hospital MR imaging unit in Huddinge. We also acknowledge Stina Granberg, who has been helpful with graphic assistance. We further thank Karin Johnsson, Eric Westman, and Russell Ouelette for helpful comments on this article.

Disclosures: Tobias Granberg, Farouk Hashim, Yngve Forslin, Carmen Cananau, Sara Shams, Peter Aspelin, Maria Kristoffersen-Wiberg—RELATED: Grant: ALF Grant from Karolinska Institutet and Stockholm City Council.* Sten Fredrikson—UNRELATED: Payment for Lectures (including service on Speakers Bureaus): Allergan, Bayer, Biogen Idec, Genzyme, Merck, Sanofi, Teva; Payment for Development of Educational Presentations: Teva. *Money paid to the institution.

REFERENCES

1. Ma D, Gulani V, Seiberlich N, et al. **Magnetic resonance fingerprinting.** *Nature* 2013;495:187–92 CrossRef Medline
2. Riederer SJ, Suddarth SA, Bobman SA, et al. **Automated MR image synthesis: feasibility studies.** *Radiology* 1984;153:203–06 CrossRef Medline
3. Warntjes JB, Leinhard OD, West J, et al. **Rapid magnetic resonance quantification on the brain: optimization for clinical usage.** *Magn Reson Med* 2008;60:320–29 CrossRef Medline
4. Warntjes JB, Dahlqvist O, Lundberg P. **Novel method for rapid, si-**

- multaneous T1, T2*, and proton density quantification. *Magn Reson Med* 2007;57:528–37 CrossRef Medline
5. Krauss W, Gunnarsson M, Andersson T, et al. **Accuracy and reproducibility of a quantitative magnetic resonance imaging method for concurrent measurements of tissue relaxation times and proton density.** *Magn Reson Imaging* 2015;33:584–91 CrossRef Medline
 6. Ambarki K, Wählin A, Birgander R, et al. **MR imaging of brain volumes: evaluation of a fully automatic software.** *AJNR Am J Neuroradiol* 2011;32:408–12 CrossRef Medline
 7. West J, Warntjes JB, Lundberg P. **Novel whole brain segmentation and volume estimation using quantitative MRI.** *Eur Radiol* 2012;22:998–1007 CrossRef Medline
 8. Ambarki K, Lindqvist T, Wählin A, et al. **Evaluation of automatic measurement of the intracranial volume based on quantitative MR imaging.** *AJNR Am J Neuroradiol* 2012;33:1951–56 CrossRef Medline
 9. Vågberg M, Lindqvist T, Ambarki K, et al. **Automated determination of brain parenchymal fraction in multiple sclerosis.** *AJNR Am J Neuroradiol* 2013;34:498–504 CrossRef Medline
 10. West J, Blystad I, Engström M, et al. **Application of quantitative MRI for brain tissue segmentation at 1.5 T and 3.0 T field strengths.** *PLoS One* 2013;8:e74795 CrossRef Medline
 11. Blystad I, Warntjes JB, Smedby O, et al. **Synthetic MRI of the brain in a clinical setting.** *Acta Radiol* 2012;53:1158–63 CrossRef Medline
 12. West J, Aalto A, Tisell A, et al. **Normal appearing and diffusely abnormal white matter in patients with multiple sclerosis assessed with quantitative MR.** *PLoS One* 2014;9:e95161 CrossRef Medline
 13. Dua T; Rompani P; World Health Organization, Multiple Sclerosis International Federation. *Atlas: Multiple Sclerosis Resources in the World, 2008.* Geneva: World Health Organization; 2008
 14. Goodin DS, Bates D. **Treatment of early multiple sclerosis: the value of treatment initiation after a first clinical episode.** *Mult Scler* 2009;15:1175–82 CrossRef Medline
 15. Bakshi R, Thompson AJ, Rocca MA, et al. **MRI in multiple sclerosis: current status and future prospects.** *Lancet Neurol* 2008;7:615–25 CrossRef Medline
 16. Filippi M, Rocca MA. **Multiple sclerosis: new measures to monitor the disease.** *Lancet Neurol* 2013;12:12–13 CrossRef Medline
 17. Yushkevich PA, Piven J, Hazlett HC, et al. **User-guided 3D active contour segmentation of anatomical structures: significantly improved efficiency and reliability.** *Neuroimage* 2006;31:1116–28 CrossRef Medline
 18. Reuter M, Schmansky NJ, Rosas HD, et al. **Within-subject template estimation for unbiased longitudinal image analysis.** *Neuroimage* 2012;61:1402–18 CrossRef Medline
 19. Jenkinson M, Beckmann CF, Behrens TE, et al. **FSL.** *Neuroimage* 2012;62:782–90 CrossRef Medline
 20. Ashburner J, Friston KJ. **Unified segmentation.** *Neuroimage* 2005;26:839–51 CrossRef Medline
 21. Schmidt P, Gaser C, Arsic M, et al. **An automated tool for detection of FLAIR-hyperintense white-matter lesions in multiple sclerosis.** *Neuroimage* 2012;59:3774–83 CrossRef Medline
 22. Vrenken H, Jenkinson M, Horsfield MA, et al; MAGNIMS Study Group. **Recommendations to improve imaging and analysis of brain lesion load and atrophy in longitudinal studies of multiple sclerosis.** *J Neurol* 2013;260:2458–71 CrossRef Medline
 23. Popescu V, Battaglini M, Hoogstrate WS, et al; MAGNIMS Study Group. **Optimizing parameter choice for FSL-Brain Extraction Tool (BET) on 3D T1 images in multiple sclerosis.** *Neuroimage* 2012;61:1484–94 CrossRef Medline
 24. Miller DH, Barkhof F, Frank JA, et al. **Measurement of atrophy in multiple sclerosis: pathological basis, methodological aspects and clinical relevance.** *Brain* 2002;125:1676–95 CrossRef Medline
 25. Simon JH. **Brain atrophy in multiple sclerosis: what we know and would like to know.** *Mult Scler* 2006;12:679–87 CrossRef Medline
 26. Fotenos AF, Mintun MA, Snyder AZ, et al. **Brain volume decline in aging: evidence for a relation between socioeconomic status, pre-clinical Alzheimer disease, and reserve.** *Arch Neurol* 2008;65:113–20 Medline
 27. Barkhof F, Calabresi PA, Miller DH, et al. **Imaging outcomes for neuroprotection and repair in multiple sclerosis trials.** *Nat Rev Neurol* 2009;5:256–66 CrossRef Medline
 28. Molyneux PD, Filippi M, Barkhof F, et al. **Correlations between monthly enhanced MRI lesion rate and changes in T2 lesion volume in multiple sclerosis.** *Ann Neurol* 1998;43:332–39 CrossRef Medline
 29. Fisniku LK, Brex PA, Altmann DR, et al. **Disability and T2 MRI lesions: a 20-year follow-up of patients with relapse onset of multiple sclerosis.** *Brain* 2008;131:808–17 CrossRef Medline
 30. MAGNIMS study group. **Evidence-based guidelines: MAGNIMS consensus guidelines on the use of MRI in multiple sclerosis—establishing disease prognosis and monitoring patients.** *Nat Rev Neurol* 2015;11:597–606 CrossRef Medline
 31. Traboulsee A, Simon JH, Stone L, et al. **Revised Recommendations of the Consortium of MS Centers Task Force for a Standardized MRI Protocol and Clinical Guidelines for the Diagnosis and Follow-Up of Multiple Sclerosis.** *AJNR Am J Neuroradiol* 2015 Nov 12. [Epub ahead of print]
 32. Warntjes JB, Tisell A, Landtblom AM, et al. **Effects of gadolinium contrast agent administration on automatic brain tissue classification of patients with multiple sclerosis.** *AJNR Am J Neuroradiol* 2014;35:1330–36 CrossRef Medline

White Matter Diffusion Changes during the First Year of Natalizumab Treatment in Relapsing-Remitting Multiple Sclerosis

O.T. Wiebenga, M.M. Schoonheim, H.E. Hulst, G.J.A. Nagtegaal, E.M.M. Strijbis, M.D. Steenwijk, C.H. Polman, P.J.W. Pouwels, F. Barkhof, and J.J.G. Geurts



ABSTRACT

BACKGROUND AND PURPOSE: Natalizumab treatment strongly affects relapsing-remitting multiple sclerosis, possibly by restraining white matter damage. This study investigated changes in white matter diffusivity in patients with relapsing-remitting multiple sclerosis during their first year of natalizumab treatment by using diffusion tensor imaging.

MATERIALS AND METHODS: The study included patients with relapsing-remitting multiple sclerosis initiating natalizumab at baseline ($n = 22$), patients with relapsing-remitting multiple sclerosis continuing interferon- β or glatiramer acetate ($n = 17$), and healthy controls ($n = 12$). Diffusion tensor imaging parameters were analyzed at baseline and month 12. We measured the extent and severity of white matter damage with diffusion tensor imaging parameters such as fractional anisotropy, comparing the patient groups with healthy controls at both time points.

RESULTS: The extent and severity of white matter damage were reduced significantly in the natalizumab group with time (fractional anisotropy–based extent, 56.8% to 47.2%; severity, $z = -0.67$ to -0.59 ; $P = .02$); this reduction was not observed in the interferon- β /glatiramer acetate group (extent, 41.4% to 39.1%, and severity, $z = -0.64$ to -0.67 ; $P = .94$). Cognitive performance did not change with time in the patient groups but did correlate with the severity of damage ($r = 0.53$, $P = < .001$).

CONCLUSIONS: In patients with relapsing-remitting multiple sclerosis starting natalizumab treatment, the extent and severity of white matter damage were reduced significantly in the first year of treatment. These findings may aid in explaining the large observed clinical effect of natalizumab in relapsing-remitting multiple sclerosis.

ABBREVIATIONS: AD = axial diffusivity; EDSS = Expanded Disability Status Scale; FA = fractional anisotropy; GA = glatiramer acetate; IFN β = interferon β ; NBV = normalized whole-brain volume; MD = mean diffusivity; RCI = Reliable Change Index; RD = radial diffusivity; RRMS = relapsing-remitting multiple sclerosis

Multiple sclerosis is an inflammatory demyelinating disease of the central nervous system, characterized by focal damage and atrophy of the white¹ and gray matter.² Physical and

cognitive dysfunction starts early in the disease,³ with a strong impact on the quality of life.⁴ Conventional MR imaging measures, such as lesion load, only modestly relate to patient functioning and progression. Recent advanced MR imaging techniques such as diffusion tensor imaging have shown better correlations with clinical outcomes, partly due to the demonstration of subtle abnormalities in the normal-appearing white matter.^{5–8}

Natalizumab is a second-line (in most countries) treatment option for relapsing-remitting multiple sclerosis (RRMS), which has been shown to have strong anti-inflammatory effects because it prevents leukocytes from penetrating the blood-brain barrier, reducing the formation of new WM lesions⁹ and possibly preventing more subtle damage in the normal-appearing white matter. In doing so, natalizumab may lead to a more advantageous environment for axonal repair and remyelination in the normal-appearing white matter, which can only be measured with more advanced imaging techniques such as DTI. This process might explain how natalizumab seems to affect clinical measures, such as reducing the number of relapses and the progression of disability.¹⁰

Received August 17, 2015; accepted after revision November 12.

From the Departments of Radiology and Nuclear Medicine (O.T.W., G.J.A.N.†, M.D.S., F.B.), Anatomy and Neurosciences (O.T.W., M.M.S., H.E.H., G.J.A.N.†, J.J.G.G.), Neurology (E.M.M.S., C.H.P.), and Physics and Medical Technology (P.J.W.P.), Neuroscience Campus Amsterdam, VU University Medical Center, Amsterdam, the Netherlands.

†Deceased.

This investigator-initiated study was sponsored by the Dutch MS Research Foundation, grant number 09–358d. MR imaging was partly sponsored by Biogen Idec.

Biogen Idec did not participate in any aspect of the design or performance (including data collection, data management, data analysis and interpretation, or preparation) of this investigator-initiated study. Final approval for the work and article was given by the authors.

Please address correspondence to Oliver T. Wiebenga, MD, VU University Medical Center, Department of Radiology and Nuclear Medicine, PO Box 7057, 1007 MB, Amsterdam, the Netherlands; e-mail: o.wiebenga@vumc.nl

Indicates article with supplemental on-line photo.

<http://dx.doi.org/10.3174/ajnr.A4690>

In this study, we investigated the effects of natalizumab on the evolution of WM damage in the first year of treatment by measuring the extent and severity of WM damage by using DTI. Patients starting natalizumab treatment were scanned at baseline and after 1 year. A patient group continuing standard disease-modifying-drugs (ie, interferon- β or glatiramer acetate [IFNb/GA]) was also included. Both patient groups were compared with healthy controls.

MATERIALS AND METHODS

Study Design

The study was a prospective and observational study with 2 time points: baseline and month 12. The study population consisted of 22 patients with RRMS initiating natalizumab treatment and 12 healthy controls, age- and sex-matched to the patients. Before switching to natalizumab, 13 patients were receiving IFNb and 9 patients were receiving GA. To provide insight into the normal evolution of WM pathology in MS, we included 17 patients with RRMS following and continuing IFNb/GA. Patients receiving IFNb/GA were pooled (IFNb $n = 11$ and GA $n = 6$) and were matched to the patients initiating natalizumab for age, sex, disability (Expanded Disability Status Scale [EDSS]¹¹), and duration of prior IFNb/GA exposure.

Inclusion criteria for the patients with RRMS were a diagnosis of clinically definite MS¹² and being between 18 and 65 years of age. Exclusion criteria were the presence or history of psychiatric or neurologic disease (besides MS) and the presence or history of alcohol or drug abuse. The study protocol was approved by the institutional ethics review board of our center, and informed consent was obtained from all participants.

No serious or unanticipated adverse events attributed to MS medication developed in the patient groups.

Study Population

Patients initiating natalizumab at the outpatient neurology clinic of our center were screened according to the indication criteria used at our institution. These included at least 1 prior period of IFNb or GA with break-through disease with ≥ 1 relapse or rapidly evolving active RRMS defined by the occurrence of ≥ 2 relapses. Patients were only included in the study once the decision to start natalizumab treatment had already been made. At the baseline measurement, 6 patients were treatment-naïve for natalizumab; 13 patients had received 1, and 3 patients, 2 infusions. All patients continued natalizumab treatment (300 mg IV once every 4 weeks) for the duration of the study.

Patients receiving IFNb/GA were already receiving and continuing IFNb/GA as their regular medical treatment. Eleven patients were continuing IFN-b-1a/b (dose and route of administration dependent on type), and 6 patients were continuing GA (20 mg subcutaneous once daily). One patient from this group discontinued GA before the month 6 visit because of radiologic and clinically stable disease combined with occurrence of adverse effects (necrosis and scarring of the skin at injection sites). Another patient discontinued IFNb-1a 1 month before the month 12 visit due to conversion to secondary-progressive MS. Both patients remained in the study.

MR Imaging

All imaging was performed on a 1.5T whole-body scanner (Sonata; Siemens, Erlangen, Germany) by using an 8-channel phased array head coil. Structural imaging sequences included a 3D-T1-weighted magnetization-prepared rapid acquisition of gradient echo sequence (TR, 2,700 ms; TE, 5 ms; TI, 950 ms; 176 sagittal sections with 1.3-mm section thickness; $1.3 \times 1.3 \text{ mm}^2$ in-plane resolution) for brain volume measurements and an axial turbo spin-echo proton-density/T2-weighted sequence (TR, 3,130 ms; TE, 24 and 85 ms; 46 contiguous 3-mm sections; $1 \times 1 \text{ mm}^2$ in-plane resolution) for WM lesion detection. Diffusion-weighted echo-planar images (TR, 8,500 ms; TE, 86 ms; isotropic resolution, $2 \times 2 \times 2 \text{ mm}$) were acquired with 60 volumes with noncollinear diffusion gradients (b-value of 700 s/mm²) and 10 volumes without directional weighting.

Brain and Lesion Volumes

T2-hyperintense WM lesions were quantified by using an automated segmentation method.¹³ Normalized whole-brain (NBV), WM, and GM volumes were calculated by using the T1-weighted images and SIENAX (<http://fsl.fmrib.ox.ac.uk/fsl/fslwiki/SIENAX>)¹⁴ Brain volumes were calculated after lesion filling, by using (part of FSL, Version 5.02; <http://www.fmrib.ox.ac.uk/fsl>). Brain volumes were calculated after lesion filling, by using an automated lesion-filling technique (Lesion Automated Preprocessing).¹⁵

Extent and Severity of WM Integrity Damage

The diffusion parameters fractional anisotropy (FA), mean diffusivity (MD), axial diffusivity (AD), and radial diffusivity (RD) were derived for each voxel by fitting a tensor model to the raw diffusion data after motion and eddy current correction. For statistical comparisons, Tract-Based Spatial Statistics (TBSS; <http://fsl.fmrib.ox.ac.uk/fsl/fslwiki/TBSS>),¹⁶ part of FSL, was used, in which all subjects' FA maps were aligned into a common space. The mean FA image was thinned to create a mean FA skeleton and thresholded at an FA of 0.2. Each subject's aligned FA and diffusivity data were then projected onto this WM skeleton, and the resulting data were fed into the FSL Randomize tool (<http://fsl.fmrib.ox.ac.uk/fsl/fslwiki/Randomise>).

At both time points, cross-sectional group differences in FA and MD of the mean WM skeleton were analyzed by using Randomize (500 permutations) by using a family-wise error-corrected threshold of $P < .05$ and correcting for age and sex.

Following the TBSS pipeline, we calculated the extent and severity of damage as follows:

1) The "extent" of damage was calculated per group, by calculating the percentage of significantly abnormal ($P < .05$) voxels within the WM skeleton for the diffusion parameters FA and MD, compared with healthy controls.

2) The "severity" of damage within the WM skeleton was calculated per patient by converting the diffusion measures FA and MD to z scores on the basis the mean and SDs of healthy control voxels. A single whole-skeleton mean z score was calculated for the diffusion parameters FA and MD, indicating the severity of damage across the entire WM skeleton per subject. As a post hoc

exploration, the severities of AD and RD were additionally calculated at both time points.

Neuropsychological Evaluation

All subjects underwent an elaborate neuropsychological assessment on the day of scanning. The cognitive domains most frequently affected in MS were investigated by using tests from Rao's Brief Repeatable Battery for Neurologic Disease,¹⁷ including the Symbol Digit Modalities Test for information-processing speed, the Spatial Recall Task (SPART 10/36) for visuospatial memory, and the Word List Generation test for verbal fluency. Additionally, the Verbal Learning and Memory Task (the Dutch equivalent of the California Verbal Learning Test for verbal memory), the Stroop Color and Word Test for attention and inhibition, the Digit Span Forward and Digit Span Backward (part of the Wechsler Adult Intelligence Scale) for working memory, and the Delis-Kaplan Executive Function System Trail-Making Test for executive functioning were administered. Parallel versions were used for the different subtests when available (Symbol Digit Modalities Test, SPART 10/36, and Verbal Learning and Memory Task).

To uniformly quantify the deviation compared with test or subtest scores of the healthy controls, we converted the test or subtest raw baseline scores to *z* scores. An average (overall) cognition *z* score was also calculated.

The raw test or subtest scores were converted to Reliable Change Indices (RCI) to correct subtle learning effects in the longitudinal analysis.¹⁸ With this method, the reliable change on an individual test score is based on the difference between baseline and retest scores for the normative subject sample. RCI was computed as follows:

$$RCI = \frac{\{[X_2 - X_1] - [\text{mean}(hc_2) - \text{mean}(hc_1)]\}}{SED},$$

where *X* is a single-subject test score, mean[*hc*] is the mean of the healthy controls' test scores, and 1 and 2 are the different time points at which cognitive testing was performed. The SD of the mean Δ score of the healthy controls was used as the standard error of the difference score (SED).

An RCI score above zero indicates a better performance, whereas an RCI score below zero indicates a worse performance than can be expected by the normal learning curve of healthy controls.

Patient Reported Outcome Measures

Fatigue and symptoms of anxiety and depression were measured by using the Checklist Individual Strength¹⁹ and the Hospital Anxiety and Depression Scale²⁰ questionnaires, respectively.

Statistical Analysis

Statistical analyses were performed with SPSS for Windows, Version 20.0 (IBM, Armonk, New York). When the variables were normally distributed, a multivariate GLM was used to test for group differences, with age, sex, and education included as covariates. Longitudinal analyses were performed by using paired *t* tests comparing baseline with month 12. Nonparametric analysis was performed by using the Kruskal-Wallis and (post hoc) Mann-Whitney tests. All analyses were Bonferroni-corrected, and *P* < .05 was considered statistically significant.

RESULTS

Descriptives and Clinical Scores

At baseline, the 3 groups did not differ on age and sex (Table 1). Compared with the healthy controls, patients with RRMS had more depressive symptoms (Hospital Anxiety and Depression Scale-Depression: natalizumab, *P* = .004; IFNb/GA, *P* = .007) and fatigue (Checklist Individual Strength: natalizumab, *P* = .006; IFNb/GA, *P* = .001) and a slightly lower level of education (natalizumab, *P* = .008; IFNb/GA, *P* = .014). There were no differences between the patient groups for any of these measures or for EDSS, disease duration, and duration of prior IFNb/GA.

After 1 year, EDSS scores remained stable at 3.0 in patients receiving natalizumab, while the depression score (Hospital Anxiety and Depression Scale-Depression) significantly improved from 4.5 to 2.0 (*P* = .012, Table 2). In patients receiving IFNb/GA, EDSS scores significantly deteriorated from 2.5 to 3.0 (*P* = .006) with no change in depression. Fatigue levels remained constant for both groups.

Brain and Lesion Volumes

At baseline, only the IFNb/GA group showed lower NBV compared with controls (*P* = .022), while both patient groups had lower normalized WM volume (natalizumab, *P* = .044; IFNb/GA, *P* = .024). After 12 months, a further reduction was seen in both patient groups for normalized WM volume (natalizumab, *P* = .008; IFNb/GA, *P* = .004) and NBV (natalizumab, *P* = .036; IFNb/GA, *P* < .001). T2-lesion volumes remained stable in patients receiving natalizumab (*P* = .644) but increased in the IFNb/GA group (*P* = .012, Table 3).

DTI: Extent of WM Damage

At baseline, patients receiving natalizumab had reduced FA in 56.8% of the investigated WM skeleton voxels, including major WM bundles of the corpus callosum, the capsula externa, forceps major, corticospinal tract, corona radiata, and superior longitudinal fasciculus (Fig 1). At month 12, this dropped to 47.2%. For MD, the extent with time was 54.3% and 55.7%, respectively (Fig 2). Increased MD was generally seen in those parts of the WM skeleton where the FA was also decreased. Patients receiving IFNb/GA had reduced FA in 41.4% of the skeleton at baseline and 39.1% at month 12; for MD, this was 33.7% and 36.1%. Affected areas overlapped with the regions damaged in the natalizumab group but were generally smaller.

DTI: Severity of WM Damage

In the patients receiving natalizumab, the severity of FA damage at baseline was *z* = -0.67. At month 12, however, the severity was reduced to *z* = -0.59 (*P* = .02 compared with baseline, Table 3), indicating that regional FA values were improved in these patients. In the patients receiving IFNb/GA, the severity remained stable at both time points, from *z* = -0.64 to -0.67, with no significant change with time (*P* = .94).

No significant changes in whole-skeleton MD, AD, and RD severity *z* scores of WM damage were found in any group between baseline and month 12 (Table 3).

Table 1: Baseline variables of patients with MS and controls (mean)^a

	Patients with Natalizumab (n = 22)	Patients with IFNb/GA (n = 17)	Healthy Controls (n = 12)	P Value
MS therapy	Starting natalizumab at baseline	Continuing IFNb/GA at baseline	NA	
Descriptives				
Age (yr)	37.2 ± 8.8	38.2 ± 5.0	35.1 ± 5.3	.492
Sex (male/female) ^b	9:3	8:9	3:9	.322
Education ^c (mean) (range)	6.0 (4–7)	6.0 (5–7)	7.0 (5–7)	.016 ^e
HADS-A ^c (mean) (range)	6.0 (1–13)	6.6 (1–14)	4.8 (1–12)	.369
HADS-D ^c (mean) (range)	4.5 (0–18)	5.0 (0–12)	1.8 (0–10)	.008 ^e
CIS-20 ^c (mean) (range)	68.5 (14–125)	86 (31–114)	42.5 (17–85)	.002 ^e
MS characteristics				
EDSS ^{b,c}	3.0 (1.5–6.5)	2.5 (1.0–6.5)	NA	.615
Disease duration since onset (yr)	8.3 ± 6.2	9.1 ± 5.2	NA	.662
Prior IFNb/GA duration at baseline (yr)	2.9 ± 3.1	4.5 ± 4.0	NA	.169
Volumes				
NGMV (L)	0.75 ± 0.04	0.73 ± 0.06	0.77 ± 0.04	.134
NWMV (L)	0.69 ± 0.04	0.69 ± 0.04	0.73 ± 0.03	.020 ^e
NBV (L)	1.44 ± 0.06	1.42 ± 0.08	1.50 ± 0.06	.025 ^f
T2 lesion volume (mL) ^d	6.2 (2.4–14.9)	4.9 (2.5–12.0)	NA	.281
Cognition z scores				
Symbol Digit Modalities Test	−2.17 ± 0.92	−1.71 ± 1.13	0.00 ± 1.00	<.001 ^e
SPART-total recall	−1.90 ± 1.94	−0.82 ± 1.83	0.00 ± 1.00	.021 ^g
SPART-delayed recall	−1.42 ± 1.57	−0.80 ± 1.93	0.00 ± 1.00	.076
VLGT-immmediate recall	−1.33 ± 1.84	−1.66 ± 1.53	0.00 ± 1.00	.052
VLGT-short-term free recall	−1.66 ± 1.89	−1.40 ± 1.64	0.00 ± 1.00	.068
VLGT-long-term free recall	−1.65 ± 1.86	−1.48 ± 1.72	0.00 ± 1.00	.070
WLG-Animals	−0.97 ± 0.73	−0.75 ± 0.81	0.00 ± 1.00	.019 ^g
WLG-Professions	−1.69 ± 1.15	−1.79 ± 1.58	0.00 ± 1.00	.001 ^e
WLG-4 letter “M” words	−0.81 ± 1.0	−0.85 ± 0.94	0.00 ± 1.00	.072
Digit Span Forward	−0.62 ± 1.06	−0.29 ± 0.98	0.00 ± 1.00	.670
Digit Span Backward	−0.96 ± 1.13	−0.05 ± 1.36	0.00 ± 1.00	.067
TMT-Letter-Number Switching	−2.33 ± 2.45	−1.58 ± 2.08	0.00 ± 1.00	.059
Stroop-interference	−0.28 ± 1.44	−0.63 ± 1.25	0.00 ± 1.00	.697
Average cognition	−1.61 ± 0.73	−1.22 ± 1.01	0.00 ± 1.00	<.001 ^e

Note:—CIS-20 indicates Checklist for Individual Strength questionnaire; HADS, Hospital Anxiety and Depression Scale; A, Anxiety; D, Depression; SPART, Spatial Recall Task; NGMV, normalized gray matter volume; NWMV, normalized white matter volume; VLGT, Verbal Memory and Learning Task; WLG, Word List Generation; TMT, Trail-Making Test; L, liter; NA, not applicable.

^a When normally distributed, a multivariate General Linear Model was used with age, sex, and education included as covariates; General Linear Model main effect *P* values are shown. Nonparametric testing was performed using the Kruskal-Wallis and post hoc Mann-Whitney tests. *P* values < .05 are considered significant.

^b χ^2 test.

^c Median and range.

^d Median and interquartile range.

^e Significant in both patient groups compared with healthy controls.

^f Only significant between patients receiving IFNb/GA and healthy controls.

^g Only significant between patients receiving natalizumab and healthy controls.

Table 2: Clinical scales of baseline and month 12 (median and range)^a

Time Point	Baseline	Month 12	P Value
Patients on natalizumab			
EDSS	3.0 (1.5–6.5)	3.0 (1.0–6.5)	1.0
HADS-A	6.0 (1–13)	6.0 (0–15)	1.0
HADS-D	4.5 (0–18)	2.0 (0–17)	.012 ^b
CIS-20	68.5 (14–125)	62.0 (10–117)	.036
Patients on IFNb/GA (n = 17)			
EDSS	2.5 (1.0–6.5)	3.0 (1.5–7.0)	.006 ^b
HADS-A	7.0 (1–14)	5.0 (1–11)	.609
HADS-D	5.0 (0–12)	3.0 (0–14)	.855
CIS-20	86.0 (31–114)	81.0 (16–105)	.177
Healthy controls (n = 12)			
HADS-A	3.5 (1–12)	2.5 (0–9)	1.0
HADS-D	1.0 (0–10)	0.0 (0–5)	1.0
CIS-20	42.5 (17–85)	52.0 (17–82)	.744

Note:—CIS-20 indicates Checklist Individual Strength questionnaire; HADS, Hospital Anxiety and Depression Scale; A, Anxiety; D, Depression.

^a EDSS, HADS, and CIS were tested with the related-samples Wilcoxon signed rank test (Bonferroni-corrected).

^b Significant difference.

Cognition

At baseline, both patient groups had lower z scores for the Symbol Digit Modalities Test (natalizumab, *P* = .001; IFNb/GA, *P* < .001) and the Word List Generation-Professions (natalizumab, *P* = .003; IFNb/GA, *P* = .002) (Table 1) compared with healthy controls. The average cognition z score was significantly lower for both patient groups (natalizumab, *P* < .001; IFNb/GA, *P* = .005) compared with the healthy controls, but no difference between the patient groups (*P* = .370) was found.

Overall, cognition scores were stable with time for both groups (Table 4), apart from the immediate recall of the

Table 3: DTI and volumetric variables of baseline and month 12 visit (mean)

	Baseline	Month 12	P Value
Patients on natalizumab (n = 22)			
FA severity (z score)	-0.67 ± 0.65	-0.59 ± 0.69	.02 ^a
MD severity (z score)	0.89 ± 0.92	0.93 ± 0.98	.81
AD severity (z score)	0.36 ± 0.40	0.43 ± 0.39	.34
RD severity (z score)	0.94 ± 1.00	0.94 ± 1.07	1.0
NGMV (L)	0.75 ± 0.04	0.75 ± 0.05	1.0
NWMV (L)	0.69 ± 0.04	0.67 ± 0.03	.008 ^a
NBV (L)	1.44 ± 0.06	1.42 ± 0.06	.036 ^a
T2 lesion volume (mL) ^b	6.2 (2.4–14.9)	6.9 (2.2–13.6)	.644
Patients on IFNβ/GA (n = 17)			
FA severity (z score)	-0.64 ± 0.43	-0.67 ± 0.48	.94
MD severity (z score)	0.74 ± 0.58	0.78 ± 0.58	.64
AD severity (z score)	0.26 ± 0.35	0.26 ± 0.28	1.0
RD severity (z score)	0.82 ± 0.59	0.87 ± 0.62	.43
NGMV (L)	0.73 ± 0.06	0.74 ± 0.05	1.0
NWMV (L)	0.69 ± 0.04	0.67 ± 0.03	.004 ^a
NBV (L)	1.42 ± 0.08	1.41 ± 0.07	<.001 ^a
T2 lesion volume (mL) ^b	4.9 (0.25–12.0)	5.4 (0.28–13.3)	.012 ^a

Note:—NGMV indicates normalized gray matter volume; NWMV, normalized white matter volume.

^a Significant difference between the time points (Bonferroni-corrected).

^b Median and interquartile range.

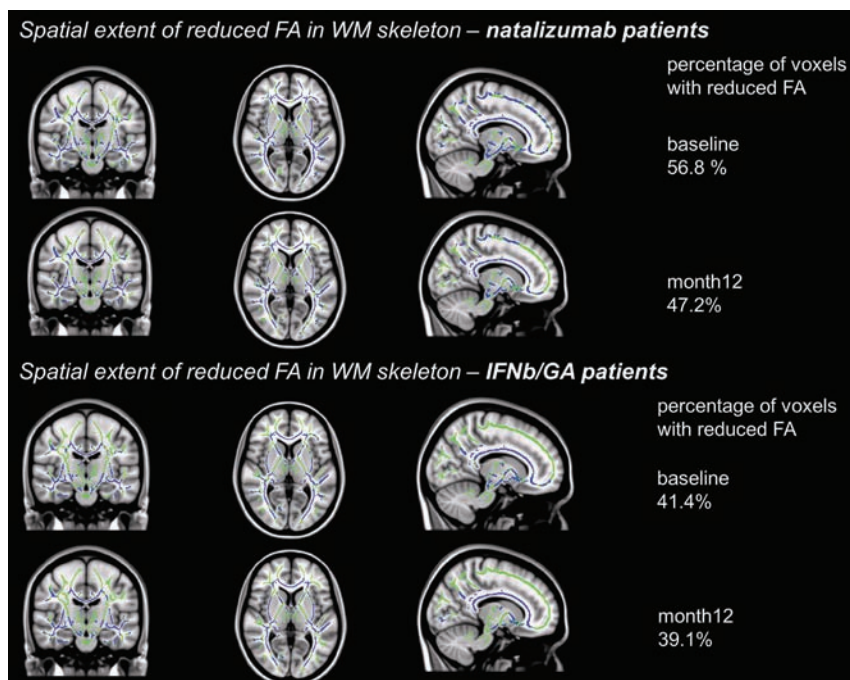


FIG 1. Spatial extent of lowered FA (in blue) of white matter voxels in the TBSS skeleton (green) ($X = 77, Y = 109, Z = 77$) of patients treated with natalizumab (upper 2 rows) and those treated with IFNβ/GA (lower 2 rows). Patients starting natalizumab had reduced FA in 56.8% ($P < .05$) of the WM skeleton at baseline and improved to 47.2% at month 12. Patients continuing IFNβ/GA had reduced FA in 41.4% of the WM skeleton at baseline and 39.1% at month 12.

Verbal Learning and Memory Task, in which only scores of patients receiving natalizumab declined with time ($P = .024$), compared with a relatively stable score in patients receiving IFNβ/GA.

In the total patient group (those receiving both natalizumab and IFNβ/GA), a significant correlation was found between average cognition and the FA severity z score ($r = 0.525, P < .001$ at month 12; On-line Figure), indicating that patients with more severe WM damage have worse cognitive impairment.

DISCUSSION

In this longitudinal study, the clinical and radiologic evolution of patients with MS initiating natalizumab treatment was monitored for 12 months. Additionally, we also followed age-, sex-, and disability-matched patients with MS continuing IFNβ/GA and healthy controls. In natalizumab-treated patients, the severity of WM damage and depressive symptoms improved during 12 months, while lesion volumes and disability levels remained constant. In patients treated with IFNβ/GA, lesion volumes and disability levels worsened, with no improvement in WM damage or depression. Both patient groups had reduced normalized WM volume and NBV at month 12.

Previous in vivo studies have shown FA reductions in focal lesions in MS, as well as in the normal-appearing white matter,^{6,21} though increases with time have not previously been reported. In animal models, reduced FA was found to be the result of less axonal integrity (related to AD^{22,23}) or demyelination (related to RD^{24,25}). This finding was confirmed in a postmortem histopathologic DTI study of MS brain sections showing a strong correlation of FA with the level of myelination as well as the number of axons in both WM lesions and normal-appearing white matter.²⁶ Because we have observed increases in FA with time, the strong anti-inflammatory effect of natalizumab,²⁷ in which leukocytes are prevented from penetrating the blood-brain barrier, may therefore have led to a more advantageous environment for axonal repair and remyelination in the normal-appearing white matter. This supposition was supported by a previous study on natalizumab, in which FA values within gadolinium-enhancing WM lesions were found to increase with time. Additionally, in this study, FA decreases were in normal-appearing brain tissue in this time period (pooled ROIs of normal-appearing white matter and GM).²⁸ In the current study, however, we did not differentiate between lesional WM and normal-appearing white matter and we did not observe decreases in FA in the natalizumab group. Future work is required to specifically follow diffusion metrics in lesional WM under natalizumab treatment because the anti-inflammatory effect could particularly prevent damage or improve integrity in preactive or active lesions but could not be investigated in the current study because we did not have sufficient gadolinium-enhanced MR images available.

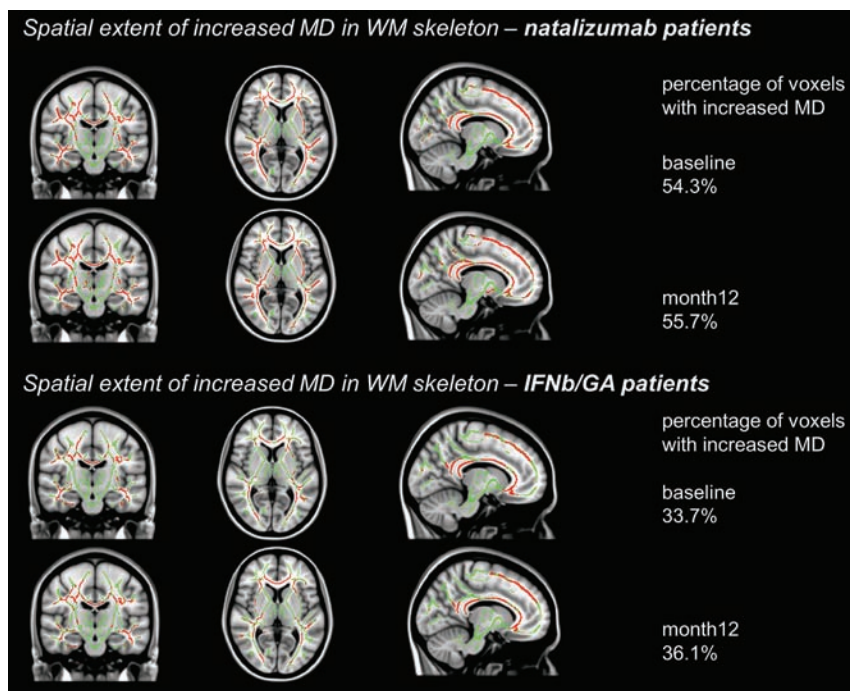


FIG 2. Spatial extent of increased MD (in red) in white matter voxels in the TBSS skeleton (green) ($X = 101, Y = 109, Z = 77$) of patients treated with natalizumab (*upper 2 rows*) and those treated with IFN β /GA (*lower 2 rows*). Patients starting natalizumab had increased MD in 54.3% ($P < .05$) of the WM skeleton at baseline and 55.7% at month 12. Patients continuing IFN β /GA had increased MD in 33.7% of the WM skeleton at baseline and 36.1% at month 12.

Table 4: RCI (mean) of patients on natalizumab and IFN β /GA between baseline and month 12

RCI Baseline–Month 12	Patients on Natalizumab	Patients on IFN β /GA	P Value
Symbol Digit Modalities Test	-0.02 ± 0.68	-0.04 ± 0.77	.993
SPART-total	0.18 ± 1.46	-0.49 ± 1.42	.432
SPART-delayed	0.54 ± 1.69	0.06 ± 1.99	.629
VLGT–immediate recall	-0.67 ± 0.88	0.20 ± 1.03	.024 ^a
VLGT–short-term free recall	-0.15 ± 1.01	0.06 ± 0.75	.575
VLGT–long-term free recall	-0.21 ± 1.36	0.47 ± 0.84	.211
WLG–Animals	0.15 ± 0.90	-0.40 ± 0.81	.185
WLG–Professions	-0.19 ± 0.88	0.04 ± 1.17	.835
WLG–4 letter “M” words	-0.61 ± 0.88	-0.36 ± 1.08	.129
Digit Span Forward	-0.01 ± 0.87	0.06 ± 0.85	.842
Digit Span Backward	-0.31 ± 0.89	-0.34 ± 1.42	.572
TMT–Letter–Number Switching	0.41 ± 3.23	0.59 ± 2.91	.922
Stroop–interference	-1.00 ± 2.14	-0.78 ± 1.63	.595

Note:—SPART indicates Spatial Recall Task; VLGT, Verbal Memory and Learning Task; WLG, Word List Generation; TMT, Trail-Making Test.

^a A significant difference between the patient groups.

Both patient groups had reduced normalized WM volume and NBV at the month 12. In the patients receiving natalizumab, this finding might be caused by the well-known pseudoatrophy effect, in which the anti-inflammatory effect of natalizumab reduces the edema during the first 12 months of treatment.^{9,29,30}

Clinically, natalizumab appeared to stabilize EDSS scores and reduce symptoms of depression, as observed in our data. No effect on cognitive functioning was found in this study. Although the patients receiving natalizumab had a significantly lower RCI in only 1 subtest (short-term verbal memory) compared with patients receiving IFN β /GA, the score of patients receiving natalizumab, in an absolute sense, at month 12 was comparable with the

baseline. This outcome is in contrast to previous studies showing improvement in cognition under natalizumab treatment with a short treatment window.^{31–37} In those studies, however, no controls were included and scores were not corrected for normal learning effects, such as by using the RCI. Here, both patient and control groups showed positive learning curves in most tests (see RCI scores in Table 4). This finding indicates normal improvement in raw cognitive scores with time, stressing the need for healthy control scores for future longitudinal studies looking at cognition in MS.

If the observed increases in FA persist for longer follow-up times, it is possible that natalizumab-induced improvement and/or stabilizations in brain tissue could affect cognitive function in these patients, given the strong correlation between the severity of FA abnormalities and overall cognition found in our data, as well as in other previous studies^{5,7,38} and the previously shown slow rate of cognitive decline in MS.³⁹ It is currently unclear, however, whether this could be in the form of actual increases in cognitive scores or merely the slowing down of cognitive decline. Therefore studies with longer follow-up times are needed. Future studies could also investigate regional WM FA changes and possibly GM FA changes (which we did not investigate in this study) and correlate these potential improvements to change in cognition.

The nonrandomized observational study design and a relatively small study population might be seen as limitations of the current study. Patients starting natalizumab might have a more severe disease (as natalizumab is a second-line therapy at our center), though in our study sample, the patient groups did not differ in physical disability, cognitive performance, disease duration, lesion load, or the severity of FA damage of the whole skeleton. Patients receiving natalizumab did show a higher extent of FA damage in WM compared with those receiving IFN β /GA (56.8% versus 41.4%) however. Therefore, we did not directly compare patient groups but merely added the interferon- β and glatiramer acetate groups, in which clinical and MR imaging effects seem to be similar,⁴⁰ to illustrate longitudinal changes in the MS brain that occur in patients with less aggressive disease. Besides the study design, the relatively short follow-up time indicates the need for future studies with longer treatment windows and larger sample sizes, per-

haps by using a baseline measurement after several months of anti-inflammatory treatment, to reduce the effects of acute inflammation. This need is especially indicated for studies looking at cognitive decline in MS.

CONCLUSIONS

We found that after 12 months of natalizumab treatment, patients with MS showed a reduction in the severity of WM damage, combined with a stabilization of EDSS scores and lesion loads and improved depressive symptoms. Carefully matched patients receiving IFN β /GA did not have reduced WM damage, showing larger lesion volumes and worsened disability. Future studies with longer follow-up times are now required to investigate the long-term effects of these improvements on clinical measures like cognition in MS.

Disclosures: Menno Schoonheim—UNRELATED: Consultancy: Genzyme*; Grants/Grants Pending: Dutch MS Research Foundation,* Comments: The MS Center Amsterdam was supported by grants from the Dutch MS Research Foundation; Payment for Lectures (including service on Speakers Bureaus): Excellence in Medical Education,* Comments: Our center has received financial compensation for lectures I have given for Excellence in Medical Education to Neurologists on several occasions. Hanneke Hulst—UNRELATED: Consultancy: Biogen Idec,* Teva Pharmaceutical Industries, Genzyme,* Novartis,* Merck Serono.* Chris Polman—RELATED: Grant: Biogen Idec; UNRELATED: Board Membership: Receptos/PPD, MorphoSys; Consultancy: Actelion, Biogen Idec, GlaxoSmithKline, Merck Serono, Novartis, Teva Pharmaceutical Industries*; Grants/Grants Pending: Biogen Idec,* Bayer Schering,* Novartis,* Teva Pharmaceutical Industries.* Frederik Barkhof—UNRELATED: Board Membership: Radiology, Neurology, Brain; Consultancy: Roche, Novartis, Synthon, Teva Pharmaceutical Industries,* Schering, Merck Serono, Biogen Idec, Comments: advice to pharmaceutical companies. Jeroen Geurts—UNRELATED: Board Membership: MSJ editorial work*; Consultancy: Hertie Foundation,* National MS Society,* Biogen,* Novartis,* Teva Pharmaceutical Industries*; Grants/Grants Pending: Biogen,* Novartis,* Dutch Foundation MS Research,* Canadian MS Society.* *Money paid to the institution.

REFERENCES

- Compston A, Coles A. **Multiple sclerosis.** *Lancet* 2008;372:1502–17 CrossRef Medline
- Geurts JJ, Calabrese M, Fisher E, et al. **Measurement and clinical effect of grey matter pathology in multiple sclerosis.** *Lancet Neurol* 2012;11:1082–92 CrossRef Medline
- Schulz D, Kopp B, Kunkel A, et al. **Cognition in the early stage of multiple sclerosis.** *J Neurol* 2006;253:1002–10 CrossRef Medline
- Chiaravalloti ND, DeLuca J. **Cognitive impairment in multiple sclerosis.** *Lancet Neurol* 2008;7:1139–51 CrossRef Medline
- Hulst HE, Steenwijk MD, Versteeg A, et al. **Cognitive impairment in MS: impact of white matter integrity, gray matter volume, and lesions.** *Neurology* 2013;80:1025–32 CrossRef Medline
- Roosendaal SD, Geurts JJ, Vrenken H, et al. **Regional DTI differences in multiple sclerosis patients.** *Neuroimage* 2009;44:1397–403 CrossRef Medline
- Schoonheim MM, Vigeveno RM, Rueda Lopes FC, et al. **Sex-specific extent and severity of white matter damage in multiple sclerosis: implications for cognitive decline.** *Hum Brain Mapp* 2014;35:2348–58 CrossRef Medline
- Dineen RA, Vilisaar J, Hlinka J, et al. **Disconnection as a mechanism for cognitive dysfunction in multiple sclerosis.** *Brain* 2009;132:239–49 Medline
- Miller DH, Soon D, Fernando KT, et al; RM Investigators. **MRI outcomes in a placebo-controlled trial of natalizumab in relapsing MS.** *Neurology* 2007;68:1390–401 CrossRef Medline
- Polman CH, O'Connor PW, Havrdova E, et al; RM Investigators. **A randomized, placebo-controlled trial of natalizumab for relapsing multiple sclerosis.** *N Engl J Med* 2006;354:899–910 CrossRef Medline
- Kurtzke JF. **Rating neurologic impairment in multiple-sclerosis: an expanded disability status scale (EdSS).** *Neurology* 1983;33:1444–52 CrossRef Medline
- Polman CH, Reingold SC, Edan G, et al. **Diagnostic criteria for multiple sclerosis: 2005 revisions to the “McDonald Criteria.”** *Ann Neurol* 2005;58:840–46 Medline
- Steenwijk MD, Pouwels PJ, Daams M, et al. **Accurate white matter lesion segmentation by k nearest neighbor classification with tissue type priors (kNN-TTPs).** *Neuroimage Clin* 2013;3:462–69 CrossRef Medline
- Smith SM, Zhang Y, Jenkinson M, et al. **Accurate, robust, and automated longitudinal and cross-sectional brain change analysis.** *Neuroimage* 2002;17:479–89 Medline
- Chard DT, Jackson JS, Miller DH, et al. **Reducing the impact of white matter lesions on automated measures of brain gray and white matter volumes.** *J Magn Reson Imaging* 2010;32:223–28 CrossRef Medline
- Smith SM, Jenkinson M, Johansen-Berg H, et al. **Tract-based spatial statistics: voxelwise analysis of multi-subject diffusion data.** *Neuroimage* 2006;31:1487–505 Medline
- Rao SM, Leo GJ, Bernardin L, et al. **Cognitive dysfunction in multiple-sclerosis, I: frequency, patterns, and prediction.** *Neurology* 1991;41:685–91 Medline
- Walker LAS, Mendella PD, Stewart A, et al. **Meaningful change in cognition in multiple sclerosis: method matters.** *Can J Neurol Sci* 2011;38:282–88 Medline
- Vercoulen JH, Swanink CM, Fennis JF, et al. **Dimensional assessment of chronic fatigue syndrome.** *J Psychosom Res* 1994;38:383–92 Medline
- Zigmond AS, Snaith RP. **The hospital anxiety and depression scale.** *Acta Psychiatr Scand* 1983;67:361–70 Medline
- Bammer R, Augustin M, Strasser-Fuchs S, et al. **Magnetic resonance diffusion tensor imaging for characterizing diffuse and focal white matter abnormalities in multiple sclerosis.** *Magn Reson Med* 2000;44:583–91 Medline
- Budde MD, Xie M, Cross AH, et al. **Axial diffusivity is the primary correlate of axonal injury in the experimental autoimmune encephalomyelitis spinal cord: a quantitative pixelwise analysis.** *J Neurosci* 2009;29:2805–13 CrossRef Medline
- Budde MD, Kim JH, Liang HF, et al. **Toward accurate diagnosis of white matter pathology using diffusion tensor imaging.** *Magn Reson Med* 2007;57:688–95 Medline
- Song SK, Sun SW, Ramsbottom MJ, et al. **Dysmyelination revealed through MRI as increased radial (but unchanged axial) diffusion of water.** *Neuroimage* 2002;17:1429–36 Medline
- Song SK, Yoshino J, Le TQ, et al. **Demyelination increases radial diffusivity in corpus callosum of mouse brain.** *Neuroimage* 2005;26:132–40 Medline
- Schmierer K, Wheeler-Kingshott CA, Boulby PA, et al. **Diffusion tensor imaging of post mortem multiple sclerosis brain.** *Neuroimage* 2007;35:467–77 Medline
- Yednock TA, Cannon C, Fritz LC, et al. **Prevention of experimental autoimmune encephalomyelitis by antibodies against alpha 4 beta 1 integrin.** *Nature* 1992;356:63–66 Medline
- Fox RJ, Cronin T, Lin J, et al. **Measuring myelin repair and axonal loss with diffusion tensor imaging.** *AJNR Am J Neuroradiol* 2011;32:85–91 CrossRef Medline
- Magraner M, Coret F, Casanova B. **The relationship between inflammatory activity and brain atrophy in natalizumab treated patients.** *Eur J Radiol* 2012;81:3485–90 CrossRef Medline
- Sastre-Garriga J, Tur C, Pareto D, et al. **Brain atrophy in natalizumab-treated patients: a 3-year follow-up.** *Mult Scler* 2015;21:749–56 CrossRef Medline
- Iaffaldano P, Viterbo RG, Paolicelli D, et al. **Impact of natalizumab on cognitive performances and fatigue in relapsing multiple sclerosis: a prospective, open-label, two years observational study.** *PLoS One* 2012;7:e35843 CrossRef Medline
- Lang C, Reiss C, Mürer M. **Natalizumab may improve cognition and mood in multiple sclerosis.** *Eur Neurol* 2012;67:162–66 CrossRef Medline
- Mattioli F, Stampatori C, Bellomi F, et al. **Natalizumab efficacy on**

- cognitive impairment in MS.** *Neurol Sci* 2011;31(suppl 3):321–23 CrossRef Medline
34. Mattioli F, Stampatori C, Capra R. **The effect of natalizumab on cognitive function in patients with relapsing-remitting multiple sclerosis: preliminary results of a 1-year follow-up study.** *Neurol Sci* 2011;32:83–88 CrossRef Medline
35. Portaccio E, Stromillo ML, Goretti B, et al. **Natalizumab may reduce cognitive changes and brain atrophy rate in relapsing-remitting multiple sclerosis: a prospective, non-randomized pilot study.** *Eur J Neurol* 2013;20:986–90 CrossRef Medline
36. Stephenson JJ, Kern DM, Agarwal SS, et al. **Impact of natalizumab on patient-reported outcomes in multiple sclerosis: a longitudinal study.** *Health Qual Life Outcomes* 2012;10:155 CrossRef Medline
37. Svenningsson A, Falk E, Celius EG, et al; Tynergy Trial Investigators. **Natalizumab treatment reduces fatigue in multiple sclerosis: results from the TYNERGY trial—a study in the real life setting.** *PLoS One* 2013;8:e58643 CrossRef Medline
38. Yu HJ, Christodoulou C, Bhise V, et al. **Multiple white matter tract abnormalities underlie cognitive impairment in RRMS.** *Neuroimage* 2012;59:3713–22 CrossRef Medline
39. Weinstein A, Schwid SR, Schiffer RB, et al. **Neuropsychologic status in multiple sclerosis after treatment with glatiramer.** *Arch Neurol* 1999;56:319–24 Medline
40. La, ML, Di Pietrantonj C, Rovaris, M, et al. **Interferons-beta versus glatiramer acetate for relapsing-remitting multiple sclerosis.** *Cochrane Database Syst Rev* 2014;7:CD009333 CrossRef Medline

Computer-Assisted Detection of Cerebral Aneurysms in MR Angiography in a Routine Image-Reading Environment: Effects on Diagnosis by Radiologists

S. Miki, N. Hayashi, Y. Masutani, Y. Nomura, T. Yoshikawa, S. Hanaoka, M. Nemoto, and K. Ohtomo



ABSTRACT

BACKGROUND AND PURPOSE: Experiences with computer-assisted detection of cerebral aneurysms in diagnosis by radiologists in real-life clinical environments have not been reported. The purpose of this study was to evaluate the usefulness of computer-assisted detection in a routine reading environment.

MATERIALS AND METHODS: During 39 months in a routine clinical practice environment, 2701 MR angiograms were each read by 2 radiologists by using a computer-assisted detection system. Initial interpretation was independently made without using the detection system, followed by a possible alteration of diagnosis after referring to the lesion candidate output from the system. We used the final consensus of the 2 radiologists as the reference standard. The sensitivity and specificity of radiologists before and after seeing the lesion candidates were evaluated by aneurysm- and patient-based analyses.

RESULTS: The use of the computer-assisted detection system increased the number of detected aneurysms by 9.3% (from 258 to 282). Aneurysm-based analysis revealed that the apparent sensitivity of the radiologists' diagnoses made without and with the detection system was 64% and 69%, respectively. The detection system presented 82% of the aneurysms. The detection system more frequently benefited radiologists than being detrimental.

CONCLUSIONS: Routine integration of computer-assisted detection with MR angiography for cerebral aneurysms is feasible, and radiologists can detect a number of additional cerebral aneurysms by using the detection system without a substantial decrease in their specificity. The low confidence of radiologists in the system may limit its usefulness.

ABBREVIATIONS: CAD = computer-assisted detection; FP = false-positive; TP = true-positive

Detection of unruptured cerebral aneurysms is a challenging task for radiologists. Unenhanced MRA has been widely accepted as a technique for initial screening because it is noninvasive and requires no contrast agent or ionizing radiation.¹ Considering its role as a screening technique, MRA requires high sensitivity. At present, catheter DSA is still the criterion standard of diagnosis. The limitations of MRA compared with DSA include the limited spatial resolution and artifacts such as motion, susceptibility, and flow.² Nevertheless, an increasing number of recent studies suggest that DSA is no longer considered essential for es-

tablishing the diagnosis of cerebral aneurysms,^{3,4} particularly when 3T MR imaging scanners are used.^{2,5,6}

Despite the continuing sophistication of the imaging technique, 1 important cause of the limited sensitivity of MRA is the detection failures of radiologists. Interpretation of both source and reconstructed images is recommended to achieve good sensitivity of MRA,⁷⁻⁹ but detecting relatively small lesions is a time-consuming and difficult task.

Computer-assisted detection (CAD) of cerebral aneurysms may play a role in improving the accuracy of aneurysm detection by MRA. Stand-alone performance figures of various CAD algorithms for cerebral aneurysms have been studied mainly by using datasets of known aneurysms, and high sensitivities have been reported.¹⁰⁻¹³

Previous observer performance studies showed that CAD for cerebral aneurysms raises the sensitivity of radiologists^{14,15} or reduces reading time while maintaining the sensitivity.¹⁶ However, those studies were performed under experimental conditions with a relatively small number of aneurysms. The high prevalence

Received August 12, 2015; accepted after revision November 19.

From the Departments of Computational Diagnostic Radiology and Preventive Medicine (S.M., N.H., Y.N., T.Y., M.N.) and Radiology (S.H., K.O.), The University of Tokyo Hospital, Tokyo, Japan; and Faculty of Information Sciences and Graduate School of Information Sciences (Y.M.), Hiroshima City University, Hiroshima, Japan.

Please address correspondence to Soichiro Miki, MD, PhD, 7-3-1 Hongo, Bunkyo-ku, Tokyo 113-0033, Japan; e-mail: smiki-tky@umin.ac.jp

Indicates open access to non-subscribers at www.ajnr.org

<http://dx.doi.org/10.3174/ajnr.A4671>

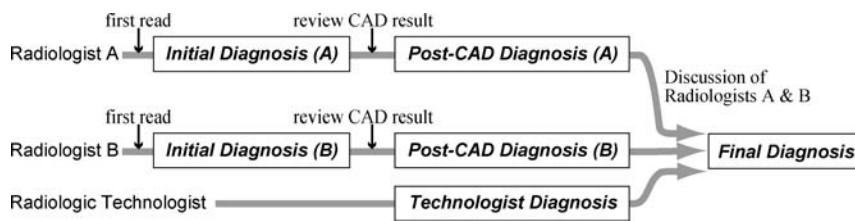


FIG 1. Flow chart of the image-reading process. Two radiologists independently interpreted MR angiograms and then reviewed the CAD results. The final diagnosis was made by consensus of the 2 radiologists. Moreover, the report of a radiologic technologist was taken into account during discussion, to minimize detection failures in the final diagnosis.

of aneurysms (19%–44%^{14–16}) may have resulted in a higher estimate of accuracy owing to observer expectation bias.^{17,18} In some studies, the mean diameters of aneurysms were relatively large (7.1 mm¹⁴ and 5.0 mm¹⁶) and radiologists had access to only MIP images; neither of these are found in recent routine screening. Recently, Štěpán-Buksakowska et al¹⁵ have investigated the detection performance of radiologists in an experimental environment closer to modern clinical settings. Still, to the best of our knowledge, experience with CAD of cerebral aneurysms in real-life clinical environments has not been reported in the literature. The purpose of our study, therefore, was to evaluate the usefulness of CAD of cerebral aneurysms in diagnosis by radiologists in a routine image-reading environment.

MATERIALS AND METHODS

Subjects

This study was approved by the ethics review board of the University of Tokyo Hospital. The subjects were a successive series of adults who were referred to our institution for their annual whole-body general medical examinations between October 2010 and December 2013. Written informed consent to use their clinical images for research about CAD conducted in our institution was obtained from all the subjects. All the subjects underwent a medical interview by a physician, in which their detailed medical history was taken. The initial inclusion criteria were as follows: 1) first-time visit to our institution, 2) MRA completed without contraindication, and 3) no known history of cerebral aneurysms. 3D time-of-flight unenhanced MRA was performed as part of brain screening, with three 3T MR units (2 Signa HDxt scanners and 1 Discovery MR750 scanner; GE Healthcare, Milwaukee, Wisconsin). The acquisition parameters were as follows: FOV, 240 mm; matrix size, 512 × 512; pixel spacing, 0.469 mm; section thickness, 1.2 mm; section interval, 0.6 mm (ie, there was a 50% overlap for each section); TR, 25 ms; TE, 2.7 ms for the Signa HDxt and 2.9 ms for the Discovery MR750. Rotational volume-rendered images around the x-, y-, and z-axes were reconstructed by radiologic technologists. Automatically generated MIP images were also transferred.

Imaging Interpretation

Within the data-acquisition period, MR angiograms were interpreted by 26 radiologists as part of daily routine diagnosis. Their years of experience in MRA interpretation in their daily routine ranged from 3 to 21 years. Three of the authors of this article (S.M., N.H., and T.Y.) also participated in the interpretation. Subject information such as age, sex, and current symptoms, if

any, was not masked. The image reading method is illustrated in Fig 1. Two radiologists and 1 radiologic technologist were assigned to each subject on a day-to-day basis.

First, the 2 radiologists independently interpreted an MR angiogram without seeing the CAD results. This stage is defined as the “initial diagnosis.” Second, the 2 radiologists independently reviewed the CAD results displayed by a Web-based CAD server, the details of

which are described later. Here, the 2 radiologists independently registered their personal “feedback” into the CAD server, to record the location of aneurysms detected and whether they had changed their diagnosis after seeing the CAD results, thus yielding the “post-CAD diagnosis.” The technologist also independently interpreted the images and made his or her personal report. Finally, after the 3 reading reports (1 from each of the radiologists and 1 from the technologist) were made, the 2 radiologists reviewed the 3 personal reading reports and discussed and made a single report by consensus, termed the “final diagnosis.” This review process was helped by a customized, structured reporting system, which automatically showed the 3 reading reports side by side. The diagnostic criterion for aneurysms was a saccular protrusion of ≥ 2 mm; lesions smaller than this were not included because of the limited spatial resolution of MRA. Fusiform aneurysms were also excluded. The sizes of the aneurysms in millimeter precision were also determined by consensus of the 2 radiologists. Each radiologist was able to interpret the source axial sections, volume-rendered images, and MIP images on computer displays.

CAD Software

The CAD software used in this study was developed by our team. The details of the algorithm are published elsewhere.¹⁹ Briefly, after a lesion candidate detection based on curvatures²⁰ and Hessian eigenvalues,²¹ a classifier ensemble trained by the boosting algorithm²² was used to determine the likelihood of an aneurysm on the basis of 63 feature values of the candidates, such as statistics of voxel values, curvatures, and features derived from Hessian eigenvalues. This software was installed as a plug-in for a Web-based CAD server developed by Nomura et al²³ (Fig 2).

The system was configured to always display the top 3 lesion candidates in likelihood per study rather than displaying variable numbers of candidates above a certain threshold of likelihood. One merit for this strategy was that the radiologists could stabilize the interpretation time. This strategy is also robust against the overall likelihood shift due to the inevitable image-quality variation between studies. We have confirmed in our preliminary study (not published) that our CAD system can maintain its sensitivity by using this “show 3” method compared with the variable number method.

A radiologist categorized each lesion candidate as either a “known true-positive (TP),” a “missed TP,” a “false-positive (FP),” or “pending.” Definitions were as follows: “known TP,” a true aneurysm that the radiologist had already recognized before

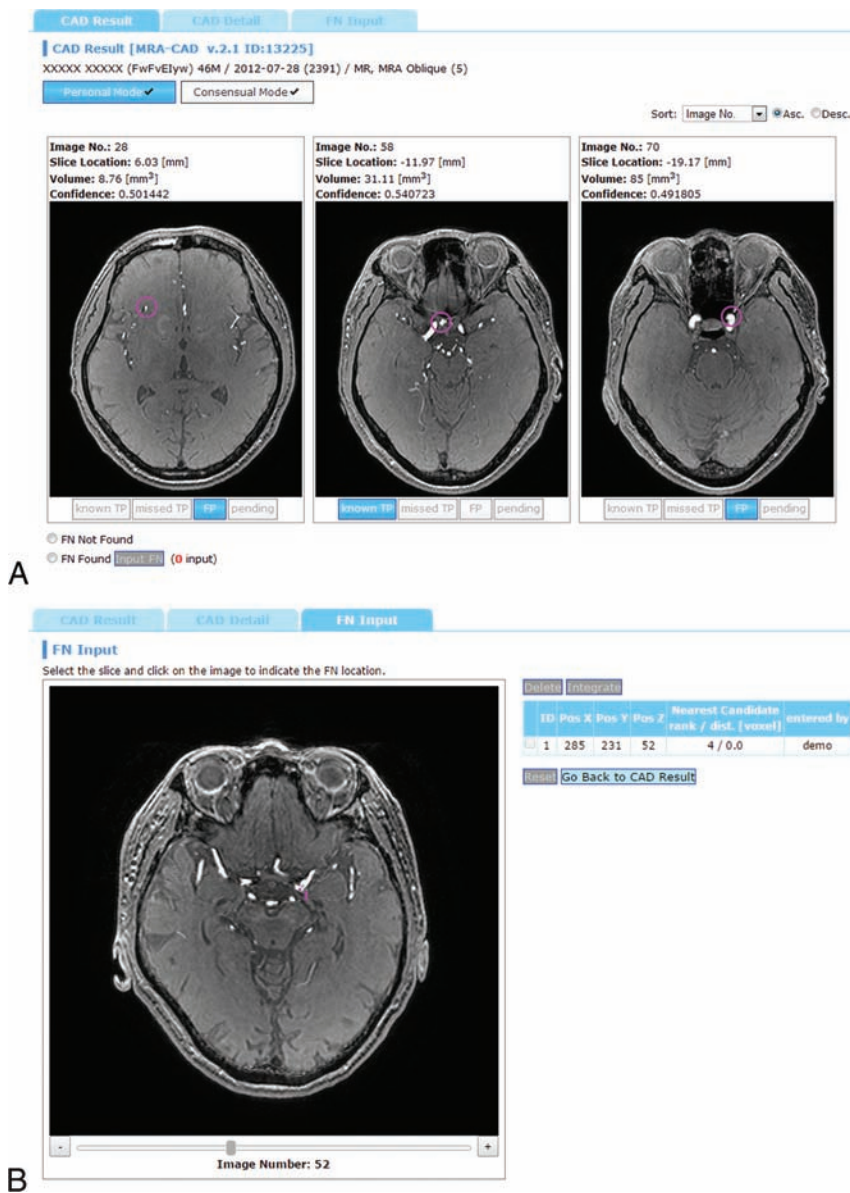


FIG 2. Example of CAD results displayed in the CAD server. A, Lesion classification interface. The top 3 lesion candidates are displayed, each of which has toggle buttons to select “known TP,” “missed TP,” “FP,” or “pending.” B, False-negative input interface. Radiologists recorded the locations of an aneurysm by a mouse click if it was not presented by the CAD system.

seeing the CAD results; “missed TP,” a lesion that he or she overlooked before seeing the CAD results; and “FP,” a false-positive candidate (ie, not an aneurysm). The “pending” selection in the final diagnosis indicated that the 2 radiologists did not reach a positive consensus, mainly because the lesion was too small. Such subjects were not referred to experts for further evaluation; thus, we did not include such pending selections as positive aneurysms. If a lesion detected by the radiologist was not included in the 3 candidates displayed by the CAD system, the radiologist manually recorded the coordinates of the aneurysm by a mouse click (Fig 2B). Thus, by combining all these data, the server collected the following items: 1) all the locations of aneurysms determined by consensus, 2) whether each radiologist successfully detected the lesion before reviewing the CAD results, and 3) whether each positive lesion was successfully included in the CAD results as one

of the top 3 candidates. Additionally, the median time for reviewing CAD results and giving feedback was determined by using the server log for the last 2 months of the data-acquisition period, by which time the radiologists were well-acquainted to the system.

Data Analysis

Statistical analysis was performed by using R, Version 3.1.2, statistical and computing software (<http://www.r-project.org/>). The sensitivity and the specificity of the radiologists were calculated by using the final diagnosis as the reference standard. The sensitivity of CAD was calculated as the successful presentation rate of positive lesions in the top 3 candidates. Then, 95% confidence intervals were computed on the basis of binomial distribution. The sensitivities of the radiologists before and after the CAD reference were compared by using the McNemar test. Additionally, the detection performance figures for both CAD and radiologists were compared between small (≤ 3 mm) and large (≥ 4 mm) aneurysms by using the χ^2 test.

RESULTS

Characteristics of Patients and Aneurysms

During the study period, 2804 first-time visitors to our institution completed the annual health checkup examination program. Among them, 39 subjects did not meet the initial inclusion criteria because MR imaging was contraindicated/refused ($n = 21$) or they had a history of known cerebral aneurysms ($n = 18$). Moreover, 64 were excluded from further evaluations because the assigned radiologists did not complete the feedback

registration. None of the MR angiograms were excluded because of poor image quality, and all of them were successfully processed by the CAD system. Thus, MR angiograms of 2701 subjects (1674 men, 1027 women) were included in this analysis. Subject median age was 54 years (range, 22–90 years). Two hundred three aneurysms from 189 subjects were determined in the final diagnosis (prevalence rate, 7.0%), the details of which are shown in the Table.

Performance of the CAD System

Overall, our CAD system successfully presented 166 (82%; 95% CI, 0.76%–0.87%) of the 203 aneurysms as the top 3 lesion candidates. Twenty-six aneurysms were detected but not presented as the top 3 candidates, and 11 aneurysms were not detected by CAD. The performance of the CAD system in relation to aneu-

Characteristics of 203 detected aneurysms in the final diagnosis

Feature	Number
Sex ^a	
Male	101
Female	88
Age ^a	
Younger than 50 yr	50
50 yr and older, younger than 60 yr	54
60 yr and older	85
Multiplicity ^a	
Single	177
Double	10
Triple	2
Location ^b	
ACA territory	54
MCA territory	31
ICA territory	107
PCA territory	5
Other	6
Size (mm) ^b	
2	97
3	61
4	29
≥5	16

Note:—ACA indicates anterior cerebral artery; PCA, posterior cerebral artery.

^a Data are number of subjects.

^b Data are number of lesions.

rysm size is shown in Fig 3. The CAD system successfully presented 124 of 158 (78%) aneurysms of 2–3 mm and 42 of 45 (93%) aneurysms of ≥4 mm. The sensitivity for the larger aneurysms was significantly higher than that for the smaller aneurysms ($P = .040$, χ^2 test). The details of the 3 missed aneurysms of ≥4 mm were as follows: 1) a 4-mm right internal carotid aneurysm, which was detected as the fourth candidate but not presented as a top 3 candidate; 2) a 4-mm left internal carotid artery aneurysm, which was not detected; and 3) a 6-mm right internal carotid artery aneurysm, which was detected as the sixth candidate but not presented.

Performances of the Radiologists

With the final diagnosis as the reference standard, the aneurysm-based overall sensitivity of the 26 radiologists in their initial diagnoses was 64% (258 of the 406 independent interpretations regarding the 203 aneurysms; 95% CI, 0.59–0.68). The sensitivity for small (≤3 mm) aneurysms was 59% (185/316), and that for large aneurysms (≥4 mm) was 81% (73/90), showing a significant difference ($P < .001$, χ^2 -test). Other statistical details are shown in Fig 4.

During the study period, the radiologists changed their initial negative diagnosis to a positive one after seeing the CAD results in 26 cases. Among these, the final diagnosis was also positive in 24 (92%). In the remaining 2 cases, aneurysms were “noticed” by 1 radiologist with the aid of the CAD system but were dismissed in the final diagnosis after discussion with the other radiologist. Thus, the CAD system more frequently benefited the radiologists in terms of detection of additional aneurysms than being detrimental in terms of introducing overdiagnosis. The interpretation-based analysis showed that the specificities of the radiologists’ diagnoses before and after seeing the CAD results were 98.9% and 98.8%, respectively.

Of the 24 aneurysms in which the CAD system benefited the

radiologists, 6 were in the anterior cerebral artery circulation, 11 were in the internal carotid artery circulation, 5 were in the middle cerebral artery circulation, and 2 were in the posterior circulation. Twenty-one aneurysms were small (≤3 mm), 2 aneurysms were 4 mm, and the remaining aneurysm was 5 mm, protruding medially from the cavernous portion of the left internal carotid artery. The use of the CAD system increased the number of aneurysms detected by 9.3% (from 258 to 282, $P < .001$ by using the McNemar test), giving an overall sensitivity of 69% in the post-CAD diagnosis (282/406; 95% CI, 0.65–0.74). However, true aneurysms were still not detected even after the radiologists saw the CAD results in 124 interpretations, including 90 interpretations in which the CAD system had presented true aneurysms but the radiologists failed to change their diagnoses. Figure 5 shows a summary of the relationship between the initial diagnoses and post-CAD diagnoses of the radiologists. In 3 cases, neither the 2 radiologists nor the CAD system found the aneurysms but they were detected by the radiologic technologist.

Of the 32 interpretations regarding the 16 aneurysms of ≥5 mm, aneurysms were detected in the initial diagnosis in 29 (91%) cases, detected in the post-CAD diagnosis in 30 (94%) cases, and remained undetected even with the aid of the CAD system in 2 (6%) interpretations (1 with a 5-mm left cavernous aneurysm and 1 with a 5-mm left internal carotid posterior communicating aneurysm protruding caudally).

The median time required for reviewing the CAD results and giving feedback was 16 seconds.

DISCUSSION

In the present study, we evaluated the usefulness of a CAD system for cerebral aneurysms in a routine clinical diagnosis environment. To the best of our knowledge, this is the first study to evaluate the impact of CAD of cerebral aneurysms on radiologists in a large general population. The CAD system showed a sensitivity (82%) comparable with that of radiologists (64%) in the detection of both small and large cerebral aneurysms. The number of detected aneurysms increased by 9.3%, while preserving specificity. The additional time required for checking the CAD results was short. Our findings suggest that there were certain benefits from CAD even for radiologists who interpreted source images from 3T scanners in routine clinical practice.

Hirai et al¹⁴ reported that under experimental conditions, radiologists benefited (increase of >20 units by a using 0–100 confidence rating scale) from the CAD results in 10% of positive aneurysms. Compared with the study by Hirai et al in which only MIP images from a 1.5T scanner were presented to the radiologists, our study used both source and reconstructed images obtained by using 3T scanners. This difference means that even without CAD, a relatively high sensitivity of radiologists was expected, which might limit the benefit obtained from our CAD system. In addition, the benefit from CAD may be underestimated in this study compared with the previous study because our data-collection method focused only on the pure detection failures of radiologists. In reviewing the CAD results, radiologists had the opportunity to reconsider the lesion candidates they had already noticed, possibly changing their level of confidence in the

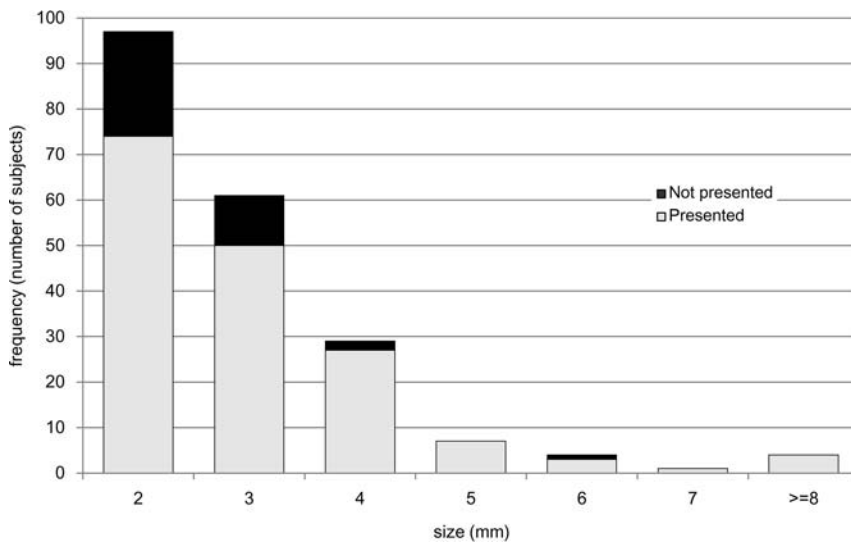


FIG 3. Performance of the CAD system in relation to aneurysm size.

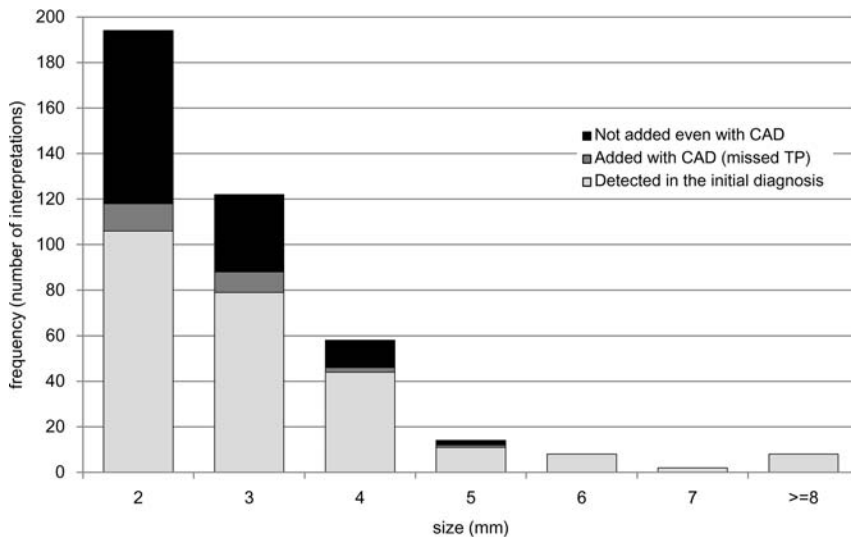


FIG 4. Performance of radiologists in relation to aneurysm size. Data are the number of interpretations (2 independent interpretations per study).

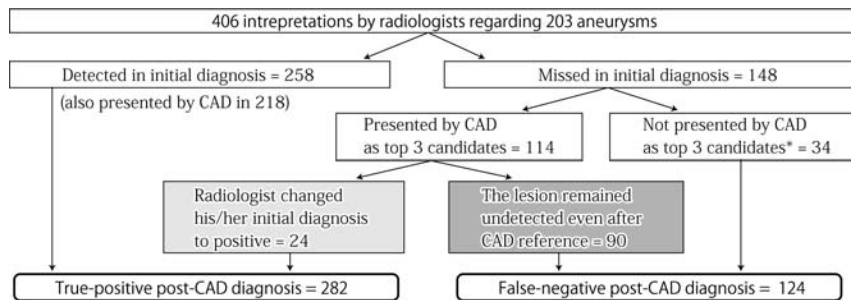


FIG 5. Relationship between initial diagnosis and post-CAD diagnosis based on 406 interpretations regarding 203 aneurysms determined in the final diagnosis. The *asterisk* indicates an aneurysm found by the other radiologist or solely by a radiologic technologist.

diagnosis. However, collecting such confidence level data in a routine environment was considered impractical.

This study demonstrated that the specificity of radiologists was not considerably decreased by CAD. This finding implies that FP lesion candidates presented by the CAD system can be easily

dismissed by radiologists. This finding is also consistent with that in the previous study.¹⁴ On the other hand, in our series, radiologists dismissed many lesion candidates presented by the CAD system that were true-positives thereafter in the final diagnosis—that is, despite the high sensitivity of our CAD, radiologists were far less affected by the CAD results than by human opinions. In at least some cases, obvious aneurysms were overlooked even with the aid of the CAD system. In our opinion, this low confidence in the CAD system is partly because our CAD system provided little qualitative information about its results and it produced many false-positive marks. In addition, the CAD system presented its results on only axial sections, which might have made the referencing process difficult. Further investigation is needed to develop more efficient methods of displaying results to realize the full potential of CAD.

The prevalence rate of cerebral aneurysms in our reference standard (7.0%) is apparently higher than previously reported figures from angiography studies (3.0%–6.0%)²⁴ but not as high as the prevalence rate (8.4%) reported by Igase et al,⁶ in which only a 3T MR imaging scanner was used to detect cerebral aneurysms in the Japanese population. They suggested that the excellent resolution of 3T MR imaging and the appropriate use of the volume-rendered technique contributed to the detection of additional aneurysms that could not be detected by other modalities. As we previously noted, owing to the recent advancements in MRA technology, invasive procedures with the sole purpose of establishing the diagnosis of cerebral aneurysms are becoming less justified. Although the true nature of the discrepancy in prevalence rates between DSA and MRA is still inconclusive, we believe that the use of 3T scanners and the reading of both source and volume-rendered images provide the highest practically possible accuracy in our reference standard diagnosis.

Our study had some limitations.

First, the sensitivity of the radiologists in our method should be regarded as a rough estimate. The reference standard diagnosis was not independent of the diagnosis of the observers being tested, and there was considerable interobserver disagreement between the 2 radiologists. Second, despite the 39-month study pe-

riod, the number of positive aneurysms was small, owing to the relatively low prevalence of the disease. In particular, the experience regarding relatively larger aneurysms (≥ 4 mm) was not sufficient. We are still using this system in daily practice, and further knowledge should be accumulated in the future.

CONCLUSIONS

The computer-assisted diagnosis of cerebral aneurysms is feasible, and radiologists can detect more cerebral aneurysms by using the CAD system without a substantial decrease in specificity. Radiologists are less likely affected by true-positive CAD results compared with the opinion of a different radiologist in double-reading settings.

Disclosures: Soichiro Miki—UNRELATED: Payment for Lectures (including service on Speakers Bureaus): AZE, Bayer Yakuhin; Payment for Manuscript Preparation: Inner Vision, Medical Eye. Naoto Hayashi—RELATED: Grant: HIMEDIC,* Siemens Healthcare KK,* GE Healthcare Japan.* Yukihiko Nomura—UNRELATED: Grants/Grants Pending: Japan Society for the Promotion of Science Grants-in-Aid for Scientific Research (Nos. 23700573, 25750182, 15K01325).† Takeharu Yoshikawa—RELATED: Grant: HIMEDIC,* Siemens Healthcare KK.*† Shouhei Hanaoka—UNRELATED: Grants/Grants Pending: Association for Research, Advancement and Promotion of Imaging Diagnostics. Kuni Ohtomo—UNRELATED: Bayer Yakuhin,* Daiichi Sankyo Healthcare,* Fuji Pharma.* Eisai*. Payment for Lectures (including service on Speakers Bureaus): Bayer Yakuhin, Daiichi Sankyo Healthcare, Fuji Pharma. *Money paid to the institution. †The Department of Computational Diagnostic Radiology and Preventive Medicine is an endowed division supported by HIMEDIC, Siemens Healthcare KK, and GE Healthcare Japan. However, these companies did not play any direct role in running this specific study, including the study design.

REFERENCES

- Bederson JB, Connolly ES Jr, Batjer HH, et al; American Heart Association. **Guidelines for the management of aneurysmal subarachnoid hemorrhage: a statement for healthcare professionals from a special writing group of the Stroke Council, American Heart Association.** *Stroke* 2009;40:994–1025 CrossRef Medline
- Kapsalaki EZ, Rountas CD, Fountas KN. **The role of 3 Tesla MRA in the detection of intracranial aneurysms.** *Int J Vasc Med* 2012;2012:792834 CrossRef Medline
- Jäger HR, Mansmann U, Hausmann O, et al. **MRA versus digital subtraction angiography in acute subarachnoid haemorrhage: a blinded multireader study of prospectively recruited patients.** *Neuroradiology* 2000;42:313–26 CrossRef Medline
- Shahzad R, Younas F. **Detection and characterization of intracranial aneurysms: magnetic resonance angiography versus digital subtraction angiography.** *J Coll Physicians Surg Pak* 2011;21:325–29 CrossRef Medline
- Li MH, Li YD, Tan HQ, et al. **Contrast-free MRA at 3.0T for the detection of intracranial aneurysms.** *Neurology* 2011;77:667–76 CrossRef Medline
- Igase K, Matsubara I, Igase M, et al. **Initial experience in evaluating the prevalence of unruptured intracranial aneurysms detected on 3-Tesla MRI.** *Cerebrovasc Dis* 2012;33:348–53 CrossRef Medline
- Korogi Y, Takahashi M, Mabuchi N, et al. **Intracranial aneurysms: diagnostic accuracy of MR angiography with evaluation of maximum intensity projection and source images.** *Radiology* 1996;199:199–207 CrossRef Medline
- Kouskouras C, Charitanti A, Giavroglou C, et al. **Intracranial aneurysms: evaluation using CTA and MRA—correlation with DSA and intraoperative findings.** *Neuroradiology* 2004;46:842–50 CrossRef Medline
- Adams WM, Laitt RD, Jackson A. **The role of MR angiography in the pretreatment assessment of intracranial aneurysms: a comparative study.** *AJNR Am J Neuroradiol* 2000;21:1618–28 Medline
- Hayashi N, Masutani Y, Masumoto T, et al. **Feasibility of a curvature-based enhanced display system for detecting cerebral aneurysms in MR angiography.** *Magn Reson Med Sci* 2003;2:29–36 CrossRef Medline
- Arimura H, Li Q, Korogi Y, et al. **Computerized detection of intracranial aneurysms for three-dimensional MR angiography: feature extraction of small protrusions based on a shape-based difference image technique.** *Med Phys* 2006;33:394–401 CrossRef Medline
- Kobashi S, Kondo K, Hata Y. **Computer-aided diagnosis of intracranial aneurysms in MRA images with case-based reasoning.** *IEICE Trans Inf Syst* 2006;E89-D:340–50 CrossRef
- Yang X, Blezek DJ, Cheng LT, et al. **Computer-aided detection of intracranial aneurysms in MR angiography.** *J Digit Imaging* 2011;24:86–95 CrossRef Medline
- Hirai T, Korogi Y, Arimura H, et al. **Intracranial aneurysms at MR angiography: effect of computer-aided diagnosis on radiologists' detection performance.** *Radiology* 2005;237:605–10 CrossRef Medline
- Štěpán-Buksakowska IL, Accurso JM, Diehn FE, et al. **Computer-aided diagnosis improves detection of small intracranial aneurysms on MRA in a clinical setting.** *AJNR Am J Neuroradiol* 2014;35:1897–902 CrossRef Medline
- Kakeda S, Korogi Y, Arimura H, et al. **Diagnostic accuracy and reading time to detect intracranial aneurysms on MR angiography using a computer-aided diagnosis system.** *Am J Roentgenol* 2008;190:459–65 CrossRef Medline
- White PM, Wardlaw JM, Easton V. **Can noninvasive imaging accurately depict intracranial aneurysms? A systematic review.** *Radiology* 2000;217:361–70 CrossRef Medline
- Wolfe JM, Horowitz TS, Kenner NM. **Cognitive psychology: rare items often missed in visual searches.** *Nature* 2005;435:439–40 CrossRef Medline
- Nomura Y, Masutani Y, Miki S, et al. **Performance improvement in computerized detection of cerebral aneurysms by retraining classifier using feedback data collected in routine reading environment.** *J Biomed Graph Comput* 2014;4:12–21
- Dorai C, Jain AK. **COSMOS: a representation scheme for 3D free-form objects.** *IEEE Trans Pattern Anal Mach Intell* 1997;19:1115–30 CrossRef
- Sato Y, Nakajima S, Shiraga N, et al. **Three-dimensional multi-scale line filter for segmentation and visualization of curvilinear structures in medical images.** *Med Imag Anal* 1998;2:143–68 CrossRef Medline
- Schapire RE, Freund Y, Bartlett P, et al. **Boosting the margin: a new explanation for the effectiveness of voting methods.** *Ann Stat* 1998;26:1651–86 CrossRef
- Nomura Y, Hayashi N, Masutani Y, et al. **CIRCUS: an MDA platform for clinical image analysis in hospitals.** *Transactions on Mass-Data Analysis of Images and Signals* 2010;2:112–27
- Rinkel GJ, Djibuti M, Algra A, et al. **Prevalence and risk of rupture of intracranial aneurysms: a systematic review.** *Stroke* 1998;29:251–56 CrossRef Medline

Brain MR Imaging Findings of Cardiac-Type Fabry Disease with an IVS4 + 919G>A Mutation

H.-J. Lee, S.-C. Hung, T.-R. Hsu, S.-C. Ko, T. Chui-Mei, C.-C. Huang, D.-M. Niu, and C.-P. Lin

ABSTRACT

BACKGROUND AND PURPOSE: A high incidence of cardiac-type Fabry disease with an α -galactosidase A mutation, IVS4 + 919 G>A, has been identified in the Taiwanese population. The neurologic manifestation has not been understood in this specific cardiac variant. This study aimed to investigate the typical imaging features of classic Fabry disease in patients with IVS4 Fabry disease.

MATERIALS AND METHODS: Twenty-six patients with IVS4-type Fabry disease (20 men and 6 women; age range, 43–71 years; median age, 61 years) and 26 age- and sex-matched healthy controls (age range, 44–68 years; median age, 60 years) were analyzed for white matter hyperintensities, the pulvinar sign, and basilar artery diameter. The volumes of white matter hyperintensities were calculated by comparison with an in-house data base of 276 controls.

RESULTS: Infarctions were found in 9 patients with IVS4 Fabry disease (35%) and in none of the healthy controls ($P = .001$). A pulvinar sign was found in 8 patients with IVS4 Fabry disease (30%) and in none of the healthy controls ($P = .002$). No significant difference was found in Fazekas scale scores for white matter hyperintensities; however, white matter hyperintensity volume in the deep white matter was higher in patients with IVS4 Fabry disease than in those from the healthy control data base ($P = .004$).

CONCLUSIONS: Along with its involvement of the cardiac system, IVS4-type Fabry disease has features similar to those of classic Fabry disease and a higher frequency of deep white matter hyperintensities and a higher incidence of infarctions and pulvinar signs than in healthy controls.

ABBREVIATIONS: BA = basilar artery; GLA = α -galactosidase A; WMH = white matter hyperintensity

Classic Fabry disease is a multisystem X-linked lysosomal disorder due to lysosomal α -galactosidase A (GLA) deficiency, which subsequently leads to accumulation of glycosphingolipids, primarily globotriaosylceramide, throughout the body.¹ The disease results in severe renal, cardiac, and central nervous system complications in adulthood. On brain MR imaging, classic Fabry disease is characterized by white matter hyperintensities, infarcts, and dolichoectasia.²

In the general population, the incidence of Fabry disease has

been reported as 1 in 40,000–117,000 live births. However, our previous studies by using neonate screening had identified a high incidence (approximately 1 in 1600 males) of a cardiac variant resulting from a GLA mutation, IVS4 + 919G>A (IVS4-type).^{3,4} Another study revealed that 12 of 10,499 males (1/875) and 24 of the 9564 females (1/399) had the IVS4 + 919G>A mutation in neonate screening.⁵ The natural course of the IVS4-type Fabry disease is still largely unknown. The intronic mutation (IVS4 + 919G>A) was reported to be a “cardiac-type” Fabry mutation,⁶ which may present with asymptomatic, mild symptomatic as microalbuminuria and retinal vessel tortuosity, to severe cardiac symptoms causing significant morbidity after the fifth decade of life. However, the neurologic symptoms in the specific subtype have never been understood. Therefore, the current study aimed to analyze the degrees of CNS involvement in IVS4-type Fabry disease by retrospectively comparing brain imaging results of this patient population with images from a healthy control data base.

MATERIALS AND METHODS

Population

This study was approved by the institutional review board at our institution. In total, 920 patients (498 men and 422 women) were

Received August 27, 2015; accepted after revision November 29.

From the Departments of Radiology (H.-J.L., S.-C.H., T.C.-M.) and Pediatrics (T.-R.H., D.-M.N.) and Taiwan Health-Tech Imaging Center (S.-C.K.), Taipei Veterans General Hospital, Taipei, Taiwan; and School of Medicine (H.-J.L., S.-C.H., T.-R.H., S.-C.K., T.C.-M., C.-C.H., D.-M.N., C.-P.L.) and Department of Biomedical Imaging and Radiological Sciences (S.-C.H., C.-C.H., C.-P.L.), National Yang-Ming University, Taipei, Taiwan.

H.-J. Lee and S.-C. Hung are co-first authors.

Please address correspondence to Ching-Po Lin, PhD, Department of Biomedical Imaging and Radiological Sciences, National Yang-Ming University, 155, Li-Nong St, Section 2, Peitou, Taipei, Taiwan, 112, Republic of China; e-mail: cplin@ym.edu.tw; and Dau-Ming Niu, MD, Department of Pediatrics, Taipei Veterans General Hospital, 201 Shih-Pai Rd, Section 2, Peitou, Taipei, Taiwan, 112, Republic of China; e-mail: dmniu111@yahoo.com.tw

<http://dx.doi.org/10.3174/ajnr.A4677>

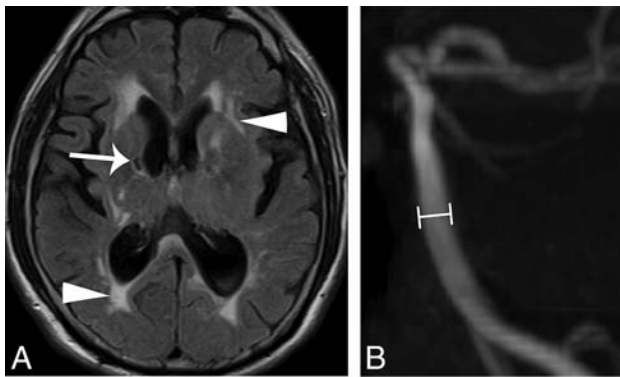


FIG 1. A 54-year-old man with IVS4-type Fabry disease had hypertrophic cardiomyopathy, headache, and stroke. Brain MR (A) axial T2 FLAIR image reveals old lacunar infarcts at the bilateral internal capsules (*arrow*) and increased deep white matter hyperintensities (*arrowheads*). B, The diameter at the middle segment of the basilar artery (*lines*) was measured as 3.2 mm on a 3D time-of-flight MR angiogram.

diagnosed with Fabry disease with IVS4 + 919G>A mutation. Twenty-six patients (20 men and 6 women; age range, 43–71 years; median age, 61 years) who had brain MR imaging examinations from 2010 to 2014 were enrolled in the study. The MR images were retrospectively reviewed by 2 certified neuroradiologists (S.-C.H. and H.-J.L.) by consensus and were compared with those of 26 sex- and age-matched healthy controls (20 men and 6 women; age range, 44–68 years; median age, 60 years). The age of healthy controls was matched to the patient age \pm 2 years. The MR imaging findings in the sexes between IVS4-type of Fabry disease and age-matched healthy controls were also compared to understand the sex-based differences. For the healthy control groups, we excluded individuals with abnormal renal function and abnormal electrocardiogram findings to lower the possibility of undiagnosed Fabry disease, and we excluded patients with bilateral fetal origin of the posterior cerebral artery to avoid the normal variation of a small-sized basilar artery (BA).

The volumes of white matter hyperintensities of patients with Fabry disease were also quantitatively calculated and compared with another in-house data base of 276 healthy controls.

Clinical Assessment

With the exception of 1 patient who was lost to follow-up, a questionnaire of neurologic and neuropsychiatric symptoms was administered to the 25 patients. The questionnaire evaluated symptoms of stroke, sudden onset of numbness or weakness in the extremities, asymmetric facial expression, dysarthria, sudden onset of blurred vision or diplopia, depression, personality changes, forgetfulness, tinnitus, and vertigo.

Qualitative and Semi-Quantitative Evaluation

The presence and location of an infarction was categorized into the following groups: none, anterior circulation alone, posterior circulation alone, and both anterior and posterior circulations (Fig 1A). High signal changes on T1-weighted images at the bilateral lateral pulvinar were considered pulvinar signs (Fig 2).⁷

Deep white matter hyperintensities (WMHs) on T2-weighted images were semi-quantitatively graded by using the Fazekas scale,⁸ in which WMHs are classified by the following scoring

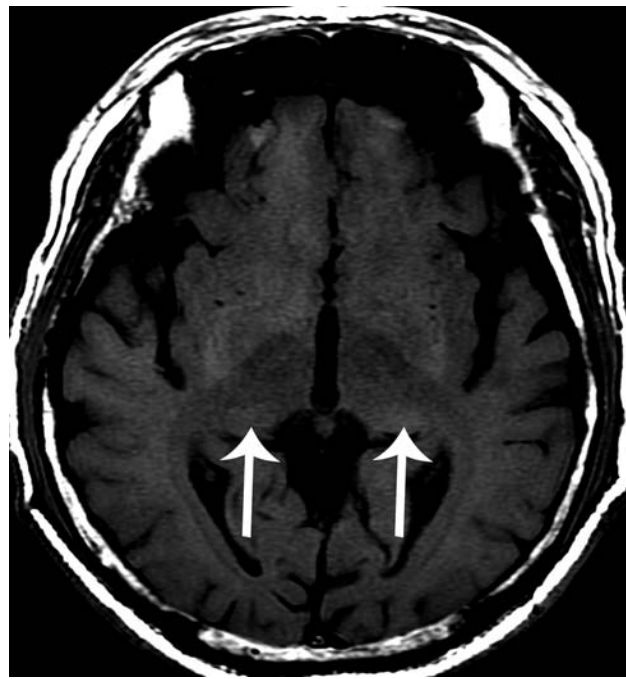


FIG 2. A 63-year-old man with cardiac-type Fabry disease and an IVS4 + 919G>A mutation. A brain MR axial T1-weighted image reveals high signal changes at the bilateral posterior thalamus (*arrows*), the “pulvinar sign.”

system: 0, absent; 1, punctate foci; 2, beginning confluence; and 3, large, confluent.

The degree of elongation and tortuosity of the BA was semi-quantitatively evaluated by using the criteria of Smoker et al⁹ according to the height of the bifurcation of the BA and its most lateral position. The scale used to categorize the height of the bifurcation of the BA was as follows: 0, at or below the dorsum sellae; 1, within the suprasellar cistern; 2, at the level of the floor of the third ventricle; and 3, indenting and elevating the floor of the third ventricle. Finally, throughout its course, the most lateral position of the BA was graded as 0 for midline, 1 for the medial-to-lateral margins of the clivus or dorsum sellae, 2 for the lateral-to-lateral margins of the clivus or dorsum sellae, and 3 for a position in the cerebellopontine angle cistern.

Quantitative Evaluation

The diameter of the BA was measured on a workstation (AZE Virtual Place Plus; AZE, Tokyo, Japan). An observer blinded to the clinical information of each case drew a line perpendicular to the middle portion of the BA on a sagittal view of the maximum-intensity-projections of a 3D time-of-flight MR angiogram (Fig 1B). The observer then recorded the full width at half maximum as the diameter. Vascular stenosis was identified when the BA was determined to be <2 mm in diameter.

WMHs were quantitatively calculated by using methods previously described in the literature.¹⁰ To optimize the accuracy of the WMH registration procedure in a voxelwise analysis scheme, we combined the Diffeomorphic Anatomical Registration Through Exponentiated Lie Algebra–based T1 voxel-based morphometry approach¹¹ by using the Gaser voxel-based morphometry 8 toolbox (<http://www.neuro.uni-jena.de/vbm/download/>)

Table 1: The brain MR imaging findings of patients with IVS4-type Fabry disease and healthy controls

	IVS4 Fabry Disease	Healthy Control	P Value ^a
No.	26	26	
Mean age (SD) (years)	59.3 (7.2)	58.4 (6.48)	.680
Sex (M/F)	20:6	20:6	1.000
Infarction	9 (35%)	0 (0%)	.001
Area of infarction (anterior circulation/posterior circulation/both)	3/2/4	0/0/0	.012
Hemorrhage/microbleeds	0 (0%)	0 (0%)	1.000
White matter scores ^b	15/8/2/1	19/6/1/0	.554
Pulvinar sign	8 (30%)	0 (0%)	.002
Chiari I malformation	0 (0%)	0 (0%)	1.000
Vascular stenosis ^c	2 (8%)	2 (8%)	1.000
Mean diameter of BA (SD) (mm)	2.75 (0.62)	2.47 (0.66)	.245
Laterality of BA ^b	12/13/1/0	6/18/1/1	.283
Height of BA bifurcation ^b	6/10/10	9/11/6	.436

^a P, unadjusted.

^b Scale of 0/1/2/3.

^c Presence of focal stenosis of all intracranial arteries.

with the lesion-segmentation toolbox,¹² which was implemented in Statistical Parametric Mapping (SPM8; <http://www.fil.ion.ucl.ac.uk/spm/software/spm8>). First, all T1- and T2-weighted images were imported into the lesion-segmentation toolbox with default settings to generate WMH probability maps and binary maps in individual space. Second, all T1-weighted MR images were corrected for bias-field inhomogeneities and were affine-registered to tissue probability maps in the Montreal Neurological Institute standard space (<http://www.mni.mcgill.ca/>) after tissue segmentation with the same generative model.¹³ These affined tissue segments were iteratively registered to the group-based template, which was generated from all images included in the current study through nonlinear deformation by using the Diffeomorphic Anatomical Registration Through Exponentiated Lie Algebra. Third, all resulting WMH maps (probability and binary) in the individual space were then normalized and modulated by applying nonlinear deformations to compare actual WMH volumetric measurements in the Montreal Neurological Institute standard space.

We divided the whole brain into 2 traditional subtypes according to their location: periventricular WMHs, defined as a 13-mm lining from the ventricle surface, or deep WMHs, which comprised the remaining white matter. This brain atlas with the 2 subtypes was subsequently applied to WMH volume maps to automatically localize the WMH loci in the Montreal Neurological Institute standard space. Global and regional WMH volumes in various regions were subsequently extracted and calculated. To further control the effect of differences in brain size on global and regional WMH volumes, we used total intracranial volume for each participant to normalize WMH volume information into a whole-brain ratio.¹⁰

Statistical Analysis

Statistical analysis was performed by using the Statistical Package for Social Sciences software package (SPSS 18 for Windows; IBM, Armonk, New York). Semi-quantitative evaluations and BA diameters of patients with late-onset Fabry disease were compared with those of 26 healthy controls. Differences in brain MR imaging findings were analyzed by χ^2 and Fisher exact tests. Compar-

isons of BA diameters between groups were evaluated by using a nonparametric Kruskal-Wallis test.

For the analysis of quantitative WMHs, which was associated with total intracranial volume, we normalized each WMH volume by this variable to rule out an effect of brain size in our statistical models. Three ANCOVAs (periventricular white matter hyperintensity, deep white matter hyperintensity, and total WMH volume) were applied to show group differences in normalized WMH volumes, and we controlled for age as a nuisance variable; the significance level was corrected for multiple comparison issue by using the Bonferroni correction ($P = .016$). The other threshold for

statistical significance was at the $P < .05$ level.

RESULTS

Fabry Disease versus Healthy Controls

Twenty-six patients with Fabry disease and IVS4 + 919G>A mutations, and 26 sex- and age-matched healthy controls underwent MR imaging (Table 1).

The neurologic symptoms in the group with IVS4-type Fabry disease were forgetfulness ($n = 6$, 24%), tinnitus ($n = 4$, 16%), vertigo ($n = 3$, 12%), sudden onset of numbness or weakness ($n = 3$, 12%), depression ($n = 2$, 8%), asymmetric facial expression ($n = 1$, 4%), blurred vision or diplopia ($n = 1$, 4%), and personality changes ($n = 1$, 4%). Fourteen patients had symptoms, while the other 12 patients were free of neurologic symptoms. No significant correlation was found between neurologic manifestations and MR imaging findings.

Infarctions were found in 9 patients with IVS4-type Fabry disease (35%), including 6 men and 3 women, and no infarctions were identified in healthy controls ($P = .001$). All were lacunar infarctions involving the anterior and/or posterior circulation variably. A 54-year-old man had symptomatic lacunar infarctions, and the other 8 patients were asymptomatic.

Positive pulvinar signs were found in 8 patients with Fabry disease (30%) and in no individual in the healthy control group (0%) ($P = .002$). In terms of WMHs, no significant difference was found in the Fazekas scores in all groups; however, quantitative deep WMH volume was significantly higher in patients with IVS4-type Fabry disease (1.1583 cm^3) than in individuals in the healthy control data base (0.1354 cm^3) ($P = .004$) (Fig 3).

Mean BA diameter was 2.75 ± 0.62 mm in the IVS4-type Fabry disease and 2.47 ± 0.66 mm in the healthy control group ($P = .245$). A 63-year-old male patient with Fabry disease was excluded from further analysis due to dissection of the BA. There was no significant difference in the height of the BA bifurcation ($P = .436$) and the laterality of the BA ($P = .283$) between those with IVS4-type Fabry disease and healthy controls.

Infarction versus Noninfarction Groups

Comparisons of brain MR imaging findings in patients with the IVS4-type Fabry disease revealed that patients with infarctions were older (age range, 54–71 years; median age, 65 years) than patients without infarctions (age range, 43–64 years; median age, 58 years) ($P = .009$) (Table 2). In the infarction group, the Fazekas scale scores for deep white matter hyperintensities were also higher than those of noninfarction group ($P = .023$). Moreover, 2 and no patients had vascular stenosis in the infarction and noninfarction groups, respectively ($P = .041$). There was no significant difference in the mean BA diameter between the infarction and noninfarction groups ($P = .301$).

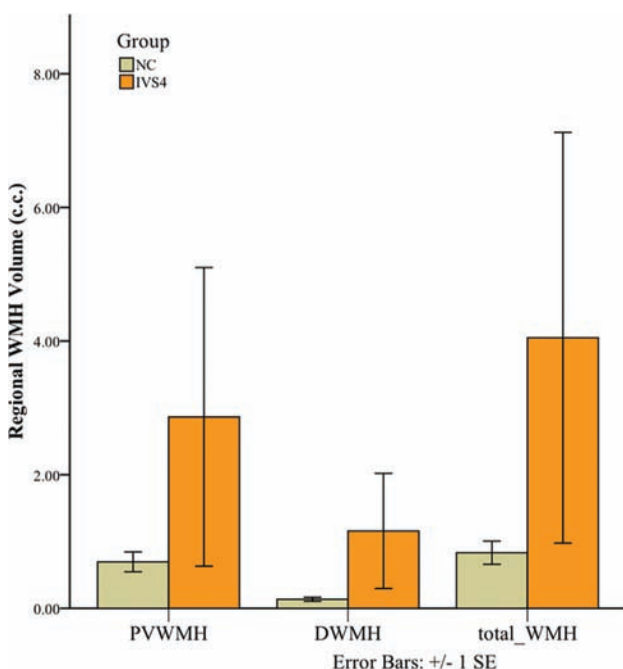


FIG 3. Bar graph of the averaged volume of regional white matter hyperintensities at the periventricular white matter (PVWMH), deep white matter (DWMH), and total white matter in both patients with IVS4-type Fabry disease and healthy controls.

Table 2: Comparison of brain MR imaging findings in patients with IVS4-type Fabry disease, with and without brain infarctions

	Infarction	Noninfarction	P Value ^a
No.	9	17	
Mean age (SD) (years)	64.0 (5.2)	56.8 (7.0)	.009
Sex (M/F)	6:3	14:3	.332
Area of infarction (anterior circulation/posterior circulation/both)	3/2/4	0/0/0	.012
Hemorrhage/microbleeds	0 (0%)	0 (0%)	1.000
White matter scores ^b	2/4/2/1	13/4/0/0	.023
Pulvinar sign	3 (33%)	5 (29%)	.837
Chiari I malformation	0 (0%)	0 (0%)	1.000
Vascular stenosis ^c	2 (22%)	0 (0%)	.041
Mean diameter of BA (SD) (mm)	2.57 (0.64)	2.86 (0.61)	.301
Laterality of BA ^b	4/5/0/0	8/8/1/0	.732
Height of BA bifurcation ^b	3/5/1	3/5/9	.114

^a P , unadjusted.

^b Scale of 0/1/2/3.

^c Presence of focal stenosis of all intracranial arteries.

Sex-Based Differences between Patients with IVS4 Fabry Disease versus Healthy Controls

There was no difference in brain MR imaging findings between female patients having Fabry disease and healthy controls (Table 3). However, in male patients with Fabry disease (Table 4), we observed a higher incidence of infarctions ($P = .010$) and pulvinar signs ($P = .004$) and larger BA diameters (2.91 ± 0.60 mm, $P = .041$) compared with healthy controls. A receiver operating characteristic curve analysis of the BA diameter in male patients revealed that a threshold of 2.95 mm could achieve a sensitivity of 53% and a specificity of 85% in differentiating IVS4-type Fabry disease and healthy controls (area under the curve = 0.69; 95% confidence interval, 0.52–0.86).

DISCUSSION

In classic Fabry disease, stroke is a common and important manifestation.^{5–16} It could be a consequence of cardiogenic embolism from cardiomyopathy, valvular heart disease, ischemic heart disease, and/or arrhythmias. Besides, due to the deposition of neutral glycosphingolipids in vascular endothelial cells, the potential cerebrovascular damage or alterations in brain perfusion should be considered.¹⁷ The prevalence of stroke in patients with IVS4-type Fabry disease was similar to that reported by a previous retrospective study of classic Fabry disease.¹⁵ However, the median age of our patients having IVS4-type Fabry disease with infarctions was older than the prior reported median age, which ranged from 28 to 54 years.¹⁸ Furthermore, none of the young patients with IVS4-type Fabry disease (younger than 54 years of age) in our cohort had experienced stroke or asymptomatic infarctions, even though Fabry disease poses a higher relative risk of stroke across all age groups.¹⁴ In our cohort, the mean age of patients with infarctions was older than that in patients without infarctions. This study demonstrated that Fabry disease with IVS4 + 919G>A mutations, though previously categorized as a cardiac variant, also increased the risk of stroke in a late-onset fashion.

Multiple or confluent WMHs on T2-weighted images are one of the characteristic neuroradiologic signs of classic Fabry disease. The injury is caused by globotriaosylceramide (GL-3)-related endothelial damage and subsequent microvascular degeneration.¹⁹ Although we observed no significant difference in WMH severity between the 2 groups by using the semi-quantitative Fazekas

score, the quantitative deep WMH volumes of IVS4-type Fabry disease were significantly higher than those in healthy controls; this finding was consistent with the higher sensitivity of the automated segmentation method for WMHs.²⁰

Vertebrobasilar dolichoectasia is thought to be an early and frequent sign of classic Fabry disease.²¹ For example, Fellgiebel et al^{22,23} demonstrated that the BA diameter was superior to white matter lesions as a diagnostic tool of Fabry disease and that this sign could be used for screening in young patients who have experienced stroke. More specifically, their group used a diameter of 2.98 mm as a cutoff value with a sensi-

Table 3: Brain MR imaging findings of female patients with IVS4-type Fabry disease and healthy controls

	Late-Onset Fabry Disease	Healthy Control	P Value ^a
No.	6	6	
Mean age (SD) (years)	57.8 (6.5)	58.0 (6.2)	.937
Infarction	3 (50%)	0 (0%)	.091
Area of infarction (anterior circulation/posterior circulation/both)	2/1/0	0/0/0	.135
Hemorrhage/microbleeds	0 (0%)	0 (0%)	1.000
White matter scores ^b	2/3/1/0	5/1/0/0	.193
Pulvinar sign	1 (17%)	0 (0%)	.500
Chiari I malformation	0 (0%)	0 (0%)	1.000
Vascular stenosis ^c	1 (17%)	0 (0%)	.500
Mean diameter of BA (SD) (mm)	2.25 (0.41)	2.62 (0.42)	.180
Laterality of BA ^b	1/5/0/0	1/4/0/1	.574
Height of BA bifurcation ^b	2/2/2	2/1/3	.766

^a P, unadjusted.^b Scale of 0/1/2/3.^c Presence of focal stenosis of all intracranial arteries.**Table 4: Brain MR imaging findings of male patients with IVS4 + 919G>A and healthy controls**

	Late-Onset Fabry Disease	Healthy Control	P Value ^a
No.	20	20	
Mean age (SD) (years)	59.7 (7.5)	58.5 (6.7)	.547
Infarction	6 (30%)	0 (0%)	.010
Area of infarction (anterior circulation/posterior circulation/both)	1/1/4	0/0/0	.070
Hemorrhage/microbleeds	0 (0%)	0 (0%)	1.000
White matter scores ^b	13/5/1/1	14/5/1/0	.792
Pulvinar sign	7 (35%)	0 (0%)	.004
Chiari I malformation	0 (0%)	0 (0%)	1.000
Vascular stenosis ^c	1 (5%)	2 (10%)	.513
Mean diameter of BA (SD) (mm)	2.91 (0.60)	2.43 (0.72)	.041
Laterality of BA ^b	11/8/1/0	5/14/1/0	.143
Height of BA bifurcation ^b	4/8/8	7/10/3	.191

^a P, unadjusted.^b Scale of 0/1/2/3.^c Presence of focal stenosis of all intracranial arteries.

tivity of 84% and a specificity of 88.5%. Furthermore, Uçeyler et al²⁴ proposed that a BA diameter of >3.2 mm could distinguish a male patient with Fabry disease and healthy controls with a sensitivity of 87% and specificity of 86%. In our cohort, male patients with IVS4 Fabry disease had significantly larger BA diameters than healthy controls, while female patients did not. A cutoff of 3.2 mm for late-onset Fabry disease had a low sensitivity, while a cutoff of 2.95 mm had fair sensitivity and specificity. This difference is probably because this was a group with late-onset disease. Thus, long-term follow-up of these patients is needed for a more thorough understanding of the progression and severity of IVS4-type Fabry disease. The concept offered an explanation for no significant difference in MR imaging findings of the female group between healthy controls and those with late-onset X-linked disease.

The characteristic “pulvinar sign,” which comprises hyperintensities of the posterior thalamus on T1-weighted images, is presumed to occur secondary to increased cerebral blood flow in the posterior circulation.^{7,25} In our patient cohort, we observed this sign in 8 (30%) patients with IVS4-type Fabry disease (Fig 2). This result is consistent with the hypothesis that this mutated form of Fabry disease comprises neurovascular alterations and cardiac and renal involvement.

This study had some limitations. First, IVS4-type Fabry disease has been previously considered a cardiac variant, which the pathologic changes of the brain was not well recognized. This limitation explains the small number of brain MRIs in this retrospective study, though the incidence of this type of Fabry disease is common in our population. An aim of this study was also to demonstrate that involvement of this type is not limited to the heart alone. Second, Fabry disease involves multiple organs, and our patients often had hypertension and cardiac and renal disease. We did not evaluate the effects of these comorbidities on intracranial conditions due to the small number of cases reviewed. Third, despite healthy controls not having cardiac and renal abnormalities, our retrospective study could not exclude the possibility of asymptomatic or undiagnosed Fabry disease in the healthy control group. Fourth, the sample size of patients with IVS4 mutation is small and may not allow detection of the milder and later-onset pathologic changes in female patients as opposed to male patients. A larger sample size and long-term follow-up are crucial for understanding late manifestations of clinical symptoms and imaging findings. Last, the age and sex-matched comparison between IVS4-type and classic Fabry disease

was not included in this study due to the rarity of classic Fabry disease.

CONCLUSIONS

This study demonstrated that the cardiac-type Fabry disease with a mutation of IVS4 + 919G>A was not limited to involvement of the cardiac system. Patients with this form of the disease presented with a greater amount of deep white matter intensities and higher incidences of infarctions and pulvinar signs than healthy controls. Finally, the use of a BA cutoff diameter of 2.95 mm achieved fair sensitivity and specificity in differentiating male patients with IVS4-type Fabry disease and healthy controls. Awareness of the neuroimaging findings helps early detection and treatment of the specific type of Fabry disease.

REFERENCES

- Desnick RJ, Ioannou YA, Eng CM. α -galactosidase A deficiency: Fabry disease. In: Scriver CR, ed. *The Metabolic and Molecular Bases of Inherited Disease*. 8th ed. New York: McGraw-Hill; 2001:3733–74
- Reisin RC, Romero C, Marchesoni C, et al. Brain MRI findings in patients with Fabry disease. *J Neurol Sci* 2011;305:41–44 CrossRef Medline
- Chong KW, Lu YH, Hsu JH, et al. High incidence of cardiac variant of Fabry disease in Taiwanese revealed by newborn screening. In:

Proceedings of the Taiwan Human Genetics Society Autumn Symposium, Hualien, Taiwan. October 4–5, 2008

4. Lin HY, Chong KW, Hsu JH, et al. **High incidence of the cardiac variant of Fabry disease revealed by newborn screening in the Taiwan Chinese population.** *Circ Cardiovasc Genet* 2009;2:450–56 CrossRef Medline
5. Chien YH, Lee NC, Chiang SC, et al. **Fabry disease: incidence of the common later-onset α -galactosidase A IVS4+919G→A mutation in Taiwanese newborns: superiority of DNA-based to enzyme-based newborn screening for common mutations.** *Mol Med* 2012;18:780–84 CrossRef Medline
6. Ishii S, Nakao S, Minamikawa-Tachino R, et al. **Alternative splicing in the alpha-galactosidase A gene: increased exon inclusion results in the Fabry cardiac phenotype.** *Am J Hum Genet* 2002;70:994–1002 CrossRef Medline
7. Takanashi Ji, Barkovich AJ, Dillon WP, et al. **T1 hyperintensity in the pulvinar: key imaging feature for diagnosis of Fabry disease.** *AJNR Am J Neuroradiol* 2003;24:916–21 Medline
8. Fazekas F, Chawluk JB, Alavi A, et al. **MR signal abnormalities at 1.5 T in Alzheimer's dementia and normal aging.** *AJR Am J Roentgenol* 1987;149:351–66 CrossRef Medline
9. Smoker WR, Corbett JJ, Gentry LR, et al. **High-resolution computed tomography of the basilar artery, 2: vertebrobasilar dolichoectasia—clinical-pathologic correlation and review.** *AJNR Am J Neuroradiol* 1986;7:61–72 Medline
10. Tsai A, Huang CC, Yang AC, et al. **Association of BACE1 gene polymorphism with cerebellar volume but not cognitive function in normal individuals.** *Dement Geriatr Cogn Dis Extra* 2012;2:632–37 CrossRef Medline
11. Ashburner J. **A fast diffeomorphic image registration algorithm.** *Neuroimage* 2007;38:95–113 CrossRef Medline
12. Schmidt P, Gaser C, Arsic M, et al. **An automated tool for detection of FLAIR-hyperintense white-matter lesions in multiple sclerosis.** *Neuroimage* 2012;59:3774–83 CrossRef Medline
13. Ashburner J, Friston KJ. **Unified segmentation.** *Neuroimage* 2005;26:839–51 CrossRef Medline
14. Sims K, Politei J, Banikazemi M, et al. **Stroke in Fabry disease frequently occurs before diagnosis and in the absence of other clinical events: natural history data from the Fabry registry.** *Stroke* 2009;40:788–94 CrossRef Medline
15. Buechner S, Moretti M, Burlina AP, et al. **Central nervous system involvement in Anderson-Fabry disease: a clinical and MRI retrospective study.** *J Neurol Neurosurg Psychiatry* 2008;79:1249–54 CrossRef Medline
16. Rolfs A, Böttcher T, Zschesche M, et al. **Prevalence of Fabry disease in patients with cryptogenic stroke: a prospective study.** *Lancet* 2005;366:1794–96 CrossRef Medline
17. Fellgiebel A, Müller MJ, Ginsberg L. **CNS manifestations of Fabry's disease.** *Lancet Neurol* 2006;5:791–95 CrossRef Medline
18. Kolodny E, Fellgiebel A, Hilz MJ, et al. **Cerebrovascular involvement in Fabry disease: current status of knowledge.** *Stroke* 2015;46:302–13 CrossRef Medline
19. deVeber GA, Schwarting GA, Kolodny EH, et al. **Fabry disease: immunocytochemical characterization of neuronal involvement.** *Ann Neurol* 1992;31:409–15 CrossRef Medline
20. Prins ND, van Straaten EC, van Dijk EJ, et al. **Measuring progression of cerebral white matter lesions on MRI: visual rating and volumetrics.** *Neurology* 2004;62:1533–39 CrossRef
21. Politei J, Schenone AB, Burlina A, et al. **Vertebrobasilar dolichoectasia in Fabry disease: the earliest marker of neurovascular involvement?** *JIEMS* 2014;2:2326409814541246 CrossRef
22. Fellgiebel A, Keller I, Marin D, et al. **Diagnostic utility of different MRI and MR angiography measures in Fabry disease.** *Neurology* 2009;72:63–68 CrossRef Medline
23. Fellgiebel A, Keller I, Martus P, et al. **Basilar artery diameter is a potential screening tool for Fabry disease in young stroke patients.** *Cerebrovasc Dis* 2011;31:294–99 CrossRef Medline
24. Uçeyler N, Homola GA, Guerrero González H, et al. **Increased arterial diameters in the posterior cerebral circulation in men with Fabry disease.** *PLoS One* 2014;9:e87054 CrossRef Medline
25. Moore DF, Ye F, Schiffmann R, et al. **Increased signal intensity in the pulvinar on T1-weighted images: a pathognomonic MR imaging sign of Fabry disease.** *AJNR Am J Neuroradiol* 2003;24:1096–101 Medline

Automated Hippocampal Subfield Segmentation at 7T MRI

L.E.M. Wisse, H.J. Kuijf, A.M. Honingh, H. Wang, J.B. Pluta, S.R. Das, D.A. Wolk, J.J.M. Zwanenburg, P.A. Yushkevich, and M.I. Geerlings



ABSTRACT

BACKGROUND AND PURPOSE: High resolution 7T MRI is increasingly used to investigate hippocampal subfields in vivo, but most studies rely on manual segmentation which is labor intensive. We aimed to evaluate an automated technique to segment hippocampal subfields and the entorhinal cortex at 7T MRI.

MATERIALS AND METHODS: The cornu ammonis (CA), CA2, CA3, dentate gyrus, subiculum, and entorhinal cortex were manually segmented, covering most of the long axis of the hippocampus on 0.70-mm³ T2-weighted 7T images of 26 participants (59 ± 9 years, 46% men). The automated segmentation of hippocampal subfields approach was applied and evaluated by using leave-one-out cross-validation.

RESULTS: Comparison of automated segmentations with corresponding manual segmentations yielded a Dice similarity coefficient of >0.75 for CA1, the dentate gyrus, subiculum, and entorhinal cortex and >0.54 for CA2 and CA3. Intraclass correlation coefficients were >0.74 for CA1, the dentate gyrus, and subiculum; and >0.43 for CA2, CA3, and the entorhinal cortex. Restricting the comparison of the entorhinal cortex segmentation to a smaller range along the anteroposterior axis improved both intraclass correlation coefficients (left: 0.71; right: 0.82) and Dice similarity coefficients (left: 0.78; right: 0.77). The accuracy of the automated segmentation versus a manual rater was lower, though only slightly for most subfields, than the intrarater reliability of an expert manual rater, but it was similar to or slightly higher than the accuracy of an expert-versus-manual rater with ~170 hours of training for almost all subfields.

CONCLUSIONS: This work demonstrates the feasibility of using a computational technique to automatically label hippocampal subfields and the entorhinal cortex at 7T MRI, with a high accuracy for most subfields that is competitive with the labor-intensive manual segmentation. The software and atlas are publicly available: <http://www.nitrc.org/projects/ashs/>.

ABBREVIATIONS: ASHS = automated segmentation of hippocampal subfields; CA = cornu ammonis; DSC = Dice similarity coefficient; DG = dentate gyrus; ERC = entorhinal cortex; ICC = intraclass correlation coefficient; SUB = subiculum

The segmentation of subfields within the hippocampal formation on in vivo MRI is of major interest because these small anatomic subregions are potentially differentially affected in neu-

ropsychiatric and neurologic disorders, including Alzheimer disease, major depressive disorder, posttraumatic stress disorder, and schizophrenia.¹ In the previous decade, >20 segmentation protocols for MRI have been published for the hippocampal subfields and adjacent medial temporal lobe structures.² Most of these protocols rely on manual segmentation,³⁻⁹ which is labor-intensive, requires a long training period, and is often difficult to reproduce between research centers. Automated segmentation methods can help overcome these problems. To our knowledge, currently, only 4 automated segmentation methods exist,¹⁰⁻¹² 3 of which were developed and evaluated on scans acquired at 3T MR imaging. Only the new FreeSurfer

Received July 31, 2015; accepted after revision November 19.

From the Penn Image Computing and Science Laboratory, Department of Radiology (L.E.M.W., J.B.P., S.R.D., P.A.Y.), and Penn Memory Center, Department of Neurology (J.B.P., D.A.W.), University of Pennsylvania, Philadelphia, Pennsylvania; Image Sciences Institute (H.J.K.), Julius Center for Health Sciences and Primary Care (A.M.H., M.I.G.), and Department of Radiology (J.J.M.Z.), UMC Utrecht, Utrecht, the Netherlands; and Almaden Research Center (H.W.), IBM Research, Almaden, California.

Paul A. Yushkevich and Mirjam I. Geerlings shared last authorship and contributed equally to this work.

This work was funded by the National Institute on Aging, grant Nos. K23 AG028018, P30AG010124, and R01 AG037376; the National Institute of Biomedical Imaging and Bioengineering, grant Nos. R01 EB014346 and R01 EB017255. Hugo Kuijf was financially supported by the project Brainbox (quantitative analysis of MR brain images for cerebrovascular disease management), funded by the Netherlands Organisation for Health Research and Development in the framework of the research program Innovative Medical Devices Initiative, project 104002002. This research was also supported by a grant from the Dutch Brain Foundation (Hersensichting Nederland; project No. 2012 [1]-43).

Please address correspondence to Laura E.M. Wisse, PhD, 3700 Hamilton Walk, Richards Building, Philadelphia, PA 19104; e-mail: Laura.Wisse@uphs.upenn.edu

Indicates open access to non-subscribers at www.ajnr.org

Indicates article with supplemental on-line appendix and table.

Indicates article with supplemental on-line photos.

<http://dx.doi.org/10.3174/ajnr.A4659>

method (<http://surfer.nmr.mgh.harvard.edu>), developed by Iglesias et al,¹³ was developed by using a higher resolution 7T postmortem atlas set, though its application has only been demonstrated at lower field strengths. The advantage of in vivo 7T MRI is that high-resolution 3D images can be generated with a relatively short scanning time, making it possible to visualize hippocampal anatomy in greater detail.

Recently, an increasing number of 7T studies have been published on the hippocampal subregional morphology.¹⁴⁻¹⁶ Several manual segmentation protocols exist for 7T MRI,^{5,7,17} and a semi-automatic technique for measuring the thickness of hippocampal subfields and layers in the hippocampal body was developed by Kerchner et al.¹⁸ In this study, we evaluated the performance of a fully automated segmentation technique for labeling hippocampal subfields and the entorhinal cortex (ERC) at 7T MR imaging, which comes with a new set of challenges, including field inhomogeneity artifacts and increased image size. We do so by adapting a technique previously developed for 3T MRI¹² to 7T MRI, labeled by using the manual annotation protocol developed by Wisse et al (2012).⁵ This protocol and the resulting automatic segmentation cover most of the longitudinal axis of the hippocampal formation. In addition, this article is the first to show that automatic segmentation performs competitively with interrater manual segmentation when the whole length of the hippocampus is labeled. Previously, only Yushkevich et al¹⁹ performed a comparison of automatic hippocampal subfield segmentation and interrater manual segmentation reliability, doing so at 3T and only in the body of the hippocampus.

MATERIALS AND METHODS

Participants

Participants were included from the PREDICT-MR,¹⁶ an ancillary study to the PREDICT-NL study,²⁰ which aimed to investigate determinants and consequences of brain changes on MR imaging in general practice attendees. The cohort included individuals 18 years of age or older who were asked to participate while in the waiting room of their general practitioner, irrespective of their symptoms.

The studies were performed in accordance with the principles of the Declaration of Helsinki and approved by the local ethics committee from the University Medical Center in Utrecht. Written informed consent was obtained from all participants.

Study Sample for the Atlas Set, Intrarater Reliability, and the Interrater Reliability Set

For the atlas set, 30 participants with a 7T T2-weighted MRI scan, required for the hippocampal subfield segmentation protocol, were randomly selected from the 47 participants in total. Images of 4 were considered to have relatively poor quality due to excessive subject motion, leaving 26 participants for the current study (mean age, 59 ± 9 years; 46% men; median Mini-Mental State Examination score,²¹ 29; range, 25-30).

As a comparison for the reliability of the automated segmentation, we included overlap and reliability values of a single rater (L.E.M.W., rater 1; intrarater reliability) and of 2 raters (L.E.M.W., rater 1, and A.M.H., rater 2; interrater reliability).

The intrarater reliability was established in a previous study,⁵ and the dataset consisted of the first 14 participants of the PREDICT-MR study (overlap with the atlas set, $n = 7$).⁵ For the interrater reliability, a random set of 14 MRI scans of PREDICT-MR was selected for segmentation (overlap with the atlas set, $n = 12$). The reliability analysis was after a training period of rater 2 of approximately 5 months, 1 day a week.

See On-line Fig 1 for a Venn diagram describing the samples.

Image Acquisition

All scans were performed on a 7T MR imaging scanner (Philips Healthcare, Best, the Netherlands) by using a volume transmit coil and a 16-channel receive coil (Nova Medical, Wilmington, Massachusetts) (participants included in the study later than May 2011 were scanned with a volume-transmit and 32-channel receive head coil [Nova Medical]). The 7T protocol included $0.70 \times 0.70 \times 0.70$ mm³ 3D T2-weighted TSE with a TR of 3158 milliseconds, a nominal TE of 301 milliseconds (with a contrast equivalent to a TE of 58 ms for brain tissue in spin-echo sequences with full refocusing angles), a flip angle of 120° (to partly compensate inhomogeneity in the radiofrequency field), a TSE factor of 182, a matrix size of $356 \times 357 \times 272$, the application of 2D sensitivity encoding with acceleration factors of 2.0×2.8 (anterior-posterior \times right-left), and a scan duration of 10 minutes and 15 seconds.⁵ The images were interpolated by zero-filling during reconstruction to a nominal spatial resolution of $0.35 \times 0.35 \times 0.35$ mm³. Moreover, the 7T MRI protocol included a $1.00 \times 1.00 \times 1.00$ mm³ T1-weighted sequence with a TR of 4.8 ms, TE of 2.2 ms, TI of 1240 ms, a TR of the inversion pulses of 3500 ms, a matrix size of $200 \times 250 \times 200$, and a scan duration of 1 minute and 57 seconds.

Manual Segmentation

The cornu ammonis (CA) fields CA1, CA2, CA3 and the dentate gyrus (DG) (the dentate gyrus label includes both the granular cell layer of the dentate gyrus and the hilar region, sometimes called CA4), subiculum (SUB), and ERC were manually segmented, blinded to participant information, by using in-house-developed software²² based on MeVisLab (MeVis Medical Solutions, Bremen, Germany²³). Segmentations were performed on coronal images, angulated perpendicular to the long axis of the hippocampal formation. The ERC was segmented according to the protocol by Goncharova et al,²⁴ except for the posterior border, for which we followed the protocol of Insausti et al.²⁵ CA1, CA2, CA3, DG, and SUB were segmented according to a previously published protocol,⁵ covering most of the long axis of the hippocampal formation. The anterior border was the most anterior section on which the hippocampus could be observed. The posterior border was defined as the section in which the total length of the fornix was visible. This was the most posterior section on which hippocampal subfields were segmented. Beyond this point, subfields fused together and could not be delineated reliably.

Automated Segmentation

We applied the automated segmentation of hippocampal subfields (ASHS) technique by using this atlas set. Briefly, the method applies deformable registration of the T1- and T2-

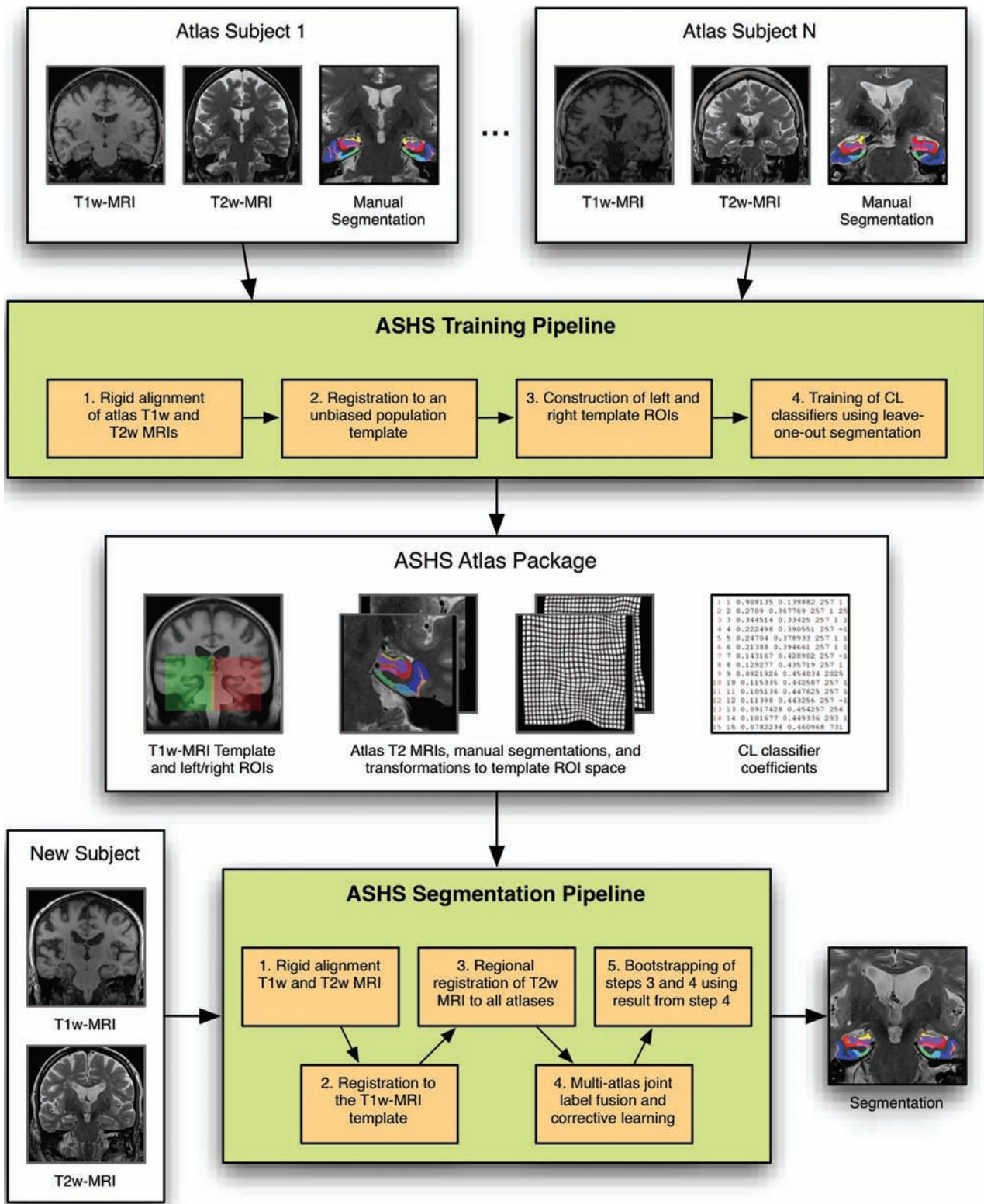


FIG 1. Training and segmentation pipelines in ASHS. Reprinted with permission from Yushkevich et al.¹² Copyright 2014 Wiley Periodicals.

weighted images,²⁶ multi-atlas joint label fusion,²⁷ and voxel-wise learning-based error correction,²⁸ to propagate anatomic labels from a set of manually labeled training images to an unlabeled image. ASHS was evaluated by using a leave-one-out cross-validation (ie, when automatically segmenting the 7T scan of 1 participant in the study, the scans of the remaining 25

participants were used as training data). The resulting automatic segmentation was then compared with the manual segmentation of the same participant. Certain parameters of the method were modified for the 7T segmentation to account for differences in image size and resolution. More details are provided in Fig 1 and the On-line Appendix.

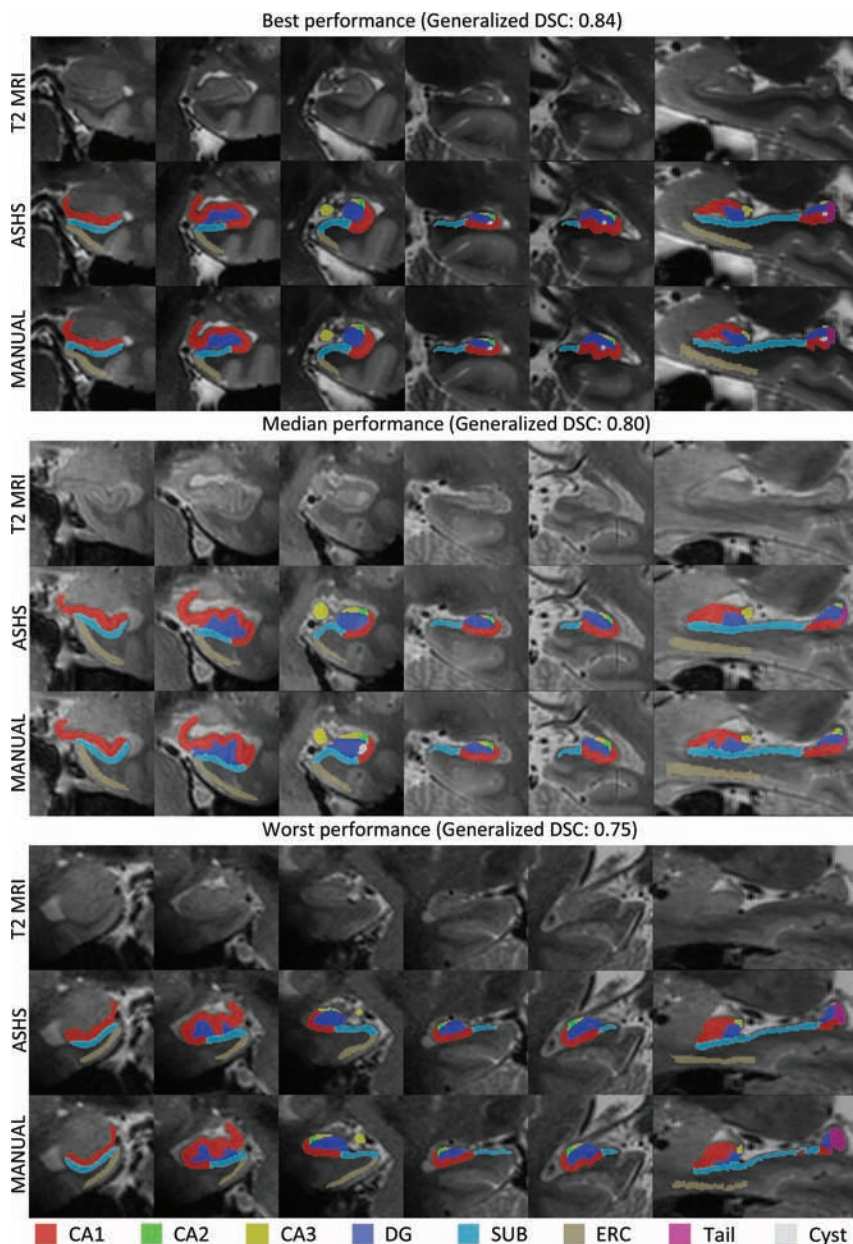


FIG 2. Examples of results from the automated segmentation from the cross-validation experiment with the best (upper panel, left hemisphere), median (middle panel, left hemisphere), and worst performance (lower panel, right hemisphere). In each panel in the top row, the raw T2 image is shown; in the second row, the automated segmentation of hippocampal subfields is shown; and the third row, the manual segmentation is shown.

Statistical Analyses

Volumes generated by manual and automated segmentations were compared by using a paired *t* test. The accuracy of automatic segmentation relative to manual segmentation (ASHS versus rater 1) was assessed in terms of relative overlap by using the Dice similarity coefficient (DSC).²⁹ The DSC was computed separately for each subfield and jointly for all subfields (generalized DSC,³⁰ see the On-line Appendix for a definition). The consistency of volume measurements derived from automatic and manual segmentations was measured by using the intraclass correlation coefficient (ICC) by using SPSS, Version 20 (IBM, Armonk, New York). The ICC variant that measured absolute agreement under a 2-way random analysis of variance model was used. Analogous

statistical methods were used to compute the ICC and DSC between repeat segmentations of the same scans by rater 1 (intrarater reliability) and between 2 raters (rater 1 versus 2, interrater reliability).

In the 12 subjects who were included in the atlas set and the sample for the interrater reliability of the 2 manual raters, we performed additional analyses to test whether the DSCs of ASHS versus rater 1 were significantly different from the DSCs of rater 2 versus rater 1, by using Wilcoxon signed rank tests (2-sided).

In addition, we evaluated the ERC segmentation without the most anterior and posterior sections. We created a mask for the manual segmentation by removing the sections anterior to the head of the hippocampus and by removing the 4 most anterior and posterior sections of the resulting set of sections.

RESULTS

Figure 2 presents a visualization of the comparison of the automated and corresponding manual segmentation from the cross-validation experiment. Based on the generalized DSC, the best, median, and worst performances are shown. This figure shows that in the upper and middle panel (the best and median performance), the automated segmentations look very similar to the manual segmentations, though in the middle panel, small localized differences can be observed. For example, the segmentation of CA3 (yellow) and the ERC (light brown) is generally smaller/thinner in the automated-versus-manual segmentation. In the lower panel, showing the segmentation with the lowest generalized DSC, the overall location of

the subfields is still similar in the manual and automated segmentation. However, local differences can be observed. For example, CA2 (green) and CA3 (yellow) are smaller in the automated-versus-manual segmentation. In addition, we observed that the mismatch occurs mainly in the segmentation of the most anterior sections for CA2, CA3, and the ERC. The automated segmentation of CA2, CA3, and the ERC included mostly fewer sections but sometimes more sections than the manual segmentation, which was likely a major source of inconsistency between the annotations. We will address this issue later in the “Results” for the ERC and in the “Discussion.” Figure 3 shows a 3D rendering of the automated segmentation of hippocampal subfields and the ERC.

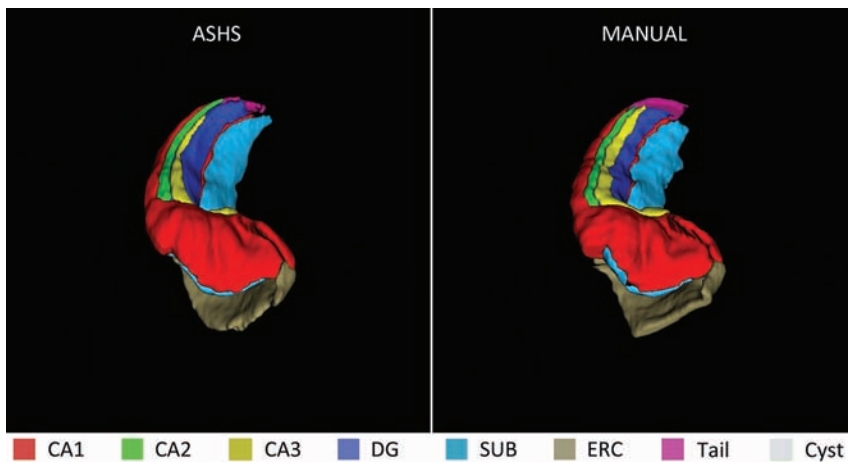


FIG 3. 3D rendering of an automated (ASHS) and a manual segmentation.

Table 1: Volumes of manual and automated segmentation

	Automated Segmentation Volume (Mean) (mL)		Manual Segmentation Volume (Mean) (mL)	
	Left	Right	Left	Right
CA1	1.43 ± 0.22	1.54 ± 0.24	1.42 ± 0.22	1.53 ± 0.23
CA2	0.054 ± 0.008 ^a	0.066 ± 0.012 ^a	0.060 ± 0.013	0.071 ± 0.013
CA3	0.10 ± 0.03 ^a	0.09 ± 0.03 ^a	0.12 ± 0.04	0.12 ± 0.05
CA2+3	0.15 ± 0.03 ^a	0.16 ± 0.04 ^a	0.18 ± 0.04	0.19 ± 0.05
DG	0.79 ± 0.12	0.79 ± 0.12	0.79 ± 0.12	0.80 ± 0.12
SUB	0.61 ± 0.09	0.64 ± 0.09	0.61 ± 0.14	0.65 ± 0.13
ERC	0.47 ± 0.07 ^a	0.49 ± 0.07 ^a	0.52 ± 0.11	0.53 ± 0.08

^a Significantly different from volumes generated by manual segmentation.

Mean volumes of the manual and automated segmentation are shown in Table 1. CA1, DG, and SUB volumes generated by the automated segmentation were similar to those of manual segmentation, but CA2, CA3, and ERC volumes were smaller compared with the manual segmentation ($P < .05$). The DSC of ASHS versus rater 1 was >0.75 for the larger subfields CA1, DG, SUB, and ERC; however it was lower for the smaller subfields CA2 and CA3 (Table 2). The mean generalized DSC across all subfields in the left hemisphere was 0.80 ± 0.03 , and for the right hemisphere, it was 0.79 ± 0.03 . The ICC was >0.74 for the larger subfields CA1, DG, and SUB; however, it was lower for the ERC and the smaller subfields of CA2 and 3. Combining CA2 and 3 into a single label increased the bilateral DSC values and the right ICC compared with the segmentation of CA2 and CA3 alone.

Notably, the above results show a discrepancy between the ICC and the DSC values for the ERC. As described above, the automated segmentation of the ERC included mostly fewer sections, but sometimes more sections than the manual segmentation, which likely affected the ICC more than the DSC. We recalculated the ICC and DSC in a restricted range, as described in the “Materials and Methods” section, and found higher ICC values (left: 0.71, right: 0.82) and slightly higher DSC values (left: 0.78 ± 0.08 ; right: 0.77 ± 0.06).

Table 2 also shows the intrarater reliability of manual segmentation by rater 1.⁵ Overall, the intrarater reliability was higher than the agreement between the automated and manual segmentations. However, for automatic techniques such as ASHS that are trained on manual segmentations, the intrarater reliability of manual segmentation represents the theoretic upper bound for

the agreement of automatic segmentation with manual segmentation. In addition, Table 2 shows the interrater reliability and overlap for 2 manual raters. The DSC values of ASHS versus rater 1 were higher for the larger subfields than the DSCs of rater 1 versus 2, and there were similar values for the smaller subfields. In additional analyses in the subjects who were included in both the atlas set and the set for the interrater reliability for the 2 manual raters, the DSC of ASHS versus rater 1 was significantly higher than the DSC of rater 1 versus 2 for the left ERC ($P = .04$), left and right SUB ($P < .01$; $P < .01$), right CA1 ($P = .03$), and left and right DG ($P = .02$; $P < .01$), and at a trend level for the right ERC ($P = .08$). It was equal for left CA1 ($P = .14$), left and right CA2 ($P = .48$; $P = .58$), and left CA3 ($P = .43$). Only for right CA3 was the DSC of the second rater higher at a trend level ($P = .08$) than that of ASHS. ASHS also had slightly higher or similar ICC values for most the subfields compared with the second rater, except for the DG, CA3, and right CA2.

DISCUSSION

The current study demonstrates that automated segmentation of hippocampal subfields and the ERC at 7T MRI is feasible and that the errors of automatic segmentation are comparable with and in some cases even lower than the disagreement between 2 manual raters applying the same segmentation protocol. ASHS attained high accuracy (ICC > 0.74 , DSC > 0.75) for larger subfields, including CA1, the DG, and SUB and lower accuracy for the ERC and smaller subfields, including CA2 and CA3. The anterior and posterior boundaries of the ERC were an important source of disagreement between the manual and automated segmentation. Restricting the range of ERC segmentation increased the accuracy, indicating that the ERC segmentation is accurate except at its anterior and posterior segments.

The high accuracy for the larger subfields, which is close to the intrarater reliability of this manual protocol,⁵ is promising and highly relevant, given the increasing number of sites using 7T MRI for hippocampal subfield research.^{5,14,17,31} The lower accuracy of the small subfields is consistent, to some extent, with that of the manual rater.⁵ It should be noted that small or thin structures are penalized by the DSC; as also mentioned by Pipitone et al,¹¹ who showed that when comparing the automated segmentation with the manual segmentation shifted by 1 voxel, the DSCs of smaller structures were affected most.

As Table 1 shows, smaller structures (CA2, CA3, and ERC) were undersegmented by ASHS. The tendency of multiatlas label fusion algorithms to undersegment certain structures is a known limitation,³² and the machine learning corrective learning step in ASHS²⁸ is meant to mitigate this effect, though it is not theoretically guaranteed to do so. In this study, corrective learning only partially reduced the undersegmentation error for CA2, CA3, and ERC (CA2 left: from 0.050 to 0.054; right: from 0.055 to 0.066;

Table 2: ICC and DSC among automated and corresponding manual segmentations, intrarater reliability of a single manual rater, and interrater reliability of 2 independent manual raters

	ICC and DSC of Automated vs Manual Rater (ASHS vs Rater 1)				ICC and DSC of a Single Manual Rater (Rater 1) ^a				ICC and DSC of 2 Independent Manual Raters (Rater 1 vs 2)			
	DSC (mean ± SD)		ICC		DSC (mean ± SD)		ICC		DSC (mean ± SD)		ICC	
	Left	Right	Left	Right	Left	Right	Left	Right	Left	Right	Left	Right
CA1	0.84 ± 0.03	0.83 ± 0.02	0.93	0.97	0.86 ± 0.02	0.86 ± 0.03	0.98	0.98	0.82 ± 0.03	0.81 ± 0.02	0.73	0.94
CA2	0.64 ± 0.08	0.65 ± 0.09	0.55	0.67	0.66 ± 0.05	0.66 ± 0.10	0.83	0.74	0.65 ± 0.06	0.66 ± 0.05	0.34	0.88
CA3	0.58 ± 0.11	0.54 ± 0.13	0.43	0.45	0.70 ± 0.10	0.71 ± 0.08	0.82	0.85	0.57 ± 0.09	0.59 ± 0.10	0.60	0.60
CA2+3	0.66 ± 0.08	0.64 ± 0.10	0.42	0.49	0.73 ± 0.07	0.74 ± 0.07	0.80	0.81	0.65 ± 0.07	0.67 ± 0.06	0.52	0.63
DG	0.85 ± 0.03	0.84 ± 0.03	0.84	0.84	0.87 ± 0.02	0.87 ± 0.02	0.96	0.98	0.83 ± 0.03	0.81 ± 0.03	0.92	0.89
SUB	0.80 ± 0.03	0.78 ± 0.04	0.74	0.75	0.83 ± 0.03	0.81 ± 0.04	0.98	0.97	0.75 ± 0.03	0.71 ± 0.05	0.78	0.58
ERC	0.75 ± 0.07	0.75 ± 0.06	0.49	0.51	0.80 ± 0.06	0.79 ± 0.05	0.80	0.82	0.71 ± 0.05	0.72 ± 0.06	0.27	0.54

^a Retrieved from Wisse et al (2012).⁵ Note that an error was detected in the original script for calculating the DSC values. The corrected DSC values are displayed in the table and have also been published in a corrigendum to the original article.

CA3 left: from 0.09 to 0.10; right: from 0.08 to 0.09; ERC left: from 0.46 to 0.47; right: from 0.47 to 0.49). As described in the “Results” section, the mismatch between the automated and manual method occurs mainly in the segmentation of the most anterior and posterior sections for CA2, CA3, and the ERC. This finding is not surprising, given that the anterior and posterior boundaries of CA2, CA3, and the ERC are based on a heuristic geometric rule rather than specific boundaries visible in the images. Restricting the range of the ERC indeed greatly increased the accuracy which is much closer to the intrarater reliability. In addition, the automated method slightly but systematically undersegments CA3 and the ERC in-plane. This undersegmentation might be a point for future improvement, for example, by incorporating a statistical shape or by manually retouching the automated segmentation of CA3. The reliability of the CA2 and CA3 segmentation warrants caution for future studies. Investigators might consider excluding these subfields from analyses or grouping them with either CA1 or the DG, depending on their research interests.

Notably, the automated segmentation performs similar or, in some cases, slightly better than a novice second rater for most of the subfields. Training a second rater takes considerable time in general, and specifically for this high-resolution data and detailed segmentation protocol, which includes several subfields and extends along most of the long axis of the hippocampus. The segmentation of one hippocampus can take up to 8 hours initially and 2 hours after 5 months of training. Training on the whole protocol can therefore take several months, underlining the need for an automated segmentation method. ASHS makes it feasible to perform automatic subfield segmentation and morphometry in large datasets, where manual segmentation by a single rater is prohibitive.

In the context of other automated segmentation methods,^{10–12,33} the current method has a comparable and even slightly higher accuracy for the segmentation of almost all subfields. Only CA2 and 3 in the protocol of Van Leemput et al¹⁰ had higher accuracy values (DSC is approximately 0.09 higher). However, the segmentation protocol by Van Leemput et al has received considerable critiques,^{34,35} among others, on the placement of the boundaries that resulted in a larger CA2 and 3 volume in the Van Leemput protocol compared with our protocol. This probably explains the difference in DSC values. DSC values for the CA1, DG, and SUB were 0.03–0.28, 0.02–0.20, and 0.03–0.38 higher

than those in prior studies,^{10–12,33} most of which were performed at 3T MR imaging. For the smaller subfields CA2 and CA3 or the combined CA2+3, DSC values were 0.09–0.10, 0.01–0.05, and 0.23–0.25 higher than the DSC values of previous studies that used subfield boundaries comparable with those in the current study.^{11,12} Most interesting, the accuracy for segmenting hippocampal subfields in the current 7T study was slightly higher compared with a recent study using the same ASHS technique on anisotropic 3T data,¹² despite the fact that the intrarater reliability of the 3T study was higher than that for the 7T study. This result indicates that there might be added value in using 7T data for the segmentation of hippocampal subfields.

The overlap and ICC values for the whole ERC are lower but approach the values of other automated segmentation methods.^{12,36,37} After restricting the range of the ERC segmentation, the accuracy improved and was well within the range of previous studies. This suggests that despite variability in the anterior and posterior boundary of the ERC, reliable measures of part of the ERC volume can be derived from ASHS segmentation. Another option for future work would be to manually correct the segmentation of the ERC, which would still take less time than a full segmentation.

A limitation of the current study, shared with all other published manual hippocampal subfield segmentation methods, is that in many cases, the actual anatomic boundaries between subfields cannot be inferred on in vivo MR imaging and are partly based on geometric rules. Resulting subfields may, therefore, include parts of neighboring regions. Another limitation is that ASHS is a computationally intensive method and requires >24 hours on a single central processing unit core to perform the segmentation of 1 participant. Furthermore, neither the current evaluation of ASHS nor the previous evaluation in Yushkevich et al^{12,19} has examined the ability of the ASHS atlases to generalize to scans obtained on different MR imaging scanners and with different MR imaging parameters. Considering that the MR imaging scanner and isotropic acquisition used in this study are used by very few research centers, it is unlikely that by directly using our atlas, other research groups will attain the same segmentation performance as reported in this article. However, ASHS is, by design, an adaptable technique and can be retrained by other groups by using different MR imaging protocols, provided that a set of manual segmentations is available. Moreover, in previous work, we have used atlases constructed by using MRI scans with

one protocol to label medial temporal lobe subregions in scans obtained with a different protocol and field strength. For instance, we used an atlas developed on 4T MRI to investigate hippocampal subfields on 3T MRI and demonstrated stronger discrimination of CA1 compared with total hippocampal volume between those with prodromal Alzheimer disease and controls,³⁸ but also showed that manual correction of ASHS results further improved discrimination of the CA1. Similarly, ASHS trained on data from a single 3T scanner was applied to multisite data from Alzheimer's Disease Neuroimaging Initiative 2 in Mueller et al,³⁹ with sensible results. Although we have not validated the current 7T ASHS approach on other datasets, we have applied it on a few $0.4 \times 0.4 \times 1.0 \text{ mm}^3$ 7T scans obtained on a Siemens scanner (Siemens, Erlangen, Germany) with visually satisfactory segmentation results (see On-line Fig 2 for an example). In future work, it will be important to quantitatively evaluate the accuracy of ASHS in cross-scanner applications, as well as to measure how differences in the presence and severity of neurodegenerative disease in the atlas set and the target images affect segmentation accuracy. The fact that the current evaluation was performed in patients without known neurodegenerative disease is a limitation, though, in Yushkevich et al (2015),¹² ASHS accuracy did not differ significantly between patients with mild cognitive impairment and controls. Finally, the datasets to evaluate the accuracy of ASHS versus rater 1 and the inter- and intrarater reliability of the manual raters only partially overlapped, which may have introduced a bias, though it should be noted that they were all drawn, without any consideration of image or segmentation quality, from the same study population and the scan quality in the resulting datasets was comparable among subjects. When comparing the DSCs of ASHS versus rater 1 with the DSCs for the intrarater reliability and the DSCs of ASHS versus rater 1 versus those of rater 1 versus 2 in the smaller, overlapping datasets, we saw no notable difference in the results (On-line Table). This finding indicates that the reliability of the segmentation was similar in all subjects and that the selection of scans probably did not introduce a bias.

CONCLUSIONS

We present a fully automated segmentation method of hippocampal subfields at 7T MRI with high accuracy for most of the subfields. The accuracy of this method is competitive with other published automated methods and with the interrater reliability for manual segmentation. Both the software and the atlas are publicly available at <http://www.nitrc.org/projects/ashs/>.

ACKNOWLEDGMENTS

We acknowledge the use of MeVisLab by MeVis Medical Solutions, Bremen, Germany.

Disclosures: David A. Wolk—UNRELATED: Consultancy: Piramal, Comments: consulting on the use of amyloid imaging in Alzheimer disease. Paul A. Yushkevich—RELATED: Grant: National Institutes of Health (AG037376)*; UNRELATED: Royalties: University of North Carolina, Chapel Hill,* Comments: I am on a patent for unrelated technology and receive royalties of about US \$200.00 every year. Mirjam I. Geerlings—RELATED: Grant: Dutch Brain Foundation (Nederlandse Hersenstichting) project No. number 2012(1)-43.* *Money paid to the institution.

REFERENCES

- Small SA, Schobel SA, Buxton RB, et al. **A pathophysiological framework of hippocampal dysfunction in ageing and disease.** *Nat Rev Neurosci* 2011;12:585–601 CrossRef Medline
- Yushkevich PA, Amaral RS, Augustinack JC, et al; Hippocampal Subfields Group (HSG). **Quantitative comparison of 21 protocols for labeling hippocampal subfields and parahippocampal subregions in in vivo MRI: towards a harmonized segmentation protocol.** *Neuroimage* 2015;111:526–41 CrossRef Medline
- Mueller SG, Stables L, Du AT, et al. **Measurement of hippocampal subfields and age-related changes with high resolution MRI at 4T.** *Neurobiol Aging* 2007;28:719–26 CrossRef Medline
- Malykhin NV, Lebel RM, Coupland NJ, et al. **In vivo quantification of hippocampal subfields using 4.7T fast spin echo imaging.** *Neuroimage* 2010;49:1224–30 CrossRef Medline
- Wisse LE, Gerritsen L, Zwanenburg JJ, et al. **Subfields of the hippocampal formation at 7T MRI: in vivo volumetric assessment.** *Neuroimage* 2012;61:1043–49 CrossRef Medline
- La Joie R, Fouquet M, Mézenge F, et al. **Differential effect of age on hippocampal subfields assessed using a new high-resolution 3T MR sequence.** *Neuroimage* 2010;53:506–14 CrossRef Medline
- Kerchner GA, Hess CP, Hammond-Rosenbluth KE, et al. **Hippocampal CA1 apical neuropil atrophy in mild Alzheimer disease visualized with 7-T MRI.** *Neurology* 2010;75:1381–87 CrossRef Medline
- Raz N, Daugherty AM, Bender AR, et al. **Volume of the hippocampal subfields in healthy adults: differential associations with age and a pro-inflammatory genetic variant.** *Brain Struct Funct* 2015;220:2663–74 CrossRef Medline
- Winterburn JL, Pruessner JC, Chavez S, et al. **A novel in vivo atlas of human hippocampal subfields using high-resolution 3 T magnetic resonance imaging.** *Neuroimage* 2013;74:254–65 CrossRef Medline
- Van Leemput K, Bakbour A, Benner T, et al. **Automated segmentation of hippocampal subfields from ultra-high resolution in vivo MRI.** *Hippocampus* 2009;19:549–57 CrossRef Medline
- Pipitone J, Park MT, Winterburn J, et al; Alzheimer's Disease Neuroimaging Initiative. **Multi-atlas segmentation of the whole hippocampus and subfields using multiple automatically generated templates.** *Neuroimage* 2014;101:494–512 CrossRef Medline
- Yushkevich PA, Pluta JB, Wang H, et al. **Automated volumetry and regional thickness analysis of hippocampal subfields and medial temporal cortical structures in mild cognitive impairment.** *Hum Brain Mapp* 2015;36:258–87 CrossRef Medline
- Iglesias JE, Augustinack JC, Nguyen K, et al; Alzheimer's Disease Neuroimaging Initiative. **A computational atlas of the hippocampal formation using ex vivo, ultra-high resolution MRI: application to adaptive segmentation of in vivo MRI.** *Neuroimage* 2015;115:117–37 CrossRef Medline
- Cho ZH, Han JY, Hwang SI, et al. **Quantitative analysis of the hippocampus using images obtained from 7.0 T MRI.** *Neuroimage* 2010;49:2134–40 CrossRef Medline
- Thomas BP, Welch EB, Niederhauser BD, et al. **High-resolution 7T MRI of the human hippocampus in vivo.** *J Magn Reson Imaging* 2008;28:1266–72 CrossRef Medline
- Wisse LE, Biessels GJ, Heringa SM, et al; Utrecht Vascular Cognitive Impairment (VCI) Study Group. **Hippocampal subfield volumes at 7T in early Alzheimer's disease and normal aging.** *Neurobiol Aging* 2014;35:2039–45 CrossRef Medline
- Boutet C, Chupin M, Lehericy S, et al. **Detection of volume loss in hippocampal layers in Alzheimer's disease using 7T MRI: a feasibility study.** *Neuroimage Clin* 2014;5:341–48 CrossRef Medline
- Kerchner GA, Deutsch GK, Zeineh M, et al. **Hippocampal CA1 apical neuropil atrophy and memory performance in Alzheimer's disease.** *Neuroimage* 2012;63:194–202 CrossRef Medline
- Yushkevich PA, Wang H, Pluta J, et al. **Nearly automatic segmentation of hippocampal subfields in in vivo focal T2-weighted MRI.** *Neuroimage* 2010;53:1208–24 CrossRef Medline
- Stegenga BT, Kamphuis MH, King M, et al. **The natural course and outcome of major depressive disorder in primary care: the**

- PREDICT-NL study. *Soc Psychiatry Psychiatr Epidemiol* 2012;47:87–95 CrossRef Medline
21. Folstein MF, Folstein SE, McHugh PR. **“Mini-mental state”: a practical method for grading the cognitive state of patients for the clinician.** *J Psychiatr Res* 1975;12:189–98 CrossRef Medline
 22. Kuijf HJ. *Image Processing Techniques for Quantification and Assessment of Brain MRI* [dissertation]. Utrecht: Utrecht University Repository; 2013
 23. Ritter F, Boskamp T, Homeyer A, et al. **Medical image analysis.** *IEEE Pulse* 2011;2:60–70 CrossRef Medline
 24. Goncharova II, Dickerson BC, Stoub TR, et al. **MRI of human entorhinal cortex: a reliable protocol for volumetric measurement.** *Neurobiol Aging* 2001;22:737–45 CrossRef Medline
 25. Insausti R, Juottonen K, Soininen H, et al. **MR volumetric analysis of the human entorhinal, perirhinal, and temporopolar cortices.** *AJNR Am J Neuroradiol* 1998;19:659–71 Medline
 26. Avants BB, Epstein CL, Grossman M, et al. **Symmetric diffeomorphic image registration with cross-correlation: evaluating automated labeling of elderly and neurodegenerative brain.** *Med Image Anal* 2008;12:26–41 CrossRef Medline
 27. Wang H, Suh JW, Das SR, et al. **Multi-atlas segmentation with joint label fusion.** *IEEE Trans Pattern Anal Mach Intell* 2013;35:611–23 CrossRef Medline
 28. Wang H, Das SR, Suh JW, et al; Alzheimer’s Disease Neuroimaging Initiative. **A learning-based wrapper method to correct systematic errors in automatic image segmentation: consistently improved performance in hippocampus, cortex and brain segmentation.** *Neuroimage* 2011;55:968–85 CrossRef Medline
 29. Dice LR. **Measures of the amount of ecologic association between species.** *Ecology* 1945;26:297–302 CrossRef
 30. Crum WR, Camara O, Hill DL. **Generalized overlap measures for evaluation and validation in medical image analysis.** *IEEE Trans Med Imaging* 2006;25:1451–61 CrossRef Medline
 31. Kerchner GA, Boxer AL. **Bapineuzumab.** *Expert Opin Biol Ther* 2010;10:1121–30 CrossRef Medline
 32. Wang H, Yushkevich PA. **Spatial bias in multi-atlas based segmentation.** *Conf Comput Vis Pattern Recognit Workshops* 2012;2012:909–16 Medline
 33. Flores GS, de Haan G, Jasinschi R, et al. *Automatic Segmentation of Hippocampal Substructures* [master’s thesis]. Eindhoven: Technische Universiteit Eindhoven; 2012
 34. de Flores R, La Joie R, Landeau B, et al. **Effects of age and Alzheimer’s disease on hippocampal subfields: comparison between manual and FreeSurfer volumetry.** *Hum Brain Mapp* 2015;36:463–74 CrossRef Medline
 35. Wisse LE, Biessels GJ, Geerlings MI. **A critical appraisal of the hippocampal subfield segmentation package in FreeSurfer.** *Front Aging Neurosci* 2014;6:261 CrossRef Medline
 36. Desikan RS, Ségonne F, Fischl B, et al. **An automated labeling system for subdividing the human cerebral cortex on MRI scans into gyral based regions of interest.** *Neuroimage* 2006;31:968–80 CrossRef Medline
 37. Klein A, Tourville J. **101 labeled brain images and a consistent human cortical labeling protocol.** *Front Neurosci* 2012;6:171 CrossRef Medline
 38. Pluta J, Yushkevich P, Das S, et al. **In vivo analysis of hippocampal subfield atrophy in mild cognitive impairment via semi-automatic segmentation of T2-weighted MRI.** *J Alzheimers Dis* 2012;31:85–99 CrossRef Medline
 39. Mueller S, Yushkevich P, Wang L, et al. **Collaboration for a systematic comparison of different techniques to measure subfield volumes: announcement and first results.** *Alzheimer’s & Dementia* 2013;9:P51

New Clinically Feasible 3T MRI Protocol to Discriminate Internal Brain Stem Anatomy

 M.J. Hoch,  S. Chung,  N. Ben-Eliezer,  M.T. Bruno,  G.M. Fatterpekar, and  T.M. Shepherd



ABSTRACT

SUMMARY: Two new 3T MR imaging contrast methods, track density imaging and echo modulation curve T2 mapping, were combined with simultaneous multisection acquisition to reveal exquisite anatomic detail at 7 canonical levels of the brain stem. Compared with conventional MR imaging contrasts, many individual brain stem tracts and nuclear groups were directly visualized for the first time at 3T. This new approach is clinically practical and feasible (total scan time = 20 minutes), allowing better brain stem anatomic localization and characterization.

ABBREVIATIONS: DEC = direction-encoded color; EMC = echo modulation curve; MLF = medial longitudinal fasciculus; PD = proton-density; stDEC-TDI = short-track direction-encoded color track density imaging; stTDI = short-track track density imaging; TDI = track density imaging

The brain stem contains many small but essential nuclei and fiber tracts that play key roles in motor, sensory, and autonomic regulation.¹ Due to the compact, complex, and nonredundant anatomy of the brain stem, even small pathologic changes or lesions can have substantial clinical consequences. In particular, specific brain stem structures are affected in different subcortical neurodegenerative diseases such as Parkinson disease, multisystem atrophy, and progressive supranuclear palsy.²⁻⁵ Unfortunately, routine MR imaging by using thin-cut T1- and T2-weighted images cannot resolve these individual small brain stem structures or measure subtle quantitative MR imaging tissue property changes that may escape visual detection by a

neuroradiologist in the prodromal or early clinical stages of neurodegeneration.

MR imaging of the postmortem human brain stem by using >1-hour scan times, motionless dissected small samples, and contrast agent doping can generate high-quality, high-spatial-resolution structural MR imaging aids to guide image interpretation of in vivo subjects,^{6,7} but the MR imaging properties of postmortem nervous tissue are altered.^{8,9} The spatial and contrast resolution of conventional MR imaging obtainable in living subjects, particularly patients, is much more limited. Instead, in vivo brain stem MR imaging anatomy is inferred on the basis of craniocaudal section position, a few internal anatomic landmarks, and known surface topography. 7T MR imaging and alternative contrasts have been explored and have advantages over conventional MR imaging acquisitions.¹⁰⁻¹⁶ However, the sparse clinical availability of ultra-high-field MR imaging and extended scan times of advanced sequences (some individually >20 minutes) are both limitations. Susceptibility-weighted imaging of the brain stem can be limited by skull base artifacts, particularly at high magnetic fields.

Track density imaging (TDI) is a novel MR imaging postprocessing technique based on high-angular-resolution diffusion acquisitions that generate super-resolution images derived by whole-brain probabilistic streamline tractography.^{17,18} Images of 500- μm isotropic resolution can be created in which pixel intensity reflects the number of probabilistic streamlines traversing the voxel and color reflects diffusion streamline orientations similar to those of conventional diffusion tensor imaging.¹⁹ These contrasts have been validated by using histology in animal models.^{20,21} We have combined a track density approach with recently developed simultaneous multisection acquisition diffusion MR

Received September 10, 2015; accepted after revision December 4.

From the Department of Radiology (M.J.H., S.C., N.B.-E., M.T.B., G.M.F., T.M.S.) New York University Langone School of Medicine, New York, New York; and Center for Advanced Imaging Innovation and Research (S.C., N.B.-E., T.M.S.), New York, New York.

Timothy Shepherd received research support from the National Institute of Aging (National Institutes of Health 1K23 AG048622-01). This research was supported, in part, by the Center for Advanced Imaging Innovation and Research, a National Institutes of Health National Institute of Biomedical Imaging and Bioengineering Biomedical Technology Resource Center (grant P41EB017183).

Abstract previously presented at: American Society of Neuroradiology Annual Meeting and the Foundation of the ASNR Symposium, April 25–30, 2015; Chicago, Illinois.

Please address correspondence to Timothy Shepherd, MD, PhD, Department of Radiology, Room 230D, New York University Langone School of Medicine, 660 First Ave, New York, NY 10016; e-mail: timothy.shepherd@nyumc.org

 Indicates open access to non-subscribers at www.ajnr.org

 Indicates article with supplemental on-line table.

 Indicates article with supplemental on-line photos.

 Indicates article with supplemental on-line video.

<http://dx.doi.org/10.3174/ajnr.A4685>

imaging²² to obtain TDI maps of brain stem structures in living subjects with clinically feasible scan times at 3T. We also have applied a new robust method for quantitating T2 and proton density in brain tissue on the basis of multisection, multiecho, spin-echo acquisitions and a novel echo modulation curve (EMC) software package.^{23–25} We demonstrate the advantages of combining these 2 techniques to generate detailed in vivo depiction of internal brain stem anatomy with clinically feasible acquisition times at 3T MR imaging.

MATERIALS AND METHODS

MR Imaging Acquisition

Three healthy right-handed (mean Edinburgh Handedness Inventory score of 78.6) adult subjects (mean age, 31 ± 1 years; 2 women) underwent noncontrast MR imaging of the head by using a 20-channel head and neck coil on a 3T MR imaging scanner (Skyra; Siemens, Erlangen, Germany). For quantitative T2 mapping, the multiecho spin-echo sequence included 15 echoes at 10-ms intervals (TE, 10–150 ms; TR, 5100 ms; matrix, 384×234 ; integrated Parallel Acquisition Techniques 2; 2-mm section thickness; 2 averages) and required 6 minutes. The high-angular-resolution diffusion sequence (3-mm isotropic resolution; matrix, 80×80 ; 2-section acceleration; 256 diffusion directions with b -value = 2500 s/mm^2 ; 8 images with $b=0$; TR/TE, 3816/98 ms; 50 sections; phase-encoding in the anteroposterior direction) required 14 minutes. For susceptibility-induced distortion correction, 1 image with $b=0$ was acquired with phase-encoding in the posteroanterior direction. Additional conventional MR imaging sequences for comparison purposes included axial 2-mm-thick dual-echo T2-weighted MR imaging, 1-mm isotropic MPRAGE, 5-mm-thick axial FLAIR, and SWI (approximately 20 minutes additional scan time). Total scan time was 40 minutes. The above protocol was repeated on 1 subject 7 weeks after the initial scan to assess repeatability of the MR imaging contrasts.

Quantitative T2 Maps

T2 and proton density (PD) maps of the brain stem were postprocessed from the multi-spin-echo datasets by using a recently developed EMC T2 fitting software package, which relies on accurate Bloch simulations to model the exact signal evolution in multi-spin-echo pulse sequences by using the exact radiofrequency pulse shapes and other experimental parameters.^{23,24} Simulations were repeated for a range of T2 values (1–1000 ms) and B_1^+ inhomogeneity values ($B_1^+ = 50\% \dots 130\%$), producing a data base of EMCs, each associated with a unique (B_1^+ , T2) value pair. The T2 parametric map was generated by matching experimentally acquired multi-spin-echo data to the EMC data base via l2-norm minimization of the difference between experimental and precalculated EMCs. PD maps were subsequently calculated by back-projecting the first echo image to time $t = 0$ by using the calculated T2 map. The software package is custom-written in Matlab (MathWorks, Natick, Massachusetts) and C++ and then is executed with Matlab scripts and a graphic user interface. Detailed information and the software package can be found at <http://cai2r.net/resources/software/emc-based-t2-mapping-package>. All figures were created with a consistent T2 dynamic range of 20–120 ms and a normalized PD dynamic range of

0.2–0.6 (no units) for optimal brain stem contrast across the 7 canonical levels.

Track Density Imaging

The diffusion-weighted images were first corrected for susceptibility-induced distortion by using a phase reversal distortion-correction method (Topup tool in FSL; <http://fsl.fmrib.ox.ac.uk/fsl/fslwiki/topup>),²⁶ which is a part of the FSL toolbox (FMRIB Software Library; <http://www.fmrib.ox.ac.uk/fsl>).²⁷ To generate the track density maps, we performed whole-brain probabilistic fiber-tracking by randomly seeding 4,000,000 tracks throughout the brain by using the MRtrix software package (<http://neuro.debian.net/pkgs/mrtrix.html>).²⁸ The constrained spherical deconvolution technique²⁹ with probabilistic streamlines was used to model multiple fiber orientations. The relevant fiber-tracking parameters were the following: 0.3-mm step size, 90° maximum angle between steps, 2.0-cm maximum and 1.5-cm minimum track length, and maximum harmonic order $l_{\text{max}} = 8$. Super-resolution TDI and direction-encoded color (DEC) TDI maps were generated with a $500\text{-}\mu\text{m}$ isotropic resolution. A “short-track” method was used for both TDI and DEC-TDI (now referred to as stTDI and stDEC-TDI) in which the maximum-to-minimum track length ratio approached 1.²¹ We used the conventional color scheme: blue (inferior-superior), green (anteroposterior), and red (left-right). In the case of stDEC-TDI, the color in each voxel can be determined by averaging the colors of all the streamline segments contained within the voxel.¹⁷

MR Imaging Data Anatomic Analysis

Postacquisition processing time for the quantitative T2 and track density maps was 15 and 180 minutes, respectively, by using an independent workstation. All MRIs were obtained with axial sections parallel to the anterior/posterior commissure line. For each subject, we then characterized anatomic detail in axial MR imaging sections from the conventional MR imaging protocol, quantitative T2, and short-track TDI parameter maps at 7 canonical anatomic levels of the brain stem (similar to Hirsch et al³⁰): rostral and caudal midbrain; rostral, middle, and caudal pons; and rostral and caudal medulla (Fig 1). The MR images were labeled according to the standard anatomic text of *Duvernoy's Atlas of the Human Brain Stem and Cerebellum*³¹ by consensus among 3 board-certified neuroradiologists. Schematics were derived from Warner's *Atlas of Neuroanatomy: With Systems Organization and Case Correlations*.³² All figures were labeled with white matter tracts on the radiologic left and nuclei on the right of the image unless the structures were in a central location. A paired structure was only labeled unilaterally to avoid cluttering the image. Anatomic detail in the axial sections was compared across the 3 subjects and between different scan sessions for the single subject with repeat imaging.

RESULTS

Coregistered axial images of the brain stem at 7 discrete anatomic levels are shown in Figs 2–7 and On-line Figs 1 and 2 with labeled substructures (see the On-line Table for the complete list of labeled substructures, which are indicated in parentheses below). While brain stem anatomy is typically characterized in the axial plane, Fig 1 also demonstrates stDEC-TDI in a selected parasagittal section orientation for depicting axial section positions. Fig

ure 7 demonstrates reproducibility of brain stem anatomic assignments for 3 subjects, and Fig 8 demonstrates reproducibility for the same subject on different days. Movies of the various MR imaging parameter maps are provided on-line for the interested reader (On-line Videos). A detailed, exhaustive discussion of the wealth of data available for each subject is beyond the scope of this current report. Below is a succinct discussion of the craniocaudal evolution of stTDI, stDEC-TDI, T2, and PD maps highlighting key findings.

The pyramidal tracts (16) were separable from the frontopontine (22) and occipitotemporal and parietopontine fibers (23) at the rostral midbrain on EMC PD maps (Fig 2E). The stDEC-TDI map (Fig 2G) shows the oculomotor nuclear complex (33) in green and the medial longitudinal fasciculus (MLF) (34) in light blue,

whereas the DEC-DTI map in this region shows a uniform green (Fig 2C). The decussation of the superior cerebellar peduncles (9) at the level of the caudal midbrain is well-demarcated on EMC T2 maps (Fig 3F). The conventional T2-weighted image fails to distinguish the decussation (Fig 3B).

The high-intensity MLF (34) is clearly identified centrally on rostral pons stTDI maps (Fig 4H). On EMC maps, the pyramidal tracts (16) lose their conspicuity at the pons levels from intertwined traversing pontocerebellar fibers (14) (Fig 4E, -F). Within the midpons, the EMC PD image (On-line Fig 1E) better depicts the motor nucleus of the trigeminal nerve (46), and the medial lemnisci (15) and spinothalamic tract (26) are more conspicuous on the EMC T2 image (On-line Fig 1F) compared with their respective conventional images (On-line Fig 1A, -B). The stTDI maps show the facial nerve fascicles (50) from the colliculus and exiting the caudal pons (On-line Fig 2H).

The rostral or open medulla shows that the medial lemnisci (15) are easily distinguished from the pyramidal tract (16) on EMC T2 (Fig 5F). Dorsal plate nuclei of the hypoglossal (55) and the dorsal motor nucleus of the vagus nerve (56) are noted on stDEC-TDI maps (Fig 5G) dorsal to the MLF (34). Neither the conventional T2-weighted (Fig 5B) nor the DEC-DTI maps (Fig 5C) can directly demonstrate these structures. There is an intensity increase of the descending pyramidal tracts (16) on stTDI maps (Fig 6H) just superior to their medullary decussation.

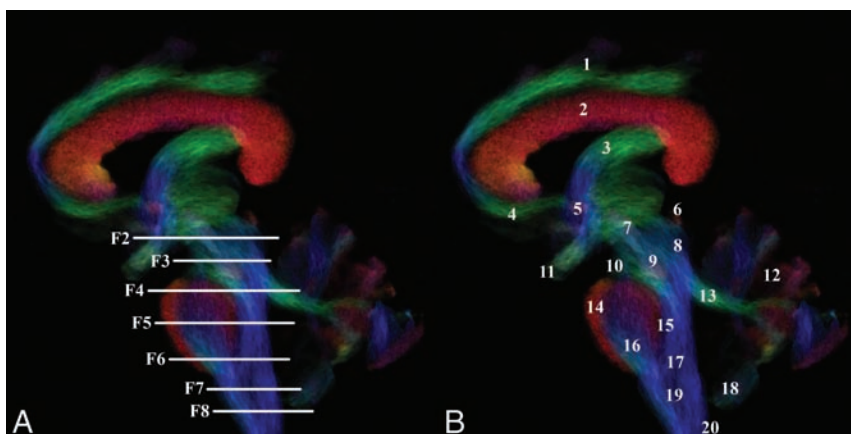


FIG 1. Parasagittal short-track direction-encoded color track density image of the brain stem. *A*, The 7 canonical axial anatomic levels of the brain stem are depicted with the section planes for Figs 2–6 and On-line Figs 1 and 2. *B*, Selected brain stem substructures are labeled to illustrate that TDI can also be used to make anatomic assignments in all 3 planes. Please refer to the On-line Table throughout this report for a complete list of labeled substructures for all figures.

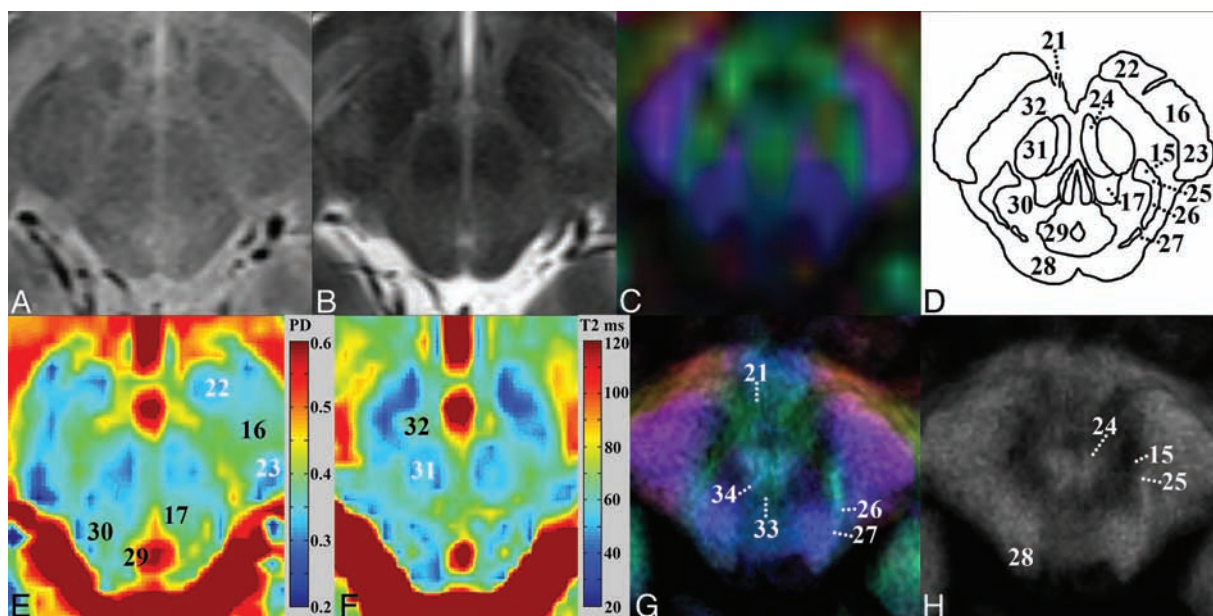


FIG 2. Rostral midbrain. Upper row: *A*, Proton-density weighted. *B*, T2-weighted. *C*, DEC-DTI. *D*, Anatomic schematic. Bottom row: *E*, EMC PD map. *F*, EMC T2 map. *G*, stDEC-TDI. *H*, stTDI. The lower row novel contrast images better depict brain stem anatomy compared with the upper row conventional images. Notice the appreciable difference in the EMC T2 value between the red nuclei (31) and the substantia nigra (32) compared with that of the standard multi-spin-echo T2 image. The stDEC-TDI map shows the oculomotor nuclear complex (33) in green and the MLF (34) in light blue, whereas the DEC-DTI map in this region shows a uniform green.

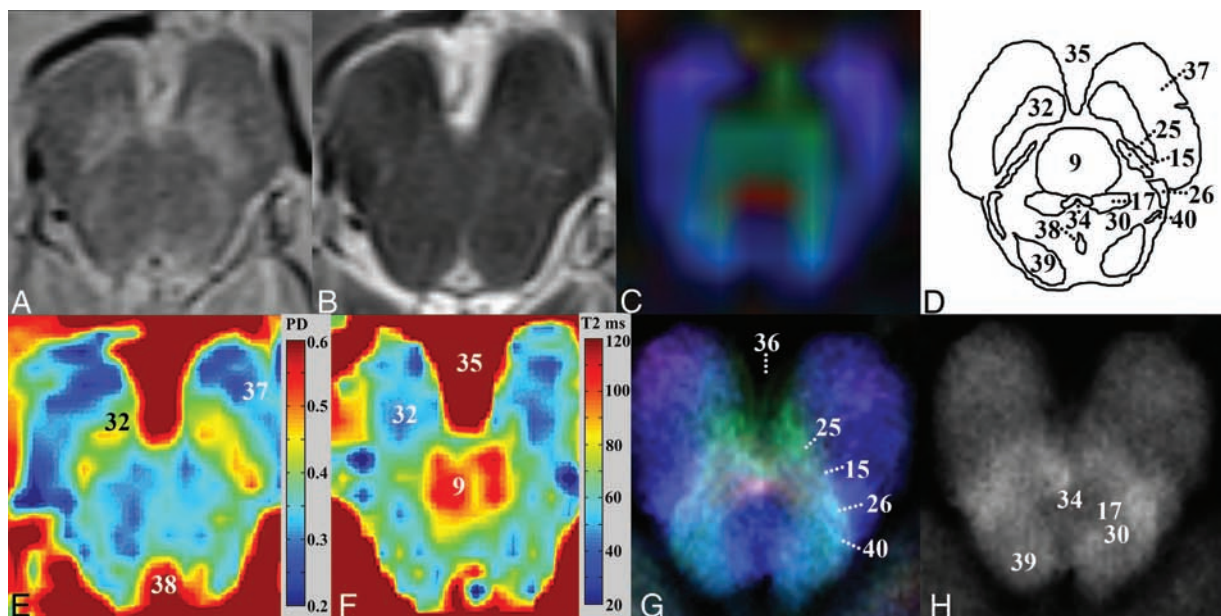


FIG 3. Caudal midbrain. Upper row: *A*, Proton-density weighted. *B*, T2-weighted. *C*, DEC-DTI. *D*, Anatomic schematic. Lower row: *E*, EMC PD map. *F*, EMC T2 map. *G*, stDEC-TDI. *H*, stTDI. The ventral trigeminothalamic tract (25), medial lemniscus (15), spinothalamic tract (26), and lateral lemniscus (40) are better outlined on stDEC-TDI compared with conventional DEC-DTI. The EMC T2 map clearly shows the decussation of the superior cerebellar peduncle (9) as an intense red structure. The conventional T2-weighted image fails to distinguish the decussation from adjacent structures.

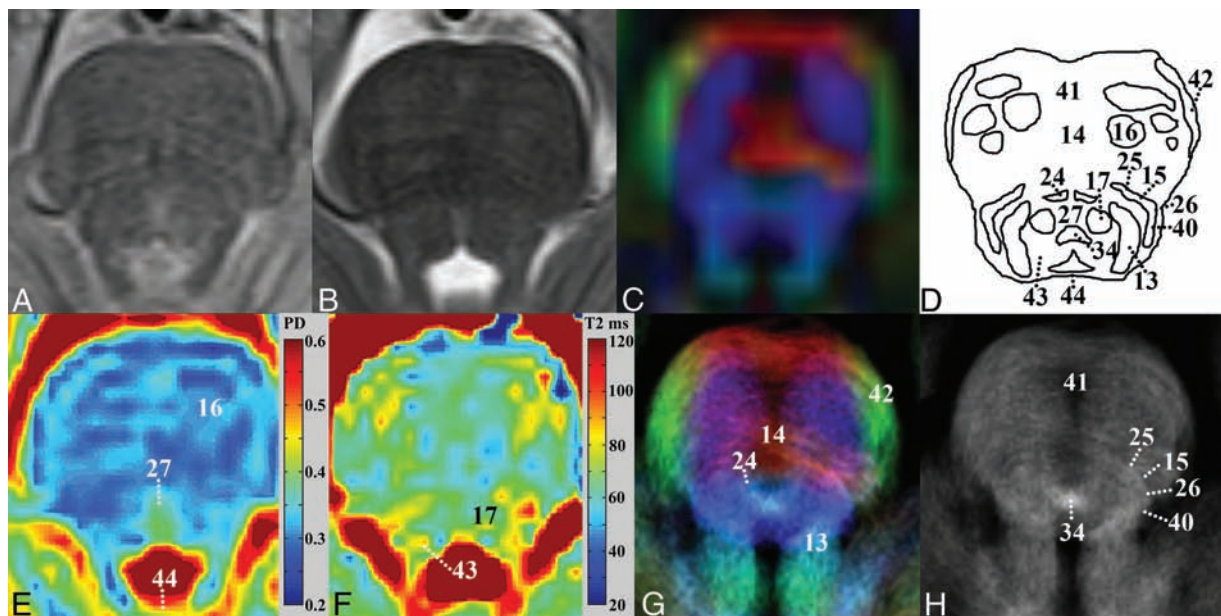


FIG 4. Rostral pons. Upper row: *A*, Proton-density weighted. *B*, T2-weighted. *C*, DEC-DTI. *D*, Anatomic schematic. Lower row: *E*, EMC PD map. *F*, EMC T2 map. *G*, stDEC-TDI. *H*, stTDI. The MLF (34) qualitatively has the highest signal intensity on stTDI and stDEC-TDI, suggesting that many probabilistic streamlines cross through these imaging voxels. The DEC-DTI map has uniform intensity, and the MLF cannot be appreciated. The locus coeruleus (43) can now be seen medial to the superior cerebellar peduncles (13) on EMC T2 and PD maps.

EMC PD maps appeared consistently superior to T2 maps for identifying nuclear groups, for example the trigeminal motor nuclei (46) on On-line Fig 1*E*, *-F*. Overall, 15 groups of bilateral paired nuclei (19, 28, 31, 32, 33, 39, 43, 45, 46, 51, 55, 56, 57, 63, 64) were identified on PD maps as opposed to T2 maps where only 9 nuclear pairs (19, 28, 31, 32, 39, 43, 46, 55, 56) were identified. Both stTDI and stDEC-TDI identified 11 pairs of nuclei (19, 28, 31, 32, 33, 39, 51, 55, 56, 63, 64), especially those with identifiable fascicles (eg, oculomotor [33] and trigeminal nuclei

[51]). Additional small nuclei were not distinct on any of the new MR imaging parameter maps (including the abducens, ambiguus, trochlear, cochlear, salivatory, and superior olives).

Aside from structures that can be recognized on conventional MR imaging from their characteristic surface topography, our protocol revealed many deeper substructures. The spinal tract of cranial nerve V (58) was seen on stTDI and stDEC-TDI maps in the dorsolateral midpons extending to the caudal medulla (Figs 5–6 and On-line Figs 1 and 2*G*, *-H*). Descending small central

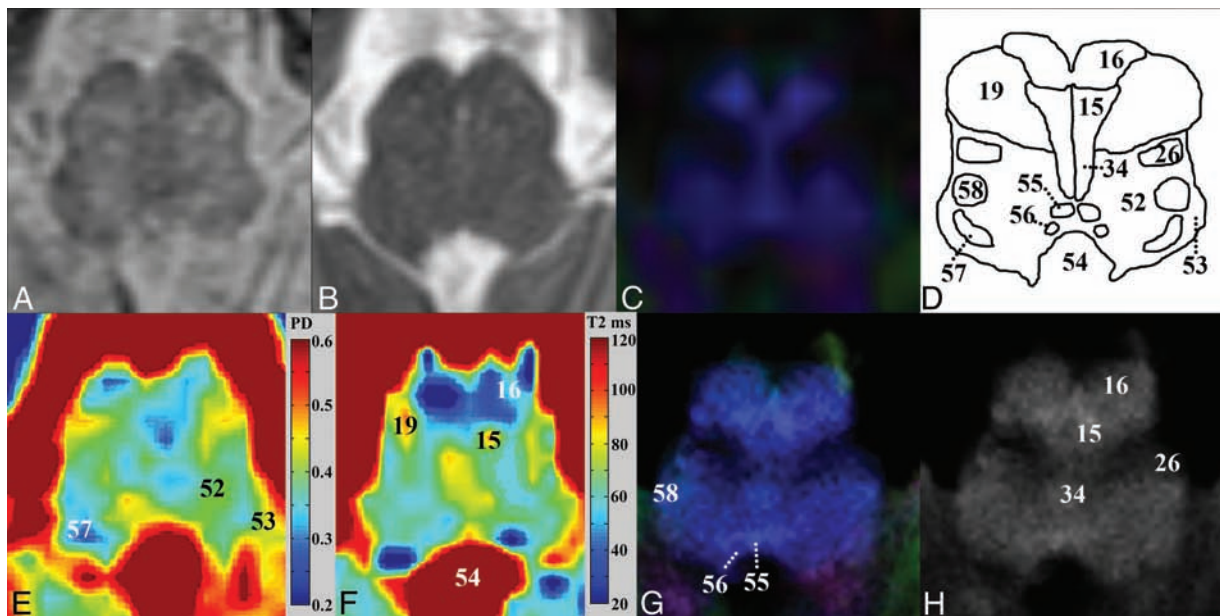


FIG 5. Rostral medulla. Upper row: *A*, Proton-density weighted. *B*, T2-weighted. *C*, DEC-DTI. *D*, Anatomic schematic. Lower row: *E*, EMC PD map. *F*, EMC T2 map. *G*, stDEC-TDI. *H*, stTDI. More brain stem substructures are directly identified with our protocol. For example, the medial lemnisci (15) are easily distinguished from the pyramidal tracts (16) on EMC T2. Dorsal plate nuclei of the hypoglossal (55) and the dorsal motor nucleus of the vagus nerve (56) are noted on both stTDI maps. Neither the conventional T2-weighted nor the DEC-DTI map can directly demonstrate these structures.

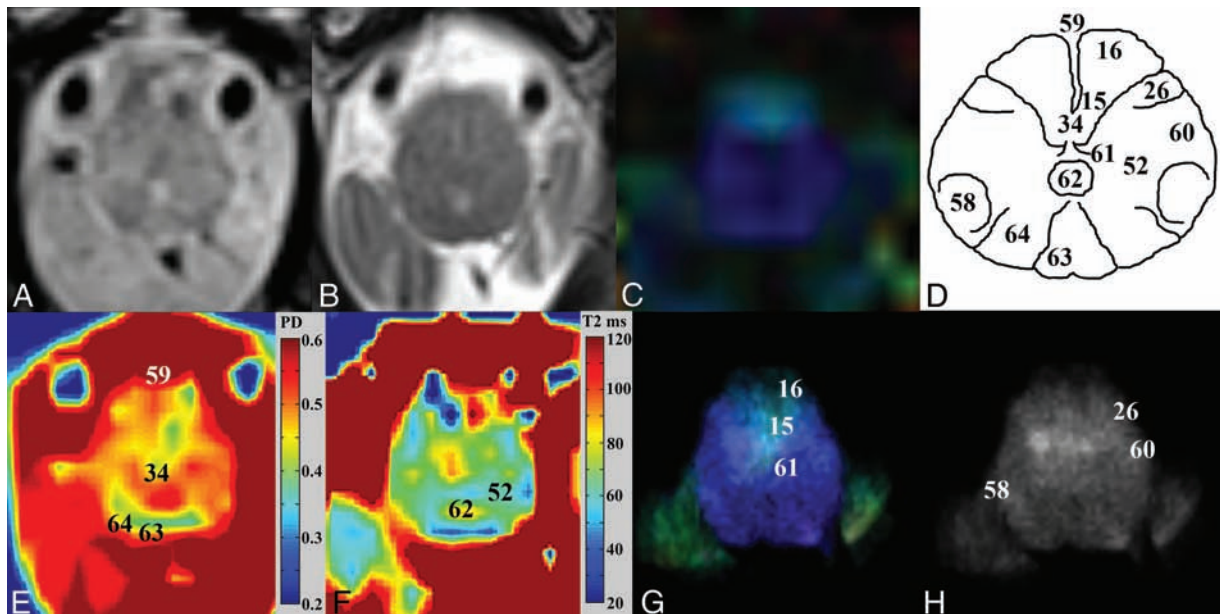


FIG 6. Caudal medulla. Upper row: *A*, Proton-density weighted. *B*, T2-weighted. *C*, DEC-DTI. *D*, Anatomic schematic. Lower row: *E*, EMC PD map. *F*, EMC T2 map. *G*, stDEC-TDI. *H*, stTDI. There is a qualitative difference in the T2, PD, and stTDI values between the right and left pyramidal tracts (16) above the decussation, which may reflect right-handedness in this subject (best seen in *E*). This left-versus-right signal difference is not appreciable on the routine T2- or PD-weighted images or the DEC-DTI. In addition, stDEC-TDI can show the subtle red streamline internal arcuate (61) crossing the midline, another advantage over DEC-DTI.

tracts that synapse with the spinal cord, the central tegmental tract (17) and reticular formation (30, 48, 52), were not seen in their entirety because they are difficult to distinguish from each other. However, on stTDI, the rubrospinal tracts were seen medial to the red nuclei (31) in the rostral midbrain (Fig 2*H*). The tectospinal tract (27) could be seen at the rostral midbrain and rostral pons levels (Figs 2*G* and 4*E*). Furthermore, stTDI clearly was superior to conventional DTI parameter maps derived of these sample

data—that is, in the caudal midbrain, the ventral trigeminothalamic tract (25), spinothalamic tract (26), and lateral lemniscus (40) were obvious on stTDI and stDEC-TDI, but not appreciated on DEC-DTI (Fig 3*C*).

DISCUSSION

Our new multicontrast protocol with clinically feasible acquisition times gains spatial resolution and anatomic contrast by using

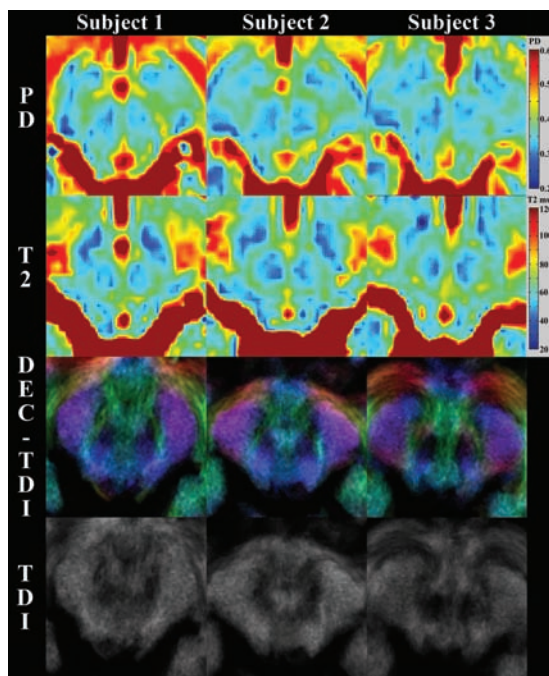


FIG 7. EMC PD and T2, stDEC-TDI, and stTDI maps at the rostral midbrain for 3 right-handed subjects (mean age, 31 ± 1 years; 2 women; mean Edinburgh Handedness Inventory score, 78.6) demonstrate excellent reproducibility for the novel MR imaging acquisition and post-processing protocol among healthy controls. Detailed anatomy for the different MR imaging contrast at this axial level is depicted in Fig 2. There are subtle differences in the subthalamic anatomy ventral and superior to the midbrain (note subject 2 in the stDEC-TDI and stTDI images) attributed to slight angulation differences in the placement of the imaging plane parallel to the anterior/posterior commissure line.

postprocessing methods to reveal structures beyond the grasp of conventional MR imaging. This protocol has the potential to become widely applicable to many brain stem pathologies and generate new specific imaging biomarkers. Furthermore, *in vivo* visualization of these small structures does not have to be limited to large academic centers with ultra-high-field MR imaging or opportunities for extended-length scan protocols. The only caveat is that radiologists may need to relearn detailed brain stem anatomy not typically required when reading conventional MR imaging.

A goal is clinical implementation, and a whole-brain diffusion sequence was chosen because patients may have diffusion abnormalities outside the brain stem. To decrease our scan time, we applied a simultaneous multisection acquisition to acquire the data.²² Whole-brain coverage is not always necessary, and a reduced z-FOV covering only the brain stem may be an alternative option in research subjects. TDI needs a sufficient number of DWI directions and SNR to reduce uncertainty in estimating white matter fiber tracts. TDI benefits from high-angular-resolution diffusion imaging and higher b-values to resolve areas of “crossing fibers.”³³ It is essential to use an MR imaging model that accounts for the presence of multiple fiber directions within a voxel; therefore, the constrained spherical deconvolution method and probabilistic streamlines are used.²⁹ The gain in actual resolution beyond the authentic imaging voxel differs from image interpolation that does not provide any extra information.

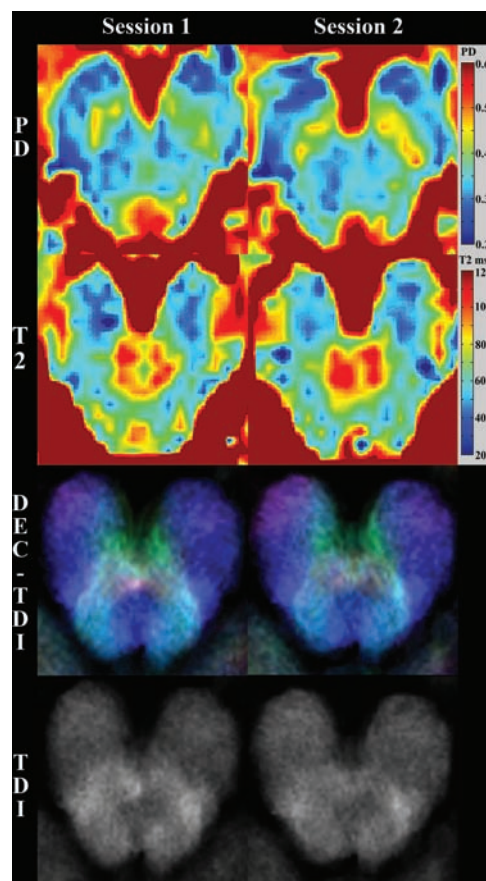


FIG 8. Single axial section at the caudal midbrain with EMC and stTDI maps repeated in the same subject 7 weeks apart demonstrating consistent contrasts within the subject. Detailed anatomy for the different MR imaging contrast at this axial level is depicted in Fig 3.

Nervous tissue water diffusion behavior is field-independent but technically challenging to characterize at 7T. Deistung et al¹⁶ used TDI to successfully parcellate individual brain stem substructures at 7T. Our TDI maps show more structures than same-source DTI color maps and the TDI maps of Deistung et al because we used a short-track TDI scaling method. Short brain stem fiber tracks have fewer streamlines due to the random seed point placement technique, which leads to a reduced intensity of the generated tracts in whole-brain TDI maps.¹⁸ With a short-track method and increasing the number of seed points, this effect is alleviated and a reasonable contrast-to-noise ratio is sustained.^{18,21} Spherical-deconvolution informed filtering is a recently introduced alternative scaling method, which could be useful in future anatomic studies.³⁴

TDI has the potential to quantitatively characterize healthy and diseased local structure connectivity³⁵ if acquisition parameters are consistent.²⁹ Ziegler et al³⁶ showed nigrostriatal changes in Parkinson disease. Currently, there is debate on the validity of quantification due to tractography biases and errors and which method should be used. Average pathlength mapping was first introduced³⁷ and has now been followed by the more direct apparent fiber density.³⁸ The source DWI resolution (3 mm isotropic) is relatively coarse and could potentially cause quantification errors in our maps.

EMC T2 mapping models both stimulated echoes and radio-

frequency inhomogeneities inherent to clinical 3T imaging in real patients. This feature allows the quantification of T2 and PD values in a manner independent of the scanner and parameter values and at clinically feasible time scales.²⁵ These maps can be used to increase anatomic contrast by emphasizing subtle tissue property differences over a dynamic range that remains compressed on standard T2-weighted images.

SWI delineates some in vivo brain stem anatomy well; however, the best results have required 7T MR imaging. Eapen et al¹⁴ focused on the human midbrain dopaminergic system. Gizewski et al¹⁰ and Deistung et al¹⁶ also used SWI in their protocols at 7T to parcellate individual brain stem substructures. However, in addition to increased aliasing and susceptibility artifacts at 7T, such high-field systems are not widely available or currently approved for clinical use in the United States. Instead of SWI, our protocol focuses on robust T2 characterization at clinically available 3T, in which there is less field-dependent T2 shortening compared with 7T.³⁹

A limitation of using fast T2 mapping protocols, similar to routine spin-echo imaging, is pulsation artifacts from nearby blood vessels. The vertebral and basilar arteries and the sigmoid sinuses can cause artifactual low T2 and PD values within the lower brain stem. In initial studies, we realized that increasing the bandwidth from 199 to 600 Hz/pixel helped reduce these pulsation artifacts.

The protocol makes direct identification of more structures possible, with additional structures identified by the positions relative to other structures. Before clinical implementation, anatomic assignments in correlation with reconstructed T2 and TDI images have to be verified with larger postmortem studies. Our method is by no means perfection but is an improvement in the ratio of directly versus indirectly visualized structures at 3T. A full assessment of the range of quantitative values for these new MR imaging parameter maps of the brain stem is beyond the scope of this initial report but will be the subject of ongoing follow-up research in a larger cohort of subjects that also assesses differences in age, sex, and handedness.

CONCLUSIONS

Clinically feasible MR imaging at 3T with novel TDI and T2 mapping better characterizes the detailed anatomy of the in vivo human brain stem compared with routine clinical sequences. Increased contrast EMC PD maps excelled at identifying nuclear groups. Super-resolution TDI maps showed several small fiber tracts not previously seen at 3T. Each contrast map has its own advantages, but for best results, use of multiple independent maps provides the optimal approach to identify different anatomic substructures. We are optimistic that this protocol has the potential to identify future imaging biomarkers for a wide assortment of clinical pathologies in the brain stem.

Disclosures: Noam Ben-Eliezer—RELATED: Grant: National Institutes of Health (P41 EB017183)*; UNRELATED: Patents (planned, pending or issued): New York University School of Medicine.* Comments: Ben-Eliezer N, Block KT, "Method and Device For Accurate Quantification of T2 Relaxation Times based on Fast Spin-Echo NMR Sequences," 2013 (provisional patent application number 61/767,663). Timothy M. Shepherd—RELATED: Grant: National Institute of Aging (1K23 AG048622–01)*; UNRELATED: Patents (planned, pending or issued): I have 3 provisional or pending patents,

devices for image-guided procedures that are unrelated to this work. Neither I nor my institution has received royalties or license fees for these inventions at this time; Other: I spoke for Siemens at both the International Society for Magnetic Resonance in Medicine and Human Brain Mapping 2015 meetings but did not accept any fees, honorarium, or reimbursement for travel. *Money paid to the institution.

REFERENCES

1. Carpenter MB, Strong OS, Truex RC. *Human Neuroanatomy: (Formerly Strong and Elwyn's Human Neuroanatomy)*. 7th ed. Baltimore: Lippincott Williams & Wilkins; 1976
2. Urbain P. *Brainstem Disorders*. Berlin: Springer-Verlag; 2011
3. Janzen J, van 't Ent D, Lemstra AW. **The pedunculopontine nucleus is related to visual hallucinations in Parkinson's disease: preliminary results of a voxel-based morphometry study.** *J Neurol* 2012; 259:147–54 CrossRef Medline
4. Rolland Y, Verin M, Payan CA, et al; NNIPPS Study Group. **A new MRI rating scale for progressive supranuclear palsy and multiple system atrophy: validity and reliability.** *J Neurol Neurosurg Psychiatry* 2011;82:1025–32 CrossRef Medline
5. Makino T, Ito S, Kuwabara S. **Involvement of pontine transverse and longitudinal fibers in multiple system atrophy: a tractography-based study.** *J Neurol Sci* 2011;303:61–66 CrossRef Medline
6. Solsberg MD, Fournier D, Potts DG. **MR imaging of the excised human brainstem: a correlative neuroanatomic study.** *AJNR Am J Neuroradiol* 1990;11:1003–13 Medline
7. Soria G, De Notaris M, Tudela R, et al. **Improved assessment of ex vivo brainstem neuroanatomy with high-resolution MRI and DTI at 7 Tesla.** *Anat Rec (Hoboken)* 2011;294:1035–44 CrossRef Medline
8. Shepherd TM, Flint JJ, Thelwall PE, et al. **Postmortem interval alters the water relaxation and diffusion properties of rat nervous tissue: implications for MRI studies of human autopsy samples.** *Neuroimage* 2009;44:820–26 CrossRef Medline
9. Shepherd TM, Thelwall PE, Stanisz GJ, et al. **Aldehyde fixative solutions alter the water relaxation and diffusion properties of nervous tissue.** *Magn Reson Med* 2009;62:26–34 CrossRef Medline
10. Gizewski ER, Maderwald S, Linn J, et al. **High-resolution anatomy of the human brain stem using 7-T MRI: improved detection of inner structures and nerves?** *Neuroradiology* 2014;56:177–86 CrossRef Medline
11. Naganawa S, Yamazaki M, Kawai H, et al. **Anatomical details of the brainstem and cranial nerves visualized by high resolution read-out-segmented multi-shot echo-planar diffusion-weighted images using unidirectional MPG at 3 T.** *Magn Reson Med Sci* 2011;10: 269–75 CrossRef Medline
12. Nagae-Poetscher LM, Jiang H, Wakana S, et al. **High-resolution diffusion tensor imaging of the brain stem at 3 T.** *AJNR Am J Neuroradiol* 2004;25:1325–30 Medline
13. Salamon N, Sicotte N, Alger J, et al. **Analysis of the brain-stem white matter tracts with diffusion tensor imaging.** *Neuroradiology* 2005; 47:895–902 CrossRef Medline
14. Eapen M, Zald DH, Gatenby JC, et al. **Using high-resolution MR imaging at 7T to evaluate the anatomy of the midbrain dopaminergic system.** *AJNR Am J Neuroradiol* 2011;32:688–94 CrossRef Medline
15. Cho ZH. *7.0 Tesla MRI Brain White Matter Atlas*. 2nd ed. Berlin: Springer-Verlag; 2015
16. Deistung A, Schäfer A, Schweser F, et al. **High resolution MR imaging of the human brainstem in vivo at 7 Tesla.** *Front Hum Neurosci* 2013; 7:710 CrossRef Medline
17. Calamante F, Tourneir JD, Jackson GD, et al. **Track density imaging (TDI): super-resolution white matter imaging using whole-brain track density mapping.** *Neuroimage* 2010;53:1233–43 CrossRef Medline
18. Calamante F, Tourneir JD, Heidemann RM, et al. **Track density imaging (TDI): validation of super resolution property.** *Neuroimage* 2011;56:1259–66 CrossRef Medline
19. Pajevic S, Pierpaoli C. **Color schemes to represent the orientation of anisotropic tissues from diffusion tensor data: application to white**

- matter fiber tract mapping in the human brain. *Magn Reson Med* 2000;43:921 Medline
20. Ullmann JF, Calamante F, Collin SP, et al. **Enhanced characterization of the zebrafish brain as revealed by super-resolution track-density imaging.** *Brain Struct Funct* 2015;220:457–68 CrossRef Medline
 21. Calamante F, Tournier JD, Kurniawan ND, et al. **Super-resolution track-density imaging studies of mouse brain: comparison to histology.** *Neuroimage* 2012;59:286–96 CrossRef Medline
 22. Setsompop K, Gagoski BA, Polimeni JR, et al. **Blipped-controlled aliasing in parallel imaging for simultaneous multislice echo planar imaging with reduced g-factor penalty.** *Magn Reson Med* 2012;67:1210–24 CrossRef Medline
 23. Ben-Eliezer N, Sodickson DK, Block KT. **Rapid and accurate T2 mapping from multi-spin-echo data using Bloch-simulation-based reconstruction.** *Magn Reson Med* 2015;73:809–17 CrossRef Medline
 24. Ben-Eliezer N, Feng L, Block KT, et al. **Accelerated in vivo mapping of T2 relaxation from radially undersampled datasets using compressed sensing and model-based reconstruction.** In: *Proceeding of the Annual Meeting of International Society for Magnetic Resonance in Medicine*, Milan, Italy. May 10–16, 2014
 25. Ben-Eliezer N, Sodickson DK, Shepherd T, et al. **Accelerated and motion-robust in vivo T2 mapping from radially undersampled data using Bloch-simulation-based iterative reconstruction.** *Magn Reson Med* 2015 Apr 17. [Epub ahead of print] CrossRef Medline
 26. Andersson JL, Skare S, Ashburner J. **How to correct susceptibility distortions in spin-echo echo-planar images: application to diffusion tensor imaging.** *Neuroimage* 2003;20:870–88 CrossRef Medline
 27. Smith SM, Jenkinson M, Woolrich MW, et al. **Advances in functional and structural MR image analysis and implementation as FSL.** *Neuroimage* 2004;23(suppl 1):S208–19 CrossRef Medline
 28. Tournier JD, Calamante F, Connelly A. **MRtrix: diffusion tractography in crossing fiber regions.** *Int J Imaging Syst Technol* 2012;22:53–66 CrossRef
 29. Tournier JD, Calamante F, Connelly A. **Robust determination of the fibre orientation distribution in diffusion MRI: non-negativity constrained super-resolved spherical deconvolution.** *Neuroimage* 2007;35:1459–72 CrossRef Medline
 30. Hirsch WL, Kemp SS, Martinez AJ, et al. **Anatomy of the brainstem: correlation of in vitro MR images with histologic sections.** *AJNR Am J Neuroradiol* 1989;10:923–28 Medline
 31. Naidich TP, Duvernoy HM, Delman BD, et al. *Duvernoy's Atlas of the Human Brain Stem and Cerebellum.* Vienna: Springer-Verlag; 2008
 32. Warner JJ. *Atlas of Neuroanatomy: With Systems Organization and Case Correlations.* Boston: Butterworth-Heinemann; 2001
 33. Tuch DS, Reese TG, Wiegell MR, et al. **High angular resolution diffusion imaging reveals intravoxel white matter fiber heterogeneity.** *Magn Reson Med* 2002;48:577–82 CrossRef Medline
 34. Smith RE, Tournier JD, Calamante F, et al. **SIFT: spherical-deconvolution informed filtering of tractograms.** *Neuroimage* 2013;67:298–312 CrossRef Medline
 35. Willats L, Raffelt D, Smith RE, et al. **Quantification of track-weighted imaging (TWI): characterisation of within-subject reproducibility and between-subject variability.** *Neuroimage* 2014;87:18–31 CrossRef Medline
 36. Ziegler E, Rouillard M, André E, et al. **Mapping track density changes in nigrostriatal and extranigral pathways in Parkinson's disease.** *Neuroimage* 2014;99:498–508 CrossRef Medline
 37. Calamante F, Tournier JD, Smith RE, et al. **A generalised framework for super-resolution track-weighted imaging.** *Neuroimage* 2012;59:2494–503 CrossRef Medline
 38. Calamante F, Smith RE, Tournier JD, et al. **Quantification of voxel-wise total fibre density: investigating the problems associated with track-count mapping.** *Neuroimage* 2015;117:284–93 CrossRef Medline
 39. Levitt MH. *Spin Dynamics: Basics of Nuclear Magnetic Resonance.* 2nd ed. Chichester: John Wiley & Sons; 2008

Super-Resolution Track Density Imaging: Anatomic Detail versus Quantification

I have read with great interest the article by Hoch et al,¹ in this issue of the *American Journal of Neuroradiology* describing an MR imaging protocol to discriminate the internal anatomy of the human brain stem. Their study provides a very nice illustration of one of the key strengths of MR imaging, in which multiple MR imaging contrast mechanisms/parameters can complement each other and provide an enhanced visualization of brain structures. In this particular study, the synergy of a recently proposed echo modulation curve (EMC) method for T2 mapping² and the super-resolution track density imaging (TDI) method³ is shown to visualize many of the tracts and nuclear groups within the brain stem, to a level not previously shown before with in vivo 3T MR imaging. Most important, this combined protocol was achieved with a total acquisition time that is feasible for clinical investigations (though it relies on postprocessing methods that may be, so far, available only at large specialized centers, a limitation likely to be overcome in the future, with the widespread use of these methodologies).

The results of the study by Hoch et al,¹ demonstrating the synergy of TDI with other MR imaging parameters to achieve enhanced anatomic delineation are consistent with the findings from previous studies, such as the combination of super-resolution TDI and ultra-high-field T1-weighted images to delineate the substructures of the thalamus at 7T MR imaging.⁴

A related issue, also briefly mentioned in the article by Hoch et al,¹ is that of quantification. While T2 is a well-studied parameter and one that has been used quantitatively for clinical applications in the past (eg, in epilepsy,⁵ Friedreich ataxia,⁶ and multiple sclerosis,⁷ among others), quantification of TDI has been the subject of recent controversy, with some studies reporting successful clinical applications⁸⁻¹⁰ and others emphasizing its potential limitations for quantitative studies.¹¹⁻¹⁴

The super-resolution TDI method was initially developed primarily as a qualitative imaging method with high anatomic contrast.³ Despite its potential role as a quantitative parameter for fiber-density mapping (given that TDI is a measure of the density of streamlines from fiber tracking), recent studies have highlighted its limitations as a fully quantitative parameter, including

relatively low quantitative reproducibility¹² and sensitivity to detecting false-positives and false-negatives.¹⁴

Given these limitations, it could be argued that the power of super-resolution TDI is not as a quantitative tool but rather in the high anatomic contrast and detail it provides (as illustrated by the results from Hoch et al,¹ and other related studies^{3,4,15,16}). Quantification is therefore better performed on the basis of, for example, other complementary track-based parameters, such as track-weighted apparent diffusion coefficient (TW-ADC), track-weighted fractional anisotropy (TW-FA), and track-weighted fiber-orientation distribution (TW-FOD),^{12,17} or even on the basis of other properties of the streamlines themselves (such as their lengths in the average pathlength map [APM] method)¹³ or on measures of the voxelwise fiber-orientation distribution (such as those related to the apparent fiber density [AFD] method).^{14,18} While these maps have reduced anatomic contrast relative to that seen in TDI maps, they have more reliable quantitative properties^{12,13} and are therefore more suitable for quantitative analysis in clinical applications.

In this context, one could envisage a scenario in which the protocol proposed by Hoch et al¹ is used to identify and delineate the structures of interest (eg, specific tracts and nuclear groups within the brain stem, as in Figs 2–8 in that study), but then these other complementary parameters are used for quantification within those specific structures. Thus, some maps (eg, EMC and super-resolution TDI) are used to define the structures of interest (on the basis of their high anatomic contrast and detail), while other maps (eg, TW-ADC, TW-FA, TW-FOD, APM, total AFD, and so forth) are used to provide more reliable quantitative measures. This approach, in turn, emphasizes once again the strength in the synergy of multiple MR imaging parameters or as Aristotle once said, “The whole is greater than the sum of its parts.”

REFERENCES

1. Hoch MJ, Chung S, Ben-Eliezer N, et al. **New clinically feasible 3T MRI protocol to discriminate internal brain stem anatomy.** *AJNR Am J Neuroradiol* 2016 Feb 11. [Epub ahead of print] CrossRef Medline
2. Ben-Eliezer N, Sodickson DK, Block KT. **Rapid and accurate T2**

- mapping from multi-spin-echo data using Bloch-simulation-based reconstruction. *Magn Reson Med* 2015;73:809–17 CrossRef Medline
3. Calamante F, Tournier JD, Jackson GD, et al. **Track density imaging (TDI): super-resolution white matter imaging using whole-brain track-density mapping.** *Neuroimage* 2010;53:1233–43 CrossRef Medline
 4. Calamante F, Oh SH, Tournier JD, et al. **Super-resolution track-density imaging of thalamic substructures: comparison with high-resolution anatomical magnetic resonance imaging at 7.0T.** *Hum Brain Mapping* 2013;34:2538–48 CrossRef Medline
 5. Jackson GD, Connelly A, Duncan JS, et al. **Detection of hippocampal pathology in intractable partial epilepsy: increased sensitivity with quantitative magnetic resonance T2 relaxometry.** *Neurology* 1993; 43:1793–99 CrossRef Medline
 6. Bonilha da Silva C, Bergo FP, D'Abreu A, et al. **Dentate nuclei T2 relaxometry is a reliable neuroimaging marker in Friedreich's ataxia.** *Eur J Neurol* 2014;21:1131–36 CrossRef Medline
 7. Bonnier G, Roche A, Romascano D, et al. **Advanced MRI unravels the nature of tissue alterations in early multiple sclerosis.** *Ann Clin Transl Neurol* 2014;1:423–32 CrossRef Medline
 8. Ziegler E, Rouillard M, André E, et al. **Mapping track density changes in nigrostriatal and extranigral pathways in Parkinson's disease.** *Neuroimage* 2014;99:498–508 CrossRef Medline
 9. Barajas RF Jr, Hess CP, Phillips JJ, et al. **Super-resolution track density imaging of glioblastoma: histopathologic correlation.** *AJNR Am J Neuroradiol* 2013;34:1319–25 CrossRef Medline
 10. Bozzali M, Parker GJ, Spanò B, et al. **Brain tissue modifications induced by cholinergic therapy in Alzheimer's disease.** *Hum Brain Mapp* 2013;34:3158–67 CrossRef Medline
 11. Besseling RM, Jansen JF, Overvliet GM, et al. **Tract specific reproducibility of tractography based morphology and diffusion metrics.** *PLoS One* 2012;7:e34125 CrossRef Medline
 12. Willats L, Raffelt D, Smith RE, et al. **Quantification of track-weighted imaging (TWI): characterisation of within-subject reproducibility and between-subject variability.** *Neuroimage* 2014;87: 18–31 CrossRef Medline
 13. Pannek K, Mathias JL, Bigler ED, et al. **The average pathlength map: a diffusion MRI tractography-derived index for studying brain pathology.** *Neuroimage* 2011;55:133–41 CrossRef Medline
 14. Calamante F, Smith RE, Tournier JD, et al. **Quantification of voxel-wise total fibre density: investigating the problems associated with track-count mapping.** *Neuroimage* 2015;117:284–93 CrossRef Medline
 15. Calamante F, Tournier JD, Kurniawan ND, et al. **Super-resolution track-density imaging studies of mouse brain: comparison to histology.** *Neuroimage* 2012;59:286–96 CrossRef Medline
 16. Cho ZH, Calamante F, Chi JG. *7.0 Tesla MRI Brain White Matter Atlas*. 2nd ed. Berlin: Springer-Verlag; 2015
 17. Calamante F, Tournier JD, Smith RE, et al. **A generalised framework for super-resolution track-weighted imaging.** *Neuroimage* 2012;59: 2494–503 CrossRef Medline
 18. Raffelt D, Tournier JD, Rose S, et al. **Apparent fibre density: a novel measure for the analysis of diffusion-weighted magnetic resonance images.** *Neuroimage* 2012;59:3976–94 CrossRef Medline

F. Calamante

Florey Institute of Neuroscience and Mental Health
Heidelberg, Victoria, Australia
Florey Department of Neuroscience and Mental Health
University of Melbourne
Melbourne, Victoria, Australia
Department of Medicine
Austin Health and Northern Health, University of Melbourne
Melbourne, Victoria, Australia

<http://dx.doi.org/10.3174/ajnr.A4721>

Endovascular Treatment versus Best Medical Treatment in Patients with Acute Ischemic Stroke: A Meta-Analysis of Randomized Controlled Trials

A.I. Qureshi, M.F. Ishfaq, H.A. Rahman, and A.P. Thomas



ABSTRACT

BACKGROUND AND PURPOSE: Endovascular treatment has emerged as a minimally invasive technique for patients with acute ischemic stroke to achieve recanalization. Our aim was to determine the effects of endovascular treatment on clinical and safety outcomes compared with best medical treatment.

MATERIALS AND METHODS: Fifteen randomized trials that compared endovascular treatment with best medical treatment in patients with acute ischemic stroke met the inclusion criteria. We calculated pooled odds ratios and 95% CIs by using random-effects models. The primary end point was a favorable outcome defined by a modified Rankin Scale score of 0 (no symptoms), 1 (no significant disability), or 2 (slight disability) at 90 days postrandomization.

RESULTS: Of the 2980 subjects randomized, the proportion of subjects who achieved a favorable outcome was significantly greater among those randomized to endovascular treatment compared with best medical treatment (2949 subjects analyzed; odds ratio, 1.82; 95% CI, 1.38–2.40; $P < .001$). Excellent outcome (modified Rankin Scale score of 0 or 1) was also significantly greater among those randomized to endovascular treatment (2791 subjects analyzed; odds ratio, 1.77; 95% CI, 1.29–2.43, $P < .001$). Risk of symptomatic intracranial hemorrhage was similar between endovascular treatment and best medical treatment (2906 subjects analyzed; odds ratio, 1.19; 95% CI, 0.84–1.68; $P = .34$).

CONCLUSIONS: Compared with best medical treatment, the odds of achieving a favorable outcome or excellent outcome at 3 months postrandomization are approximately 80% higher with endovascular treatment among patients with acute ischemic stroke.

ABBREVIATION: ICH = intracranial hemorrhage

Endovascular treatment was introduced for patients with ischemic stroke in whom limited benefit with intravenous recombinant tissue plasminogen activator was expected or for those in whom IV thrombolytics was not indicated. There has been a

6-fold increase in the use of endovascular treatment among patients with acute ischemic stroke in the past few years,¹ and availability of endovascular treatment has been identified as a mandatory component of comprehensive stroke centers in the United States.^{2,3} Several randomized trials have compared the efficacy of endovascular treatment with best medical treatment, which may include IV thrombolytic administration. Because of the small sample sizes or the limited representation of patients most likely to benefit from endovascular treatment within a study population, the results have been conflicting.⁴⁻⁷ We performed this meta-analysis to combine the results of all existing trials to provide a comprehensive assessment of the benefit and risk associated with endovascular treatment in patients with acute ischemic stroke.

MATERIALS AND METHODS

Study Design

We performed a meta-analysis of relevant randomized controlled trials and stratified analyses by important differences in trial characteristics. We followed the Preferred Reporting Items for Systematic Reviews and Meta-Analyses guidelines. We performed a

Received August 5, 2015; accepted after revision December 1.

From the Zeenat Qureshi Stroke Institute (A.I.Q., M.F.I.), St. Cloud, Minnesota; and Department of Neurology (H.A.R., A.P.T.), Houston Methodist Hospital–Texas Medical Center, Houston, Texas.

Adnan I. Qureshi was responsible for the literature search, study design, data analysis, data interpretation, figures, and manuscript writing and revisions. Muhammad F. Ishfaq was responsible for the literature search, figures, data collection, data analysis, data interpretation, manuscript revision, and study design. Haseeb A. Rahman conducted the literature search, data collection, data interpretation, and manuscript revision. Abraham P. Thomas conducted the literature search, data collection, data interpretation, and manuscript revision.

Abstract previously presented at: European Stroke Conference, May 12–15, 2015; Vienna, Austria.

Please address correspondence to Adnan I. Qureshi, MD, 519 2nd St N, St. Cloud, MN 56303; e-mail: qureshai@gmail.com



Indicates article with supplemental on-line tables.



Indicates article with supplemental on-line photos.



Evidence-Based Medicine Level 1.

<http://dx.doi.org/10.3174/ajnr.A4775>

computerized literature search of the Medline and Cochrane data bases on April 17, 2015, with the following search terms: “endovascular treatment,” “thrombectomy devices,” “acute ischemic stroke,” “proximal intracranial occlusion in the anterior circulation,” “randomized control trial,” “intra-arterial revascularization,” “retrievable stents,” “alteplase,” “endovascular thrombectomy with the Solitaire FR stent retriever,” “recombinant pro-urokinase,” and “intravenous and intra-arterial recombinant tissue plasminogen activator (rtPA).” No other search restrictions were applied.

We included trials if they enrolled patients with acute ischemic stroke (within 24 hours of symptom onset) for endovascular treatment (intra-arterial thrombolysis and mechanical thrombectomy alone or in combination) and randomly assigned patients to endovascular treatment or medical treatment with or without IV thrombolysis. Trials in which endovascular treatment was performed after administering IV thrombolysis were included. Trials that included <10 subjects, those that did not report clinical outcomes according to grades of modified Rankin Scale postrandomization, or those that performed any procedure for prevention of new or recurrent ischemic stroke were excluded.

Outcomes

The primary efficacy end point was the proportion of randomized subjects who achieved a modified Rankin Scale score of 0 (no symptoms), 1 (no significant disability), or 2 (slight disability) at 90 days postrandomization.⁸ Secondary efficacy end points were the proportion of randomized subjects who achieved a modified Rankin Scale score of 0 or 1 and survival at 3 months postrandomization. Posttreatment symptomatic intracranial hemorrhage was the safety end point analyzed. Information on these end points was abstracted by M.F.I. and H.A.R. independently and entered into a structured dataset and compared. All disagreements were resolved by reaching a consensus, and there was complete agreement on abstracted results in the final dataset.

Statistical Analysis

We calculated odds ratios and 95% CIs by using Comprehensive Meta-Analysis 2·2·048 (Biostat, Englewood, New Jersey) for each of the trials. We compared the calculated odds ratios with the odds ratios or hazard ratios reported in the original article when available to ensure congruence. If specific end points were not reported in a trial, that trial was excluded only from the pooled analyses of the specific end points that were not reported. We calculated pooled odds ratios by using a random-effects model by using the method of DerSimonian and Laird.⁹ Heterogeneity was assessed by using the Cochran Q statistic, and when there was heterogeneity, we assessed the magnitude of heterogeneity with the I^2 measure (the percentage of total variability due to true between-study heterogeneity). We stratified results by key trial characteristics, including the type of subjects recruited (exclusively within 4.5 hours of symptom onset and/or confirmation of arterial occlusion before randomization), the type of endovascular treatment performed (intra-arterial thrombolysis or a combination of intra-arterial thrombolysis and mechanical thrombec-

tomy or mechanical thrombectomy alone), the administration of IV thrombolysis (before endovascular treatment), and the treatment in subjects randomized to medical treatment (received IV thrombolysis).

In sensitivity analyses, we restricted the analyses to trials with at least 50 randomized subjects who achieved a modified Rankin Scale score of 0, 1, or 2 at 3 months postrandomization, and we analyzed for heterogeneity on the basis of masking within the trial. We analyzed the results only for trials that assessed the primary outcome at 90 days postrandomization by using blinded ascertainment. We assessed publication bias by visual inspection of funnel plots and by calculation of the P value (2-sided) for the Egger intercept. We did not make corrections for multiple hypotheses testing because of the exploratory nature of the analyses. All tests were 2-sided, with $P < .05$ deemed as significant.¹⁰

RESULTS

We identified 18 randomized clinical trials evaluating endovascular treatment in patients with acute ischemic stroke (On-line Fig 1).^{11–28} Three trials^{26–28} (87 subjects randomized) were excluded because they either used the Scandinavian Stroke Scale or the National Institutes of Health Stroke Scale as outcome measures or endovascular treatment was used in both treatment groups. The remaining 15 trials^{11–25} met the inclusion criteria and were included in the meta-analysis (see On-line Table 1), resulting in 2980 patients. One trial²² ascertained outcome at 6 months postrandomization, and we accepted the reported outcome as a surrogate for outcome at 90 days postrandomization. The characteristics of included studies are provided in the On-line Table. Six trials enrolled patients exclusively within ≤ 4.5 hours of symptom onset, and 12 trials required confirmed arterial occlusion before randomization (by conventional angiography in 3 and CT or MR angiography in 9). Endovascular treatment consisted of intra-arterial thrombolysis alone in 5 trials, and a combination of intra-arterial thrombolysis with mechanical thrombectomy or mechanical thrombectomy alone was used in 10 trials. Seven trials permitted the administration of IV thrombolysis before endovascular treatment. In 11 trials, subjects randomized to medical treatment received IV thrombolysis when indicated.

Among 2980 subjects randomized, 1114 (37.4%) achieved a modified Rankin Scale score of 0, 1, or 2 at 3 months postrandomization. The proportion of randomized subjects with acute ischemic stroke who achieved a modified Rankin Scale score of 0, 1, or 2 at 90 days postrandomization was significantly greater among those randomized to endovascular treatment (689 [43.1%] of 1597 subjects) compared with best medical treatment (425 [31.4%] of 1352 subjects) (2949 subjects analyzed; odds ratio, 1.82; 95% CI, 1.38–2.40; $P < .001$) as demonstrated in Fig 1. However, there was significant heterogeneity among the trials (Cochran Q statistic, 34.35; 14 df ; $P = .002$; $I^2 = 59.24\%$). In the first sensitivity analysis, the proportion of randomized subjects with acute ischemic stroke who achieved a modified Rankin Scale score of 0, 1, or 2 at 3 months postrandomization was significantly greater among those randomized to endovascular treatment (2906 subjects analyzed; odds ratio, 1.78; 95% CI, 1.34–2.37; $P < .001$) after exclusion of trials that had <50 subjects who achieved a modified Rankin Scale score of 0, 1, or 2 at 3 months postran-

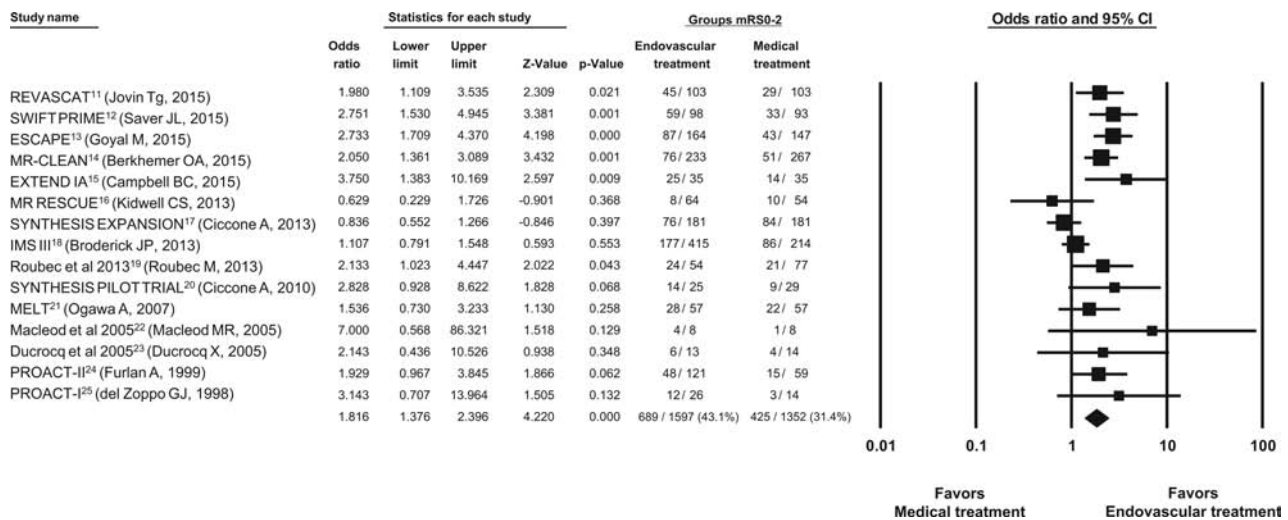


FIG 1. Odds of favorable outcome (modified Rankin Scale scores, 0, 1, or 2) at 90 days postrandomization.

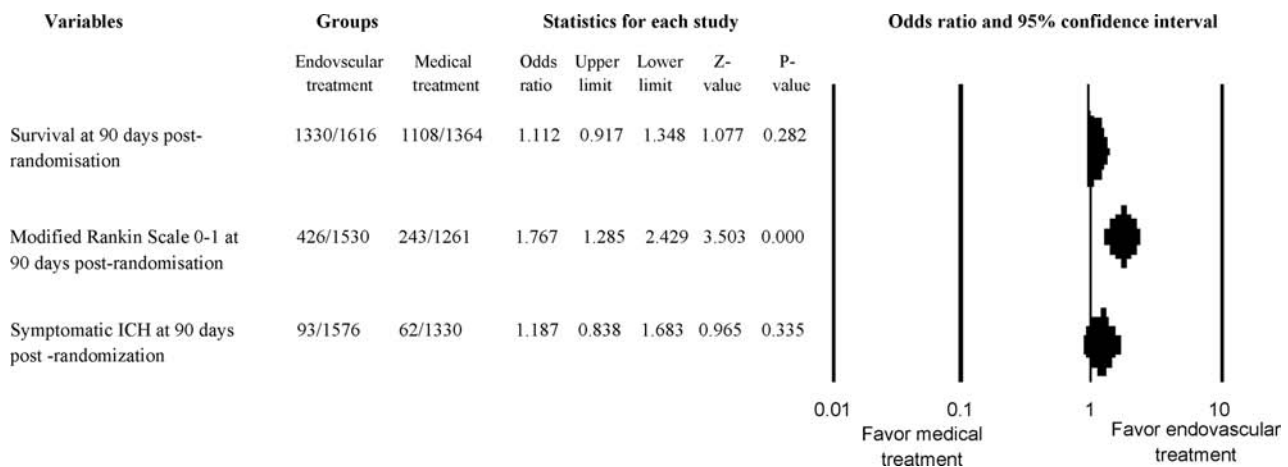


FIG 2. Odds of excellent outcome (modified Rankin Scale scores, 0 or 1), survival at 90 days postrandomization, and posttreatment intracranial hemorrhage.

domization. In the second sensitivity analysis, the results were unchanged after exclusion of trials that did not use blinded outcome ascertainment or did not assess outcome at 90 days postrandomization (2818 subjects analyzed; odds ratio, 1.80; 95% CI, 1.34–2.42; $P < .001$).

The proportion of randomized subjects with acute ischemic stroke who achieved a modified Rankin Scale score of 0 or 1 at 90 days postrandomization was significantly greater among those randomized to endovascular treatment (426 [27.8%] of 1530 subjects) compared with best medical treatment (243 [19.3%] of 1261 subjects) (2791 subjects analyzed; odds ratio, 1.77; 95% CI, 1.29–2.43; $P < .001$; Fig 2 and On-line Fig 2). There was significant heterogeneity among the trials (Cochran Q statistic, 27.79; 12 df ; $P = .006$; $I^2 = 56.83\%$). There was no difference in survival at 90 days postrandomization between subjects randomized to endovascular treatment compared with those randomized to best medical treatment (2980 subjects analyzed; odds ratio, 1.11; 95% CI, 0.92–1.35; $P = .28$; Fig 2). The specific definition of symptomatic intracranial hemorrhage varied among trials (On-line Table 2), but 155 patients had a symptomatic intracranial hemorrhage. In pooled analyses, there was no difference in the risk of symp-

tomatic intracranial hemorrhage between subjects randomized to endovascular treatment and those randomized to medical treatment (2906 subjects analyzed; odds ratio, 1.19; 95% CI, 0.84–1.68; $P = .34$). There was no heterogeneity among the trials concerning survival (Cochran Q statistic, 10.98; 14 df ; $P = .687$; $I^2 = 0\%$) or symptomatic intracerebral hemorrhage (Cochran Q statistic, 8.52; 12 df ; $P = .744$; $I^2 = 0\%$).

The odds ratios in various strata based on trial design, defined by type of subjects recruited, endovascular treatment performed, and treatment in subjects randomized to medical treatment, are provided in Fig 3. The odds of favorable outcomes were somewhat higher in trials that enrolled subjects within 24 hours of symptom onset (1627 subjects analyzed; OR, 2.02; 95% CI, 1.62–2.51; $P < .001$) compared with those that exclusively recruited within 4.5 hours of symptom onset (1322 subjects analyzed; OR, 1.81; 95% CI, 1.05–3.11; $P = .03$), with nonsignificant test for heterogeneity (Cochran Q statistic, 7.635; 8 df ; $P = .470$; $I^2 = 0.000\%$). Notably, the patient populations are not independent because trials that included subjects within 24 hours also included those enrolled within 4.5 hours. The odds of favorable outcome were somewhat higher in 12 trials that required angiographic confirmation of

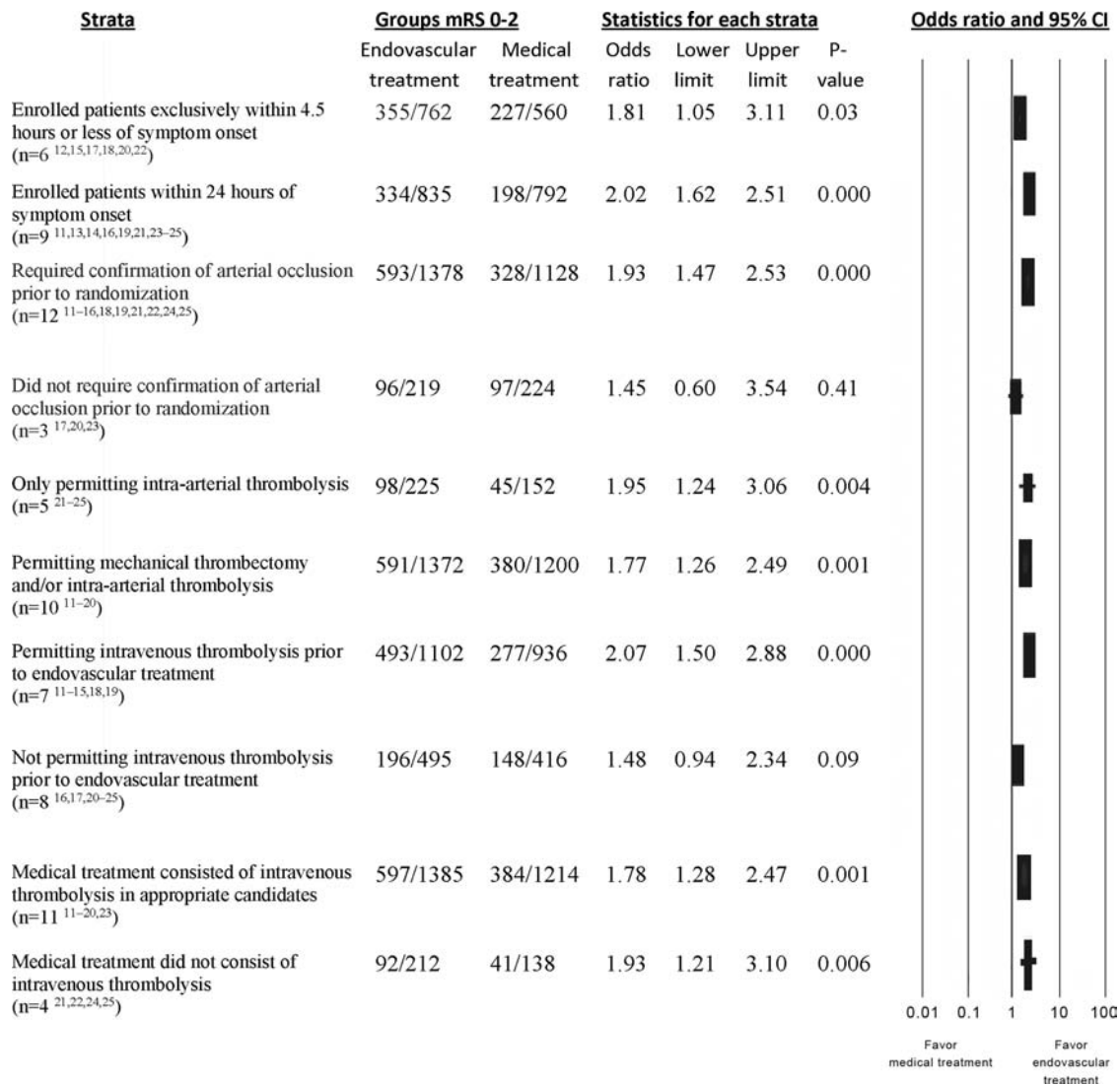


FIG 3. Odds of favorable outcome (modified Rankin Scale scores, 0, 1, or 2) at 90 days postrandomization in various strata based on trial design.

arterial occlusion before randomization (2506 subjects analyzed; OR, 1.93; 95% CI, 1.47–2.53; $P < .001$) but not in the 3 trials that did not require confirmation of arterial occlusion (443 subjects analyzed; OR, 1.45; 95% CI, 0.60–3.54; $P = .41$). The odds of favorable outcome were higher in trials that permitted a combination of pharmacologic thrombolysis with mechanical thrombectomy or mechanical thrombectomy alone (2572 subjects analyzed; OR, 1.77; 95% CI, 1.26–2.49; $P = .001$) and those that permitted intra-arterial thrombolytic treatment alone (377 subjects analyzed; OR, 1.95; 95% CI, 1.24–3.06; $P = .004$). The odds of favorable outcome appeared higher with endovascular treatment in trials that permitted IV thrombolytic treatment before or with endovascular treatment than in trials that did not permit IV thrombolysis before endovascular treatment.

There was a trend toward higher odds of symptomatic intracranial hemorrhage in trials that enrolled subjects within 24 hours of symptom onset (1600 subjects analyzed; OR, 1.48; 95% CI, 0.91–2.40; $P = .11$; On-line Table 3) but not in those trials that exclusively recruited within 4.5 hours of symptom onset. The odds of symptomatic intracranial hemorrhage were higher in tri-

als that permitted only intra-arterial thrombolytic treatment (377 subjects analyzed; OR, 4.19; 95% CI, 1.42–12.31; $P = .009$) but not in trials that permitted a combination of pharmacologic thrombolysis and mechanical thrombectomy or mechanical thrombectomy alone. There was no difference in 90-day survival with endovascular treatment in any of the strata based on trial design (On-line Table 3).

There was no evidence of publication bias having a significant effect on the results (Egger regression intercept P value [2-tailed] = 0.13; On-line Fig 3).

DISCUSSION

We demonstrate the therapeutic benefit of endovascular treatment in 2980 subjects with acute ischemic stroke randomized in 15 controlled trials. The analysis included data from more recent trials in contrast to previous meta-analyses and systematic reviews.^{29,30} Such a design allowed incorporation of technologic advancements and larger sample sizes within the analysis. The magnitude of benefit associated with endovascular treatment appeared higher in more recent trials (Fig 1), presumably due to the

use of new thrombectomy devices such as stent retrievers and appropriate patient selection. The odds of a favorable outcome were higher in trials that required angiographic confirmation of arterial occlusion before randomization. In a subset analysis of the Interventional Management of Stroke III trial,³¹ when only those subjects with arterial occlusion before randomization were analyzed, the magnitude of benefit with endovascular treatment was higher among such subjects (7% absolute increase in favorable outcome, $P = .011$ by ordinal shift analysis). The odds of a favorable outcome were higher with endovascular treatment, even in trials that enrolled subjects after 4.5 hours of symptom onset and those trials that enrolled subjects after receiving IV thrombolytics.

Some issues should be considered before interpretation of the results of the meta-analysis. We observed significant heterogeneity among results as observed in previous systematic review or meta-analysis of other clinical trials because of either clinical or methodologic diversity.³² Because of significant heterogeneity among studies, we used a random-effects model to take into account both within- and between-study variability.^{33,34} The model assumes that the effect is not the same in all studies and provides a much wider confidence interval (compared with a fixed-effects model).³³ We also attempted to provide explanatory data by performing stratified analyses by key trial characteristics and sensitivity analyses. We acknowledge that another option would be to just perform a narrative review, but we chose to perform a meta-analysis because these studies represented treatments in which the value of the average effect will be of interest.^{35,36} We used trial-level data because patient-level data were not available. Patient-level data are unlikely to change the overall findings but may provide insight into confounding effects of patient and procedure-related variables.

The possibility of publication bias cannot be completely excluded due to the borderline value for nonsignificance (Egger test, $P = .13$). There is a small chance that the estimate of the beneficial effect of endovascular treatment in patients with acute ischemic stroke may be exaggerated due to selective publication of trials with positive findings.³⁷ We presented data for outcomes at 90 days because data were available at that time point in most trials and the time point has been used consistently in most trials of acute ischemic stroke.⁸ The analysis does not provide any data on the effect of endovascular treatment on quality of life, cognitive deficits, and 1-year death and disability. There are also trials that are either ongoing or whose results have not yet been published after peer review, such as Assess the Penumbra System in the Treatment of Acute Stroke (THERAPY), Pragmatic Ischaemic Stroke Thrombectomy Evaluation (PISTE), and Trial and Cost Effectiveness Evaluation of Intra-arterial Thrombectomy in Acute Ischemic Stroke (THRACE), which were not included to avoid flaws such as failure to assess the methodologic quality of the included primary studies in this meta-analysis.³⁸

CONCLUSIONS

Our results support the recent focused update in the American Heart Association/American Stroke Association guidelines³⁹ strongly recommending that patients with acute ischemic stroke receive endovascular therapy with a stent retriever if they meet

specified criteria (Class I; Level of Evidence A). Our results also support administering IV thrombolysis in appropriate candidates and confirmation of major arterial occlusion before selection for endovascular treatment. The implementations of the results of the meta-analysis into clinical practice may vary in different settings on the basis of the availability of triage patterns, advanced imaging, and endovascular treatment.

Disclosures: Abraham P. Thomas—UNRELATED: Payment for Lectures (including service on Speakers Bureaus); Genentech; Other: TTI Home Health Care,* Accel at Herman Park,* Comments: Medical Directorship. *Money paid to the institution.

REFERENCES

- Hassan AE, Chaudhry SA, Grigoryan M, et al. **National trends in utilization and outcomes of endovascular treatment of acute ischemic stroke patients in the mechanical thrombectomy era.** *Stroke* 2012;43:3012–17 CrossRef Medline
- Alberts MJ, Latchaw RE, Selman WR, et al; Brain Attack Coalition. **Recommendations for comprehensive stroke centers: a consensus statement from the Brain Attack Coalition.** *Stroke* 2005;36:1597–616 CrossRef Medline
- Grigoryan M, Chaudhry SA, Hassan AE, et al. **Neurointerventional procedural volume per hospital in United States: implications for comprehensive stroke center designation.** *Stroke* 2012;43:1309–14 CrossRef Medline
- Qureshi AI, Abd-Allah F, Aleu A, et al. **Endovascular treatment for acute ischemic stroke patients: implications and interpretation of IMS III, MR RESCUE, and SYNTHESIS EXPANSION trials—a report from the Working Group of International Congress of Interventional Neurology.** *J Vasc Interv Neurol* 2014;7:56–75 Medline
- Patil CG, Long EF, Lansberg MG. **Cost-effectiveness analysis of mechanical thrombectomy in acute ischemic stroke.** *J Neurosurg* 2009;110:508–13 CrossRef Medline
- Chimowitz MI. **Endovascular treatment for acute ischemic stroke—still unproven.** *N Engl J Med* 2013;368:952–55 CrossRef Medline
- Blackham KA, Meyers PM, Abruzzo TA, et al; Society for NeuroInterventional Surgery. **Endovascular therapy of acute ischemic stroke: report of the Standards of Practice Committee of the Society of NeuroInterventional Surgery.** *J Neurointerv Surg* 2012;4:87–93 CrossRef Medline
- Quinn TJ, Dawson J, Walters MR, et al. **Reliability of the modified Rankin Scale: a systematic review.** *Stroke* 2009;40:3393–95 CrossRef Medline
- DerSimonian R, Laird N. **Meta-analysis in clinical trials.** *Control Clin Trials* 1986;7:177–88 CrossRef Medline
- Cavender MA, Sabatine MS. **Bivalirudin versus heparin in patients planned for percutaneous coronary intervention: a meta-analysis of randomized controlled trials.** *Lancet* 2014;384:599–606 CrossRef Medline
- Jovin TG, Chamorro A, Cobo E, et al; REVASCAT Trial Investigators. **Thrombectomy within 8 hours after symptom onset in ischemic stroke.** *N Engl J Med* 2015;372:2296–306 CrossRef Medline
- Saver JL, Goyal M, Bonafe A, et al; SWIFT PRIME Investigators. **Stent-retriever thrombectomy after intravenous t-PA vs. t-PA alone in stroke.** *N Engl J Med* 2015;372:2285–95 CrossRef Medline
- Goyal M, Demchuk AM, Menon BK, et al; ESCAPE Trial Investigators. **Randomized assessment of rapid endovascular treatment of ischemic stroke.** *N Engl J Med* 2015;372:1019–30 CrossRef Medline
- Berkhemer OA, Fransen PS, Beumer D, et al. **A randomized trial of intraarterial treatment for acute ischemic stroke.** *N Engl J Med* 2015;372:11–20 CrossRef Medline
- Campbell BC, Mitchell PJ, Kleinig TJ, et al; EXTEND-IA Investigators. **Endovascular therapy for ischemic stroke with perfusion-imaging selection.** *N Engl J Med* 2015;372:1009–18 CrossRef Medline
- Kidwell CS, Jahan R, Gornbein J, et al; MR RESCUE Investigators. **A**

- trial of imaging selection and endovascular treatment for ischemic stroke.** *N Engl J Med* 2013;368:914–23 CrossRef Medline
17. Ciccone A, Valvassori L, Nichelatti M, et al; SYNTHESIS Expansion Investigators. **Endovascular treatment for acute ischemic stroke.** *N Engl J Med* 2013;368:904–13 CrossRef Medline
 18. Broderick JP, Palesch YY, Demchuk AM, et al; Interventional Management of Stroke (IMS) III Investigators. **Endovascular therapy after intravenous t-PA versus t-PA alone for stroke.** *N Engl J Med* 2013;368:893–903 CrossRef Medline
 19. Roubec M, Kuliha M, Procházka V, et al. **A controlled trial of revascularization in acute stroke.** *Radiology* 2013;266:871–78 CrossRef Medline
 20. Ciccone A, Valvassori L, Ponzio M, et al; SYNTHESIS Investigators. **Intra-arterial or intravenous thrombolysis for acute ischemic stroke? The SYNTHESIS pilot trial.** *J Neurointerv Surg* 2010;2:74–79 CrossRef Medline
 21. Ogawa A, Mori E, Minematsu K, et al; MELT Japan Study Group. **Randomized trial of intraarterial infusion of urokinase within 6 hours of middle cerebral artery stroke: the middle cerebral artery embolism local fibrinolytic intervention trial (MELT) Japan.** *Stroke* 2007;38:2633–39 CrossRef Medline
 22. Macleod MR, Davis SM, Mitchell PJ, et al. **Results of a multicenter, randomized controlled trial of intra-arterial urokinase in the treatment of acute posterior circulation ischemic stroke.** *Cerebrovasc Dis* 2005;20:12–17 CrossRef Medline
 23. Ducrocq X, Bracard S, Taillandier L, et al. **Comparison of intravenous and intra-arterial urokinase thrombolysis for acute ischaemic stroke.** *J Neuroradiol* 2005;32:26–32 CrossRef Medline
 24. Furlan A, Higashida R, Wechsler L, et al. **Intra-arterial prourokinase for acute ischemic stroke: the PROACT II study—a randomized controlled trial, Prolyse in Acute Cerebral Thromboembolism.** *JAMA* 1999;282:2003–11 CrossRef Medline
 25. del Zoppo GJ, Higashida RT, Furlan AJ, et al. **PROACT: a phase II randomized trial of recombinant pro-urokinase by direct arterial delivery in acute middle cerebral artery stroke: PROACT Investigators—Prolyse in Acute Cerebral Thromboembolism.** *Stroke* 1998;29:4–11 CrossRef Medline
 26. Lewandowski CA, Frankel M, Tomsick TA, et al. **Combined intravenous and intra-arterial r-TPA versus intra-arterial therapy of acute ischemic stroke: Emergency Management of Stroke (EMS) Bridging Trial.** *Stroke* 1999;30:2598–605 CrossRef Medline
 27. Keris V, Rudnicka S, Vorona V, et al. **Combined intraarterial/intravenous thrombolysis for acute ischemic stroke.** *AJNR Am J Neuroradiol* 2001;22:352–58 Medline
 28. Sen S, Huang DY, Akhavan O, et al. **IV vs. IA TPA in acute ischemic stroke with CT angiographic evidence of major vessel occlusion: a feasibility study.** *Neurocrit Care* 2009;11:76–81 CrossRef Medline
 29. Fargen KM, Neal D, Fiorella DJ, et al. **Meta-analysis of prospective randomized controlled trials evaluating endovascular therapies for acute ischemic stroke.** *J Neurointerv Surg* 2015;7: 84–89 CrossRef Medline
 30. Fields JD, Khatri P, Nesbit GM, et al. **Meta-analysis of randomized intra-arterial thrombolytic trials for the treatment of acute stroke due to middle cerebral artery occlusion.** *J Neurointerv Surg* 2011;3: 151–55 CrossRef Medline
 31. Demchuk AM, Goyal M, Yeatts SD, et al; IMS III Investigators. **Recanalization and clinical outcome of occlusion sites at baseline CT angiography in the Interventional Management of Stroke III trial.** *Radiology* 2014;273:202–10 CrossRef Medline
 32. Higgins J, Thompson S, Deeks J, et al. **Statistical heterogeneity in systematic reviews of clinical trials: a critical appraisal of guidelines and practice.** *J Health Serv Res Policy* 2002;7:51–61 CrossRef Medline
 33. Hedges LV, Vevea JL. **Fixed- and random-effects models in meta-analysis.** *Psychological Methods* 1998;3:486–504 CrossRef
 34. Field AP. **The problems in using fixed-effects models of meta-analysis on real-world data.** *Understanding Statistics* 2003;2:105–24 CrossRef
 35. Owen C, Whincup PH, Gilg JA, et al. **Effect of breast feeding in infancy on blood pressure in later life: systematic review and meta-analysis.** *BMJ* 2003;327:1189–95 CrossRef Medline
 36. Thompson SG. **Why sources of heterogeneity in meta-analysis should be investigated.** *BMJ* 1994;309:1351–55 CrossRef Medline
 37. Reid EK, Tejani AM, Huan LN, et al. **Managing the incidence of selective reporting bias: a survey of Cochrane review groups.** *Syst Rev* 2015;4:85 CrossRef Medline
 38. Garg AX, Hackam D, Tonelli M. **Systematic review and meta-analysis: when one study is just not enough.** *Clin J Am Soc Nephrol* 2008;3:253–60 CrossRef Medline
 39. Powers WJ, Derdeyn CP, Biller J, et al; American Heart Association Stroke Council. **2015 American Heart Association/American Stroke Association Focused Update of the 2013 Guidelines for the Early Management of Patients with Acute Ischemic Stroke Regarding Endovascular Treatment: a Guideline for Healthcare Professionals From the American Heart Association/American Stroke Association.** *Stroke* 2015;46:3020–35 CrossRef Medline
 40. Jadad AR, Moore RA, Carroll D, et al. **Assessing the quality of reports of randomized clinical trials: is blinding necessary?** *Control Clin Trials* 1996;17:1–12 CrossRef Medline

Clinical Impact of Ventilation Duration in Patients with Stroke Undergoing Interventional Treatment under General Anesthesia: The Shorter the Better?

O. Nikoubashman, K. Schürmann, T. Probst, M. Müller, J.P. Alt, A.E. Othman, S. Tauber, M. Wiesmann, and A. Reich



ABSTRACT

BACKGROUND AND PURPOSE: Whether general anesthesia for neurothrombectomy in patients with ischemic stroke has a negative impact on clinical outcome is currently under discussion. We investigated the impact of early extubation and ventilation duration in a cohort that underwent thrombectomy under general anesthesia.

MATERIALS AND METHODS: We analyzed 103 consecutive patients from a prospective stroke registry. They met the following criteria: CTA-proved large-vessel occlusion in the anterior circulation, ASPECTS above 6 on presenting cranial CT, revascularization by thrombectomy with the patient under general anesthesia within 6 hours after onset of symptoms, and available functional outcome (mRS) 90 days after onset.

RESULTS: The mean ventilation time was 128.07 ± 265.51 hours (median, 18.5 hours; range, 1–1244.7 hours). Prolonged ventilation was associated with pneumonia during hospitalization and unfavorable functional outcome (mRS ≥ 3) and death at follow-up (Mann-Whitney *U* test; $P \leq .001$). According to receiver operating characteristic analysis, a cutoff after 24 hours predicted unfavorable functional outcome with a sensitivity and specificity of 60% and 78%, respectively. Our results imply that delayed extubation was not associated with a less favorable clinical outcome compared with immediate extubation after the procedure.

CONCLUSIONS: Short ventilation times are associated with a lower pneumonia rate and more favorable clinical outcome. Cautious interpretation of our data implies that whether patients are extubated immediately after the procedure is irrelevant for clinical outcome as long as ventilation does not exceed 24 hours.

ABBREVIATION: GA = general anesthesia

Recently, 5 prospective, randomized, open-label, blinded endpoint–designed clinical trials have established endovascular thrombectomy as the preferred treatment technique for acute ischemic stroke caused by large-vessel occlusion.^{1–5} These studies showed that endovascular recanalization in the anterior circulation 6–8 hours after stroke onset is associated with favorable functional outcome in 33%–60% of cases (mRS ≤ 2 at day 90).^{1–5} Basic cornerstones of the procedures such as the use of modern stent retrievers were comparable in the different studies. One con-

troversial difference, however, was the use of intubation and general anesthesia (GA) during the procedures.^{1–5} In fact, GA rates ranged from 6.7% to 37.8% in the mentioned prospective studies.^{1–5} Most active members of the Society of Vascular and Interventional Neurology stated, in a recent survey, that they preferred general anesthesia over conscious sedation for recanalization treatment of acute ischemic stroke.⁶ Patients with stroke are often noncompliant during endovascular procedures.⁶ Conscious sedation and local anesthesia do not immobilize agitated patients and are not apt to secure the patient's airway and thus may lead to aspiration.^{6,7} General anesthesia and intubation, however, allow complete immobilization and comfort of the patient, thereby allowing better image quality.^{7,8} On the other hand, it is assumed that delays in door-to-puncture time, development of ventilator-associated pneumonia, and ventilation-induced hypotension and hypocapnia may negatively influence clinical outcome in patients treated under GA.^{9,10} In a recent retrospective study >500 patients who were treated under GA were matched with patients treated under conscious sedation.¹¹ Patients with GA were found

Received September 17, 2015; accepted after revision November 18.

From the Departments of Neuroradiology (O.N., T.P., M.M., J.P.A., M.W.) and Neurology (K.S., S.T., A.R.), University Hospital Aachen, Aachen, Germany; Institute of Neuroscience and Medicine 4 (O.N.), Forschungszentrum Jülich, Jülich, Germany; and Department of Radiology (A.E.O.), University Hospital Tübingen, Tübingen, Germany.

Please address correspondence to Omid Nikoubashman, MD, Klinik für Neuroradiologie, Universitätsklinikum Aachen, Pauwelsstr 30, 52074 Aachen, Germany; e-mail: onikoubashman@ukaachen.de

 Indicates article with supplemental on-line tables.

<http://dx.doi.org/10.3174/ajnr.A4680>

to have a higher in-hospital mortality and higher rate of pneumonia.¹¹ However, patients were not matched for stroke severity (NIHSS scores were not reported), and this omission could account for the worse outcome.^{11,12}

In the end, one can break the debate down to the following 2 questions: 1) Is GA per se a risk factor for unfavorable clinical outcome? 2) Are prolonged ventilation times associated with unfavorable clinical outcome? Only a prospective, randomized study can address the first question. The second question, however, can be approached by examining a cohort that was treated predominantly under GA. Given that this was the case in the patients treated in our institution, our aim was to determine whether short ventilation times and early extubation in the angiography suite are associated with a more favorable clinical outcome.

MATERIALS AND METHODS

Patients

Our analysis was based on a prospective observational registry of all consecutive patients of the RWTH University Hospital Aachen (Germany) tertiary stroke center who had undergone endovascular recanalization of acute ischemic stroke in the anterior circulation since February 2010. Between February 2010 and January 2015, 318 patients with acute ischemic stroke underwent endovascular treatment for large-vessel occlusion in the anterior circulation. One hundred twenty-five patients (39.3%) met the inclusion criteria of revascularization within 6 hours after onset of symptoms, ASPECTS above 6 on presenting cranial CT, and CTA-proved large-vessel occlusion in the anterior circulation (the distal intracranial internal carotid artery including carotid T and M1 ± M2 segments of the middle cerebral artery). In 22 patients (17.4%), the clinical end point (mRS 90 days after onset) could not be evaluated. Thus, 103 patients were included in our analysis.

Procedures

Standard endovascular treatment with and without stent retrievers was performed as reported previously.¹³ Interventionalists with an individual annual experience of at least 15–20 thrombectomies in large-vessel-occlusion acute ischemic stroke performed the interventions. The anesthesiologic and postinterventional workflow was as follows: The anesthesiologist in charge is always informed when a stroke is announced. An emergency anesthesiologic team is present in the angiography suite when a patient is moved from the CT to the angiography suite. Induction of GA and puncture of the groin are performed simultaneously whenever possible.

The type of anesthesia and the choice of medication were at the discretion of the treating anesthesiologist. Usually, after the airway was secured with a rapid-sequence intubation, general anesthesia was maintained with intravenous anesthetics such as propofol and remifentanyl. A moderate hypertension (systolic blood pressure, 140–160 mm Hg) was induced until revascularization was achieved to improve cerebral perfusion.⁷ After revascularization was achieved, normotension (systolic pressure, 110–130 mm Hg) was restored to reduce the risk of reperfusion injury.¹⁴

After the procedure, patients were extubated in the angiogra-

phy suite or after postinterventional CT whenever possible. Post-acute work-up and treatment were performed in a certified stroke unit or neurologic intensive care unit. Criteria for extubation followed general guidelines for discontinuation of ventilatory support.¹⁵ These criteria comprised end of sedation and/or reversal of the underlying cause of respiratory failure, sufficient oxygenation (PaO_2 /fraction of inspired oxygen ≥ 120 –150 or saturation of peripheral oxygen $\geq 90\%$ on fraction of inspired oxygen $\leq 40\%$ and positive end-expiratory pressure ≤ 5 [–8] cm H_2O , pH > 7.25), hemodynamic stability (no or low-dose vasopressor medications), ability to initiate an inspiratory effort, hemoglobin ≥ 7 –10 mg/dL, core temperature (> 36.0 and ≤ 38 – 38.5°C), and mental status (awake/alert or easily arousable). Not all criteria were mandatory. In our cohort, neurologic deficits, especially those associated with increased risk of pneumonia (ie, dysphagia) and diminished respiratory drive (ie, decreased vigilance); neurologic prognosis; anticipated treatment options (ie, early carotid endarterectomy; early hemicraniectomy; conservative treatment of raised intracranial pressure); and overall treatment concept after intervention (curative versus palliative) influenced individual decisions for extubation. Withdrawal of care was always based on a consensus of the treating medical team, considering the patient's individual medical situation, prognosis, and putative wish. In case of ambiguous situations, our institution offered support by a palliative care team and/or ethical committee.

Clinical and Radiologic Data

After obtaining permission from our local ethics board, we assessed demographics (age, sex), clinical presentation (NIHSS), disability (mRS) at admission and disability at follow-up (mRS at discharge and day 90), cerebrovascular risk factors and primary and secondary prophylactic use of antiplatelet/-coagulant medication, serum glucose level (admission), and ischemic stroke etiology (adapted from the Trial of ORG 10172 in Acute Stroke Treatment, TOAST).¹⁶ Radiologic data were assessed by the primary treating neuroradiologist and re-evaluated by a blinded colleague. A reference standard was established for statistical analyses in a consensus reading for cases in which there was disagreement. Radiologic and procedural data comprised initial and postinterventional/follow-up imaging for the site of large-vessel occlusion and the extent of initial and final ischemic changes (ASPECTS), time from onset of symptoms to imaging and beginning of treatment, type of intra-arterial treatment (including bridging therapy) and devices, procedural time intervals, result of recanalization (TICI), and peri- and posttreatment complications (hemorrhagic and local events, secondary hemicraniectomy).¹⁷ Hemorrhagic events were reported according to the European Cooperative Acute Stroke Study (ECASS) definition.¹⁸ The most common definition of ventilator-associated pneumonia requires pneumonia occurring 48 hours after intubation and new or progressive and persistent infiltrates on a chest radiograph plus 2 of the following: abnormal white blood cell count (< 4000 white blood cells/mL or $> 12,000$ white blood cells/mL), the presence of hypothermia or fever ($< 36^\circ\text{C}$ or $> 38^\circ\text{C}$), purulent sputum, and deterioration in gas exchange.¹⁹ The role of chest radiographs in the diagnosis of pneumonia, however, has been discussed controversially, because the sensitivity of chest radiographs for the de-

tection of infiltrates is poor.²⁰ Therefore, we chose a more pragmatic approach in daily clinical care and treated all patients with clinical and laboratory and/or radiologic examinations suggestive of pneumonia. Accordingly, we chose to include these patients in our pneumonia analysis and to rather overestimate than underestimate pneumonia rates.

Primary outcome measures were the occurrence of ventilator-associated pneumonia during hospitalization, functional outcome defined as an mRS of ≤ 2 , and mortality on follow-up after 90 days.

Statistical Analysis

We used the Student *t*, Mann-Whitney *U*, Pearson χ^2 , and Fisher exact tests, depending on the type of data and data distribution. Binary logistic regression and Cox regression were used for multivariate analyses. Receiver operating characteristics were used for threshold estimation. *P* values under the α level of .05 were significant. All statistical analyses were performed with SPSS 23 software (IBM, Armonk, New York).

RESULTS

Clinical Data

Revascularization was successful in 90/99 (90.9%) procedures that involved mechanical stent-assisted thrombectomy. On average, 2.4 stent-retriever passes were needed for vessel recanalization. There were 4 cases of procedure-related intracranial SAH caused by vessel perforation, with consecutive parenchymal hemorrhage (ECASS-PH2) in 2 of these 4 cases. The rate of intracranial bleeding (SAH and PH2), which included all postinterventional imaging results regardless of cause and clinical impact, was 7.8% (8/103). The rate of symptomatic intracranial hemorrhages was 4.8% (5/103).

Forty of 42 patients in whom pneumonia was suspected underwent chest radiography. Thirty of these 40 (75%) patients had pathologic chest radiographs and ≥ 2 clinical and/or laboratory criteria for pneumonia. Chest radiographs were not conclusive in the remaining 10 patients. Clinical and laboratory criteria were highly suggestive of pneumonia in 8 of these 10 patients. All 8 patients received antibiotic treatment for suspected pneumonia. Accordingly, we classified these 8 patients as pneumonia cases. In the remaining 2 of 10 patients with nonconclusive chest radiographs, clinical and laboratory examinations eventually did not confirm the suspected diagnosis of pneumonia. Hence, these patients were not classified as having pneumonia. A chest radiograph was not performed due to palliative management in 2 patients, in whom pneumonia was suspected. Both patients died due to multiorgan failure when intensive care measures were terminated according to the patients' wishes. One patient who was treated for pneumonia and died 4 days after admission was included in our pneumonia calculation. The other patient died within 36 hours after admission before the suspected diagnosis of pneumonia could have been proved or disproved. This patient was not classified as a ventilator-associated pneumonia case. In summary, there were 39 cases of ventilator-associated pneumonia, which included 9 (23%) cases of pneumonia-associated sepsis. Diagnoses were based on clinical, laboratory, and radiologic

findings in 30 (77%) cases and on clinical and laboratory examinations alone in 9 cases (23%).

The end point of death at 3 months showed a marked non-normal distribution, with 50% of deaths occurring within 3 days and 75% of deaths occurring within 2 weeks after treatment (mean, 11.0 ± 18.3 days; range, 0–75 days). Early death was primarily attributed to secondary complications due to unsuccessful stroke treatment and consecutive switch to palliative care. Causes of death were cerebrovascular complications (12 cases), sepsis due to pneumonia (3 cases), respiratory failure due to pneumonia (3 cases), cardiac causes (4 cases), competing causes (4 cases), and unknown (2 cases).

Anesthesia

An overview of clinical, radiologic, and procedural characteristics can be found in On-line Table 1. All patients received intra-arterial treatment under general anesthesia. Intubation was performed immediately before or simultaneous with the initiation of endovascular therapy in 98 of 103 (95.1%) patients. The remaining 5 patients were intubated by the emergency physician on the way to our hospital. Extubation within 24 hours after interventional therapy was achieved in 58 of 103 (56.3%) patients. This included 30 patients (29.1%) who were extubated immediately after the procedure. Mean ventilation time of these 30 patients was 2.77 ± 1.43 hours (median, 2.5 hours; range, 1–6 hours). The Table shows the impact of various clinical and procedural factors on pneumonia rates and morbidity and mortality. Prolonged ventilation was associated with pneumonia during hospitalization and unfavorable functional outcome (mRS ≥ 3) and death at follow-up (Mann-Whitney *U* test; $P \leq .001$) (Figs 1 and 2 and On-line Table 2). Linear regression analysis was not possible due to the non-normal distribution of our data. Results of binary logistic regression analyses for various ventilation cutoffs are found in On-line Table 2. Cox regression implied that pneumonia rates, morbidity, and mortality did not depend on the respective covariants (Table) ($P \geq .052$). Receiver operating characteristic analysis implied that a cutoff after 24 hours correlated fairly well (area under the curve, 0.704) with favorable functional outcome (mRS ≤ 2) (sensitivity, 60%; specificity, 78%). Delayed extubation compared with extubation immediately after the procedure was associated with increased pneumonia rates and unfavorable clinical outcome (Fig 3). Univariate and multivariate analyses, however, implied that the impact of delayed extubation on pneumonia rates and clinical outcome was not significant (On-line Tables 3 and 4). Only when our dataset was artificially doubled did our data show that delayed extubation after 24 hours was associated with a less favorable clinical outcome compared with immediate extubation after the procedure (On-line Table 3).

DISCUSSION

General Anesthesia in Interventional Stroke Treatment

Whether general anesthesia for neurothrombectomy in patients with ischemic stroke has a negative impact on clinical outcome is currently under discussion. When we established interventional thrombectomy treatment for large-vessel occlusion, we had better experience with intubation and general anesthesia than with conscious sedation in terms of safe procedural performance and com-

Univariate analysis (Pearson χ^2 and Student *t* tests) of factors influencing pneumonia rates and clinical outcome

Characteristics	Pneumonia (P Value)	mRS >2 (P Value)	Death (P Value)
Hypertension	.919	.565	.195
Diabetes	.364	.001 ^a	.001 ^a
Fat metabolism disorder	.061	.834	.542
Adiposity	.069	.775	.921
Nicotine	.645	.001 ^a	.239
Alcohol	.145	.354	.283
Cardiovascular disease	.709	.708	.783
Atrial fibrillation	.404	.215	.667
Prior stroke	.727	.078	.070
Age older than 70 yr	.260	<.001 ^a	.079
Antiplatelet medication	.170	.599	.761
Anticoagulant medication	.206	.755	.815
Onset to recanalization	.268	.630	.884
TICI $\geq 2b$.947	.237	.059
>1/3 MCA territory	.004 ^a	<.001 ^a	<.001 ^a
Pneumonia	—	.001 ^a	.274
Intracerebral hemorrhage	.450	.170	.092

^a Significant.

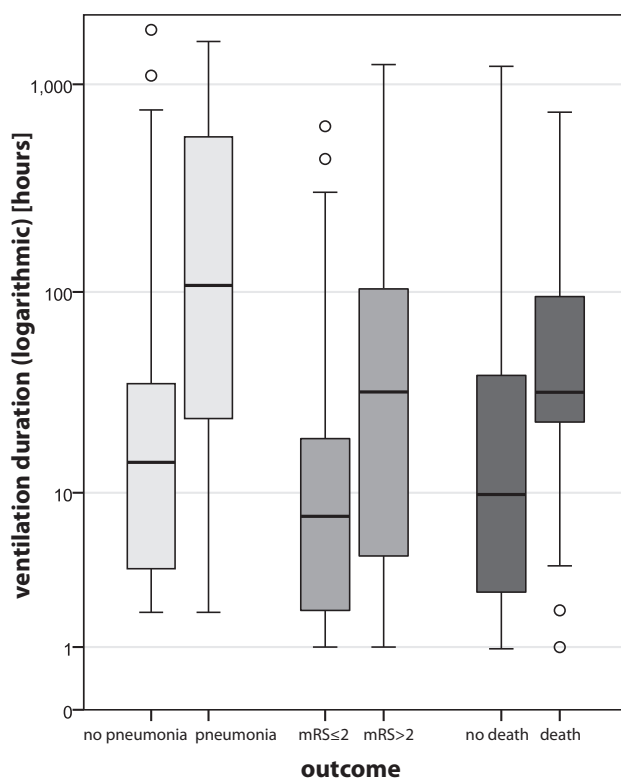


FIG 1. Boxplots illustrating the association between outcome measures and ventilation times. Clinical measures (mRS and death) as assessed after 90 days.

fort of the patient. Even though these advantages come at the price of a considerable pneumonia rate of 38%, we produced satisfactory results with regard to clinical outcome and standard procedural time intervals by establishing an optimized setting with parallel instead of serial anesthesiologic and neuroradiologic workflow.¹⁻⁵ Mean procedure times were significantly shorter than procedure times during conscious sedation as calculated by Brinjikji et al¹² in their meta-analysis of 9 studies that deal with GA versus conscious sedation (mean time to groin, 117 minutes; mean procedural time, 89 minutes) ($P < .001$, Student *t* test).

Considering that our patient cohort was older than that in the prospective, randomized, open-label, blinded end point studies, our favorable functional outcome rate (mRS ≤ 2) of 40.8% compared reasonably well with the average rate of 52.1% in the prospective, randomized, open-label, blinded end point studies.¹⁻⁵ In fact, when our cohort was adjusted for comparable age (younger than 70 years), favorable functional outcome (mRS ≤ 2) was achieved in 66.7% of cases, which is comparable with the rate of 65% reported by Berkhemer et al⁵ in the Solitaire with the Intention for Thrombectomy as Primary Endovascular Treatment for Acute Ischemic Stroke study (GA rate of 36%). Our results are also in accordance with results from a meta-analysis by Brinjikji et al.¹² The authors reported that differences between patients treated under GA and those under conscious sedation in functional outcome (defined as mRS ≤ 2), mortality, and respiratory complications were not significant after adjusting for stroke severity (NIHSS on symptom-onset).¹² Furthermore, the authors did not find statistically significant differences in mean time to groin, mean procedural time, and time from symptom onset to revascularization between patients with GA and conscious sedation.¹² In the end, the nature of our data does not allow determining the influence of GA on clinical outcome. Nevertheless, our everyday practice showed that routinely applied general anesthesia produces comparative results with regard to procedural and clinical outcome.

Ventilation Duration and Clinical Outcome

To the best of our knowledge, the question of whether short ventilation times and early extubation after neurointerventional stroke treatment are associated with a more favorable clinical outcome has not been addressed. In fact, longer ventilation times were associated with higher pneumonia rates, less favorable functional outcome, and higher mortality rates (Figs 1 and 2, and On-line Table 2). Hence, our results support the hypothesis that shorter ventilation times are associated with lower pneumonia rates and a more favorable clinical outcome.²¹⁻²³ When we investigated the influence of ventilation times via various cutoffs, multivariate analyses indicated that longer ventilation times resulted in higher pneumonia rates, regardless of the time of cutoff (On-line Table 2). However, multivariate analysis also indicated that longer ventilation times per se had no independent impact on unfavorable functional outcome ($P \geq .075$). With regard to mortality, only a cutoff after 24 hours discriminated between favorable and unfavorable outcome ($P = .020$, On-line Table 2). This result, which implies that ventilation duration does not affect clinical outcome, is counterintuitive because it would imply that clinical outcome did not depend on whether a patient was ventilated for 3 hours or 300 hours. Nonetheless, this finding would support the hypothesis that intubation per se has a negative impact on clinical outcome. However, data from the literature and a more elaborate interpretation of our results imply that ventilation duration may nevertheless have an impact on clinical outcome.^{8,9,21,23} A more thorough insight into our data shows that the missing significance at early and late cutoffs may be partly attributed to the non-normal distribution of our data. In fact, 33 of 42 (78.6%) patients with favorable functional outcome were ventilated for ≤ 24 hours and only 3 of 42 (7.1%) patients with

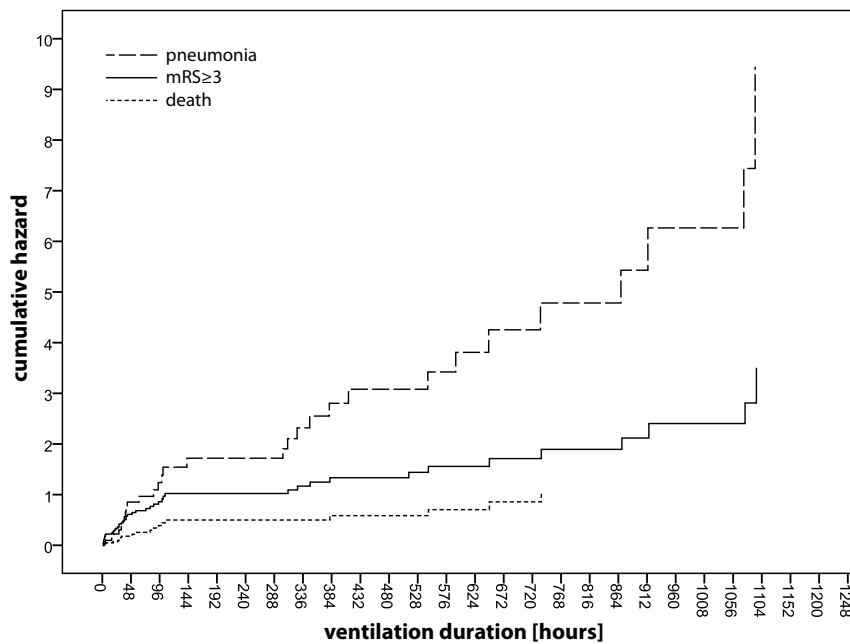


FIG 2. Cox regression showing the cumulative hazard for pneumonia during hospitalization and unfavorable clinical outcome (mRS ≥ 3 and death assessed after 90 days), depending on ventilation duration.

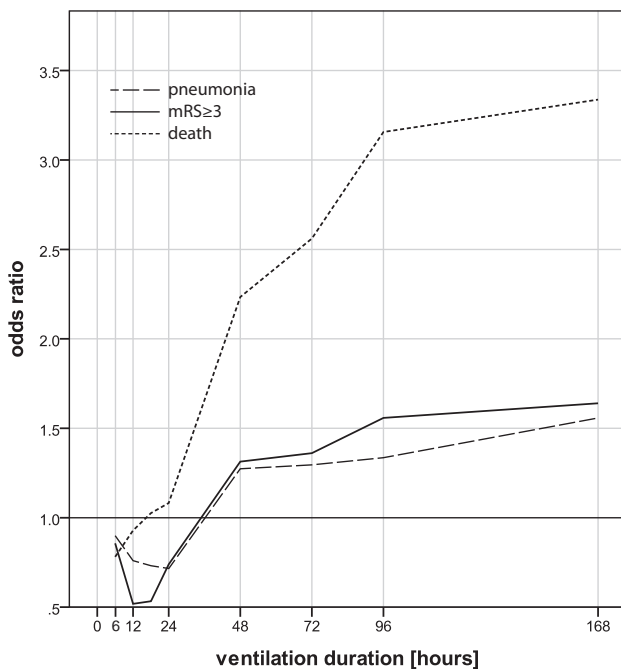


FIG 3. Odds ratios for pneumonia during hospitalization and unfavorable clinical outcome (mRS ≥ 3 and death assessed after 90 days), depending on whether extubation was performed immediately after the procedure or within time windows of 6, 12, 18.5, 24, 48, 72, 96 hours, and 1 week.

favorable clinical outcome were ventilated for >1 week. Consequently, early cutoffs that result in cohorts with equal numbers of patients with favorable or unfavorable outcomes are likely to become nonsignificant. In addition, ventilation time is not an independent variable because it is always the aim to extubate as soon as possible. Accordingly, multivariate analysis revealed that clinical factors such as age ($P = .001$), infarction size ($P \leq .013$), and

pneumonia ($P \leq .041$), which is again strongly related to ventilation duration, have the most important impact on functional outcome (On-line Table 2). Hence, in simple terms, our results reflect that long-term ventilation is associated with a less favorable clinical course, even though the difference between cause and effect is not always clear. Nonetheless, our results may serve as a first guide to estimating the clinical prognosis of ventilated patients.

Immediate versus Delayed Extubation

It has been shown that longer duration of ventilation increases the risk of ventilator-associated pneumonia.^{21,24} Thus, we always attempt to extubate patients immediately after the procedure to reduce the risk of pneumonia and to assess an early neurologic status.²³ However, sometimes extubation may be delayed due to medical (eg, dysphagia, low pharyngeal muscle tone, and impaired co-

operation or level of consciousness; see the “Materials and Methods” section for further extubation criteria) or nonmedical reasons (eg, reduced staff capacities due to other medical emergencies). Therefore, we investigated whether delayed extubation (outside the angiography suite) was associated with a higher pneumonia rate and a less favorable clinical outcome. In fact, the longer extubation was delayed, the more patients experienced ventilator-associated pneumonia. In addition, odds ratios for death (90 days) tripled and odds ratios for unfavorable functional outcome (90 days) doubled when patients were not extubated immediately after the procedure but within 1 week (Fig 3 and On-line Table 4). However, these effects failed to reach statistical significance in multivariate analysis (On-line Tables 3 and 4). Thus, strict interpretation of our data implies that delayed extubation within 1 week had no impact on pneumonia rates and clinical outcome. However, Cox regression and Mann-Whitney U tests showed that long ventilation was indeed associated with higher pneumonia rates and unfavorable outcome (Figs 1 and 2). Hence, our own results and data from the literature contradict the above-mentioned hypothesis to some extent.^{8,9,21,23} In summary, our results support the hypothesis that intubation per se is a risk factor for pneumonia and unfavorable clinical outcome. Nonetheless, our results are possibly also affected by the small sample size and the non-normal distribution of our data. In fact, when we artificially doubled our sample size, it became apparent that our sample size was too small for the Pearson χ^2 test to reveal statistical significances at cutoffs after 48 hours. In the end, cautious interpretation of our data indicates that extubation immediately after the procedure does not necessarily have an impact on clinical outcome, as long as patients are extubated within 24 hours (Fig 3 and On-line Table 3).

Limitations

The major limitation of our study is the relatively small sample size and the retrospective approach, both of which provoke speculative interpretation of our data to some extent. Nevertheless, our results may serve as a cornerstone for future multicenter studies and may be useful for centers where GA is the first choice or for patients in whom GA cannot be avoided.

CONCLUSIONS

Short ventilation times are associated with a lower pneumonia rate and more favorable clinical outcome. Cautious interpretation of our data implies that whether patients are extubated immediately after the procedure is irrelevant for pneumonia rates and clinical outcome, as long as ventilation does not exceed 24 hours.

Disclosures: Martin Wiesmann—UNRELATED: Consultancy: Stryker Neurovascular, Silk Road Medical; Grants/Grants Pending: Siemens*; Payment for Lectures (including service on Speakers Bureaus): Bracco, Covidien, Siemens, Stryker Neurovascular; Payment for Development of Educational Presentations: Abbott,* ab medica,* Acandis,* Bayer HealthCare,* Bracco,* B. Braun,* Codman Neurovascular,* Covidien,* Dahlhausen,* MicroVention,* Penumbra,* phenox,* Philips Healthcare,* Siemens,* Silk Road Medical,* St. Jude,* Stryker Neurovascular.* *Money paid to the institution.

REFERENCES

1. Saver JL, Goyal M, Bonafe A, et al; SWIFT PRIME Investigators. **Stent-retriever thrombectomy after intravenous t-PA vs. t-PA alone in stroke.** *N Engl J Med* 2015;372:2285–95 CrossRef Medline
2. Jovin TG, Chamorro A, Cobo E, et al; REVASCAT Trial Investigators. **Thrombectomy within 8 hours after symptom onset in ischemic stroke.** *N Engl J Med* 2015;372:2296–306 CrossRef Medline
3. Goyal M, Demchuk AM, Menon BK, et al; ESCAPE Trial Investigators. **Randomized assessment of rapid endovascular treatment of ischemic stroke.** *N Engl J Med* 2015;372:1019–30 CrossRef Medline
4. Campbell BC, Mitchell PJ, Kleinig TJ, et al; EXTEND-IA Investigators. **Endovascular therapy for ischemic stroke with perfusion-imaging selection.** *N Engl J Med* 2015;372:1009–18 CrossRef Medline
5. Berkhemer OA, Fransen PS, Beumer D, et al. **A randomized trial of intraarterial treatment for acute ischemic stroke.** *N Engl J Med* 2015; 372:11–20 CrossRef Medline
6. McDonagh DL, Olson DM, Kalia JS, et al. **Anesthesia and sedation practices among neurointerventionalists during acute ischemic stroke endovascular therapy.** *Front Neurol* 2010;1:118 CrossRef Medline
7. Brekenfeld C, Mattle HP, Schroth G. **General is better than local anesthesia during endovascular procedures.** *Stroke* 2010;41: 2716–17 CrossRef Medline
8. Froehler MT, Fifi JT, Majid A, et al. **Anesthesia for endovascular treatment of acute ischemic stroke.** *Neurology* 2012;79:S167–73 CrossRef Medline
9. Takahashi C, Liang CW, Liebeskind DS, et al. **To tube or not to tube? The role of intubation during stroke thrombectomy.** *Front Neurol* 2014;5:170 CrossRef Medline
10. Hassan AE, Chaudhry SA, Zacharatos H, et al. **Increased rate of aspiration pneumonia and poor discharge outcome among acute ischemic stroke patients following intubation for endovascular treatment.** *Neurocrit Care* 2012;16:246–50 CrossRef Medline
11. McDonald JS, Brinjikji W, Rabinstein AA, et al. **Conscious sedation versus general anaesthesia during mechanical thrombectomy for stroke: a propensity score analysis.** *J Neurointerv Surg* 2015;7: 789–94 CrossRef Medline
12. Brinjikji W, Murad MH, Rabinstein AA, et al. **Conscious sedation versus general anesthesia during endovascular acute ischemic stroke treatment: a systematic review and meta-analysis.** *AJNR Am J Neuroradiol* 2015;36:525–29 CrossRef Medline
13. Nikoubashman O, Reich A, Pjontek R, et al. **Postinterventional subarachnoid haemorrhage after endovascular stroke treatment with stent retrievers.** *Neuroradiology* 2014;56:1087–96 CrossRef Medline
14. Nour M, Scalzo F, Liebeskind DS. **Ischemia-reperfusion injury in stroke.** *Interv Neurol* 2013;1:185–99 CrossRef Medline
15. MacIntyre NR, Cook DJ, Ely EW Jr, et al; American College of Chest Physicians, American Association for Respiratory Care, American College of Critical Care Medicine. **Evidence-based guidelines for weaning and discontinuing ventilatory support: a collective task force facilitated by the American College of Chest Physicians, the American Association for Respiratory Care, and the American College of Critical Care Medicine.** *Chest* 2001;120:375S–95S CrossRef Medline
16. Adams HP Jr, Bendixen BH, Kappelle LJ, et al. **Classification of subtype of acute ischemic stroke: definitions for use in a multicenter clinical trial—TOAST. Trial of Org 10172 in Acute Stroke Treatment.** *Stroke* 1993;24:35–41 CrossRef Medline
17. Fugate JE, Klunder AM, Kallmes DF. **What is meant by “TICI”?** *AJNR Am J Neuroradiol* 2013;34:1792–97 CrossRef Medline
18. Trouillas P, von Kummer R. **Classification and pathogenesis of cerebral hemorrhages after thrombolysis in ischemic stroke.** *Stroke* 2006;37:556–61 CrossRef Medline
19. Muscedere J, Sinuff T, Heyland DK, et al; Canadian Critical Care Trials Group. **The clinical impact and preventability of ventilator-associated conditions in critically ill patients who are mechanically ventilated.** *Chest* 2013;144:1453–60 CrossRef Medline
20. Esayag Y, Nikitin I, Bar-Ziv J, et al. **Diagnostic value of chest radiographs in bedridden patients suspected of having pneumonia.** *Am J Med* 2010;123:88.e1–5 CrossRef Medline
21. Byers JF, Sole ML. **Analysis of factors related to the development of ventilator-associated pneumonia: use of existing databases.** *Am J Crit Care* 2000;9:344–49; quiz 351 Medline
22. Kasuya Y, Hargett JL, Lenhardt R, et al. **Ventilator-associated pneumonia in critically ill stroke patients: frequency, risk factors, and outcomes.** *J Crit Care* 2011;26:273–79 CrossRef Medline
23. Talke PO, Sharma D, Heyer EJ, et al. **Republished: Society for Neuroscience in Anesthesiology and Critical Care expert consensus statement—anesthetic management of endovascular treatment for acute ischemic stroke.** *Stroke* 2014;45:e138–50 CrossRef Medline
24. Muscedere J. **Which antibiotic for hospital acquired pneumonia caused by MRSA?** *BMJ* 2014;348:g1469 CrossRef Medline

Outcomes Are Not Different between Patients with Intermediate and High DWI-ASPECTS after Stent-Retriever Embolectomy for Acute Anterior Circulation Stroke

S.K. Kim, W. Yoon, M.S. Park, T.W. Heo, B.H. Baek, and Y.Y. Lee

ABSTRACT

BACKGROUND AND PURPOSE: Questions remain as to what benefits embolectomy provides to patients presented with considerable early ischemic changes on baseline imaging studies. This study aimed to investigate the impact of the Alberta Stroke Program Early CT Score applied to DWI on treatment outcomes in patients with acute stroke undergoing stent-retriever embolectomy.

MATERIALS AND METHODS: We retrospectively analyzed the clinical and DWI data from 171 patients with acute anterior circulation stroke who were treated with stent-retriever embolectomy within 6 hours of symptom onset. DWI-ASPECTS scores were analyzed with the full scale or were dichotomized (4–6 versus 7–10). Patients with DWI-ASPECTS ≤ 3 were excluded from the study. Associations between outcome and clinical and radiologic factors were determined with a multivariate logistic regression analysis. A good outcome was defined as a modified Rankin Scale score of 0–2 at 3 months.

RESULTS: The median DWI-ASPECTS was 7 (interquartile range, 6–8). The rates of good outcome, symptomatic hemorrhage, and mortality were not different between high DWI-ASPECTS (scores of 7–10) and intermediate DWI-ASPECTS (scores of 4–6) groups. In patients with an intermediate DWI-ASPECTS, good outcome was achieved in 46.5% (20/43) of patients with successful revascularization, whereas no patients without successful revascularization had a good outcome ($P = .016$). In multivariate logistic regression analysis, independent predictors of good outcome were age and successful revascularization.

CONCLUSIONS: Our study suggested that there were no differences in outcomes between patients with a high DWI-ASPECTS and those with an intermediate DWI-ASPECTS who underwent stent-retriever embolectomy for acute anterior circulation stroke. Thus, patients with an intermediate DWI-ASPECTS otherwise eligible for endovascular therapy may not be excluded from stent-retriever embolectomy or stroke trials.

ABBREVIATION: IQR = interquartile range

Recent randomized controlled trials have shown that stent-retriever embolectomy in addition to standard care was associated with improved functional outcome in patients with acute anterior circulation stroke due to large-vessel occlusion within 6–8 hours of symptom onset.^{1–5} For further advancement in treating acute anterior circulation stroke, it is becoming important to more clearly refine the selection criteria for stent-retriever embolectomy. Several clinical and imaging factors are known to be associated with functional outcomes after endovascular treat-

ment for acute anterior circulation stroke.^{6–9} However, questions remain as to what benefits embolectomy provides to patients who present at extended time periods or those with considerable early ischemic changes on baseline imaging studies. Furthermore, the imaging technique that best determines candidacy for embolectomy in these patients remains unknown.

ASPECTS is a 10-point semiquantitative scoring system, which was developed to offer the simplicity and reliability of CT to assess early ischemic changes in patients with acute ischemic stroke in the anterior circulation.¹⁰ ASPECTS has recently been applied to DWI, which is much more sensitive and accurate in the detection of acute infarction than noncontrast CT.^{11–14} A recent study showed that interrater agreement for DWI-ASPECTS was superior to that for CT-ASPECTS and that DWI-ASPECTS outperformed CT-ASPECTS in predicting functional outcome at 90 days.⁹ The DWI-ASPECTS can also provide similar risk assessment far more rapidly than measurement of the infarct volume

Received September 15, 2015; accepted after revision November 23.

From the Departments of Radiology (S.K.K., W.Y., T.W.H., B.H.B., Y.Y.L.) and Neurology (M.S.P.), Chonnam National University Medical School, Chonnam National University Hospital, Gwangju, Republic of Korea.

Please address correspondence to Woong Yoon, MD, Department of Radiology, Chonnam National University Hospital, 42 Jebong-ro, Dong-gu, Gwangju, 501-757, Republic of Korea; e-mail: radyoon@jnu.ac.kr

<http://dx.doi.org/10.3174/ajnr.A4663>

on DWI, an independent predictable marker of the clinical outcome, in patients with anterior circulation stroke.^{9,15-17} However, few studies have investigated the association between pretreatment DWI-ASPECTS and functional outcome after stent-retriever embolectomy in patients with acute anterior circulation stroke.^{9,14,18}

Although several studies showed that a DWI-ASPECTS of 7 was the optimal cutoff value for predicting clinical outcomes in patients undergoing intra-arterial or IV pharmacologic thrombolysis,¹⁹⁻²¹ results of recent studies have suggested that some patients with a DWI-ASPECTS of <7 may still benefit from complete recanalization.¹⁴ Successful revascularization can be achieved more frequently by using stent-based embolectomy than by using pharmacologic thrombolysis or other mechanical devices.¹⁻⁵ In this context, patients with acute stroke and a DWI-ASPECTS of <7 might have a similar chance of a good outcome compared with those with a higher DWI-ASPECTS if they are treated with stent-retriever embolectomy in a short time window. However, this hypothesis has not been tested. Thus, this study aimed to investigate the impact of DWI-ASPECTS on functional outcome in patients with acute anterior circulation stroke who underwent stent-retriever embolectomy.

MATERIALS AND METHODS

Patients

From December 2010 to December 2013, 190 consecutive patients presenting with acute ischemic stroke due to internal carotid artery or middle cerebral artery occlusions were treated with stent-retriever embolectomy at a comprehensive regional stroke center. Patients underwent a nonenhanced CT scan and multimodal MR imaging before endovascular embolectomy procedures. Of these patients, those who had DWI of insufficient quality for reliable evaluation ($n = 3$) or a DWI-ASPECTS of ≤ 3 ($n = 6$) or a previous modified Rankin Scale score of ≥ 2 ($n = 4$) or concomitant anterior and posterior circulation infarction ($n = 6$) were excluded; thus, 171 patients were left in this study. We prospectively collected the following clinical and radiologic data of these 171 patients: demographic features, cerebrovascular risk factors, NIHSS scores on admission, use of IV thrombolysis, time to endovascular treatment, procedure time, time to reperfusion, revascularization status, and clinical outcome. The institutional ethics committee approved this study. For each patient, written informed consent for endovascular therapy was obtained from a family member.

MR Imaging Analysis

MR imaging examinations were performed by using a 1.5T unit (Signa HDxt; GE Healthcare, Milwaukee, Wisconsin). Before the endovascular procedure, patients underwent MR imaging, including DWI, gradient-echo imaging, a FLAIR sequence, 3D TOF-MRA, and perfusion imaging. DWI sequences were obtained in the axial plane by using a single-shot, spin-echo echoplanar technique with the following parameters: TR of 9000 ms, TE of 80 ms, section thickness of 4 mm, intersection gap of 0 mm, FOV of 260 × 260 mm, and b-values of 0 and 1000 s/mm². DWI-ASPECTS was assessed by 2 neuroradiologists (with 2 and 4 years of experience, respectively) who were

blinded to any clinical information. Conclusions were reached by consensus.

Endovascular Treatment

On admission, a stroke neurologist performed a neurologic assessment based on the NIHSS. The inclusion criteria for stent-retriever embolectomy were as follows: presentation within 6 hours of stroke onset, baseline NIHSS score of ≥ 4 , no intracranial hemorrhage detected on cranial CT or MR imaging, a target mismatch pattern on multimodal MR imaging based on visual estimation (time-to-peak map of perfusion imaging showing a lesion volume $\geq 30\%$ larger than that detected with diffusion imaging), and infarct volume on diffusion imaging or nonenhanced CT of less than one-third of the MCA territory.

Cerebral angiography and endovascular therapy were performed with the patient under conscious sedation. In cases of agitation, an intravenous bolus of midazolam was given and repeated if necessary. Stent-based embolectomy with a Solitaire stent (Covidien, Irvine, California) was performed as the first-line endovascular treatment. When stent-based embolectomy was unsuccessful, additional mechanical approaches were performed, including manual aspiration embolectomy with a Penumbra System reperfusion catheter (Penumbra, Alameda, California). The details of the techniques used for mechanical embolectomy were previously described.^{22,23} Revascularization status was assessed on the final angiogram and was classified according to the modified TICI scale,²⁴ and successful revascularization was defined as a modified TICI grade of 2b or 3. Clinical outcome was assessed by a stroke neurologist by using the mRS during an outpatient visit 3 months after treatment. If patients were unable to attend the outpatient clinic, outcomes were obtained via telephone interview. A good clinical outcome was defined as an mRS score of ≤ 2 .

Statistical Analysis

Continuous variables are presented as medians and interquartile ranges (IQRs). Discrete variables are presented as counts and percentages. First, the area under the receiver operating characteristic curve was applied to evaluate the prognostic performance of DWI-ASPECTS and the optimal cutoff value for discriminating a good outcome (defined as mRS 0–2 at 3 months). Second, the differences in baseline characteristics and treatment outcomes between DWI-ASPECTS subgroups were determined. Patients were divided into 2 groups according to baseline DWI-ASPECTS for analysis of the prognostic impact on functional outcome; namely, a high DWI-ASPECTS group (scores of 7–10) and an intermediate DWI-ASPECTS group (scores of 4–6). The χ^2 or Fisher exact test was used for comparing categorical variables, and the Mann-Whitney U test was used for comparing continuous variables. Third, independent associations between functional outcome and clinical and radiologic factors were determined with a multivariate logistic regression analysis. The variables tested in the multivariate logistic regression models were those with $P < .2$ in the univariate analysis and time to treatment. Fourth, we further compared functional outcome between patients with or without successful revascularization (modified TICI, $\geq 2b$) according to the DWI-ASPECTS subgroups to evaluate the impact of DWI-ASPECTS on the success of endovascular therapy. The χ^2 or

Table 1: Baseline clinical characteristics of the study population

	Total (N = 171)	DWI-ASPECTS		P Value
		7–10 (n = 120)	4–6 (n = 51)	
Age (yr) (median) (IQR)	72 (63.5–78)	73 (65–78)	68 (60–74)	.014
Male sex	88 (51.5%)	58 (48.3%)	30 (58.8%)	.209
Risk factors				
Hypertension	95 (55.6%)	69 (57.5%)	26 (51%)	.432
Diabetes mellitus	32 (18.7%)	22 (18.3%)	10 (19.6%)	.845
Coronary artery disease	20 (11.7%)	14 (11.7%)	6 (11.8%)	.985
Dyslipidemia	42 (24.6%)	35 (29.2%)	7 (13.7%)	.034 ^a
Smoking	46 (26.9%)	27 (22.5%)	19 (37.3%)	.059 ^a
Atrial fibrillation	87 (50.9%)	64 (53.3%)	23 (45.1%)	.324
Congestive heart failure	6 (3.5%)	5 (4.2%)	1 (1.9%)	.670 ^a
History of stroke or TIA	22 (12.9%)	18 (15%)	4 (7.8%)	.317 ^a
Intravenous thrombolysis	104 (60.8%)	71 (59.2%)	33 (64.7%)	.497
Time to treatment (min) (median) (IQR)	245 (190–310)	257.5 (190–315)	220 (190–281)	.155
Procedure time (min) (median) (IQR)	33 (20–50)	34 (20.5–50)	30 (20–43.5)	.444
Time to revascularization (min) (median) (IQR)	280 (223.5–352)	297.5 (228.5–355)	252 (221.5–326)	.136
Baseline NIHSS score (median) (IQR)	13 (10–16)	12 (9–15)	15 (12–18)	<.001
Stroke etiology				
Large-artery atherosclerosis	43 (25.1%)	32 (26.7%)	11 (21.6%)	.482
Cardioembolism	99 (57.9%)	70 (58.3%)	29 (56.9%)	.859
Undetermined	28 (16.4%)	17 (14.2%)	11 (21.6%)	.231

^a Comparisons were performed using the Fisher exact test. Comparisons of categoric variables were performed using χ^2 tests unless otherwise indicated.

Table 2: Outcomes after stent-retriever embolectomy in 171 patients

	Total (N = 171)	DWI-ASPECTS		P Value
		7–10 (n = 120)	4–6 (n = 51)	
Modified TIC1 2b or 3	144 (84.2%)	101 (84.2%)	43 (84.3%)	.981
Good outcome	81 (47.4%)	61 (50.8%)	20 (39.2%)	.164
Symptomatic hemorrhage	6 (3.5%)	4 (3.3%)	2 (3.9%)	1.000 ^a
Mortality	16 (9.4%)	9 (7.5%)	7 (13.7%)	.201

^a Comparisons were performed using the Fisher exact test. Comparisons of categoric variables were performed using χ^2 tests unless otherwise indicated.

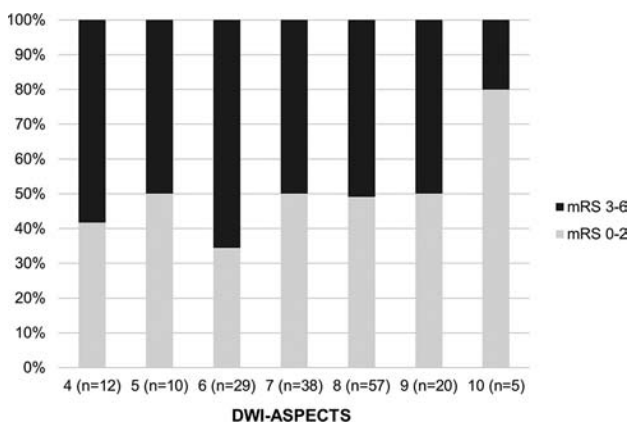


FIG 1. Functional outcome (mRS 0–6) of 171 patients with acute anterior circulation stroke according to pretreatment DWI-ASPECTS. The proportion of outcomes (mRS 0–2 versus mRS 3–6) within each DWI-ASPECTS is shown.

Fisher exact test was used for comparison. All statistical analyses were performed with SPSS software (Version 21.0; IBM, Armonk, New York). A *P* value < .05 was significant.

RESULTS

One hundred seventy-one eligible patients (88 men and 83 women; mean age, 69.9 years; age range, 23–92 years) were identified. Clinical characteristics of the patients are shown in Table 1.

Of the 171 patients, 127 had occlusions in the middle cerebral

artery and 44 had occlusions in the internal carotid artery. Overall, the median NIHSS score on admission was 13 (IQR, 10–16). The median time from symptom onset to endovascular therapy was 245 minutes (IQR, 190–310 minutes), and the median procedure time was 33 minutes (IQR, 20–50 minutes).

The median time from symptom onset to revascularization was 280 minutes (IQR, 223.5–352 minutes).

In the entire cohort, the median DWI-ASPECTS was 7 (IQR, 6–8); 120 patients had a DWI-ASPECTS of ≥ 7 , and 51 patients had a DWI ASPECTS of 4–6. The median NIHSS score was significantly higher in patients with a DWI-ASPECTS of 4–6 than in those with a DWI-ASPECTS of ≥ 7 (15 versus 12, *P* < .001). There was a significant correlation between DWI-ASPECTS and admission NIHSS score (*P* < .001). Age and dyslipidemia were also associated with DWI-ASPECTS (Table 1). Patients with an intermediate DWI-ASPECTS were significantly younger than those with a high DWI-ASPECTS (*P* = .014).

Treatment outcomes of patients are summarized in Table 2. Overall, successful revascularization (modified TIC1 2b or 3) was achieved in 84.2% (144/171). In the entire cohort, 47.4% (81/171) had a good outcome and 3.5% (6/171) had a symptomatic hemorrhage. Mortality was 9.4% (16/171) at 3 months.

Impact of DWI-ASPECTS on Outcomes

Three-month outcomes according to pretreatment DWI-ASPECTS are shown in the Fig 1. Receiver operating characteristic curve analysis showed that a DWI-ASPECTS of ≥ 7 was the optimal cutoff to predict a good outcome at 3 months with an area under the curve of 0.57 (95% CI, 0.483–0.656), a sensitivity of 75.3%, and a specificity of 34.4% (Fig 2). Overall, 50.8% (61/120) of patients with a DWI-ASPECTS of ≥ 7 and 39.2% (20/51) of patients with a DWI-ASPECTS of 4–6 had a good outcome; this difference was not statistically significant (*P* = .164) (Table 2).

There were also no significant differences in the rates of successful revascularization, symptomatic hemorrhage, and mortality between patients with DWI-ASPECTS of 7–10 and those with scores of 4–6.

When each year of age, each point of the NIHSS, time to treatment, symptomatic hemorrhage, DWI-ASPECTS (each score or dichotomized into 7–10 versus 4–6), and successful revascularization were selected into the multivariate logistic regression analysis, independent predictors of good outcome were age (OR, 0.941; 95% CI, 0.909–0.974; $P = .001$) and successful revascularization (OR, 8.511; 95% CI, 2.298–31.525; $P = .001$) (Table 3).

Impact of Revascularization on Outcomes among DWI-ASPECTS Subgroups

There was no significant difference in the rate of successful revascularization between patients with a DWI-ASPECTS of 7–10 and those with a DWI-ASPECTS of 4–6 (84.2% versus 84.3%). In the high DWI-ASPECTS group, a good outcome was achieved more frequently in patients with successful revascularization than in those without (58.4% versus 10.5%, $P < .001$). In this group, the OR for good outcome with successful revascularization was 11.94 (95% CI, 2.62–54.47; $P < .001$). A similar relationship was found for the intermediate DWI-ASPECTS group. In this group, a good outcome was achieved in 46.5% (20/43) of patients with successful revascularization, whereas no patients without successful revascularization had a good outcome ($P = .016$) (Fig 3).

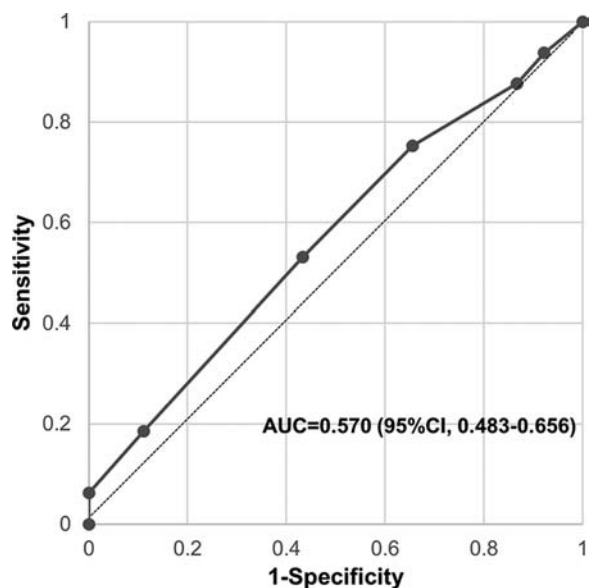


FIG 2. Receiver operating characteristic curve of DWI-ASPECTS for prediction of a good outcome (mRS 0–2 at 3 months). AUC indicates area under the curve.

Table 3: Logistic regression analysis of predictors of good outcome

	Unadjusted OR	95% CI	P Value	Adjusted OR	95% CI	P Value
Age per 1-yr increase	0.947	0.918–0.976	<.001	0.941	0.909–0.974	.001
Baseline NIHSS, per 1-point increase	0.900	0.834–0.971	.006	–	–	–
Time to treatment	1	0.996–1.004	.999	–	–	–
Modified TIC1 2b or 3	9.455	2.725–32.808	<.001	8.511	2.298–31.525	.001
Symptomatic hemorrhage	0.213	0.240–1.859	.125	–	–	–
DWI-ASPECTS, per 1-point increase	1.150	0.930–1.421	.196	–	–	–
DWI-ASPECTS ≥ 7 vs < 7	1.603	0.823–3.120	.165	–	–	–

DISCUSSION

The present study showed that treatment outcomes are not significantly different between patients with a high DWI-ASPECTS of 7–10 and those with an intermediate DWI-ASPECTS of 4–6 who underwent stent-retriever embolectomy for acute anterior circulation stroke. There were no significant differences in the rates of successful revascularization, good outcome, symptomatic hemorrhage, and mortality between the 2 groups in our study.

Several factors might explain the finding that patients with an intermediate DWI-ASPECTS benefited from stent-retriever embolectomy in our study. First, stent-retriever embolectomy can achieve a dramatically increased rate of successful recanalization of up to 80%–90% without an increased risk of symptomatic hemorrhage, compared with intra-arterial pharmacologic thrombolysis or previous mechanical approaches.²³ Recanalization is one of the most powerful independent predictors of good outcome in patients with acute stroke undergoing endovascular treatment.^{16,25–27} In our study, the overall rate of successful revascularization was 84%, and it was identical among high and intermediate DWI-ASPECTS groups. The rate of symptomatic hemorrhage was quite low (3.5%) in our study. Among the intermediate DWI-ASPECTS group, almost half of patients with recanalization had a good outcome in the present study. In addition, recanalization was one of the independent predictors of good outcome (OR = 8.512), while DWI-ASPECTS was not. This finding is consistent with the results of a previous study by Inoue et al.¹⁴ In their study, patients with anterior circulation stroke were treated with various endovascular therapies, including IV/intra-arterial thrombolysis and mechanical embolectomy with a snare or Solitaire stent, and 50% of patients with complete recanalization (Thrombolysis in Myocardial Infarction score of 3) in the subgroup with DWI-ASPECTS of ≤ 5 had a good outcome.¹⁴ Thus, the results of our study and the study of Inoue et al.¹⁴ suggest that recanalization is far more important than pretreatment DWI-ASPECTS to predict good outcome in patients with anterior circulation stroke after endovascular therapy.

Second, the DWI-ASPECTS cannot substitute for DWI lesion volume in patients with anterior circulation stroke and an intermediate ASPECTS of 4–6 because an intermediate DWI-ASPECTS corresponds to a wide range of lesion volumes.²⁸ It has been reported that DWI lesion volume is a strong predictor of clinical outcome after endovascular treatment.^{16,29} Recently, Ribo et al²⁹ suggested the concept of the maximal admission lesion volume compatible with favorable outcome, which was defined as the admission core volume above which the possibility of favorable outcome (mRS 0–2) was $< 10\%$ in patients with acute anterior circulation stroke. In their study, maximal admission lesion volume compatible with favorable outcome was found to

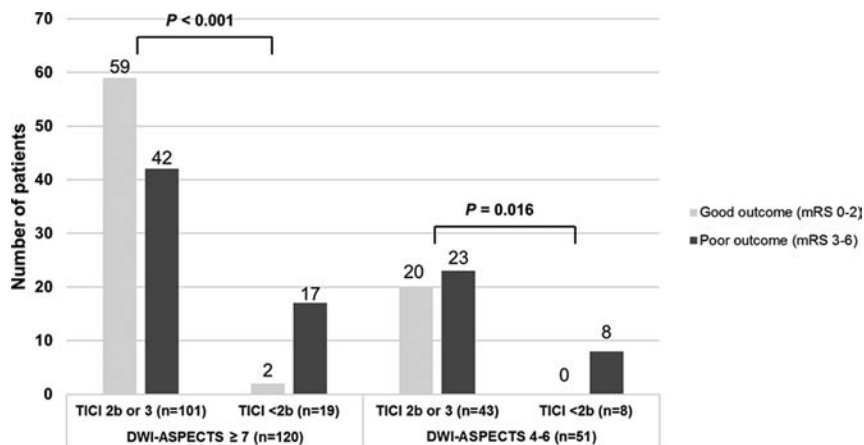


FIG 3. Impact of successful revascularization on functional outcome according to DWI-ASPECTS.

be 39 mL and was shown to be a potent predictor of favorable outcome (OR, 9.3; $P = .01$), independent of recanalization and age.²⁹

DWI-ASPECTS is commonly used as surrogate for lesion volume to save time in an acute setting. However, a previous study showed that DWI lesion volume in patients with a DWI-ASPECTS 4–6 ranged from 10 to 197 mL (median, 66 mL; IQR, 41–97 mL).²⁸ An explanation for this variability is that ASPECTS regions are weighed unequally and in favor of the striatocapsular region.³⁰ Another recent study showed that there is a striking disparity of DWI ASPECTS–DWI lesion volume correlations between the superficial (cortical) and the deep (striatocapsular) MCA regions.³¹ DWI-ASPECTS showed only a poor correlation to DWI lesion volume for stroke lesions in the striatocapsular region in that study. In this regard, patients with a DWI-ASPECTS of 4–6 but small ischemic lesion volume are likely to have a chance of a good outcome after stent-retriever embolectomy, especially when successful revascularization occurs.

Third, patients with a high DWI-ASPECTS were significantly older than those with an intermediate ASPECTS, and age was one of the independent predictors of good outcome in the present study. This might attenuate the positive effect of DWI-ASPECTS on outcome in the high DWI-ASPECTS group and thus contribute to the statistical insignificance of the DWI-ASPECTS.

Our study result has an important clinical implication, in that patients with an intermediate DWI-ASPECTS otherwise eligible for endovascular therapy, especially with scores of 4 and 5, may not be excluded from stent-retriever embolectomy or stroke trials on the basis of the DWI-ASPECTS alone. Our study suggested that the DWI-ASPECTS may not be a relevant imaging predictor of outcome in patients with anterior circulation stroke presenting within 6 hours. The DWI-ASPECTS was not significantly associated with outcomes in univariate and multivariate analysis in the present study. The results of our study are consistent with a recent study by Danière et al.¹⁸ Among 26 patients with a DWI-ASPECTS of <5 in their study, 60% of patients younger than 70 years of age had a good outcome, whereas 10% of those 70 years of age and older had a good outcome after stent-retriever embolectomy. The authors suggested that younger patients may still benefit from recanalization despite a DWI-ASPECTS of <5. In the present study, the absence of statistical significance of

DWI-ASPECTS on outcome may be partly because patients with a low DWI-ASPECTS of ≤ 3 were not included. Previous studies showing a positive correlation between DWI-ASPECTS and outcome after endovascular therapy mostly included patients with an ASPECTS of 0–3, and most of these patients had an mRS of 5–6, which might explain any statistically significant relationship between DWI-ASPECTS and outcome in their analyses.^{9,14}

Although the DWI-ASPECTS may not be suitable for prediction of infarction volume and outcome in patients with intermediate-to-high ASPECTS, it can still be used to predict a lesion volume cut-

point of >100 mL, which corresponds to a traditional concept of greater than one-third of the middle cerebral artery territory and serves as an exclusion criterion for endovascular therapy in ongoing trials. In a study by de Margerie-Mellon et al.,²⁸ 94% of patients (32/34) with a DWI-ASPECTS of ≤ 3 had a lesion volume of >100 mL and the lowest lesion volume in those patients was 93 mL. While DWI-ASPECTS may not predict outcome in patients with acute anterior circulation stroke, it may be useful for defining the presence of a benign imaging pattern to establish candidacy in the new embolectomy era.

Our study has several limitations, including a retrospective and monocentric study design. We did not measure DWI lesion volume and thus did not examine the relationship between lesion volume and ASPECTS. However, that relationship has been well documented in previous studies,^{28,31} and the aim of our study was to investigate whether the DWI-ASPECTS can be used as an imaging predictor of clinical outcome after stent-retriever embolectomy in anterior circulation stroke. The patients were selected for endovascular therapy by using perfusion imaging and a target mismatch profile. The results of the study might be different if patients with a nontarget mismatch profile were included. Finally, the patient number in the high DWI-ASPECTS group was larger than that of the intermediate group.

CONCLUSIONS

Our study suggested that treatment outcomes were not different between patients with a high DWI-ASPECTS of 7–10 and those with an intermediate DWI-ASPECTS of 4–6 who underwent stent-retriever embolectomy for acute anterior circulation stroke. Thus, patients with intermediate DWI-ASPECTS otherwise eligible for endovascular therapy may not be excluded from stent-retriever embolectomy or stroke trials.

REFERENCES

1. Berkhemer OA, Fransen PS, Beumer D, et al. **A randomized trial of intraarterial treatment for acute ischemic stroke.** *N Engl J Med* 2015; 372:11–20 CrossRef Medline
2. Campbell BC, Mitchell PJ, Kleinig TJ, et al; EXTEND-IA Investigators. **Endovascular therapy for ischemic stroke with perfusion-imaging selection.** *N Engl J Med* 2015;372:1009–18 CrossRef Medline
3. Goyal M, Demchuk AM, Menon BK, et al; ESCAPE Trial Investiga-

- tors. **Randomized assessment of rapid endovascular treatment of ischemic stroke.** *N Engl J Med* 2015;372:1019–30 CrossRef Medline
4. Saver JL, Goyal M, Bonafe A, et al; SWIFT PRIME Investigators. **Stent-retriever thrombectomy after intravenous t-PA vs. t-PA alone in stroke.** *N Engl J Med* 2015;372:2285–95 CrossRef Medline
 5. Jovin TG, Chamorro A, Cobo E, et al; REVASCAT Trial Investigators. **Thrombectomy within 8 hours after symptom onset in ischemic stroke.** *N Engl J Med* 2015;372:2296–306 CrossRef Medline
 6. Yoo AJ, Chaudhry ZA, Nogueira RG, et al. **Infarct volume is a pivotal biomarker after intra-arterial stroke therapy.** *Stroke* 2012;43:1323–30 CrossRef Medline
 7. Shi ZS, Liebeskind DS, Xiang B, et al; Multi MERCI, TREVO, and TREVO 2 Investigators. **Predictors of functional dependence despite successful revascularization in large-vessel occlusion strokes.** *Stroke* 2014;45:1977–84 CrossRef Medline
 8. Linfante I, Starosciak AK, Walker GR, et al. **Predictors of poor outcome despite recanalization: a multiple regression analysis of the NASA registry.** *J Neurointerv Surg* 2015 Jan 6. [Epub ahead of print] CrossRef Medline
 9. McTaggart RA, Jovin TG, Lansberg MG, et al; DEFUSE 2 Investigators. **Alberta stroke program early computed tomographic scoring performance in a series of patients undergoing computed tomography and MRI: reader agreement, modality agreement, and outcome prediction.** *Stroke* 2015;46:407–12 CrossRef Medline
 10. Barber PA, Demchuk AM, Zhang J, et al. **Validity and reliability of a quantitative computed tomography score in predicting outcome of hyperacute stroke before thrombolytic therapy: ASPECTS Study Group—Alberta Stroke Programme Early CT Score.** *Lancet* 2000;355:1670–74 CrossRef Medline
 11. Barber PA, Hill MD, Eliasziw M, et al; ASPECTS Study Group. **Imaging of the brain in acute ischaemic stroke: comparison of computed tomography and magnetic resonance diffusion-weighted imaging.** *J Neurol Neurosurg Psychiatry* 2005;76:1528–33 CrossRef Medline
 12. Butcher K, Parsons M, Allport L, et al; EPITHET Investigators. **Rapid assessment of perfusion-diffusion mismatch.** *Stroke* 2008;39:75–81 CrossRef Medline
 13. Kimura K, Iguchi Y, Shibazaki K, et al. **Large ischemic lesions on diffusion-weighted imaging done before intravenous tissue plasminogen activator thrombolysis predicts a poor outcome in patients with acute stroke.** *Stroke* 2008;39:2388–91 CrossRef Medline
 14. Inoue M, Olivot JM, Labreuche J, et al. **Impact of diffusion-weighted imaging Alberta stroke program early computed tomography score on the success of endovascular reperfusion therapy.** *Stroke* 2014;45:1992–98 CrossRef Medline
 15. Vogt G, Laage R, Shuaib A, et al; VISTA Collaboration. **Initial lesion volume is an independent predictor of clinical stroke outcome at day 90: an analysis of the Virtual International Stroke Trials Archive (VISTA) database.** *Stroke* 2012;43:1266–72 CrossRef Medline
 16. Olivot JM, Mosimann PJ, Labreuche J, et al. **Impact of diffusion-weighted imaging lesion volume on the success of endovascular reperfusion therapy.** *Stroke* 2013;44:2205–11 CrossRef Medline
 17. Lin K, Lee SA, Zink WE. **What ASPECTS value best predicts the 100-mL threshold on diffusion weighted imaging? Study of 150 patients with middle cerebral artery stroke.** *J Neuroimaging* 2011;21:229–31 CrossRef Medline
 18. Danière F, Lobotesis K, Machi P, et al. **Patient selection for stroke endovascular therapy—DWI-ASPECTS thresholds should vary among age groups: insights from the RECAST study.** *AJNR Am J Neuroradiol* 2015;36:32–39 CrossRef Medline
 19. Singer OC, Kurre W, Humpich MC, et al; MR Stroke Study Group Investigators. **Risk assessment of symptomatic intracerebral hemorrhage after thrombolysis using DWI-ASPECTS.** *Stroke* 2009;40:2743–48 CrossRef Medline
 20. Nezu T, Koga M, Kimura K, et al. **Pretreatment ASPECTS on DWI predicts 3-month outcome following rt-PA: SAMURAI rt-PA Registry.** *Neurology* 2010;75:555–61 CrossRef Medline
 21. Aoki J, Kimura K, Shibazaki K, et al. **DWI-ASPECTS as a predictor of dramatic recovery after intravenous recombinant tissue plasminogen activator administration in patients with middle cerebral artery occlusion.** *Stroke* 2013;44:534–37 CrossRef Medline
 22. Yoon W, Jung MY, Jung SH, et al. **Subarachnoid hemorrhage in a multimodal approach heavily weighted toward mechanical embolectomy with Solitaire stent in acute stroke.** *Stroke* 2013;44:414–19 CrossRef Medline
 23. Kim SK, Yoon W, Moon SM, et al. **Outcomes of manual aspiration thrombectomy for acute ischemic stroke refractory to stent-based embolectomy.** *J Neurointerv Surg* 2015;7:473–77 CrossRef Medline
 24. Zaidat OO, Yoo AJ, Khatri P, et al; STIR Revascularization working group, STIR Thrombolysis in Cerebral Infarction (TICI) Task Force. **Recommendations on angiographic revascularization grading standards for acute ischemic stroke: a consensus statement.** *Stroke* 2013;44:2650–63 CrossRef Medline
 25. Rha JH, Saver JL. **The impact of recanalization on ischemic stroke outcome: a meta-analysis.** *Stroke* 2007;38:967–73 CrossRef Medline
 26. Abilleira S, Cardona P, Ribó M, et al; Catalan Stroke Code and Reperfusion Consortium. **Outcomes of a contemporary cohort of 536 consecutive patients with acute ischemic stroke treated with endovascular therapy.** *Stroke* 2014;45:1046–52 CrossRef Medline
 27. Yoon W, Kim SK, Park MS, et al. **Endovascular treatment and the outcomes of atherosclerotic intracranial stenosis in patients with hyperacute stroke.** *Neurosurgery* 2015;76:680–86; discussion 686 CrossRef Medline
 28. de Margerie-Mellon C, Turc G, Tisserand M, et al. **Can DWI-ASPECTS substitute for lesion volume in acute stroke?** *Stroke* 2013;44:3565–67 CrossRef Medline
 29. Ribo M, Tomasello A, Lemus M, et al. **Maximal admission core lesion compatible with favorable outcome in acute stroke patients undergoing endovascular procedures.** *Stroke* 2015;46:2849–52 CrossRef Medline
 30. Phan TG, Donnan GA, Koga M, et al. **The ASPECTS template is weighted in favor of the striatocapsular region.** *Neuroimage* 2006;31:477–81 CrossRef Medline
 31. Schröder J, Cheng B, Ebinger M, et al; STIR and VISTA Imaging Investigators. **Validity of acute stroke lesion volume estimation by diffusion-weighted imaging—Alberta Stroke Program Early Computed Tomographic Score depends on lesion location in 496 patients with middle cerebral artery stroke.** *Stroke* 2014;45:3583–88 CrossRef Medline

Angiographic Structural Differentiation between Native Arteriogenesis and Therapeutic Syngangiosis in Intracranial Arterial Steno-Occlusive Disease

Y.C. Ooi, A.N. Laiwalla, R. Liou, and N.R. Gonzalez



ABSTRACT

BACKGROUND AND PURPOSE: Encephaloduroarteriosyngangiosis has been shown to generate collateral vessels from the extracranial-to-intracranial circulation in patients with Moyamoya disease and intracranial arterial steno-occlusive disease. The mechanisms involved are not well-understood. We hypothesized that angiogenesis is the leading mechanism forming collaterals after encephaloduroarteriosyngangiosis because there are no pre-existing connections. Angiogenesis-generated collaterals should exhibit higher architectural complexity compared with innate collaterals.

MATERIALS AND METHODS: Pre- and postoperative digital subtraction angiograms were analyzed in patients enrolled in a prospective trial of encephaloduroarteriosyngangiosis surgery. Branching angioscore, tortuosity index, and local connected fractal dimension were compared between innate and postoperative collaterals.

RESULTS: One hundred one angiograms (50 preoperative, 51 postoperative) were analyzed from 44 patients (22 with intracranial atherosclerosis and 22 with Moyamoya disease). There was a significantly higher median branching angioscore (13 versus 4, $P < .001$) and a lower median tortuosity index (1.08 versus 1.76, $P < .001$) in the encephaloduroarteriosyngangiosis collaterals compared with innate collaterals. Higher mean local fractal dimension peaks (1.28 ± 0.1 versus 1.16 ± 0.11 , $P < .001$) were observed in the encephaloduroarteriosyngangiosis collaterals compared with innate collaterals for both intracranial atherosclerosis ($P < .001$) and Moyamoya disease ($P < .001$) groups. The observed increase in high connectivity was greater in the intracranial atherosclerosis group compared with patients with Moyamoya disease ($P = .01$).

CONCLUSIONS: The higher median branching angioscore and local connected fractal dimension, along with the lower median tortuosity index of encephaloduroarteriosyngangiosis collaterals, are consistent with the greater complexity observed in the process of sprouting and splitting associated with angiogenesis.

ABBREVIATIONS: EDAS = encephaloduroarteriosyngangiosis; ICAS = intracranial atherosclerosis; ICASD = intracranial arterial steno-occlusive disease; LCFD = local connected fractal dimension; MMD = Moyamoya disease

Intracranial arterial steno-occlusive disease (ICASD) is one of the most common vascular abnormalities found worldwide in patients with acute ischemic stroke.¹ ICASD accounts for 10% of strokes in whites and as much as 67% of strokes in Asian, His-

panic, and black patients.¹ ICASD carries a worse prognosis than other stroke etiologies, with a rate of recurrent stroke and death between 15% and 25% per year despite maximal medical therapy.² While patients with ICASD develop spontaneous collaterals to areas of ischemia, these alternative conduits fail with time and lead to a progression of their symptoms, resulting in transient ischemic attacks, strokes, or even death.³ Indirect cerebral revascularization via encephaloduroarteriosyngangiosis (EDAS) has been successful in establishing collateral flow in several forms of ICASD, including Moyamoya disease (MMD) and intracranial atherosclerosis (ICAS).^{4,5} However, the mechanisms involved in

Received June 30, 2015; accepted after revision December 1.

From the Departments of Neurosurgery (Y.C.O., A.N.L., R.L., N.R.G.) and Radiology (N.R.G.), David Geffen School of Medicine at the University of California, Los Angeles, Los Angeles, California.

This work was supported by the Ruth and Raymond Stotter Endowed Chair in Neurosurgery and the National Institutes of Health—National Institute of Neurological Disorders and Stroke award, K23NS079477.

The authors have no personal, financial, or institutional interest in any of the drugs, materials, or devices described in this article.

Paper previously presented in part at: Annual Scientific Meeting of the American Association of Neurological Surgeons, May 2–6, 2015; Washington, DC; and Annual Meeting of the California Association of Neurological Surgeons, January 16–18, 2015; Newport Beach, California.

Please address correspondence to Nestor R. Gonzalez, MD, David Geffen School of Medicine at UCLA, 300 Stein Plaza, Suite 562, Los Angeles, CA 90095; e-mail: ngonzalez@mednet.ucla.edu

Indicates open access to non-subscribers at www.ajnr.org

<http://dx.doi.org/10.3174/ajnr.A4675>

innate collateral formation and neovascularization induced by EDAS are not fully understood.

Innate collateral vessels that occur spontaneously in ICASD are formed by arteriogenesis.⁶ The formation of collaterals via arteriogenesis is driven by sheer stress and involves the recruitment and enlargement of preexisting vessels in a flow-dependent hypoxia-independent process.⁶ Conversely, due to the lack of preexisting collateral vessels between the portions of the external carotid artery used during EDAS and the ICA, formation of EDAS should be primarily driven by angiogenesis.⁷ Angiogenesis is induced by hypoxia and involves the formation of new collateral vessels via sprouting or splitting from preexisting vascular structures, resulting in collaterals of greater complexity.

A better understanding of the differences in morphology and clinical implications of these features between spontaneously occurring collaterals in ICASD and new collaterals formed after EDAS may provide valuable insight into ICASD and its treatment. We designed an angiography-based study by using patients from a prospective trial of EDAS surgery to test the hypothesis that neovascularization generated after EDAS has greater angioarchitectural complexity compared with spontaneously formed innate collaterals in ICASD. To quantify the complexity of the vascular trees, we measured branching pattern, tortuosity, and fractal connectivity.

MATERIALS AND METHODS

Pre- and postoperative digital subtraction angiograms were analyzed in patients enrolled in a prospective trial of EDAS surgery (Surgical Indirect Revascularization for Symptomatic Intracranial Arterial Stenosis [ERSIAS] trial; clinicaltrials.gov identifier: NCT01819597). The study was conducted with institutional review board approval. All patients enrolled in the study had experienced either a TIA or nonsevere stroke. All EDAS operations were performed by 1 of 2 senior vascular neurosurgeons. EDAS is a form of indirect revascularization or external carotid–internal carotid bypass. It involves the dissection and relocation of superficial temporal artery and/or middle meningeal artery branches. These arterial branches are separated from their surrounding tissues under microscopic visualization, rerouted through a craniotomy, and then placed intracranially in close proximity to branches of the MCA. The MCA branches are dissected in the arachnoid space, and the superficial temporal artery and/or middle meningeal artery branches are kept in position with microsutures to the arachnoid or dural cuffs, maintaining close contact between the external carotid and MCA branches.^{2,4,5} Preoperative angiograms were obtained within a week before the operation. Postoperative angiograms were obtained at the 3-, 6-, and 12-month intervals postoperatively. The most recent postoperative angiogram available was used for this study. All angiograms were obtained by a senior neuroradiologist, by using standard lateral and posterior-anterior views at 3 frames per second. Selective ICA and external carotid artery injections were performed to minimize vessel overlap.

Innate collaterals for patients with ICAS were defined by first establishing the angiographic limits among the major branches of the anterior cerebral artery, middle cerebral artery, and posterior cerebral artery territories and then identifying leptomeningeal

collateral vessels crossing these territories (Figs 1 and 2). For patients with MMD, “innate collaterals” were defined as deep collaterals with a Moyamoya-like appearance. “EDAS collaterals” were defined as new branches observed from the superficial temporal artery or middle meningeal artery that produced cerebral blush and subsequently drained into cerebral veins. Selected collateral vessels were isolated by dynamic delineation for further analysis. With dynamic delineation, vessel flow was followed through the arterial phases of the catheter angiogram, establishing the continuity of vessels. These vessels were traced and marked, excluding any overlapping and/or underlying vessels. Delineated vessels were analyzed by 3 independent observers, including 2 neuroradiologists and 1 senior neuroradiologist. The interobserver agreement (κ) was calculated. Marked vessels were converted to a binary black and white image (Fig 3). All image processing was performed by using ImageJ software (National Institutes of Health, Bethesda, Maryland).⁸

Angioarchitectural differences between innate and EDAS collaterals were evaluated by comparing the quantitative measures of branching pattern and tortuosity. Branching pattern was measured by using the branching angioscore (Fig 4).⁹ A 10,000-pixel-per-box grid was overlaid on the delineated vessels. The branching angioscore was defined as the total number of branching points within a single box. This was measured in all boxes within the grid containing portions of the delineated vessel, and the box with the highest branching angioscore was selected. Tortuosity was measured with the artery tortuosity index, by using the longest branch of the delineated vessel between 2 branching points (Fig 5).¹⁰ The artery tortuosity index was calculated by the quotient of the actual vessel length and the straight-line distance of a delineated vessel between 2 branching points. Group indices were compared with the Wilcoxon rank sum test.

The local connected fractal dimension (LCFD) of delineated vessels was measured by using the Fraclac plugin for Image J.¹¹ LCFD provides an index of complexity by measuring changes in connectivity with varying scales, allowing quantification of non-Euclidean geometric patterns. Fraclac performs LCFD analysis by selecting a seed pixel on the marked vessel and calculating the total number of pixels connected to the seed in a square area around the seed. The process is repeated for concentric squares of different sizes. On the basis of the rate of change of connected pixels within the different sizes of squares, it computes the fractal dimension for that pixel (Fig 6). This process is iterated over each pixel of the delineated vessel. High connectivity was defined as $LCFD \geq 1.2$. Log-transformations were used for skewed data. Comparison of means was performed by using a 2-tailed unpaired *t* test for the aggregate group and a 2-tailed paired *t* test for matched samples for MMD and ICAS. The Spearman correlation was used to test the associations among the variables.

RESULTS

The study population included 44 patients (4–84 years of age; mean, 35 ± 19.2 years), 30 females (68%) and 14 males (32%). Twenty-two patients had ICAS (7–84 years of age; mean, 49 ± 16.9 years) with stenosis in the intracranial ICA and/or MCA. Twenty-two patients had MMD (4–56 years of age; mean, 29 ± 14.6 years), with 13 patients (59%) at Suzuki stage 3 and 9

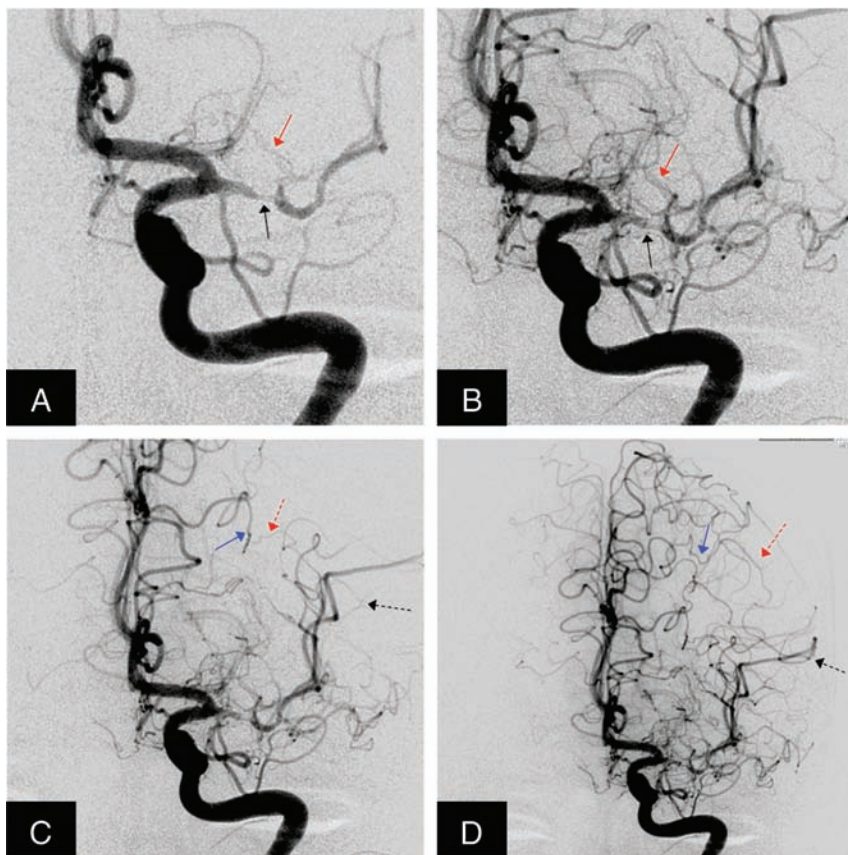


FIG 1. Cerebral angiogram anteroposterior views of the left internal carotid artery injection in a patient with intracranial atherosclerosis involving the middle cerebral artery that identify innate deep collaterals and leptomeningeal collaterals. Early arterial phase (A) and late arterial phase (B) show stenosis involving the middle cerebral artery (black arrow), with collaterals arising from the medial lenticulostriate arteries and connecting to the lateral lenticulostriate arteries, corresponding to deep collaterals providing flow to the MCA circulation. In the midarterial phase (C) and late arterial phase (D), normal branches of the anterior cerebral artery (blue arrow) are seen extending beyond the normal watershed territory. There is a delay in filling of the MCA branches (black dotted arrow). Leptomeningeal collaterals (red dotted arrow) are seen between the ACA and MCA branches.

patients (41%) at Suzuki stage 4. The mean age in the MMD group was significantly lower than that of the ICAS group ($P < .001$). There were 15 females (68%) in both the ICAS and MMD groups. Seven patients required bilateral EDAS (6 females, 1 male). Of 102 angiograms (51 preoperative, 51 postoperative), 1 preoperative angiogram was excluded due to a lack of identifiable collaterals. The interobserver agreement (κ) for delineated vessels in both pre- and postoperative angiograms was 0.813.

Branching Angioscore

The branching angioscores were not normally distributed. There was a significantly higher median branching angioscore in the EDAS collaterals compared with the innate collaterals (13 versus 4, $P < .001$). This was significantly different for both the ICAS and MMD groups (ICAS: 11 versus 4, $P < .001$; MMD: 15 versus 5, $P < .001$). The Table provides additional details of the branching angioscores.

Tortuosity Index

The tortuosity indices were not normally distributed. There was a significantly lower median tortuosity index in the EDAS collaterals compared with the innate collaterals (1.08 versus 1.76, $P < .001$).

.001). This was significantly different for both the ICAS and MMD groups (ICAS: 1.91 versus 1.08, $P < .001$; MMD: 1.73 versus 1.09, $P < .001$).

Local Connected Fractal Dimension

The LCFDs were normally distributed. There was a significantly higher mean LCFD in the EDAS collaterals compared with the innate collaterals (1.28 ± 0.1 versus 1.16 ± 0.11 , $P < .001$). The proportion of high connectivity (LCFD ≥ 1.2) in the entire study population was significantly greater in the EDAS collaterals ($P < .001$) than in the innate collaterals. In the ICAS group, the mean LCFD was significantly higher in the EDAS collaterals (1.27 ± 0.11) versus innate collaterals (1.13 ± 0.12 , $P < .001$). This relationship also held in the MMD group, with the mean LCFD in EDAS collaterals being 1.29 ± 0.09 versus 1.17 ± 0.1 in the innate collaterals ($P < .001$). The proportion of high connectivity was also greater in the MMD group ($P < .001$) and the ICAS group ($P < .001$) separately. The Spearman correlation showed a strong association between LCFD peaks and both the branching angioscore ($P < .001$) and the tortuosity index ($P < .001$).

DISCUSSION

Indirect cerebral revascularization via EDAS has been shown to establish new collaterals through the development of vessels from the external carotid artery to the internal carotid artery in patients with ICASD.^{4,5} This phenomenon has been extensively described in the literature¹²⁻²¹; however, the mechanism involved in the formation of EDAS collaterals remains poorly understood. This is the first study to quantitatively compare the angioarchitecture of newly formed EDAS collaterals with that of existing innate collaterals in patients with ICASD, providing insight into the underlying mechanisms involved in collateral vessel formation.

Angiogenesis, primarily driven by hypoxia, involves the formation of new vessels through sprouting and splitting from pre-existing vascular structures.^{7,22} Hypoxia regulates angiogenesis by activation of the hypoxia-inducible factor, which, in turn, modifies a variety of pro- and antiangiogenic factors, causing a shift toward an angiogenic phenotype.²³⁻²⁵ Animal studies performed by Luo et al,²⁶ have shown that despite this shift toward a proangiogenic state, hypoxia ultimately leads to the inhibition of new vessel formation by brain endothelial cells. The failure to produce a neovascularization response has been attributed to the highly specialized nature of brain endothelial cells and the pleiotropic effects of the angiogenic factors produced by them.²⁶ Native collaterals, however, occur via a process known as arteriogenesis,

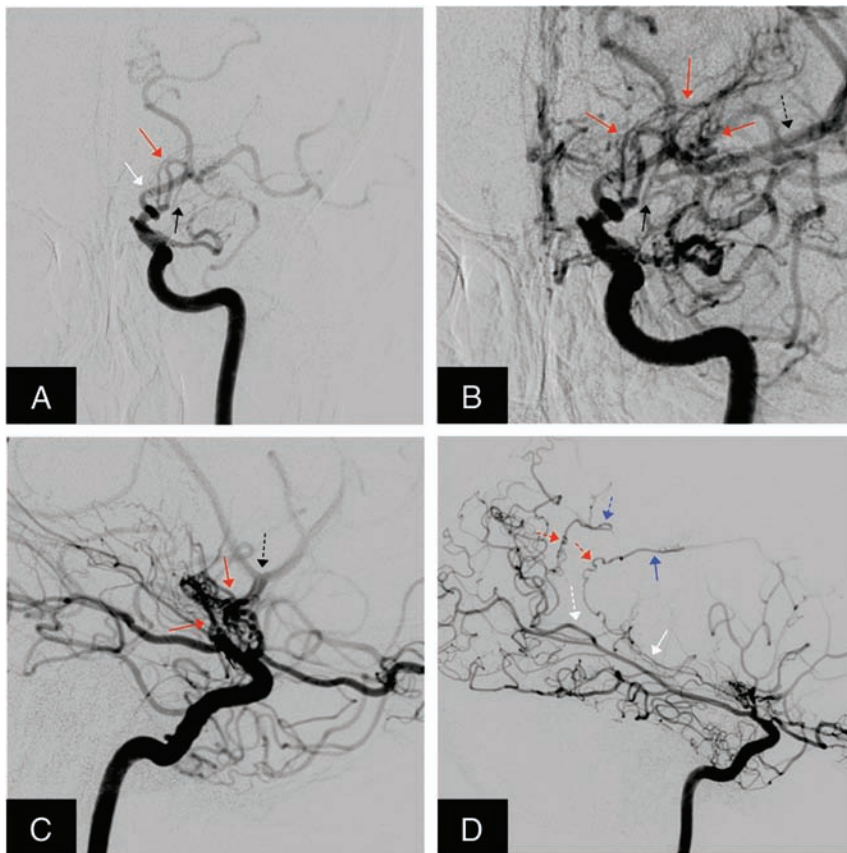


FIG 2. Cerebral angiogram anteroposterior (A and B) and lateral (C and D) views in a patient with Moyamoya disease with narrowing of the middle cerebral artery, identify innate deep collaterals and leptomeningeal collaterals. Early arterial phase (A) and late arterial phase (B) show normal posterior cerebral artery (white arrow), stenosis involving the middle cerebral artery (black arrow), with deep collaterals arising from the anterior choroidal artery (red arrow), providing collateral flow to the MCA, which fills in a delayed fashion (black dotted arrow). Early arterial phase (C) demonstrates deep collaterals from the anterior choroidal artery (red arrow), providing collateral flow to the MCA, which fills in a delayed fashion (black dotted arrow). Late arterial phase (D) shows leptomeningeal collaterals (red dotted arrows) arising from branches of the anterior choroidal artery (white arrow), providing collateral flow to the distal portion of the pericallosal artery (blue arrow), which fills in a delayed fashion. Also visible are leptomeningeal collaterals (red dotted arrows) arising from posterior cerebral artery (white dotted arrow), supplying the distal portion of the callosomarginal artery (blue dotted arrow).

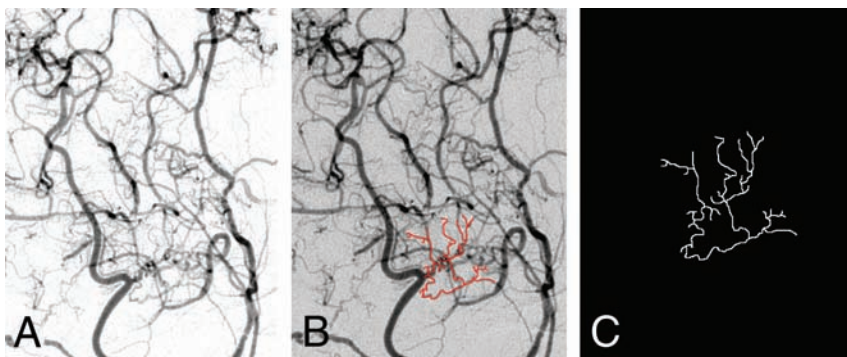


FIG 3. Isolation of collaterals by dynamic delineation. Selected vessels are followed through the arterial phase of the digital subtraction angiograms to establish continuity of vessels. Vessels are traced and marked, excluding other overlapping or underlying vessels; then they are converted to a binary black and white image. A, Selective postoperative lateral external carotid artery injection. B, Branches of the superficial temporal artery traced and marked. C, Converted binary image.

which is flow-dependent and hypoxia-independent. In arteriogenesis, preexisting vessels with stenotic segments are exposed to increased shear stress due to a high-pressure gradient between 2 vascular territories.^{6,22} Arteriogenesis involves the recruitment and enlargement of preexisting vessels, leading to the formation of large tortuous vessels. Because sprouting and splitting are not part of this process, it is expected that vessels formed by arteriogenesis will be of lower complexity than those formed by angiogenesis.

Our study shows that there is a distinct difference in angioarchitecture between postsurgical EDAS collaterals and innate collaterals. These differences were detected by analyzing 3 different aspects of the morphology of the collaterals: the branching pattern, tortuosity, and fractal connectivity. While these have been previously established in the description of vascular morphology in the systemic circulation,^{9,10,27,28} this is the first study to use all 3 indices in tandem to differentiate and characterize cerebrovasculature. The branching angioscore has previously been used as a marker for angiogenesis.⁹ The tortuosity index has proved to be useful in analyzing coronary arteries to differentiate patients with chronic pressure and volume overload and as a marker of adverse outcomes in connective tissue disorders.^{10,27,28} Local connected fractal dimensions have been used previously to compare differences in retinal vasculature and to differentiate oral epithelium according to the degree of malignancy.^{29,30}

Imaging study of the angioarchitecture of cerebral vasculature poses a challenge due to the 3D orientation of intracranial vessels. While 3D imaging such as CTA and MRA can provide adequate representation of the angioarchitecture, these imaging modalities have a limited resolution for the evaluation of new collaterals.^{31,32} For optimal resolution, we selected conventional angiography, which has a spatial resolution of 200 μm . However, catheter angiograms have the potential limitation of obscuring the true angioarchitecture of cerebral vessels due to overlapping vasculature when projected on a 2D image. By obtaining selective external carotid ar-

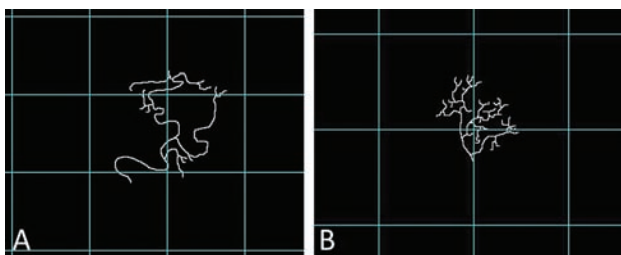


FIG 4. A 10,000-pixel-per-box grid is overlaid on the delineated vessels. The branching angioscore is defined as the total number of branching points within a single box. This is measured in all boxes within the grid containing portions of the delineated vessel, and the box with the highest branching angioscore is selected (highlighted in red). A, Innate collaterals. B, EDAS collaterals.

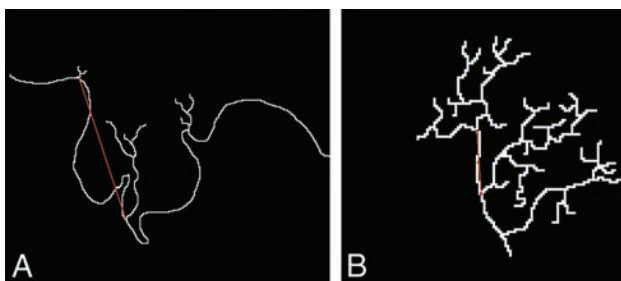


FIG 5. The artery tortuosity index is measured by using the longest branch of the delineated vessel between 2 branching points. The artery tortuosity index is calculated by the quotient of the actual vessel length and the straight-line distance (red line) of a delineated vessel between 2 branching points. A, Innate collaterals. B, EDAS collaterals.

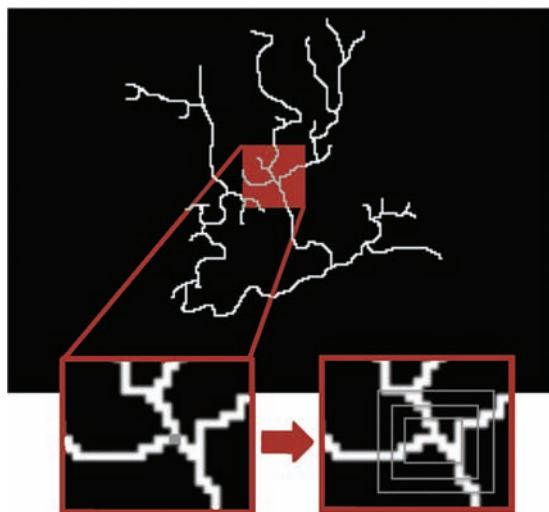


FIG 6. Local connected fractal dimension of delineated vessels. The Fraclac plugin for ImageJ selects seed pixels and measures the total number of connected pixels within a predetermined square area. The process is repeated for increasing concentric areas, and the rate of change of connected pixels is used to calculate the LCFD. The process is repeated for each pixel of the delineated vessel. High connectivity is defined as $LCFD \geq 1.2$.

tery and ICA images, we were able to minimize vessel overlap. Furthermore, dynamic delineation allowed us to isolate targeted vessels for analysis by observing the sequential filling of vessels with time, and by tracing these, we established the continuity of the individual vessels. This method is subject to interobserver

Branching angioscore, tortuosity index, and local connected fractal dimension¹ by collateral type

	Type of Collateral	
	Innate	EDAS
No.	51	51
Branching angioscore		
Mean	4.61	14.12
SD	2.40	5.27
Median	4	13
IQR	3	9
Tortuosity index		
Mean	1.81	1.09
SD	0.66	0.07
Median	1.76	1.08
IQR	0.71	0.07
Peak LCFD ¹		
Mean	1.16	1.28
SD	0.11	0.1
Median	1.16	1.27
IQR	0.17	0.12

Note:—IQR indicates interquartile range.

variability; however, observations were validated internally with good interobserver reliability.

Our study shows that innate collaterals in patients with ICASD display the characteristic high tortuosity and low branching seen in arteriogenesis, affirming the hypothesis that spontaneously occurring collaterals in the brain occur via a hypoxia-independent process and rely on preexisting networks of vessels. In contrast, postsurgical EDAS collaterals have a significantly higher vascular complexity and branching rate. This feature is consistent with the complex branching pattern observed with the formation of new vessels through sprouting and splitting from a parent vessel via angiogenesis. The results of our study support arteriogenesis as the primary mechanism of innate collateral vessel formation within cerebral vasculature in the setting of intracranial arterial stenosis. Our results also suggest that the process of angiogenesis occurs in adult patients with ICASD, leading to the formation of new collateral vessels after EDAS.

Despite the encouraging findings, further studies are necessary to determine whether the postsurgical EDAS vessels are newly formed or correspond to the integration of native vascular networks through new small connections from the external carotid artery. Both scenarios could lead to the same pattern of high LCFD and branching angioscore because the same process forms the vessels of the brain. The low tortuosity index seen in postsurgical collaterals suggests that despite the gradient pressure, these vessels do not become tortuous as seen in native collaterals. This finding may indicate that these vessels do not have high shear stress. Reduced tortuosity and shear stress could be associated with the absence of hemorrhages from EDAS collaterals as shown in our prior work after up to 7 years of follow-up.⁴

CONCLUSIONS

The higher complexity and branching rate of collateral vessels formed after EDAS, indicative of sprouting and splitting from a parent vessel, suggest angiogenesis as the primary mechanism of EDAS collateralization. The lower complexity and branching rate and the higher tortuosity index of innate collaterals in patients with ICASD, consistent with large tortuous vessels, suggest

that arteriogenesis is the primary mechanism for innate collateralization.

Disclosures: Nestor R. Gonzalez—RELATED: Grant: Ruth and Raymond Stotter Endowed Chair in Neurosurgery and the National Institutes of Health—National Institute of Neurological Disorders and Stroke award, K23NS079477. Comments: Research reported in this publication was supported by the National Institute of Neurological Disorders and Stroke of the National Institutes of Health under award No. K23NS079477. The content is solely the responsibility of the authors and does not necessarily represent the official views of the National Institutes of Health.

REFERENCES

1. Gorelick PB, Wong KS, Bae HJ, et al. **Large artery intracranial occlusive disease: a large worldwide burden but a relatively neglected frontier.** *Stroke* 2008;39:2396–99 CrossRef Medline
2. Gonzalez NR, Liebeskind DS, Dusick JR, et al. **Intracranial arterial stenoses: current viewpoints, novel approaches, and surgical perspectives.** *Neurosurg Rev* 2013;36:175–84; discussion 184–85 CrossRef Medline
3. Liebeskind DS, Cotsonis GA, Saver JL, et al; Warfarin-Aspirin Symptomatic Intracranial Disease (WASID) Investigators. **Collaterals dramatically alter stroke risk in intracranial atherosclerosis.** *Ann Neurol* 2011;69:963–74 CrossRef Medline
4. Dusick JR, Gonzalez NR, Martin NA. **Clinical and angiographic outcomes from indirect revascularization surgery for Moyamoya disease in adults and children: a review of 63 procedures.** *Neurosurgery* 2011;68:34–43; discussion 43 CrossRef Medline
5. Dusick JR, Liebeskind DS, Saver JL, et al. **Indirect revascularization for nonmoyamoya intracranial arterial stenoses: clinical and angiographic outcomes.** *J Neurosurg* 2012;117:94–102 CrossRef Medline
6. Schirmer SH, van Nooijen FC, Piek JJ, et al. **Stimulation of collateral artery growth: travelling further down the road to clinical application.** *Heart* 2009;95:191–97 CrossRef Medline
7. Saito N, Imai H. **Insights on the revascularization mechanism for treatment of Moyamoya disease based on the histopathologic concept of angiogenesis and arteriogenesis.** *World Neurosurg* 2011;75:204–05 CrossRef Medline
8. Schneider CA, Rasband WS, Eliceiri KW. **NIH Image to ImageJ: 25 years of image analysis.** *Nat Methods* 2012;9:671–75 Medline
9. Gowdak LH, Poliakova L, Wang X, et al. **Adenovirus-mediated VEGF(121) gene transfer stimulates angiogenesis in normoperfused skeletal muscle and preserves tissue perfusion after induction of ischemia.** *Circulation* 2000;102:565–71 Medline
10. Morris SA, Orbach DB, Geva T, et al. **Increased vertebral artery tortuosity index is associated with adverse outcomes in children and young adults with connective tissue disorders.** *Circulation* 2011;124:388–96 CrossRef Medline
11. Karperien A. FracLac for Image J. <http://rsb.info.nih.gov/ij/plugins/fraclac/FLHelp/Introduction.htm>. Accessed March 30, 2015
12. Sakamoto S, Ohba S, Shibukawa M, et al. **Angiographic neovascularization after bypass surgery in Moyamoya disease: our experience at Hiroshima University Hospital.** *Hiroshima J Med Sci* 2007;56:29–32 Medline
13. Matsushima Y, Aoyagi M, Fukai N, et al. **Angiographic demonstration of cerebral revascularization after encephalo-duro-arterio-synangiosis (EDAS) performed on pediatric Moyamoya patients.** *Bull Tokyo Med Dent Univ* 1982;29:7–17 Medline
14. Kim DS, Kang SG, Yoo DS, et al. **Surgical results in pediatric Moyamoya disease: angiographic revascularization and the clinical results.** *Clin Neurol Neurosurg* 2007;109:125–31 CrossRef Medline
15. Matsushima Y, Suzuki R, Ohno K, et al. **Angiographic revascularization of the brain after encephaloduroarteriosynangiosis: a case report.** *Neurosurgery* 1987;21:928–34 Medline
16. Demartini Z Jr, Martins RT, Rocha CE, et al. **Surgical treatment of Moyamoya disease in children.** *Arq Neuropsiquiatr* 2008;66:276–78 Medline
17. Veeravagu A, Guzman R, Patil CG, et al. **Moyamoya disease in pediatric patients: outcomes of neurosurgical interventions.** *Neurosurg Focus* 2008;24:E16 CrossRef Medline
18. O'Donnell TF Jr, Callow AD, Scott G, et al. **Ultrasound characteristics of recurrent carotid disease: hypothesis explaining the low incidence of symptomatic recurrence.** *J Vasc Surg* 1985;2:26–41 Medline
19. Yamada I, Matsushima Y, Suzuki S. **Childhood Moyamoya disease before and after encephalo-duro-arterio-synangiosis: an angiographic study.** *Neuroradiology* 1992;34:318–22 Medline
20. Scott RM, Smith JL, Robertson RL, et al. **Long-term outcome in children with Moyamoya syndrome after cranial revascularization by pial synangiosis.** *J Neurosurg* 2004;100(2 Suppl Pediatrics):142–49 CrossRef Medline
21. Houkin K, Kuroda S, Ishikawa T, et al. **Neovascularization (angiogenesis) after revascularization in Moyamoya disease: which technique is most useful for Moyamoya disease?** *Acta Neurochir (Wien)* 2000;142:269–76 Medline
22. Heil M, Eitenmüller I, Schmitz-Rixen T, et al. **Arteriogenesis versus angiogenesis: similarities and differences.** *J Cell Mol Med* 2006;10:45–55 Medline
23. Enholm B, Paavonen K, Ristimäki A, et al. **Comparison of VEGF, VEGF-B, VEGF-C and Ang-1 mRNA regulation by serum, growth factors, oncoproteins and hypoxia.** *Oncogene* 1997;14:2475–83 CrossRef Medline
24. Liu Y, Cox SR, Morita T, et al. **Hypoxia regulates vascular endothelial growth factor gene expression in endothelial cells: identification of a 5' enhancer.** *Circ Res* 1995;77:638–43 Medline
25. Oh H, Takagi H, Takagi C, et al. **The potential angiogenic role of macrophages in the formation of choroidal neovascular membranes.** *Invest Ophthalmol Vis Sci* 1999;40:1891–98 Medline
26. Luo J, Martinez J, Yin X, et al. **Hypoxia induces angiogenic factors in brain microvascular endothelial cells.** *Microvasc Res* 2012;83:138–45 CrossRef Medline
27. Wang Q, Liu C, Yan B, et al. **Correlation of extracranial internal carotid artery tortuosity index and intraprocedural complications during carotid artery stenting.** *Eur Neurol* 2012;68:65–72 CrossRef Medline
28. Jakob M, Spasojevic D, Krogmann ON, et al. **Tortuosity of coronary arteries in chronic pressure and volume overload.** *Cathet Cardiovasc Diagn* 1996;38:25–31 CrossRef Medline
29. Landini G, Rippon JW. **How important is tumour shape? Quantification of the epithelial-connective tissue interface in oral lesions using local connected fractal dimension analysis.** *J Pathol* 1996;179:210–17 CrossRef Medline
30. Landini G, Murray PI, Misson GP. **Local connected fractal dimensions and lacunarity analyses of 60 degrees fluorescein angiograms.** *Invest Ophthalmol Vis Sci* 1995;36:2749–55 Medline
31. Karamessini MT, Kagadis GC, Petsas T, et al. **CT angiography with three-dimensional techniques for the early diagnosis of intracranial aneurysms: comparison with intra-arterial DSA and the surgical findings.** *Eur J Radiol* 2004;49:212–23 CrossRef Medline
32. Green D, Parker D. **CTA and MRA: visualization without catheterization.** *Semin Ultrasound, CT MR* 2003;24:185–89 CrossRef Medline

Occlusion of Posterior Fossa Dural Sinuses in Vein of Galen Malformation

A. Berenstein, N. Toma, Y. Niimi, and S. Paramasivam

ABSTRACT

BACKGROUND AND PURPOSE: Spontaneous or progressive occlusion of the posterior fossa dural sinuses is often observed in patients with vein of Galen malformation, which can affect the clinical course. The aim of this study was to examine the patency of the posterior fossa dural sinuses in patients with vein of Galen malformation and to analyze the clinical and angiographic course of this condition.

MATERIALS AND METHODS: We retrospectively reviewed 61 consecutive children with vein of Galen malformations. Clinical presentation, management, outcome, and angiographic change were analyzed for the patients with attention paid to all dural sinus occlusions.

RESULTS: Twenty patients (32.8%) demonstrated spontaneous sinus occlusion, mostly in the sigmoid sinus. This condition was not observed in neonates and was first discovered during infancy or childhood. Progression of sinus occlusion was seen in 10 patients, and the conditions of 6 of them deteriorated in accordance with the progression of sinus occlusion. After total or subtotal obliteration of the malformation by transarterial glue embolization, 13 patients recovered to healthy, 3 patients had only mild developmental delay, and 4 patients remained neurologically disabled.

CONCLUSIONS: Spontaneous sinus occlusion is not a rare condition and can result in neurologic deterioration in the natural history of untreated vein of Galen malformation. If signs of progressive sinus occlusion are noticed, early arteriovenous shunt reduction or elimination by transarterial glue embolization is expected to prevent permanent brain damage.

ABBREVIATION: VGM = vein of Galen malformation

Vein of Galen malformations (VGMs) are direct arteriovenous shunts in the subarachnoid space of the velum interpositum cistern and quadrigeminal cistern, supplied by the choroidal and quadrigeminal arteries and drained by the dilated median prosencephalic vein of Markowski, the embryonic precursor of the vein of Galen.^{1,2} This malformation is considered to form between 6 and 11 weeks of gestational age when this transient embryonic vein exists.

The clinical presentation of VGM varies depending on the age of the patient. Neonates typically present with high-output congestive heart failure due to high-flow shunt producing cardiac overload, whereas infants and children usually present with hy-

drovenous disorders, such as macrocrania, prominent facial and scalp veins, and hydrocephalus.^{2,3} Hydrovenous disorders result from diminished absorption of CSF due to cerebral venous hypertension.⁴ Development of outflow restriction in the posterior fossa dural sinuses will improve the cardiac overload but will lead to further intracranial venous hypertension, which will not only interfere with absorption of CSF but will also create congestion within cerebral veins. Venous hypertension consequently results in brain tissue loss and hence developmental delay.^{2,3}

Thus, posterior fossa dural sinus occlusion is thought to aggravate the clinical course of VGM. However, its incidence, pathogenic mechanism, and the effect of endovascular embolization are unknown. The aim of this study was to analyze the clinical and angiographic course of patients with VGM with sinus occlusion and to determine whether embolization can prevent clinical deterioration in these patients.

MATERIALS AND METHODS

Retrospective review of the institutional data base during January 2005 to December 2012 revealed 61 patients with VGM. We collected information from the clinical case records, MR images at

Received August 25, 2015; accepted after revision November 30.

From the Hyman Newman Institute of Neurology and Neurosurgery (A.B., S.P.), Ichan School of Medicine at Mount Sinai Hospital, New York, New York; Department of Neurosurgery (N.T.), Mie University Graduate School of Medicine, Tsu, Mie, Japan; and Department of Neuroendovascular Therapy (Y.N.), St. Luke's International Hospital, Tokyo, Japan.

Please address correspondence to Naoki Toma, MD, Department of Neurosurgery, Mie University Graduate School of Medicine, 2-174 Edobashi, Tsu, Mie, 514-8507, Japan; e-mail: toma0511@gmail.com

<http://dx.doi.org/10.3174/ajnr.A4688>

Table 1: Demographics and clinical characteristics of 61 patients with VGM comparing patients with and without sinus occlusion

	Sinus Occlusion Group (n = 20)		Nonocclusion Group (n = 41)		P Value ^a
Male/female	9:11		24:17		NS
Age at the first treatment					
Neonates (0–30 days)	2	10.0%	17	41.5%	<.05
Infants (1–24 mo)	13	65.0%	21	51.2%	NS
Children (2–15 yr)	5	25.0%	3	7.3%	NS
Presentation					
Congestive heart failure	3	15.0%	20	48.8%	<.05
Hydrovenous disorder	15	75.0%	12	29.3%	<.001
Developmental delay	5	25.0%	2	4.9%	<.05
Seizure	3	15.0%	2	4.9%	NS
Headache	0	0.0%	1	2.4%	NS
Asymptomatic	0	0.0%	9	22.0%	<.05
Embryonic sinus					
Falcine sinus	13	65.0%	24	58.5%	NS
Occipital sinus	14	70.0%	25	61.0%	NS

Note:—NS indicates not significant.

^a P value was calculated using the Fisher exact test.

presentation and during follow-up, and DSA at the time of each endovascular embolization and follow-up.

All patients were examined for the patency of the posterior fossa dural sinuses, including transverse, sigmoid, and occipital sinuses and jugular bulbs, on the basis of bilateral common or internal carotid and at least unilateral vertebral arteriography.

All patients except 1 who demonstrated spontaneous thrombosis of the VGM on the initial angiogram were treated with single or multiple sessions of endovascular treatment at the Hyman Newman Institute for Neurology and Neurosurgery. All patients were treated primarily by transarterial embolization by using *n*-BCA. Transarterial embolization with ethylene vinyl alcohol copolymer (Onyx; Covidien, Irvine, California) mostly via dural feeders or a transvenous approach with detachable coils was added, if necessary, to obtain complete obliteration of the VGM.

Fifteen patients who were referred to us after partial embolization at an outside institution were also included in this study. Although available data were limited, the initial status of the posterior fossa dural sinuses could be evaluated with DSA or MR venography in all of these cases. At outside institutions, 4 of 15 patients had been treated with *n*-BCA in the same manner as ours, 7 patients had undergone proximal feeder occlusion with coils, and the remaining 4 patients had been treated exclusively with Onyx.

To clarify the impact of the age of the patient on occlusive changes in the posterior fossa dural sinuses, we categorized the patients into 3 age groups: neonates (≤ 30 days after birth), infants (1–24 months of age), and children (2–15 years of age), according to the age at the initial treatment either in our center or outside.

Angiographic changes in the posterior fossa dural sinuses were categorized into progression, no change, and regression. New development of sinus occlusion or an increase in the extent of the occluded segment before the first treatment by us or during the course of treatment was defined as “progression.” Reopening of the occluded sinus or a decrease in the extent of the occluded segment was defined as “regression.”

Clinical factors were compared between patients with and

without sinus occlusion by using Fisher exact tests, and we considered a *P* value $< .05$ statistically significant.

RESULTS

Demographics and Clinical Characteristics

We identified 61 patients with VGM referred to our center between January 2005 and December 2012 (Table 1). Nineteen patients were first treated within 30 days after birth (neonate group); 34 patients, at 1 to 24 months of age (infant group); and 8 patients at 2–15 years of age (children’s group).

Twenty patients (32.8%) demonstrated occlusion of the posterior fossa dural sinuses. In the neonate group, sinus occlusion was considerably less likely to occur compared with the other

groups. All 19 neonates demonstrated well-developed sigmoid sinuses and internal jugular veins on the initial angiograms. Occipital sinuses were also observed in all neonates. Only 2 (cases 16 and 19) of them, who had been referred late to our center owing to previous complications after early treatment, developed sinus occlusion during their infancy.

With respect to the clinical presentation, hydrovenous disorders, such as macrocrania, prominent facial and scalp veins, and hydrocephalus, were most closely correlated with sinus occlusion (75% in sinus occlusion group and 29.3% in nonocclusion group; $P < .001$). Developmental delay was also more common in the patients with sinus occlusion (25% in the sinus occlusion group and 4.9% in the nonocclusion group, $P < .05$). All asymptomatic patients were not associated with sinus occlusion. Although the persistence of the occipital sinus could function as an alternative venous outlet when the sigmoid sinus was occluded, the prevalence of embryonic sinuses, such as the falcine and occipital sinuses, was not correlated statistically with the development of posterior fossa dural sinus occlusion.

Representative Cases

Case 8. A 13-month-old boy, who had been diagnosed with VGM due to macrocrania and prominent scalp and facial veins at 6 months of age, was referred to our center for endovascular treatment (Fig 1). The initial angiogram demonstrated VGM and complete occlusion of the left sigmoid sinus and near-occlusion of the right sigmoid sinus. There was an alternative venous pathway via the emissary vein to the jugular bulb on the right side. After subtotal obliteration of the VGM achieved by staged transarterial embolization, the bilateral sigmoid sinuses reopened and the patient has been developing normally.

Case 14. A 3-month-old girl with a prenatal diagnosis of VGM presented with hydrocephalus (Fig 2). She underwent the first embolization at 3 months of age. Angiography showed stenosis of the left sigmoid sinuses and jugular bulbs. Intraventricular hemorrhage occurred after the first embolization procedure, and resulted in progression of hydrocephalus. However, the patient re-

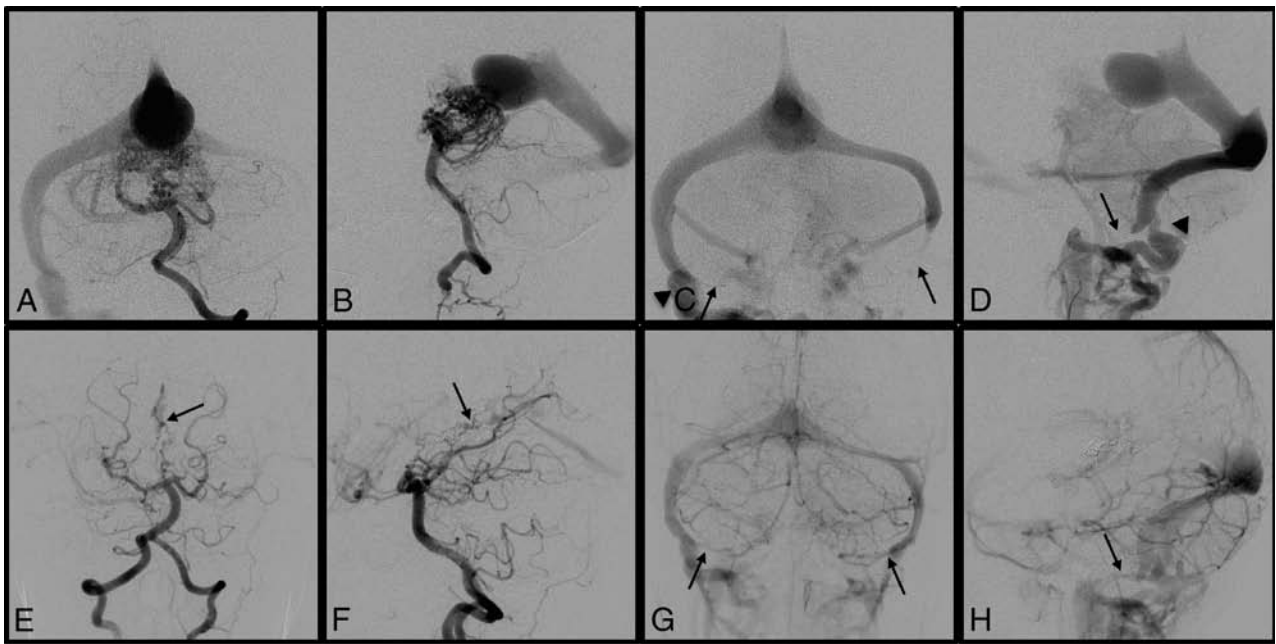


FIG 1. Case 8. A 13-month-old boy was diagnosed with VGM due to macrocrania and prominent scalp and facial veins. Left vertebral artery angiograms before the first embolization demonstrated a VGM in the arterial phase (A and B) and complete occlusion of the left sigmoid sinus and near-occlusion of the right sigmoid sinus in the venous phase (C and D, *arrows*). There was an alternative venous pathway via the emissary vein to the jugular bulb on the right side (C and D, *arrowheads*). Left vertebral artery angiograms in the midarterial phase (E and F) and the late venous phase (G and H) after subtotal obliteration of VGM achieved by staged transarterial embolization (E and F, *arrows*) demonstrate the reopened bilateral sigmoid sinuses (G and H, *arrows*). The patient is developing normally.

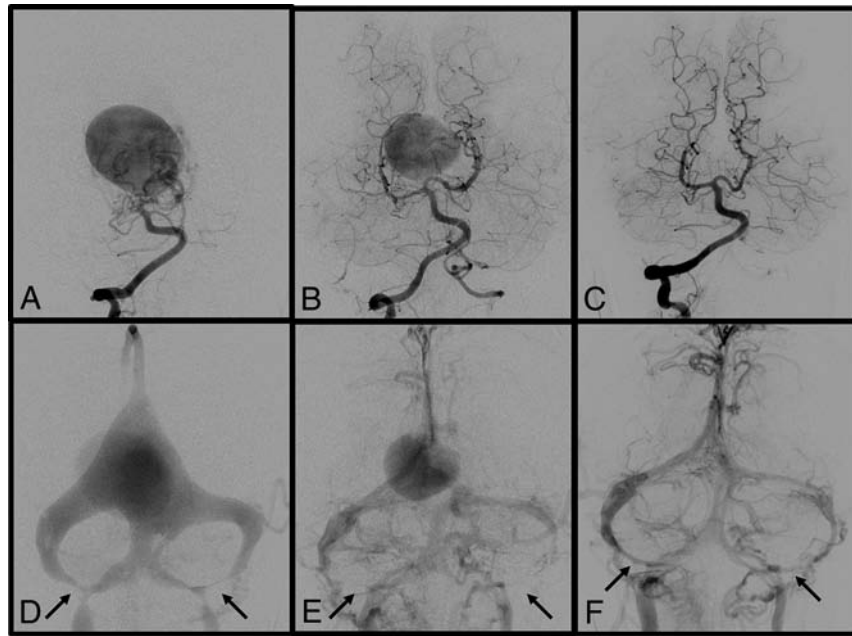


FIG 2. Case 14. A 3-month-old girl with a prenatal diagnosis of VGM who presented with hydrocephalus. Right vertebral artery angiograms before the first embolization at 3 months of age (A and D) show a VGM with multiple feeders and stenosis of bilateral sigmoid sinuses and jugular bulbs (D, *arrows*). The first embolization was complicated by intraventricular hemorrhage resulting in hydrocephalus. However, the patient recovered well after ventriculoperitoneal shunt placement. Right vertebral artery angiograms before the second embolization at 7 months of age (B and E) show a decrease in the size of the VGM and progression to bilateral sigmoid sinus occlusion (E, *arrows*). Note the partial regression of the occipital sinuses. The third embolization at 13 months of age led to subtotal obliteration of the VGM (data not shown). Right vertebral artery angiograms at 2 years of age (C and F) show total exclusion of VGM and regression of bilateral sigmoid sinuses (F, *arrows*). Her neurologic status had improved except for a slight developmental delay at the last follow-up.

covered well after ventriculoperitoneal shunt placement. She underwent the second embolization at 7 months of age. Angiography showed a decrease in size of the VGM and progression to

bilateral sigmoid sinus occlusion. The third embolization at 13 months of age led to subtotal obliteration of the VGM (data not shown). At 2 years of age, angiography showed total exclusion of

Table 2: Summary of patients with posterior fossa dural sinus occlusion

Case No.	Sex	Presentation		Location of Sinus Occlusion		Procedural Complications	Neurologic Deficit
		Initial	Later	Right	Left		
Neonates							
16	F	CHF	HC, DD, SZ	SJ		Ischemic stroke	Severe DD, hemiparesis
19	M	CHF	HC, DD	TSJ	SJ	SDH and ischemic stroke	Severe DD
Infants							
6	M	MC	HC	S	S	None	None
11	F	HC		S	S	None	None
14	F	HC	DD	S	S	IVH	Mild DD
12	F	MC, HC		S	S	None	None
7	F	MC, HC		TSJ	T	None	None
13	M	MC	HA, DD	TSJ	TSJ	None	Mild DD
15	M	HC, DD, SZ		TSJ		Ischemic stroke	Moderate DD, hemiparesis
4	M	MC		S	TSJ	None	None
1	M	HC		S		None	None
2	M	MC, HC		S		None	None
10	F	MC		S	SJ	None	None
8	M	MC		S	SJ	None	None
5	F	SZ			TSJ	None	None
Children							
3	F	MC		SJ		None	None
20	M	MC, DD		S	S	Ischemic stroke	Moderate DD, hemiparesis
18	M	MC, DD			SJ	None	Mild DD
9	F	DD		SJ	SJ	None	None
17	M	MC			SJ	None	None

Note:—CHF indicates congestive heart failure; MC, macrocrania; HC, hydrocephalus; DD, developmental delay; SZ, seizure; HA, headache; T, transverse sinus; S, sigmoid sinus; J, jugular bulb; SDH, subdural hematoma; IVH, intraventricular hemorrhage.

the VGM and regression of the bilateral sigmoid sinus occlusion. Her neurologic status has improved except for a slight developmental delay at the last follow-up.

Clinical and Angiographic Courses

With respect to the location of occluded sinuses, 9 patients had unilateral and 11 patients had bilateral occlusion, most commonly at the sigmoid sinus (Table 2 and Fig 3). Sinus occlusion was not observed in neonates and was first discovered during infancy in 13 patients and during childhood in 7 patients. In these patients, we found spontaneous occlusion at the first angiogram but before the first treatment in 13 patients and newly developed occlusions during the course of treatment in 7 patients. In all of these 7 patients, angiograms after any session of embolization showed no embolic material in the area where sinus occlusion later occurred.

Progression of sinus occlusion was identified in 10 patients, and conditions of 6 of them deteriorated in accordance with the progression of sinus occlusion. Regression of sinus occlusion was also identified in 7 patients (3 patients first showed progression and showed regression afterward during the course of treatment).

In 8 of 10 patients who showed progression, sinus occlusion was identified while a significant amount of shunt flow of the VGM still existed, largely from 2 months to 3 years of age. The remaining 2 patients (cases 1 and 6) demonstrated sinus occlusion with well-developed collateral venous pathways when the VGM was totally obliterated. Regression of sinus occlusion was found when VGM was totally or subtotally excluded in all 7 patients (6 infants and a 2-year-old child). There was no change in 6 patients (2 infants and 4 children).

Seven (70%) of 10 patients with hydrocephalus, including 1

patient (case 11) who developed progressive hydrocephalus during treatment, showed a decrease in the ventricular size after embolization and did not have any symptom or neurologic deficit on the last follow-up. Of the patients with sinus occlusion, only case 14 underwent a shunt operation for hydrocephalus. Four (50%) (cases 9, 13, 14, and 18) of 8 patients who presented with developmental delay demonstrated significant improvement on the last follow-up.

Five patients had procedural complications. One patient who underwent glue embolization at our center had a small thalamic hemorrhage with ventricular extension after embolization and had mild developmental delay (case 14). Four patients who underwent early treatment at outside institutions had ischemic stroke (cases 15, 16, 19, and 20), resulting in hemiparesis in 3 and moderate-to-severe developmental delay in 4. On the last follow-up, 13 patients were neurologically intact, 3 patients had only mild developmental delay without focal signs, and all 4 patients who underwent early treatment at outside institutions had significant neurologic deficits.

DISCUSSION

Posterior fossa dural sinus occlusion is a common finding in patients with VGM.^{2,5} However, few descriptions have focused on this condition in the previous literature, and the pathogenic mechanism remains unknown. Raybaud et al,¹ in their series of 23 patients with VGM, identified complete angiographic absence of both transverse and sigmoid sinuses in 5 patients, and they found that the venous drainage channels are patent more often in neonates than in older children. Geibprasert et al⁶ reported that significant jugular bulb stenosis was present in 7 of 25 patients (28%) and was associated with hydrocephalus in 6 patients. Chow et al,⁷

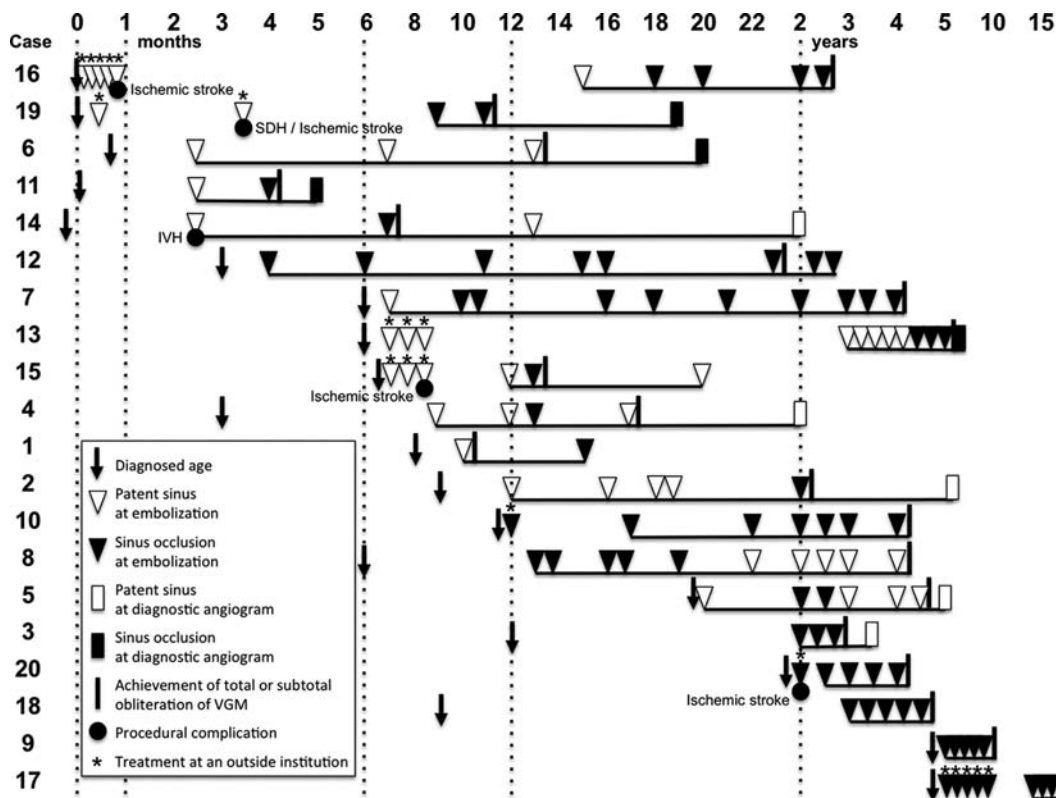


FIG 3. Angiographic patency of the posterior fossa dural sinuses in each patient is chronologically shown. Time points of the initial diagnosis and total or subtotal obliteration of the VGM and procedural complications are also shown. *Underlines* indicate the follow-up periods in our center. SDH indicates subdural hematoma; IVH, intraventricular hemorrhage.

in their recent review of 41 patients with VGM, also identified 16 patients (39.0%) with sinus stenosis and 4 patients (4.9%) with venous sinus thrombus or occlusion on the angiograms. The overall frequency (32.8%) of this condition and rare incidence in neonates in our series are consistent with those in these previous studies.

As the pathogenic mechanism of sinus occlusion, dysmaturation of the jugular bulb due to the arteriovenous shunt or persistence of the occipital sinus,² embryologic segmental sinus atresia,¹ progressive jugular bulb stenosis resulting from expansion of the cranial vault,⁸ and the induced intimal hyperplasia from increased shear stress due to the high-flow shunt have been speculated.⁸

In the normal development of the cerebral venous system, adult arrangement of the transverse and sigmoid sinuses and the jugular bulbs can be seen at 3 months of gestational age.⁹ After 4 months of gestational age, the transverse sinus begins to expand with marked increase in venous flow from the rapidly growing cerebral hemispheres. In contrast to the ballooning of the transverse sinus, the sigmoid sinus and jugular bulb are poorly developed at this stage because the jugular bulb, which is surrounded by cartilaginous and osseous structures, has difficulty expanding during fetal life. After birth, the hemodynamic change from a fetal to a postnatal type of circulation eventually promotes the jugular bulb maturation.¹⁰ Meanwhile, considerable high-flow shunts from VGM could presumably trigger the development of the sigmoid sinus and the jugular bulb by overcoming the surrounding cartilaginous and osseous structures during fetal life or immediately after birth. Consequently, neonates with VGM who present

with high-output congestive heart failure usually have well-developed sigmoid sinuses and jugular bulbs as observed in our series. This finding suggests that posterior fossa dural sinus occlusion in VGM is not developmental but is acquired after birth, as we have also seen in other high-flow intracranial AVFs presenting in neonates and infants (A.B., unpublished data, date unknown).

Recently, we reported that the outcome of patients with VGM who presented with heart failure in the neonatal period has significantly improved by timely endovascular treatment.¹¹ Those patients who undergo appropriate treatment from the neonatal period will not develop sinus occlusion and can achieve angiographic obliteration of VGMs with normal neurologic development.

When shunt flow through the VGM is relatively low, the patient is asymptomatic during the neonatal period and is often diagnosed after developing hydrovenous disorders during infancy. In such patients, enlargement of the cranial vault and specific growth patterns of the posterior fossa may interfere with the development of the jugular foramen.² In our series, most sinus occlusion occurred during the infantile period when the cranial vault was expanding. Progression of sinus occlusion might be associated with the growth pattern of the posterior fossa during infancy.

Posterior fossa dural sinus occlusion will be a cause of worsening of the hydrovenous disorder; at the same time, it may be a secondary change due to intracranial hypertension. Sainte-Rose et al¹² reported that the increased superior sagittal sinus pressure in infantile hydrocephalus is due to a reversible collapse of the

sinus caused by the intracranial hypertension. It is very likely that the collapse takes place in the posterior fossa at the level of the sigmoid sinuses. Also in patients with VGM, persistent intracranial high pressure may mechanically compress the sigmoid sinus causing reversible stenosis/occlusion. In our series, 7 patients (6 infants and a 2-year-old child) demonstrated regression of sinus occlusion when intracranial pressure decreased by total or subtotal obliteration of the VGM. However, long-term compression of the sinus may cause irreversible occlusion. The patients exposed to prolonged intracranial hypertension due to treatment delay demonstrated persistent occlusion of the posterior fossa dural sinuses despite successful shunt reduction by endovascular treatment.

Hydrovenous Disorder due to Sinus Occlusion

In a patient with a VGM, high-flow arteriovenous shunts draining into the torcular Herophili increase the superior sagittal sinus pressure.¹³ Raised pressure in the superior sagittal sinus causes cortical cerebral vein stagnation, resulting in increased pial venous pressure, resulting in progressive impairment of CSF absorption, which is further aggravated by the occlusion, and consequently progressive diffuse brain damage. Therefore, the prognosis of an untreated VGM depends on pial venous pressure, which is affected by the timing of the development of sinus occlusion and alternative venous pathways to drain the VGM and the brain. If sinus occlusion develops slowly, collateral pathways may develop and adapt to the increased venous pressure, allowing the patients to grow normally at the beginning.

However, the long-term pial venous congestion may eventually result in developmental delay due to chronic ischemia in untreated VGM.² Therefore, patients with increased pial venous pressure have an urgent need to reduce shunt flow of the VGM to avoid permanent brain damage. Reduction in shunt flow of the VGM by embolization might stop progression of sinus occlusion and consequently prevent progression of symptoms.

Effectiveness of Endovascular Embolization

If endovascular embolization is started in the neonatal period and substantial reduction of the shunt flow of the VGM is achieved in time, patency of the posterior fossa dural sinuses seems to be preserved, as seen in 16 patients of our 19 neonates, excluding 3 patients who died within 30 days, achieved total obliteration of the VGM before 2 years of age. Among them, the posterior fossa dural sinuses remained patent during the course of treatment in 14 patients treated early in our series. In contrast, 2 patients who were referred to us late after early initial treatment developed sinus occlusion.

We believe that transarterial glue embolization is the best way to achieve on-target obliteration at the fistula site of the VGM, leading to effective shunt reduction. Although sinus occlusion may initially progress despite effective glue embolization in the early phases of the staged embolization, continuous shunt reduction by further glue embolization will eventually stop progression and sometimes reopen occluded sinuses; this treatment will prevent or even reverse development of symptoms of the hydrovenous disorder.

Proximal feeder occlusion should be avoided because it not only leaves the fistula site patent but also eliminates future transarterial access to the fistula. In the patient with sinus occlusion, the transvenous access route is often impeded. Transvenous sinus

stent placement in patients with progressive jugular bulb stenosis has been reported¹⁴ but should be performed only when the transarterial approach is not possible because of limited experience with and unknown long-term effects of this placement.

Two patients who underwent proximal coil occlusion without sufficient shunt reduction developed hydrocephalus and sinus occlusion and consequently had significant developmental delay despite late total exclusion of the VGM. Because proximal coil occlusion did not close the fistula itself, there was persistent prolonged intracranial venous hypertension before the fistulas were sufficiently occluded with *n*-BCA.

Therefore, it is important to shorten the duration of patient exposure to high-flow shunts leading to intracranial venous hypertension. Careful observation of head circumference and developmental milestones will be helpful in detecting a patient who is predisposed to progressive posterior fossa dural sinus occlusion. When a patient with VGM shows signs of progressive hydrovenous disorder, early arteriovenous shunt reduction by transarterial glue embolization is the best option to prevent permanent brain damage.

CONCLUSIONS

Patients with VGM are frequently associated with posterior fossa dural sinus occlusion, typically during their infancy. Sinus occlusion will aggravate a hydrovenous disorder and vice versa. Early arteriovenous shunt flow reduction and total obliteration by transarterial glue embolization may have the potential to prevent progressive sinus occlusion and its symptoms and may even reverse some of the symptoms. Therefore, recognition of the frequent occurrence of this condition and careful observation of early signs of hydrovenous disorder are important for the management of patients with VGM.

REFERENCES

1. Raybaud CA, Strother CM, Hald JK. **Aneurysms of the vein of Galen: embryonic considerations and anatomical features relating to the pathogenesis of the malformation.** *Neuroradiology* 1989;31:109–28 CrossRef Medline
2. Lausjaunias P, ter Brugge KG, Berenstein A. *Surgical Neuroangiography: Vol. 3: Clinical and Interventional Aspects in Children.* Berlin: Springer-Verlag; 2006
3. Lasjaunias PL, Chng SM, Sachet M, et al. **The management of vein of Galen aneurysmal malformations.** *Neurosurgery* 2006;59:S184–94; discussion S3–S13 Medline
4. Zerah M, Garcia-Monaco R, Rodesch G, et al. **Hydrodynamics in vein of Galen malformations.** *Childs Nerv Syst* 1992;8:111–17; discussion 117 CrossRef Medline
5. Lasjaunias P, Ter Brugge K, Lopez Ibor L, et al. **The role of dural anomalies in vein of Galen aneurysms: report of six cases and review of the literature.** *AJNR Am J Neuroradiol* 1987;8:185–92 Medline
6. Geibprasert S, Krings T, Armstrong D, et al. **Predicting factors for the follow-up outcome and management decisions in vein of Galen aneurysmal malformations.** *Childs Nerv Syst* 2010;26:35–46 CrossRef Medline
7. Chow ML, Cooke DL, Fullerton HJ, et al. **Radiological and clinical features of vein of Galen malformations.** *J Neurointerv Surg* 2015;7:443–48 CrossRef Medline
8. Raybaud C. **Normal and abnormal embryology and development of the intracranial vascular system.** *Neurosurg Clin N Am* 2010;21:399–426 CrossRef Medline
9. Padgett DH. **The development of the cranial venous system in man,**

- from the viewpoint of comparative anatomy. *Contrib Embryol* 1957;36:79–140
10. Okudera T, Huang YP, Ohta T, et al. **Development of posterior fossa dural sinuses, emissary veins, and jugular bulb: morphological and radiologic study.** *AJNR Am J Neuroradiol* 1994;15:1871–83 Medline
 11. Berenstein A, Fifi JT, Niimi Y, et al. **Vein of Galen malformation in neonates: new management paradigms for improving outcomes.** *Neurosurgery* 2012;70:1207–14 CrossRef Medline
 12. Sainte-Rose C, LaCombe J, Pierre-Kahn A, et al. **Intracranial venous sinus hypertension: cause or consequence of hydrocephalus in infants?** *J Neurosurg* 1984;60:727–36 CrossRef Medline
 13. Quisling RG, Mickle JP. **Venous pressure measurements in vein of Galen aneurysms.** *AJNR Am J Neuroradiol* 1989;10:411–17 Medline
 14. Brew S, Taylor W, Reddington A. **Stenting of a venous stenosis in vein of Galen aneurysmal malformation: a case report.** *Interv Neuroradiol* 2001;7:237–40 Medline

Association between Postprocedural Infarction and Antiplatelet Drug Resistance after Coiling for Unruptured Intracranial Aneurysms

M.S. Kim, K.I. Jo, J.Y. Yeon, J.S. Kim, K.H. Kim, P. Jeon, and S.C. Hong

ABSTRACT

BACKGROUND AND PURPOSE: Procedure-related thromboembolism is a major limitation of coil embolization, but the relationship between thromboembolic infarction and antiplatelet resistance is poorly understood. The purpose of this study was to verify the association between immediate postprocedural thromboembolic infarction and antiplatelet drug resistance after endovascular coil embolization for unruptured intracranial aneurysm.

MATERIALS AND METHODS: This study included 338 aneurysms between October 2012 and March 2015. All patients underwent postprocedural MR imaging within 48 hours after endovascular coil embolization. Antiplatelet drug resistance was checked a day before the procedure by using the VerifyNow system. Abnormal antiplatelet response was defined as >550 aspirin response units and >240 P2Y12 receptor reaction units. In addition, we explored the optimal cutoff values of aspirin response units and P2Y12 receptor reaction units. The primary outcome was radiologic infarction based on postprocedural MR imaging.

RESULTS: Among 338 unruptured intracranial aneurysms, 134 (39.6%) showed diffusion-positive lesions on postprocedural MR imaging, and 32 (9.5%) and 105 (31.1%) had abnormal aspirin response unit and P2Y12 receptor reaction unit values, respectively. Radiologic infarction was associated with advanced age (65 years and older, $P = .024$) only with defined abnormal antiplatelet response (aspirin response units ≥ 550 , P2Y12 receptor reaction units ≥ 240). P2Y12 receptor reaction unit values in the top 10th percentile (>294) were associated with radiologic infarction ($P = .003$). With this cutoff value, age (adjusted odds ratio, 2.29; 95% confidence interval, 1.28–4.08), P2Y12 receptor reaction units (>294 ; OR, 3.43; 95% CI, 1.53–7.71), and hyperlipidemia (OR, 2.05; 95% CI, 1.04–4.02) were associated with radiologic infarction in multivariate analysis.

CONCLUSIONS: Radiologic infarction after coiling for unruptured aneurysm was closely associated with age. Only very high P2Y12 receptor reaction unit values (>294) predicted postprocedural infarction. Further controlled studies are needed to determine the precise cutoff values, which could provide information regarding the optimal antiplatelet regimen for aneurysm coiling.

ABBREVIATIONS: ARU = aspirin response unit; DPL = diffusion-positive lesion; PRU = P2Y12 receptor reaction unit

Endovascular coil embolization is a well-established treatment method for intracranial aneurysms. Recent evidence suggests that this procedure can be considered a first-line treatment for both ruptured and unruptured intracranial aneurysms.^{1,2} However, endovascular coil embolization still has major drawbacks, including procedural rupture, thromboembolic complications, and durability issues. Among these shortcomings, thromboembolism is

the most common problem.^{3–5} To reduce thromboembolic complications, many studies investigated the association between thromboembolism and aneurysm and/or patient factors.^{5–8} Previous studies have demonstrated that 30%–60% of endovascular coil embolizations for unruptured aneurysms show ischemic lesions on postprocedural diffusion-weighted images. Although most of the lesions seem to be benign, some could result in permanent neurologic sequelae. Recent studies demonstrated that antiplatelet resistance was associated with ischemic complications after coil embolization and that drug adjustment could lower the risk.^{9,10} Still, these results are controversial, and the association between antiplatelet drug resistance and diffusion lesions has not yet been fully elucidated.^{11,12}

Therefore, the purpose of this study was to verify the association between thromboembolic infarction and antiplatelet drug resistance after endovascular coil embolization for unruptured intracranial aneurysms. We also explored other risk factors for thromboembolic complications.

Received August 4, 2015; accepted after revision November 19.

From the Departments of Neurosurgery (M.S.K., J.Y.Y., J.S.K., S.C.H.) and Radiology (K.H.K., P.J.), Division of Interventional Neuroradiology, Samsung Medical Center, Sungkyunkwan University School of Medicine, Seoul, Korea; and Department of Neurosurgery (K.I.J.), Hana General Hospital, Cheongju, Korea.

Min Soo Kim and Kyung Il Jo contributed equally to this work.

Please address correspondence to Seung Chyul Hong, MD, Department of Neurosurgery, Samsung Medical Center, Sungkyunkwan University School of Medicine, 81 Irwon-ro, Gangnam-gu, Seoul 135-710, Korea; e-mail: nsschong@skku.edu

<http://dx.doi.org/10.3174/ajnr.A4777>

MATERIALS AND METHODS

This retrospective study included patients from a data base prospectively collected between October 2012 and March 2015. This study was approved by the institutional review board, and informed consent was waived. During the given period, 470 unruptured aneurysms were treated in a single tertiary hospital. Among these, 129 cases were excluded due to lack of postprocedural MR imaging. There were no symptomatic infarctions among the excluded patients. Three cases with procedural rupture were also excluded, leaving 309 patients with 338 unruptured intracranial aneurysms for inclusion in this study.

Patient information, including sex, age, diabetes mellitus, hypertension, hyperlipidemia, smoking history, aneurysm profile including the size and location of the aneurysm, medical history, and pre- and postprocedural neurologic symptoms, was obtained from retrospective chart review. We also reviewed the number of angiograms obtained per intervention and total procedural time, which was considered to total anesthesia time.

Aneurysm size was categorized according to the long diameter on 3D digital subtraction angiography as small (<7 mm) and large (≥ 7 mm).¹³ Aneurysm location was categorized into internal carotid artery, anterior cerebral artery, middle cerebral artery, and posterior circulation systems. Postprocedural MR imaging was performed between 24 and 48 hours after the embolization procedure, and included diffusion-weighted imaging and time-of-flight (with 3D volume-rendered imaging). MRIs were reviewed by 2 independent board-certified radiologists. If hyperintense diffusion-positive lesions (DPLs) were detected on DWI, details of the lesions, including location, number, and size, were analyzed. The primary outcome of this study was the presence of DPL. Because there were only a small number ($n = 2$) of symptomatic lesions in this study population, we assumed that multiple lesions ($n \geq 6$) were more severe lesions.⁵ Additionally, the degree of embolization was determined by immediate postprocedural MR imaging.¹⁴

Antiplatelet Therapy and Antiplatelet Function Test

Preprocedural antiplatelet therapy included aspirin (100 mg) and clopidogrel (75 mg) daily for 7 days before the elective endovascular coil embolization, regardless of stent usage. Response to the antiplatelet agents was evaluated in all patients the day before the procedure by using the VerifyNow P2Y12 assay (Accumetrics, San Diego, California). Because there was no definite evidence of association between antiplatelet drug resistance and immediate thromboembolic complications after coil embolization, the antiplatelet regimen was altered according to stent usage and the attending physician's discretion. An abnormal antiplatelet response was defined as >550 aspirin response units (ARUs) and/or >240 P2Y12 receptor reaction units (PRUs).^{15,16} Also, we tried to investigate and clarify the optimal cutoff values of both ARUs and PRUs that were associated with DPL, which have been controversial in the literature.^{11,17,18}

Coil Embolization Procedures

Endovascular coil embolization was performed with the patient under general anesthesia. All procedures were performed by 2

neurointerventional experts at our center by using a biplane angiographic unit (Artis zee; Siemens, Erlangen, Germany). During the procedure, all patients were injected intravenously with heparin to prevent thromboembolic infarction. If thrombus was caused by using a catheter or wire during the procedure, the thrombus was immediately dissolved by using intravenous glycoprotein IIb/IIIa receptor inhibitor (tirofiban, Aggrastat), and the remission of the thrombus was confirmed with subsequent angiography.¹⁹ A bolus of intravenous heparin (60 IU/kg) was injected at the time of catheter insertion, and activated clotting times were assessed hourly. If the activated clotting time after heparinization was shorter than 2–3 times from the baseline, an additional 1000 IU of heparin was injected to maintain an acceptable activated clotting time throughout the procedure. In cases with stent-assisted coil embolization, heparinization was maintained until 24 hours postprocedure on the basis of activated partial thromboplastin time tests performed every 4 hours. In addition, although we mostly used the single-catheter technique, we recorded the use of multiple catheters because using an additional catheter was reported to increase the risk of thromboembolic complications during the procedure.²⁰

Statistical Analysis

Statistical analyses were performed with SPSS, Version 22.0 (IBM, Armonk, New York); SAS, Version 9.4 (SAS Institute, Cary, North Carolina); and R Project Statistical and Computing software, R3.0.3 (<http://www.R-project.org/>). Univariate analysis was performed with the χ^2 , Fisher exact, and Student *t* tests after dichotomizing patient clinical, laboratory, and procedural data. Variables with $P < .100$ in univariate analysis were chosen for multivariable models by using multivariate logistic regression models. Results of ARUs and PRUs were included in the multivariate analysis regardless of the results of univariate analysis because these were the variables of interest in this study. To explore the optimal cutoff values of ARUs and PRUs, we used a scatterplot to investigate the correlation among the ARU, PRU, and infarction event. We found that the ARU had no significant clinical correlation with an infarction event, whereas the PRU was significantly correlated. Thus, we divided the patients into 10 equal groups based on the PRU value used generally. In all analyses, $P \leq .05$ was statistically significant.

RESULTS

Baseline characteristics of patients are detailed in Table 1. Among 338 unruptured intracranial aneurysms, 263 (77.8%) were small (<7 mm) and 75 (22.2%) were large (≥ 7 mm). Stent-assisted embolization was performed in 148 (43.8%) cases, and a multiple microcatheter technique was performed in 118 (34.9%) cases. Antiplatelet function tests showed 32 (9.5%) ARU abnormalities and 105 (31.1%) PRU abnormalities. Complete embolization was achieved in 290 (85.8%) cases based on postprocedural MR imaging. Mean total procedural time was 168 ± 49 minutes. Because lack of precise value of total procedure time, this value was excluded in multivariate analysis. The univariate analysis showed that total procedural time was significantly associated with DPL (DPL versus no DPL, 193 ± 61 minutes versus 166 ± 48 minutes; $P = .04$).

Table 1: Baseline patient characteristics according to antiplatelet resistance status

	Total (N = 338)	Abnormal ARU (n = 32)	P Value ^a	Abnormal PRU (n = 105)	P Value ^a
Clinical					
Age (≥65 yr)	204 (60.4%)	14 (43.8%)	.061	33 (31.4%)	.433
Sex (female)	225 (66.6%)	23 (71.9%)	.560	83 (79.0%)	.001 ^b
Diabetes	23 (6.8%)	7 (21.9%)	.003 ^b	11 (10.5%)	.100
Hypertension	146 (43.2%)	16 (50.0%)	.456	48 (45.7%)	.554
Hyperlipidemia	53 (15.7%)	5 (15.6%)	1.000	12 (11.4%)	.196
Smoking	59 (17.5%)	5 (15.6%)	.816	20 (19.0%)	.643
TIA or stroke history	16 (4.7%)	3 (9.4%)	.381	3 (2.9%)	.408
Procedure					
Dome size of aneurysm ≥7 mm	75 (22.2%)	11 (34.4%)	.114	28 (26.7%)	.204
Location of aneurysm					
ICA	198 (58.6%)	18 (56.3%)	.636 ^c	62 (59.0%)	.588 ^c
MCA	80 (23.7%)	11 (34.4%)		20 (19.0%)	
ACA	28 (8.3%)	1 (3.1%)		12 (11.4%)	
Posterior circulation	32 (9.5%)	2 (6.3%)		11 (10.5%)	
Technique					
Assist with stent	149 (44.1%)	14 (43.8%)	1.000	45 (42.9%)	.813
Double catheter	116 (34.3%)	14 (43.8%)	.246	42 (40.0%)	.173
Incomplete occlusion	48 (14.2%)	4 (12.5%)	.804	18 (17.1%)	.315
Thrombus formation	5 (1.5%)	2 (6.3%)	.073	2 (1.9%)	1.000
Mean No. of angiograms ± SD	6.87 ± 2.34	6.53 ± 1.93	.386	7.17 ± 2.36	.115

Note:—ACA indicates anterior cerebral artery.

^a P value was obtained by comparing patients with normal response with a χ^2 , Fischer exact, or Student t test for each variable.

^b Significant.

^c These values were obtained by comparing ICA versus MCA, ACA, or posterior circulation with linear-by-linear association.

Comparisons between the normal and abnormal antiplatelet response groups showed that diabetes was more frequent in the abnormal ARU group, while the abnormal PRU group showed a higher female/male ratio. No other variables showed a statistically significant difference between groups (Table 1).

Of 338 cases, 134 (39.6%) showed DPLs on postprocedural MR imaging. Among cases with a DPL, 89 had ipsilateral lesions, 16 had contralateral lesions, and 29 had both ipsilateral and contralateral lesions. One hundred twenty-one cases (90.3%) were small-dot (<15 mm) lesions, and 13 cases (9.7%) had large (>15 mm) lesions. Twenty-nine cases had multiple (≥6) lesions on postprocedural DWI. There were no territorial infarctions in this study population. Thrombus formation during the procedure occurred in 5 patients, and they received intravenous tirofiban immediately. None of the patients with procedural thrombus formation showed neurologic deterioration.

Only 2 patients showed neurologic deficits associated with ischemic lesions on postprocedural MR imaging. One patient showed only an abnormal ARU value, and the other patient showed normal ARU and PRU values. One patient had a persistent deficit despite improvement (Fig 1), while the other patient experienced a full recovery (Fig 2).

Any Diffusion-Positive Lesion

Univariate analyses showed that advanced age (65 years or older) ($P = .006$), incomplete occlusion ($P = .016$), and dome size of the aneurysm (≥7 mm) ($P = .016$) were associated with the presence of a DPL ($P < .05$). However, ARU ($P = .448$) and PRU ($P = .337$) abnormalities were not associated with DPL in this data-

set ($P > .05$). According to multivariate logistic regression analysis, advanced age (65 years or older; $P = .024$; OR, 1.78; 95% confidence interval, 1.08–2.93) was associated with the presence of a DPL ($P < .05$). Detailed statistical results are described in Table 2.

Multiple Diffusion-Positive Lesions (n ≥ 6)

Advanced age (65 years or older) ($P = .017$), incomplete occlusion ($P = .033$), and large aneurysm size (≥7 mm) ($P = .012$) were associated with multiple DPLs. ARU ($P = .215$) and PRU ($P = .399$) abnormalities were not associated with multiple (≥6) DPLs. Multivariate analysis showed that advanced age (65 years or older) ($P = .030$; OR, 2.47; 95% CI, 1.09–5.59), incomplete occlusion ($P = .039$; OR, 2.66; 95% CI, 1.05–6.76), and thrombus formation ($P = .010$; OR, 9.93; 95% CI, 1.86–97.10) were associated with multiple DPLs ($P < .05$).

Optimal Cutoff Value of Antiplatelet Resistance

DPLs were not associated with ARUs by scatterplot (Fig 3). The number of infarctions tended to increase along with PRU values but did not show statistical significance ($P = .090$; estimated OR, 1.00; 95% CI, 1.00–1.01; Fig 3). PRU values in the top 10% (>294) were associated with DPLs ($P = .003$; OR, 4.8; 95% CI, 1.71–13.50; Fig 4). With this cutoff value, advanced age (65 years or older) (OR, 2.29; 95% CI, 1.28–4.08), PRU (≥294) (OR, 3.43; 95% CI, 1.53–7.71), and hyperlipidemia (OR, 2.05; 95% CI, 1.04–4.02) were associated with DPL in multivariate analysis.

DISCUSSION

Recent studies have demonstrated that high-on-treatment platelet reactivity was associated with symptomatic infarction and an increased the risk of mortality.^{11,21,22} However, patients in these studies regarding antiplatelet resistance were mostly those with atherosclerotic steno-occlusive disease, especially in cardiointerventions.^{23,24} Unlike atherosclerotic vessels, unruptured aneurysms do not always cause significant atherosclerotic burden. High-on-treatment platelet reactivity should be individualized by receiver operating characteristics; therefore, different conclusions can be drawn from previous studies.

Several studies support the idea that clopidogrel resistance can increase postprocedural thromboembolic complications, and our preliminary study showed similar results.^{4,11,12,22} Hwang et al¹⁰ recently reported that abnormal PRUs were associated with symptomatic infarction and that modified antiplatelet preparation could reduce the rate of thromboembolic events in coil embolization. In contrast, in this study, the occurrence of immediate

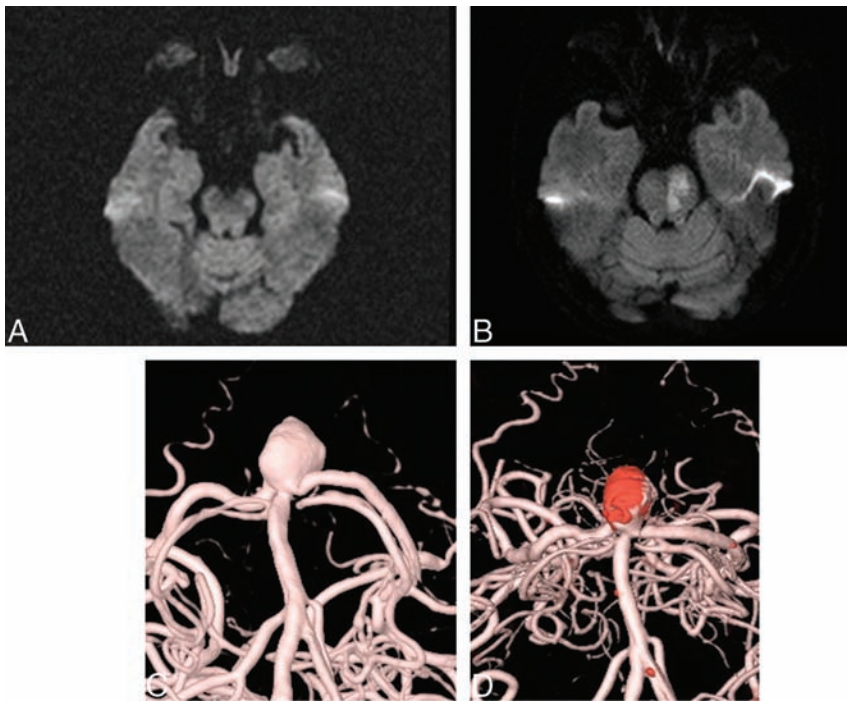


FIG 1. A 75-year-old woman with a 10.81-mm basilar tip aneurysm underwent endovascular coil embolization. *A*, Preprocedural MR imaging (DWI). *B*, Postprocedural MR imaging (DWI). *C*, Preprocedural angiography. *D*, Postprocedural angiography.

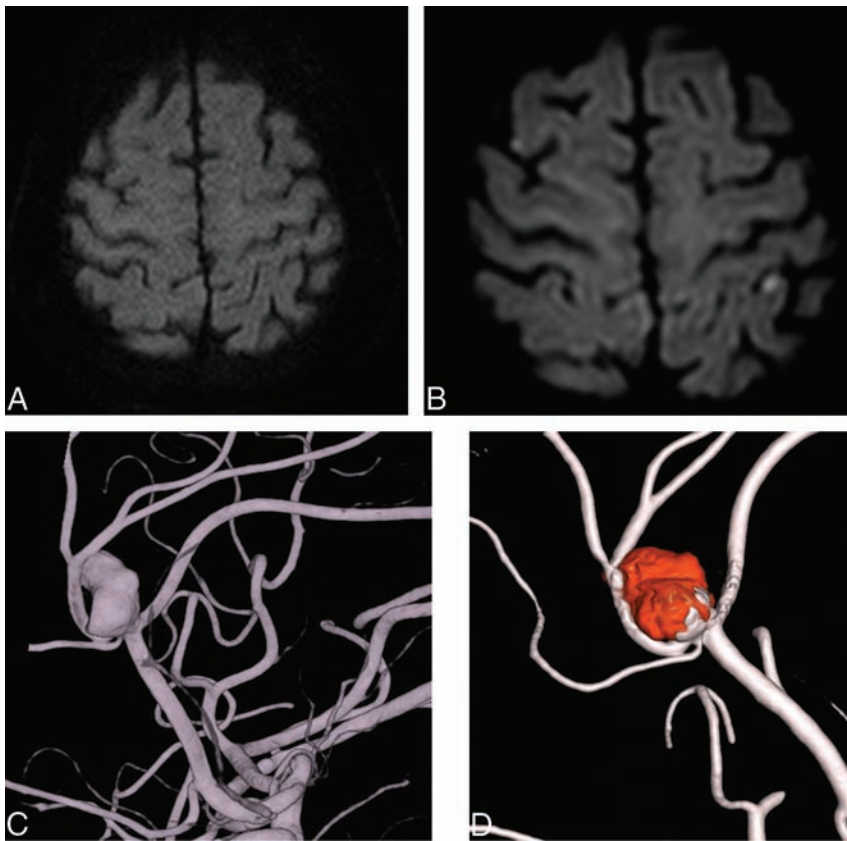


FIG 2. A 71-year-old woman with an aneurysm with a maximal diameter of 12.32 mm on the A2/3 segment. *A*, Preprocedural MR imaging (DWI). *B*, Postprocedural MR imaging (DWI). *C*, Preprocedural angiography. *D*, Postprocedural angiography.

postprocedural thromboembolic infarction was not closely associated with antiplatelet hyporesponders. This disparity is likely the result of different definitions of abnormal antiplatelet response and different outcome measurements because the PRU cutoff value varied widely among studies.^{4,10,11} Our results showed that abnormal PRUs (>240) were not associated with DPL, but PRU values in the upper 10th percentile (>294) were associated with DPL. These different results suggest that only nonresponse is associated with a higher thromboembolic risk.

Different outcome-measurement approaches could be another source of the contradictory results. Hwang et al¹⁰ used symptomatic infarction and procedural thrombus formation as the primary outcome. In this study, the primary outcome was the presence of a diffusion-positive lesion rather than symptomatic infarction because there were only 2 cases of symptomatic infarction in this case series. Instead, multiple (≥ 6) small-dot lesions were categorized, and the association with variables was studied because multiple (≥ 6) small-dot lesions on immediate postprocedural MR imaging were closely associated with symptomatic infarction in a previous study.⁷ We hypothesized that image-guided analysis would be more objective and that the possibility of missing a thromboembolic event would be lower. If a patient had a silent infarction, his or her death could be confused with that of a patient without complications.

A previous study showed that advanced age (65 years or older) was the only predictor of diffusion lesions after coil embolization. The authors suggested that tortuous vascular structures and underlying atherosclerotic burden could cause these results.⁸ Our findings support the findings of this previous study. Almekhlafi et al²⁵ reported that during carotid artery stent placement, microemboli could occur during stent deployment or advancement through the stenosis. Thromboembolic complications could occur by dislodging thrombi from atherosclerotic vessels proximal to the target site and cracking the atherosclerotic plaque.¹² Therefore, the use of wires or a catheter at the target site would cause thromboembolic

Table 2: Patient clinical, laboratory, and procedural variables associated with any DPL and multiple DPLs (≥ 6) on univariate and multivariate logistic analyses

	Any DPL			DPL ≥ 6		
	Univariate (P Value)	Multivariate (P Value)	OR (95% CI)	Univariate (P Value)	Multivariate (P Value)	OR (95% CI)
Clinical						
Age (≥ 65 yr)	.006	.024	1.78 (1.08–2.93)	.017	.030	2.47 (1.09–5.59)
Sex (female)	.556			.309		
Diabetes	.508			.123		
Hypertension	.502			.239		
Hyperlipidemia	.092	.065	1.76 (0.97–3.27)	1.000		
Smoking	.884			.327		
TIA or stroke history	1.000			.149		
Laboratory						
ARU (≥ 550)	.448	.802	1.11 (0.51–2.41)	.755	.215	0.33 (0.06–1.90)
PRU (> 240)	.337	.357	1.23 (0.76–2.01)	.294	.399	1.42 (0.63–3.20)
Procedure						
Dome size of aneurysm ≥ 7 mm	.016	.112	1.57 (0.90–2.74)	.033	.267	1.65 (0.68–3.99)
Location of aneurysm	.111			.551		
Technique						
Assist with stent	.145			.437		
Multiple catheters	1.000			.418		
Incomplete occlusion	.016	.085	1.78 (0.92–3.44)	.012	.039	2.66 (1.05–6.76)
Thrombus formation	.083	.082	7.32 (0.78–69.24)	.060	.010	9.93 (1.86–97.10)
No. of angiograms	.341			.954		

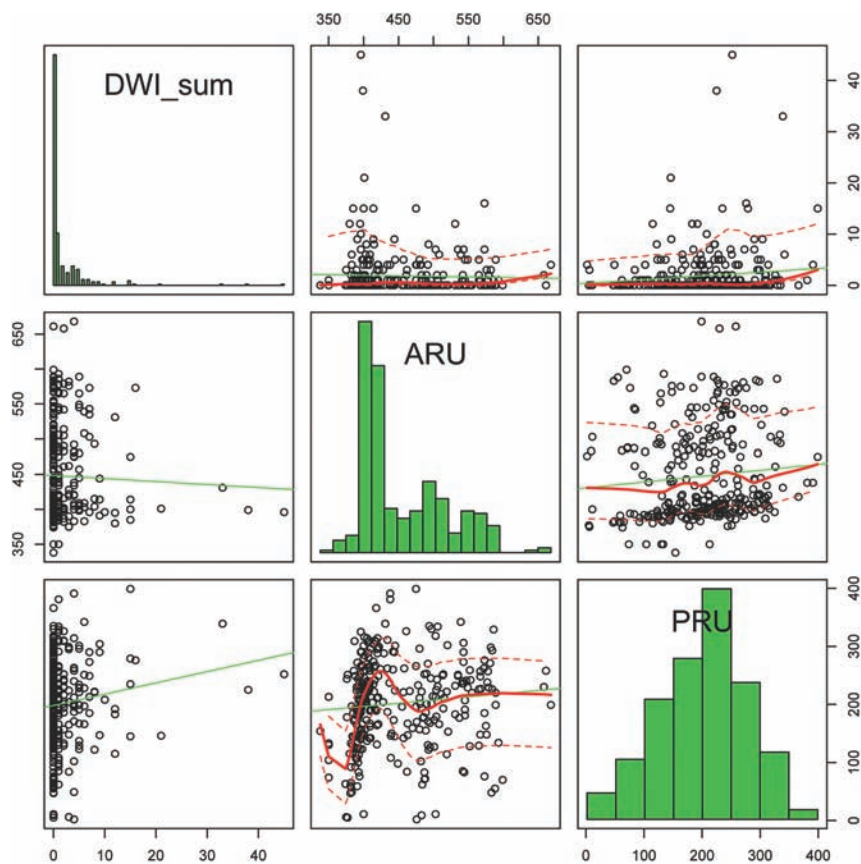


FIG 3. A scatterplot shows that the number of infarctions tends to increase along with PRU. ARU did not show a similar tendency.

events by dislodging thrombi from the atherosclerotic vessels at the aortic arch level. In this situation, nonipsilateral DPL occurred after the procedure. However, there are no data regarding the degree of atherosclerosis and tortuosity of the aortic arch.

variable aneurysm diameters, neck sizes, and antiplatelet resistance. Among these patients, 4 had asymptomatic DPLs on post-procedural MR imaging and 1 showed no DPL or symptoms. Although thrombus formation during the procedure showed a statistically significant difference on multiple (≥ 6) DPLs in mul-

For further evaluation and to identify the source of thromboembolism during coiling, CT angiography including the aortic arch could be helpful. Softer and smaller caliber catheters and wires and more skillful techniques could reduce the chance of dislodging thrombi during the procedure. Hwang et al²⁶ reported that incomplete occlusion is a risk factor for delayed ischemic stroke due to induced blood flow disturbance or stagnation. This study suggests that incomplete occlusion could be a source of infarction in both immediate and delayed thromboembolism. In addition, incomplete occlusion and large aneurysm size could explain frequent thromboembolism due to struggling to achieve complete occlusion of an aneurysm. These attempts could prolong the duration of procedure.^{20,27} Therefore, increased procedural time could possibly lead to thromboembolic complications in the postprocedural period. Mani and Eisenberg²⁸ reported that the thromboembolic complication rate increases when the arteriographic procedure exceeds 80 minutes. Our study also showed that procedural time was associated with postprocedural DPL.

The 5 patients experiencing thrombus formation during the procedure had

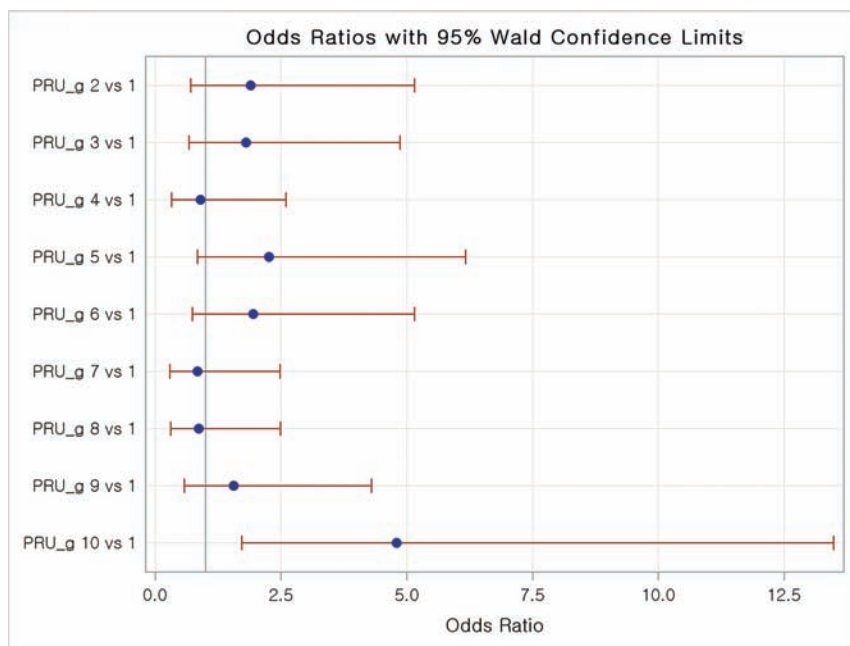


FIG 4. Association between PRU values and diffusion-positive lesions. The top 10% of PRU values (>294) were associated with higher thromboembolic risk ($P = .0029$).

tivariate logistic regression analysis, thrombus formation during embolization of unruptured aneurysm seems to be benign with the appropriate usage of a glycoprotein IIb/IIIa inhibitor.

Limitations

Several limitations of this study should be noted. First, although this study uses prospectively collected data, patient data were obtained from retrospective chart review. Therefore, minimal, transient symptoms could be missed in this analysis. Second, this study did not include the effect of systemic heparinization during the procedure. Despite maintaining heparinization during the procedure, precise activated clotting time control was difficult due to various patient responses to injected heparin. Third, the primary outcome of this study was DPL rather than symptomatic infarction. Although we hypothesized that image-based analysis could be more objective, these data may not have clinical significance. Fourth, these data were analyzed at an aneurysm level due to classification difficulties. Difficulties occurred when an individual patient had multiple aneurysms. Analyzing the patient at an aneurysm level prevents such difficulties because the individual aneurysms are checked into the data base separately. Additionally, we analyzed the data at a patient level and found that there were no significant differences in the patient-level clustering data results.

Last, some experts recommended analyzing the clinical association with procedural time, the number of angiograms performed per intervention, and DPL.^{20,29-31} The exact time of each procedure was not included in our registry data base. According to our retrospective chart review, we could only obtain anesthesia time, not procedural time. The univariate analysis revealed that anesthesia time was solely associated with DPL but not the number of angiograms performed per intervention. However, anesthesia time could differ from procedure time due to other procedure time associated with anesthesia. Therefore, we did not include total procedural time in multivariate analysis. In addition, we did not

include the number of angiograms obtained per intervention in multivariate analysis because they were associated with DPL in univariate analysis. Procedural time could be a potential predictor of DPL because it relates to the difficulty of coil embolization. These variables could be potential predictors of postprocedural DPL and could be considered important variables in further study.

CONCLUSIONS

Postprocedural DPL was closely associated with advanced age. Only clopidogrel nonresponse (PRU >294) could predict DPL after unruptured aneurysm coiling. The antiplatelet regimen should be individualized on the basis of the receiver operating characteristics. Further studies are needed to determine precise cutoff values, which may provide a rationale for the optimal antiplatelet regimen for aneurysm coiling.

REFERENCES

- Ruan C, Long H, Sun H, et al. **Endovascular coiling vs. surgical clipping for unruptured intracranial aneurysm: a meta-analysis.** *Br J Neurosurg* 2015;29:485-92 CrossRef Medline
- Norback O, Gál G, Johansson M, et al. **The establishment of endovascular aneurysm coiling at a neurovascular unit: report of experience during early years.** *Neuroradiology* 2005;47:144-52 CrossRef Medline
- Rahme RJ, Zammar SG, El Ahmadi TY, et al. **The role of antiplatelet therapy in aneurysm coiling.** *Neurol Res* 2014;36:383-88 CrossRef Medline
- Kim B, Kim K, Jeon P, et al. **Thromboembolic complications in patients with clopidogrel resistance after coil embolization for unruptured intracranial aneurysms.** *AJNR Am J Neuroradiol* 2014;35:1786-92 CrossRef Medline
- Kang DH, Kim BM, Kim DJ, et al. **MR-DWI-positive lesions and symptomatic ischemic complications after coiling of unruptured intracranial aneurysms.** *Stroke* 2013;44:789-91 CrossRef Medline
- Hahnemann ML, Ringelstein A, Sandalcioglu IE, et al. **Silent embolism after stent-assisted coiling of cerebral aneurysms: diffusion-weighted MRI study of 75 cases.** *J Neurointerv Surg* 2014;6:461-65 CrossRef Medline
- Cronqvist M, Wirestam R, Ramgren B, et al. **Diffusion and perfusion MRI in patients with ruptured and unruptured intracranial aneurysms treated by endovascular coiling: complications, procedural results, MR findings and clinical outcome.** *Neuroradiology* 2005;47:855-73 CrossRef Medline
- Soeda A, Sakai N, Sakai H, et al. **Thromboembolic events associated with Guglielmi detachable coil embolization of asymptomatic cerebral aneurysms: evaluation of 66 consecutive cases with use of diffusion-weighted MR imaging.** *AJNR Am J Neuroradiol* 2003;24:127-32 Medline
- Oxley TJ, Dowling RJ, Mitchell PJ, et al. **Antiplatelet resistance and thromboembolic complications in neurointerventional procedures.** *Front Neurol* 2011;2:83 CrossRef Medline
- Hwang G, Huh W, Lee JS, et al. **Standard vs modified antiplatelet preparation for preventing thromboembolic events in patients with high on-treatment platelet reactivity undergoing coil embolization for an unruptured intracranial aneurysm: a randomized clinical trial.** *JAMA Neurol* 2015;72:764-72 CrossRef Medline

11. Kang HS, Kwon BJ, Kim JE, et al. **Preinterventional clopidogrel response variability for coil embolization of intracranial aneurysms: clinical implications.** *AJNR Am J Neuroradiol* 2010;31:1206–10 CrossRef Medline
12. Kim BJ, Kwon JY, Jung JM, et al. **Association between silent embolic cerebral infarction and continuous increase of P2Y12 reaction units after neurovascular stenting.** *J Neurosurg* 2014;121:891–98 CrossRef Medline
13. Wiebers DO, Whisnant JP, Huston J 3rd, et al; International Study of Unruptured Intracranial Aneurysms Investigators. **Unruptured intracranial aneurysms: natural history, clinical outcome, and risks of surgical and endovascular treatment.** *Lancet* 2003;362:103–10 CrossRef Medline
14. Ernst M, Yoo AJ, Kriston L, et al. **Is visual evaluation of aneurysm coiling a reliable study end point? Systematic review and meta-analysis.** *Stroke* 2015;46:1574–81 CrossRef Medline
15. Delgado Almandoz JE, Crandall BM, Scholz JM, et al. **Pre-procedure P2Y12 reaction units value predicts perioperative thromboembolic and hemorrhagic complications in patients with cerebral aneurysms treated with the Pipeline Embolization Device.** *J Neurointerv Surg* 2013;5(suppl 3):iii3–10 CrossRef Medline
16. Maruyama H, Takeda H, Dembo T, et al. **Clopidogrel resistance and the effect of combination cilostazol in patients with ischemic stroke or carotid artery stenting using the VerifyNow P2Y12 assay.** *Intern Med* 2011;50:695–98 CrossRef Medline
17. Godino C, Mendolicchio L, Figini F, et al. **Comparison of VerifyNow-P2Y12 test and flow cytometry for monitoring individual platelet response to clopidogrel: what is the cut-off value for identifying patients who are low responders to clopidogrel therapy?** *Thromb J* 2009;7:4 CrossRef Medline
18. Park KW, Park JJ, Jeon KH, et al. **Clinical predictors of high post-treatment platelet reactivity to clopidogrel in Koreans.** *Cardiovasc Ther* 2012;30:5–11 CrossRef Medline
19. Jeon JS, Sheen SH, Hwang G, et al. **Intraarterial tirofiban thrombolysis for thromboembolisms during coil embolization for ruptured intracranial aneurysms.** *J Cerebrovasc Endovasc Neurosurg* 2012;14:5–10 CrossRef Medline
20. Bendszus M, Koltzenburg M, Burger R, et al. **Silent embolism in diagnostic cerebral angiography and neurointerventional procedures: a prospective study.** *Lancet* 1999;354:1594–07 CrossRef Medline
21. Ozben S, Ozben B, Tanrikulu AM, et al. **Aspirin resistance in patients with acute ischemic stroke.** *J Neurol* 2011;258:1979–86 CrossRef Medline
22. Yamada NK, Cross DT 3rd, Pilgram TK, et al. **Effect of antiplatelet therapy on thromboembolic complications of elective coil embolization of cerebral aneurysms.** *AJNR Am J Neuroradiol* 2007;28:1778–82 CrossRef Medline
23. Lev EI, Patel RT, Maresh KJ, et al. **Aspirin and clopidogrel drug response in patients undergoing percutaneous coronary intervention: the role of dual drug resistance.** *J Am Coll Cardiol* 2006;47:27–33 CrossRef Medline
24. Saw J, Densem C, Walsh S, et al. **The effects of aspirin and clopidogrel response on myonecrosis after percutaneous coronary intervention: a BRIEF-PCI (Brief Infusion of Intravenous Eptifibatide Following Successful Percutaneous Coronary Intervention) trial substudy.** *JACC Cardiovasc Interv* 2008;1:654–59 CrossRef Medline
25. Almekhlafi MA, Demchuk AM, Mishra S, et al. **Malignant emboli on transcranial Doppler during carotid stenting predict postprocedure diffusion-weighted imaging lesions.** *Stroke* 2013;44:1317–22 CrossRef Medline
26. Hwang G, Kim JG, Song KS, et al. **Delayed ischemic stroke after stent-assisted coil placement in cerebral aneurysm: characteristics and optimal duration of preventative dual antiplatelet therapy.** *Radiology* 2014;273:194–201 CrossRef Medline
27. Dion JE, Gates PC, Fox AJ, et al. **Clinical events following neuroangiography: a prospective study.** *Stroke* 1987;18:997–1004 CrossRef Medline
28. Mani RL, Eisenberg RL. **Complications of catheter cerebral arteriography: analysis of 5,000 procedures, III: assessment of arteries injected, contrast medium used, duration of procedure, and age of patient.** *AJR Am J Roentgenol* 1978;131:871–74 CrossRef Medline
29. Kato K, Tomura N, Takahashi S, et al. **Ischemic lesions related to cerebral angiography: evaluation by diffusion weighted MR imaging.** *Neuroradiology* 2003;45:39–43 Medline
30. Britt PM, Heiserman JE, Snider RM, et al. **Incidence of postangiographic abnormalities revealed by diffusion-weighted MR imaging.** *AJNR Am J Neuroradiol* 2000;21:55–59 Medline
31. Hähnel S, Bender J, Jansen O, et al. **Clinically silent cerebral embolisms after cerebral catheter angiography [in German].** *Rofo* 2001;173:300–05 CrossRef Medline

Current Trends and Results of Endovascular Treatment of Unruptured Intracranial Aneurysms at a Single Institution in the Flow-Diverter Era

O. Petr, W. Brinjikji, H. Cloft, D.F. Kallmes, and G. Lanzino



ABSTRACT

BACKGROUND AND PURPOSE: During the past several years, the number of unruptured aneurysms treated with endovascular techniques has increased. Traditionally, coil embolization was the treatment of choice for these lesions; however, recently flow diversion has become a viable, and in some cases superior, treatment option. The current single-center study presents results and trends of endovascular treatment with flow diversion and coil embolization in an unselected group of patients with unruptured intracranial aneurysms in a “real world” setting during the flow-diverter era.

MATERIALS AND METHODS: Three hundred ten patients with 318 treated unruptured aneurysms from June 2009 to May 2015 were included. Patient demographics, clinical characteristics, aneurysm/treatment characteristics, and outcomes were collected prospectively. We studied the following: intensive care unit admission/reasons, perioperative and mid-/long-term complications, target aneurysm rupture, retreatment/recurrence rates, and long-term neurologic outcome using the mRS.

RESULTS: The flow-diverter group had a larger mean aneurysm size (12.3 ± 8.6 mm versus 8.7 ± 6.3 mm, $P < .0001$). There were no significant differences in the immediate ($P = .43$) and mid-/long-term complication rates ($P = .54$) between groups. Perioperative neurologic morbidity and mortality rates were 2.1% and 0.5% in the coiling group and 2.5% and 1.6% in the flow-diverter group. Patients with coiling were more likely to be retreated than those with flow diversion (14.8% versus 5.7%, $P = .009$). Worsening of the mRS due to the target aneurysm was noted in only 3.2% of patients.

CONCLUSIONS: The endovascular treatment of unruptured aneurysms can be performed with very low rates of neurologic complications. Both flow-diverter and coil therapy were safe and effective.

ABBREVIATIONS: FD = flow diverter; ICU = intensive care unit; PED = Pipeline Embolization Device

During the past several years, the number of unruptured aneurysms treated with endovascular techniques has increased. Traditionally coil embolization was the treatment of choice for these lesions; however, the introduction of endoluminal flow diversion has heralded the beginning of a new endovascular era. Flow diversion achieves high rates of aneurysm occlusion with acceptable safety profiles.¹⁻⁶ However, with increasing experience and widespread use of flow diversion, several problems and complications have been recognized.^{7,8} These include intraparenchymal hemorrhage, postprocedural subarachnoid hemorrhage, and ischemic stroke.^{9,10}

Newer endovascular treatment options allow better patient selection for flow-diversion and coiling techniques. At this stage, the potential influence of flow diversion on the use of coils in treatment of intracranial aneurysms remains unknown.¹¹ These devices are being used in greater numbers of patients with various aneurysm locations and morphologies.^{6,12-14} While observing the changing endovascular treatment trends is interesting, it is crucial to assess the risk-benefit ratio for treatment by flow diverters (FDs) compared with coiling. The current single-center study presents results and trends of endovascular treatment with flow diversion and coil embolization in a group of unselected patients with unruptured intracranial aneurysms in a “real world” setting.

MATERIALS AND METHODS

Patient Population and Data Collection

Following institutional review board approval, all patients included in a prospective database of unruptured aneurysms from June 2009 to May 2015 were included in this study. Information collected in this database included patient demographics and

Received August 25, 2015; accepted after revision November 18.

From the Departments of Neurologic Surgery (O.P., G.L.) and Radiology (W.B., H.C., D.F.K., G.L.), Mayo Clinic, Rochester, Minnesota; and Department of Neurosurgery, (O.P.), Medical University, Innsbruck, Austria.

Please address correspondence to Giuseppe Lanzino, MD, Mayo Clinic, 200 1st St SW, Rochester, MN 55905; e-mail: lanzino.giuseppe@mayo.edu; @WBrinjikji

 Indicates article with supplemental on-line photos.

<http://dx.doi.org/10.3174/ajnr.A4699>

baseline clinical characteristics, aneurysm characteristics, treatment characteristics, and treatment outcomes. Patient demographic data collected included age, sex, baseline symptoms, baseline neurologic status, history of subarachnoid hemorrhage, and family history of intracranial aneurysms. Aneurysm characteristics included location and size. Treatment characteristics included type of device used, number of flow diverters used, and use of stent or balloon assistance.

The periprocedural pharmacologic protocol for patients undergoing flow-diverter therapy was uniform throughout the study period. Starting clopidogrel (Plavix), 75 mg, and aspirin, 325 mg, daily for 5 days before the procedure was recommended. Postoperatively, patients were maintained on the same clopidogrel and aspirin dosage for 3 months. After 3 months, clopidogrel was discontinued for patients undergoing on-label treatment (ie, aneurysms of the internal carotid artery proximal to the takeoff of the posterior communicating artery). For cases that were not off-label, and especially in high-risk locations, we have continued antiplatelet therapy for a longer time due to a potentially higher risk of thromboembolic events. Patients with aneurysms distal to the origin of the posterior communicating artery or involving the posterior circulation were usually maintained on clopidogrel for a longer time, and the antiplatelet therapy was recommended according to the results of their follow-up conventional angiography. After discontinuation of clopidogrel, low-dose aspirin (81 mg/day) indefinitely was recommended. Loading doses of clopidogrel and aspirin were given on the day before or the day of the procedure for patients who were not electively admitted. Platelet reactivity was not tested in any patient.

Outcomes

Treatment outcomes included intraprocedural and periprocedural technical events, clinical events (including aneurysm perforation, thrombosis, neurologic symptoms, medical symptoms, ophthalmologic symptoms, and groin complications), and late technical and clinical events at follow-up. Periprocedural complications were defined as those occurring within 30 days following the procedure, and late events were defined as events occurring after 30 days. Clinical follow-up was collected by telephone within the first 30 days, at the time of radiographic follow-up at 6 and 12 months and 3 years, and by telephone at 24 months. Clinical follow-up was obtained by a specialized nurse not directly involved with the original procedure. At the time of follow-up, patients were asked to rate themselves on the basis of the modified Rankin Scale. Patients were also asked to specify the reason for any score higher than zero. A baseline assessment, following the same methodology, was also obtained at the first encounter before aneurysm treatment.

For patients with flow diverters, radiologic follow-up with conventional angiography was recommended at 6, 12, and 36 months, and for patients with coiling, conventional angiography or MRA was recommended 6 or 12 months after the original procedure, depending on aneurysm characteristics. Afterward, imaging follow-up for patients with coiling was individualized according to various patient and aneurysm factors. Aneurysm occlusion on follow-up angiography, MRA, and/or CTA was categorized as “complete” (no filling of the aneurysm sac), “near-

complete” (>90% occlusion), and “incomplete” (<90% occlusion). We also reported FD angiographic outcomes by the number of FDs used in treatment.

We studied the following outcomes: 1) the presence of perioperative complications, 2) mid- and long-term complications, 3) target aneurysm rupture, 4) retreatment rates, 5) major recurrence rates, and 6) long-term neurologic outcome. Long-term neurologic outcome was assessed by using the modified Rankin Scale and with the methodology detailed above. We also determined whether neurologic disability was secondary to the aneurysm or other symptoms (ie, back pain, intercurrent nonrelated illness, and so forth). “Neurologic morbidity” was defined as any neurologic deficit that appeared either due to target aneurysms or their endovascular treatment. “Neurologic mortality” was defined as any death of the patient related to target aneurysms and/or their treatment complications.

Statistical Analysis

Baseline characteristics and outcomes were compared between the flow-diverter and coiling groups. Descriptive statistics are presented as means and proportions. Means are presented with SDs. Categorical variables were compared by using a χ^2 test, and continuous variables were compared by using a Student *t* test. Statistical significance was a *P* value < .05. All statistical analysis was performed by using JMP 10.0 (SAS Institute, Cary, North Carolina).

RESULTS

Patient Population

During the study period (September 2009 to April 2015), 332 patients were recommended for endovascular treatment of 341 unruptured intracranial aneurysms. Twenty-two patients with 23 target aneurysms were excluded due to missing Minnesota Research Authorization. Three hundred ten patients with 318 target aneurysms treated with endovascular coiling or flow diverters were included in the study. One hundred ninety-six aneurysms were initially treated with coiling, and 87 aneurysms were initially treated with flow diversion. Thirty-five aneurysms were treated with flow diversion following recanalization after coiling (these aneurysms were either coiled at other institutions or coiled at our institution prior to the study period). Of the 318 target aneurysms treated during the study period, 34 required retreatment. Thus, there were 352 aneurysm treatments during the study period. Demographic and aneurysm characteristics are listed in Table 1. Two hundred forty-nine patients (80.3%) were women, and 61 patients (19.7%) were men. The mean age at presentation was 57.4 years (range, 20–83 years). Most of the treated aneurysms were asymptomatic (249 aneurysms, 78.3%), while 69 aneurysms (21.7%) were symptomatic. Headache (11.0%) and visual problems (5.7%) were the most common presenting symptoms. Two hundred ten aneurysms (66.0%) were incidentally discovered.

Radiologic follow-up was available for 290 aneurysms (91.2%), while 28 aneurysms (8.8%) have not yet undergone radiologic follow-up because they were recently treated. The mean length of radiologic follow-up was 20 months (range, 0–67 months), and the mean clinical follow-up was 23.4 months (range, 1–67 months). From 2009 to 2014, the proportion of aneurysms treated with flow diversion increased from 15.8% to

Table 1: Demographic characteristics

	All Patients (n = 310)	Patients with Coiling (n = 188)	Patients with Flow Diverters (n = 122)	P Value
Mean age (SD) (yr)	57.4 (20–83)	57.9 (24–80)	55.7 (23–80)	.10
Female sex (No.) (%)	249 (80.3%)	145 (77.1%)	104 (85.2%)	.01
Mean (range) follow-up (mo)	23.4 (1–67)	24.5 (1–67)	22.4 (1–61)	
No. of aneurysms	318	196	122	
Aneurysm location				<.0001
Cavernous ICA	27 (8.5%)	1 (0.5%)	26 (21.3%)	
Paraclinoid/supraclinoid ICA	104 (32.7%)	34 (17.3%)	70 (57.4%)	
ICA terminus	13 (4.1%)	10 (5.1%)	3 (2.5%)	
ICA PcomA	36 (11.3%)	24 (12.2%)	12 (9.8%)	
MCA	19 (6.0%)	16 (8.2%)	3 (2.5%)	
ACA/AcomA	56 (17.6%)	56 (28.6%)	0 (0%)	
Vertebral artery	2 (0.6%)	1 (0.5%)	1 (0.8%)	
Basilar artery	37 (11.6%)	35 (17.9%)	2 (1.6%)	
PICA	10 (3.2%)	7 (3.6%)	3 (2.5%)	
Other	14 (4.4%)	12 (6.1%)	2 (1.6%)	
Anterior circulation	263 (82.7%)	148 (75.5%)	115 (94.3%)	
Posterior circulation	55 (17.3%)	48 (24.5%)	7 (5.7%)	
Mean size (SD)		8.7 (±6.3 mm)	12.3 (±8.6 mm)	<.0001
Small (<5 mm)	60 (18.9%)	46 (23.5%)	14 (11.5%)	
Medium (5–15 mm)	207 (65.1%)	131 (66.8%)	76 (62.3%)	
Large (16–25 mm)	26 (8.2%)	11 (5.6%)	15 (12.3%)	<.0001
Giant (>25 mm)	25 (7.9%)	8 (4.1%)	17 (13.9%)	<.0001
Symptoms				
Asymptomatic	249 (78.3%)	159 (81.1%)	90 (73.8%)	
Symptomatic	69 (21.7%)	37 (18.9%)	32 (26.2%)	
Headaches	35 (11.0%)	21 (10.7%)	14 (11.5%)	
Visual problems	18 (5.7%)	9 (4.6%)	9 (7.4%)	
Aneurysm discovered incidentally	210 (66.0%)	144 (73.5%)	66 (54.1%)	

Note:—PcomA indicates posterior communicating artery; AcomA, anterior communicating artery; ACA, anterior cerebral artery; PICA, posterior inferior cerebellar artery.

48.8% (On-line Fig 1). Accordingly, in the proximal (to the origin of the posterior communicating artery) ICA aneurysm group, the proportion of aneurysms treated with flow diverters increased from 27.3% to 88.9% (On-line Fig 2).

Basic demographic characteristics between the 2 groups are summarized in Table 1. The flow-diverter group had a higher mean aneurysm size (12.3 ± 8.6 mm versus 8.7 ± 6.3 mm, $P < .0001$). There were more large and giant aneurysms in the FD group compared with the coiling group (26.2% versus 9.7%, $P < .0001$). There was a significant difference in the location of treated aneurysms between the 2 groups ($P < .0001$): Twenty-six cavernous sinus aneurysms (21.3%) were treated with FDs compared with 1 (0.5%) in the coil embolization group; 70 (57.4%) supraclinoid/paraclinoid aneurysms were treated in the FD group versus 34 (17.3%) aneurysms in the coiling group. All anterior cerebral artery/anterior communicating artery aneurysms (56/17.6%) were treated with coiling only. Characteristics of treated aneurysms are summarized in Table 1.

Angiographic Results

Angiographic results and basic characteristics of techniques and devices are listed in Table 2. Radiologic follow-up was available for 290 (91.2%) aneurysms, after a mean time of 20 months (range, 0–67 months), while 28 aneurysms (8.8%) have not yet undergone radiologic follow-up.

Complete occlusion at the last radiologic follow-up was achieved in 165 (51.9%) aneurysms, and near-complete occlusion, in 112 (35.2%) aneurysms. Among patients with at least 6 months of imaging follow-up, the complete occlusion rate was

55.1% (147/267) and the near-complete occlusion rate was 34.5% (92/267). For patients with flow diverters with 6 months of imaging follow-up, the complete occlusion rate was 64.4% (67/104) and the near-complete occlusion rate was 22.1% (23/104). For patients with coiling with at least 6 months of imaging follow-up, the complete occlusion rate was 49.1% (80/163) and the near-complete occlusion rate was 42.3% (69/163).

Of 352 endovascular treatments and 318 treated unruptured aneurysms, major recurrences were present and retreated in 29 aneurysms (14.8%) in the coiling group. In the FD group, there were no instances of recanalization; however, 7 aneurysms (5.7%) were retreated due to persistent filling of the aneurysm sac. The rate of retreatment was significantly higher in the coiling group ($P = .009$). Of 29 aneurysm retreatments in the coiling group, 18 (9.2%) were retreated with recoiling; 2 (1.0%), with surgical clipping; and 8 (4.1%), with FDs. All 7 retreatments (5.7%) from the FD group were retreated with the Pipeline Embolization Device (PED; Covidien, Irvine, California).

In the FD group, the overall rate of complete occlusion at last follow-up was 56.6% (69/122) and the near-complete occlusion rate was 21.3% (26/122). Complete occlusion rates were 49.5% (45/91) for patients treated with 1 FD, 66.7% (12/18) for patients treated with 2 FDs, and 92.3% (12/13) for patients treated with ≥3 FDs. These data are summarized in Table 3.

Technical Outcomes and Immediate Complications

Immediate complications following the endovascular procedure occurred in 32 patients (10.3%). These complications included 20 patients (10.6%) from the coiling group and 12 patients (9.8%)

Table 2: Technical and angiographic outcomes^a

	All Patients/ Treatments (N = 310/352)	Patients with Coiling/ Treatments (n = 188/223)	Patients with Flow Diverters/Treatments (n = 122/129)	P Value
Coiling-assist devices				
Balloon	9/352 (2.6%)	9/223 (4.0%)	NA	–
Stent	10/352 (2.8%)	10/223 (4.5%)	NA	
Flow diverter used				
Pipeline	124/352 (35.2%)	NA	124/129 (96.1%)	–
Surpass ^b	5/352 (1.4%)	NA	5/129 (3.9%)	
Angiographic occlusion at last follow-up				
Complete	165/318 (51.9%)	96/196 (49.0%)	69/122 (56.6%)	<.0001
Near-complete	112/318 (35.2%)	86/196 (43.9%)	26/122 (21.3%)	
Incomplete	41/318 (12.9%)	14/196 (7.1%)	27/122 (22.1%)	
Angiographic follow-up for patients with imaging ≥6 mo posttreatment				<.0001
Complete	147/267 (55.1%)	80/163 (49.1%)	67/104 (64.4%)	
Near-complete	92/267 (34.5%)	69/163 (42.3%)	23/104 (22.1%)	
Incomplete	28/267 (10.5%)	14/163 (8.6%)	14/104 (13.5%)	
Mean radiologic follow-up time (mo)	20 (0–67)	20 (0–67)	20 (0–61)	.46
Retreatment				.009
Recoiling	18/318 (5.7%)	18/196 (9.2%)	0/122 (0.0%)	
Retreatment with FD	15/318 (4.7%)	8/196 (4.1%)	7/122 (5.7%)	
Clipping	2/318 (0.6%)	2/186 (1.0%)	0/122 (0.0%)	
Recurrence	36/318 (11.3%)	29/196 (14.8%)	7/122 (5.7%)	.009

Note:—NA indicates not available.

^a Three hundred ten patients received 352 treatments; 188 patients with coiling received 223 treatments, and 122 patients with flow diverters received 129 treatments.

^b Stryker Neurovascular, Kalamazoo, Michigan.

Table 3: Outcomes by number of flow diverters

Angiographic Occlusion at Last Follow-Up	1 Device	2 Devices	≥3 Devices	122 Aneurysms
Complete	45 (49.5%)	12 (66.7%)	12 (92.3%)	69 (56.6%)
Near-complete	22 (24.1%)	4 (22.2%)	0 (0%)	26 (21.3%)
Incomplete	24 (26.4%)	2 (11.1%)	1 (7.7%)	27 (22.1%)

from the FD group and are summarized in Table 4. Seven patients experienced TIAs (2.3%), and 1 patient noted a deterioration of ophthalmoplegia (0.3%). There was no significant difference in the immediate complication rate between both groups ($P = .43$). Neurologic mortality rates were 0.5% in the coiling group and 1.6% in the FD group ($P = .70$). Neurologic morbidity rates were 2.1% in the coiling group and 2.5% in the FD group ($P = .85$).

The mean length of the hospital stay was not significantly different between the 2 groups (1.2 days for the coiling group and 1.3 days for the FD group, $P = .54$). There was a decreasing trend in the proportion of patients with flow diverters going to the intensive care unit (ICU) between 2009 and 2014 (100% to 15.8%). The same was true for patients with coiling (50% to 16.7%) (On-line Fig 3).

Midterm and Long-Term Clinical Outcomes

Midterm and long-term complications following endovascular procedures occurred in 12 patients (3.9%) and are listed in Table 4. Midterm/long-term complications occurred in 6 patients (3.2%) from the coiling group and 6 patients (4.9%) from the FD group ($P = .54$). Six patients (1.9%) had thromboembolic complications, and 4 patients (1.3%) experienced periorbital pain. Only 1 of all mid-/long-term complications (0.3%) resulted in a permanent neurologic deficit. This 73-year-old woman with a left-sided giant symptomatic carotid cavernous aneurysm treated with flow diversion developed a permanent mild right-sided hemiparesis.

Clinical follow-up with mRS assessment before and after treatment was available for all patients, with a mean follow-up time of 23.4 months (range, 1–67 months). The mean length of clinical follow-up was not significantly different between groups (24.5 months; range, 1–67 months in the coiling group; and 22.4 months; range, 1–61 months in the FD group).

Ten patients (3.2%) reported mRS worsening due to the target aneurysm or endovascular therapy (7 in the coiling group and 3 in the FD group). Three patients experienced postoperative rupture (1.0%). Twenty-two patients (7.1%) died during the study period; however, only 3 (1.0%) of the deaths were related to their target aneurysms or stroke. One patient died following delayed rupture of a previously coiled unruptured aneurysm, 1 patient died from a distal intraparenchymal hemorrhage 8 days after treatment with a PED, and 1 patient had a posttreatment rupture from a giant left ICA aneurysm 11 months after PED deployment. Long-term neurologic outcomes are listed in Table 5. A summary of patients who experienced postoperative rupture is provided in Table 6.

DISCUSSION

Our consecutive prospective series of 318 aneurysms in 310 unselected patients demonstrated that endovascular treatment of unruptured aneurysms can be performed with low rates of neurologic complications and high rates of satisfactory angiographic occlusion. Both flow-diverter and coil therapy were safe and effective. However, coil treatment was associated with higher rates of recurrence and retreatment. Only 3.2% of patients noticed a deterioration of symptoms due to aneurysm or endovascular treatment. Our study also demonstrated that since the introduction of flow diversion at our institution, there has been a significant upward trend in the use of FDs as approximately 50% of unruptured aneurysms are now treated by using these methods.

Table 4: Clinical outcomes

	All Patients (N = 310)	All Treatments (n = 352)	Patients with Coiling (n = 188)	Coiling Treatments (n = 223)	Patients with Flow Diverters (n = 122)	Flow-Diverter Treatments (n = 129)	P Value
ICU admission							
Yes	82 (26.5%)	93 (26.4%)	37 (19.7%)	45 (20.2%)	45 (36.9%)	48 (37.2%)	.005
No	228 (73.5%)	259 (73.6%)	151 (80.3%)	178 (79.8%)	77 (63.1%)	81 (62.8%)	
Reason for ICU admission							
1) Complexity	39 (12.6%)	45 (12.8%)	16 (8.5)	20 (9.0)	23 (18.9%)	25 (19.4%)	
2) Neurologic deterioration	4 (1.3%)	4 (1.1%)	3 (1.6%)	3 (1.3%)	1 (0.8%)	1 (0.8%)	
3) Intraoperative rupture	3 (1.0%)	3 (0.9%)	3 (1.6%)	3 (1.3%)	0 (0%)	0 (0%)	
4) Vessel occlusion	6 (1.9%)	6 (1.7%)	1 (0.5%)	1 (0.4%)	5 (4.1%)	5 (3.9%)	
5) Coil dislocation	1 (0.3%)	1 (0.3%)	1 (0.5%)	1 (0.4%)	NA	NA	
6) Pipeline	14 (4.5%)	15 (4.3%)	NA	NA	14 (11.5%)	15 (11.6%)	
Immediate complications (<30 days)	32 (10.3%)	32 (9.1%)	20 (10.6%)	20 (9.0%)	12 (9.8%)	12 (9.3%)	.43
Intraoperative rupture	3 (1.0%)	3 (0.9%)	3 (1.6%)	3 (1.3%)	0 (0%)	0 (0%)	
Thromboembolic	5 (1.6%)	5 (1.4%)	4 (2.1%)	4 (1.8%)	1 (0.8%)	1 (0.8%)	
TIA	7 (2.3%)	7 (2.0%)	5 (2.7%)	5 (2.2%)	2 (1.6%)	2 (1.6%)	
Thrombus formation	7 (2.3%)	7 (2.0%)	3 (1.6%)	3 (1.3%)	4 (3.3%)	4 (3.1%)	
Groin hematoma	5 (1.6%)	5 (1.4%)	3 (1.6%)	3 (1.3%)	2 (1.6%)	2 (1.6%)	
Intraoperative aneurysm perforation	3 (1.0%)	3 (0.9%)	3 (1.6%)	3 (1.3%)	0 (0%)	0 (0%)	
Complication-related morbidity	4 (1.3%)	4 (1.1%)	2 (1.1%)	2 (0.9%)	2 (1.6%)	2 (1.6%)	
Complication-related mortality	3 (1.0%)	3 (0.9%)	1 (0.5%)	1 (0.4%)	2 (1.6%)	2 (1.6%)	
Mid- and long-term complications	12 (3.9%)	12 (3.4%)	6 (3.2%)	6 (2.7%)	6 (4.9%)	6 (4.7%)	.54
Thromboembolic, stroke	6 (1.9%)	6 (1.7%)	4 (2.1%)	4 (1.8%)	2 (1.6%)	2 (1.6%)	
Periorbital pain	4 (1.3%)	4 (1.1%)	2 (1.1%)	2 (0.9%)	2 (1.6%)	2 (1.6%)	
Vessel stenosis/occlusion	2 (0.6%)	2 (0.6%)	0 (0%)	0 (0%)	2 (1.6%)	2 (1.6%)	
Persistent complication-related morbidity	3 (1.0%)	3 (0.9%)	2 (1.1%)	2 (0.9%)	1 (0.8%)	1 (0.8%)	
Complication-related mortality	0 (0%)	0 (0%)	0 (0%)	0 (0%)	0 (0%)	0 (0%)	
Target aneurysm rupture	2 (0.6%)	2 (0.6%)	1 (0.5%)	1 (0.4%)	1 (0.8%)	1 (0.8%)	.19
PcomA (giant)	1 (0.3%)	1 (0.3%)	0 (0%)	0 (0%)	1 (0.8%)	1 (0.8%)	
MCA (large)	1 (0.3%)	1 (0.3%)	1 (0.5%)	1 (0.4%)	0 (0%)	0 (0%)	
Neurologic mortality	3 (1.0%)	3 (0.9%)	1 (0.5%)	1 (0.4%)	2 (1.6%)	2 (1.6%)	.70
Neurologic morbidity	7 (2.3%)	7 (2.0%)	4 (2.1%)	4 (1.8%)	3 (2.5%)	3 (2.3%)	.85
All-cause mortality	19 (6.1%)	19 (5.4%)	14 (7.4%)	14 (6.3%)	5 (4.1%)	5 (3.9%)	.15

Table 5: Aneurysm-related clinical outcomes

	All Patients (N = 310)	Patients with Coiling (n = 188)	Patients with Flow Diverters (n = 122)	P Value
Mortality related to target aneurysm rupture or stroke	9 (2.9%)	5 (2.7%)	4 (3.3%)	.15
Worsening of aneurysm-related symptoms	10 (3.2%)	7 (3.7%)	3 (2.5%)	.79
Long-term good neurologic outcomes (mRS ≤ 2)	264 (85.2%)	155 (82.4%)	109 (89.3%)	.33

Given the high safety profile of endovascular treatment, we have stopped routinely admitting patients to the ICU for monitoring posttreatment and are now sending more patients to a hospital floor after a brief stay in the postoperative recovery unit. These findings are important because they highlight the outcomes of contemporary endovascular treatment options of unruptured aneurysms in a real world setting and in a consecutive series of unselected patients.

Angiographic Outcomes

The incomplete degree of angiographic aneurysm occlusion and the risk of aneurysm recurrence remain the major limitations of endovascular treatment of cerebral aneurysms.¹⁵ In our series, we found cumulative complete/near-complete aneurysm occlusion rates of 87.1%. Cumulative complete/near-complete occlusion rates were 92.9% in the coiling group and 77.9% in the FD group. The high rate of angiographic occlusion at follow-up in aneurysms treated with coil embolization that we observed is in line with other recently published study results. For example, in a series of 4665 treated unruptured aneurysms, Shigematsu et al¹⁶ demonstrated a cumulative complete/near-complete aneurysm occlusion rate of 89.6%. Of these, 2690 aneurysms (57.7%) were completely occluded and

1490 (31.9%) had small residual necks. The rate of incomplete occlusion following coiling ranged from 1.2% to 20.8% in larger studies,¹⁷⁻²³ similar to our finding of 8% in the coiling group.

The rate of complete occlusion in the FD group with at least 6 months of follow-up of 64.4% is lower than that in other flow-diverter studies; however, the low rate of retreatment (6%) is in line with those previously reported.²⁴⁻²⁸ In the Pipeline for Uncoilable or Failed Aneurysms Study,²⁴ the rate of complete occlusion was 82% at 6 months and 86% at 12 months. Likewise, in a large single-center consecutive series of 54 patients, Lylyk et al²⁵ found high rates of complete - aneurysm occlusion of 93% and 96% at 6 and 12 months, respectively.

In our series, we encountered 3 cases of posttreatment rupture. In comparison, the Cerebral Aneurysm Rerupture After Treatment (CARAT) investigators reported annual rates of rupture after 1 year of 0.11% (95% CI, 0%–0.63%) for coiling. However, rerupture rates of incompletely obliterated aneurysms were as high as 17.6% during a mean follow-up of 4 years, when <70% of the aneurysm was occluded. In large series of flow-diversion treatments,^{2,27-30} the incidence of an-

Table 6: Cases of aneurysm rupture posttreatment

Rupture of Target Aneurysm after Treatment	R MCA	L PcomA Partially Thrombosed	R Carotid Ophthalmic
Aneurysm size (mm)	11	38	20
Initial treatment	Simple coiling	Partial coiling/PED	PED
No. of devices	6 Coils	3 Coils/1 PED	1 PED
Initial degree of occlusion	Near-complete	Incomplete	Incomplete
Follow-up imaging			
Complete radiologic/angiographic time (mo)	25.4	9.1	0.27
First imaging follow-up	DSA	MRA	CTA (emergency)
Timing of first imaging follow-up (mo)	7	3	8 Days (emergency)
Degree of occlusion at first follow-up	Incomplete/recurrence	Incomplete (decrease)	Incomplete
Degree of occlusion at last follow-up	Near-complete	Incomplete (decrease)	NA
Recurrence/retreatment	2×/2×	NA	NA
Retreatment			
Size of recurrence (mm)	5		
Time (mo)	7		
Endovascular technique	Simple coiling		
No. of devices	2 Coils		
Immediate degree of occlusion	Near-complete		
Retreatment			
Size of recurrence (mm)	13		
Time (mo)	18.5		
Endovascular technique	Simple coiling		
No. of devices	7 Coils		
Immediate degree of occlusion	Near-complete		
Rupture time	2.5 mo	9.1 mo	8 days

Note:—R indicates right; L, left; PcomA, posterior communicating artery.

aneurysm rupture was found to be between 0.4% and 2.6%. Brinjikji et al³¹ reported similar results (3%) in their meta-analysis of published case series.

Clinical Outcomes

In our series, we observed neurologic morbidity and mortality rates of 2.3% and 1.0% for patients, respectively. Only a minority of patients (3.2%) reported mRS worsening related to the target aneurysm or endovascular therapy (3.7% in the coiling group and 2.5% in the FD group). Neurologic morbidity and mortality rates in the FD group were 2.5% and 1.6%, respectively. This is lower than that reported in the International Retrospective Study of the Pipeline Embolization Device (IntrePED), which reported a combined neurologic morbidity and mortality rate of 8.4%.²⁹ This rate may be due to patient selection because the proportion of patients with treated non-ICA aneurysms in our study was lower than that in IntrePED. Other previously published studies^{8,26,32-34} have reported morbidity and mortality rates following FD treatment ranging from 0% to 12% and 0% to 7%, respectively.³¹

During our study period, we have changed our daily practice of admitting patients with unruptured intracranial aneurysms after treatment directly to the ICU. Arias et al³⁵ showed that most significant postprocedural events (74%) after uncomplicated aneurysm intervention occur within 4 hours. These events become less frequent with increasing time. Likewise, Eisen et al³⁶ found that in the absence of intraoperative events with the potential for ongoing cerebral ischemia, most patients undergoing elective endovascular treatment of unruptured cerebral aneurysms can be managed without direct ICU admission. Our experience and findings have been similar.³⁷ Improved ICU admission rates are likely due to a combination of increasing operator experience and patient selection.

Limitations

The limitations of this study are related to the absence of randomization and the variable duration of follow-up. However, the data for all patients were collected prospectively. This was a single-center case series of aneurysms treated by a group of experienced neurointerventionalists and endovascular neurosurgeons. Thus, our data may not be generalizable to other practices. With increasing experience with the PED, the off-label use of the PED has been widening in our practice, which could contribute to higher complication rates. Another limitation of the study is that there was no independent assessment of angiographic or clinical outcomes. The determination of final radiologic results was by the treating physician. In addition, there were significant differences in the baseline characteristics of patients undergoing coiling and flow-diverter therapy, which could confound our statistical analyses. These limitations notwithstanding, our study summarizes the results in an unselected group of patients with unruptured aneurysms in a real world setting and provides a contemporary view indicating that both endovascular techniques are safe and clinically effective in treating unruptured intracranial aneurysms. No patient was lost to follow-up. Moreover, clinical outcome, in accordance with International Subarachnoid Aneurysm Trial methodology, was by a patient self-assessment.³⁸

CONCLUSIONS

Our study of >300 patients with 318 unruptured aneurysms treated with flow-diverter therapy or coil embolization found that endovascular treatment of unruptured aneurysms is both safe and effective. Coil embolization was associated with higher recurrence and retreatment rates, but the rates of poor neurologic outcome were similar between groups. Flow diversion has been a disruptive technology at our institution because >50% of unruptured aneu-

rysms are now treated with this technique. Last, we found that in most cases, routine ICU admission is not necessary, and we have changed our practice accordingly. Our findings highlight the safety and efficacy profile of the endovascular treatment of unruptured aneurysms in a real world setting.

Disclosures: David F. Kallmes—UNRELATED: Board Membership: GE Healthcare (Cost-Effectiveness Board)*; Consultancy: ev3/Covidien/Medtronic,* Comments: planning and implementing clinical trials; Grants/Grants Pending: Sequent Medical,* SurModics,* NeuroSigma,* Codman,* Medtronic,* MicroVenton*;* Comments: pre-clinical research and clinical trials; Travel/Accommodations/Meeting Expenses Unrelated to Activities Listed: Medtronic,* Comments: presentation at an FDA panel meeting. Giuseppe Lanzino—UNRELATED: Consultancy: Covidien.* *Money paid to the institution.

REFERENCES

1. Yu SC, Kwok CK, Cheng PW, et al. **Intracranial aneurysms: mid-term outcome of Pipeline embolization device—a prospective study in 143 patients with 178 aneurysms.** *Radiology* 2012;265:893–901 CrossRef Medline
2. Saatci I, Yavuz K, Ozer C, et al. **Treatment of intracranial aneurysms using the Pipeline flow-diverter embolization device: a single-center experience with long-term follow-up results.** *AJNR Am J Neuroradiol* 2012;33:1436–46 CrossRef Medline
3. Deutschmann HA, Wehrschoetz M, Augustin M, et al. **Long-term follow-up after treatment of intracranial aneurysms with the Pipeline embolization device: results from a single center.** *AJNR Am J Neuroradiol* 2012;33:481–86 CrossRef Medline
4. Maimon S, Gonen L, Nossek E, et al. **Treatment of intra-cranial aneurysms with the SILK flow diverter: 2 years' experience with 28 patients at a single center.** *Acta Neurochir* 2012;154:979–87 CrossRef Medline
5. Chiu AH, Cheung AK, Wenderoth JD, et al. **Long-term follow-up results following elective treatment of unruptured intracranial aneurysms with the Pipeline embolization device.** *AJNR Am J Neuroradiol* 2015;36:1728–34 CrossRef Medline
6. McAuliffe W, Wycoco V, Rice H, et al. **Immediate and midterm results following treatment of unruptured intracranial aneurysms with the Pipeline embolization device.** *AJNR Am J Neuroradiol* 2012; 33:164–70 CrossRef Medline
7. Lanzino G. **Editorial: flow diversion for intracranial aneurysms.** *J Neurosurg* 2013;118:405–06; discussion 406–07 CrossRef Medline
8. McDonald RJ, McDonald JS, Kallmes DF, et al. **Periprocedural safety of Pipeline therapy for unruptured cerebral aneurysms: analysis of 279 patients in a multihospital database.** *Interv Neuroradiol* 2015;21: 6–10 CrossRef Medline
9. Burrows AM, Cloft H, Kallmes DF, et al. **Periprocedural and mid-term technical and clinical events after flow diversion for intracranial aneurysms.** *J Neurointerv Surg* 2015;7:646–51 CrossRef Medline
10. Cruz JP, Chow M, O'Kelly C, et al. **Delayed ipsilateral parenchymal hemorrhage following flow diversion for the treatment of anterior circulation aneurysms.** *AJNR Am J Neuroradiol* 2012;33:603–08 CrossRef Medline
11. Crobeddu E, Lanzino G, Kallmes DF, et al. **Marked decrease in coil and stent utilization following introduction of flow diversion technology.** *J Neurointerv Surg* 2013;5:351–53 CrossRef Medline
12. de Barros Faria M, Castro RN, Lundquist J, et al. **The role of the Pipeline embolization device for the treatment of dissecting intracranial aneurysms.** *AJNR Am J Neuroradiol* 2011;32:2192–95 CrossRef Medline
13. Kulcsár Z, Ernemann U, Wetzel SG, et al. **High-profile flow diverter (Silk) implantation in the basilar artery: efficacy in the treatment of aneurysms and the role of the perforators.** *Stroke* 2010;41:1690–96 CrossRef Medline
14. Pistocchi S, Blanc R, Bartolini B, et al. **Flow diverters at and beyond the level of the circle of Willis for the treatment of intracranial aneurysms.** *Stroke* 2012;43:1032–38 CrossRef Medline
15. Lanzino G, Crobeddu E, Cloft HJ, et al. **Efficacy and safety of flow diversion for paraclinoid aneurysms: a matched-pair analysis compared with standard endovascular approaches.** *AJNR Am J Neuroradiol* 2012;33:2158–61 CrossRef Medline
16. Shigematsu T, Fujinaka T, Yoshimine T, et al; JR-NET Investigators. **Endovascular therapy for asymptomatic unruptured intracranial aneurysms: JR-NET and JR-NET2 findings.** *Stroke* 2013;44:2735–42 CrossRef Medline
17. Pierot L, Spelle L, Vitry F. **Immediate anatomic results after the endovascular treatment of unruptured intracranial aneurysms: analysis of the ATENA series.** *AJNR Am J Neuroradiol* 2010;31:140–44 CrossRef Medline
18. Oishi H, Yamamoto M, Shimizu T, et al. **Endovascular therapy of 500 small asymptomatic unruptured intracranial aneurysms.** *AJNR Am J Neuroradiol* 2012;33:958–64 CrossRef Medline
19. Gonzalez N, Murayama Y, Nien YL, et al. **Treatment of unruptured aneurysms with GDCs: clinical experience with 247 aneurysms.** *AJNR Am J Neuroradiol* 2004;25:577–83 Medline
20. van Rooij WJ, Sluzewski M. **Durability of treatment of intracranial aneurysms with Hydrocoils is not different from standard platinum coils.** *Stroke* 2006;37:2874; author reply 2875 Medline
21. Yue W. **Endovascular treatment of unruptured intracranial aneurysms.** *Interv Neuroradiol* 2011;17:420–24 CrossRef Medline
22. Song JH, Chang IB, Ahn JH, et al. **Angiographic results of wide-necked intracranial aneurysms treated with coil embolization: a single center experience.** *J Korean Neurosurg Soc* 2015;57:250–57 CrossRef Medline
23. Raymond J, Guilbert F, Weill A, et al. **Long-term angiographic recurrences after selective endovascular treatment of aneurysms with detachable coils.** *Stroke* 2003;34:1398–403 CrossRef Medline
24. Becske T, Kallmes DF, Saatci I, et al. **Pipeline for uncoilable or failed aneurysms: results from a multicenter clinical trial.** *Radiology* 2013; 267:858–68 CrossRef Medline
25. Lylyk P, Miranda C, Ceratto R, et al. **Curative endovascular reconstruction of cerebral aneurysms with the Pipeline embolization device: the Buenos Aires experience.** *Neurosurgery* 2009;64:632–42; discussion 642–43; quiz N6 CrossRef Medline
26. Chalouhi N, Zanaty M, Whiting A, et al. **Safety and efficacy of the Pipeline embolization device in 100 small intracranial aneurysms.** *J Neurosurg* 2015;122:1498–502 CrossRef Medline
27. Chalouhi N, Starke RM, Yang S, et al. **Extending the indications of flow diversion to small, unruptured, saccular aneurysms of the anterior circulation.** *Stroke* 2014;45:54–58 CrossRef Medline
28. Zanaty M, Chalouhi N, Starke RM, et al. **Flow diversion versus conventional treatment for carotid cavernous aneurysms.** *Stroke* 2014; 45:2656–61 CrossRef Medline
29. Kallmes DF, Hanel R, Lopes D, et al. **International retrospective study of the Pipeline embolization device: a multicenter aneurysm treatment study.** *AJNR Am J Neuroradiol* 2015;36:108–15 CrossRef Medline
30. Briganti F, Napoli M, Tortora F, et al. **Italian multicenter experience with flow-diverter devices for intracranial unruptured aneurysm treatment with periprocedural complications—a retrospective data analysis.** *Neuroradiology* 2012;54:1145–52 CrossRef Medline
31. Brinjikji W, Murad MH, Lanzino G, et al. **Endovascular treatment of intracranial aneurysms with flow diverters: a meta-analysis.** *Stroke* 2013;44:442–47 CrossRef Medline
32. Berge J, Biondi A, Machi P, et al. **Flow-diverter Silk stent for the treatment of intracranial aneurysms: 1-year follow-up in a multicenter study.** *AJNR Am J Neuroradiol* 2012;33:1150–55 CrossRef Medline
33. Leonardi M, Cirillo L, Toni F, et al. **Treatment of intracranial aneurysms using flow-diverting Silk stents (BALT): a single centre experience.** *Interv Neuroradiol* 2011;17:306–15 Medline
34. Velioglu M, Kizilkilic O, Selcuk H, et al. **Early and midterm results of complex cerebral aneurysms treated with Silk stent.** *Neuroradiology* 2012;54:1355–65 CrossRef Medline
35. Arias EJ, Patel B, Cross DT 3rd, et al. **Timing and nature of in-house**

- postoperative events following uncomplicated elective endovascular aneurysm treatment. *J Neurosurg* 2014;121:1063–70 CrossRef Medline
36. Eisen SH, Hindman BJ, Bayman EO, et al. **Elective endovascular treatment of unruptured intracranial aneurysms: a management case series of patient outcomes after institutional change to admit patients principally to postanesthesia care unit rather than to intensive care.** *Anesth Analg* 2015;121:188–97 CrossRef Medline
37. Burrows AM, Rabinstein AA, Cloft HJ, et al. **Are routine intensive care admissions needed after endovascular treatment of unruptured aneurysms?** *AJNR Am J Neuroradiol* 2013;34:2199–201 CrossRef Medline
38. Molyneux A, Kerr R, Stratton I, et al; International Subarachnoid Aneurysm Trial (ISAT) Collaborative Group. **International Subarachnoid Aneurysm Trial (ISAT) of neurosurgical clipping versus endovascular coiling in 2143 patients with ruptured intracranial aneurysms: a randomised trial.** *Lancet* 2002;360:1267–74 CrossRef Medline

Differential Gene Expression in Coiled versus Flow-Diverter-Treated Aneurysms: RNA Sequencing Analysis in a Rabbit Aneurysm Model

A. Rouchaud, C. Johnson, E. Thielen, D. Schroeder, Y.-H. Ding, D. Dai, W. Brinjikji, J. Cebral, D.F. Kallmes, and R. Kadirvel



ABSTRACT

BACKGROUND AND PURPOSE: The biologic mechanisms leading to aneurysm healing or rare complications such as delayed aneurysm ruptures after flow-diverter placement remain poorly understood. We used RNA sequencing following implantation of coils or flow diverters in elastase aneurysms in rabbits to identify genes and pathways of potential interest.

MATERIALS AND METHODS: Aneurysms were treated with coils ($n = 5$) or flow diverters ($n = 4$) or were left untreated for controls ($n = 6$). Messenger RNA was isolated from the aneurysms at 4 weeks following treatment. RNA samples were processed by using RNA-sequencing technology and were analyzed by using the Ingenuity Pathway Analysis tool.

RESULTS: With RNA sequencing for coiled versus untreated aneurysms, 464/9990 genes (4.6%) were differentially expressed (58 down-regulated, 406 up-regulated). When we compared flow-diverter versus untreated aneurysms, 177/10,041 (1.8%) genes were differentially expressed (8 down-regulated, 169 up-regulated). When we compared flow-diverter versus coiled aneurysms, 13/9982 (0.13%) genes were differentially expressed (8 down-regulated, 5 up-regulated). Keratin 8 was overexpressed in flow diverters versus coils. This molecule may potentially play a critical role in delayed ruptures due to plasmin production. We identified overregulation of apelin in flow diverters, supporting the preponderance of endothelialization, whereas we found overexpression of molecules implicated in wound healing (dectin 1 and hedgehog interacting protein) for coiled aneurysms. Furthermore, we identified metalloproteinases 1, 12, and 13 as overexpressed in coiled versus untreated aneurysms.

CONCLUSIONS: We observed different physiopathologic responses after endovascular treatment with various devices. Flow diverters promote endothelialization but express molecules that could potentially explain the rare delayed ruptures. Coils promote wound healing and express genes potentially implicated in the recurrence of coiled aneurysms.

ABBREVIATIONS: *DAPL1* = death associated protein-like 1; *FGFBP1* = fibroblast growth factor binding protein 1; *HHIP* = hedgehog-interacting protein; IA = intracranial aneurysm; *IL6* = interleukin 6; IPA = Ingenuity Pathway Analysis; *MMP* = matrix metalloproteinase; mRNA = messenger RNA; *PRND* = prion protein 2; RNA-seq = RNA sequencing; *SRCIN1* = SRC kinase signaling inhibitor 1

Endovascular treatment is now considered the standard of care for most intracranial aneurysms (IAs). Numerous endovascular tools exist for the treatment of IAs, and flow-diverting devices

have elicited much interest, with good occlusion rates.¹ However, the biologic mechanisms driving IA physiopathology remain poorly understood, including the mechanisms for formation, rupture, growth, healing, or device-related complications, and need further elucidation. Indeed, endovascular devices used for the treatment of IAs are not simply inert mechanical devices used to seal the aneurysm neck without any interaction with the host; rather, they interact with different biologic processes with the aim of definitely healing the aneurysm. Those biologic interactions may vary according to the device used or depending on the local biologic conditions and sometimes lead to nonocclusion of the aneurysm or to very rare but devastating complications such as delayed rupture.²⁻⁴ It is important to understand the biologic processes after endovascular treatment to optimize the devices used for the treatment of IAs and try to prevent potential complications.

Received September 16, 2015; accepted after revision November 10.

From the Applied Neuroradiology Laboratory (A.R., C.J., E.T., D.S., Y.-H.D., D.D., W.B., D.F.K., R.K.) and Department of Radiology (W.B., D.F.K.), Mayo Clinic, Rochester, Minnesota; and Department of Bioengineering (J.C.), George Mason University, Fairfax, Virginia.

This work was supported by research grant NS076491 from the National Institutes of Health. Aymeric Rouchaud was supported by a research grants from the French Society of Radiology and the Therese Planiol Foundation.

Please address correspondence to Aymeric Rouchaud, MD, Neuroradiology Research Laboratory, Mayo Clinic, 200 First St SW, Rochester, MN 55905; e-mail: Rouchaud.Aymeric@mayo.edu, aymeric.rouchaud@gmail.com

Indicates open access to non-subscribers at www.ajnr.org

Indicates article with supplemental on-line tables.

<http://dx.doi.org/10.3174/ajnr.A4648>

Previous studies explored the mechanisms of aneurysm healing following endovascular treatments, but they have mostly focused at the tissue, cellular, or molecular levels.⁵⁻⁷ Endovascular coiling primarily elicits thrombus formation in the aneurysm cavity and then promotes neointima formation across the neck to seal the aneurysm cavity from the circulation,^{5,8} but long-term occlusion rates are poor, with high rates of recanalization due to lack of aneurysm healing.^{9,10} On the contrary, occlusions rates following flow diversion are high and likely driven by endothelialization of the device from endothelial cells originating from the parent artery.^{6,11} However, despite high rates of occlusion and good clinical outcomes,⁵ flow-diverter devices have been associated with the occurrence of previously unobserved complications. Indeed, several cases of delayed aneurysm rupture have been reported with fatal outcomes.^{3,4}

Even if this complication is very rare and occurs in <1% of cases, controversy exists surrounding the mechanism, and it appears important to try to explain it. Several mechanisms have been proposed to explain this complication, such as flow modifications² or a deleterious impact of the intra-aneurysm thrombus trapped by the flow diverter.³ Gene-regulation studies have previously investigated the impact of selected key molecules such as metalloproteinases, fibronectin, and collagen, potentially involved in the healing of aneurysms following coil or flow-diverter embolization.¹²⁻¹⁴ However, these prior studies did not provide a global overview of the biologic pathways involved in those different treatment options.¹⁵ Recently, microarray and RNA sequencing (RNA-seq) have been used to compare messenger RNA (mRNA) and microRNA expression in both humans and animal models to better understand the molecular mechanisms of aneurysm healing.^{16,17} However, none of these previous studies have compared coiled or flow-diverter-treated aneurysms.¹⁸ We used RNA-seq technology following implantation of coils or flow diverters in elastase-induced saccular aneurysms in rabbits to identify genes and pathways of potential clinical interest and to determine whether differential pathways exist for the healing of coiled and flow-diverter-treated aneurysms.

MATERIALS AND METHODS

Aneurysm Creation, Treatment, and Follow-Up

The Mayo Clinic Animal Care and Use Committee approved all procedures before initiation of the study. Some of the rabbits used in this study were originally used as part of another investigation, in which we compared the gene expression between untreated aneurysms with contralateral carotid arteries¹⁶ and prior analyses of the expression of selected vascular remodeling molecules following coil and flow-diverter treatment.¹⁵ Elastase-induced saccular aneurysms were created in 16 New Zealand white rabbits (body weight, 3–4 kg). Detailed procedures for aneurysm creation have been previously described in depth.¹⁹ Aneurysms were permitted to mature for at least 3 weeks after creation. Then they were either embolized with platinum coils ($n = 5$) or treated with flow diverters (Pipeline Embolization Device; Covidien, Irvine, California) as previously described²⁰ ($n = 4$) or left untreated ($n = 6$). At 4 weeks following treatment, follow-up DSA of the

aortic arch was performed. The animals were then euthanized by using a lethal injection of pentobarbital. Animals with untreated aneurysms were euthanized at 12 weeks following aneurysm creation. The aneurysm samples were harvested, and the samples were immediately snap frozen in liquid nitrogen and kept frozen at -70°C until use.

RNA Extraction

RNA was isolated from frozen tissues by using the miRNeasy Mini Kit (Qiagen, Valencia, California). The quantity of the RNA was measured by using spectrophotometry, and the integrity of the RNA was confirmed by electrophoretic separation by using the 2100 Bioanalyzer (Agilent Technologies, Santa Clara, California).

RNA Sequencing

RNA libraries were prepared according to the manufacturer's instructions for the TruSeq RNA Sample Prep Kit v2 (Illumina, San Diego, California). Then the libraries were loaded onto paired end-flow cells following the standard protocol of Illumina by using the cBot and cBot Paired-End Cluster Kit, Version 3, and HCS, Version 2.0.12 data collection software (Illumina). Base calling was performed by using RTA, Version 1.17.21.3 (Illumina).

Bioinformatics Analysis

The processing of the mRNA and microRNA data was performed by using MAP-RSeq (Version 1.2.1.3).²¹ MAP-RSeq consists of the following steps: alignment, quality control, obtaining genomic features per sample, and finally summarizing the data across samples. The pipeline provides detailed quality control data to estimate the distance between paired-end reads, evaluates the sequencing depth for alternate splicing analysis, determines the rate of duplicate reads, and calculates the read depth across genes by using the RSeQC (Version 2.3.2)²² software. Paired-end reads are aligned by Tophat (Version 2.0.6; <https://ccb.jhu.edu/software/tophat/index.shtml>)²³ against the April 2009 OryCun2 genome build by using the Bowtie1.aligner²⁴ option (<http://www.broadinstitute.org/cancer/software/genepattern/modules/docs/Bowtie.aligner/4>). Gene counts were generated by using HTSeq (Version 0.5.3p9)²⁵ software, and the gene annotation files were obtained from Ensembl (ftp://ftp.ensembl.org/pub/release75/gtf/oryctolagus_cuniculus/Oryctolagus_cuniculus.OryCun2.0.75.gtf.gz) and the University of California, Santa Cruz (<http://hgdownload.soe.ucsc.edu/downloads.html#rabbit>). Differential expression comparing the normal tissue versus aneurysm in the same rabbit was computed by using the edgeR algorithm (Version 2.6.2) across all samples. Human orthologs were assigned by using ExoLocator (<http://exolocator.bii.a-star.edu.sg/>).²⁶ The pathway analysis leveraged the Ingenuity Pathway Analysis (IPA; <http://www.winsite.com/ingenuity/ingenuity+pathway+analysis/>)²⁷ software to identify pathways enriched with human ortholog targets. IPA identified the involvement of different pathways according to the number of genes of the specific pathway that were differentially expressed in the compared groups. A pathway is considered more involved than another one if more genes of this specific pathway are found up- or down-regulated according to the prespecified values.

Table 1: Top up- and down-regulated molecules comparing coiled versus untreated aneurysms, determined by IPA^a

Top Up-Regulated Molecules			Top Down-Regulated Molecules		
Gene Name	Description	Exp. Value	Gene Name	Description	Exp. Value
<i>MMP1</i>	Matrix metalloproteinase 1 (interstitial collagenase)	8.407	<i>SRCIN1</i>	SRC kinase signaling inhibitor 1	-4.210
<i>MAP3K19</i>	Mitogen-activated protein kinase kinase kinase 19	7.854	<i>DAPL1</i>	Death associated protein-like 1	-3.922
<i>TREML2</i>	Triggering receptor expressed on myeloid cells-like 2	7.583	<i>HHIP</i>	Hedgehog interacting protein	-3.512
<i>FGF23</i>	Fibroblast growth factor 23	7.423	<i>MPZ</i>	Myelin protein zero	-3.400
<i>MMP13</i>	Matrix metalloproteinase 13 (collagenase 3)	7.201	<i>MYH7B</i>	Myosin, heavy chain 7B, cardiac muscle, β	-3.342
<i>SLAMF7</i>	SLAM family member 7	6.670	<i>PCDHAC2</i>	Protocadherin α subfamily C, 2	-3.112
<i>CXCL13</i>	Chemokine (C-X-C motif) ligand 13	6.490	<i>THrsp</i>	Thyroid hormone responsive	-3.089
<i>XDH</i>	Xanthine dehydrogenase	6.298	<i>CYP2D6</i>	Cytochrome P450, family 2, subfamily D, polypeptide 6	-2.991
<i>IBSP</i>	Integrin-binding sialoprotein	6.221	<i>USH2A</i>	Usher syndrome 2A (autosomal recessive, mild)	-2.932
<i>MMP12</i>	Matrix metalloproteinase 12 (macrophage elastase)	6.206	<i>SORCSI</i>	Sortilin-related VPS10 domain containing receptor 1	-2.703

Note:—Exp. indicates expression.

^a Values are expressed as log-fold change.

Quantitative Real-Time Polymerase Chain Reaction Analysis

The mRNA expression of selected genes was assessed by quantitative real-time polymerase chain reaction. These selected genes were prion protein 2 (*PRND*), fibroblast growth factor-23, matrix metalloproteinase (*MMP*) 1, SRC kinase signaling inhibitor 1 (*SRCIN1*), death associated protein-like 1 (*DAPL1*), and hedgehog-interacting protein (*HHIP*). Briefly, first, strand complementary DNAs were synthesized from 500 ng of total RNA by using a synthesis system (SuperScript III First-Strand Synthesis System; Invitrogen, Grand Island, New York). Then, real-time polymerase chain reaction was performed with a cycler (iCycler; Bio-Rad, Hercules, California) by using the SYBR Green PCR kit (Quantigen, Hilden, Germany). The specific primers were designed from corresponding sequences obtained from the GenBank by using a Web tool (Primer 3; <http://frodo.wi.mit.edu/primer3/>).

Statistical Analysis

The *t* test statistics and corresponding *P* values were used as a measure of the mean change in expression between the test and control groups relative to the variability. The primary assessment compared each treatment group versus the control group. We additionally had a secondary assessment comparing treatment groups against each other. The EdgeR tool was used to test for a normal distribution of the data. The *t* test-based *P* values were adjusted for multiple comparisons by using the false discovery rate multiple-correction approach.²⁸ Genes were considered differentially expressed in case of a fold change of 2 (a log-value of >2 was considered up-regulated, whereas a log-value of ≤ 2 was considered down-regulated), with a false discovery rate ≤ 0.1 and a *P* value $< .05$.

RESULTS

Coiled versus Untreated Aneurysms

All aneurysm treatments with coils were successful without any recurrence at follow-up. Using the criteria above for differential expression, we identified 464 of 9990 (4.6%) genes as being dif-

ferentially expressed compared with untreated aneurysms. Of these 464 genes, 58 were down-regulated and 406 were up-regulated (On-line Table 1). The most up- and down-regulated molecules are presented in Table 1. Of the 10 most up-regulated, 3 are metalloproteinases: *MMP1* (8.4-fold), *MMP12* (6.1-fold), and *MMP13* (7.2-fold) involved in the breakdown of extracellular matrix and interstitial collagen for tissue remodeling. The most down-regulated protein is *HHIP*, decreased 3.5-fold compared with untreated aneurysms. The most involved pathways are shown in On-line Table 2. Those pathways are generally related to inflammatory responses, including T- and B-cell and interleukin-10 involvement and cell-to-cell signaling as well as granulocyte and agranulocyte adhesion and diapedesis. Those pathways involve up-regulation of *MMPs* such as *MMP1*, *MMP3*, *MMP12*, *MMP13*, and interleukins.

Flow-Diverter-Treated versus Untreated Aneurysms

All aneurysm treatments with flow diverters were successful without any delayed rupture at follow-up. Using the criteria above for differential expression, we identified 177 of 10,041 (1.8%) genes as being differentially expressed. Of these 177 genes, 8 were down-regulated and 169 were up-regulated (On-line Table 3). The most up- and down-regulated molecules are presented in Table 2. Of the 10 most up-regulated, fibroblast growth factor 23 increased 5.7-fold, keratin 8 increased 6.2-fold, *MMP1* increased 4.5-fold, apelin increased 4.4-fold, and interleukin 6 (*IL6*) increased 4.4-fold compared with untreated aneurysms. Of the most down-regulated molecules, *DAPL1* decreased by 3.8-fold, *SRCIN1* decreased by 3.3-fold, macrophage receptor with collagenous structure decreased by 2.4-fold, and fibroblast growth factor binding protein 1 (*FGFBP1*) decreased by 2.2-fold. The most involved pathways are shown in On-line Table 4. The most involved pathway was the atherosclerosis signaling pathway with 9 up-regulated genes compared with nontreated aneurysms. Similar to coiled aneurysms, agranulocyte adhesion and diapedesis pathways and the cell-to-cell signaling pathway were involved with flow diverters.

Table 2: Top up- and down-regulated molecules comparing flow-diverted versus untreated aneurysms, determined by IPA^a

Top Up-Regulated Molecules			Top Down-Regulated Molecules		
Gene Name	Description	Exp. Value	Gene Name	Description	Exp. Value
<i>PRND</i>	Prion protein 2 (dublet)	8.719	<i>DAPL1</i>	Death associated protein-like 1	-3.752
<i>KRT8</i>	Keratin 8	6.233	<i>SRCIN1</i>	SRC kinase signaling inhibitor 1	-3.295
<i>FGF23</i>	Fibroblast growth factor 23	5.662	<i>FAM150A</i>	Family with sequence similarity 150, member A	-2.555
<i>SIRPB1</i>	Signal-regulatory protein β 1	5.463	<i>MARCO</i>	Macrophage receptor with collagenous structure	-2.396
<i>CXCL8</i>	Chemokine (C-X-C motif) ligand 8	4.781	<i>LECT1</i>	Leukocyte cell derived chemotaxin 1	-2.373
<i>GPR158</i>	G protein-coupled receptor 158	4.747	<i>SCIN</i>	Scinderin	-2.287
<i>MMP1</i>	Matrix metalloproteinase 1 (interstitial collagenase)	4.467	<i>FGFBP1</i>	Fibroblast growth factor binding protein 1	-2.183
<i>HMGA2</i>	High mobility group AT-hook 2	4.412	<i>MYH7B</i>	Myosin, heavy chain 7B, cardiac muscle, β	-2.107
<i>APLN</i>	Apelin	4.412			
<i>IL6</i>	Interleukin 6 (interferon, β 2)	4.375			

Note:—Exp. indicates expression.

^a Values are expressed as log-fold change.

Table 3: Top up- and down-regulated molecules comparing flow-diverted versus coiled aneurysms, determined by IPA^a

Top Up-Regulated Molecules			Top Down-Regulated Molecules		
Gene Name	Description	Exp. Value	Gene Name	Description	Exp. Value
<i>KRT8</i>	Keratin 8	4.266	<i>PDILT</i>	Protein disulfide isomerase-like, testis expressed	-4.172
<i>BSG</i>	Basigin/EMMPRIN	3.799	<i>LIPA</i>	Lipase A, lysosomal acid, cholesterol esterase	-3.820
<i>TLDC2</i>	TBC/LysM-associated domain containing 2	3.363	<i>EXPH5</i>	Exophilin 5	-2.872
<i>PRPH</i>	Peripherin	2.895	<i>ZNF483</i>	Zinc finger protein 483	-2.667
<i>RMRP</i>	RNA component of mitochondrial RNA processing endoribonuclease	2.671	<i>KLHL14</i>	Kelch-like family member 14	-2.470
			<i>CLEC7A</i>	C-type lectin domain family 7 member A	-2.451
			<i>TCN1</i>	Transcobalamin I (vitamin B12 binding protein, R binder family)	-2.432
			<i>COL25A1</i>	Collagen, type XXV, α	-2.285

Note:—Exp. indicates expression.

^a Values are expressed as log-fold change.

Flow-Diverter-Treated versus Coiled Aneurysms

Using the criteria above for differential expression, we identified 13 of 9982 (0.13%) genes as being differentially expressed. Of these 13 genes, 8 were down-regulated and 5 were up-regulated (Table 3). Of the 13 differentially expressed molecules when comparing flow-diverter-treated IAs with coiled aneurysms, keratin 8 increased 4.3-fold, and basigin increased 3.8-fold. Protein disulfide isomerase-like was overexpressed in the coiled group compared with the flow-diverter group at 4.2-fold; and C-type lectin domain family 7, member A (also called dectin 1) was over-expressed 2.5-fold in the coiled group. Due to the low number of differentially expressed molecules when comparing coiled with flow-diverter-treated aneurysms, it was not possible to identify specific pathways differentially involved.

Validation of Microarray Data

Verification of differential gene expression in the aneurysm and control artery was performed in 5 selected genes from the top up- or down-regulated genes identified by RNA-seq. Those selected genes were *PRND*, fibroblast growth factor 23, *MMP1*, *SRCIN1*, *DAPL1*, and *HHIP*. Results obtained by reverse transcription polymerase chain reaction for gene expression levels varied in the same way and in comparable amplitude as those obtained with RNA-seq. Results of reverse transcription polymerase chain reaction are presented in On-line Table 5.

DISCUSSION

This study found differential expression in a large assortment of genes in tissue from coiled or flow-diverter-treated aneurysms compared with untreated aneurysms. The differentially expressed genes are mostly related to the inflammatory response and cellular migration. These findings may provide insight into the biologic effects of coils and flow diverters and highlight pathways to better understand and optimize the outcomes after endovascular treatment of intracranial aneurysms.

Our results showed that relatively few genes were differentially expressed when comparing coiled versus flow-diverter-treated aneurysms. These findings show that despite 2 different approaches, the response to the device used for the endovascular treatment of IAs did not vary substantially. These findings further demonstrate that the observed gene modifications were mostly driven by the aneurysm itself rather than by the device and imply that the mechanisms leading to aneurysm occlusion are somewhat similar, regardless of the device used. However, some genes were differentially expressed in the flow-diverter-treated group compared with the coiled group.

Specifically, the most up-regulated molecule was keratin 8, which acts as a binding site for plasminogen.²⁹ This overexpression of plasminogen receptors could be deleterious to the treated aneurysms. Indeed, the association of plasminogen with cellular

receptors facilitates its activation in plasmin.^{30,31} Then, plasmin generated from plasminogen is able to degrade extracellular matrix components directly or indirectly by activating (*MMP-1*, 3, and 9).^{32,33}

Our study also found that apelin is up-regulated in flow-diverter-treated aneurysms compared with coiled aneurysms. This molecule significantly reduces aneurysm formation in the elastase model of abdominal aortic aneurysms by decreasing macrophage burden likely due to an apelin-mediated decrease in proinflammatory cytokine and chemokine activation.^{34,35} It has also been demonstrated that apelin is present to a limited degree in endothelial cells, with a potent ability to stimulate the proliferation of cultured human umbilical vein endothelial cells.³⁶ In our study, apelin was overexpressed in flow-diverter-treated aneurysms compared with coiled aneurysms; this overexpression is potentially a key factor for the promotion of endothelial cells, leading to stent endothelialization and aneurysm occlusion.³⁷

These current results also confirm the role of inflammation after the implantation of devices for the treatment of IAs. Metalloproteinases are known to be involved in thrombus homeostasis in IAs, but mainly *MMP2* and *MMP9* have been described in this pathology.³⁸⁻⁴¹ Here, we report the important role of other *MMP* molecules (*MMP1*, -12, and -13) overexpressed in coiled versus untreated IAs. These *MMPs* have been reported as being implicated in abdominal aortic aneurysm formation and progression.⁴²⁻⁵² However their impact has not been extensively described in the setting of IAs.⁵⁰ We suspect that this increased level of *MMPs* in coiled aneurysms is linked to recanalization because *MMP-9* levels are associated with aneurysm recanalization and recurrence.⁵³ The RNA-seq also found that basigin (also known as extracellular matrix metalloproteinase inducer) is up-regulated in flow-diverter-treated aneurysms compared with coiled aneurysms. This molecule is known to regulate different *MMPs*, especially *MMP2* and *MMP9*.^{54,55} The increased level of basigin in flow diverters could explain the higher level of those *MMPs* in flow-diverter-treated aneurysms as previously described.¹⁵

Furthermore, the macrophage receptor with collagenous structure is another differentially expressed gene in our study. This molecule is associated with thrombus-free aneurysms in a study comparing thrombus-free and thrombus-covered walls of abdominal aortic aneurysms.⁵⁶ In our study, we observed a down-regulation of macrophage receptor with collagenous structure in the flow-diverter group, suggesting an increased implication of intra-aneurysmal thrombosis compared with untreated aneurysms and the potential role of intra-aneurysmal thrombus for delayed aneurysm rupture associated with flow diverters.^{3,57}

Regarding the potential deleterious role of keratin 8 in flow diverters, the generation of plasmin induces neutrophil aggregation, monocyte chemotaxis, and expression of proinflammatory molecules⁵⁸ via multiple signaling pathways, including nuclear factor- κ B.⁵⁹ This involvement of the fibrinolytic system has been previously highlighted in abdominal aortic aneurysm pathology.⁶⁰ In abdominal aortic aneurysms, plasminogen is present in the mural thrombus.⁶¹ This mural thrombus, by trapping polymorphonuclear leukocytes and adsorbing plasma components, could act as a source of proteases in aneurysms, which may play a

critical role in enlargement and rupture.⁵⁷ Furthermore, abdominal aortic aneurysm diameter is correlated with the level of plasmin activity in the abdominal aortic aneurysm wall.⁶¹ The overexpression of keratin 8 in flow-diverter-treated IAs could explain the deleterious issue in the rare cases of delayed aneurysm rupture after flow diverters. This overexpression of keratin 8 associated with a large amount of intrasaccular thrombus after flow-diverter placement supports intra-aneurysmal thrombosis as a possible cause of delayed aneurysm rupture after flow-diversion treatment³; however, the confirmation of this hypothesis would need further dedicated experiments to precisely determine the impact of keratin 8.

Another important function for aneurysm occlusion after endovascular treatment is wound healing, consisting subsequently of thrombus formation, myofibroblast invasion, and extracellular matrix deposition.^{5,12,62} C-type lectin domain family 7, member A (dectin 1) is a molecule promoting wound healing by the enhanced production of collagen matrices with β -glucans.⁶³⁻⁶⁵ Our results show that dectin 1 is approximately 4 times overexpressed in coiled IAs compared with flow-diverter-treated IAs. This finding suggests that wound healing is a process that is much more preponderant in coils than in flow-diverter treatment. *FGFBP1* is another molecule promoting wound healing.^{66,67} The present results show that *FGFBP1* is decreased in flow-diverter-treated aneurysms compared with untreated aneurysms; this decrease supports the idea that aneurysm occlusion after flow-diverter therapy is not related to wound-healing mechanisms but mostly to endothelial cell proliferation originating from the parent artery, as previously demonstrated.⁶ We also identified another molecule of interest, *HHIP*, which is abundantly expressed in vascular endothelial cells and involved in angiogenesis.⁶⁸ We observed in our study that the expression of *HHIP* is down-regulated in coiled aneurysms. *HHIP* down-regulation is involved in the promotion of angiogenesis and could be involved in the neovascularization of the wound during the healing of coiled aneurysms.^{5,69}

Limitations

Our study has several limitations. We used the rabbit elastase model and acknowledge that animal models are imperfect predictors of the human response. Indeed, the created aneurysms are in the mediastinum rather than the subarachnoid space and thus subject to different perianeurysmal modulations compared with berry aneurysms. Another limitation in using a model is the high degree of homogeneity among the different aneurysms, which is not the same in unselected human IAs. However, this model has been evaluated with RNA-seq and has expression patterns similar to those in human intracranial aneurysms.¹⁶ However, this aneurysm model is not one of spontaneous rupture, and some biologic pathways may differ when considering rupture-prone aneurysms. To explore these mechanisms, analyzing gene expressions in new models for active aneurysms with inflamed aneurysm walls or bioactive thrombus would be interesting.^{70,71} Also, time intervals between the creation of an aneurysm and the time of euthanizing the animals were different between untreated and treated aneurysms, which could introduce a difference in the healing process. Given the differences between the human and the rabbit genomes, the observed findings may not be directly applicable to the clinical

system. As with most gene-expression studies, we recognize that any results obtained are exploratory in nature and need to be explored further; to that end, we did validate several results with reverse transcription polymerase chain reaction and will continue to explore these results further in other models.

Likewise, because of normal variations, there very likely are genes for which our threshold levels were not achieved, which may have an effect in humans. Just because a gene is not significantly up- or down-regulated does not necessarily imply that it is not relevant. Similarly, a gene found up- or down-regulated is not necessarily related to the specific question. The aim of this study was to give a general overview of gene modifications after coiling or flow-diverter treatment, not to describe all the gene variations following coil embolization or flow-diverter therapy or to identify and focus on a specific pathways or molecules. This study identifies some new parameters to explore that could be potential key factors in improving endovascular devices. This will require further validation with specific experiments to precisely describe the role of each molecule of interest.

CONCLUSIONS

RNA-sequencing analysis of rabbit aneurysms showed that despite different approaches, the response to the device used for the endovascular treatment of IAs does not vary substantially and that the mechanisms leading to aneurysm occlusion are somewhat similar, regardless of the device used. However, it revealed differential regulation of some key pathways, including inflammation and cellular migration that could explain the different biologic mechanisms implicated in aneurysm healing after either coiling or flow-diverter treatments and could be key molecules to explore to explain related complications. This study confirms wound healing being preponderant after coiling compared with flow-diverter-treated aneurysms. In addition, this study identified in the flow-diverter-treated IAs an overexpression of keratin 8 and basigin, implicated in the inflammatory response and in the plasminogen system.

Disclosures: Juan Cebral—RELATED: Grant: National Institutes of Health;* Comments: research grant; UNRELATED: Grants/Grants Pending: National Institutes of Health, Philips Healthcare, Comments: research grants. David F. Kallmes—RELATED: Grant: Covidien/Medtronic,* Comments: provided devices at no cost; UNRELATED: Board Membership: GE Healthcare (Cost-Effectiveness Board)*; Consultancy: Medtronic,* Comments: planning and implementing clinical trials; Grants/Grants Pending: MicroVention,* Sequent Medical,* SurModics,* Codman Neurovascular,* ev3/Covidien/Medtronic,* NeuroSigma,* Comments: preclinical and clinical research; Travel/Accommodations/Meeting Expenses Unrelated to Activities Listed: Medtronic,* Comments: presentation at FDA panel meeting. Ramanathan Kadirvel—RELATED: Grant: National Institutes of Health (grant number NS076491). *Money paid to the institution.

REFERENCES

- Brinjikji W, Murad MH, Lanzino G, et al. **Endovascular treatment of intracranial aneurysms with flow diverters: a meta-analysis.** *Stroke* 2013;44:442–47 CrossRef Medline
- Cebral JR, Mut F, Raschi M, et al. **Aneurysm rupture following treatment with flow-diverting stents: computational hemodynamics analysis of treatment.** *AJNR Am J Neuroradiol* 2011;32:27–33 CrossRef Medline
- Kulcsár Z, Houdart E, Bonafé A, et al. **Intra-aneurysmal thrombosis as a possible cause of delayed aneurysm rupture after flow-diverter treatment.** *AJNR Am J Neuroradiol* 2011;32:20–25 CrossRef Medline
- Kulcsár Z, Szikora I. **The ESMINT Retrospective Analysis of Delayed Aneurysm Ruptures after flow diversion (RADAR) study.** *The eJournal of the European Society of Minimally Invasive Neurological Therapy* 2012. <http://www.ejmint.org/original-article/1244000088>. Accessed December 15, 2015
- Brinjikji W, Kallmes DF, Kadirvel R. **Mechanisms of healing in coiled intracranial aneurysms: a review of the literature.** *AJNR Am J Neuroradiol* 2015;36:1216–22 CrossRef Medline
- Kadirvel R, Ding YH, Dai D, et al. **Cellular mechanisms of aneurysm occlusion after treatment with a flow diverter.** *Radiology* 2014;270:394–99 CrossRef Medline
- Rouchaud A, Journé C, Louedec L, et al. **Autologous mesenchymal stem cell endografting in experimental cerebrovascular aneurysms.** *Neuroradiology* 2013;55:741–49 CrossRef Medline
- Kallmes DF, Helm GA, Hudson SB, et al. **Histologic evaluation of platinum coil embolization in an aneurysm model in rabbits.** *Radiology* 1999;213:217–22 CrossRef Medline
- Crobeddu E, Lanzino G, Kallmes DF, et al. **Review of 2 decades of aneurysm-recurrence literature, part 1: reducing recurrence after endovascular coiling.** *AJNR Am J Neuroradiol* 2013;34:266–70 CrossRef Medline
- Raymond J, Guilbert F, Weill A, et al. **Long-term angiographic recurrences after selective endovascular treatment of aneurysms with detachable coils.** *Stroke* 2003;34:1398–403 CrossRef Medline
- Li ZF, Fang XG, Yang PF, et al. **Endothelial progenitor cells contribute to neointima formation in rabbit elastase-induced aneurysm after flow diverter treatment.** *CNS Neurosci Ther* 2013;19:352–57 CrossRef Medline
- Kadirvel R, Ding YH, Dai D, et al. **Differential gene expression in well-healed and poorly healed experimental aneurysms after coil treatment.** *Radiology* 2010;257:418–26 CrossRef Medline
- Mangrum WI, Farassati F, Kadirvel R, et al. **mRNA expression in rabbit experimental aneurysms: a study using gene chip microarrays.** *AJNR Am J Neuroradiol* 2007;28:864–69 Medline
- Kadirvel R, Ding YH, Dai D, et al. **Gene expression profiling of experimental saccular aneurysms using deoxyribonucleic acid microarrays.** *AJNR Am J Neuroradiol* 2008;29:1566–69 CrossRef Medline
- Puffer C, Dai D, Ding YH, et al. **Gene expression comparison of flow diversion and coiling in an experimental aneurysm model.** *J Neurointerv Surg* 2015;7:926–30 CrossRef Medline
- Holcomb M, Ding YH, Dai D, et al. **RNA-sequencing analysis of messenger RNA/microRNA in a rabbit aneurysm model identifies pathways and genes of interest.** *AJNR Am J Neuroradiol* 2015;36:1710–15 CrossRef Medline
- Nakaoka H, Tajima A, Yoneyama T, et al. **Gene expression profiling reveals distinct molecular signatures associated with the rupture of intracranial aneurysm.** *Stroke* 2014;45:2239–45 CrossRef Medline
- Roder C, Kasuya H, Harati A, et al. **Meta-analysis of microarray gene expression studies on intracranial aneurysms.** *Neuroscience* 2012;201:105–13 CrossRef Medline
- Altes TA, Cloft HJ, Short JG, et al. **1999 ARRS Executive Council Award: creation of saccular aneurysms in the rabbit: a model suitable for testing endovascular devices—American Roentgen Ray Society.** *AJR Am J Roentgenol* 2000;174:349–54 CrossRef Medline
- Kallmes DF, Ding YH, Dai D, et al. **A new endoluminal, flow-disrupting device for treatment of saccular aneurysms.** *Stroke* 2007;38:2346–52 CrossRef Medline
- Kalari KR, Nair AA, Bhavsar JD, et al. **MAP-RSeq: Mayo Analysis Pipeline for RNA sequencing.** *BMC Bioinformatics* 2014;15:224 CrossRef Medline
- Wang L, Wang S, Li W. **RSeQC: quality control of RNA-seq experiments.** *Bioinformatics* 2012;28:2184–85 CrossRef Medline
- Trapnell C, Pachter L, Salzberg SL. **TopHat: discovering splice junctions with RNA-Seq.** *Bioinformatics* 2009;25:1105–11 CrossRef Medline
- Langmead B, Trapnell C, Pop M, et al. **Ultrafast and memory-efficient**

- cient alignment of short DNA sequences to the human genome. *Genome Biol* 2009;10:R25 CrossRef Medline
25. Anders S, Pyl PT, Huber W. **HTSeq—a Python framework to work with high-throughput sequencing data.** *Bioinformatics* 2015;31:166–69 CrossRef Medline
 26. Khoo AA, Ogrizek-Tomas M, Bulovic A, et al. **ExoLocator—an online view into genetic makeup of vertebrate proteins.** *Nucleic Acids Res* 2014;42:D879–81 CrossRef Medline
 27. Krämer A, Green J, Pollard J Jr, et al. **Causal analysis approaches in Ingenuity Pathway Analysis.** *Bioinformatics* 2014;30:523–30 CrossRef Medline
 28. Reiner A, Yekutieli D, Benjamin Y. **Identifying differentially expressed genes using false discovery rate controlling procedures.** *Bioinformatics* 2003;19:368–75 CrossRef Medline
 29. Obermajer N, Doljak B, Kos J. **Cytokeratin 8 ectoplasmic domain binds urokinase-type plasminogen activator to breast tumor cells and modulates their adhesion, growth and invasiveness.** *Mol Cancer* 2009;8:88 CrossRef Medline
 30. Didiysova M, Wujak L, Wygrecka M, et al. **From plasminogen to plasmin: role of plasminogen receptors in human cancer.** *Int J Mol Sci* 2014;15:21229–52 CrossRef Medline
 31. Syrovets T, Lunov O, Simmet T. **Plasmin as a proinflammatory cell activator.** *J Leukoc Biol* 2012;92:509–19 CrossRef Medline
 32. Lijnen HR. **Plasmin and matrix metalloproteinases in vascular remodeling.** *Thromb Haemostasis* 2001;86:324–33 Medline
 33. Carmeliet P, Moons L, Lijnen R, et al. **Urokinase-generated plasmin activates matrix metalloproteinases during aneurysm formation.** *Nat Genet* 1997;17:439–44 CrossRef Medline
 34. Leeper NJ, Tedesco MM, Kojima Y, et al. **Apelin prevents aortic aneurysm formation by inhibiting macrophage inflammation.** *Am J Physiol Heart Circ Physiol* 2009;296:H1329–35 CrossRef Medline
 35. Zhou Y, Wang Y, Qiao S. **Apelin: a potential marker of coronary artery stenosis and atherosclerotic plaque stability in ACS patients.** *Int Heart J* 2014;55:204–12 CrossRef Medline
 36. Masri B, Morin N, Cornu M, et al. **Apelin (65–77) activates p70 S6 kinase and is mitogenic for umbilical endothelial cells.** *FASEB J* 2004;18:1909–11 Medline
 37. Du X, Kang JP, Wu JH, et al. **Elevated high sensitive C-reactive protein and apelin levels after percutaneous coronary intervention and drug-eluting stent implantation.** *J Zhejiang Univ Sci B* 2010;11:548–52 CrossRef Medline
 38. Tulamo R, Frösen J, Hernesniemi J, et al. **Inflammatory changes in the aneurysm wall: a review.** *J Neurointerv Surg* 2010;2:120–30 CrossRef Medline
 39. Frösen J. **Smooth muscle cells and the formation, degeneration, and rupture of saccular intracranial aneurysm wall: a review of current pathophysiological knowledge.** *Transl Stroke Res* 2014;5:347–56 CrossRef Medline
 40. Aoki T, Kataoka H, Morimoto M, et al. **Macrophage-derived matrix metalloproteinase-2 and -9 promote the progression of cerebral aneurysms in rats.** *Stroke* 2007;38:162–69 CrossRef Medline
 41. Kadirvel R, Dai D, Ding YH, et al. **Endovascular treatment of aneurysms: healing mechanisms in a swine model are associated with increased expression of matrix metalloproteinases, vascular cell adhesion molecule-1, and vascular endothelial growth factor, and decreased expression of tissue inhibitors of matrix metalloproteinases.** *AJNR Am J Neuroradiol* 2007;28:849–56 Medline
 42. Courtois A, Nurgens BV, Hustinx R, et al. **18F-FDG uptake assessed by PET/CT in abdominal aortic aneurysms is associated with cellular and molecular alterations prefacing wall deterioration and rupture.** *J Nucl Med* 2013;54:1740–47 CrossRef Medline
 43. Morris DR, Biros E, Cronin O, et al. **The association of genetic variants of matrix metalloproteinases with abdominal aortic aneurysm: a systematic review and meta-analysis.** *Heart* 2014;100:295–302 CrossRef Medline
 44. Saracini C, Bolli P, Sticchi E, et al. **Polymorphisms of genes involved in extracellular matrix remodeling and abdominal aortic aneurysm.** *J Vasc Surg* 2012;55:171–79 e2 CrossRef Medline
 45. Wilson WR, Anderton M, Choke EC, et al. **Elevated plasma MMP1 and MMP9 are associated with abdominal aortic aneurysm rupture.** *Eur J Vasc Endovasc Surg* 2008;35:580–84 CrossRef Medline
 46. Chase AJ, Newby AC. **Regulation of matrix metalloproteinase (matrixin) genes in blood vessels: a multi-step recruitment model for pathological remodelling.** *J Vasc Res* 2003;40:329–43 CrossRef Medline
 47. Xiong W, Knispel R, MacTaggart J, et al. **Membrane-type 1 matrix metalloproteinase regulates macrophage-dependent elastolytic activity and aneurysm formation in vivo.** *J Biol Chem* 2009;284:1765–71 CrossRef Medline
 48. Dai X, Shen J, Annam NP, et al. **SMAD3 deficiency promotes vessel wall remodeling, collagen fiber reorganization and leukocyte infiltration in an inflammatory abdominal aortic aneurysm mouse model.** *Sci Rep* 2015;5:10180 CrossRef Medline
 49. Didangelos A, Yin X, Mandal K, et al. **Extracellular matrix composition and remodeling in human abdominal aortic aneurysms: a proteomics approach.** *Mol Cell Proteomics* 2011;10:M111.008128 CrossRef Medline
 50. Zhang B, Dhillon S, Geary I, et al. **Polymorphisms in matrix metalloproteinase-1, -3, -9, and -12 genes in relation to subarachnoid hemorrhage.** *Stroke* 2001;32:2198–202 CrossRef Medline
 51. Curci JA, Liao S, Huffman MD, et al. **Expression and localization of macrophage elastase (matrix metalloproteinase-12) in abdominal aortic aneurysms.** *J Clin Invest* 1998;102:1900–10 CrossRef Medline
 52. Tromp G, Gatalica Z, Skunca M, et al. **Elevated expression of matrix metalloproteinase-13 in abdominal aortic aneurysms.** *Ann Vasc Surg* 2004;18:414–20 CrossRef Medline
 53. Bouzeghrane F, Darsaut T, Salazkin I, et al. **Matrix metalloproteinase-9 may play a role in recanalization and recurrence after therapeutic embolization of aneurysms or arteries.** *J Vasc Interv Radiol* 2007;18:1271–79 CrossRef Medline
 54. Chen XF, Wang JA, Hou J, et al. **Extracellular matrix metalloproteinase inducer (EMMPRIN) is present in smooth muscle cells of human aneurysmal aorta and is induced by angiotensin II in vitro.** *Clin Sci (Lond)* 2009;116:819–26 CrossRef Medline
 55. Lizarbe TR, Tarín C, Gómez M, et al. **Nitric oxide induces the progression of abdominal aortic aneurysms through the matrix metalloproteinase inducer EMMPRIN.** *Am J Pathol* 2009;175:1421–30 CrossRef Medline
 56. Kazi M, Zhu C, Roy J, et al. **Difference in matrix-degrading protease expression and activity between thrombus-free and thrombus-covered wall of abdominal aortic aneurysm.** *Arterioscler Thromb Vasc Biol* 2005;25:1341–46 CrossRef Medline
 57. Fontaine V, Jacob MP, Houard X, et al. **Involvement of the mural thrombus as a site of protease release and activation in human aortic aneurysms.** *Am J Pathol* 2002;161:1701–10 CrossRef Medline
 58. Li Q, Laumonier Y, Syrovets T, et al. **Plasmin triggers cytokine induction in human monocyte-derived macrophages.** *Arterioscler Thromb Vasc Biol* 2007;27:1383–89 CrossRef Medline
 59. Burysek L, Syrovets T, Simmet T. **The serine protease plasmin triggers expression of MCP-1 and CD40 in human primary monocytes via activation of p38 MAPK and janus kinase (JAK)/STAT signaling pathways.** *J Biol Chem* 2002;277:33509–17 CrossRef Medline
 60. Reilly JM. **Plasminogen activators in abdominal aortic aneurysmal disease.** *Ann N Y Acad Sci* 1996;800:151–56 CrossRef Medline
 61. Coutard M, Touat Z, Houard X, et al. **Thrombus versus wall biological activities in experimental aortic aneurysms.** *J Vasc Res* 2010;47:355–66 CrossRef Medline
 62. Killer M, Plenk H, Minnich B, et al. **Histological demonstration of healing in experimental aneurysms.** *Minim Invasive Neurosurg* 2009;52:170–75 CrossRef Medline
 63. Daley JM, Brancato SK, Thomay AA, et al. **The phenotype of murine wound macrophages.** *J Leukoc Biol* 2010;87:59–67 CrossRef Medline
 64. van den Berg LM, Zijlstra-Willems EM, Richters CD, et al. **Dectin-1 activation induces proliferation and migration of human keratino-**

- cytes enhancing wound re-epithelialization. *Cell Immunol* 2014; 289:49–54 CrossRef Medline
65. Roy S, Dickerson R, Khanna S, et al. **Particulate β -glucan induces TNF- α production in wound macrophages via a redox-sensitive NF- κ B-dependent pathway.** *Wound Repair Regen* 2011;19:411–19 CrossRef Medline
 66. Beer HD, Bittner M, Niklaus G, et al. **The fibroblast growth factor binding protein is a novel interaction partner of FGF-7, FGF-10 and FGF-22 and regulates FGF activity: implications for epithelial repair.** *Oncogene* 2005;24:5269–77 CrossRef Medline
 67. Tassi E, McDonnell K, Gibby KA, et al. **Impact of fibroblast growth factor-binding protein-1 expression on angiogenesis and wound healing.** *Am J Pathol* 2011;179:2220–32 CrossRef Medline
 68. Olsen CL, Hsu PP, Glienke J, et al. **Hedgehog-interacting protein is highly expressed in endothelial cells but down-regulated during angiogenesis and in several human tumors.** *BMC Cancer* 2004;4:43 CrossRef Medline
 69. Wong VW, Crawford JD. **Vasculogenic cytokines in wound healing.** *Biomed Res Int* 2013;2013:190486 CrossRef Medline
 70. Gounis MJ, van der Bom IM, Wakhloo AK, et al. **MR imaging of myeloperoxidase activity in a model of the inflamed aneurysm wall.** *AJNR Am J Neuroradiol* 2015;36:146–52 CrossRef Medline
 71. Delbosc S, Alsac JM, Journe C, et al. **Porphyromonas gingivalis participates in pathogenesis of human abdominal aortic aneurysm by neutrophil activation: proof of concept in rats.** *PLoS One* 2011;6:e18679 CrossRef Medline

Smoking Does Not Affect Occlusion Rates and Morbidity-Mortality after Pipeline Embolization for Intracranial Aneurysms

A. Rouchaud, W. Brinjikji, H.J. Cloft, G. Lanzino, T. Becske, and D.F. Kallmes

ABSTRACT

BACKGROUND AND PURPOSE: Smoking is a major risk factor for patients with intracranial aneurysms, yet the effects of smoking on outcomes of aneurysm with flow-diverter treatment remain unknown. We studied the impact of smoking on long-term angiographic and clinical outcomes after flow-diverter treatment of intracranial aneurysms.

MATERIALS AND METHODS: We retrospectively reviewed data from patients treated with the Pipeline Embolization Device and included in the International Retrospective Study of the Pipeline Embolization Device, the Pipeline for Uncoilable or Failed Aneurysms Study, and the Aneurysm Study of Pipeline in an Observational Registry. Patients were stratified according to smoking status into 3 groups: 1) never smoker, 2) current smoker, and 3) former smoker. We studied angiographic and clinical outcomes. Outcomes were compared by using χ^2 and Student *t* tests. A multivariate analysis was performed to determine whether smoking was independently associated with poor outcomes.

RESULTS: Six hundred sixteen patients with 694 aneurysms were included. Current smokers had a smaller mean aneurysm size compared with the other 2 groups ($P = .005$) and lower rates of multiple Pipeline Embolization Device use ($P = .015$). On multivariate analysis, former smokers (OR, 1.08; 95% CI, 0.43–2.71; $P = .57$) and current smokers (OR, 0.70; 95% CI, 0.27–1.77; $P = .38$) had similar odds of long-term angiographic incomplete occlusion compared with never smokers. Former smokers (OR, 1.27; 95% CI, 0.64–2.52; $P = .25$) and current smokers (OR, 0.74; 95% CI, 0.37–1.46; $P = .22$) had similar odds of major morbidity and neurologic mortality compared with never smokers.

CONCLUSIONS: These results suggest that smoking is not associated with angiographic and clinical outcomes among patients treated with the Pipeline Embolization Device. Nonetheless, patients with intracranial aneurysms should continue to be counseled about the risks of tobacco smoking.

ABBREVIATION: PED = Pipeline Embolization Device

Tobacco smoking is one of the most important risk factors for intracranial aneurysm formation and subarachnoid hemorrhage.¹⁻⁷ Previous studies have shown that cigarette smoking is associated with a 6-fold increased risk of SAH.^{1,6} Controversy exists regarding smoking as a risk factor for aneurysm recurrence after endovascular coiling of intracranial aneurysms.^{8,9} It is possible that smoking could affect aneurysm occlusion rates following flow-diverter therapy because a number of preclinical studies

have demonstrated that cigarette smoking reduces the number of circulating endothelial progenitor cells,¹⁰ cells essential to aneurysm healing following flow-diverter therapy.¹¹ In addition, smoking has been associated with poor postoperative clinical outcomes for a number of surgical and endovascular procedures.^{12,13}

Given the widespread acceptance and use of flow-diverter therapy in the treatment of intracranial aneurysms, it is important to know what affect, if any, modifiable risk factors such as smoking have on clinical and angiographic outcomes. To gain a better understanding of the impact of smoking on long-term outcomes after flow diversion for intracranial aneurysms, we studied angiographic and clinical outcomes of patients included in 3 large clinical studies of the Pipeline Embolization Device (PED; Covidien, Irvine, California): the International Retrospective Study of the Pipeline Embolization Device (IntrePED), the Pipeline for Uncoilable or Failed Aneurysms study (PUFS), and the Aneurysm Study of Pipeline in an Observational Registry (ASPIRE), strati-

Received September 16, 2015; accepted after revision November 18.

From the Departments of Radiology (A.R., W.B., H.J.C., D.F.K.) and Neurosurgery (G.L.), Mayo Clinic, Rochester, Minnesota; and University of Rochester (T.B.), Rochester, New York.

Please address correspondence to Aymeric Rouchaud, MD, Neuroradiology Research Laboratory, Mayo Clinic, 200 First St SW, Rochester, MN 55905; e-mail: Rouchaud.Aymeric@mayo.edu or aymeric.rouchaud@gmail.com

Indicates article with supplemental on-line table.

<http://dx.doi.org/10.3174/ajnr.A4664>

fying patients into 3 groups: 1) never smoker, 2) current smoker, and 3) former smoker. The goal of this study was to determine whether smoking is an independent risk factor for long-term aneurysm incomplete occlusion and major neurologic morbidity-mortality after PED treatment. We hypothesized that patients who smoked or had a history of smoking would have a lower rate of aneurysm occlusion and higher morbidity-mortality rates.

MATERIALS AND METHODS

Patient Population

Patients were selected from the PUFs,¹⁴ IntrePED,¹⁵ and the ASPIRE (<https://www.clinicaltrials.gov/ct2/show/NCT01557036>) studies. PUFs was a prospective single-arm clinical trial of 108 patients with 108 aneurysms, including only patients with wide-neck (≥ 4 mm) and large (10–24.9 mm) or giant (≥ 25 mm) aneurysms of the internal carotid artery from the petrous to the superior hypophyseal segments with a follow-up of 5 years. IntrePED was a retrospective postmarket registry of 793 patients with 906 aneurysms with no size or location criteria with a follow-up of 3 years. ASPIRE was a prospective postmarket registry with 191 patients with 207 aneurysms, in which size and location inclusion criteria followed the country-specific PED instruction for use with a follow-up of 2 years. The patients included in this study have already been included in previous studies that did not focus on the impact of smoking.

We pooled data from these 3 studies including patients with unruptured and ruptured aneurysms in which information on smoking status was available. Patients were divided into 3 groups based on smoking status: 1) current smoker, 2) previous smoker and 3) never smoker. For previous smokers, no data were available regarding the last time the patient smoked cigarettes. We collected and analyzed the following baseline characteristics: age, sex, number of aneurysms, aneurysm size, aneurysm type (saccular, fusiform, dissecting, and other), aneurysm location, rupture status, and use of multiple PEDs.

Outcomes

The primary outcomes of this study were complete aneurysm occlusion at last follow-up and major neurologic morbidity and neurologic mortality. Secondary outcomes included major ipsilateral ischemic stroke, ipsilateral intracranial hemorrhage, all-cause mortality, and in-stent stenosis at last follow-up. “Major” adverse events were defined as ongoing clinical deficits at 7 days following the event. All major adverse events are included in the neurologic morbidity and mortality rates. All adverse events were adjudicated by the Adverse Events Review Committee of each study. An independent core lab adjudicated all angiographic outcomes. ASPIRE, IntrePED, and PUFs all reported clinical outcomes while only ASPIRE and PUFs reported angiographic outcomes.

Statistical Analysis

Statistical analyses were performed by using SAS, Version 9.1 or higher (SAS Institute, Cary, North Carolina). Summary statistics are presented for all data available by using means and SDs for continuous variables and frequency tabulations for categorical variables. Comparisons among groups for continuous variables were

evaluated by using *t* tests or ANOVAs and the Fisher exact or Pearson χ^2 test for binary categorical variables. Most statistical analyses were performed across patient groups—that is, on a per-patient basis. Because some patients had >1 aneurysm, however, each patient’s first aneurysm treated was used to classify patients into the 4 anatomic/size subgroups and the largest aneurysm was used to classify patients into the 3 aneurysm-size categories. The first aneurysm treated was defined a priori. A multivariate logistic regression analysis was performed to determine whether smoking status was independently associated with the above outcomes. Adjusted variables in this model were baseline variables that were significantly different among groups. For the multivariate analysis, the never-smoker group was the reference group. Given the wide variability in the length of follow-up, we performed a survival analysis on aneurysm occlusion by smoking status.

RESULTS

Baseline Patient and Aneurysm Characteristics

Six hundred sixteen patients with 694 treated aneurysms were included. Long-term clinical follow-up was available for 616 patients. Angiographic follow-up >6 months was available for 210 patients. Baseline demographics and aneurysms characteristics according to the smoking status are presented in the On-line Table.

The mean age of all patients was 57.4 ± 14.2 years. The mean length of follow-up was 22.2 ± 18.5 months for the clinical evaluation and 28.9 ± 23.7 months for the angiographic follow-up. One hundred seventy-nine patients with 214 aneurysms (30.8%) were current smokers, 111 patients with 120 aneurysms (17.3%) were former smokers, and 326 patients with 360 aneurysms (51.9%) had never smoked. In general, baseline characteristics were similar among groups except that current smokers had a smaller mean aneurysm size (11.2 ± 7.1 mm) compared with the previous smoker (13.4 ± 7.6 mm) and never smoker (13.2 ± 8.1 mm) groups ($P = .005$). Fewer patients in the current smoker group were treated with multiple PEDs (31.0%, 66/213) than in the previous smoker (44.5%, 53/119) and never smoker (41.8%, 150/359) groups ($P = .015$).

Univariate Analysis

Univariate analysis is presented in Table 1. Major neurologic morbidity and mortality rates were similar among groups (7.3% for current smokers, 14.4% for previous smokers, and 10.5% for never smokers, $P = .15$). Complete occlusion rates at last follow-up were similar among groups as well (86.2% for current smokers, 79.6% for previous smokers, and 82.5% for never smokers, $P = .64$). Previous smokers did have higher rates of major ipsilateral ischemic stroke (9.9%, 11/111) compared with current smoker (3.4%, 6/179) and never smoker groups (4.3%, 14/325) ($P = .04$). Previous smokers also had higher rates of major neurologic morbidity (13.5%, 15/111) compared with current smokers (4.5%, 8/179) and those who never smoked (8.0%, 26/325) ($P = .02$). There were no differences in rates of major ipsilateral intracranial hemorrhage ($P = .22$), neurologic mortality ($P = .93$), all-cause mortality ($P = .56$), and in-stent stenosis ($P = .80$).

Table 1: Univariate analysis of patient groups

Outcome	Current Smoker	Previous Smoker	Never Smoker	Total	P Value
Major ipsilateral ischemic stroke	3.4% (6/179)	9.9% (11/111)	4.3% (14/325)	5.0% (31/615)	.043 ^a
Major ipsilateral intracranial hemorrhage	1.1% (2/179)	3.6% (4/111)	3.7% (12/325)	2.9% (18/615)	.216
Major morbidity	4.5% (8/179)	13.5% (15/111)	8.0% (26/325)	8.0% (49/615)	.024 ^a
Neurologic mortality	3.9% (7/179)	4.5% (5/111)	4.6% (15/325)	4.4% (27/615)	.931
Major morbidity and neurologic mortality	7.3% (13/179)	14.4% (16/111)	10.5% (34/325)	10.2% (63/615)	.146
All-cause mortality	4.5% (8/179)	7.2% (8/111)	5.2% (17/325)	5.4% (33/615)	.564
Complete aneurysm occlusion					
180 days (−20/+42 days)	75.0% (30/40)	73.7% (28/38)	76.1% (51/67)	75.2% (109/145)	.969
1 yr (±42 days)	96.9% (31/32)	80.6% (25/31)	80.9% (38/47)	85.5% (94/110)	.068
3 yr	95.2% (20/21)	92.0% (23/25)	93.3% (28/30)	93.4% (71/76)	1.000
5 yr	94.1% (16/17)	100.0% (19/19)	92.3% (24/26)	95.2% (59/62)	.615
Last follow-up visit	86.2% (50/58)	79.6% (39/49)	82.5% (80/97)	82.8% (169/204)	.638
In stent stenosis at last angiographic follow-up					
>50%–75%	1.9% (1/52)	2.2% (1/45)	0.0% (0/81)	1.1% (2/178)	.296
>75%	1.9% (1/52)	0.0% (0/45)	2.5% (2/81)	1.7% (3/178)	.795

^a Significant.

Table 2: Multivariate logistic regression analysis

Outcome/Smoke Status	Odds Ratio (CI 95%)	P Value
Major ipsilateral ischemic stroke		
Current vs never	0.94 (0.36–2.42)	.40
Previous vs never	1.91 (0.79–4.60)	.12
Major ipsilateral intracranial hemorrhage		
Current vs never	0.41 (0.11–1.56)	.18
Previous vs never	1.04 (0.35–3.08)	.41
Major morbidity		
Current vs never	0.65 (0.29–1.44)	.11
Previous vs never	1.49 (0.73–3.06)	.09
Neurologic mortality		
Current vs never	0.85 (0.33–2.16)	.76
Previous vs never	0.96 (0.33–2.78)	.94
Major morbidity and neurologic mortality		
Current vs never	0.74 (0.37–1.46)	.22
Previous vs never	1.27 (0.64–2.52)	.25
All-cause mortality		
Current vs never	0.88 (0.36–2.14)	.46
Previous vs never	1.50 (0.61–3.67)	.29
Without complete aneurysm occlusion at last follow-up		
Current vs never	0.70 (0.27–1.77)	.38
Previous vs never	1.08 (0.43–2.71)	.57
Stenosis >50% at last follow-up		
Current vs never	2.30 (0.37–14.21)	.45
Previous vs never	1.46 (0.17–12.43)	.97

Multivariate Analysis

The multivariate logistic regression analysis is presented in Table 2. Previous smokers had similar odds of major neurologic morbidity and mortality compared with the never smoker group (OR, 1.27; 95% CI, 0.64–2.52; $P = .25$). The same was true for current smokers (OR, 0.74; 95% CI, 0.37–1.46; $P = .22$). Previous smokers also had similar odds of incomplete angiographic occlusion at last follow-up compared with the never smoker group (OR, 1.08; 95% CI, 0.43–2.71; $P = .57$). The same was true for current smokers (OR, 0.70; 95% CI, 0.27–1.77; $P = .38$). The odds of all other complications were similar between never smokers and current/previous smokers as well.

According to the survival analysis on aneurysm occlusion by smoking status, there was no significant difference in freedom

from occlusion across the smoking-status groups (log-rank test, P value = .52); survival curves are presented in the Figure.

DISCUSSION

Our study of >600 patients with nearly 700 treated aneurysms demonstrates that tobacco smoking is not independently associated with aneurysm occlusion rates or higher rates of poor clinical outcome following PED embolization of intracranial aneurysms. In both uni- and multivariate analyses of the entire cohort and in a subgroup analysis, we failed to detect an association between smoking and long-term angiographically confirmed occlusion rates or with combined neurologic morbidity and mortality. However, the multivariate analysis showed a tendency for lower rates of complete occlusion for current smokers. The nonsignificance of these results may be due to potential lack of statistical power of the analyses even if the population of the study was quite large. Rates of stroke, hemorrhage, and in-stent stenosis were similar between groups on multivariate analysis. These findings suggest that smoking status should not be a factor for excluding patients from PED embolization of intracranial aneurysms.

This study is the first, to our knowledge, to specifically analyze the impact of smoking on angiographic and clinical outcomes after PED treatment of intracranial aneurysms. Understanding the effect of smoking on outcomes related to the PED is important because previous studies have shown that cigarette smoking is a risk factor for both intracranial aneurysm formation and recurrence after endovascular coiling.⁹ In their study of 100 patients, Ortiz et al⁹ found that cigarette smokers had higher odds of recanalization following endovascular coiling than never smokers. However, larger follow-up studies by Brinjikji et al⁸ and Chen et al¹⁶ demonstrated no association between aneurysm occlusion and smoking status.

Our study found no association between smoking status and clinical outcomes following flow-diverter treatment of intracranial aneurysms with the PED. While no prior studies have examined the association between clinical outcomes and flow-diverter treatment, other studies have reported clinical outcomes following stent placement of intracranial arteries. In a study of 125 patients undergoing stent-assisted coiling with the Enterprise self-expanding stent (Codman & Shurtleff, Raynham, Massachusetts),

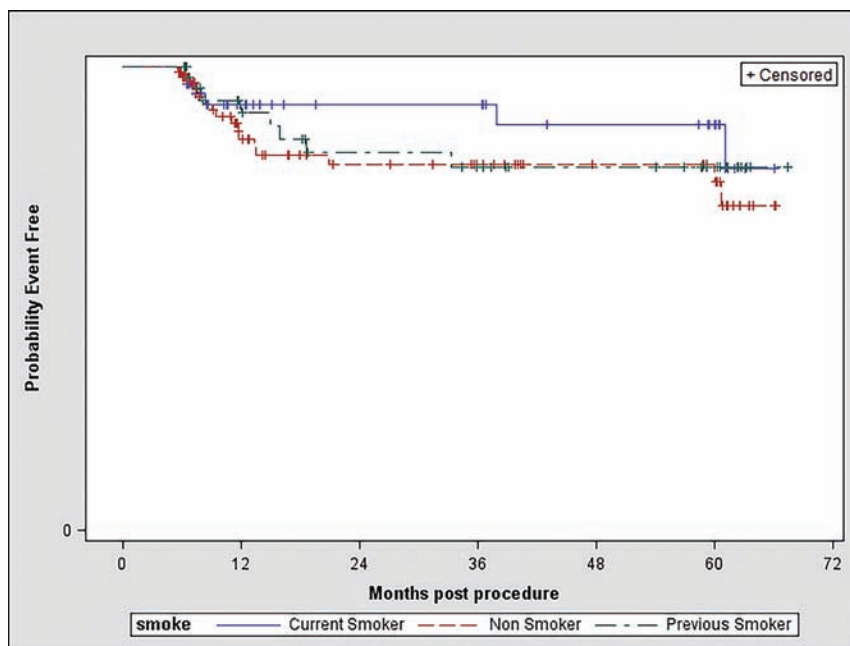


FIGURE. Survival analysis on aneurysm occlusion by smoking status. Log-rank test, P value = .52.

Song et al¹⁷ found that active smoking was associated with higher rates of delayed thromboembolic events. In a study of 45 aneurysms in 41 patients receiving covered stents for treatment of distal internal carotid and vertebral artery aneurysms, Zhu et al¹⁸ found that smoking was an independent predictor of late in-stent stenosis. In the setting of carotid stenosis, a subgroup analysis of the Carotid Revascularization Endarterectomy versus Stenting Trial found that smoking predicted an increased rate of restenosis after carotid endarterectomy but not after carotid stent placement.¹⁹

Prior studies have demonstrated that smoking is associated with worse clinical outcomes following stent placement in other locations as well. In a study of >9000 patients undergoing percutaneous coronary intervention with drug-eluting stents, Matteau et al²⁰ found that smoking was an independent risk factor for postoperative ischemic events and bleeding. Similar to patients with PEDs, patients with percutaneous coronary intervention are required to receive dual antiplatelet therapy following their intervention. Yeo et al²¹ found that active smoking was independently associated with higher rates of in-stent thrombosis following percutaneous coronary intervention. In a subgroup analysis of the Synergy Between Percutaneous Coronary Intervention With TAXUS and Cardiac Surgery (See more at <http://www.acc.org/Latest-in-Cardiology/Clinical-Trials/2014/08/19/16/32/SYNTAX#sthash.u3T0dfPw.dpuf>), Zhang et al²² found that smoking was associated with poor clinical outcomes after revascularization in patients with complex coronary artery disease with higher rates of in-stent thrombosis, death, myocardial infarction, and stroke. Smoking has also been associated with decreased odds of primary stent patency following endovascular treatment of subclavian artery disease.¹²

Limitations

Our study has several limitations. Some patients from the PUFs, IntrePED, and ASPIRE studies were not included in the present

pooled analysis because of missing data regarding their smoking status. This noninclusion of some patients could be a potential selection bias, but we doubt that this has skewed the results because the availability of their smoking status is not likely to be related to their actual smoking habits. The patients in our study were stratified into those who never, currently, or formerly smoked, but we did not further stratify smokers by pack-year because such data were not available. Previous studies have shown that increased pack-years are associated with an increased risk of SAH.^{23,24} Also, we performed the analysis on the basis of the smoking status of the patients at the time of the treatment and did not have information regarding their smoking habits after the treatment, which might have changed during the course of follow-up. We acknowledge that this feature might introduce a bias if many patients

stopped smoking after the treatment or restarted smoking during the follow-up period. Because our study was retrospective, we did not perform a power calculation before data collection. This omission might introduce a potential bias due to low statistical power, and multiple comparisons may raise the false-positivity issue or not reach it as well. However, our study is the largest study examining the association between smoking and outcomes of intracranial aneurysm treatment to date. Last, we have no data or information as to whether smokers were managed differently than never smokers. It is possible that smokers were more likely to undergo more careful intraprocedural and periprocedural monitoring of antiplatelet and anticoagulation status or closer angiographic follow-up.

CONCLUSIONS

The results of our study show that smoking is not an independent risk factor for worse clinical outcomes, aneurysm occlusion rates, or in-stent stenosis after PED treatment of intracranial aneurysms. Nonetheless, patients with intracranial aneurysms should continue to be counseled about the risks of cigarette smoking.

Disclosures: Giuseppe Lanzino—UNRELATED: Consultancy: Covidien/Medtronic.* Tibor Becske—UNRELATED: Consultancy: Covidien/Medtronic; Other: proctoring fees from Covidien/Medtronic. David F. Kallmes—RELATED: Grant: Medtronic (Principal Investigator of clinical trial)*; Consulting Fee or Honorarium: Medtronic (Steering Committee participation)*; UNRELATED: Board Membership: GE Healthcare (Cost-Effectiveness Board)*; Consultancy: Medtronic.* Comments: planning and implementing clinical trials; Grants/Grants Pending: MicroVention,* Sequent Medical,* SurModics,* Codman Neurovascular,* ev3/Covidien/Medtronic,* NeuroSigma*; Travel/Accommodations/Meeting Expenses Unrelated to Activities Listed: Medtronic.* Comments: presentation at FDA panel meeting. *Money paid to the institution.

REFERENCES

1. Bonita R. Cigarette smoking, hypertension and the risk of subarachnoid hemorrhage: a population-based case-control study. *Stroke* 1986;17:831–35 CrossRef Medline

2. Juvela S, Hillbom M, Numminen H, et al. **Cigarette smoking and alcohol consumption as risk factors for aneurysmal subarachnoid hemorrhage.** *Stroke* 1993;24:639–46 CrossRef Medline
3. Juvela S, Poussa K, Porras M. **Factors affecting formation and growth of intracranial aneurysms: a long-term follow-up study.** *Stroke* 2001;32:485–91 CrossRef Medline
4. Knekt P, Reunanen A, Aho K, et al. **Risk factors for subarachnoid hemorrhage in a longitudinal population study.** *J Clin Epidemiol* 1991;44:933–39 CrossRef Medline
5. Kang HS, Han MH, Kwon BJ, et al. **Repeat endovascular treatment in post-embolization recurrent intracranial aneurysms.** *Neurosurgery* 2006;58:60–70; discussion 60–70 CrossRef Medline
6. Petitti DB, Wingerd J. **Use of oral contraceptives, cigarette smoking, and risk of subarachnoid haemorrhage.** *Lancet* 1978;2:234–35 Medline
7. Sacco RL, Wolf PA, Bharucha NE, et al. **Subarachnoid and intracerebral hemorrhage: natural history, prognosis, and precursive factors in the Framingham Study.** *Neurology* 1984;34:847–54 CrossRef Medline
8. Brinjikji W, Lingineni RK, Gu CN, et al. **Smoking is not associated with recurrence and retreatment of intracranial aneurysms after endovascular coiling.** *J Neurosurg* 2015;122:95–100 CrossRef Medline
9. Ortiz R, Stefanski M, Rosenwasser R, et al. **Cigarette smoking as a risk factor for recurrence of aneurysms treated by endosaccular occlusion.** *J Neurosurg* 2008;108:672–75 CrossRef Medline
10. Wei HJ, Wang D, Chen JL, et al. **Mobilization of circulating endothelial progenitor cells after endovascular therapy for ruptured cerebral aneurysms.** *Neurosci Lett* 2011;498:114–18 CrossRef Medline
11. Kadivel R, Ding YH, Dai D, et al. **Cellular mechanisms of aneurysm occlusion after treatment with a flow diverter.** *Radiology* 2014;270:394–99 CrossRef Medline
12. Soga Y, Tomoi Y, Fujihara M, et al. **Perioperative and long-term outcomes of endovascular treatment for subclavian artery disease from a large multicenter registry.** *J Endovasc Ther* 2015;22:626–33 CrossRef Medline
13. Musallam KM, Rosendaal FR, Zaatari G, et al. **Smoking and the risk of mortality and vascular and respiratory events in patients undergoing major surgery.** *JAMA Surg* 2013;148:755–62 CrossRef Medline
14. Becske T, Kallmes DF, Saatci I, et al. **Pipeline for uncoilable or failed aneurysms: results from a multicenter clinical trial.** *Radiology* 2013;267:858–68 CrossRef Medline
15. Kallmes DF, Hanel R, Lopes D, et al. **International retrospective study of the Pipeline embolization device: a multicenter aneurysm treatment study.** *AJNR Am J Neuroradiol* 2015;36:108–15 CrossRef Medline
16. Chen JX, Lai LF, Zheng K, et al. **Influencing factors of immediate angiographic results in intracranial aneurysms patients after endovascular treatment.** *J Neuro* 2015;262:2115–23 CrossRef Medline
17. Song J, Yeon JY, Kim JS, et al. **Delayed thromboembolic events more than 30 days after self-expandable intracranial stent-assisted embolization of unruptured intracranial aneurysms.** *Clin Neurol Neurosurg* 2015;135:73–78 CrossRef Medline
18. Zhu YQ, Li MH, Lin F, et al. **Frequency and predictors of endoleaks and long-term patency after covered stent placement for the treatment of intracranial aneurysms: a prospective, non-randomised multicentre experience.** *Eur Radiol* 2013;23:287–97 CrossRef Medline
19. Lal BK, Beach KW, Roubin GS, et al; CREST Investigators. **Restenosis after carotid artery stenting and endarterectomy: a secondary analysis of CREST, a randomised controlled trial.** *Lancet Neurol* 2012;11:755–63 CrossRef Medline
20. Matteau A, Yeh RW, Camenzind E, et al. **Balancing long-term risks of ischemic and bleeding complications after percutaneous coronary intervention with drug-eluting stents.** *Am J Cardiol* 2015;116:686–93 CrossRef Medline
21. Yeo KK, Armstrong EJ, Soni K, et al. **Long-term outcomes of angiographically confirmed coronary stent thrombosis: results from a multicentre California registry.** *EuroIntervention* 2015;11:188–95 CrossRef Medline
22. Zhang YJ, Iqbal J, van Klaveren D, et al. **Smoking is associated with adverse clinical outcomes in patients undergoing revascularization with PCI or CABG: the SYNTAX trial at 5-year follow-up.** *J Am Coll Cardiol* 2015;65:1107–15 CrossRef Medline
23. Anderson CS, Feigin V, Bennett D, et al; Australasian Cooperative Research on Subarachnoid Hemorrhage Study (ACROSS) Group. **Active and passive smoking and the risk of subarachnoid hemorrhage: an international population-based case-control study.** *Stroke* 2004;35:633–37 CrossRef Medline
24. Kim CK, Kim BJ, Ryu WS, et al. **Impact of smoking cessation on the risk of subarachnoid haemorrhage: a nationwide multicentre case control study.** *J Neurol Neurosurg Psychiatry* 2012;83:1100–03 CrossRef Medline

Pipeline Embolization Device with or without Adjunctive Coil Embolization: Analysis of Complications from the IntrePED Registry

M.S. Park, C. Kilburg, P. Taussky, F.C. Albuquerque, D.F. Kallmes, E.I. Levy, P. Jabbour, I. Szikora, E. Boccardi, R.A. Hanel, A. Bonafé, and C.G. McDougall

ABSTRACT

SUMMARY: Flow diversion to treat cerebral aneurysms has revolutionized neurointerventional surgery. Because the addition of coils potentially increases the time and complexity of endovascular procedures, we sought to determine whether adjunctive coil use is associated with an increase in complications. Patients in the International Retrospective Study of Pipeline Embolization Device registry were divided into those treated with the Pipeline Embolization Device alone ($n = 689$ patients; $n = 797$ aneurysms; mean aneurysm size, 10.3 ± 7.6 mm) versus those treated with the Pipeline Embolization Device and concurrent coil embolization ($n = 104$ patients; $n = 109$ aneurysms; mean aneurysm size, 13.6 ± 7.8 mm). Patient demographics and aneurysm characteristics were examined. Rates of neurologic morbidity and mortality were compared between groups. The Pipeline Embolization Device with versus without coiling required a significantly longer procedure time (135.8 ± 63.9 versus 96.7 ± 46.2 min; $P < .0001$) and resulted in higher neurological morbidity (12.5% versus 7.8%; $P = .13$). These data suggest that either strategy represents an acceptable risk profile in the treatment of complex cerebral aneurysms and warrants further investigation.

ABBREVIATIONS: IntrePED = International Retrospective Study of Pipeline Embolization Device; PED = Pipeline Embolization Device

The recent development of flow diversion for cerebral aneurysms that are difficult to treat has ushered in an exciting time in the world of neurointerventional surgery.¹⁻¹⁷ Reports in the literature, however, are conflicting concerning the optimal strategy in using this new device.^{1,2,4,13,15,16,18-21} The addition of coil embolization to flow diversion, while prevalent in daily use, has not been subjected to a large systematic analysis.^{7-11,16,21-24} The earliest case report hypothesized that coils within the aneurysm sac can augment the degree of flow diversion with the goal of improved occlusion of the aneurysm.¹ Others believe that adjunctive coil embolization does little to improve the already high occlusion rates obtained by using the Pipeline Embolization Device (PED; Covidien, Irvine, California) alone.²¹ Furthermore, there

have been reports of complications associated with overly dense coil embolization of aneurysms in this setting.²²

We analyzed the International Retrospective Study of Pipeline Embolization Device (IntrePED [ClinicalTrials.gov identifier: NCT01558102]) data to determine whether there was an increase in neurologic complications associated with the use of the PED and adjunctive coil embolization.

MATERIALS AND METHODS

This study is a subanalysis of IntrePED registry data obtained from a multicenter, observational, international registry of patients treated with the PED. The primary objective of IntrePED was to identify any neurologic events following treatment with the PED. The IntrePED registry includes patients treated with the PED starting in July 2008 and concluding in July 2013, following the enrollment of 793 patients. Because the study was conducted retrospectively, the protocol did not specify the coiling methodology, and the decision to use coils with the PED was left to the discretion of the treating physician. Details regarding the institutional review board and ethics committee approvals, patient population, and protocol requirements are described in the primary IntrePED article.¹⁷

This subanalysis was performed to compare the safety outcomes of patients treated with the PED alone (PED group) with those of patients treated with the PED and adjunctive coil embolization (PED/coil group). Data collected for analysis were basic

Received July 14, 2015; accepted after revision November 18.

From the Department of Neurosurgery (M.S.P., C.K., P.T.), University of Utah Health Care, Salt Lake City, Utah; Department of Neurosurgery (F.C.A., C.G.M.), Barrow Neurological Institute, Phoenix, Arizona; Department of Radiology (D.F.K.), Mayo Clinic, Rochester, Minnesota; Department of Neurosurgery (E.I.L.), University of Buffalo, Buffalo, New York; Department of Neurosurgery (P.J.), Thomas Jefferson University, Philadelphia, Pennsylvania; Department of Neurointerventions (I.S.), National Institute of Neurosciences, Budapest, Hungary; Department of Neuroradiology (E.B.), Ospedale Niguarda Ca' Granda, Milan, Italy; Department of Neurosurgery (R.A.H.), Baptist Health, Jacksonville, Florida; and Department of Neuroradiology (A.B.), Hôpital Gui de Chauliac, Montpellier, France.

Please address correspondence to Cameron G. McDougall, MD, c/o Neuroscience Publications; Barrow Neurological Institute, St. Joseph's Hospital and Medical Center, 350 W Thomas Rd, Phoenix, AZ 85013; e-mail: Neuropub@dignityhealth.org

<http://dx.doi.org/10.3174/ajnr.A4678>

Table 1: Patient details

Patient Characteristics	PED/Coils	PED Alone	P Value ^a
No. (%) of aneurysms	109 (12.0%)	797 (88.0%)	
No. (%) of patients	104 (13.1%)	689 (86.9%)	
Age (yr)			.279
Mean	57.6 ± 15.1	56.8 ± 14.0	
Median, range	61.5; 3–81	57; 9–86	
Sex (No., %)			.435
Male	24 (23.1%)	137 (19.9%)	
Female	80 (76.9%)	552 (80.1%)	
Follow-up duration (mo)			.718
Mean	21.1 ± 8.8	22.1 ± 8.8	
Median, range	20.8; 0.1–45.0	21.0; 0.1–60.5	
Procedure time (min)			<.0001
Mean	135.8 ± 63.9	96.7 ± 46.2	
Median, range	120; 46–365	87; 10–376	

^a P values for age, duration of follow-up, and procedure time were calculated with Wilcoxon rank sum tests. P value for sex was calculated with the χ^2 test.

demographic information, including patient age, sex, and history of aneurysm rupture; aneurysm characteristics, including aneurysm size, neck size, shape, and location; procedural data, including procedure time and devices used; and follow-up data, including any complications. The primary outcomes were neurologic mortality and combined neurologic morbidity and mortality. Neurologic morbidity was predefined as the composite of the following neurologic complications: spontaneous aneurysm rupture, ipsilateral intracranial hemorrhage, ischemic stroke, parent artery stenosis, and cranial neuropathy. These complications were characterized as major or minor, with “major” defined as an ongoing clinical deficit at 7 days after the event. All major adverse events are included in the neurologic morbidity and mortality rates.

The data were analyzed to determine whether there were any significant differences between those patients treated with the PED alone versus those treated with the PED and adjunctive coils. Differences in continuous variables between the 2 groups were tested by using the Wilcoxon rank sum test. Differences in categorical variables between groups were analyzed by using the χ^2 or Fisher exact test. Data are presented as the number of events and percentage or mean ± SD unless otherwise noted; P values < .05 were statistically significant. Most statistical analyses were performed across patient groups on a per-patient basis. When determining aneurysm size, we categorized patients with multiple aneurysms on the basis of the size of the largest aneurysm. Analysis of aneurysm characteristics was performed across all aneurysms rather than across patients.

RESULTS

The registry included 793 patients with 906 aneurysms: 689 patients with 797 aneurysms were treated with the PED alone, and 104 patients with 109 aneurysms were treated with PED/coil (Table 1). While the patient ages, sex, and length of follow-up were well matched, procedure times were significantly increased for the PED/coil cohort compared with the PED alone group (135.8 ± 63.9 minutes versus 96.7 ± 46.2 minutes, $P < .0001$).

The mean aneurysm and neck sizes were statistically larger in the PED/coil cohort than in the PED alone group (aneurysm size, 13.6 ± 7.8 mm versus 10.3 ± 7.6 mm, $P < .0001$; neck size, 6.4 ± 3.0 mm versus 6.2 ± 5.1 mm, $P = .017$) (Table 2). These larger

Table 2: Aneurysm characteristics

Aneurysm Characteristics	PED/Coils	PED Alone	P Value ^a
No. of aneurysms	109	797	
No. of patients	104	689	
Aneurysm size (mm) ^b			<.0001
Mean	13.6 ± 7.8	10.3 ± 7.6	
Median, range	12; 1.6–45.0	8; 1.0–55.0	
Aneurysm neck (mm)			.017
Mean	6.4 ± 3.0	6.2 ± 5.1	
Median, range	6; 0.8–16.0	5; 0.9–53.0	
Aneurysm shape (No., %)			.3366
Fusiform	13 (11.9%)	103 (12.9%)	
Saccular	85 (78.0%)	604 (75.8%)	
Dissecting	3 (2.8%)	51 (6.4%)	
Other	8 (7.3%)	39 (4.9%)	
Aneurysm location (No., %)			<.0001
Internal carotid artery	70 (64.2%)	614 (77.0%)	
Middle cerebral artery	8 (7.3%)	35 (4.4%)	
Posterior cerebral artery	0 (0%)	15 (1.9%)	
Basilar artery	16 (14.7%)	28 (3.5%)	
Other	15 (13.8%)	105 (13.2%)	
Aneurysm ruptured at initial presentation (No., %)	13 (11.9%)	63 (7.9%)	.155
Multiple PEDs used ^c (No., %)	34 (31.2%)	274 (34.5%)	.499

^a P values for aneurysm size and neck size were calculated with Wilcoxon rank sum tests. P values for categorical variables were calculated with χ^2 tests.

^b Of the 797 aneurysms treated with PEDs alone, size data were not available for 8 aneurysms. Of the 109 aneurysms treated with PED/coil, size data were not available for 2 aneurysms.

^c Of the 797 aneurysms treated with PEDs alone, data regarding the number of PEDs used were not reported for 2 aneurysms.

aneurysms were also more likely to require multiple PEDs during treatment (Table 3). There was also a statistically significant difference in the location of aneurysms treated between the 2 groups ($P < .0001$). There were significantly fewer internal carotid artery aneurysms treated in the PED/coil cohort compared with the PED alone group (64.2% versus 77%, $P = .006$). There were significantly more basilar artery aneurysms treated by PED/coil compared with PED alone (14.7% versus 3.5%, $P < .0001$). There was no statistically significant difference in presentation with subarachnoid hemorrhage between the 2 groups (PED/coil 11.9% versus PED alone 7.9%, $P = .155$).

Overall, 13 of 104 (12.5%) patients in the PED/coil cohort experienced a major neurologic complication and/or mortality versus 54 of 689 (7.8%) patients in the PED alone cohort ($P = .13$) (Table 4). Neither the overall nor the individual complication rates reached statistical significance.

DISCUSSION

While the use of adjunctive coil embolization with the PED is not novel, there are questions regarding the efficacy of, and the potential for, increased complications with this strategy compared with PED embolization alone. Certain authors have advocated coil embolization as a method of improving occlusion rates and minimizing the potential for catastrophic aneurysm rupture following the use of flow-diverting stents.^{23,25,26} Others have argued that the addition of coil embolization to the procedure yields no significant added advantage in regard to treatment efficacy.²¹ However, our single-center results, which have been previously presented, did identify a statistically significant increase in the need for retreatment with a strategy of PED alone versus PED/coil.²⁷

Table 3: Multiple PED use

Procedure	Aneurysm Size (%) (n/N)			P Value ^a	Total
	Small	Large	Giant		
PED alone ^b	25.8% (113/438)	43.7% (129/295)	53.7% (29/54)	<.001	34.5% (274/795)
PED/coil ^c	18.2% (6/33)	32.3% (20/62)	66.7% (8/12)	.010	31.2% (34/109)
All subjects	25.3% (119/471)	41.7% (149/357)	56.1% (37/66)	<.001	34.1% (308/904)

^a P values were calculated using Fisher exact tests.

^b Of the 797 aneurysms treated with the PED alone, data regarding the number of PEDs used were not available for 2 aneurysms treated; thus, 795 is used as the total denominator. Of these 795 aneurysms, size data were not available for 8 aneurysms. All 795 are included in the total calculation, but only 787 are included in the aneurysm-size categories.

^c Of the 109 aneurysms treated with PED/coil, size data were not available for 2 aneurysms. All 109 are included in the total calculation, but only 107 are included in the aneurysm-size categories.

Table 4: Patient outcomes

Major Complications	PED/Coils (n, %) (Patients = 104; Aneurysms = 109)	PED Alone (n, %) (Patients = 689; Aneurysms = 797)	P Value ^a
Neurologic morbidity	11 (10.6%)	48 (7.0%)	.226
Spontaneous rupture	0 (0%)	5 (0.7%)	>.99
Ipsilateral intracranial hemorrhage	3 (2.9%)	17 (2.5%)	.738
Ischemic stroke	7 (6.7%)	29 (4.2%)	.307
Parent artery stenosis	0 (0%)	2 (0.3%)	>.99
Cranial neuropathy	1 (1.0%)	1 (0.1%)	.245
Neurologic mortality	7 (6.7%)	23 (3.3%)	.099
Neurologic morbidity and mortality	13 (12.5%)	54 (7.8%)	.128

^a P values were calculated using Fisher exact tests.

Additionally, we previously reported our overall (31.7%) and permanent complication (3.2%) rates following use of the PED.¹⁹ However, we did not examine any potential differences in complications between these 2 treatment strategies. In an earlier report on the PED, Siddiqui et al²² described a patient with a giant middle cerebral artery aneurysm treated with 2 PEDs and dense coil embolization. The patient had an acute thrombosis of the PED following the procedure, which was attributed to the dense coil mass. The authors recommended avoiding dense packing of aneurysms when coil embolization is used as an adjunctive treatment with the PED.

In a recent series published by Lin et al,²³ 75 patients treated with the PED alone were compared with 29 patients treated with the PED and adjunctive coil embolization. There was no statistically significant difference in the complication rates between the 2 groups (10.3% with PED/coil versus 8.0% with PED alone, $P = .7$). Lin et al found, as we did in the IntrePED study, that aneurysms treated with a strategy of PED/coil were statistically larger than aneurysms treated with PED alone (16.3 versus 12.4 mm, $P = .02$). Nosseck et al²⁶ also found similar results in 25 consecutive patients with unruptured aneurysms treated with the PED and adjunctive coiling.

Szikora et al²¹ described their series of 19 patients with wide-neck intracranial aneurysms treated with a strategy of both PED/coil and PED alone. Initially, they treated patients with adjunctive coil embolization, maintaining low coil-packing densities; however, they switched to a strategy of overlapping PEDs without coiling in the latter part of their series. Despite the 2 differing strategies, they had similar occlusion rates at the 6-month follow-up interval. Although their overall complication rate (1 permanent nonrestricting morbidity and 1 mortality) was within the rates published in the literature, they did not specify which treatment strategy was associated with these complications.

In the IntrePED registry, there was a statistically significant

difference in the aneurysm size between the 2 cohorts we evaluated ($P < .0001$). Aneurysms treated with adjunctive coil embolization were larger in both aneurysm size and aneurysm neck size. These differences are likely related to the individual clinician's judgment in regard to the efficacy of stand-alone PED placement for this subset of aneurysms. There may have been a stronger desire to have more immediate contrast stasis during the initial treatment of larger aneurysms due to the higher chance of spontaneous rupture with increasing aneurysm size. In this instance, 2 options for increasing stasis would be to add coil embolization or to place multiple PEDs across the aneurysm neck. Potentially, the use of multiple PEDs may also increase the rate of complications during the procedure. However, we did not identify a difference in the percentage of aneurysms treated with multiple PEDs in either cohort. Patients with larger aneurysms,

however, were more likely to have multiple PEDs deployed in both groups (PED alone versus PED/coil).

Another interesting finding in our analysis is the statistically significant difference in the location of aneurysms treated by either strategy. Again, this is likely related to clinical judgment in terms of the aneurysm characteristics and their relationship to the parent vessel. Additionally, endovascular surgeons may be more reluctant to use adjunctive coil embolization when using flow diverters in the posterior cerebral artery/posterior circulation, which is currently an off-label indication in some countries.

While one may presuppose a higher intraprocedural rupture rate with a strategy of PED and adjunctive coils, this was not apparent in our findings. Even with manipulation of the aneurysm wall/dome during coil embolization, there was no statistically significant increased rate of ipsilateral intracranial hemorrhage during or following the procedure. While the anatomical differences between the aneurysms in the 2 cohorts may have certainly influenced the practitioner's judgment as to the optimal treatment strategy, there were no statistically significant differences in the primary or secondary end points for either treatment strategy. Overall, the complication rates reported for the patients in the IntrePED registry for either treatment strategy are in line with those in the published literature for use of flow-diverting stents.¹⁹

Once the decision is made to use adjunctive coil embolization, the setup and performance of the procedure may be distinctly different from those used in deploying a PED alone. First, one must decide whether to coil the aneurysm before or after placement of the flow-diverting stent. One can choose to proceed first with primary or balloon-assisted coil embolization followed by PED deployment. While this strategy would not significantly affect the deployment of the PED from a guide catheter standpoint, it does add the time required to perform the initial embolization

to the overall procedure. Once coils are placed within the aneurysm, the microcatheter or balloon microcatheter or both are removed, allowing unencumbered navigation of the catheters for PED deployment. This technique, however, can potentially obscure visualization of the PED during deployment.

Alternatively, one can jail a microcatheter within the aneurysm and initially place the PED followed by aneurysm coiling. This strategy, however, may affect the choice of support catheters. One must ensure that the inner diameter of the guide catheter is sufficiently large enough to support simultaneous navigation of the Marksman catheter (Covidien) and the microcatheter to be used for coil embolization. The use of a second microcatheter for coiling placed through the same guide catheter as the Marksman catheter would likely preclude the use of additional catheters (ie, distal-access catheters) to support PED deployment due to limitations in guide-catheter size. Despite the increase in procedural times and/or case complexity, there was no statistically significant increase in the overall complication rate in terms of neurologic morbidity and mortality in our analysis.

Limitations

Our study is limited by its retrospective nature, with participating sites following their standard practice for treating aneurysms with PEDs. As a result, the decision to use adjunctive coil embolization was left to the discretion of the treating physician and was not standardized across centers. Because the IntrePED study was a retrospective, observational study without preplanned subgroup analysis, no prespecified differences were expected between these 2 cohorts. Additionally, no power analysis was performed. While there are certain inherent limitations with this type of study, we believe that the conclusions may still be clinically relevant.

CONCLUSIONS

Decisions about which strategy to use when faced with a complex cerebral aneurysm are made largely at the discretion of, and with the judgment of, the practitioner. There have been few large series comparing PED alone versus PED with coiling in terms of overall efficacy in aneurysm treatment. While there was a statistically significant difference in aneurysm size and location and procedural times in the IntrePED registry between our 2 cohorts, there was no statistically significant difference in overall complications. These data suggest that either strategy represents an acceptable risk profile in the treatment of complex cerebral aneurysms and warrants further investigation.

ACKNOWLEDGMENTS

We thank Ms Suzanne LaScalza and Mei Jiang, PhD, for assistance with statistical analysis. The IntrePED observational registry was funded and supported by Covidien/Medtronic, with scientific oversight of the study by the steering committee.

Disclosures: Min S. Park—RELATED: Other: Covidien/Medtronic, Comments: Covidien provided statistical analysis support for the article (as described in our acknowledgments). No money was provided as part of the preparation, writing, submission, or any other aspects of this work. Philipp Taussky—RELATED: Consulting Fee or Honorarium: Covidien/Medtronic (Pipeline proctor). David F. Kallmes—RELATED: Grant: ev3/Covidien/Medtronic.* Comments: support for clinical trial; Consulting Fee or Honorarium: ev3/Covidien/Medtronic.* Comments: Steering Committee for clinical trial; Fees for Participation in Review Activities, Such as Data Monitoring

Boards, Statistical Analysis, Endpoint Committees, and the Like: ev3/Covidien/Medtronic.* Comments: Safety Committee; UNRELATED: Board Membership: GE Healthcare Cost-Effectiveness Board*; Consultancy: ev3/Covidien/Medtronic.* Comments: clinical trials support; Grants/Grants Pending: MicroVention,* Codman Neuro/DePuy Synthes,* NeuroSigma,* SurModics,* Sequent Medical.* ev3/Covidien/Medtronic,* Comments: support for clinical and preclinical research; Patents (planned, pending or issued): Mayo Medical Ventures.* Comments: augmentation patent; Royalties: University of Virginia Patent Foundation (Spine Fusion); Travel/Accommodations/Meeting Expenses Unrelated to Activities Listed: ev3/Covidien/Medtronic.* Comments: travel to FDA panel meeting. Elad I. Levy—UNRELATED: Board Membership: Stryker (American Spinal Injury Association Impairment Scale [AIS] Clinical Advisory Board), Next-Gen Biologics (Advisory Board); Consultancy: Pulsar Vascular (unpaid); Expert Testimony: renders medical/legal opinion as an expert witness; Payment for Lectures (including service on Speakers Bureaus): Covidien/Medtronic (honorarium for lectures), Stryker; Payment for Development of Educational Presentations: Covidien/Medtronic Abbott, Comments: honorarium for training for Covidien/Medtronic and carotid training sessions for Abbott for physicians; Stock/Stock Options: Blockade Medical, Intratech Medical, Medina Medical; Other: Covidien/Medtronic (National Principal Investigator for Solitaire with the Intention for Thrombectomy as Primary Endovascular Treatment for Acute Ischemic Stroke trials). Pascal Jabbour—UNRELATED: Consultancy: Covidien (Pipeline proctor). István Szikora—RELATED: Consulting Fee or Honorarium: Covidien/Medtronic; Support for Travel to Meetings for the Study or Other Purposes: Covidien/Medtronic; UNRELATED: Consultancy: Covidien/Medtronic, Stryker, Codman, Sequent Medical. Edoardo Boccardi—RELATED: Consulting Fee or Honorarium: Covidien/Medtronic; UNRELATED: Consultancy: Covidien/Medtronic, Stryker, MicroVention. Ricardo A. Hanel—RELATED: Consulting Fee or Honorarium: Covidien/Medtronic; UNRELATED: Board Membership: Medina Medical; Consultancy: Stryker, Codman, MicroVention; Stock/Stock Options: Blockade Medical. Alain Bonafé—UNRELATED: Consultancy: Covidien/Medtronic. Cameron G. McDougall—RELATED: Consulting Fee or Honorarium: Covidien/Medtronic; UNRELATED: Consultancy: MicroVention.* Money paid to the institution.

REFERENCES

1. Fiorella D, Woo HH, Albuquerque FC, et al. **Definitive reconstruction of circumferential, fusiform intracranial aneurysms with the Pipeline embolization device.** *Neurosurgery* 2008;62:1115–20; discussion 1120–21 CrossRef Medline
2. Lylyk P, Miranda C, Ceratto R, et al. **Curative endovascular reconstruction of cerebral aneurysms with the Pipeline embolization device: the Buenos Aires experience.** *Neurosurgery* 2009;64:632–42; discussion 642–43; quiz N6 CrossRef Medline
3. Nelson PK, Lylyk P, Szikora I, et al. **The Pipeline embolization device for the intracranial treatment of aneurysms trial.** *AJNR Am J Neuroradiol* 2011;32:34–40 CrossRef Medline
4. Chalouhi N, Zanaty M, Whiting A, et al. **Safety and efficacy of the Pipeline embolization device in 100 small intracranial aneurysms.** *J Neurosurg* 2015;122:1498–502 CrossRef Medline
5. Zanaty M, Chalouhi N, Starke RM, et al. **Flow diversion versus conventional treatment for carotid cavernous aneurysms.** *Stroke* 2014; 45:2656–61 CrossRef Medline
6. Tse MM, Yan B, Dowling RJ, et al. **Current status of Pipeline embolization device in the treatment of intracranial aneurysms: a review.** *World Neurosurg* 2013;80:829–35 CrossRef Medline
7. Saatci I, Yavuz K, Ozer C, et al. **Treatment of intracranial aneurysms using the Pipeline flow-diverter embolization device: a single-center experience with long-term follow-up results.** *AJNR Am J Neuroradiol* 2012;33:1436–46 CrossRef Medline
8. Fischer S, Vajda Z, Aguilar Perez M, et al. **Pipeline embolization device (PED) for neurovascular reconstruction: initial experience in the treatment of 101 intracranial aneurysms and dissections.** *Neuroradiology* 2012;54:369–82 CrossRef Medline
9. McAuliffe W, Wycoco V, Rice H, et al. **Immediate and midterm results following treatment of unruptured intracranial aneurysms with the Pipeline embolization device.** *AJNR Am J Neuroradiol* 2012; 33:164–70 CrossRef Medline
10. Chitale R, Gonzalez LF, Randazzo C, et al. **Single center experience with Pipeline stent: feasibility, technique, and complications.** *Neurosurgery* 2012;71:679–91; discussion 691 CrossRef Medline
11. Becske T, Kallmes DF, Saatci I, et al. **Pipeline for uncoilable or failed**

- aneurysms: results from a multicenter clinical trial. *Radiology* 2013; 267:858–68 CrossRef Medline
12. Deutschmann HA, Wehrschoetz M, Augustin M, et al. **Long-term follow-up after treatment of intracranial aneurysms with the Pipeline embolization device: results from a single center.** *AJNR Am J Neuroradiol* 2012;33:481–86 CrossRef Medline
 13. Briganti F, Delehaye L, Leone G, et al. **Flow diverter device for the treatment of small middle cerebral artery aneurysms.** *J Neurointerv Surg* 2015 Jan 20. [Epub ahead of print] CrossRef Medline
 14. Zanaty M, Chalouhi N, Barros G, et al. **Flow-diversion for ophthalmic segment aneurysms.** *Neurosurgery* 2015;76:286–89; discussion 289–90 CrossRef Medline
 15. Navarro R, Brown BL, Beier A, et al. **Flow diversion for complex intracranial aneurysms in young children.** *J Neurosurg Pediatr* 2015; 15:276–81 CrossRef Medline
 16. Chalouhi N, Zanaty M, Whiting A, et al. **Treatment of ruptured intracranial aneurysms with the Pipeline embolization device.** *Neurosurgery* 2015;76:165–72; discussion 172 CrossRef Medline
 17. Kallmes DF, Hanel R, Lopes D, et al. **International retrospective study of the Pipeline embolization device: a multicenter aneurysm treatment study.** *AJNR Am J Neuroradiol* 2015;36:108–15 CrossRef Medline
 18. Chalouhi N, Tjoumakaris S, Phillips JL, et al. **A single Pipeline embolization device is sufficient for treatment of intracranial aneurysms.** *AJNR Am J Neuroradiol* 2014;35:1562–66 CrossRef Medline
 19. Park MS, Albuquerque FC, Nanaszko M, et al. **Critical assessment of complications associated with use of the Pipeline embolization device.** *J Neurointerv Surg* 2015;7:652–69 CrossRef Medline
 20. Siddiqui AH, Abla AA, Kan P, et al. **Panacea or problem: flow diverters in the treatment of symptomatic large or giant fusiform vertebrobasilar aneurysms.** *J Neurosurg* 2012;116:1258–66 CrossRef Medline
 21. Szikora I, Berentei Z, Kulcsar Z, et al. **Treatment of intracranial aneurysms by functional reconstruction of the parent artery: the Budapest experience with the Pipeline embolization device.** *AJNR Am J Neuroradiol* 2010;31:1139–47 CrossRef Medline
 22. Siddiqui AH, Kan P, Abla AA, et al. **Complications after treatment with Pipeline embolization for giant distal intracranial aneurysms with or without coil embolization.** *Neurosurgery* 2012;71:E509–13; discussion E513 CrossRef Medline
 23. Lin N, Brouillard AM, Krishna C, et al. **Use of coils in conjunction with the Pipeline embolization device for treatment of intracranial aneurysms.** *Neurosurgery* 2015;76:142–49 CrossRef Medline
 24. Dornbos D 3rd, Pillai P, Sauvageau E. **Flow diverter assisted coil embolization of a very small ruptured ophthalmic artery aneurysm.** *J Neurointerv Surg* 2013 Dec 11. [Epub ahead of print] CrossRef Medline
 25. Turowski B, Macht S, Kulcsár Z, et al. **Early fatal hemorrhage after endovascular cerebral aneurysm treatment with a flow diverter (SILK-Stent): do we need to rethink our concepts?** *Neuroradiology* 2011;53:37–41 CrossRef Medline
 26. Nossek E, Chalif DJ, Chakraborty S, et al. **Concurrent use of the Pipeline embolization device and coils for intracranial aneurysms: technique, safety, and efficacy.** *J Neurosurg* 2015;122:904–11 CrossRef Medline
 27. Park MS, Nanaszko M, Sanborn MR, et al. **Re-treatment rates after treatment with the Pipeline embolization device alone versus Pipeline and coil embolization of cerebral aneurysms: a single-center experience.** *J Neurosurg* 2015 Dec 18. [Epub ahead of print] CrossRef Medline

Interrogating the Functional Correlates of Collateralization in Patients with Intracranial Stenosis Using Multimodal Hemodynamic Imaging

B.A. Roach, M.J. Donahue, L.T. Davis, C.C. Faraco, D. Arteaga, S.-C. Chen, T.R. Ladner, A.O. Scott, and M.K. Strother



ABSTRACT

BACKGROUND AND PURPOSE: The importance of collateralization for maintaining adequate cerebral perfusion is increasingly recognized. However, measuring collateral flow noninvasively has proved elusive. The aim of this study was to assess correlations among baseline perfusion and arterial transit time artifacts, cerebrovascular reactivity, and the presence of collateral vessels on digital subtraction angiography.

MATERIALS AND METHODS: The relationship between the presence of collateral vessels on arterial spin-labeling MR imaging and DSA was compared with blood oxygen level–dependent MR imaging measures of hypercapnic cerebrovascular reactivity in patients with symptomatic intracranial stenosis ($n = 18$). DSA maps were reviewed by a neuroradiologist and assigned the following scores: 1, collaterals to the periphery of the ischemic site; 2, complete irrigation of the ischemic bed via collateral flow; and 3, normal antegrade flow. Arterial spin-labeling maps were scored according to the following: 0, low signal; 1, moderate signal with arterial transit artifacts; 2, high signal with arterial transit artifacts; and 3, normal signal.

RESULTS: In regions with normal-to-high signal on arterial spin-labeling, collateral vessel presence on DSA strongly correlated with declines in cerebrovascular reactivity (as measured on blood oxygen level–dependent MR imaging, $P < .001$), most notably in patients with nonatherosclerotic disease. There was a trend toward increasing cerebrovascular reactivity with increases in the degree of collateralization on DSA ($P = .082$).

CONCLUSIONS: Collateral vessels may have fundamentally different vasoreactivity properties from healthy vessels, a finding that is observed most prominently in nonatherosclerotic disease and, to a lesser extent, in atherosclerotic disease.

ABBREVIATIONS: ASL = arterial spin-labeling; ATA = arterial transit artifacts; BOLD = blood oxygen level–dependent; CVR = cerebrovascular reactivity; IC = intracranial

The presence of intracranial collateral blood flow in steno-occlusive disease has consistently been shown to be one of the most important variables for predicting response to treatment

and clinical outcome.^{1–5} Speculations regarding the anatomic and physiologic properties of collateral vessels are frequently debated, and there is still much controversy on how collateralization contributes to prognosis in acute stroke and chronic hypoperfusion.^{6,7} New imaging approaches are being developed with sensitivity to collateralization, yet there is currently insufficient information on how these new techniques relate to objective measures of intracranial circulation in vascular insufficiency.^{8,9}

More specifically, intracranial arterioles have the ability to dilate and/or remodel to meet the oxygen-delivery requirements of downstream tissue in response to a vascular insult. The ability of arterioles to modulate cerebral blood volume (milliliters of blood/milliliters of parenchyma) and cerebral blood flow (milliliters of blood/100 g tissue/min) is commonly referred to as cerebrovascular reactivity (CVR) and can be assessed using functional MR imaging or SPECT techniques during the administration of vasoactive stimuli (eg, hypercapnia or acetazolamide). If the ability of the intracranial circulation to increase CBV in response to re-

Received August 3, 2015; accepted after revision November 28.

From the Departments of Radiology and Radiological Sciences (B.A.R., M.J.D., L.T.D., C.C.F., D.A., T.R.L., A.O.S., M.K.S.), Neurology (M.J.D.), and Psychiatry (M.J.D.) and the Vanderbilt Center for Quantitative Sciences (S.-C.C.), Vanderbilt Medical Center, Nashville, Tennessee.

This work was supported by National Institutes of Health/National Institute of Neurological Disorders and Stroke grant 5R01NS078828-03 and the American Heart Association grant 14GRNT20150004.

Paper previously presented at: Annual Meeting of the American Society of Neuro-radiology and the Foundation of the ASNR Symposium, April 25–30, 2015; Chicago, Illinois.

Please address correspondence to Manus J. Donahue, PhD, Vanderbilt University Institute of Imaging Science, Medical Center North, AAA-3115, 1161 21st Ave South, Nashville, TN 37232; e-mail: mj.donahue@vanderbilt.edu

 Indicates open access to non-subscribers at www.ajnr.org

 Indicates article with supplemental on-line table

<http://dx.doi.org/10.3174/ajnr.A4758>

duced perfusion pressure is inadequate, the oxygen extraction fraction (the ratio of oxygen consumed to oxygen delivered) may increase, and in advanced stages, oxygen metabolism (cerebral metabolic rate of O₂, micromole/100 g/min) will decline and an infarct may result.

Collaterals are thought to arise when growth factors, released to reduce metabolic strain, stimulate neoangiogenesis. Collaterals may be recruited from both the affected circulation and uninvolvement territories. As the vascular insult evolves, collateral vessels may become more robust, increasing in number and size.¹⁰ Previous studies have demonstrated that CVR in the presence of steno-occlusive disease and collateralization ranges from reduced to essentially normal compared with healthy tissue.^{11–14} The variability of these findings may relate to the chronicity of the vascular insult and a spectrum of evolving intracranial angiogenesis or remodeling.

The current criterion standard for assessing collateral vessels is digital subtraction angiography, a technique that provides both spatial and temporal information. However, DSA is limited by the inherent procedural risks related to its invasive nature. As our understanding of the importance of collaterals evolves, a less invasive and more time-efficient measure of collaterals is needed to guide treatment decisions. Multiphase CTA, which assesses intracranial collaterals via additional delayed equilibrium and late venous phase acquisitions, has recently been shown to be useful in triaging patients with stroke compared with single-phase CTA.¹⁵ As with DSA, however, multiphase CTA is constrained by radiation dose concerns and limitations related to intravenous contrast requirements.

Alternatively, information regarding collateralization can be derived from noninvasive CBF-weighted arterial spin-labeling (ASL) or blood oxygenation-weighted blood oxygen level-dependent (BOLD) MR imaging. In ASL, blood water protons are labeled magnetically; this feature creates an endogenous tracer that can be used to assess CBF and blood arrival times on the timescale of the longitudinal blood water relaxation time (T₁ ~ 1.65 seconds at 3T).¹⁶ At typical so-called postlabeling delay times of 1.5–2 seconds, labeled blood water exchanges with tissue and creates a small (1%–2%) perfusion signal. However, when the arterial arrival time is much longer, as is the case in collateral vessels, the label will remain in the vasculature and create well-known arterial transit artifacts (ATA, signal > 2%). Thus, temporal vascular information can be provided in the presence of parenchyma with collateral vessels. Recently, it has been shown that ASL MR imaging can provide information similar to that of DSA for assessing the presence and intensity of collateral flow.^{17,18}

Additionally, more common BOLD MR imaging can provide complementary qualitative information, often with higher temporal resolution and reduced insensitivity to slow blood arrival than ASL. In evoked BOLD MR imaging, T₂* images are obtained during periods of a vasodilatory stimulus such as hypercapnia. Here, the larger increases in CBF and arterial CBV in relation to small-to-negligible changes in the cerebral metabolic rate of O₂ lead to a higher fractional concentration of oxyhemoglobin relative to deoxyhemoglobin in capillaries and veins, which translates to a lengthening of the surrounding blood and tissue water T₂* and an increase in the MR signal. BOLD MR imaging can be

performed at much higher temporal resolution than ASL (eg, 1–2 seconds for BOLD relative to 4–8 seconds for ASL), yet its contrast is more qualitative, with contributions primarily from CBF, CBV, and the cerebral metabolic rate of O₂.

The primary aim of this study was to assess the presence and intensity of collateral vessels by using baseline ASL MR imaging and DSA hemodynamic imaging in sequence with hypercapnic BOLD MR imaging in the setting of steno-occlusive disease and, specifically, to understand the vascular compliance of collateral vessels. The hypothesis investigated was that parenchyma perfused by collateral vessels has reduced CVR relative to healthy parenchyma.

MATERIALS AND METHODS

Participants

Patients (*n* = 18; mean age, 49 years; age range, 25–71 years; 10 women, 8 men) were recruited as part of a prospective longitudinal clinical trial (Vanderbilt Assessment of Multimodal MRI in Patients at-Risk for stroke with Intracranial Stenosis) that has been approved by the institutional review board. Patients provided informed, written consent as required by the local institutional review board on presentation with symptoms consistent with ischemic cerebrovascular disease. Those selected for this study either presented with atherosclerotic intracranial (IC) stenosis (*n* = 9; mean age, 56 years; 3 women and 6 men) or non-atherosclerotic IC stenosis (*n* = 9; 7 with Moyamoya disease, 1 with fibromuscular dysplasia, and 1 with Takayasu arteritis; mean age, 42 years; 7 women and 2 men). Hypercapnic BOLD and baseline ASL MR imaging was performed within 30 days of the DSA acquisition. Imaging in all patients was performed before revascularization.

MR Imaging

Patients were scanned at 3T (Achieva; Philips Healthcare, Best, the Netherlands) by using body coil transmission and neurovascular 16-channel sensitivity encoding reception.

Patients underwent a multimodal imaging protocol consisting of the following scans: 1) T₁-weighted (MPRAGE: 1 × 1 × 1 mm³; TR/TE = 8.9/4.6 ms; duration = 3 minutes 47 seconds); 2) T₂-weighted FLAIR (0.9 × 0.9 × 1 mm³; TR/TE = 11,000/120 ms; multishot turbo spin-echo inversion recovery; duration = 1 minute 39 seconds); 3) baseline (normocapnic normoxic) CBF-weighted pseudocontinuous ASL (3.5 × 3.5 × 7 mm³; TR/TE/postlabeling delay times = 4500/11/1600 ms; 17 sections; ascending acquisition; 1500-ms Hanning-windowed pulse train; 90-mm labeling offset); and 4) hypercapnic BOLD (single-shot gradient-echo EPI with TR/TE = 2000/35 ms, duration = 12 minutes). For BOLD, patients were fitted with a nasal cannula to measure end-tidal CO₂ levels and a nonbreathing mask to supply medical-grade room air (21% O₂, 79% N₂) or a carbogen mixture (5% CO₂, 95% O₂); other patient vitals (eg, peripheral arterial oxygen saturation, heart rate, and blood pressure) were monitored by a respiratory therapist. A 2-block paradigm consisting of 180-second blocks of breathing carbogen interleaved with a block of breathing room air was used during the BOLD MR imaging acquisition, with 90-second blocks of room air breathing at the beginning and end of the paradigm. Quantitative differences be-

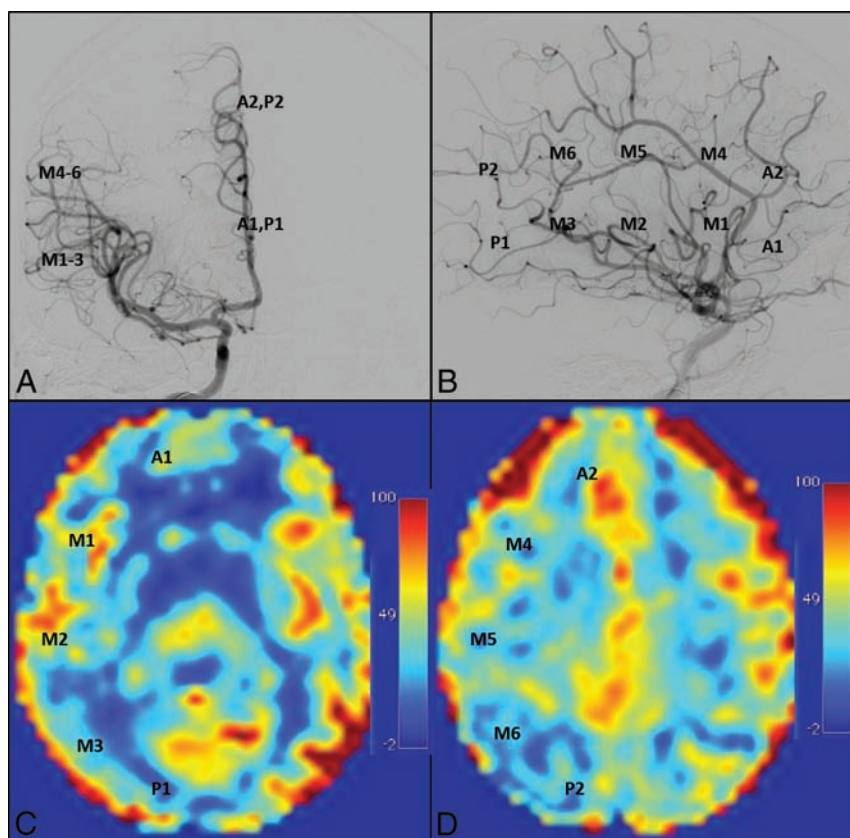


FIG 1. ASPECTS territories superimposed on normal DSA and ASL MR images. A and B, Territories superimposed on anteroposterior and lateral projections during intracranial ICA angiography. C and D, Territories superimposed at the ganglionic and supraganglionic levels, respectively.

tween carbogen and a simpler hypercapnic normoxic stimulus have been reported in the literature.¹⁹

Digital Subtraction Angiography

DSA was performed clinically in the neuroangiography suite by using an Allura Xper biplane neuro x-ray system (Philips Healthcare). Selected catheterizations of carotid and vertebral arteries were performed in multiple projections by using nonionic, water-soluble intra-arterial contrast. Stenoses were graded on DSA by using established criteria by a board-certified neuroradiologist (M.K.S.).²⁰

BOLD and ASL Analysis

MR imaging data were analyzed by using an in-house Matlab (MathWorks, Natick, Massachusetts) code and routines available from the fMRI of the Brain Software Library (FSL; <http://www.fmrib.ox.ac.uk/fsl>). First, affine motion correction, linear slice time correction, and spatial smoothing (full width at half maximum = 6 mm with a Gaussian kernel) were applied. Baseline drift correction was performed on a voxelwise basis by quadratic polynomial regression. Subsequently, functional data were coregistered to a standard atlas (Montreal Neurological Institute; spatial resolution = 4 mm isotropic) to enable spatial comparison across subjects. Z-statistic and signal change maps were calculated from the BOLD data as has been described in the literature.¹⁹

All cerebral blood flow quantification was performed in Matlab. Surround subtractions were performed between the label and

control images. CBF maps were quantified in absolute units (milliliters/100 g/min) by applying a 2-compartment perfusion model by using constrained nonlinear optimization with identical parameters as outlined in the literature.^{21,22} CBF maps were transformed to standard space (4-mm isotropic resolution) by applying the same affine transformation matrix calculated from the BOLD images.

Twenty brain regions in territories defined by the Alberta Stroke Programme Early CT Score criteria¹⁸ were considered in each subject (eg, 360 regions evaluated across all volunteers).

Collateral Grading

A neuroradiologist (M.K.S., with 10 years' experience), blinded to ASL findings, graded the presence and intensity of collateral vessels on DSA in 20 territories defined by the ASPECTS criteria (Fig 1).¹⁸ A previously established 4-point scoring system was used as follows: 0, no collaterals visible; 1, collaterals to the periphery of the ischemic site; 2, complete irrigation of the ischemic bed with collateral flow; and 3, normal antegrade flow. Flow was then assessed in the corresponding anatomic locations

on ASL MR images by 3 separate graders (2 board-certified neuroradiologists, M.K.S. and L.T.D., and 1 imaging physicist, M.J.D.), blinded to non-ASL findings. A similar scoring system was used for ASL MR imaging: 0, no or minimal ASL signal; 1, moderate ASL signal with ATA; 2, high ASL signal with ATA; and 3, normal perfusion without ATA.^{8,17,23} Scoring was then converted to a simple 2-point system: 0, collaterals absent; 1, collaterals present. A score of 1 (presence of collaterals) was assigned to regions with DSA or ATA scores of 1 or 2, while a score of zero (absence of collaterals) was assigned to regions with DSA or ATA scores of 0 or 3. A representative image with ATA in the right M3 region correlating with collaterals on DSA is shown in Fig 2.

Statistical Analysis

The first aim was to understand the similarities between the collateral grading from ASL and DSA. Due to the relative novelty of the ASL scoring system, interreader agreement was first evaluated with Cohen κ analysis with the common criteria: poor agreement, 0–0.20; fair agreement, 0.20–0.40; moderate agreement, 0.40–0.60; good agreement, 0.60–0.80; very good agreement, 0.80–1.00. The analysis was performed for the binary scoring system. Analyses were also performed separately for atherosclerosis-versus-nonatherosclerosis subtypes.

Next, to understand the CVR in regions with collaterals, territories with or without collaterals were placed into 2 groups by using DSA. CVR values were normalized to the cerebellum in the

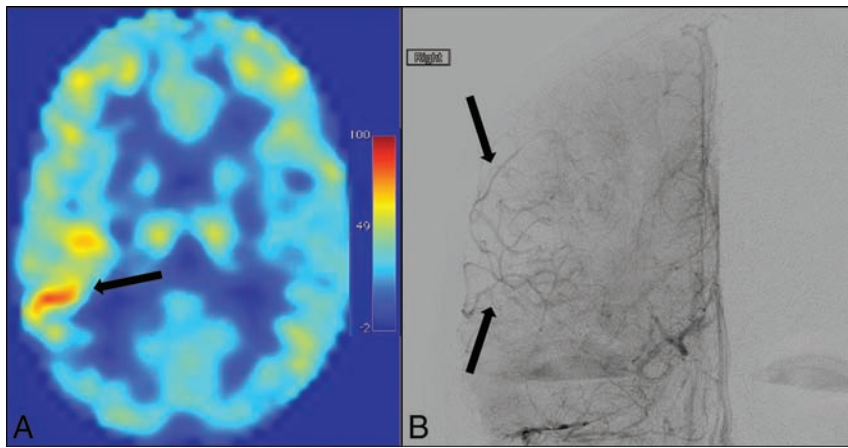


FIG 2. A, Arterial transit artifacts (arrow) at the ganglionic level on ASL MR imaging in the M3 region (ASPECTS designation criteria) representing leptomeningeal collateralization. B, A similar distribution is shown in an early venous phase anteroposterior right ICA angiogram showing leptomeningeal collaterals (arrows) arriving at the periphery of the ischemic site.

Table 1: Modified Suzuki scale

Score	Description of Classification
0	No evidence of disease
I	Mild-to-moderate stenosis around the ICA bifurcation with absent or slightly developed ICA MMD
II	Severe stenosis around the ICA bifurcation or occlusion of either proximal anterior or MCA branches with well-developed ICA MMD
III	Occlusion of both anterior and MCA branches with well-developed ICA MMD
IV	Complete occlusion of both anterior and MCA branches with an absent or small amount of ICA MMD

Note:—MMD indicates Moyamoya disease.

Table 2: Collaterals on ASL (presence of ATA) versus DSA-confirmed collaterals—nonatherosclerosis

		DSA	
		Yes	No
ASL	Yes	48	50
	No	9	25
$P = .022 (\chi^2)$ Sensitivity, 84.2% (78.0%–90.4%) Specificity, 33.3% (25.3%–41.4%) PPV, 49.0% (40.5%–57.5%) NPV, 73.5% (66.0%–81.1%)			

Note:—PPV indicates positive predictive value; NPV, negative predictive value.

Table 3: Collaterals on ASL (presence of ATA) versus DSA-confirmed collaterals—atherosclerosis

		DSA	
		Yes	No
ASL	Yes	24	130
	No	9	44
$P = .811 (\chi^2)$ Sensitivity, 72.7% (65.1%–80.3%) Specificity, 25.3% (17.9%–32.7%) PPV, 15.6% (9.4%–21.8%) NPV, 83.0% (76.6%–89.4%)			

Note:—PPV indicates positive predictive value; NPV, negative predictive value.

corresponding territories and compared by using an unpaired 2-tailed *t* test, separately for all patients, patients with atherosclerosis, and those without atherosclerosis to understand whether

CVR trends are different between subgroups. To compare the influence that collateralization has on measures of hemodynamic reserve, we separated territories into 4 groups based on the DSA score, and corresponding mean normalized cerebrovascular reactivity values were calculated. An unpaired 2-tailed *t* test with $P < .05$ was applied to assign significance.

RESULTS

Patient Characteristics

Patient demographics and severity/extent of disease, including the presence and location of infarction, are detailed in the On-line Table. No areas of infarction occupied >50% of any individual territory analyzed; infarct volume was generally much smaller than the territory volume considered. Table 1 illustrates the components of the modified Suzuki Scale score.^{24,25}

Table 1 illustrates the components of the modified Suzuki Scale score.^{24,25}

Collateral Grading

For the 3 raters, ASL scores between raters were found to have fair agreement ($\kappa = 0.31$ – 0.36) for patients with and without atherosclerosis when raters 1 and 2 were compared (both board-certified neuroradiologists). Raters 1 and 3 (a board-certified neuroradiologist and an imaging physicist) provided moderate agreement ($\kappa = 0.48$ – 0.56). Due to variation in the ASL scoring, the more standardized DSA scoring metric was used for all further comparisons of the effect of collaterals on cerebrovascular reactivity (Tables 2 and 3).

Collateral Effect on Functional Hemodynamic Imaging (BOLD MR Imaging)

As shown in Fig 3, territories perfused by collateral vessels on DSA that also had ASL scores of >0 demonstrated significantly decreased CVR ($P < .001$). When considered separately, regions in patients with nonatherosclerotic IC stenosis demonstrated significantly decreased CVR compared with normally perfused regions ($P = .022$), while the atherosclerosis subset showed no significant correlation ($P = .338$).

Influence of Collateralization on Measures of Hemodynamic Reserve

The number of regions considered for patients with atherosclerosis was 5 (DSA score = 0), 39 (DSA score = 1), 28 (DSA score = 2), and 68 (DSA score = 3) for patients without atherosclerosis and 0 (DSA score = 0), 16 (DSA score = 1), 25 (DSA score = 3), and 179 (DSA score = 3) for the patients with atherosclerosis. Due to the low number of subjects with a DSA score of zero, this group was not considered statistically.

When territories were separated on the basis of the DSA score for collateralization (Fig 4), CVR was significantly decreased in regions with both collaterals to the periphery of the ischemic site (DSA = 1, $P < .05$) and complete irrigation of the ischemic bed with collateral flow (DSA = 2, $P < .05$) compared with normally perfused territories (DSA = 3). A positive trend was shown when comparing CVR between territories with scores of DSA = 1 and

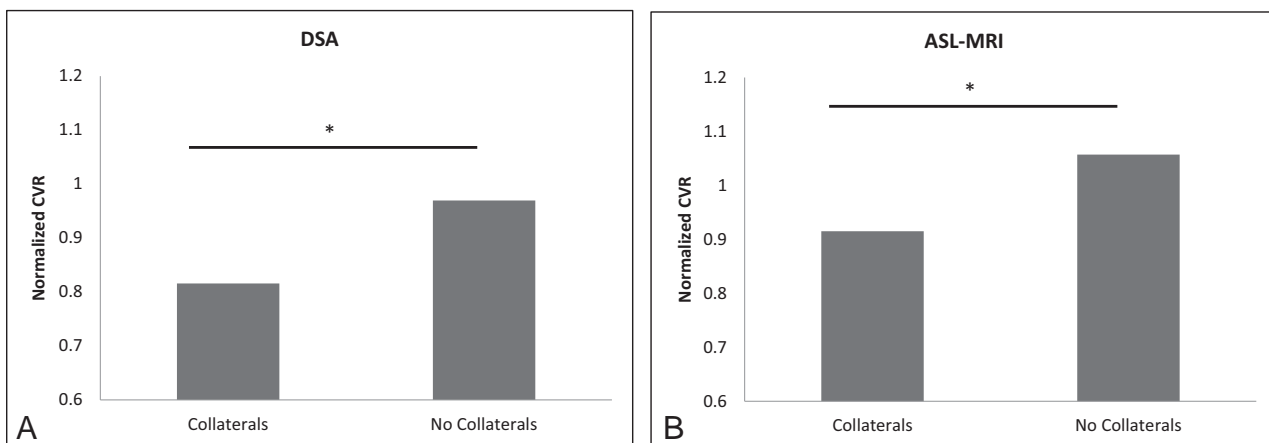


FIG 3. CVR normalized to the cerebellum (y-axis) is shown to be significantly decreased in regions perfused by collaterals on both DSA (A) and ASL MR imaging (B) ($P < .001$ and $P = .0012$, respectively).

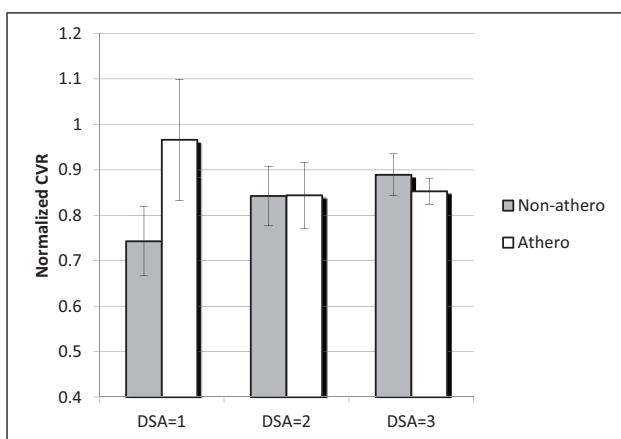


FIG 4. CVR is known to be decreased in the presence of collaterals; however, the graph above shows that CVR tends to increase along with increases in the degree of collateralization. These findings are generally driven by the nonatherosclerotic IC stenosis group.

DSA = 2 (2-sided $P = .082$). Findings were driven by the nonatherosclerotic group.

Representative DSA and ASL MR images from a patient with Takayasu arteritis, who presented with stroke-like symptoms from TIA as a result of near-occlusive cervical ICA stenosis caused by intimal dissections (Fig 5), demonstrated both primary and secondary collateral pathways, which developed due to flow-limiting cervical ICA stenosis.

DISCUSSION

The primary findings of this study are the following: 1) ATA from ASL MR imaging correlated significantly with collateral perfusion on DSA in patients with nonatherosclerotic IC stenosis and demonstrated a positive trend in patients with atherosclerotic IC stenosis; 2) regions with collaterals had significantly decreased CVR compared with regions without collaterals; and 3) in regions with collaterals, CVR increased with increasing levels of collateralization.

Several prior studies have examined the ability of ASL MR imaging to assess collaterals compared with DSA, with results supporting our findings.^{8,17,26} However, 1 study expressed difficulty with ASL interpretation and found no correlation with DSA for collaterals.²⁷

This study had a small patient subset ($n = 7$) with IC stenosis resulting from both Moyamoya disease ($n = 3$) and atherosclerosis ($n = 4$). We observed a similar result in a mixed atherosclerotic and nonatherosclerotic population, showing only a trend toward correlation with DSA. However, a subgroup analysis showed that the atherosclerotic group was masking a statistically significant correlation in the nonatherosclerotic group. This finding suggests that ASL MR imaging analysis for collaterals may be more reliable in the nonatherosclerotic population.

Differences between the current study and those previously reported in the literature may be driven by variability in collateral scoring by territory, most notably in the ASL scores. This variability is demonstrated by only a fair-to-moderate interrater agreement with respect to ASL scoring in the current study. A few experimental reasons potentially explain these results, likely from the variability of the arrival-time delays and the sensitivity of the ASL method used between studies. For instance, Zaharchuk et al⁸ used a 1.5T pseudocontinuous ASL sequence with a long postlabeling delay of 2 seconds. Due to the shorter blood T1 recovery time at 1.5T ($T1 \sim 1.2\text{--}1.4$ seconds) relative to 3T ($T1 \sim 1.6\text{--}1.8$ seconds) used in our study, it is possible that voxels with large endovascular signal were more noticeable relative to those with tissue perfusion because tissue T1 is much shorter (<1 second at 1.5T, depending on the white and gray matter fraction).⁸ Chng et al¹⁷ used a pulsed ASL approach at 3T with multiple delay times, which is known to be more sensitive to variation in blood-arrival times. Therefore, it is likely that ASL methods and post-labeling delay times should be adjusted for specific sensitivity to arrival-time delays. Imaging parameters used in our study were optimized for perfusion, which may not be as sensitive to the specific range of delays observed in our patients. It is likely that different ASL protocols have different discriminatory abilities to detect these effects, which also may depend on the patient population and range of blood water arrival times.

Several findings may underlie the improved correlation of collaterals and CVR from patients without atherosclerosis (largely those with Moyamoya disease) compared with those with atherosclerosis. It has been shown that regions supplied by primary collateral pathways (via communicating arteries through the circle of Willis) tend to have better CVR to hypoperfused territories, even approaching normal in 1 study.¹⁴

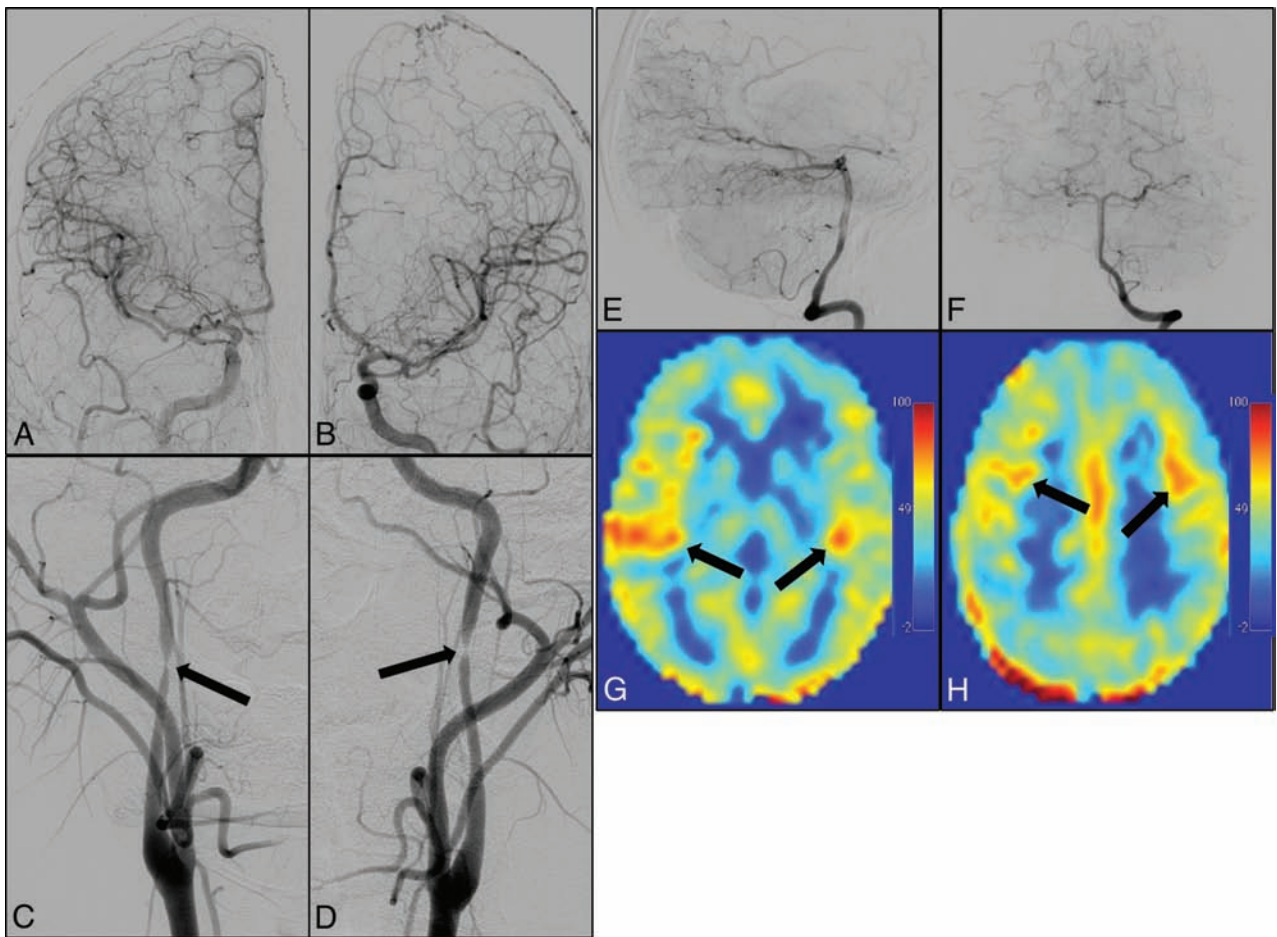


FIG 5. DSA images after injection of the ICA (A), common carotid artery (B), and vertebral artery (E and F) show multiple deep and leptomeningeal secondary collateral pathways. Collateralization is a result of poor intracranial flow due to high-grade stenoses of the cervical ICAs (arrows, C and D), shown after common carotid injection in the anteroposterior dimension. Correlative signal is shown on ASL MR images at the ganglionic (arrows, G) and supraganglionic (arrows, H) levels.

The subjects with atherosclerotic IC stenosis in our study were more likely to have isolated proximal disease (4 of 9 patients with atherosclerosis compared with 1 of 9 without it), which may preserve primary collateral pathways. Collateral flow via intact primary collaterals is not represented by ATA on ASL. It is suggested that secondary collateral pathways only become established when these primary pathways fail to sufficiently augment flow. These primary pathways are often not intact in the nonatherosclerotic group, creating more reliance on the secondary collaterals, which would be closer to autoregulatory capacity, depending on the severity of stenosis. In Moyamoya disease, collaterals have been shown to correlate with disease severity.²⁸

The significant decrease in CVR in territories perfused by collaterals, demonstrated in our study by both ASL and DSA, is consistent with findings on prior studies showing that angiogenesis occurs in response to tissue hypoxia from hypoperfusion.¹⁰ As suggested by the variability in our data, prior studies have shown a range of decreases in CVR in regions supplied by collateral vessels from markedly decreased to normal compared with normally perfused tissue.¹¹⁻¹⁴ This suggests that the presence of collaterals alone does not necessarily portend a protective effect. It is essential to correlate collateralization with a measure of hemodynamic reserve, as can be done with

BOLD MR imaging, to assess the CVR in these hypoperfused territories. Variations in contributions have been attributed to the source of collateralization, with primary pathways (anterior and posterior communicating arteries) resulting in a better protective effect compared with secondary pathways (ophthalmic artery and leptomeningeal vessels).^{13,14,29-31}

Clinical implications can be drawn from the current study. First, we add to a growing body of literature supporting the use of ASL MR imaging rather than invasive DSA to assess the presence of collateralization, even for patients with IC stenosis from non-atherosclerotic etiologies. It is imperative that this information be compared with measures of hemodynamic reserve to guide treatment decisions because the presence of collaterals does not necessarily indicate better vascular reserve. Second, we have shown that CVR is decreased in territories perfused by collaterals theoretically approaching zero, in which there is tissue without vascularity compared with normally perfused tissue, but CVR increases with increased collateralization within regions perfused by collaterals. Finally, our data suggest more variability within the atherosclerosis subset regarding how collateralization is achieved and the contribution of collaterals toward CVR. This suggestion is largely speculative, however, because our sample size limited definitive comparison of circle of Willis integrity within the atherosclerotic subset.

A limitation of our study is the relatively small patient population used for assessment. This limitation could have some bearing on our data variability, particularly in the atherosclerosis subset. Additionally, our study and those performed to date have used a standard ASL protocol, which was applied to the entire patient population. However, patients may require an ASL MR imaging protocol with signal acquisition at many different time points to fully evaluate the extent of collateralization, as previously suggested.²⁶

CONCLUSIONS

Our study demonstrates that ASL MR imaging may provide a useful noninvasive measure of collateralization, particularly in the nonatherosclerotic IC stenosis subset. Furthermore, collaterals identified on ASL MR imaging with ATA correlated with decreased CVR compared with regions not perfused via collaterals. Finally, within territories perfused by collaterals, CVR increased with higher DSA scores.

Disclosures: Brent A. Roach—RELATED: Grant: National Institutes of Health/National Institute of Neurological Disorders and Stroke grant 5R01NS078828-03.* American Heart Association grant 14GRNT20150004.* Manus J. Donahue—RELATED: Grant: National Institutes of Health/National Institute of Neurological Disorders and Stroke.* Comments: National Institutes of Health/National Institute of Neurological Disorders and Stroke R01 to support experimental costs and coinvestigator salaries. Daniel Arteaga—RELATED: Grant: American Heart Association grant 14PRE20370055, Radiological Society of North America grant RMS1402; Support for Travel to Meetings for the Study or Other Purposes: American Heart Association grant 14PRE20370055; Fees for Participation in Review Activities such as Data Monitoring Boards, Statistical Analysis, Endpoint Committees, and the Like: part of a grant used to fund statistical analysis, National Institutes of Health/National Institute of Neurological Disorders and Stroke grant 1R01NS078828.* Megan K. Strother—RELATED: Grant: National Institutes of Health.* *Money paid to the institution.

REFERENCES

- Bang OY, Saver JL, Kim SJ, et al. Collateral flow predicts response to endovascular therapy for acute ischemic stroke. *Stroke* 2011;42:693–99 CrossRef Medline
- Sheth SA, Liebeskind DS. Imaging evaluation of collaterals in the brain: physiology and clinical translation. *Curr Radiol Rep* 2014; 2:29 CrossRef Medline
- Lima FO, Furie KL, Silva GS, et al. The pattern of leptomeningeal collaterals on CT angiography is a strong predictor of long-term functional outcome in stroke patients with large vessel intracranial occlusion. *Stroke* 2010;41:2316–22 CrossRef Medline
- Bang OY, Saver JL, Buck BH, et al. Impact of collateral flow on tissue fate in acute ischaemic stroke. *J Neurol Neurosurg Psychiatry* 2008; 79:625–29 Medline
- Liebeskind DS. Collaterals in acute stroke: beyond the clot. *Neuroimaging Clin North Am* 2005;15:553–73 CrossRef Medline
- Brozici M, van der Zwan A, Hillen B. Anatomy and functionality of leptomeningeal anastomoses: a review. *Stroke* 2003;34:2750–62 CrossRef Medline
- Seeta Ramaiah S, Churilov L, et al. The impact of arterial collateralization on outcome after intra-arterial therapy for acute ischemic stroke. *AJNR Am J Neuroradiol* 2014;35:667–72 CrossRef Medline
- Zaharchuk G, Do HM, Marks MP, et al. Arterial spin-labeling MRI can identify the presence and intensity of collateral perfusion in patients with moyamoya disease. *Stroke* 2011;42:2485–91 CrossRef Medline
- Donahue MJ, Strother MK, Hendrikse J. Novel MRI approaches for assessing cerebral hemodynamics in ischemic cerebrovascular disease. *Stroke* 2012;43:903–15 CrossRef Medline
- Lehoux S, Lévy BI. Collateral artery growth: making the most of what you have. *Circ Res* 2006;99:567–69 CrossRef Medline
- Bokkers RP, van Osch MJ, Klijn CJ, et al. Cerebrovascular reactivity within perfusion territories in patients with an internal carotid artery occlusion. *J Neurol Neurosurg Psychiatry* 2011;82:1011–16 CrossRef Medline
- Norrving B, Nilsson B, Risberg J. rCBF in patients with carotid occlusion. Resting and hypercapnic flow related to collateral pattern. *Stroke* 1982;13:155–62 CrossRef Medline
- Müller M, Schimrigk K. Vasomotor reactivity and pattern of collateral blood flow in severe occlusive carotid artery disease. *Stroke* 1996;27:296–99 CrossRef Medline
- Vernieri F, Pasqualetti P, Matteis M, et al. Effect of collateral blood flow and cerebral vasomotor reactivity on the outcome of carotid artery occlusion. *Stroke* 2001;32:1552–58 CrossRef Medline
- Menon B, d'Este C, Qazi E, et al. Multiphase CT angiography: a new tool for the imaging triage of patients with acute ischemic stroke. *Radiology* 2015;275:510–20 CrossRef Medline
- Lu H, Clingman C, Golay X, et al. Determining the longitudinal relaxation time (T1) of blood at 3.0 Tesla. *Magn Reson Med* 2004;52:679–82 CrossRef Medline
- Chng SM, Petersen ET, Zimine I, et al. Territorial arterial spin labeling in the assessment of collateral circulation: comparison with digital subtraction angiography. *Stroke* 2008;39:3248–54 CrossRef Medline
- Barber PA, Demchuk AM, Zhang J, et al. Validity and reliability of a quantitative computed tomography score in predicting outcome of hyperacute stroke before thrombolytic therapy: ASPECTS Study Group—Alberta Stroke Programme Early CT Score. *Lancet* 2000; 355:1670–74 CrossRef Medline
- Donahue MJ, Dethrage LM, Faraco CC, et al. Routine clinical evaluation of cerebrovascular reserve capacity using carbogen in patients with intracranial stenosis. *Stroke* 2014;45:2335–41 CrossRef Medline
- Samuels OB, Joseph GJ, Lynn MJ, et al. A standardized method for measuring intracranial arterial stenosis. *AJNR Am J Neuroradiol* 2000;21:643–46 Medline
- Faraco CC, Strother MK, Dethrage LM, et al. Dual vessel-encoded ASL for simultaneous BOLD and CBF reactivity assessment in patients with ischemic cerebrovascular disease. *Magn Reson Med* 2015; 73:1579–92 CrossRef Medline
- Donahue MJ, Faraco CC, Strother MK, et al. Bolus arrival time and cerebral blood flow responses to hypercarbia. *J Cereb Blood Flow Metab* 2014;34:1243–52 CrossRef Medline
- Kim JJ, Fischbein NJ, Lu Y, et al. Regional angiographic grading system for collateral flow: correlation with cerebral infarction in patients with middle cerebral artery occlusion. *Stroke* 2004;35:1340–44 CrossRef Medline
- Suzuki J, Takaku A. Cerebrovascular “moyamoya” disease: disease showing abnormal net-like vessels in base of brain. *Arch Neurol* 1969;20:288–99 CrossRef Medline
- Mugikura S, Takahashi S, Higano S, et al. Predominant involvement of ipsilateral anterior and posterior circulations in moyamoya disease. *Stroke* 2002;33:1497–500 CrossRef Medline
- Wu B, Wang X, Guo J, et al. Collateral circulation imaging: MR perfusion territory arterial spin-labeling at 3T. *AJNR Am J Neuroradiol* 2008;29:1855–60 CrossRef Medline
- Chen H, Wu B, Zhu G, et al. Permeability imaging as a biomarker of leptomeningeal collateral flow in patients with intracranial arterial stenosis. *Cell Biochem Biophys* 2014 Dec 12. [Epub ahead of print] CrossRef Medline
- Strother MK, Anderson MD, Singer RJ, et al. Cerebrovascular collaterals correlate with disease severity in adult North American patients with Moyamoya disease. *AJNR Am J Neuroradiol* 2014;35:1318–24 CrossRef Medline
- Ringelstein EB, Weiller C, Weckesser M, et al. Cerebral vasomotor reactivity is significantly reduced in low-flow as compared to thromboembolic infarctions: the key role of circle of Willis. *J Neurol Sci* 1994;121:103–09 CrossRef Medline
- Tatemichi TK, Chamorro A, Petty GW, et al. Hemodynamic role of ophthalmic artery collateral in internal carotid artery occlusion. *Neurology* 1990;40:461–64 CrossRef Medline
- Rutgers DR, Klijn CJ, Kappelle LJ, et al. A longitudinal study of collateral flow patterns in the circle of Willis and the ophthalmic artery in patients with a symptomatic carotid occlusion. *Stroke* 2000;31:1913–20 CrossRef Medline

Abnormal Amygdala Resting-State Functional Connectivity in Irritable Bowel Syndrome

R. Qi, C. Liu, J. Ke, Q. Xu, Y. Ye, L. Jia, F. Wang, L.J. Zhang, and G.M. Lu



ABSTRACT

BACKGROUND AND PURPOSE: Functional neuroimaging studies in irritable bowel syndrome have revealed abnormalities in the corticolimbic regions, specifically, hyperactivity of the amygdala during visceral and somatic stimulation. This study investigated changes in the neural circuitry of the amygdala in patients with irritable bowel syndrome based on resting-state functional connectivity.

MATERIALS AND METHODS: Functional MR imaging data were acquired from 31 patients with irritable bowel syndrome and 32 healthy controls (matched for age, sex, and educational level) during rest, and the resting-state functional connectivity of bilateral amygdalae was compared. Multiple regression was performed to investigate the relationship between clinical indices of patients with irritable bowel syndrome and resting-state functional connectivity.

RESULTS: Compared with healthy controls, patients with irritable bowel syndrome had higher positive resting-state functional connectivity between the amygdala and insula, midbrain, parahippocampal gyrus, pre- and postcentral gyri, and supplementary motor area. The inclusion of anxiety and depression as covariates did not alter amygdala resting-state functional connectivity differences between the study groups. Multiple covariate regression results showed that the pain intensity in patients with irritable bowel syndrome positively correlated with resting-state functional connectivity between the amygdala and supplementary motor area, pre- and postcentral gyri, and insula, while the Irritable Bowel Syndrome–Symptom Severity Score positively correlated with resting-state functional connectivity between the amygdala and insula and midbrain.

CONCLUSIONS: Patients with irritable bowel syndrome showed disturbed amygdala resting-state functional connectivity with the corticolimbic regions, which could partly account for the enhanced emotional arousal and visceral information processing associated with irritable bowel syndrome.

ABBREVIATIONS: IBS = irritable bowel syndrome; PHG = parahippocampal gyrus; RSFC = resting-state functional connectivity; SMA = supplementary motor area

Irritable bowel syndrome (IBS) is a common chronic gastrointestinal condition characterized by abdominal pain, bloating, and disturbed defecation.^{1,2} It is thought to result from a dysregulation of the brain-gut interaction.³ With its high prevalence (ob-

served in up to 20% of the population)⁴ and the recurrent nature of the symptoms, IBS negatively affects the quality of life of individuals with this condition and is a health care burden for society⁵; however, the neural basis for IBS has not been examined in detail, to our knowledge.

Functional neuroimaging is the only means of identifying the human brain circuitry that is correlated with various phenotypic and behavioral manifestations of functional gastrointestinal disorders, including IBS⁶; convergent neuroimaging studies have implicated an abnormal emotional arousal network that encompasses emotional, cognitive, and psychological aspects.⁷ Hyperactivity of the amygdala within this network is a striking feature of IBS, which has been documented in many studies by using visceral or somatic stimuli.^{6,8} The amygdala networks are important in emotional regulation, modulation of sensory information, and processing of visceral information in relation to emotional stimuli.⁹ On the basis of the importance of the amygdala in emotional

Received August 18, 2015; accepted after revision November 16.

From the Departments of Medical Imaging (R.Q., J.K., Q.X., L.J.Z., G.M.L.), Gastroenterology (C.L., Y.Y., F.W.), and Emergency Medicine (L.J.), Jinling Hospital, Medical School of Nanjing University, Nanjing, Jiangsu, China.

R.Q., C.L., L.J.Z., and G.M.L. contributed equally to this work.

This work was supported by the grants from the Natural Scientific Foundation of China (Nos. 81322020, 81230032, and 81171313 for L.J.Z. and 81301209 for R.Q.), the Program for New Century Excellent Talents in the University (NCET-12-0260 for L.J.Z.), and the Chinese Key Program (Nos. BWS11063 and 10z026 for G.M.L.).

Please address correspondence to Long Jiang Zhang, MD, or Guang Ming Lu, MD, Department of Medical Imaging, Jinling Hospital, Medical School of Nanjing University, 305 Zhongshan East Rd, Xuanwu District, Nanjing, Jiangsu Province 210002, China; e-mail: kevinzhjl@163.com; cjr.luguangming@vip.163.com

Indicates open access to non-subscribers at www.ajnr.org

<http://dx.doi.org/10.3174/ajnr.A4655>

systems and its implication in IBS, this study focused on examining amygdala functional connectivity in patients with IBS.

Brain activity is present even in the absence of an externally activated task, which might cause fluctuations in blood oxygen level-dependent signal. Thus, in task-based activation studies, the background brain activity can distort the blood oxygen level-dependent signal, making it difficult to elucidate the brain mechanisms involved within the studies. Resting-state functional MR imaging is a fairly new approach, which could resolve this issue¹⁰ by measuring spontaneous blood oxygen level-dependent fluctuations in the brain during rest,¹¹ which has been used in the study of IBS.^{6,12} Resting-state functional connectivity (RSFC)—the quantification method most frequently used in resting-state functional MR imaging studies^{10,13}—measures interregional temporal correlation between a predefined seed region and functionally related regions¹⁴ and has been used as a reliable and sensitive index in studies of healthy subjects and patients with various brain disorders such as Alzheimer disease, depression, and attention deficit/hyperactivity disorder.^{11,15} However, there have been no prior studies using RSFC to investigate the amygdala functional connectivity in patients with IBS.

The present study examined abnormalities of the amygdala functional connectivity in IBS. We hypothesized that amygdala RSFC with corticolimbic regions associated with emotion arousal and visceral information processing would be higher in patients with IBS relative to healthy control subjects, underlying clinically well-observed IBS features such as amplified experience of pain and a negative emotional state. Moreover, given that anxiety and depression have been linked to visceral sensation processing,¹⁶ we conjectured that anxiety and depression scores would affect amygdala RSFC differences between patients with IBS and healthy controls when included as covariates in the analysis.

MATERIALS AND METHODS

Subjects

All participants provided informed consent to procedures approved by the local Medical Research Ethics Committee. Patients with IBS were recruited from the Digestive Disease Clinic of our hospital and by community advertisements. Thirty-two right-handed patients who were identified as having IBS were recruited for this study between December 2013 and December 2014. A diagnosis of IBS was made by a gastroenterologist with expertise in functional gastrointestinal disorders based on the Rome III criteria,¹⁷ which include recurrent abdominal pain or discomfort associated with ≥ 2 of the following: relief/improvement by defecation, onset related to a change in stool frequency, and onset related to a change in stool appearance.

Inclusion criteria for patient recruitment were as follows: older than 18 years of age and a diagnosis positive for IBS based on the Rome III criteria. Exclusion criteria were as follows: a history of gastrointestinal surgery; current or past psychiatric illnesses or substance abuse; treatment with any centrally acting medications such as selective serotonin reuptake inhibitors, aspirin, or nonsteroidal anti-inflammatory drugs for >2 weeks before enrollment; major medical or neurologic conditions; and head motion of >1.0 mm in translation or 1.0° in rotation during MR imaging.

One patient with IBS was excluded for excessive head motion. The remaining 31 patients with IBS (25 men, 6 women; mean age, 29.23 ± 9.69 years) were included in the final analysis.

Thirty-two age-, sex-, and educational level-matched right-handed healthy control subjects (25 men, 7 women; mean age, 27.47 ± 8.64 years) were recruited by advertisement and were screened through a medical examination for the absence of chronic pain, bowel disturbance, and visceral disease. Other exclusion criteria were the same as those applied to the IBS patient group.

Questionnaires

Before MR imaging, each subject completed a set of neuropsychological tests, which included the Mini-Mental State Examination, Montreal Cognitive Assessment, and Zung Self-Rating Anxiety and Depression Scales. When making the research plan before the experiment, we included the Mini-Mental State Examination to avoid inclusion of those subjects with possible dementia,¹⁸ especially for the older subjects who might be recruited, so this test was performed in all subjects, including those with relatively young age. The Montreal Cognitive Assessment¹⁹ was used to screen subjects for mild cognitive impairment and to evaluate their general cognition, and the Zung Self-Rating Anxiety Scale²⁰ and the Zung Self-Rating Depression Scale²¹ were used to rate anxiety-/depression-related symptoms. In addition, patients with IBS were also tested for the IBS-Symptom Severity Score,²² and the IBS-Quality of Life score,²³ and with the visual analog scale (0–100 points), which included the descriptors “no pain sensation” at zero and “the most intense pain sensation imaginable” at 100.²⁴

MR Imaging Data Acquisition

Subjects were scanned by using a 3T MR imaging scanner (Tim Trio; Siemens, Erlangen, Germany). A foam pad was used to minimize head motion. First, high-resolution T1 structural images were acquired in the sagittal orientation with a magnetization-prepared rapid acquisition of gradient echo sequence (TR/TE, 2300/2.98 ms; flip angle, 9° ; FOV, 256×256 mm²; acquisition matrix, 256×256 ; 191 sections with section thickness of 1 mm). Resting-state fMRI data were then obtained by using a single-shot, gradient-recalled echo-planar imaging sequence (250 volumes; TR/TE, 2000/30 ms; FOV, 240×240 mm; flip angle, 90° ; matrix, 64×64 ; voxel size, $3.75 \times 3.75 \times 4$ mm; 30 axial sections aligned along the anterior/posterior commissure).

Data Preprocessing

Data preprocessing was performed by using SPM8 software (<http://www.fil.ion.ucl.ac.uk/spm/software/spm8>). For each participant, the first 10 volumes were discarded to account for steady-state longitudinal magnetization and the remaining 240 images were corrected for temporal differences and head motion. Data from 1 patient with IBS were discarded because of excessive head motion. Therefore, 31 patients and 32 controls were included in the analysis. Group differences in translation and rotation of head motion were also evaluated according to the following formula²⁵:

HeadMotion/Rotation =

$$\frac{1}{L-1} \sum_{i=2}^L \sqrt{|x_i - x_{i-1}|^2 + |y_i - y_{i-1}|^2 + |z_i - z_{i-1}|^2},$$

where L is the length of the time-series ($L = 240$ in this study), and x_i , y_i , and z_i are translations/rotations at the i th time point in the x , y , and z directions, respectively. No differences in image quality were found between patients with IBS and healthy controls (2-sample t test, $t = 1.35$, $P = .18$ for translational motion and $t = 1.47$, $P = .15$ for rotational motion). In this study, T1-weighted images were used as the bridge for the fMRI scans normalized from individual space to the Montreal Neurological Institute space because these T1 structural images had higher resolution than the EPI fMRI scans, which meant that the transformation deviation of individual T1 image to Montreal Neurological Institute space would be smaller than that of the EPI. First, the T1 structural image of each subject was coregistered to the corresponding functional image. Second, the coregistered structural T1 image was segmented by using the unified segmentation algorithm,^{26,27} which can significantly improve the accuracy of spatial normalization, and it was then transformed into the Montreal Neurological Institute stereotaxic space of $3 \times 3 \times 3 \text{ mm}^3$ by applying the parameters of the structural image normalization and then smoothed by convolution with an isotropic Gaussian kernel (8-mm full width at half maximum). After smoothing, imaging data were temporally filtered (bandpass, 0.01–0.08 Hz) to remove the effects of low-frequency drift and high-frequency noise. Before functional connectivity analysis, several sources of spurious variance—including 6 head-motion parameters obtained by rigid-body head-motion correction and average signals from CSF and white matter—were removed by applying linear regression.²⁸ The global signal was not regressed according to a previous study.²⁹

Functional Connectivity Analysis

The FMRIB Integrated Registration and Segmentation Tool (FIRST; <http://fsl.fmrib.ox.ac.uk/fsl/fslwiki/FIRST>) was used on T1 images to delineate the amygdalae in each subject; the individual amygdala mask was then normalized to the Montreal Neurological Institute space. For the fMRI data of every subject, the average time-series across all voxels of each amygdala was separately computed as a reference time course and correlated with the time-series of the rest of the brain. Correlation coefficients were then converted to z values with the Fisher r -to- z transformation to standardize the statistical analysis. Thus, whole-brain RSFC maps of the bilateral amygdala were generated for each subject.

Statistical Analysis

SPSS, Version 16.0 (IBM, Armonk, New York) was used to analyze demographic and clinical data. SPM8 was used to analyze RSFC maps for each subject. A random 2-sample t test was then performed to assess differences in amygdala RSFC maps between patients with IBS and healthy controls, while eliminating the effects of age, sex, and educational level by regression. Significant clusters were identified by using the joint expected probability

Table 1: Demographic and clinical data for patients with IBS and healthy controls^a

Protocols	HC ($n = 32$)	Patients ($n = 31$)	P Value
Sex (M/F)	25:7	25:6	.81 ^b
Mean age (yr)	27.47 ± 8.64	29.23 ± 9.69	.45 ^c
Education (yr)	14.18 ± 2.33	13.87 ± 3.24	.66 ^c
SAS	34.44 ± 5.64	39.74 ± 9.64	.01 ^c
SDS	36.09 ± 8.32	41.12 ± 10.26	.04 ^c
MMSE	27–30; median, 30	28–30; median, 30	.02 ^c
MoCA	28.09 ± 2.16	27.69 ± 1.39	.39 ^c
IBS-QOL		66.05 ± 12.04	
IBS-SSS		242.48 ± 28.74	
VAS (pain) intensity		30.47 ± 14.86	
Duration (months)		32.67 ± 23.56	

Note:—HC indicates healthy controls; SAS, Self-Rating Anxiety Scale; SDS, Self-Rating Depression Scale; MMSE, Mini-Mental State Examination; MoCA, Montreal Cognitive Assessment; IBS-QOL, IBS-Quality of Life; IBS-SSS, IBS-Symptom Severity Score; VAS, visual analog scale.

^a Values are expressed as means.

^b P value for sex distribution was obtained by the χ^2 test.

^c P values for age, education, and neuropsychological test scores were obtained by the 2-sample t test.

distribution,²⁹ with height ($P < .005$) and extent ($P < .05$) thresholds corrected at the whole-brain level.

Statistical analysis was also performed by including anxiety and depression scores (along with age, sex, and educational level) as covariates³⁰ to evaluate the effect of anxiety and depression on amygdala RSFC during comparisons. Because the Zung Self-Rating Anxiety Scale and the Self-Rating Depression Scale scores showed high correlations within each group (patient group: Spearman $\rho = 0.76$, $P < .001$; control group: Spearman $\rho = 0.78$, $P < .001$), the scores were taken together (covariates 1 and 2) rather than considered separately as covariates to evaluate the psychosocial effects on the RSFC as described in a previous study of IBS.³¹

A multiple linear regression analysis was used to investigate the relationship between amygdala RSFC in patients with IBS and the IBS-Symptom Severity Score, IBS-Quality of Life score, and pain intensity in SPM8. The statistical threshold was the same as that in the above-mentioned 2-sample t test.

RESULTS

Clinical Data

Demographic and clinical information for the subjects is shown in Table 1. There were no differences in terms of age, sex, or educational level between patients with IBS and healthy controls ($P > .05$). Scores for the Mini-Mental State Examination (>26) and the Montreal Cognitive Assessment (≥ 26) for all subjects were in the normal range, while patients with IBS had lower Mini-Mental State Examination and higher Zung Self-Rating Anxiety Scale and Depression Scale scores than controls ($P < .05$) (Table 1). All cases were diarrhea-predominant based on bowel habits, with pain reported as a symptom by each patient.

Amygdala Resting-State Functional Network and Effect of Psychosocial Factors

Patients with IBS had a higher left amygdala positive RSFC with the right insula, midbrain, left pre-/postcentral gyri, right precentral gyrus, left parahippocampal gyrus (PHG), and bilateral supplementary motor areas (SMAs) and higher right amygdala positive RSFC with the right insula, midbrain, left

PHG, bilateral precentral gyri, and right SMA relative to healthy controls (Table 2 and Figs 1 and 2). No amygdala RSFC differences between patients with IBS and controls were removed when anxiety and depression were included as covariates (along with age, sex, and educational level) in the analysis.

Correlation Analysis

Multiple covariate regression results suggested that the pain intensity in patients with IBS positively correlated with RSFC be-

tween the left amygdala and bilateral SMA, pre- and postcentral gyri, and insula; and the RSFC between the right amygdala and the right precentral gyrus and right insula, while the IBS–Symptom Severity Score positively correlated with RSFC between the left amygdala and bilateral insula and the midbrain and with RSFC between the right amygdala and right insula (Fig 3).

DISCUSSION

The present study investigated changes in amygdala RSFC in IBS. The results showed that patients with IBS had higher RSFC between the amygdala and insula, midbrain, PHG, and sensorimotor regions. In addition, including anxiety and depression as covariates in the analysis had no effect on the RSFC differences between patients with IBS and controls.

Higher Amygdala-Insula RSFC in IBS

In this study, patients with IBS had higher RSFC between the left and right amygdala and the insula, a major component of the limbic system³² that is closely connected to the amygdala.⁹ The insula is involved in emotional arousal and visceral sensory, autonomic visceral motor, and pain processing³³ and is consistently activated in healthy subjects exposed to visceral stimuli.⁶ The insula is also an essential node in the homeostatic afferent network that is hyperactivated in IBS.^{8,16,34} Increased insula activities in patients with IBS during rectal distension³⁵ and in response to cutaneous heat stimuli³⁶ have been reported. Evidence also showed that a functional network between the amygdala and insula mediates anxious anticipation of a negative event, and anx-

Table 2: Brain regions showing amygdala RSFC differences between patients with IBS and healthy controls

Brain Regions	BA	MNI Coordinates (mm) (x, y, z)	Voxel No.	T Value ^a
Left amygdala				
Right insula	13	42, 6, -3	77	+3.22
Midbrain		12, -30, -21	70	+3.24
Left pre-/postcentral gyri	4,9	-60, -6, 27	78	+2.89
Right precentral gyrus	9	63, 6, 27	72	+2.94
Left PHG	35	-24, -18, -12	77	+3.31
Left SMA	6	-15, -15, 48	98	+3.18
Right SMA	6	6, -6, 60	83	+3.42
Right amygdala				
Right insula	13	42, 12, -12	75	+3.20
Midbrain		12, -30, -21	74	+3.27
Left PHG	35	-33, -21, -18	76	+3.57
Left precentral gyrus	4	-53, -8, 27	96	+2.89
Right precentral gyrus	4	63, 3, 27	80	+2.94
Right SMA	6	12, -30, 60	71	+3.37

Note:—BA indicates Brodmann area; MNI, Montreal Neurological Institute.

^aPositive value represents higher positive RSFC.

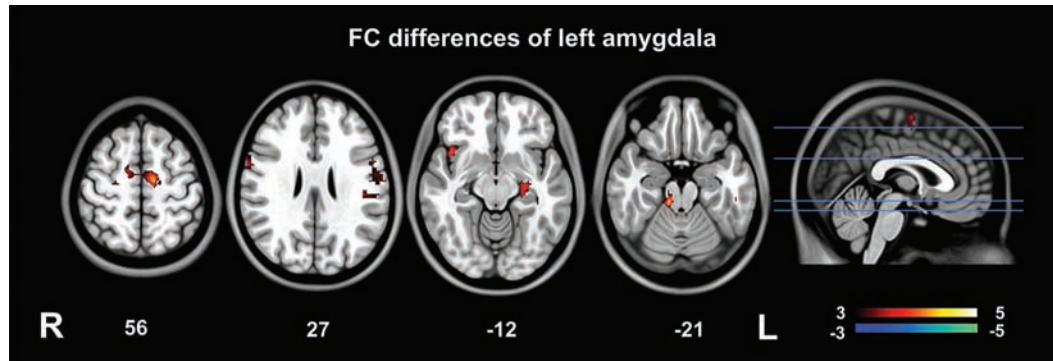


FIG 1. Functional connectivity analysis of the left amygdala. Compared with healthy controls, patients with IBS had higher positive RSFC between the left amygdala and the right insula, midbrain, left pre-/postcentral gyri, right precentral gyrus, left PHG, and bilateral SMA.

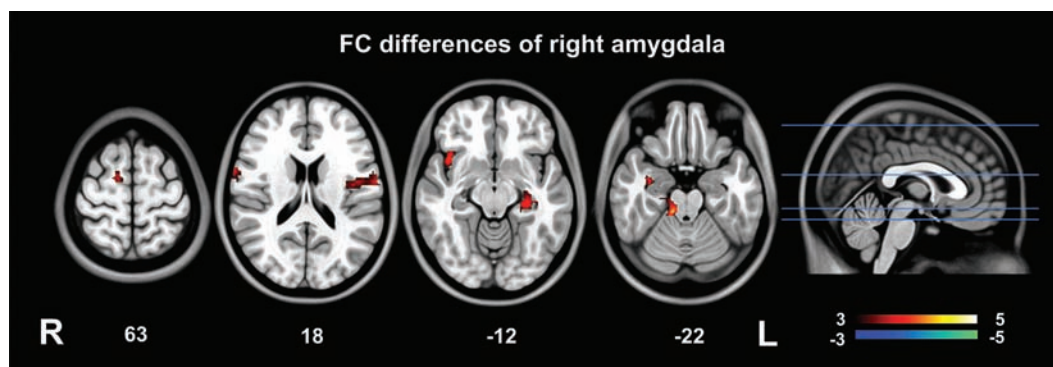


FIG 2. Functional connectivity analysis of the right amygdala. Patients with IBS had higher right amygdala–positive RSFC with the right insula, midbrain, left PHG, bilateral precentral gyri, and right SMA relative to healthy controls.

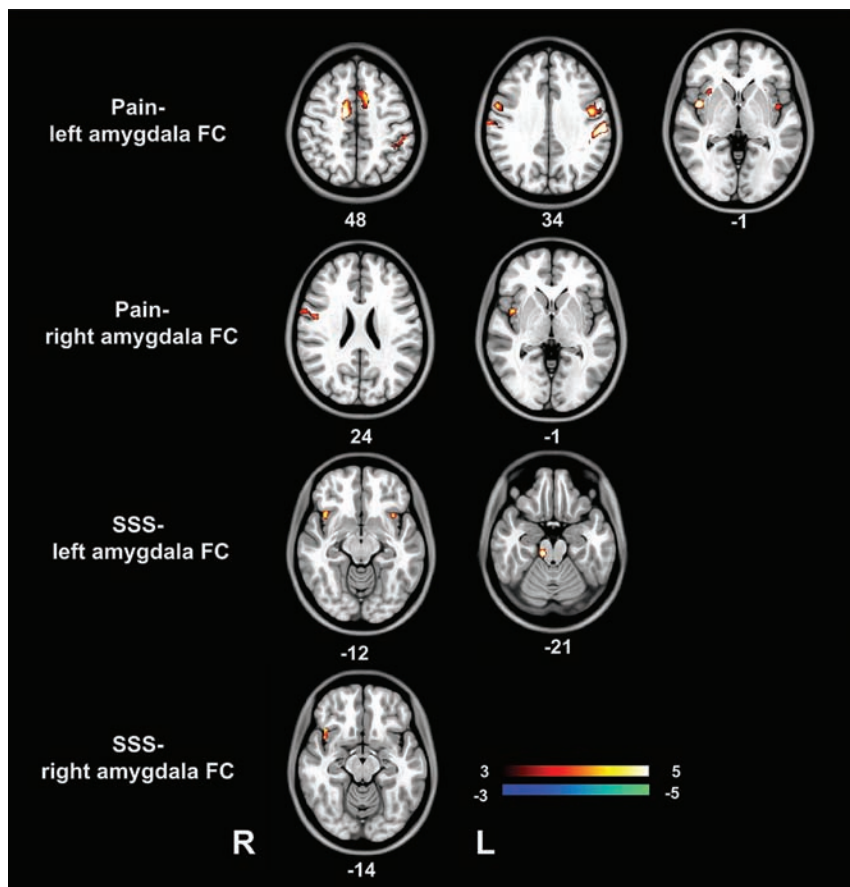


FIG 3. Correlation between amygdala RSFC and clinical indices in patients with IBS. The pain intensity in patients with IBS positively correlated with RSFC between the left amygdala and bilateral SMA, pre- and postcentral gyri, and insula, and the RSFC between the right amygdala and right precentral gyrus and right insula. The IBS–Symptom Severity Score positively correlated with RSFC between the left amygdala and bilateral insula and midbrain, and RSFC between the right amygdala and right insula. IBS–SSS indicates IBS–Symptom Severity Score; FC, functional connectivity.

ious individuals display exaggerated activity within this network during anticipation of aversive stimuli.³⁷ An increase in functional connectivity has been interpreted as increased wiring inside the network or increased neuronal synchrony and/or activity.^{38,39} Thus, the observed higher amygdala–insula functional coupling here may be a mechanism supporting the enhanced emotional arousal and visceral information processing associated with IBS. In addition, the association between insula RSFC and pain intensity in IBS implies a role for the insula in pain processing in these patients. Previous studies have also indicated that the insula is involved in the processing of the affective dimension of pain⁴⁰ and coding of pain intensity.⁴¹

Higher Amygdala–Midbrain RSFC in IBS

A higher RSFC between the amygdala and midbrain was detected in IBS relative to control subjects, which has not been previously reported. Previous studies have reported brain stem activation in healthy controls in response to visceral and somatic stimulation⁴² and higher midbrain activation in patients with IBS than in healthy controls during rectal stimulation.⁸ Animal studies have also identified strong connections between the amygdala and brain stem that are responsible for processing visceral information related to emotional stimuli.⁹ We speculate that the higher functional coupling be-

tween the amygdala and midbrain observed in this study may be related to an amplified nociceptive response to visceral information in IBS.⁶

Higher Amygdala–PHG RSFC in IBS

The RSFC between the amygdala and PHG was also higher in patients with IBS compared with control subjects. A previous fMRI study of patients with IBS showed that increased hippocampal activity was associated with the anticipation of rectal distension,⁴³ and a follow-up study reported a significant correlation between a decreased blood oxygen level–dependent response in the hippocampus during rectal distension and the improvement of gastrointestinal symptoms after the IBS was treated.⁴⁴ The amygdala has extensive connections with the hippocampus and PHG,⁴⁵ which modulate emotional memories.⁴⁶ In addition, a prior fMRI study in healthy adults showed that amygdala–hippocampal connectivity increases during encoding and retrieval of emotional memories.⁴⁷ Thus, in this study, the higher amygdala–PHG RSFC in patients with IBS may arise from long-time encoding of negative emotional memories such as visceral pain. This speculation requires further investigation examining how the amygdala–PHG RSFC changes because of treatment for IBS.

Higher Amygdala–Sensorimotor Region RSFC in IBS

We also noted a higher RSFC between the amygdala and the sensorimotor regions (SMA, pre- and postcentral gyri). The SMA plays an important role in motor inhibition and response⁴⁸ and the functional processing of painful stimuli.⁴⁹ Pre- and postcentral gyri are important components of motor and sensory areas. These sensorimotor regions, which are core regions within the so-called pain network,⁴⁰ are commonly observed with enhanced activations in IBS and other functional gastrointestinal disorders.⁵⁰ Using resting-state functional MR imaging, Cifre et al³⁹ reported increased connectivity between the primary motor cortex and SMA in patients with fibromyalgia, another chronic pain condition, and interpreted that as the result of the widespread central sensitization in patients. Thus, we speculated that the higher RSFC in this study may be related to the central pain amplification in patients with IBS.⁸

Psychosocial Effects on the Amygdala RSFC in IBS

In this study, anxiety and depression had no effect on amygdala RSFC differences between patients with IBS and healthy controls, contrary to our hypothesis that RSFC abnormalities in IBS could be partly explained by anxiety and depression symptoms. The

negative finding may be due to the small number of patients with IBS with severe anxiety or depression symptoms that was included in this study and requires confirmation in a larger sample of patients with IBS.

Limitations

This study had some limitations. First, the study population was relatively small and consisted of Chinese patients with diarrhea-predominant IBS; thus, the results may not be generalizable to patients of other ethnicities or with other subtypes of IBS. Second, the exact neurophysiologic meaning of functional connectivity still remains unclear, and much work is needed before it can be used routinely in the clinical setting. Longitudinal studies are also needed to address whether the observed results are altered by IBS treatment. Third, sex differences in IBS⁵¹ were not considered due to the small number of female patients. Sex differences in brain responses to emotion-related stimuli⁵² and in the resting state⁵³ have been observed in patients with IBS; thus, the potential role of sex in amygdala RSFC should be addressed in future studies. Fourth, although we used the whole amygdala as a seed region, previous research has shown that amygdala subregions have distinct functional networks,⁵⁴ and future investigations should consider variations in RSFC pattern across these subregions.

CONCLUSIONS

Patients with IBS had abnormalities in amygdala RSFC in several corticolimbic regions, which could, in part, underlie the enhanced emotional arousal and visceral information processing associated with IBS.

Disclosures: Long Jiang Zhang—RELATED: Grant: Natural Scientific Foundation of China; the Program for New Century Excellent Talents in the University.* Comments: grant Nos. 81322020, 81230032, and 81171313; the Program for New Century Excellent Talents in the University (NCET-12-0260). *Money paid to the institution.

REFERENCES

- Chey WD, Kurlander J, Eswaran S. Irritable bowel syndrome: a clinical review. *JAMA* 2015;313:949–58 CrossRef Medline
- Mayer EA. Clinical practice: irritable bowel syndrome. *N Engl J Med* 2008;358:1692–99 CrossRef Medline
- Mayer EA, Tillisch K. The brain-gut axis in abdominal pain syndromes. *Annu Rev Med* 2011;62:381–96 CrossRef Medline
- Longstreth GF, Wolde-Tsadik G. Irritable bowel-type symptoms in HMO examinees: prevalence, demographics, and clinical correlates. *Dig Dis Sci* 1993;38:1581–89 CrossRef Medline
- Canavan C, West J, Card T. Review article: the economic impact of the irritable bowel syndrome. *Aliment Pharmacol Ther* 2014;40:1023–34 CrossRef Medline
- Mayer EA, Aziz Q, Coen S, et al. Brain imaging approaches to the study of functional GI disorders: a Rome working team report. *Neurogastroenterol Motil* 2009;21:579–96 CrossRef Medline
- Al Omran Y, Aziz Q. Functional brain imaging in gastroenterology: to new beginnings. *Nat Rev Gastroenterol Hepatol* 2014;11:565–76 CrossRef Medline
- Tillisch K, Mayer EA, Labus JS. Quantitative meta-analysis identifies brain regions activated during rectal distension in irritable bowel syndrome. *Gastroenterology* 2011;140:91–100 CrossRef Medline
- Price JL. Comparative aspects of amygdala connectivity. *Ann N Y Acad Sci* 2003;985:50–58 Medline
- Fox MD, Raichle ME. Spontaneous fluctuations in brain activity

observed with functional magnetic resonance imaging. *Nat Rev Neurosci* 2007;8:700–11 CrossRef Medline

- Lee MH, Smyser CD, Shimony JS. Resting-state fMRI: a review of methods and clinical applications. *AJNR Am J Neuroradiol* 2013;34:1866–72 CrossRef Medline
- Rapps N, van Oudenhove L, Enck P, et al. Brain imaging of visceral functions in healthy volunteers and IBS patients. *J Psychosom Res* 2008;64:599–604 CrossRef Medline
- Fox MD, Greicius M. Clinical applications of resting-state functional connectivity. *Front Syst Neurosci* 2010;4:19 CrossRef Medline
- van de Ven VG, Formisano E, Prvulovic D, et al. Functional connectivity as revealed by spatial independent component analysis of fMRI measurements during rest. *Hum Brain Mapp* 2004;22:165–78 CrossRef Medline
- Li F, He N, Li Y, et al. Intrinsic brain abnormalities in attention deficit hyperactivity disorder: a resting-state functional MR imaging study. *Radiology* 2014;272:514–23 CrossRef Medline
- Van Oudenhove L. Visceral sensory and cognitive-affective neuroscience: towards integration? *Gut* 2010;59:431–32 CrossRef Medline
- Drossman DA. The functional gastrointestinal disorders and the Rome III process. *Gastroenterology* 2006;130:1377–90 CrossRef Medline
- Folstein MF, Robins LN, Helzer JE. The Mini-Mental State Examination. *Arch Gen Psychiatry* 1983;40:812 CrossRef Medline
- Nasreddine ZS, Phillips NA, Bédirian V, et al. The Montreal Cognitive Assessment, MoCA: a brief screening tool for mild cognitive impairment. *J Am Geriatr Soc* 2005;53:695–99 CrossRef Medline
- Zung WW. A rating instrument for anxiety disorders. *Psychosomatics* 1971;12:371–79 CrossRef Medline
- Zung WW, Richards CB, Short MJ. Self-rating depression scale in an outpatient clinic: further validation of the SDS. *Arch Gen Psychiatry* 1965;13:508–15 CrossRef Medline
- Francis CY, Morris J, Whorwell PJ. The irritable bowel severity scoring system: a simple method of monitoring irritable bowel syndrome and its progress. *Aliment Pharmacol Ther* 1997;11:395–402 CrossRef Medline
- Patrick DL, Drossman DA, Frederick IO, et al. Quality of life in persons with irritable bowel syndrome: development and validation of a new measure. *Dig Dis Sci* 1998;43:400–11 CrossRef Medline
- Price DD, Bush FM, Long S, et al. A comparison of pain measurement characteristics of mechanical visual analogue and simple numerical rating scales. *Pain* 1994;56:217–26 CrossRef Medline
- Liao W, Chen H, Feng Y, et al. Selective aberrant functional connectivity of resting state networks in social anxiety disorder. *Neuroimage* 2010;52:1549–58 CrossRef Medline
- Ashburner J, Friston KJ. Unified segmentation. *Neuroimage* 2005;26:839–51 CrossRef Medline
- Liu CH, Li F, Li SF, et al. Abnormal baseline brain activity in bipolar depression: a resting state functional magnetic resonance imaging study. *Psychiatry Res* 2012;203:175–79 CrossRef Medline
- Fox MD, Snyder AZ, Vincent JL, et al. The human brain is intrinsically organized into dynamic, anticorrelated functional networks. *Proc Natl Acad Sci U S A* 2005;102:9673–78 CrossRef Medline
- Saad ZS, Gotts SJ, Murphy K, et al. Trouble at rest: how correlation patterns and group differences become distorted after global signal regression. *Brain Connect* 2012;2:25–32 CrossRef Medline
- Poline JB, Worsley KJ, Evans AC, et al. Combining spatial extent and peak intensity to test for activations in functional imaging. *Neuroimage* 1997;5:83–96 CrossRef Medline
- Zhou G, Qin W, Zeng F, et al. White-matter microstructural changes in functional dyspepsia: a diffusion tensor imaging study. *Am J Gastroenterol* 2013;108:260–69 CrossRef Medline
- Augustine JR. Circuitry and functional aspects of the insular lobe in primates including humans. *Brain Res Brain Res Rev* 1996;22:229–44 CrossRef Medline
- Nagai M, Kishi K, Kato S. Insular cortex and neuropsychiatric

- disorders: a review of recent literature. *Eur Psychiatry* 2007;22:387–94 CrossRef Medline
34. Chang L. **Brain responses to visceral and somatic stimuli in irritable bowel syndrome: a central nervous system disorder?** *Gastroenterol Clin North Am* 2005;34:271–79 CrossRef Medline
 35. Yuan YZ, Tao RJ, Xu B, et al. **Functional brain imaging in irritable bowel syndrome with rectal balloon-distention by using fMRI.** *World J Gastroenterol* 2003;9:1356–60 CrossRef Medline
 36. Verne GN, Himes NC, Robinson ME, et al. **Central representation of visceral and cutaneous hypersensitivity in the irritable bowel syndrome.** *Pain* 2003;103:99–110 CrossRef Medline
 37. Carlson JM, Greenberg T, Rubin D, et al. **Feeling anxious: anticipatory amygdalo-insular response predicts the feeling of anxious anticipation.** *Soc Cogn Affect Neurosci* 2011;6:74–81 CrossRef Medline
 38. Bettus G, Guedj E, Joyeux F, et al. **Decreased basal fMRI functional connectivity in epileptogenic networks and contralateral compensatory mechanisms.** *Hum Brain Mapp* 2009;30:1580–91 CrossRef Medline
 39. Cifre I, Sitges C, Fraiman D, et al. **Disrupted functional connectivity of the pain network in fibromyalgia.** *Psychosom Med* 2012;74:55–62 CrossRef Medline
 40. Price DD. **Psychological and neural mechanisms of the affective dimension of pain.** *Science* 2000;288:1769–72 CrossRef Medline
 41. Derbyshire SW, Jones AK, Gyulai F, et al. **Pain processing during three levels of noxious stimulation produces differential patterns of central activity.** *Pain* 1997;73:431–45 CrossRef Medline
 42. Dunckley P, Wise RG, Fairhurst M, et al. **A comparison of visceral and somatic pain processing in the human brainstem using functional magnetic resonance imaging.** *J Neurosci* 2005;25:7333–41 CrossRef Medline
 43. Larsson MB, Tillisch K, Craig AD, et al. **Brain responses to visceral stimuli reflect visceral sensitivity thresholds in patients with irritable bowel syndrome.** *Gastroenterology* 2012;142:463–472.e3 CrossRef Medline
 44. Lowén MB, Mayer EA, Sjöberg M, et al. **Effect of hypnotherapy and educational intervention on brain response to visceral stimulus in the irritable bowel syndrome.** *Aliment Pharmacol Ther* 2013;37:1184–97 CrossRef Medline
 45. Hamann SB, Ely TD, Grafton ST, et al. **Amygdala activity related to enhanced memory for pleasant and aversive stimuli.** *Nat Neurosci* 1999;2:289–93 CrossRef Medline
 46. Izquierdo I, Medina JH. **Memory formation: the sequence of biochemical events in the hippocampus and its connection to activity in other brain structures.** *Neurobiol Learn Mem* 1997;68:285–316 CrossRef Medline
 47. Smith AP, Stephan KE, Rugg MD, et al. **Task and content modulate amygdala-hippocampal connectivity in emotional retrieval.** *Neuron* 2006;49:631–38 CrossRef Medline
 48. Nachev P, Kennard C, Husain M. **Functional role of the supplementary and pre-supplementary motor areas.** *Nat Rev Neurosci* 2008;9:856–69 CrossRef Medline
 49. Craggs JG, Price DD, Verne GN, et al. **Functional brain interactions that serve cognitive-affective processing during pain and placebo analgesia.** *Neuroimage* 2007;38:720–29 CrossRef Medline
 50. Jones MP, Dillej JB, Drossman D, et al. **Brain-gut connections in functional GI disorders: anatomic and physiologic relationships.** *Neurogastroenterol Motil* 2006;18:91–103 CrossRef Medline
 51. Chang L, Heitkemper MM. **Gender differences in irritable bowel syndrome.** *Gastroenterology* 2002;123:1686–701 CrossRef Medline
 52. Labus JS, Gupta A, Coveleskie K, et al. **Sex differences in emotion-related cognitive processes in irritable bowel syndrome and healthy control subjects.** *Pain* 2013;154:2088–99 CrossRef Medline
 53. Hong J-Y, Kilpatrick LA, Labus J, et al. **Patients with chronic visceral pain show sex-related alterations in intrinsic oscillations of the resting brain.** *J Neurosci* 2013;33:11994–2002 CrossRef Medline
 54. Amunts K, Kedo O, Kindler M, et al. **Cytoarchitectonic mapping of the human amygdala, hippocampal region and entorhinal cortex: intersubject variability and probability maps.** *Anat Embryol (Berl)* 2005;210:343–52 CrossRef Medline

Optimal MR Plaque Imaging for Cervical Carotid Artery Stenosis in Predicting the Development of Microembolic Signals during Exposure of Carotid Arteries in Endarterectomy: Comparison of 4 T1-Weighted Imaging Techniques

Y. Sato, K. Ogasawara, S. Narumi,  M. Sasaki, A. Saito, E. Tsushima, T. Namba, M. Kobayashi, K. Yoshida, Y. Terayama, and A. Ogawa



ABSTRACT

BACKGROUND AND PURPOSE: Preoperative identification of plaque vulnerability may allow improved risk stratification for patients considered for carotid endarterectomy. The present study aimed to determine which plaque imaging technique, cardiac-gated black-blood fast spin-echo, magnetization-prepared rapid acquisition of gradient echo, source image of 3D time-of-flight MR angiography, or noncardiac-gated spin-echo, most accurately predicts development of microembolic signals during exposure of carotid arteries in carotid endarterectomy.

MATERIALS AND METHODS: Eighty patients with ICA stenosis ($\geq 70\%$) underwent the 4 sequences of preoperative MR plaque imaging of the affected carotid bifurcation and then carotid endarterectomy under transcranial Doppler monitoring of microembolic signals in the ipsilateral middle cerebral artery. The contrast ratio of the carotid plaque was calculated by dividing plaque signal intensity by sternocleidomastoid muscle signal intensity.

RESULTS: Microembolic signals during exposure of carotid arteries were detected in 23 patients (29%), 3 of whom developed new neurologic deficits postoperatively. Those deficits remained at 24 hours after surgery in only 1 patient. The area under the receiver operating characteristic curve to discriminate between the presence and absence of microembolic signals during exposure of the carotid arteries was significantly greater with nongated spin-echo than with black-blood fast spin-echo (difference between areas, 0.258; $P < .0001$), MP-RAGE (difference between areas, 0.106; $P = .0023$), or source image of 3D time-of-flight MR angiography (difference between areas, 0.128; $P = .0010$). Negative binomial regression showed that in the 23 patients with microembolic signals, the contrast ratio was associated with the number of microembolic signals only in nongated spin-echo (risk ratio, 1.36; 95% confidence interval, 1.01–1.97; $P < .001$).

CONCLUSIONS: Nongated spin-echo may predict the development of microembolic signals during exposure of the carotid arteries in carotid endarterectomy more accurately than other MR plaque imaging techniques.

ABBREVIATIONS: AUC = area under the receiver operating characteristic curve; BB-FSE = black-blood fast spin-echo; CEA = carotid endarterectomy; CR = contrast ratio; MES = microembolic signals; ROC = receiver operating characteristic; SE = spin-echo; SI-MRA = source image of 3D time-of-flight MR angiography; TCD = transcranial Doppler

For appropriately selected patients, carotid endarterectomy (CEA) can effectively prevent stroke,^{1–3} with few neurologic deficits observed immediately following the procedure. Surgical

site embolism represents $>70\%$ of intraoperative procedure-related strokes.⁴ When one monitors the middle cerebral artery by using intraoperative transcranial Doppler (TCD), microembolic signals (MES) are detected in $>90\%$ of patients undergoing CEA^{4–6}; however, the quality and quantity of MES detected depends on the stage of CEA.^{5–7} During exposure procedures for the carotid arteries, plaque that represents a source of emboli and has not been removed remains exposed to blood flow. Under such conditions, manipulation of the carotid arteries can dislodge emboli from the surgical site into the intracranial arteries.⁸ Furthermore, because the target vessel remains closed during the exposure procedure, detectable MES are thought to represent solid masses, such as thrombi, necrosis, or lipid.⁶ In contrast, once the

Received July 7, 2014; accepted after revision November 27, 2015.

From the Departments of Neurosurgery (Y.S., K.O., T.N., M.K., K.Y., A.O.), Neurology and Gerontology (S.N., A.S., Y.T.), and Division of Ultra-High Field MRI and Department of Radiology (M.S.), Iwate Medical University School of Medicine, Morioka, Japan; and Graduate School of Health Sciences (E.T.), Hirosaki University, Hirosaki, Japan.

This work was partly supported by grants-in-aid for Strategic Medical Science Research (S1491001, 2014–2018) from the Ministry of Education, Culture, Sports, Science and Technology of Japan and a grant-in-aid for Scientific Research (15K10313) from the Japan Society for the Promotion of Science.

Please address correspondence to Kuniaki Ogasawara, MD, Department of Neurosurgery, Iwate Medical University, Uchimarui, 19-1, Morioka 020-8505, Japan; e-mail: kuogasa@iwate-med.ac.jp

 Indicates open access to non-subscribers at www.ajnr.org

<http://dx.doi.org/10.3174/ajnr.A4674>

walls of the carotid arteries are cut for endarterectomy, a high number of harmless gaseous MES may develop during carotid declamping due to air entering the lumen of the arteries.^{6,9} Detection of MES during the exposure procedure has been shown to correlate with postoperative neurologic deficits immediately after CEA.^{5-7,9-11}

Several investigators have compared MES during the exposure procedure for the carotid arteries in CEA with histopathologic findings of excised carotid plaque and have demonstrated that development of the MES was strongly associated with vulnerable carotid plaques consisting primarily of intraplaque hemorrhage and/or intraluminal thrombus.^{12,13} Intraplaque hemorrhage might cause formation of intraluminal thrombus likely due to chemical mediators, increased stenosis, or changes in eddy currents, though the associations among these remain unclear. Other research has shown that more cerebrovascular adverse events related to CEA occurred in patients with atheromatous plaques compared with patients with fibrous plaques.⁹ Preoperative identification of plaque vulnerability may thus allow improved risk stratification for patients considered for CEA.

Intraplaque characteristics are generally assessed by using MR imaging based on T1-weighted sequences,¹⁴ and the detection of intraplaque hemorrhage on preoperative MR imaging is associated with the development of MES during the procedure for exposure of the carotid arteries.¹² However, there has been inconsistency among published findings on vulnerable plaques.¹⁵ This could be due to interinstitutional differences in the methodology for such imaging techniques as cardiac-gated black-blood fast spin-echo (BB-FSE),¹⁶⁻¹⁹ magnetization-prepared rapid acquisition of gradient echo,^{12,20-22} source image of 3D time-of-flight MR angiography (SI-MRA),²³ and noncardiac-gated spin-echo (SE).^{15,24,25} Although the cardiac-gated BB-FSE method is most commonly used for T1-weighted MR plaque imaging,^{17,18} the TR is dependent on a single R-R interval from electrocardiography, which occasionally results in an overly long TR to diminish proton density-weighted contrast and to enhance T1-weighted contrast.²⁵

In addition to cardiac gating, proton density-weighted contrast is preserved when using T1-weighted spoiled gradient-echo techniques, which are generally used for MRA.²³ The use of T1-weighted spoiled gradient-echo techniques on SI-MRA could result in insufficient contrast between fibrous and lipid/necrotic plaques.¹⁵ Originally developed for direct thrombus imaging, MPRAGE is a modified sequence in which the TI is set to permit black-blood effects.²¹ Because the signal intensity of the lipid/necrotic component tends to show T1 values similar to those of blood, the intensity can theoretically be attenuated.¹⁵ The substantial influence of the proton density and inversion recovery pulse can be avoided in nongated SE; however, this sequence requires a relatively long acquisition time and is known to be susceptible to patient motion even when motion correction is used.¹⁵ Among these 4 kinds of imaging techniques, substantial variation is observed in the contrast provided by T1-weighted MR plaque imaging and its ability to characterize intraplaque components. Furthermore, quantitative color-coded MR plaque imaging performed by using the nongated SE sequence has recently been shown to provide accurate evaluation of the composition (ie, fi-

brous tissue, lipid/necrosis, or hemorrhage) of excised carotid plaques compared with histopathologic findings in patients undergoing CEA.²⁶

The purpose of the present study was thus to determine which plaque imaging technique, BB-FSE, MPRAGE, SI-MRA, or nongated SE, all of which are variations of T1-weighted imaging, can most accurately predict development of MES during exposure of the carotid arteries in CEA.

MATERIALS AND METHODS

Study Design

The present study was designed as prospective observational research. This protocol was reviewed and approved by the institutional ethics committee, and written informed consent was obtained from all patients or their next of kin before participation.

Patient Selection

The present study included patients with ipsilateral ICA stenosis $\geq 70\%$ as per the below-mentioned method and useful residual function (modified Rankin Scale score, 0–2) who underwent CEA of the carotid bifurcation in our institution. Patients who did not undergo any of the 4 kinds of MR plaque imaging preoperatively were excluded. Patients without reliable TCD monitoring throughout the entire operation because of failure to obtain an adequate bone window were also excluded from analysis.

Angiography and Data Processing

All patients underwent angiography with arterial catheterization, and the degree of ICA stenosis was determined by using the North American Symptomatic Carotid Endarterectomy Trial criteria³ and was based on the comment of Fox et al²⁷ as follows: Distal ICA was measured beyond the bulb, where the walls are parallel and no longer tapering. To prevent underestimation of the percentage stenosis for the distal ICA with reduced axial diameter due to near-occlusion, if the diameter of the coaxial section of the distal ICA was at least 80% smaller than the diameter on the contralateral side, we substituted the diameter of the contralateral distal ICA for calculating the degree of stenosis of the affected ICA. If the contralateral ICA was occluded or stenotic ($>70\%$) and the diameter of the distal ICA on the affected side was less than the diameter of the distal external carotid artery, the diameter of the distal external carotid artery was substituted for calculating the degree of stenosis of the affected ICA.

The length of the ICA stenotic lesion was measured, and the height of the distal end of the lesion relative to the cervical vertebra was determined in the lateral view on angiography. The inflection point was also defined as the center of stenotic lesion curvature. Lesion tortuosity was defined as the angle formed by the 2 tangential lines drawn on the ICA side and the common carotid artery side starting from the inflection point, by using the anteroposterior or lateral view on angiograms in which the curvature in the stenosis of the carotid artery was most visible.²⁸ A stenotic lesion was classified as having ulceration when it fulfilled the radiographic criteria for an ulcer niche, seen in profile as a crater penetrating a stenotic lesion in any projection on angiography.²⁹

Pre-, Intra-, and Postoperative Management

All patients received antiplatelet therapy until the morning of the day CEA was performed and underwent the operation under general anesthesia by a single senior neurosurgeon using an operative microscope from the skin incision. This neurosurgeon was blinded to the findings on MR plaque imaging. The senior neurosurgeon has experienced approximately 600 CEAs as an operator for 15 years. Dissection of the carotid sheath and exposure of the carotid arteries were routinely performed as follows³⁰: The upper plane of the carotid sheath surrounding the common carotid artery was first cut with scissors; next, the other planes of the carotid sheath were bluntly separated from the common and external carotid arteries and the ICA with Pean forceps. Scissors were used when the carotid sheath adhered to carotid arteries. The surgeon and surgical assistants were blinded to intraoperative TCD findings and consistently proceeded with surgical procedures regardless of these findings. A patient was prospectively defined as having adhesions during carotid exposure when scissors were required throughout the dissection of the carotid sheath and exposure of the carotid arteries.³⁰

During exposure of the carotid arteries, attempts were made to keep the increase in systolic blood pressure at least +10% above the preoperative value.³¹ If needed, a vasodilator (nitroglycerin or nicardipine) or a vasoconstrictor (adrenalin) was administered intravenously. No intraluminal shunt or patch graft was used in these procedures. A bolus of heparin (5000 IU) was administered before ICA clamping.

All patients were neurologically tested immediately before induction of general anesthesia and after recovery from general anesthesia by a neurologist who was blinded to patient clinical information, including intraoperative findings such as the presence or absence of MES; and the presence or absence of new postoperative neurologic deficits was recorded.

Another senior neurosurgeon blinded to the clinical and imaging findings of patients retrospectively reviewed videos recorded through an operative microscope from skin incision to carotid declamping and determined the degree of stress on the carotid arteries occurring with manipulation.

MR Plaque Imaging and Data Processing

MR plaque imaging of the affected carotid bifurcation was performed within 1 week before CEA by using a 1.5T MR imaging scanner (Echelon Vega; Hitachi Medical, Tokyo, Japan) and an 8-channel neurovascular coil under the same imaging protocol described previously.¹⁵ This scanner can image BB-FSE, MPRAGE, SI-MRA, and nongated SE in a single imaging session.¹⁵ The section direction was carefully set as perpendicular to the long axis of the carotid bifurcation on the sagittal 2D phase-contrast MR angiography, the section for BB-FSE was set at the location of most severe stenosis, and the midsections of MPRAGE, SI-MRA, and nongated SE were set at a location identical to that for BB-FSE.

Data processing was performed by one of the authors blinded to the clinical and imaging findings except the side on which CEA was performed. First, signal intensities of the carotid plaque and adjacent sternocleidomastoid muscle for the side on which CEA was performed were measured for the section in which the 4 kinds

of images were obtained. ROIs were manually traced on a liquid crystal display by using the polygon cursor of a free software package (zioTerm2009; Ziosoft, Tokyo, Japan). Each signal-intensity value was obtained, and the contrast ratio (CR) of the carotid plaque was calculated by dividing the plaque signal intensity by the muscle signal intensity.¹⁵

Second, nongated SE plaque image data from the DICOM files for the same section used in the first study were transferred to a plaque analysis software package (PlaqueViewer; Hitachi Medical). For the side on which CEA was performed, the software automatically divided internal areas of the plaques into 3 color-coded components (fibrous tissue, green; lipid/necrosis, yellow; and hemorrhage, red) according to the CRs of the plaques, with cutoff values of 1.17 (fibrous tissue versus lipid/necrosis) and 1.55 (lipid/necrosis versus hemorrhage) as obtained from previous studies.^{24,26} Next, percentage areas of each component were automatically calculated (Hemorrhage + Lipid / Necrosis + Fibrous Tissue = 100%).

TCD Monitoring

TCD was performed by using an EME Pioneer TC2020 system (Nicolet Vascular, Golden, Colorado; software Version 2.50) (probe, 2 MHz; diameter, 1.5 cm; insonation depth, 40–66 mm; scale, –100 and +150 cm/s; sample volume, 2 mm; 64-point fast Fourier transform; fast Fourier transform length, 2 mm; fast Fourier transform overlap, 60%; high-pass filter, 100 Hz; detection threshold, 9 dB; minimum increase time, 10 ms) for insonation of the MCA ipsilateral to the carotid artery undergoing CEA. TCD data were stored on a hard disk by using a coding system and were later analyzed manually by a clinical neurophysiologist who was blinded to patient information. MES were identified during exposure of the carotid arteries (from skin incision until ICA clamping) according to the recommended guidelines.³²

Statistical Analysis

Data are expressed as the mean \pm SD. We used receiver operating characteristic (ROC) curves to assess the accuracy of the CR and percentage area in predicting the development of MES during exposure of the carotid arteries. Pair-wise comparisons of the area under the receiver operating characteristic curve (AUC) for each MR image or the percentage area of each component were performed as proposed by Pepe and Longton.³³ A negative binomial model was fitted to investigate the relationship between the CR in each MR plaque sequence and the number of MES only in patients with MES during exposure of the carotid arteries. The relationship between each variable and the development of MES during exposure of the carotid arteries was evaluated with univariate analysis by using the Mann-Whitney *U* or χ^2 test. Multivariate statistical analysis of factors related to the development of MES during exposure of the carotid arteries was performed by using logistic regression modeling. Variables showing values of $P < .2$ in univariate analyses were entered into the final model. For all statistical analyses, significance was set at the $P < .05$ level, with the exception of the pair-wise comparison followed by the Bonferroni inequality correction for those differences deemed statistically significant at the level of $P < .05/6 = .0083$ (AUC for the MR

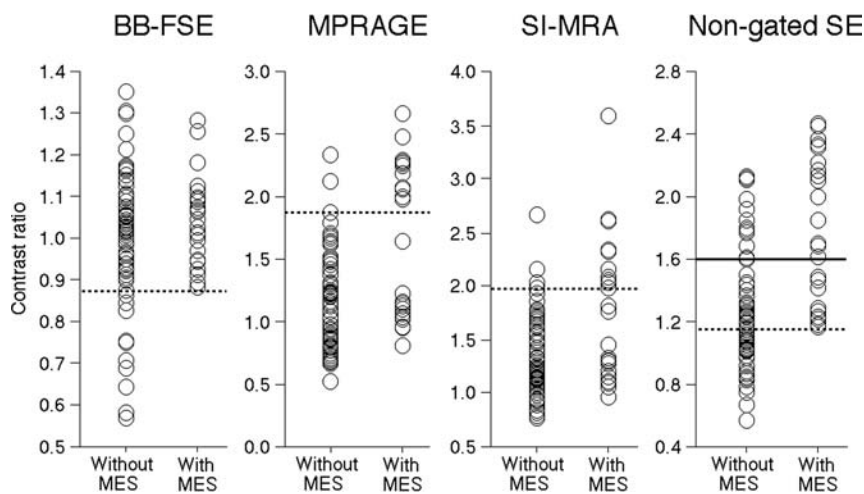


FIG 1. The relationship between contrast ratio from each MR sequence for plaque imaging and the development of microembolic signals during exposure of the carotid arteries. *Dashed horizontal lines* denote the cutoff points lying closest to the left upper corners of the receiver operating characteristic curves in predicting the development of MES during exposure of the carotid arteries. *The horizontal line* denotes the cutoff points lying closest to the left upper corners of the ROC curve in predicting the development of ≥ 6 MES during exposure of the carotid arteries.

image) or $P < .05/3 = .0167$ (AUC for percentage area of the component).

RESULTS

During the 20 months of the study, 93 patients satisfied the inclusion criteria. Of these, 2 patients who underwent urgent CEA due to crescendo transient ischemic attacks did not undergo all 4 kinds of MR plaque imaging. The remaining 91 patients successfully underwent all 4 kinds of MR plaque imaging and subsequent CEA. TCD was attempted in all 91 patients, but 11 patients did not show reliable TCD monitoring throughout the entire operation because of failure to obtain an adequate bone window. These 13 patients were excluded from analysis. Eighty patients were thus enrolled in the present study.

MES were detected in 23 of the 80 patients (29%) studied when the ICA was manipulated to allow exposure from the carotid sheath. Three (13%) of the 23 patients developed new neurologic deficits after recovery from general anesthesia. All deficits included hemiparesis contralateral to the CEA. Those deficits resolved completely within 12 hours in 2 patients. However, neurologic deficits in the remaining patient remained at 24 hours after the operation. None of the 57 patients without MES during exposure of the carotid arteries developed new neurologic deficits postoperatively.

Figures 1 and 2 show the relationship between the CR with each MR plaque imaging technique and the development of MES during exposure of the carotid arteries and the ROC curves for the former in predicting the latter, respectively. AUCs for nongated SE, MPRAGE, SI-MRA, and BB-FSE were 0.821, 0.715, 0.693, and 0.567, respectively. The AUC was significantly greater for nongated SE than for MPRAGE (difference between areas, 0.106; $P = .0023$), SI-MRA (difference between areas, 0.128; $P = .0010$), or BB-FSE (difference between areas, 0.258; $P < .0001$). No significant differences between the AUCs of other combinations (BB-FSE versus MPRAGE: difference between areas, 0.148 and $P =$

.0341; BB-FSE versus SI-MRA: difference between areas, 0.132 and $P = .0955$; MPRAGE versus SI-MRA: difference between areas, 0.022 and $P = .4124$) were observed.

Sensitivity, specificity, and positive- and negative-predictive values for CR at the cutoff point lying closest to the left upper corner of the ROC curve in predicting development of MES during exposure of the carotid arteries were 100%, 49%, 44%, and 100% (cutoff point = 1.155) for nongated SE; 48%, 97%, 85%, and 82% (cutoff point = 1.876) for MPRAGE; 44%, 95%, 77%, and 81% (cutoff point = 1.977) for SI-MRA; and 100%, 19%, 33%, and 100% (cutoff point = 0.874) for BB-FSE, respectively (Figs 1 and 2).

Figure 3 shows comparisons of CR for the 4 kinds plaque imaging and the number of MES in 23 patients with MES during exposure of the carotid arteries.

Negative binomial regression showed no effect of CR for BB-FSE, MPRAGE, or SI-MRA on the number of MES. However, CR for nongated SE had a significant association with the number of MES: For every 1.0 increase in CR for nongated SE, the expected MES count increased by a factor of 1.36 (95% confidence interval, 1.01–1.97; $P < .001$). Sensitivity, specificity, and positive- and negative-predictive values for CR on nongated SE at the cutoff point lying closest to the left upper corner of the ROC curve in predicting the development of ≥ 6 MES³⁴ during exposure of the carotid arteries were 100%, 74%, 27%, and 100% (cutoff point = 1.600), respectively (Figs 1 and 2).

Results of univariate analysis of factors related to the development of MES during exposure of the carotid arteries are summarized in the Table. The incidences of symptomatic lesions and ulceration of stenotic lesions were significantly higher in patients with MES than in those without. No other variables showed significant associations with the development of MES during exposure of the carotid arteries. None of the 80 patients studied was defined as having adhesions during carotid exposure. Although the degree of stress on carotid arteries by manipulation could not be categorized, this degree was determined to be equivalent among patients.

For multivariate statistical analysis of factors related to the development of MES during exposure of the carotid arteries, symptomatic lesions and ulceration of the stenotic lesion were adopted as confounders in the logistic regression model, as items showing $P < .2$ in univariate analyses. The CR in nongated SE, for which the AUC in predicting development of MES during exposure of the carotid arteries was greatest among the 4 kinds of MR plaque imaging, was also added as a confounder. Analysis revealed that symptomatic lesions (95% CI, 1.10–21.53; $P = .0375$) and CR in nongated SE (95% CI, 4.13–90.91; $P = .0002$) were significantly associated with the development of MES during exposure of the carotid arteries.

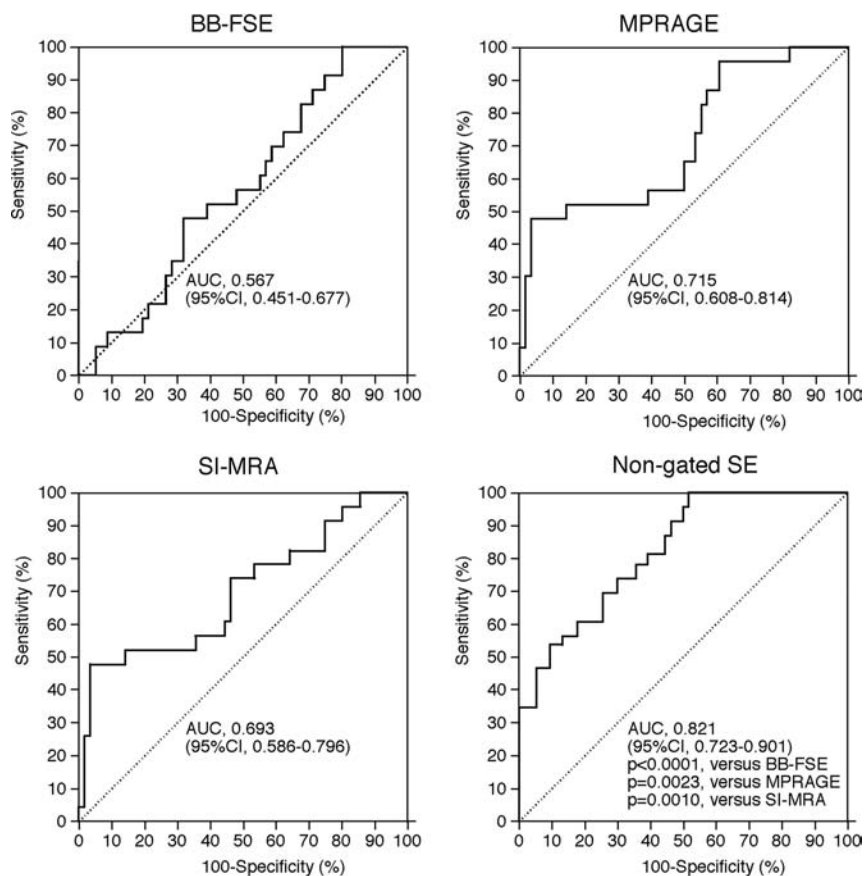


FIG 2. ROC curves used to compare accuracy among contrast ratios in each MR image for predicting the development of MES during exposure of the carotid arteries. Pair-wise comparison analysis shows a significantly greater area under the ROC curve for nongated SE compared with AUCs for BB-FSE, MPRAGE, or SI-MRA.

Figures 4 and 5 show the relationship between the percentage areas of each component in quantitative color-coded MR plaque imaging derived from the nongated SE sequence and the development of MES during exposure of the carotid arteries and ROC curves for the former in predicting the latter, respectively. AUCs for percentage areas of hemorrhage, lipid/necrosis, and fibrous tissue were 0.771, 0.533, and 0.787, respectively. The AUC was significantly greater for hemorrhage (difference between areas, 0.238; $P < .0001$) and fibrous tissue (difference between areas, 0.255; $P = .0002$) than for lipid/necrosis. No significant difference between AUCs for hemorrhage and fibrous tissue (0.016) was observed ($P = .5026$).

Sensitivity, specificity, and positive- and negative-predictive values for percentage areas of hemorrhage, lipid/necrosis, or fibrous tissue at the cutoff point lying closest to the left upper corner of the ROC curve in predicting development of MES during exposure of the carotid arteries were 70%, 73%, 52%, and 85% (cutoff point = 40.7%); 35%, 82%, 44%, and 75% (cutoff point = 12.3%); or 57%, 89%, 86%, and 83% (cutoff point = 9.0%), respectively (Figs 4 and 5).

Representative images for the 4 kinds of MR plaque imaging and quantitative color-coded MR plaque images from a single patient with MES during exposure of the carotid arteries are shown in Fig 6.

DISCUSSION

The present study demonstrated that nongated SE may predict development of MES during exposure of the carotid arteries in CEA more accurately than other MR plaque imaging.

According to the comparison of findings from different plaque imaging sequences with those from specimens obtained by CEA, nongated SE is superior to BB-FSE, MPRAGE, and SI-MRA for discriminating main intraplaque components such as hemorrhage, lipid-rich necrotic core, and fibrous tissue.¹⁵ In the present study, the ROC area to discriminate between patients with and without MES was significantly greater in nongated SE than in other MR images. In addition, among patients with MES, whereas intraplaque signal intensity in nongated SE correlated with the number of MES, no correlation was evident between intraplaque signal intensity in other MR imaging techniques and the number of MES. These findings indicate that nongated SE more accurately predicts the development of MES during exposure of the carotid arteries in CEA than other MR plaque imaging techniques, corresponding with previous results for comparing findings from different plaque imaging sequences with those from specimens obtained by CEA.

Multivariate analysis also revealed that as well as symptomatic lesions, CR in nongated SE was significantly associated with the development of MES during exposure of the carotid arteries. Furthermore, at the optimal cutoff point of ROC analysis for CR on nongated SE, while approximately half of the patients who did not develop MES were incorrectly categorized as possibly developing MES, no patients who developed MES were missed. These findings suggest that CR on preoperative nongated SE may identify patients at risk for MES during exposure of the carotid arteries in CEA as a clinical screening test. Nongated SE can avoid substantial influences of the proton density and inversion recovery pulse.¹⁵ The sequence method is also widely applicable in any scanner and may be used for multicenter trials.

The present study by using quantitative color-coded MR plaque imaging demonstrated that the increased or reduced occupation rate of hemorrhage or fibrous tissue, respectively, in carotid plaque was more strongly associated with the development of MES during exposure of the carotid arteries than the occupying rate of lipid/necrosis. The high association of hemorrhage or fibrous tissue corresponded with previous findings.^{9,12} In contrast, no reports have described the reduced association for lipid/necrosis. Signal intensity for each component in the carotid plaque is, in descending order, hemorrhage, lipid/necrosis, and fibrous tissue in any MR plaque imaging.¹⁵ However, the present

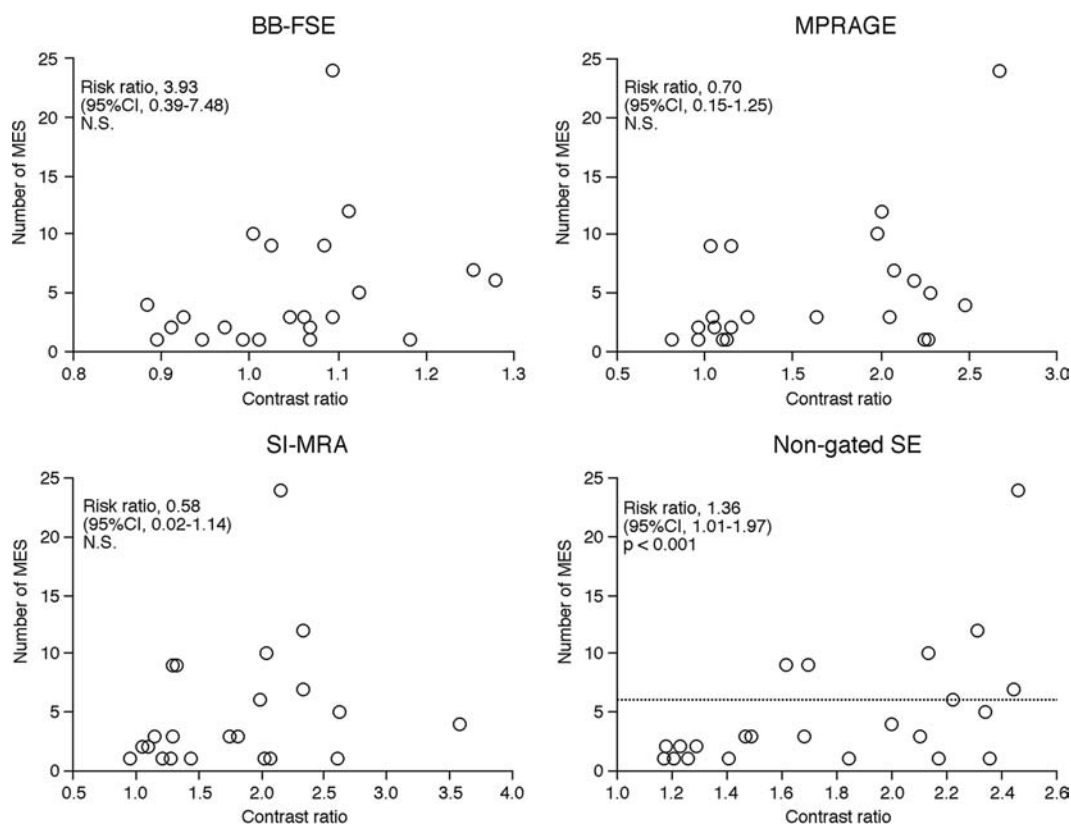


FIG 3. Comparisons of contrast ratios in each MR image and the number of MES in patients with MES during exposure of the carotid arteries. In negative binomial regression analysis, CR was associated with the number of MES only in nongated SE. The *dashed horizontal line* denotes 6 MES as the optimal cutoff point for predicting the development of new postoperative ischemic events.³⁴

Risk factors related to the development of MES during exposure of the carotid arteries

Factors	Development of MES		P Value
	Yes (n = 23)	No (n = 57)	
Age (yr) (mean)	69.8 ± 5.6	69.2 ± 7.3	.5507
Male sex	22 (95.7%)	55 (96.5%)	>.9999
Hypertension	18 (78.3%)	46 (80.7%)	>.9999
Diabetes mellitus	6 (26.1%)	20 (35.1%)	.5989
Dyslipidemia	7 (30.4%)	14 (24.6%)	.5867
Symptomatic lesions	19 (82.6%)	31 (54.4%)	.0223
Degree of ICA stenosis (%) (mean)	86.8 ± 9.3	88.8 ± 8.1	.4913
Length of stenotic lesion (mm) (mean)	52.2 ± 11.3	54.3 ± 11.9	.4003
Height of distal end of stenotic lesion relative to cervical vertebra (mean)	2.8 ± 0.9	2.9 ± 0.8	.6046
Tortuosity of stenotic lesion (mean)	107.0° ± 23.3°	111.1° ± 24.0°	.4755
Ulceration of stenotic lesion	12 (52.2%)	15 (26.3%)	.0372

results from quantitative color-coded MR plaque imaging indicated that accurate discrimination of these 3 components is necessary to predict the development of MES during exposure of the carotid arteries. Nongated SE is superior to other plaque imaging techniques for discriminating these components¹⁵; this finding supports nongated SE as suitable for predicting the development of MES during exposure of the carotid arteries.

According to the concept presented by Caplan and Hennerici,³⁵ low blood flow velocity in the cerebral arteries may impair clearance of emboli generated from a proximal lesion, subsequently facilitating the onset of ischemia due to emboli in poorly perfused areas of the brain. Actually, several investigators have demonstrated that when microemboli are generated during exposure of the carotid arteries in CEA and pass through the

MCA, low blood flow velocity in the MCA is significantly associated with the development of postoperative cerebral ischemic events,³⁶ and increased MCA flow velocity by intentional hypertension (keeping the increase in systolic blood pressure at least +10% above the preoperative value) during exposure of the carotid arteries in CEA prevents postoperative development of new cerebral ischemic events due to intraoperative MES.³¹ In the present study, positive and negative predictive values for CR on nongated SE at the optimal cutoff point of 1.155 in predicting development of MES during exposure of the carotid arteries were 44% and 100%, respectively, and the 2 values for CR on nongated SE at the optimal cutoff point of 1.600 in predicting development of ≥6 MES during exposure of the carotid arteries were 27% and 100%, respectively.

One study, performed by using the same methods for measuring the degree of stenosis in the ICA and MES on TCD as those used in the present study and with patient characteristics similar to those in the present study, showed that the optimal cutoff point for the number of MES in predicting development of new postoperative ischemic events is 6.³⁴ Another study indicated that early clamping of the common and external carotid arteries before exposure of the ICA containing fragile plaque prevents development of new postoperative ischemic events due to MES during exposure of the carotid arteries.³⁷ Intentional hypertension and early clamping of the carotid arteries are easily performed and inexpensive. On the basis of these findings, we propose a practical clinical algorithm to prevent development of MES-related ischemic events in CEA: Patients undergo preoperative MR imaging of plaque by using nongated SE; and when the CR is >1.155 , intentional hypertension is performed during exposure of the carotid arteries. Furthermore, when the CR is >1.600 , early clamp-

ing of the carotid arteries is provided; and when the CR is ≤ 1.155 , both procedures are unnecessary.

Comparison of the 4 kinds of MR plaque imaging has limitations that must be taken into account when interpreting the results, and these limitations have already been discussed in the literature.¹⁵ In the present study, the signal intensity of the carotid plaque was measured in only 1 axial section, set at the location where the stenosis was most severe. This measurement represents the most serious limitation because MES during exposure of the carotid arteries do not always originate from the location with the most severe stenosis. Novel techniques for 3D MR imaging of plaques have recently been developed.^{38,39} Further investigation of whether volumetric analysis of the whole plaque by using 3D

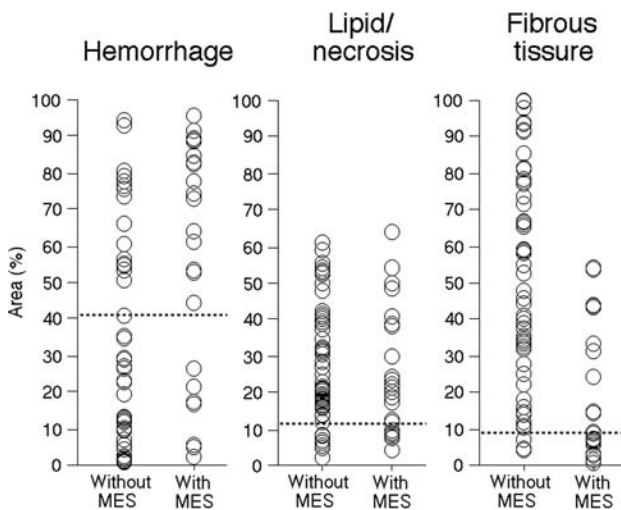


FIG 4. The relationship between the percentage area of each component in quantitative color-coded MR plaque imaging and the development of MES during exposure of the carotid arteries. The dashed horizontal lines denote the cutoff points lying closest to the left upper corners of the ROC curves in predicting the development of MES during exposure of the carotid arteries.

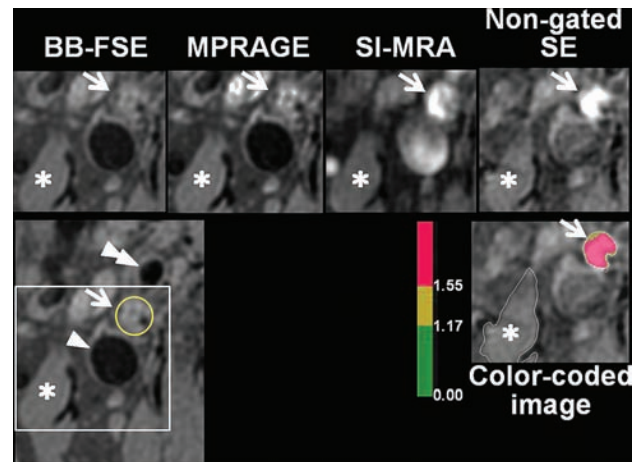


FIG 6. Four kinds of MR plaque images (upper) and quantitative color-coded MR plaque image (right lower) in the symptomatically stenosed (95%) right internal carotid artery of a 72-year-old man showing MES during exposure of the carotid arteries in endarterectomy. A larger FOV image (left lower) indicates anatomic relationships among each vessel (arrow, internal carotid artery; yellow circle, lumen of the internal carotid artery filled with plaque; single arrowhead, internal jugular vein; double arrowhead, external carotid artery; and white square, FOV identical to that of other images). Signal intensities of the plaque in the internal carotid artery (arrows) relative to those of the sternocleidomastoid muscle (asterisks) are, in ascending order, BB-FES, MPRAGE, SI-MRA, and nongated SE. The plaque comprises mainly red and partially yellow areas on the color-coded MR plaque image. On the basis of contrast ratios, hemorrhage, lipid/necrosis, and fibrous tissue are displayed as red, yellow, and green, respectively.

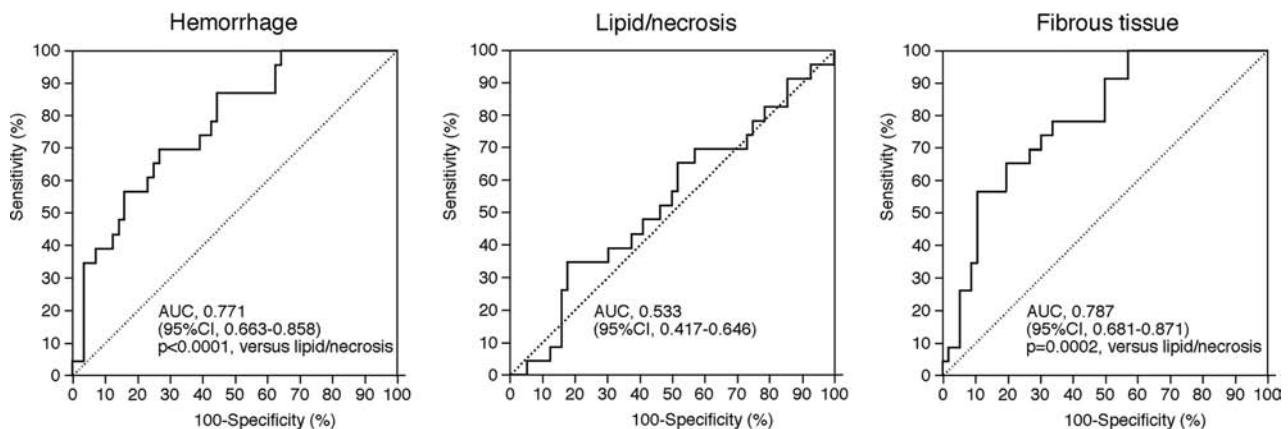


FIG 5. ROC curves used to compare accuracy among percentage areas of each component in quantitative color-coded MR plaque imaging for predicting the development of MES during exposure of the carotid arteries. Pair-wise comparison analysis shows significantly greater AUCs for hemorrhage or fibrous tissue than for lipid/necrosis.

MR imaging may improve the accuracy of predicting MES development during exposure of the carotid arteries in CEA would be of benefit. As another limitation, all patients underwent the operation by the same senior neurosurgeon, to perform surgical procedures in as standardized a manner as possible. Another senior neurosurgeon retrospectively reviewed videos that had been recorded through an operative microscope and determined that the degree of stress on the carotid arteries due to manipulation during carotid exposure was equivalent among patients. Because the degree of stress may affect the development of MES, our findings may not be generalizable to other surgeons. The small sample size (total, 80 patients; 32 patients with events) and patient selection bias (12% of patients were excluded because of failure to obtain TCD data) were also limitations. In addition, because the present study was designed as observational research, prospective studies to validate the accuracy of our data, including the cutoff point for CR in predicting development of MES during exposure of the carotid arteries, will be needed.

CONCLUSIONS

The present study demonstrated that nongated SE, which is widely applicable in any scanner, may predict development of MES during exposure of the carotid arteries in CEA more accurately than other MR imaging techniques for plaque imaging.

Disclosures: Kuniaki Ogasawara, Shinsuke Narumi—*RELATED: Grant: grant-in-aid for Strategic Medical Science Research Center of Ministry of Education, Culture, Sports, Science and Technology-Japan and Core Research for Evolutional Science and Technology of Japan Science and Technology Agency (25861122).* Makoto Sasaki—*RELATED: Consulting Fee or Honorarium: Hitachi Medical, Comments: M.S. is a consultant for Hitachi Medical Corporation and has received honoraria from them; UNRELATED: Grants/Grants Pending: Japanese Ministry,* Hitachi Medical,* Astra-Zeneca,* Mitsubishi,* Otsuka*;* Payment for Lectures (including service on Speakers Bureaus): Daiichi Sankyo, Ezai, Sanofi, Mitsubishi, Johnson & Johnson, Bayer, Astra-Zeneca, Kowa, Fuji, Hitachi Medical, GE Healthcare; Travel/Accommodations/Meeting Expenses Unrelated to Activities Listed: Olea Medical. *Money paid to the institution.*

REFERENCES

- Rothwell PM, Eliasziw M, Gutnikov SA, et al; Carotid Endarterectomy Trialists' Collaboration. **Analysis of pooled data from the randomised controlled trials of endarterectomy for symptomatic carotid stenosis.** *Lancet* 2003;361:107–16 CrossRef Medline
- Endarterectomy for asymptomatic carotid artery stenosis: Executive Committee for the Asymptomatic Carotid Atherosclerosis Study.** *JAMA* 1995;273:1421–28 Medline
- North American Symptomatic Carotid Endarterectomy Trial Collaborators. **Beneficial effect of carotid endarterectomy in symptomatic patients with high-grade carotid stenosis.** *N Engl J Med* 1991;325:445–53 CrossRef Medline
- Spencer MP. **Transcranial Doppler monitoring and causes of stroke from carotid endarterectomy.** *Stroke* 1997;28:685–91 CrossRef Medline
- Ackerstaff RG, Moons KG, van de Vlasakker CJ, et al. **Association of intraoperative transcranial Doppler monitoring variables with stroke from carotid endarterectomy.** *Stroke* 2000;31:1817–23 CrossRef Medline
- Wolf O, Heider P, Heinz M, et al. **Microembolic signals detected by transcranial Doppler sonography during carotid endarterectomy and correlation with serial diffusion-weighted imaging.** *Stroke* 2004;35:e373–e375 CrossRef Medline
- Gavrilescu T, Babikian VL, Cantelmo NL, et al. **Cerebral microembolism during carotid endarterectomy.** *Am J Surg* 1995;170:159–64 CrossRef Medline

- Rosario JA, Hachinski VC, Lee DH, et al. **Adverse reactions to duplex scanning.** *Lancet* 1987;330:1023 CrossRef Medline
- Verhoeven BA, de Vries JP, Pasterkamp G, et al. **Carotid atherosclerotic plaque characteristics are associated with microembolization during carotid endarterectomy and procedural outcome.** *Stroke* 2005;36:1735–40 CrossRef Medline
- Gaunt ME, Martin PJ, Smith JL, et al. **Clinical relevance of intraoperative embolization detected by transcranial Doppler ultrasonography during carotid endarterectomy: a prospective study of 100 patients.** *Br J Surg* 1994;81:1435–39 CrossRef Medline
- Jansen C, Ramos LM, van Heesewijk JP, et al. **Impact of microembolism and hemodynamic changes in the brain during carotid endarterectomy.** *Stroke* 1994;25:992–97 CrossRef Medline
- Altaf N, Beech A, Goode SD, et al. **Carotid intraplaque hemorrhage detected by magnetic resonance imaging predicts embolization during carotid endarterectomy.** *J Vasc Surg* 2007;46:31–36 CrossRef Medline
- Sitzer M, Müller W, Siebler M, et al. **Plaque ulceration and lumen thrombus are the main sources of cerebral microemboli in high-grade internal carotid artery stenosis.** *Stroke* 1995;26:1231–33 CrossRef Medline
- Hatsukami TS, Yuan C. **MRI in the early identification and classification of high-risk atherosclerotic carotid plaques.** *Imaging Med* 2010;2:63–75 CrossRef Medline
- Saito A, Sasaki M, Ogasawara K, et al. **Carotid plaque signal differences among four kinds of T1-weighted magnetic resonance imaging techniques: a histopathological correlation study.** *Neuroradiology* 2012;54:1187–94 CrossRef Medline
- Yoshida K, Narumi O, Chin M, et al. **Characterization of carotid atherosclerosis and detection of soft plaque with use of black-blood MR imaging.** *AJNR Am J Neuroradiol* 2008;29:868–74 CrossRef Medline
- Watanabe Y, Nagayama M, Suga T, et al. **Characterization of atherosclerotic plaque of carotid arteries with histopathological correlation: vascular wall MR imaging vs. color Doppler ultrasonography (US).** *J Magn Reson Imaging* 2008;28:478–85 CrossRef Medline
- Arai D, Yamaguchi S, Murakami M, et al. **Characteristics of carotid plaque findings on ultrasonography and black blood magnetic resonance imaging in comparison with pathological findings.** *Acta Neurochir Suppl* 2011;112:15–19 CrossRef Medline
- Boussel L, Herigault G, Sigovan M, et al. **Modified electrocardiograph-triggered black-blood turbo spin-echo technique to improve T1-weighting in contrast-enhanced MRI of atherosclerotic carotid arteries.** *J Magn Reson Imaging* 2008;28:533–37 CrossRef Medline
- Yamada N, Higashi M, Otsubo R, et al. **Association between signal hyperintensity on T1-weighted MR imaging of carotid plaques and ipsilateral ischemic events.** *AJNR Am J Neuroradiol* 2007;28:287–92 Medline
- Moody AR, Murphy RE, Morgan PS, et al. **Characterization of complicated carotid plaque with magnetic resonance direct thrombus imaging in patients with cerebral ischemia.** *Circulation* 2003;107:3047–52 CrossRef Medline
- Liu XS, Zhao HL, Cao Y, et al. **Comparison of carotid atherosclerotic plaque characteristics by high-resolution black-blood MR imaging between patients with first-time and recurrent acute ischemic stroke.** *AJNR Am J Neuroradiol* 2012;33:1257–61 CrossRef Medline
- Yoshimura S, Yamada K, Kawasaki M, et al. **High-intensity signal on time-of-flight magnetic resonance angiography indicates carotid plaques at high risk for cerebral embolism during stenting.** *Stroke* 2011;42:3132–37 CrossRef Medline
- Narumi S, Sasaki M, Ohba H, et al. **Prediction of carotid plaque characteristics using non-gated MR imaging: correlation with endarterectomy specimens.** *AJNR Am J Neuroradiol* 2013;34:191–97 CrossRef Medline
- Narumi S, Sasaki M, Ohba H, et al. **Altered carotid plaque signal among different repetition times on T1-weighted magnetic reso-**

- nance plaque imaging with self-navigated radial-scan technique. *Neuroradiology* 2010;52:285–90 CrossRef Medline
26. Narumi S, Sasaki M, Ohba H, et al. **Predicting carotid plaque characteristics using quantitative color-coded T1-weighted MR plaque imaging: correlation with carotid endarterectomy specimens.** *AJNR Am J Neuroradiol* 2014;35:766–71 CrossRef Medline
 27. Fox AJ, Symons SP, Aviv RI, et al. **Falsely claiming use of NASCET percentage stenosis method.** *Radiology* 2009;253:574–75; author reply 575 CrossRef Medline
 28. Myouchin K, Takayama K, Taoka T, et al. **Carotid Wallstent placement difficulties encountered in carotid artery stenting.** *Springerplus* 2013;2:468 CrossRef Medline
 29. Randoux B, Marro B, Koskas F, et al. **Carotid artery stenosis: prospective comparison of CT, three-dimensional gadolinium-enhanced MR, and conventional angiography.** *Radiology* 2001;220:179–85 CrossRef Medline
 30. Yoshida K, Ogasawara K, Kobayashi M, et al. **Scar formation of the carotid sheath identified during carotid endarterectomy in patients with previous cardiac surgery: significance of history of intraoperative Swan-Ganz catheter insertion—clinical article.** *J Neurosurg* 2010;113:885–89 CrossRef Medline
 31. Kobayashi M, Ogasawara K, Yoshida K, et al. **Intentional hypertension during dissection of carotid arteries in endarterectomy prevents postoperative development of new cerebral ischemic lesions caused by intraoperative microemboli.** *Neurosurgery* 2011;69:301–07 CrossRef Medline
 32. **Basic identification criteria of Doppler microembolic signals: Consensus Committee of the Ninth International Cerebral Hemodynamic Symposium.** *Stroke* 1995;26:1123 CrossRef Medline
 33. Pepe MS, Longton G. **Standardizing diagnostic markers to evaluate and compare their performance.** *Epidemiology* 2005;16:598–603 CrossRef Medline
 34. Aso K, Ogasawara K, Sasaki M, et al. **Preoperative cerebrovascular reactivity to acetazolamide measured by brain perfusion SPECT predicts development of cerebral ischemic lesions caused by microemboli during carotid endarterectomy.** *Eur J Nucl Med Mol Imaging* 2009;36:294–301 CrossRef Medline
 35. Caplan LR, Hennerici M. **Impaired clearance of emboli (washout) is an important link between hypoperfusion, embolism, and ischemic stroke.** *Arch Neurol* 1998;55:1475–82 CrossRef Medline
 36. Ogasawara K, Suga Y, Sasaki M, et al. **Intraoperative microemboli and low middle cerebral artery blood flow velocity are additive in predicting development of cerebral ischemic events after carotid endarterectomy.** *Stroke* 2008;39:3088–91 CrossRef Medline
 37. Kobayashi M, Ogasawara K, Inoue T, et al. **Urgent endarterectomy using pretreatment with free radical scavenger, edaravone, and early clamping of the parent arteries for cervical carotid artery stenosis with crescendo transient ischemic attacks caused by mobile thrombus and hemodynamic cerebral ischemia: case report.** *Neurol Med Chir (Tokyo)* 2007;47:121–25 CrossRef Medline
 38. Balu N, Chu B, Hatsukami TS, et al. **Comparison between 2D and 3D high-resolution black-blood techniques for carotid artery wall imaging in clinically significant atherosclerosis.** *J Magn Reson Imaging* 2008;27:918–24 CrossRef Medline
 39. Crowe LA, Gatehouse P, Yang GZ, et al. **Volume-selective 3D turbo spin echo imaging for vascular wall imaging and distensibility measurement.** *J Magn Reson Imaging* 2003;17:572–80 CrossRef Medline

Modified Core Biopsy Technique to Increase Diagnostic Yields for Well-Circumscribed Indeterminate Thyroid Nodules: A Retrospective Analysis

S. Han, J.H. Shin, S.Y. Hahn, and Y.L. Oh

ABSTRACT

BACKGROUND AND PURPOSE: The results of conventional core biopsy for some thyroid nodules with indeterminate cytology have still remained indeterminate. The aim of this study was to evaluate whether the ultrasonography-guided core needle biopsy technique containing the nodule, capsular portion, and surrounding parenchyma was more effective than a conventional method in enhancing diagnostic yield for circumscribed solid thyroid nodules without malignant sonographic features.

MATERIALS AND METHODS: This retrospective comparative study evaluated 26 thyroid nodules in 26 consecutive patients between 2006 and 2010. They were biopsied by using a conventional method, and 61 nodules from 60 patients were biopsied by using a modified ultrasonography-guided core needle biopsy technique in 2013. The patients enrolled in this study presented with circumscribed solid thyroid nodules without malignant sonographic features, classified as nondiagnostic or atypia/follicular lesions of undetermined significance at previous cytology. The ultrasonography-guided core needle biopsy results of the 2 groups were compared.

RESULTS: The rate of inconclusive ultrasonography-guided core needle biopsy results was 34.6% (9/26) in the conventional group and 11.4% (7/61) in the modified technique group ($P = .018$). There was no significant difference in the mean size of the nodules between the 2 groups ($P = .134$). The malignancy rate was 33% (3/9) for the conventional group and 52% (27/52) for the modified technique group ($P = .473$). The most common malignant pathology was a follicular variant of papillary thyroid carcinoma and follicular adenoma was the most common benign lesion.

CONCLUSIONS: For circumscribed solid nodules without malignant sonographic features with indeterminate cytology, the ultrasonography-guided core needle biopsy technique containing the nodule, capsular portion, and surrounding parenchyma is more effective in diagnostic yield compared with a conventional method that biopsies the intranodular portion.

ABBREVIATIONS: AUS/FLUS = atypia or follicular lesions of undetermined significance; CNB = core needle biopsy; FNA = ultrasonography-guided fine-needle aspiration; PTC = papillary thyroid carcinoma; US = ultrasonography

Despite the lack of definite malignant sonographic features, solid thyroid nodules showing nondiagnostic or atypia or follicular lesions of undetermined significance (AUS/FLUS) in fine-needle aspiration (FNA) readings by using the Bethesda System for Reporting Thyroid Cytopathology have raised concerns about the diagnosis of malignancy.¹⁻⁴ The management of nodules with nondiagnostic lesions or AUS/FLUS has been a matter of debate.^{2,3} Several studies have suggested that sonography-guided core needle biopsy (US-CNB) helps decrease the frequency of

inconclusive diagnostic results and improves the rate of accurate diagnoses.⁵⁻⁹

US-CNB is safe and well-tolerated, yields a low incidence of complications, and serves as an alternative to FNA for obtaining tissues for diagnosis.^{7,10} However, its results have remained indeterminate for up to 36% of the nodules whose cytology is insufficient to differentiate nodular hyperplasia from follicular neoplasm, even after US-CNB.⁵ On ultrasonography (US), circumscribed solid nodules without malignant features are frequently confirmed histologically as nodular hyperplasia, a follicular neoplasm (follicular/Hürthle adenoma or carcinoma), a follicular variant of papillary thyroid carcinoma (PTC), or a classic type of PTC.¹¹⁻¹⁴

The preoperative diagnosis of PTC would usually be sufficient with FNA because nuclear features are the key to diagnosis.⁴ "Follicular neoplasm" is defined as an encapsulated lesion whose growth pattern (microfollicular, macrofollicular, trabecular, or

Received July 20, 2015; accepted after revision November 11.

From the Departments of Radiology (S.H., J.H.S., S.Y.H.) and Pathology (Y.L.O.), Samsung Medical Center, Sungkyunkwan University School of Medicine, Seoul, South Korea.

Please address correspondence to Jung Hee Shin, MD, PhD, Department of Radiology, Samsung Medical Center, Sungkyunkwan University School of Medicine, 81 Irwon-ro, Gangnam-gu, Seoul 06351, South Korea; e-mail: helena35@hanmail.net

<http://dx.doi.org/10.3174/ajnr.A4650>

another growth pattern) is distinct from that of the surrounding thyroid parenchyma. Nodular hyperplasia is one of the most common pathologies in benign thyroid disease and is characterized by a densely cellular follicular proliferation that lacks a capsule on histology.^{4,15,16} Because nodular hyperplasia may sometimes be considered normal thyroid tissue after core needle biopsy diagnosis, the presence of a capsule and normal parenchyma in the thyroid nodule can be meaningful for the differentiation of a follicular neoplasm from nodular hyperplasia. Nodules with circumscribed solid features only identified on US are diagnosed as indeterminate because they have neither malignant nor benign features.¹⁷ Moreover, indeterminate FNA of these lesions may lead to an unnecessary diagnostic operation. Thus, circumscribed solid thyroid nodules not associated with other malignant features require the use of CNB techniques under US guidance other than a conventional method that biopsies the internal portion of the thyroid nodule. One recent study suggested that the use of a CNB technique that biopsied the capsule of the thyroid nodule and the surrounding parenchyma was useful for the diagnosis of cytologically indeterminate nodules.¹⁸ However, the authors did not compare the results of the conventional method with those of the modified method or focus on the diagnosis of problematic nodules by using a conventional CNB method. We evaluated whether the modified CNB technique was more effective in the diagnostic yield of circumscribed solid nodules without malignant sonographic features with indeterminate cytology compared with a conventional method. Therefore, we compared the inconclusive rate (nondiagnostic or AUS/FLUS rate) and malignant rate of CNB results between the conventional and the modified technique groups.

MATERIALS AND METHODS

Study Design and Patients

This retrospective study was approved by the institutional review board of our institution, and the requirement for informed consent was waived. However, informed consent for procedures was obtained from patients before they underwent the ultrasonography-guided fine-needle aspiration and US-CNB procedures.

From April 2006 to December 2010, US-CNB was performed on 109 patients with 109 thyroid lesions. Twenty-one patients were excluded because of the absence of a history of ultrasonography-guided fine-needle aspiration. The remaining 88 patients had inconclusive results on initial FNA readings obtained in our institution. Among them, 26 consecutive patients presented with 26 thyroid nodules, which were circumscribed solid nodules on US without typical malignant sonographic features (spiculated margins, microcalcifications, marked hypoechogenicity, and taller-than-wide shape).^{1,17} Twenty-five patients from this study had been included in our prior study by Hahn et al.⁵ At that time, we targeted the internal portion of the thyroid nodule by using US-CNB (Fig 1). The inclusion of the thyroid capsule and normal parenchyma had not been contemplated, and these patients were defined as the “conventional group.” However, a novel US-CNB technique was routinely and prospectively applied to all thyroid nodule samples from June 2013 onward. The main target tissue for biopsy was a capsular portion, including the lesion and normal parenchyma (Fig 1). From July to December 2013, 180 patients

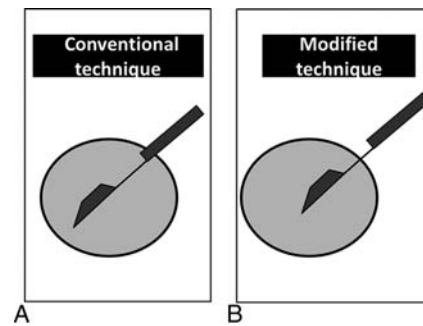


FIG 1. Schematic representation of the conventional and modified US-guided CNB techniques. In the conventional method, the specimen notch of the biopsy needle is confined to the internal portion of the thyroid nodule. In the modified US-CNB technique, the specimen notch of the biopsy needle is placed in the capsule and contains both parenchymal and nodular tissue.

underwent US-CNB. Of these, 60 consecutive patients presented with 61 nodules that were categorized as circumscribed solid nodules without coexistent suspicious features on US or nondiagnostic or AUS/FLUS at previous cytology. All patients included for statistical analysis were surgically diagnosed or followed-up for at least 2 years. We retrospectively reviewed age, sex, and complications after the procedure when present on the medical record. We compared the conclusiveness of CNB results, age, tumor size, malignancy rate, and final pathologic results between the conventional and the modified technique groups.

Ultrasonography and US-Guided CNB Procedures

All US examinations were performed by using high-resolution ultrasonography equipment (iU22 or HD I5000; Philips Healthcare, Bothell, Washington), with 5- to 12-MHz linear array transducers. US-CNB, including the scanning and interpretation of US images, was performed by 1 of 4 radiologists with ≥ 5 years' experience. In our practice, US-CNB was sometimes indicated in the diagnosis of thyroid nodules with indeterminate cytology obtained at our or another hospital or if malignant histology other than differentiated thyroid cancer was suspected on US or clinically. In our former study period, the range of indication for US-CNB was narrow because an alternative to repeat FNA and ultrasonography-guided fine-needle aspiration was performed at the request of clinicians or patients, even in nodules smaller than 0.5 cm in the period before the current published guidelines.^{2,17} US-CNB was performed by using a spring-activated, short-throw (1.1-cm excursion) 18-gauge needle (ACECUT; TSK Laboratory, Tochigi-Ken, Japan) by a freehand technique for the 2 study periods. The routine number of thyroid biopsy cores obtained at our institution was 2 or 3 per nodule in the 2 study periods. In the conventional CNB method performed before June 2013, the specimen notch of the biopsy needle and a tissue cutting were confined to the intranodular portion within the thyroid nodule. On the other hand, in the modified US-CNB technique, the specimen notch of the biopsy needle was placed in the capsule and contained both parenchymal and nodular tissue (Fig 1).

Histologic Examination

Two or 3 specimen cores were fixed in formalin and entirely embedded in a paraffin block. Immunohistochemical staining was

Table 1: Comparison of ultrasound-guided core needle biopsy for circumscribed solid thyroid nodules without malignant sonographic features with indeterminate cytology

	Conventional Group (n = 26)	Modified Technique Group (n = 61)	P Value
Mean age of patients (yr)	46.6 (range, 34–62)	49.7 (range, 26–73)	.204
Mean tumor size (mm)	18.3 (range, 4–39)	22.3 (range, 7–60)	.134
Inconclusive rate of US-CNB result	34.6% (9/26)	11.4% (7/61)	.018
Malignant rate ^a	33.3% (3/9)	51.9% (27/52)	.473

^aThe denominator is the number of the nodules that underwent surgical excision.

Table 2: Correlation with results of US-CNB and final surgical pathology of the conventional CNB group^a

CNB Results by Bethesda Category (n = 26)	Surgical Pathology (n = 9)	
	Benign (n = 6)	Malignant (n = 3)
Class I (n = 0)	–	–
Class II (n = 15)	NH (n = 1), LT (n = 1)	–
Class III (n = 9)	NH (n = 4)	PTC (n = 1)
Class IV (n = 1)	–	PTC (n = 1)
Class V (n = 0)	–	–
Class VI (n = 1)	–	MTC (n = 1)

Note:—NH, nodular hyperplasia; LT, lymphocytic thyroiditis; MTC, medullary thyroid carcinoma.

^aData are the number of nodules.

Table 3: Correlation with results of US-CNB and final surgical pathology of the modified CNB group^a

CNB Results by Bethesda Category (n = 61)	Surgical Pathology (n = 52)	
	Benign (n = 25)	Malignant (n = 27)
Class I (n = 0)	–	–
Class II (n = 7)	NH (n = 1)	–
Class III (n = 7)	NH (n = 2), FA (n = 2)	FVPTC (n = 2)
Class IV (n = 35)	FA (n = 17), NH (n = 2), HT (n = 1)	FVPTC (n = 7), FC (n = 5), FVPTC in NH (n = 1)
Class V (n = 1)	–	FVPTC (n = 1)
Class VI (n = 11)	–	PTC (n = 8), FVPTC (n = 2), WVPTC (n = 1)

Note:—FA, follicular adenoma; FC, follicular carcinoma; FVPTC, follicular variant of papillary thyroid carcinoma; HT, Hashimoto thyroiditis; WVPTC, Warthin-like variant of papillary thyroid carcinoma; NH, nodular hyperplasia.

^aData are the number of nodules.

performed when needed by pathologists. However, we did not assess the role of the immunohistochemical results for the contribution to the diagnosis. The diagnosis of CNB specimens was interpreted by 1 of 6 cytopathologists. One expert with 15 years of experience in thyroid cytopathology supervised the other cytopathologists in questionable cases. Histologic diagnosis on US-CNB reported in 2 study periods was reclassified into the same 6 categories according to the Bethesda system that was used in FNA readings because no international standardization for CNB reporting is available⁴: class I, nondiagnostic; class II, benign; class III, AUS/FLUS; class IV, follicular neoplasm/suspicious for follicular neoplasm; class V, suspicious for malignancy; and class VI, malignancy. After the final CNB results, the nodules were divided into a conclusive group (classes II, IV, V, and VI) and an inconclusive group (classes I and III).

Data and Statistical Analysis

The conclusiveness of CNB results, age, tumor size, and malignancy rate were compared between the conventional and modified technique groups by using Student *t* and Fisher exact tests, respectively. Data were analyzed by using SAS software, Version 9.4 (SAS Institute, Cary, North Carolina). All *P* values were 2-sided, and *P* < .05 was considered statistically significant.

RESULTS

The clinical parameters and final CNB results are summarized in Table 1. Of the 26 patients in the conventional group (age range, 34–62 years; mean age, 46.6 years), 3 (11.5%) were men and 23 (88.5%) were women. Of the 60 patients in the modified technique group (age range, 26–73 years; mean age, 49.7 years), 12 (20%) were men and 48 (80%) were women. There were no significant differences in age and sex between the 2 groups (*P* values = .204 and .373, respectively).

The mean size of the 26 thyroid nodules on conventional US-CNB was 18.3 mm (range, 4–39 mm). The mean size of the 61 thyroid nodules by using the modified CNB technique was 22.3 mm (range, 7–60 mm) (*P* = .134). None of the patients evaluated had significant complications. In the modified technique, perinodular hemorrhage occurred in 1 patient immediately after US-CNB but subsided after manual compression.

All specimens obtained by using the 2 US-CNB methods demonstrated adequacy for diagnosis. The CNB results according to the Bethesda system recommended for practical use showed class II in 15 (57.7%) cases, class III in 9 (34.6%) cases, class IV in 1 (3.8%) case, and class VI in 1 (3.8%) case for the 26 nodules

biopsied in the conventional group and class II in 7 (11.4%) cases, class III in 7 (11.4%) cases, class IV in 35 (57.4%) cases, class V in 1 (1.6%) case, and class VI in 11 (18.0%) cases for the 61 nodules biopsied in the modified method group, respectively. The rate of inconclusive US-CNB results was 34.6% (9/26) by using the conventional method and 11.4% (7/61) by using the modified technique (*P* = .018).

Surgical pathology on excision was present in 9 of 26 nodules in the conventional group and in 52 of 61 nodules in the modified technique group (Tables 2 and 3). The malignancy rate by surgical pathology was 33.3% (3/9) in the conventional group and 51.9% (27/52) in the modified technique group (*P* = .473), but this difference was not statistically significant. In the conventional group, surgical pathologies included nodular hyperplasia in 5 cases, chronic lymphocytic thyroiditis in 1 case, classic PTC in 2 cases, and medullary thyroid carcinoma in 1 case (Fig 2). In the modified technique group, final pathology in 52 patients included nodular hyperplasia in 5 cases, follicular adenoma in 19 cases, nodular Hashimoto thyroiditis in 1 case, follicular variant of PTC in 13 cases, classic PTC in 8 cases, follicular carcinoma in 5 cases, and Warthin-like variant of PTC in 1 case (Fig 3).

Of the circumscribed solid nodules without malignant US

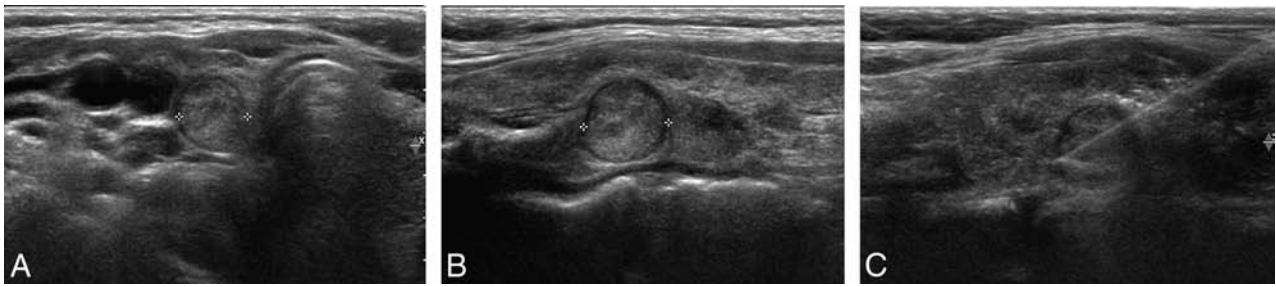


FIG 2. Ultrasound images of a 42-year-old woman who underwent conventional US-CNB. Transverse (A) and longitudinal (B) sonograms demonstrate a 1-cm circumscribed isoechoic nodule (crosses) in the right thyroid lobe. A previous cytologic result was nondiagnostic. After conventional US-CNB confined to a lesion in the thyroid nodule (C), the diagnosis of nodular hyperplasia or Hürthle cell neoplasm was inconclusive. To differentiate nodular hyperplasia from follicular neoplasm, we performed thyroidectomy, and the final pathology indicated nodular hyperplasia.

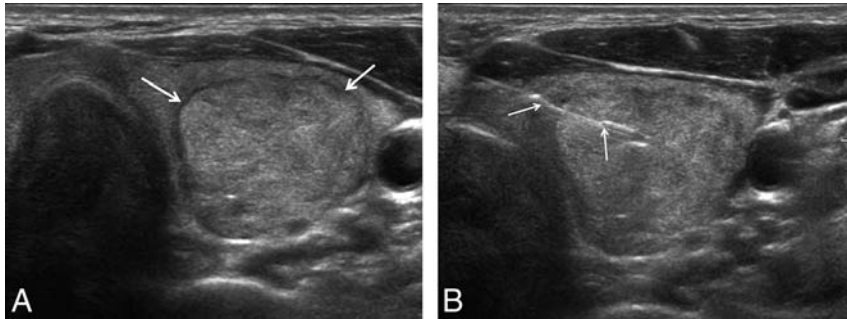


FIG 3. Ultrasound images of a 56-year-old woman who had undergone the modified US-CNB technique. The sonogram demonstrates a 3.7-cm circumscribed solid nodule (transverse image in A) without evidence of malignant features, confirmed to be a follicular lesion of undetermined significance on prior cytology. The specimen notch (arrows) of the biopsy needle before tissue excision was placed in the thyroid capsule and contained both parenchymal and nodular tissue (B). The diagnosis using the modified CNB technique indicated follicular neoplasm. Follicular adenoma was confirmed after thyroidectomy.

features, the most common malignancy was a follicular variant of PTC in 13 (43.3%) of 30 malignancy cases, and the most frequent benign pathology was follicular adenoma in 19 (61.3%) of 31 benign lesions.

DISCUSSION

Our study demonstrated that the rate of inconclusive US-CNB results in the modified technique group was significantly lower than that in the conventional group for circumscribed solid nodules without malignant US features (11.4% versus 34.6%, $P = .004$). The main issue of the present study was circumscribed solid nodules with indeterminate cytology, which addressed follicular neoplasm rather than PTC because of the presence of nodules without evidence of malignant US features indicating PTC. This modified biopsy technique is essential to differentiate follicular neoplasm from adenomatous nodules because visualization of the capsule in the specimen helps pathologists change their findings from follicular lesions of undetermined significance to follicular neoplasm, while the absence of the capsule implies nodular hyperplasia. This technique can improve identification of surgical candidates. As shown by our results, the percentage of the benign diagnoses decreased in the second cohort by using the modified technique, whereas the percentage of follicular neoplasms increased, as did the percentage of malignancies.

Although a previous study has already described this technique, it did not evaluate its effectiveness compared with a conventional method and concentrate on problematic nodules separately at diagnosis by using routinely performed conventional CNB methods.¹⁸ These problematic nodules should be diagnosed on US before any intervention. Circumscribed solid nodules without malignant features are considered an indeterminate category on US.¹⁷ These nodules are a challenge for risk stratification using US, FNA, and even conventional CNB due to the impossibility of capsule assessment.

Previous reports have shown that the CNB method is more useful than repeat FNA for the evaluation of nodules that are inconclusive on FNA.^{7-9,19} These

studies reported that the rate of inconclusive CNB results ranged between 0% and 26%. Recently, Hahn et al⁵ demonstrated that US-CNB is beneficial for the diagnosis of thyroid nodules with inconclusive US-guided FNA results. However, it is still not helpful for the differential diagnosis in 36% of nodules that are suspicious for follicular neoplasm on US, as shown by the occurrence of several indeterminate results in the differentiation of nodular hyperplasia from follicular neoplasm even after US-CNB. Nodular hyperplasia is one of the most common benign lesions of the thyroid and does not require further treatment in most patients.⁴ However, follicular neoplasms should be surgically treated because the differentiation of a follicular adenoma from a follicular carcinoma is impossible without the evaluation of the whole capsule.²⁻⁴ Unfortunately, this modified CNB technique is inadequate to differentiate benign and malignant follicular neoplasms. However, reliable diagnosis of nodules with any evidence of follicular neoplasm via presurgical interventions prevents unnecessary surgery in those patients with simple nodular hyperplasia and gives reassurance to anxious patients who are not candidates for surgery.

In the cases in which surgical pathology was available, the most common malignant subtype in circumscribed solid thyroid nodules without malignant US features with indeterminate cytology was a follicular variant of PTC, with 13 (43.3%) cases of 30 malignancies. The follicular variant of PTC frequently has cytologi-

cally inconclusive results without definite malignant features on US. This result supports a previous report in which the follicular variant of PTC showed more benign US features, and the diagnostic rate of PTC on FNA was lower compared with classic PTC.²⁰ Further studies about whether CNB is better than FNA for the preoperative diagnosis of the follicular variant of PTC are needed.

Previous reports have suggested that the incidence of conventional CNB-related hematoma was approximately 0%–1.5%.^{10,21,22} In the modified capsular biopsy technique group, 1 patient had subsequent perinodular hemorrhage, which was resolved by manual compression. Perinodular hemorrhages infrequently occur even in FNA by using 23- to 25-gauge needles.²³ Color Doppler US has to be routinely used to avoid hypervascularized perinodular vessels when the tract for biopsy is determined.

Our study has some limitations. First, this retrospective study compared the results of procedures performed in 2 different periods. Therefore, although some unidentified confounding factors may be present, we could not retrospectively estimate them, and prospective studies would be more adequate in this context. Second, the sample size was small. We did not actively perform US-CNB in the former study period because the management of inconclusive cytologic nodules was routinely performed by using repeat FNA or surgery in our institution. Third, selection bias due to technical problems associated with the biopsies may exist. In case of thyroid nodules large enough to occupy the entire ipsilateral thyroid gland, biopsying the thyroid capsule is not easy because the needle can potentially damage extrathyroidal structures. The modified technique may present limitations in biopsying large nodules and preserving normal parenchyma. The most problematic factor of CNB in small nodules (< 1 cm) would be target size. If small lesions are well-targeted, the results should be reliable because the notch can be properly positioned within the specimen to encompass 7 mm of throw.

CONCLUSIONS

For circumscribed solid thyroid nodules without malignant sonographic features and with indeterminate cytology, the US-CNB technique containing the nodule, capsular portion, and surrounding parenchyma enhances diagnostic yield compared with a conventional CNB method that biopsied only the internal portion of the nodule. This technique reduces the frequency of inconclusive CNB results and properly selects surgical candidates.

REFERENCES

1. Kim EK, Park CS, Chung WY, et al. **New sonographic criteria for recommending fine-needle aspiration biopsy of nonpalpable solid nodules of the thyroid.** *AJR Am J Roentgenol* 2002;178:687–91 CrossRef Medline
2. Cooper DS, Doherty GM, Haugen BR, et al; American Thyroid Association (ATA) Guidelines Taskforce on Thyroid Nodules and Differentiated Thyroid Cancer. **Revised American Thyroid Association management guidelines for patients with thyroid nodules and differentiated thyroid cancer.** *Thyroid* 2009;19:1167–214 CrossRef Medline
3. Gharib H, Papini E, Paschke R, et al. **American Association of Clinical Endocrinologists, Associazione Medici Endocrinologi, and European Thyroid Association Medical Guidelines for Clinical Practice for the Diagnosis and Management of Thyroid Nodules.** *Endocr Pract* 2010;16(suppl 1):1–43 CrossRef Medline
4. Cibas ES, Ali SZ. **The Bethesda System For Reporting Thyroid Cytopathology.** *Am J Clin Pathol* 2009;132:658–65 CrossRef Medline
5. Hahn SY, Shin JH, Han BK, et al. **Ultrasonography-guided core needle**

- biopsy for the thyroid nodule: does the procedure hold any benefit for the diagnosis when fine-needle aspiration cytology analysis shows inconclusive results?** *Br J Radiol* 2013;86:20130007 CrossRef Medline
6. Lee KH, Shin JH, Oh YL, et al. **Atypia of undetermined significance in thyroid fine-needle aspiration cytology: prediction of malignancy by US and comparison of methods for further management.** *Ann Surg Oncol* 2014;21:2326–31 CrossRef Medline
 7. Park KT, Ahn SH, Mo JH, et al. **Role of core needle biopsy and ultrasonographic finding in management of indeterminate thyroid nodules.** *Head Neck* 2011;33:160–65 CrossRef Medline
 8. Samir AE, Vij A, Seale MK, et al. **Ultrasound-guided percutaneous thyroid nodule core biopsy: clinical utility in patients with prior nondiagnostic fine-needle aspirate.** *Thyroid* 2012;22:461–67 CrossRef Medline
 9. Yeon JS, Baek JH, Lim HK, et al. **Thyroid nodules with initially nondiagnostic cytologic results: the role of core-needle biopsy.** *Radiology* 2013;268:274–80 CrossRef Medline
 10. Screaton NJ, Berman LH, Grant JW. **US-guided core-needle biopsy of the thyroid gland.** *Radiology* 2003;226:827–32 CrossRef Medline
 11. Rhee SJ, Hahn SY, Ko ES, et al. **Follicular variant of papillary thyroid carcinoma: distinct biologic behavior based on ultrasonographic features.** *Thyroid* 2014;24:683–88 CrossRef Medline
 12. Kim DW, Jung SJ, Eom JW, et al. **Color Doppler features of solid, round, isoechoic thyroid nodules without malignant sonographic features: a prospective cytopathological study.** *Thyroid* 2013;23:472–76 CrossRef Medline
 13. Yoon JH, Kim EK, Youk JH, et al. **Better understanding in the differentiation of thyroid follicular adenoma, follicular carcinoma, and follicular variant of papillary carcinoma: a retrospective study.** *Int J Endocrinol* 2014;2014:321595 CrossRef Medline
 14. Lee KH, Shin JH, Ko ES, et al. **Predictive factors of malignancy in patients with cytologically suspicious for Hürthle cell neoplasm of thyroid nodules.** *Int J Surg* 2013;11:898–902 CrossRef Medline
 15. Baloch ZW, Livolsi VA. **Follicular-patterned lesions of the thyroid: the bane of the pathologist.** *Am J Clin Pathol* 2002;117:143–50 CrossRef Medline
 16. Schreiner AM, Yang GC. **Adenomatoid nodules are the main cause for discrepant histology in 234 thyroid fine-needle aspirates reported as follicular neoplasm.** *Diagn Cytopathol* 2012;40:375–79 CrossRef Medline
 17. Moon WJ, Baek JH, Jung SL, et al; Korean Society of Thyroid Radiology (KSThR), Korean Society of Radiology. **Ultrasonography and the ultrasound-based management of thyroid nodules: consensus statement and recommendations.** *Korean J Radiol* 2011;12:1–14 CrossRef Medline
 18. Nasrollah N, Trimboli P, Guidobaldi L, et al. **Thin core biopsy should help to discriminate thyroid nodules cytologically classified as indeterminate: a new sampling technique.** *Endocrine* 2013;43:659–65 CrossRef Medline
 19. Na DG, Kim JH, Sung JY, et al. **Core-needle biopsy is more useful than repeat fine-needle aspiration in thyroid nodules read as nondiagnostic or atypia of undetermined significance by the Bethesda system for reporting thyroid cytopathology.** *Thyroid* 2012;22:468–75 CrossRef Medline
 20. Kim DS, Kim JH, Na DG, et al. **Sonographic features of follicular variant papillary thyroid carcinomas in comparison with conventional papillary thyroid carcinomas.** *J Ultrasound Med* 2009;28:1685–92 Medline
 21. Quinn SF, Nelson HA, Demlow TA. **Thyroid biopsies: fine-needle aspiration biopsy versus spring-activated core biopsy needle in 102 patients.** *J Vasc Interv Radiol* 1994;5:619–23 CrossRef Medline
 22. Taki S, Kakuda K, Kakuma K, et al. **Thyroid nodules: evaluation with US-guided core biopsy with an automated biopsy gun.** *Radiology* 1997;202:874–77 CrossRef Medline
 23. Zhang S, Ivanovic M, Nemcek AA Jr, et al. **Thin core needle biopsy crush preparations in conjunction with fine-needle aspiration for the evaluation of thyroid nodules: a complementary approach.** *Cancer* 2008;114:512–18 CrossRef Medline

Brain Region–Specific Degeneration with Disease Progression in Late Infantile Neuronal Ceroid Lipofuscinosis (CLN2 Disease)

J.P. Dyke, D. Sondhi, H.U. Voss, K. Yohay, C. Hollmann, D. Mancenido, S.M. Kaminsky, L.A. Heier, K.D. Rudser, B. Kosofsky, B.J. Casey, R.G. Crystal, and D. Ballon



ABSTRACT

BACKGROUND AND PURPOSE: Late infantile neuronal ceroid lipofuscinosis (CLN2 disease) is a uniformly fatal lysosomal storage disease resulting from mutations in the *CLN2* gene. Our hypothesis was that regional analysis of cortical brain degeneration may identify brain regions that are affected earliest and most severely by the disease.

MATERIALS AND METHODS: Fifty-two high-resolution 3T MR imaging datasets were prospectively acquired on 38 subjects with CLN2. A retrospective cohort of 52 disease-free children served as a control population. The FreeSurfer software suite was used for calculation of cortical thickness.

RESULTS: An increased rate of global cortical thinning in CLN2 versus control subjects was the primary finding in this study. Three distinct patterns were observed across brain regions. In the first, subjects with CLN2 exhibited differing rates of cortical thinning versus age. This was true in 22 and 26 of 34 regions in the left and right hemispheres, respectively, and was also clearly discernable when considering brain lobes as a whole and Brodmann regions. The second pattern exhibited a difference in thickness from healthy controls but with no discernable change with age (9 left hemispheres, 5 right hemispheres). In the third pattern, there was no difference in either the rate of cortical thinning or the mean cortical thickness between groups (3 left hemispheres, 3 right hemispheres).

CONCLUSIONS: This study demonstrates that CLN2 causes differential rates of degeneration across the brain. Anatomic and functional regions that degenerate sooner and more severely than others compared with those in healthy controls may offer targets for directed therapies. The information gained may also provide neurobiologic insights regarding the mechanisms underlying disease progression.

ABBREVIATION: NCLs = neuronal ceroid lipofuscinoses

The neuronal ceroid lipofuscinoses (NCLs) are the most common neurodegenerative diseases of childhood, affecting between 2 and 4 in 100,000 live births each year.^{1–4} NCLs are inher-

ited, and to date, more than a dozen genes with >430 causative mutations have been identified. While defects in lysosomal storage are a central feature of NCLs, recently the pathobiology has been determined to be more complex.^{5,6} The present study focuses on the late infantile form of CLN2 disease (classic CLN2 disease), which is an autosomal recessive disorder caused by mutations in the *CLN2* gene.⁷ *CLN2* is a 6.65-kb 13 exon gene mapped to chromosomal locus 11p15, and mutations result in a lack of production of tripeptidyl peptidase-1, a 46-kDa enzyme required by lysosomes for cleavage of N-terminal tripeptides from substrates.^{8–10} A deficiency of tripeptidyl peptidase-1 results in an accumulation of autofluorescent lipopigments in lysosomes known as lipofuscin.¹¹ Retinal endothelial cells and CNS neurons are particularly sensitive to this buildup of undegraded proteins, resulting in cell death.^{1,12,13} Disease onset begins at ages 2–4, and widespread neurodegeneration results in seizures, cognitive impairment, blindness, and a loss of motor skills.^{14,15} CLN2 disease is progressive and universally fatal, with death generally occurring by ages 8–12.¹⁶

Received April 8, 2015; accepted after revision November 30.

From the Departments of Radiology (J.P.D., H.U.V., L.A.H., D.B.), Genetic Medicine (D.S., C.H., D.M., S.M.K., R.G.C., D.B.), Pediatrics (K.Y., B.K.), and Psychiatry (B.J.C.), Weill Cornell Medical College, New York, New York; and Division of Biostatistics (K.D.R.), Clinical and Translational Science Institute, University of Minnesota, Minneapolis, Minnesota.

This work was supported in part by grants from the National Institutes of Health (R01NS061848, U54NS065768). The Lysosomal Disease Network (U54NS065768) is a part of the National Center for Advancing Translational Sciences Rare Diseases Clinical Research Network, an initiative of the Office of Rare Diseases Research, National Center for Advancing Translational Sciences, funded through a collaboration among the National Center for Advancing Translational Sciences, National Institute of Neurological Disorders and Stroke, and National Institute of Diabetes and Digestive and Kidney Diseases.

Please address correspondence to Jonathan P. Dyke, PhD, Department of Radiology, Weill Cornell Medical College, 1300 York Ave, Box 234, New York, NY 10021; e-mail: jpd2001@med.cornell.edu

Indicates open access to non-subscribers at www.ajnr.org

Indicates article with supplemental on-line tables.

<http://dx.doi.org/10.3174/ajnr.A4669>

Our previous work characterized whole-brain degeneration in CLN2 disease by using a scoring system derived from 3 MR imaging techniques.¹⁷ Specifically, principal component analysis was used to combine the apparent diffusion coefficient, percentage of CSF, and *N*-acetylaspartate creatine ratio into a single MR imaging disease severity score. While this resulted in a robust and objective measure of disease severity in the whole brain, it did not assess regional variations in the rate of progression of the disease. For the present work, our hypothesis was that CLN2 disease may affect specific cortical regions of the brain earlier and more severely than others.

Brodmann¹⁸ used neurohistologic methods to outline regions of the cerebral cortex on the basis of their distinct cytoarchitecture in 1909. However, it is only within the past 10–15 years that high-resolution (1 mm³) isotropic T1-weighted 3T MR images with sharp contrast between gray and white matter have become available to noninvasively measure individual cortical thicknesses. The cerebral cortex that composes the gray matter is a folded sheet of neurons and glia measuring from 2 to 4 mm in thickness with up to 6 functionally distinct layers. The thicknesses of both the entire cortex and individual layers vary nonuniformly throughout the brain.

Previously, outlining cortical gyri and sulci on images derived from MR imaging scans required many hours of labor-intensive manual tracing and experience. The advent of more advanced computer technology combined with MR image analysis tools such as FreeSurfer (<http://surfer.nmr.mgh.harvard.edu>) now allows nearly automated processing of cortical thickness and volume measures of gray and white matter.^{19,20} These techniques have been used to study neurodegeneration in other disease states.^{21–24} Our hypothesis was that these morphometric techniques would yield information on the regional progression of CLN2 disease. While it is well-known that CLN2 induces global cortical atrophy, we focused on identifying regional changes in cortical thickness that exhibited differential rates of degeneration as a function of age and associated disease severity. To distinguish pathologic processes from normal brain maturation, we compared changes in subjects with CLN2 with a normative control population.

MATERIALS AND METHODS

Study Population

This study was conducted under research protocols approved by the institutional review board at Weill Cornell Medical College. For subjects with CLN2 disease, both parents/guardians signed an informed consent for each subject. All were diagnosed both by disease phenotype and genetic analysis. Fifty-two MR imaging datasets were acquired from 38 subjects (2.5–8.4 years of age; median, 5.0 years; 13 males/25 females). Fourteen of these subjects were scanned at 2 time points as part of a separate therapeutic trial for CLN2, but all subjects were untreated at the time of the scans used for this study. All subjects were evaluated by 4 observers by using the Weill Cornell CLN2 Disease Severity Scale.¹⁵ The subjects' CLN2 scores (0–12 scale; 12 being unaffected) ranged from 1.5 to 11.0. To participate in this study, the subject's genotype included at least 1 of the 3 most common CLN2 mutations: C3670T (nonsense Arg207 to stop), G3556C (intron 7 splice), and

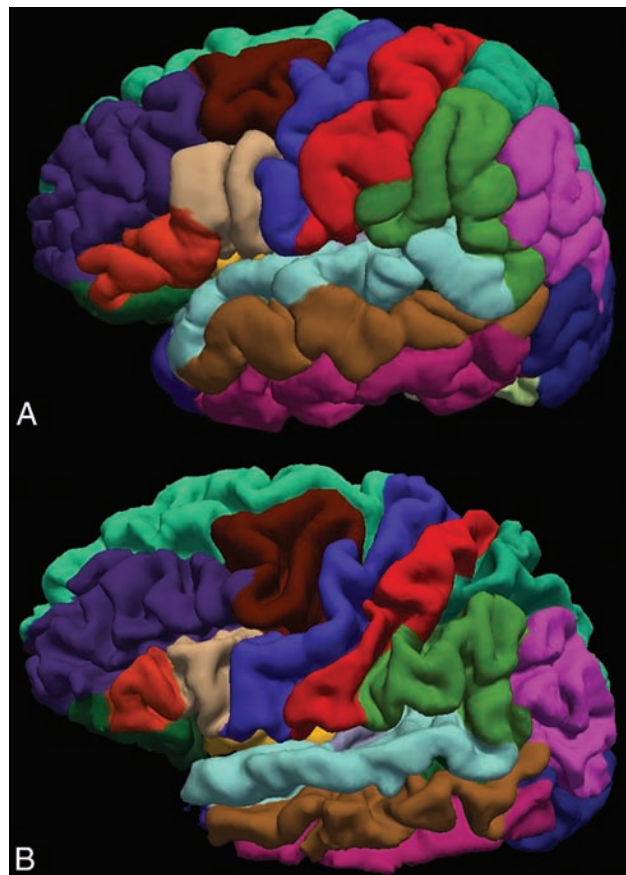


FIG 1. Surface representation of the FreeSurfer-based cortical parcellation for a control subject (A, 6.1 years of age) compared with that of an age-matched subject with CLN2 (B, 5.9 years of age; clinical CLN2 score = 1.5). Note the atrophy as evidenced by deeper sulci and less prominent gyri in the subject with more advanced disease.

G4655A (Cys365Tyr) (On-line Table 1). High-resolution T1-weighted imaging data were obtained retrospectively from a normative pediatric fMRI study provided by one of the authors (B.J.C.). For this healthy control group, 52 MR imaging datasets were acquired without anesthesia (4.8–12.0 years of age; median, 8.9 years; 24 males/28 females). Exclusion criteria stated that healthy subjects could not be born earlier than 36 weeks' gestational age or present with any diagnosis of neurologic or psychiatric disorders such as bipolar disorder, autism spectrum disorder, intellectual disability, or schizophrenia.

MR Imaging Techniques

All CLN2 imaging data were acquired by using a 3T HDx MR imaging system (GE Healthcare, Milwaukee, Wisconsin) with an 8-channel head resonator. A sagittal high-resolution isotropic 3D brain volume imaging gradient-echo pulse sequence was used to obtain optimal gray and white matter contrast. Isotropic 3D volumetric datasets were obtained at a spatial resolution of 1.0 × 1.0 × 1.0 mm with a 256 × 256 matrix, 160 sections, a TR of 12 ms, a TE of 5 ms, a TI of 450 ms, an acceleration factor of 2, a flip angle of 12°, and a bandwidth of 122 Hz/pixel. All imaging of subjects with CLN2 was performed with the patient under general anesthesia as prescribed by standard operating procedures within the Department of Anesthesiology at our institution.

Table 1: Cortical regions grouped by lobe as defined by the Desikan-Killiany atlas in FreeSurfer

Temporal Lobe	Parietal Lobe	Occipital Lobe	Cingulate Lobe	Frontal Lobe
Bankssts	Inferior parietal	Cuneus	Caudal anterior cingulate	Caudal middle frontal
Entorhinal	Postcentral	Lateral occipital	Isthmus cingulate	Frontal pole
Fusiform	Precuneus	Lingual	Posterior cingulate	Lateral orbitofrontal
Inferior temporal	Superior parietal	Pericalcarine	Rostral anterior cingulate	Medial orbitofrontal
Middle temporal	Supramarginal			Paracentral
Parahippocampal				Pars opercularis
Superior temporal				Pars orbitalis
Temporal pole				Pars triangularis
Transverse temporal				Precentral
				Rostral middle frontal
				Superior frontal

Note:—Bankssts indicates banks of the superior temporal sulcus.

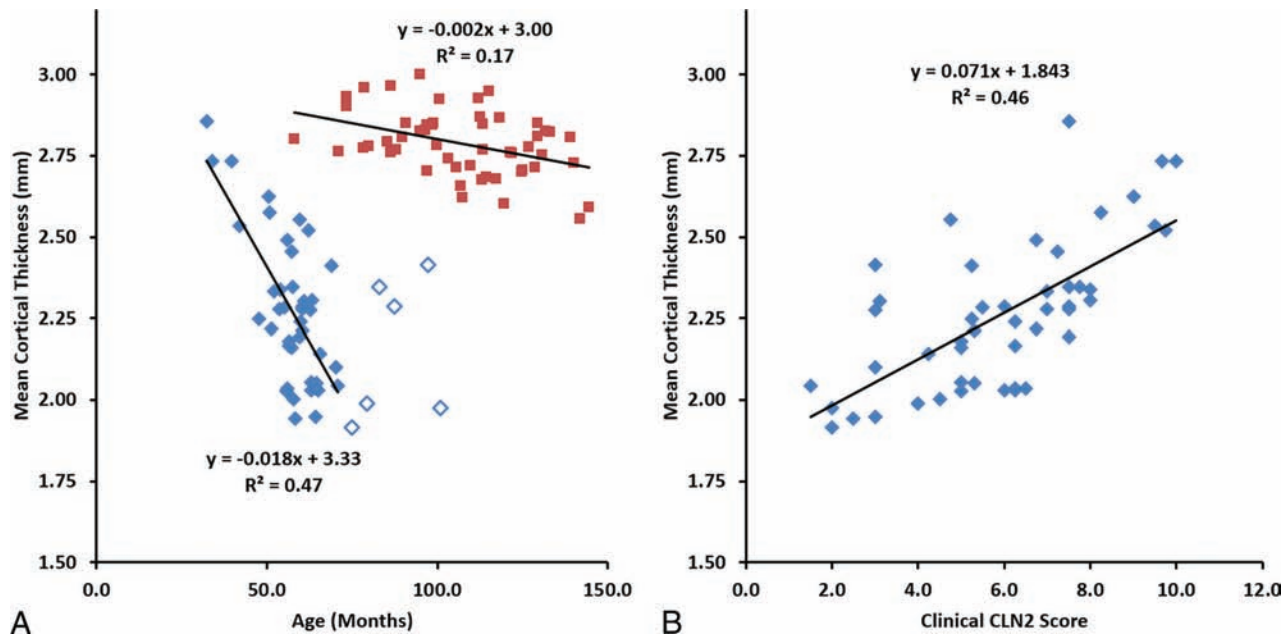


FIG 2. The mean cerebral cortical gray matter thickness as a function of subject age (A) and clinical score (B) for CLN2 (solid diamond) and control (large filled square) groups. Subjects with CLN2 older than 72 months of age (open diamond) are not included in the linear fit.

A magnetization-prepared rapid acquisition of gradient echo pulse sequence was used for 16 of the control subjects who were scanned on a 3T HDx MR imaging system (GE Healthcare). A spatial resolution of $0.94 \times 0.94 \times 1.5$ mm was achieved with a 256×192 matrix, 120 sections, TR/TE/TI of 8.3/1.7/725 ms, a flip angle of 7° , and a bandwidth of 122 Hz/pixel. An MPRAGE sequence was used for the remaining 36 control subjects by using a 12-channel head coil on a 3T Tim Trio MR imaging system (Siemens, Erlangen, Germany). A spatial resolution of $1.0 \times 1.0 \times 1.2$ mm was used with a 256×256 matrix, 160 sections, and TR/TE/TI of 2170/4.3/1100 ms with an acceleration factor of 2, a flip angle of 7° , and a bandwidth of 140 Hz/pixel. Note that the Siemens TR represents the time between slab excitations, while the GE protocol calculates the TR as the time duration between acquisitions of individual lines in *k*-space. As a result, the effective TR under this protocol was 8.5 ms.

The FreeSurfer software package was used to generate semi-automated parcellation of cortical structures from the high-resolution T1-weighted MR imaging series. FreeSurfer removes non-brain tissue, normalizes the image intensity, performs an automated Talairach transformation, and segments structures. It

corrects topology and surface deformations and identifies the gray/white matter boundary. The location of the greatest shift in intensity defines the transition between distinct tissue classes.²⁵ The skull stripping and cortical mapping were visually inspected for each subject by 2 authors (J.P.D., H.U.V.). Visualization of segmentation and cortical surface results was performed in multiple planes with output from the FreeSurfer QATools package (<http://surfer.nmr.mgh.harvard.edu/fswiki/QATools>). 3D surface renderings of cortical parcellations were also viewed to confirm correct labeling of the sulci and gyri (Fig 1). White matter control points were added, and the parcellation was rerun if white matter was underestimated in certain areas due to lower image intensity. Four CLN2 MR imaging scans displayed incorrect labeling of several cortical regions and were removed from analysis. FreeSurfer was run under a Linux environment with Version 20110522 (5.1.0) by using 8-CPU-cores. Thirty-three of 34 FreeSurfer-defined cortical regions were grouped into their respective cerebral lobes (frontal, $n = 11$; occipital, $n = 4$; parietal, $n = 5$; temporal, $n = 9$; cingulate gyrus, $n = 4$), according to their position in the Desikan-Killiany atlas (Table 1).²⁶ The remaining insula region is part of several lobes.

Table 2: The rate of decline (millimeters/month) and mean cortical thickness between CLN2 and healthy control populations in whole brain, hemispheres, and cerebral lobes

	CLN2 Slope	Control Slope	P Value	CLN2 Mean	Control Mean	P Value
Whole brain	-0.018(5)	-0.002(1)	<.001	2.26(23)	2.79(10)	<.001
LH	-0.016(5)	-0.002(1)	<.001	2.23(22)	2.78(10)	<.001
RH	-0.020(6)	-0.002(1)	<.001	2.29(24)	2.79(11)	<.001
LH cingulate	-0.018(8)	-0.003(2)	.002	2.69(32)	2.92(22)	<.001
LH frontal	-0.005(5)	-0.002(2)	.265	2.33(17)	2.87(12)	<.001
LH occipital	-0.026(10)	-0.004(3)	<.001	1.66(26)	2.16(19)	<.001
LH parietal	-0.021(5)	-0.002(1)	<.001	2.10(26)	2.71(13)	<.001
LH temporal	-0.023(4)	-0.002(3)	<.001	2.51(30)	2.99(19)	<.001
RH cingulate	-0.021(8)	-0.003(3)	<.001	2.69(40)	2.85(18)	<.001
RH frontal	-0.014(4)	-0.002(2)	<.001	2.41(21)	2.87(14)	<.001
RH occipital	-0.024(7)	-0.004(2)	<.001	1.68(24)	2.22(20)	<.001
RH parietal	-0.023(7)	-0.002(2)	<.001	2.16(27)	2.71(13)	<.001
RH temporal	-0.020(5)	-0.002(3)	<.001	2.61(28)	3.05(22)	<.001

Note:—LH indicates left hemisphere; RH, right hemisphere.

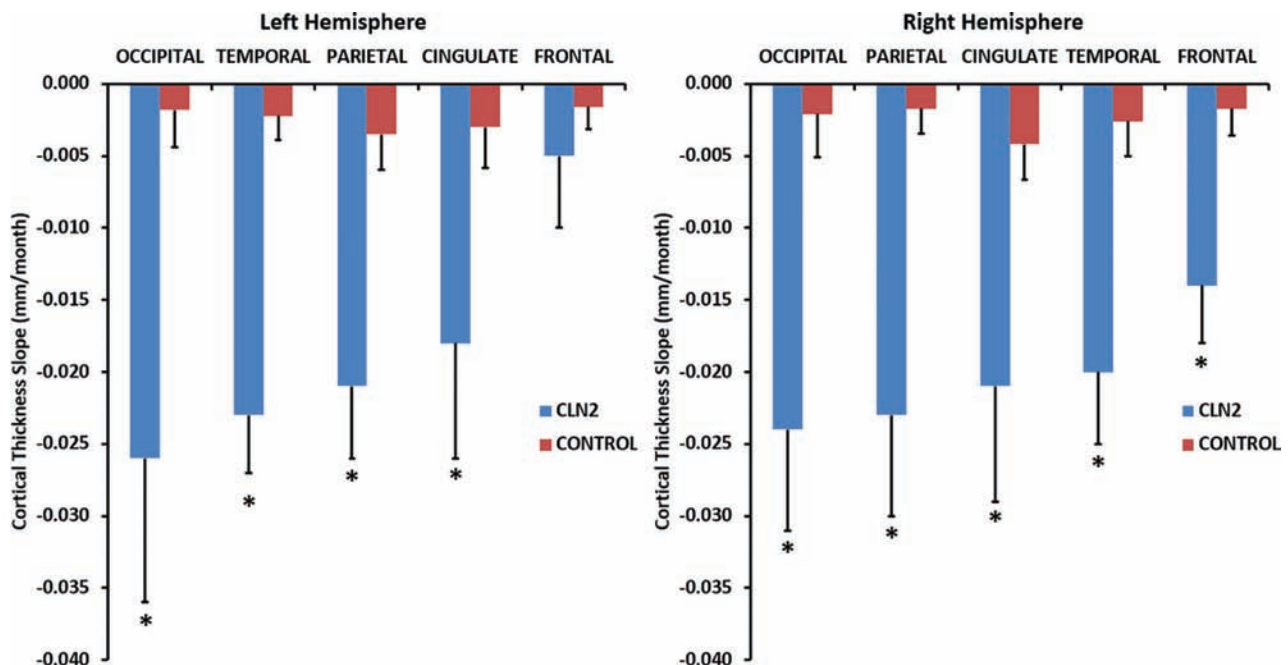


FIG 3. The rate of decline of cortical thickness with age for cerebral lobes in CLN2 ($n = 42$, blue) versus control ($n = 52$, red) groups. The 95% confidence interval of the slope is plotted as the error bar. Differences between CLN2 and control population of $P < .05$ are marked with an asterisk.

Statistical Methods

Group means of cortical thickness were evaluated by using linear regression with adjustment for age as follows:

$$1) \quad Y = m_1x_1 + m_2x_2 + b,$$

where Y represents the cortical thickness, x_1 is the subject age, and x_2 is a dichotomous variable representing the subject group (0 = control, $n = 52$; 1 = CLN2, $n = 48$). In Equation 1, m_2 represents the age-adjusted difference in the mean cortical thickness between the 2 groups. To account for any difference in the rates of decline in cortical thickness between the 2 groups, we added an interaction term:

$$2) \quad Y = m_1x_1 + m_2x_2 + m_3(x_1x_2) + b,$$

where the difference in the rate of decline is represented by m_3 . Subjects with CLN2 72 months and younger were used in estimating the slope or rate of cortical decline with time (42 MR imaging scans from 32 subjects). This estimation included a linear fit to the

cortical thickness versus age before the data became asymptotic in advanced stages of disease. To take into account the correlated nature of 2 measurements on the same subjects, we used generalized estimating equations with robust variance estimation for confidence intervals and interaction P values.²⁷ The time between measurements on the same subject varied across subjects. As such, a working independence correlation structure was used in conjunction with the robust variance estimate. Similarly, slopes across age for each group were estimated and compared by using generalized estimating equations with robust variance estimation. Multiple comparisons were addressed by using the Holm procedure within each of 7 groups of tests: global thickness of whole brain, lobes on the left and right sides each, subcortical substructures on the left and right sides each, and Brodmann areas on the left and right sides each.²⁸ $P < .05$ of adjusted P values from the Holm procedure was considered statistically significant after adjustment for multiple comparisons. All analyses were conducted

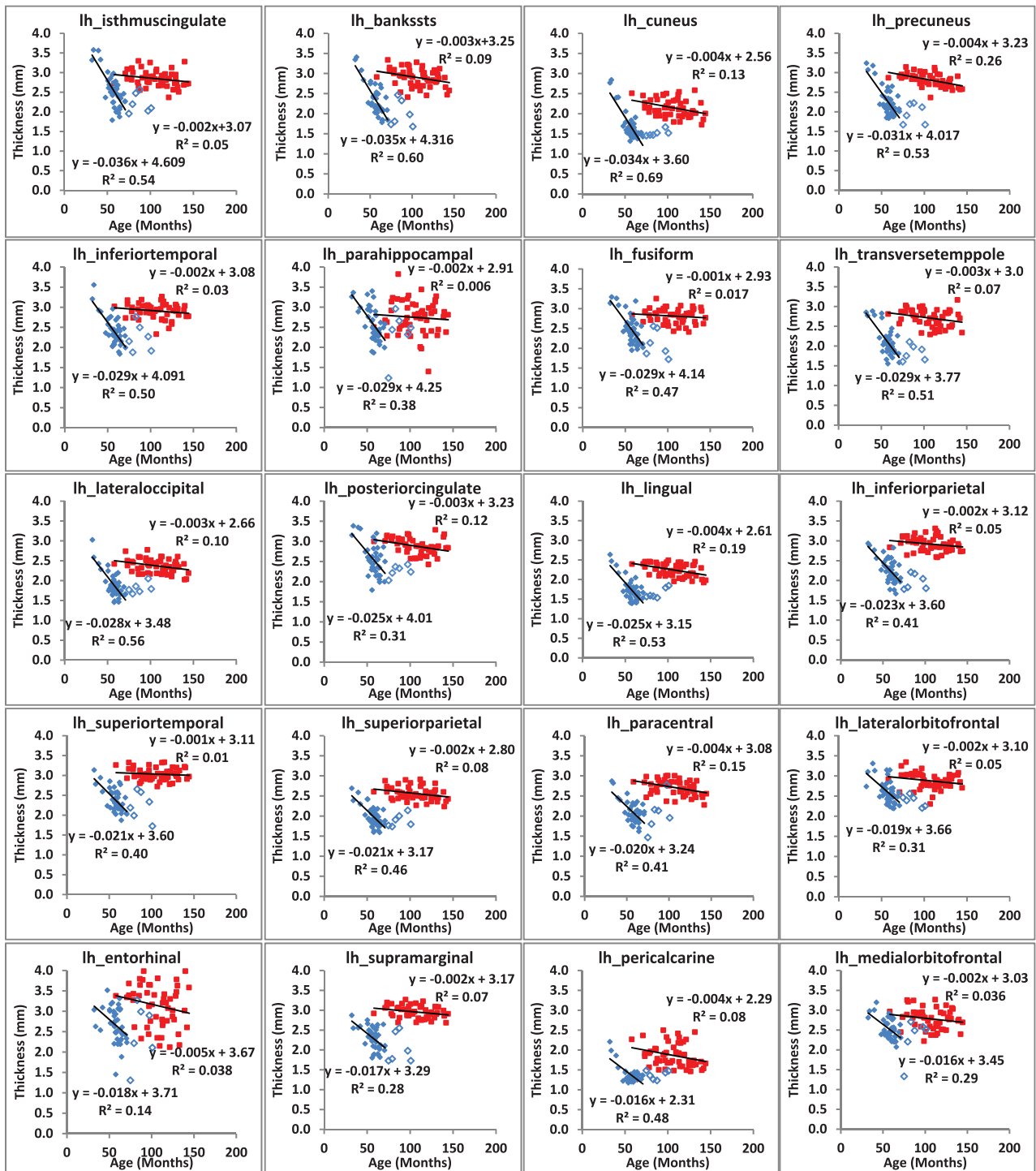


FIG 4. Regional changes in cortical thickness of the left hemisphere are plotted as a function of subject age for CLN2 (solid diamond) and control (large filled square) groups. Subjects with CLN2 older than 72 months of age (open diamond) are not included in the linear fit.

by using R statistical and computing software, Version 3.1.1 (<http://www.r-project.org/>).

RESULTS

A 3D surface representation of the FreeSurfer-based cerebral cortical parcellations of a control subject (A, 6.1 years of age) compared with that of an age-matched subject with CLN2 (B, 5.9 years of age; clinical CLN2 score, 1.5) shows distinct differences in the structure of the gyri and sulci (Fig 1). A greater degree of cortical

atrophy is apparent as the disease progresses, visualized by deeper sulci and less prominent gyri (compare A versus B). This impression was quantitatively validated by the significant differences in the decline of cortical thickness with age in CLN2 versus control groups of both the right and left hemispheres.

The change in cortical thickness with subject age for the whole brain showed a divergence between CLN2 ($n = 48$) and control ($n = 52$) groups [CLN2 slope = $-0.018(5)$ mm/month; control slope = $-0.002(1)$ mm/month, $P < .001$] (Fig 2A and Table 2),

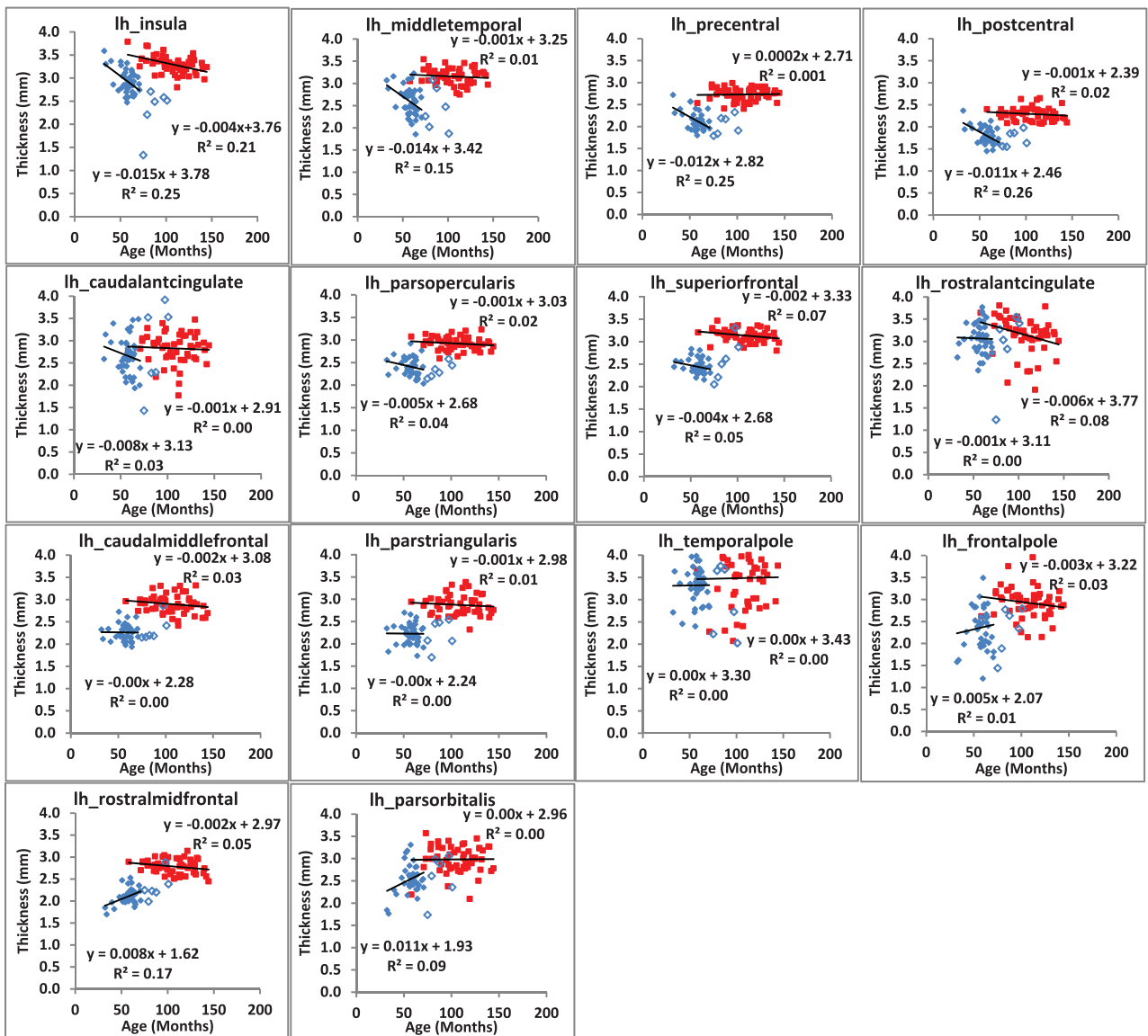


FIG 4. Continued.

with the CLN2 group thinning at a much faster rate. These changes were seen in both the left (LH) and right (RH) hemispheres, respectively: LH/RH CLN2 slope = $-0.016(5)/-0.020(6)$ mm/month versus control slope = $-0.002(1)$ mm/month, $P < .001$. This same trend of rapid degeneration was also seen when plotting cortical thickness versus the clinical CLN2 score (Fig 2B and Table 2). Thus, while there are individual differences in the age of onset of the disease, cortical thinning proceeds relentlessly with disease progression. The mean cortical thickness was also significantly less ($P < .001$) in the whole brain and left and right hemispheres in the subjects with CLN2 compared with those in the healthy control population (Table 2).

The cortical thickness was calculated for all regions ($n = 34$) separately and also was combined into specific Brodmann regions ($n = 12$) and cerebral lobes ($n = 5$) (Table 2 and On-line Tables 2–4). The mean thickness for each of the cerebral lobes was calculated as the average thickness of the regions composing that lobe. The rate of change of each of the 5 cerebral lobes of the left

and right hemispheres was plotted versus age for the CLN2 (age, 72 months and younger) and control groups in Fig 3. Cortical degeneration was significantly faster in 9 of 10 lobes (4 left and 5 right hemispheres) in the CLN2 versus control groups (Fig 3 and Table 2). The occipital, temporal, parietal, and cingulate lobes degenerated faster in both hemispheres of the CLN2 population compared with their respective lobes in the control group. The frontal lobe exhibited the slowest rate of degeneration in CLN2 and did not differ from the control group in the left hemisphere. The mean cortical thickness was significantly decreased ($P < .001$) in all lobes in subjects with CLN2 in both hemispheres compared with the control population.

The rate of change of cerebral cortical thickness with age was calculated for all regions ($n = 34$) of the brain in each hemisphere and exhibited 3 clear patterns (Figs 4 and 5). In the first, both the rate of change and mean thickness were different between subjects with CLN2 and controls (22 regions in the left hemisphere and 26 in the right hemisphere). In the second, there was no difference in the rate of change, but there was a difference in the mean cortical

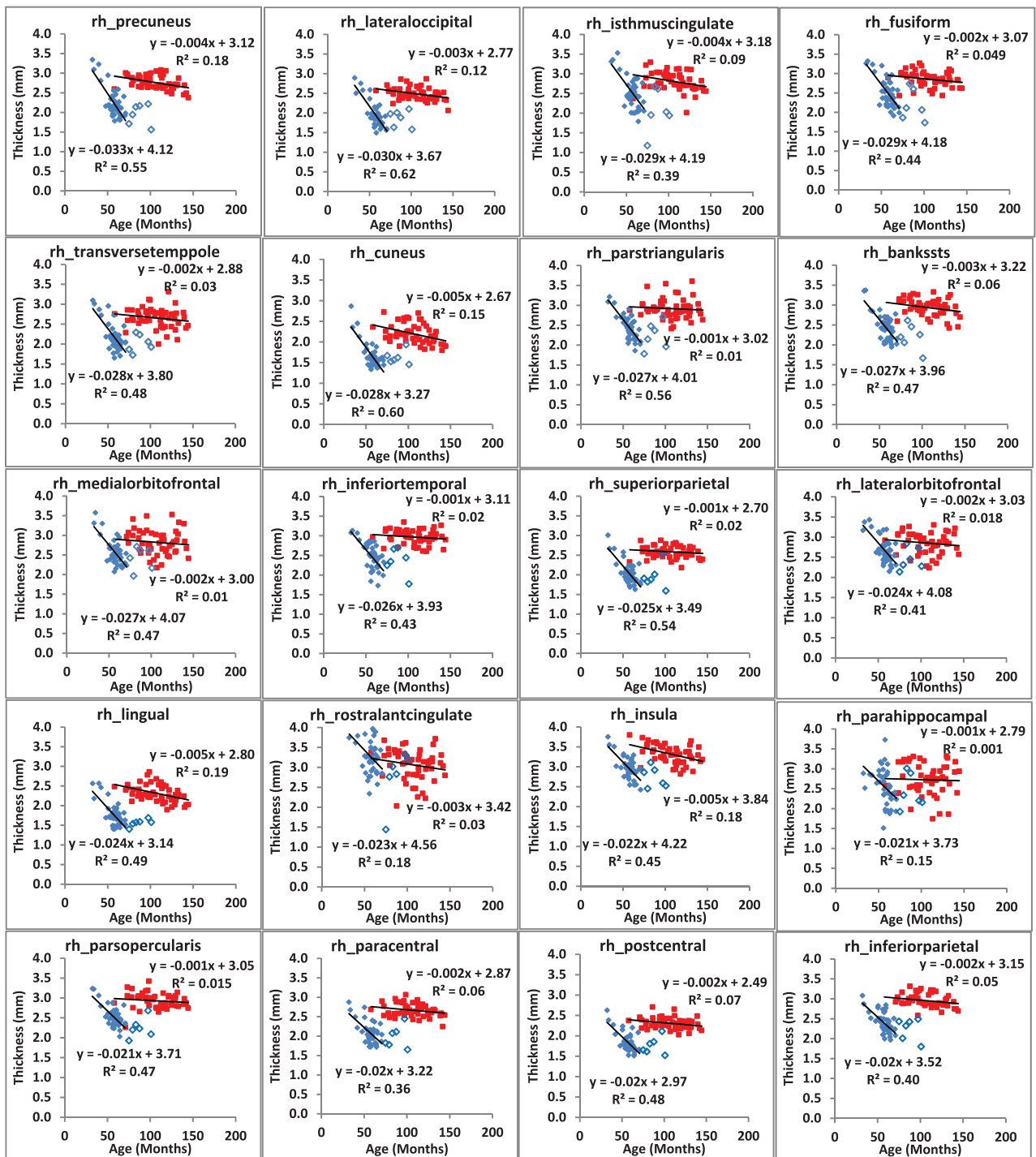


FIG 5. Regional changes in cortical thickness of the right hemisphere are plotted as a function of subject age for CLN2 (solid diamond) and control (large filled square) groups. Subjects with CLN2 older than 72 months of age (open diamond) are not included in the linear fit.

thickness (9 regions in the left hemisphere and 5 in the right hemisphere), and in the third, there was no difference in either the rate of cortical thinning or the mean cortical thickness (3 regions in the left hemisphere and 3 in the right hemisphere, On-line Table 2). Note that in cases in which there was a significant difference between the rate of cortical thinning between subjects with CLN2 and control subjects, a difference in the mean values of cortical thickness was certain. Similarly, there were no regions in which a significant rate of cortical thickness change was not accompanied

by a change in mean cortical thickness. Mean cortical thickness values in both hemispheres were different ($P < .001$) in all regions between subjects with CLN2 and controls except the caudal anterior cingulate, rostral anterior cingulate, and temporal pole. Specific Brodmann areas exhibited significant rates of decline (7 regions in the left hemisphere and 12 regions in the right hemisphere) ($P < .001$) (On-line Table 3). Mean cortical thickness values in both hemispheres showed significant differences from controls ($P < .001$) in all Brodmann regions.

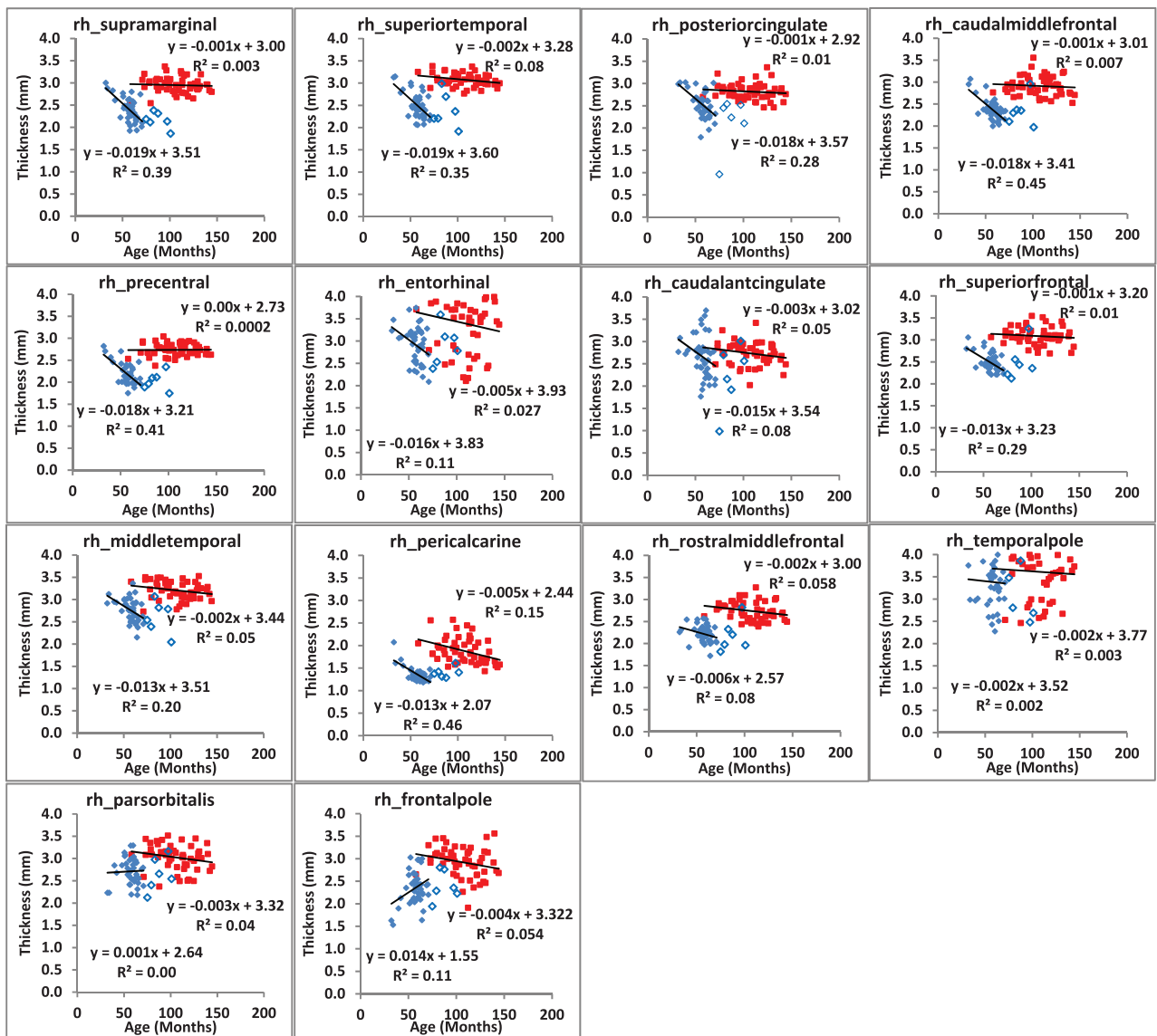


FIG 5. Continued.

DISCUSSION

The increased rate of global cortical thinning in CLN2 versus control subjects is a primary finding in this study. In addition, this quantitative human MR imaging study demonstrates differential rates of degeneration in the cerebral cortical thickness with the progression of CLN2. These rates were based on cross-sectional data from many subjects at different stages of disease and not longitudinal follow-up of individual subjects for a long time. Regions of most rapid degeneration in subjects with CLN2 with age were in the occipital, temporal, parietal, and cingulate lobes. Degeneration of the occipital lobe, which contains the visual processing center, was faster than in any other lobe. The effect of degeneration in this region and in specific Brodmann areas complements our previously published work demonstrating a direct correlation between decreased performance on an Ophthalmic Severity Scale and the Weill Cornell CLN2 Score.²⁹ In this context, impaired visual function in CLN2 may be, in part, the consequence of neuronal loss in the retina and thinning of the visual cortex.^{13,16} Most interesting,

the rate of frontal lobe degeneration was not significantly different between subjects with CLN2 and control populations in the left hemisphere. However, the mean cortical thickness was significantly reduced in all lobes of the subjects with CLN2 compared with controls.

It is essential to interpret degenerative changes in CLN2 in the context of results obtained from normally progressing pediatric control subjects. Although cortical thickness decreased in CLN2 with disease progression, a trend toward mild cortical thinning was also observed in normal pediatric aging. This trend is in concordance with several studies in the literature.³⁰⁻³² The underlying mechanism for cortical thinning in normal maturation is still being investigated. It is postulated that synaptic pruning allowing changes in plasticity to increase neuronal efficiency may play a role.³¹ It is also believed that increased myelination into the cortical periphery may account for gray matter thinning in pediatric controls and increased white matter structure in adults. Compared with controls, degenerative changes in cortical thickness in

the CLN2 population that we have reported are then specifically attributed to disease progression.

Variation in FreeSurfer cortical thickness measurements can arise from multiple sources when comparing data across platforms and institutions. In this study, the same FreeSurfer, Version 5.1.0, and a Linux operating system were used for processing of both CLN2 and control data. Studies have been performed to determine the reliability of these measures across various scanner platforms, pulse sequences, field strengths, and other differences.^{33,34} Our normative control population imaging in this study was acquired on both Siemens and GE Healthcare 3T platforms by using slightly different acquisition parameters for the MPRAGE sequence. However, no systematic difference in mean cortical thickness was observed in the healthy control population as a result of the scanner manufacturer.

CONCLUSIONS

Cortical degeneration in the brain occurs more rapidly in all lobes of subjects with CLN2 except the frontal lobe in the left hemisphere. The fact that CLN2 disease evidently affects specific cerebral lobes and cortical regions earlier and more rapidly than others may provide valuable information for enhanced diagnostic and future focal therapeutic strategies against this fatal disease. It may also provide neurobiologic insights regarding underlying mechanisms and clinical insights regarding deficits resulting from disease progression that may improve our understanding of CLN2 disease.

ACKNOWLEDGMENTS

We gratefully acknowledge aid from the following groups in recruiting subjects with CLN2 for this study: the Partnership for Cures Chicago Illinois, Nathan's Battle Foundation, Batten Disease Support and Research Association, Noah's Hope Foundation, and Hope 4 Bridget Foundation. The authors would also like to thank Dr Gary Glover of Stanford University for providing the research MPRAGE sequence for use on the GE Healthcare MR imaging platform.

Disclosures: Jonathan P. Dyke—RELATED: Grant: National Institutes of Health (U54NS065768).* Dolan Sondhi—RELATED: Grant: National Institutes of Health (R01NS061848, U54NS065768).* Kaleb Yohay—RELATED: Grant: National Institutes of Health (R01NS061848, U54NS065768)*; Support for Travel to Meetings for the Study or Other Purposes: National Institutes of Health (R01NS061848, U54NS065768).* Stephen M. Kaminsky—RELATED: Grant: National Institutes of Health (R01NS061848, U54NS065768)*; OTHER RELATIONSHIPS: I am part of the team for the clinical protocol for a gene therapy to treat the disease addressed in this article. Kyle D. Rudser—RELATED: Grant: National Institutes of Health (supported in part by award UL1TR000114 of the National Center for Advancing Translational Sciences).* Barry Kosofsky—RELATED: Grant: National Institute of Neurological Disorders and Stroke.* B.J. Casey—RELATED: Grant: National Institute on Drug Abuse (RC2 DA029475).* Douglas Ballon—RELATED: Grant: National Institutes of Health/National Institute of Neurological Disorders and Stroke (U54NS065768).* *Money paid to the institution.

REFERENCES

1. Boustany RM. **Batten disease or neuronal ceroid lipofuscinosis.** In: Moser HW, ed. *Handbook of Clinical Neurology.* Vol 22. New York: Elsevier; 1996:671–700
2. Haltia M. **The neuronal ceroid-lipofuscinoses: from past to present.** *Biochim Biophys Acta* 2006;1762:850–56 CrossRef Medline
3. Kohlschütter A, Schulz A. **Towards understanding the neuronal ceroid lipofuscinoses.** *Brain Dev* 2009;31:499–502 CrossRef Medline
4. Jalanko A, Braulke T. **Neuronal ceroid lipofuscinoses.** *Biochim Biophys Acta* 2009;1793:697–709 CrossRef Medline
5. Mole SE, Cotman SL. **Genetics of the neuronal ceroid lipofuscinoses (Batten disease).** *Biochim Biophys Acta* 2015;1852:2237–41 CrossRef Medline
6. Mole SE. NCL mutation and patient database. <http://www.ucl.ac.uk/ncl/mutation.shtml>. Accessed August 6, 2015
7. Schulz A, Kohlschütter A, Mink J, et al. **NCL diseases: clinical perspectives.** *Biochim Biophys Acta* 2013;1832:1801–06 CrossRef Medline
8. Chang M, Cooper BL, Davidson OP. **CLN2.** In: Mole S, Williams RE, Goebel HH, Mole S, eds. *The Neuronal Ceroid Lipofuscinoses (Batten Disease).* 2nd ed. Oxford: Oxford University Press; 2011:80–102
9. Vines DJ, Warburton MJ. **Classical late infantile neuronal ceroid lipofuscinosis fibroblasts are deficient in lysosomal tripeptidyl peptidase I.** *FEBS Lett* 1999;443:131–35 CrossRef Medline
10. Lin L, Sohar I, Lackland H, et al. **The human CLN2 protein/tripeptidyl-peptidase I is a serine protease that autoactivates at acidic pH.** *J Biol Chem* 2001;276:2249–55 CrossRef Medline
11. Gless P, Hasan M. **Lipofuscin in neuronal aging and diseases.** *Norm Pathol Anat (Stuttgart)* 1976;32:1–68
12. Mitchison HM, Lim MJ, Cooper JD. **Selectivity and types of cell death in the neuronal ceroid lipofuscinoses.** *Brain Pathol* 2004;14: 86–96 CrossRef Medline
13. Birch DG. **Retinal degeneration in retinitis pigmentosa and neuronal ceroid lipofuscinosis: an overview.** *Mol Genet Metab* 1999;66: 356–66 CrossRef Medline
14. Wisniewski KE, Kida E, Golabek AA, et al. **Neuronal ceroid lipofuscinoses: classification and diagnosis.** *Adv Genet* 2001;45: 1–34 CrossRef Medline
15. Worgall S, Kekatpure MV, Heier L, et al. **Neurological deterioration in late infantile neuronal ceroid lipofuscinosis.** *Neurol* 2007;69: 521–35 CrossRef Medline
16. NINDS. Batten Disease Fact Sheet. NIH Publication No. 11-2790. http://www.ninds.nih.gov/disorders/batten/detail_batten.htm. Accessed September 1, 2015
17. Dyke JP, Sondhi D, Voss HU, et al. **Assessment of disease severity in late infantile neuronal ceroid lipofuscinosis using multiparametric MR imaging.** *AJNR Am J Neuroradiol* 2013;34:884–89 CrossRef Medline
18. Brodmann K. *Vergleichende Lokalisationslehre der Grosshirnrinde.* Leipzig: J.A. Barth; 1909
19. Dale AM, Fischl B, Sereno MI. **Cortical surface-based analysis, I: segmentation and surface reconstruction.** *Neuroimage* 1999;9: 179–94 CrossRef Medline
20. Clarkon MJ, Cardoso MJ, Ridgway GR, et al. **A comparison of voxel and surface based cortical thickness estimation methods.** *Neuroimage* 2011;57:856–65 CrossRef Medline
21. Tillema JM, Marloes GM, Powels PJ, et al. **Volumetric MRI data correlate to disease severity in metachromatic leukodystrophy.** *Ann Clin Trans Neurol* 2015;2:932–40 CrossRef Medline
22. Pagonabarraga J, Corcuera-Solano I, Vives-Gilbert Y, et al. **Pattern of regional cortical thinning associated with cognitive deterioration in Parkinson's disease.** *PLoS One* 2013;8:e54980 CrossRef Medline
23. Rohrer JD, Warren JD, Modat M, et al. **Patterns of cortical thinning in the language variants of frontotemporal lobar degeneration.** *Neurology* 2009;72:1562–69 CrossRef Medline
24. Lebedeva A, Westman E, Lebedev AV, et al; Alzheimer's Disease Neuroimaging Initiative. **Structural brain changes associated with depressive symptoms in the elderly with Alzheimer's disease.** *Neurol Neurosurg Psychiatry* 2014;85:930–35 CrossRef Medline
25. Fischl B, Dale AM. **Measuring the thickness of the human cerebral cortex from magnetic resonance images.** *Proc Natl Acad Sci U S A* 2000;97:11050–55 Medline
26. Desikan RS, Ségonne F, Fischl B, et al. **An automated labeling**

- system for subdividing the human cerebral cortex on MRI scans into gyral based regions of interest. *Neuroimage* 2006;31:968–80 Medline
27. Diggle P, Heagerty P, Liang KY, et al. *Analysis of Longitudinal Data*. New York: Oxford University Press; 2002
 28. Holm S. A simple sequentially rejective multiple test procedure. *Scandinavian Journal of Statistics* 1979;6:65–70
 29. Orlin A, Sondhi D, Witmer MT, et al. Spectrum of ocular manifestations in CLN2-associated Batten (Jansky-Bielschowsky) disease correlate with advancing age and deteriorating neurological function. *PLoS One* 2013;8:e73128 CrossRef Medline
 30. Wierenga LM, Langen M, Oranje B, et al. Unique developmental trajectories of cortical thickness and surface area. *Neuroimage* 2014; 87:120–26 CrossRef Medline
 31. Muftuler LT, Davis EP, Buss C, et al. Cortical and subcortical changes in typically developing preadolescent children. *Brain Res* 2011;1399:15–24 CrossRef Medline
 32. Giedd JN, Blumenthal J, Jeffries NO, et al. Brain development during childhood and adolescence: a longitudinal MRI study. *Nat Neurosci* 1999;2:861–63 Medline
 33. Dickerson BC, Fenstermacher E, Salat DH, et al. Detection of cortical thickness correlates of cognitive performance: reliability across MRI scan sessions, scanners, and field strengths. *Neuroimage* 2008; 39:10–18 Medline
 34. Han X, Jovicich J, Salat D, et al. Reliability of MRI-derived measurements of human cerebral cortical thickness: the effects of field strength, scanner upgrade and manufacturer. *Neuroimage* 2006;32: 180–94 Medline

Differentiation of Speech Delay and Global Developmental Delay in Children Using DTI Tractography-Based Connectome

J.-W. Jeong, S. Sundaram, M.E. Behen, and H.T. Chugani



ABSTRACT

BACKGROUND AND PURPOSE: Pure speech delay is a common developmental disorder which, according to some estimates, affects 5%–8% of the population. Speech delay may not only be an isolated condition but also can be part of a broader condition such as global developmental delay. The present study investigated whether diffusion tensor imaging tractography-based connectome can differentiate global developmental delay from speech delay in young children.

MATERIALS AND METHODS: Twelve children with pure speech delay (39.1 ± 20.9 months of age, 9 boys), 14 children with global developmental delay (39.3 ± 18.2 months of age, 12 boys), and 10 children with typical development (38.5 ± 20.5 months of age, 7 boys) underwent 3T DTI. For each subject, whole-brain connectome analysis was performed by using 116 cortical ROIs. The following network metrics were measured at individual regions: strength (number of the shortest paths), efficiency (measures of global and local integration), cluster coefficient (a measure of local aggregation), and betweenness (a measure of centrality).

RESULTS: Compared with typical development, global and local efficiency were significantly reduced in both global developmental delay and speech delay ($P < .0001$). The nodal strength of the cognitive network is reduced in global developmental delay, whereas the nodal strength of the language network is reduced in speech delay. This finding resulted in a high accuracy of $>83\% \pm 4\%$ to discriminate global developmental delay from speech delay.

CONCLUSIONS: The network abnormalities identified in the present study may underlie the neurocognitive and behavioral consequences commonly identified in children with global developmental delay and speech delay. Further validation studies in larger samples are required.

ABBREVIATIONS: AAL = Automated Anatomical Labeling; GD = global developmental delay; ICA + BSM = independent component analysis with ball-stick model; IQ = intelligence quotient; SD = speech delay; TD = typical development

Global developmental delay (GD) is caused by a broad spectrum of etiologies that result in the impairment of multiple developmental domains such as language, motor function, cognition, social interaction, and activities of daily living.¹ Its prevalence is estimated to be 1%–3% in children younger than 5 years of age.¹ Children with isolated speech and language delay (SD)

represent a distinct group with specific impairment in the receptive and/or expressive language domains in the context of otherwise intact neurocognitive and social functioning. SD in children is a common condition, which, according to some estimates, affects 5%–8% of the population.^{2,3}

Even though speech and language are affected in both the GD and SD groups, the absence of additional abnormalities in other domains (ie, motor, daily living skills) characterizes the SD group. It is important to differentiate children with GD or SD into distinct subgroups as early as possible to provide accurate prognostic information and appropriate intervention.⁴ More important, direct developmental assessment by using psychometrics is often unreliable in young children, particularly those with developmental delay or impairment.^{5,6} Thus, new objective methods for potentially discriminating SD from GD in the first few years of life are needed to provide the most effective interventions in a timely manner.

Using noninvasive imaging approaches such as diffusion ten-

Received June 12, 2015; accepted after revision November 14.

From the Carman and Ann Adams Departments of Pediatrics (J.-W.J., S.S., M.E.B., H.T.C.) and Neurology (J.-W.J., S.S., M.E.B., H.T.C.), Wayne State University School of Medicine, Detroit, Michigan; and Translational Imaging Laboratory (J.-W.J., S.S., M.E.B., H.T.C.), Children's Hospital of Michigan, Detroit, Michigan.

This work was supported by grant R01-NS089659 to J.-W.J. from the National Institute of Neurological Disorders and Stroke.

Please address correspondence to Jeong-Won Jeong, PhD, Departments of Pediatrics and Neurology, Wayne State University School of Medicine, Translational Imaging Laboratory, Children's Hospital of Michigan, 3901 Beaubien St, Detroit, MI 48201; e-mail: jeongwon@pet.wayne.edu

Indicates open access to non-subscribers at www.ajnr.org

<http://dx.doi.org/10.3174/ajnr.A4662>

DTI tractography may provide critical clinical information and new insight into the neural basis of GD and SD. Conventional clinical MR imaging is typically unremarkable in most of these patients. Indeed, clinically used neuroimaging tools are of limited value in evaluating children with SD or GD except to rule out a lesional/structural etiology. Therefore, there is an urgent need to develop noninvasive neuroimaging approaches to improve our etiologic yield and understand the anatomic substrates of these disorders. With DTI tractography, it was found that a subset of children with GD showed poorly developed white matter tracts such as the arcuate fasciculus and inferior longitudinal fasciculus.⁷ In a subsequent tract-based morphometric study, it was further found that both diffusion and geometric properties of the arcuate fasciculus were abnormal in a subset of children with GD.⁸ In Angelman syndrome, a severe, syndromic form of GD, abnormalities were also found in multiple major cortical association tracts by using DTI tractography⁹ and Tract-Based Spatial Statistics (<http://fsl.fmrib.ox.ac.uk/fsl/fslwiki/TBSS>).¹⁰ Overall, white matter abnormalities in GD and other related neurodevelopmental disorders have been replicated by many studies.¹¹⁻¹³

The goal of this study was to investigate a DTI tool by using connectome analysis to refine white matter abnormalities in children with GD and SD. This tool models the human brain as a network or a graph represented by a collection of nodes (ie, cortical and subcortical regions) and links (ie, axonal fiber counts between nodes), which may provide a powerful way of examining the structural connections in specific brain networks and how these connectivity strengths are associated with specific functional phenotypes. To quantify the degree of connectivity strength in clinical DTI data that typically samples the molecular displacement of water diffusion at a lower angular resolution, a novel DTI tractography method, referred to as “independent component analysis with ball-stick model” (ICA + BSM)¹⁴ was recently developed. This method combines 2 complementary approaches, ICA and BSM, to isolate multiple fiber bundles in a single voxel: The first is ICA, to approximate fiber orientations of multiple cylindrical tensors existing in a local cluster, and the second is BSM, to refine the ICA-driven initial orientation of multiple cylindrical tensors mixed in a single voxel of a local cluster. The major advantage of ICA + BSM is that it isolates independently attenuated diffusion profiles from “neighboring voxels” to optimize initial guesses of multiple tensor orientations existing in a single voxel. The method has an outstanding accuracy to detect different white matter pathways associated with primary motor and language functions by resolving the crossing-fiber problem in clinical DTI data.^{15,16}

In this study, we used ICA + BSM tractography to determine whether abnormal connectivity patterns based on whole-brain connectome analysis can be used to improve the classification of young children with GD and SD. Several studies have noted that the volumes of the subcortical structures, including the hippocampus, correlated with intelligence quotient (IQ), which is a clinical measure defining the severity of GD.¹⁷⁻¹⁹ It seems likely that in children, poorly developed cortical/subcortical structures may exist and account for unrecognized distinctions between the subgroups of developmental delay (ie, GD versus pure SD). The present study presumes that the comprehensive evaluation by

using whole-brain connectome analysis may allow us to clearly differentiate patients with GD and SD from healthy controls. We hypothesized that compared with healthy controls, patients with GD or pure SD will both have significantly reduced efficiency in both long- and short-range axonal connections in their whole-brain network and that while children with SD will show localized cortical connectivity abnormalities centered on the frontotemporal language network, children with GD will show broader cortico-subcortical network abnormalities.

MATERIALS AND METHODS

Subjects

Fourteen children with significant global developmental delay defined by impaired global cognition (IQ < 70) and adaptive behavioral functioning impaired in at least 2 developmental domains (gross/fine motor, speech/language, daily living skills, and socialization skills) were recruited for the GD group (39.3 ± 18.2 months of age, 12 boys). In addition, 12 children with isolated speech and language delay, defined by intact global cognition and measured language functioning in the impaired range (expressive and/or receptive language score of <70) and measured adaptive behavior measured within normal limits in daily living, socialization, and motor skills were recruited for the SD group (39.1 ± 20.9 months of age, 9 boys). Ten typically developing (TD) children, defined by measured global cognition, language, and adaptive behavior (communication, daily living, socialization, motor) skills within normal limits (standard score of ≥85) were recruited for healthy controls (38.5 ± 20.5 months of age, 7 boys). These children were recruited from the local area by an active community outreach effort.

Two-sample *t* tests showed that all 3 groups did not differ on age ($P > .42$) or sex ($P > .37$). For each group, we applied the following exclusion criteria: 1) history of seizures, 2) history of prematurity or a perinatal hypoxic-ischemic event, 3) focal deficits on clinical examination by a pediatric neurologist, 4) dysmorphic features suggestive of a clinical syndrome, 5) diagnosis of an autism spectrum disorder or attention deficit/hyperactivity disorder, 6) MR imaging findings interpreted as abnormal by a pediatric neuroradiologist, 7) comparative genomic hybridization microarray and/or Fragile X tests positive, 8) an inborn error of metabolism, 9) history of maltreatment, 10) being bilingual, and 11) being left-handed.

The present study was approved by institutional review board of the university, and written informed consent was obtained from all parents/guardians.

Data Acquisition

All MR imaging scans were obtained on a 3T Signa scanner (GE Healthcare, Milwaukee, Wisconsin) equipped with an 8-channel head coil and an array spatial sensitivity encoding technique. DTI was acquired with a multisection single-shot diffusion-weighted echo-planar imaging sequence at TR = 12,500 ms, TE = 88.7 ms, FOV = 24 cm, 128 × 128 acquisition matrix, contiguous 3-mm thickness to cover entire axial sections of the whole brain by using 55 isotropic gradient directions with $b=1000$ s/mm², $b=0$ acquisition, and NEX = 1. This DTI scan takes about 11 minutes. For anatomic reference, a 3D fast spoiled gradient-echo sequence

was acquired for each participant at TR/TE/TI of 9.12/3.66/400 ms, section thickness of 1.2 mm, and planar resolution of $0.94 \times 0.94 \text{ mm}^2$, which takes approximately 3 minutes. Because the scans for children with GD and SD were clinical MR imaging studies, sedation was used as necessary by the sedation team. None of children with TD were sedated for the MR imaging. They were scanned while sleeping and were monitored for movement during scanning. If there was significant movement, the MR imaging was not used in the present study.

Data Processing

For each subject, an ICA+BSM tractography¹⁴ was applied for whole-brain tractography to avoid the intravoxel crossing-fiber problem and to isolate up to the orientations of 3 crossing-fiber bundles at every voxel. Before performing ICA+BSM tractography analysis for the structural connectivity, the National Institutes of Health TORTOISE package (<https://science.nichd.nih.gov/confluence/display/nihpd/TORTOISE>) was used to correct motion artifacts in the DTI data. Whole-brain streamline tractography was then performed by using ICA+BSM to reconstruct up to 3 crossing streamlines by applying 30 randomized seeding points at every voxel of fractional anisotropy of >0.20 . The first eigenvectors of the stick components having a fractional ratio of >0.05 were considered as the reconstructed fiber orientations and were then used for the streamline tractography at step size = 0.2 voxel width, turning angle threshold = 60° , and maximal length = 250 mm.

For the connectome analysis, 116 cortical regions (or nodes) of interest were generated by fitting a deformable template of the Automated Anatomical Labeling atlas (AAL, <http://www.cyceron.fr/index.php/en/plateforme-en/freeware>), resulting in 116×116 connectivity matrices in which the elements quantify the pair-wise connectivity scores (ie, streamline tract numbers connecting any 2 given cortical regions normalized by the corresponding tract mean lengths). The SPM8 Diffeomorphic Anatomical Registration Through Exponentiated Lie Algebra approach (<http://www.fil.ion.ucl.ac.uk/spm/software/spm12>) was used to obtain an optimal non-linear deformation to warp the AAL template to individual subjects.

One-way ANOVA followed by the Benjamini and Hochberg procedure²⁰ for multiple comparisons was applied to identify pairs of AAL regions showing significantly altered connectivity between 2 groups (TD versus GD, TD versus SD, and GD versus SD). For each of 3 between-group comparisons, the ANOVA was initially applied at each element of the upper triangular part of the 116×116 connectivity matrix to test the null hypothesis of equality in the mean value of connectivity score between groups (dependent variable: score; factor: group; covariate: age). Subsequently, the regions were combined to 6 bilateral anatomic regions (ie, frontal, temporal, parietal, occipital, cerebellum, and subcortical) to reduce the number of comparisons. The Benjamini and Hochberg procedure²⁰ was used to adjust independent P values of these regions to control the false discovery rate for multiple comparisons ($\alpha = .05$). In addition, the whole-brain false discovery rate connectome analysis by using the Network Based Statistic toolbox (<https://sites.google.com/site/bctnet/comparison/nbs>) was applied independently to determine statistical reproducibility.

For the subsequent analysis identifying specific regions with atypically altered connectivity patterns, single-subject connectivity matrices were first binarized by thresholding entire connectivity scores, whereby we only considered the existence/absence of fiber pathways (ie, the elements were considered as one if their scores were $>5\%$ of the maximal score and as zero otherwise). The proportional thresholding of 5% was heuristically selected to minimize the variances of the network metrics used in the TD group. This was performed to ensure that between-group differences reflect alterations in network organization rather than differences in absolute connectivity. The Brain Connectivity Toolbox (<https://sites.google.com/site/bctnet>) was then applied to the binary matrix to assess the following network metrics: nodal strength (the sum of links connected to the node measuring local connectivity at individual nodes), global efficiency (the average of the inverse of the shortest path lengths in the whole-brain measuring the ability of the whole-brain network for parallel information transfer), local efficiency (the inverse of the average shortest path connecting the given node with all other nodes measuring the efficiency of a given node in communicating with the rest of the nodes), cluster coefficient (the fraction of triangular links around a node measuring local aggregation at individual nodes), and betweenness (the number of all shortest paths at individual nodes measuring the importance of the node). In each of the metrics, 1-way ANOVA for the linear model (dependent variable: metric; factor: group; covariate: age) was used to assess the significance of between-group differences at each of 116 AAL regions.

Finally, a support vector machine approach²¹ was used to differentiate GD and SD by using each of the metrics, in which a grid search approach was adopted to optimize the radial basis function of each metric by using “training samples.” The optimized radial basis function was then used to classify the “testing samples.” The differentiation performance was validated by using conventional “hold-out” cross-validation—that is, in each trial, half of the entire sample in GD and SD was randomly selected as “training instances” and rest of the sample was used as “testing instances” to evaluate 3 performance measures of that trial (ie, accuracy, sensitivity, and specificity). A total of 10,000 trials were repeated in which the performance measures of each trial were averaged to assess overall performance. In addition, the permutation test was applied to evaluate the probability of getting accuracy values higher than the ones obtained during the cross-validation procedure by chance. We permuted the group labels 10,000 times without replacement, each time randomly assigning GD and SD labels to individual subjects, and we repeated the cross-validation procedure. The number of times the accuracy of the permuted labels was higher than that obtained for the real labels was reported in P values.

RESULTS

In the comparison between the TD and GD groups (Fig 1), it was observed that the TD group showed increased pair-wise connectivity ($P < .05$), leading to significantly increased node strength and/or efficiency in the bilateral hippocampi ($F > 14.44$, $P < .001$), bilateral caudate/putamen/globus pallidus/thalamus ($F > 6.52$, $P < .02$), left rectus ($F = 7.82$, $P = .01$), left inferior temporal ($F > 7.82$, $P < .01$), left postcentral ($F > 6.52$, $P < .02$), left insular ($F > 6.52$, $P < .02$), left superior parietal ($F = 6.52$, $P = .02$), left calcarine ($F = 15.24$, $P < .001$), left cuneus ($F > 13.21$, $P < .003$),

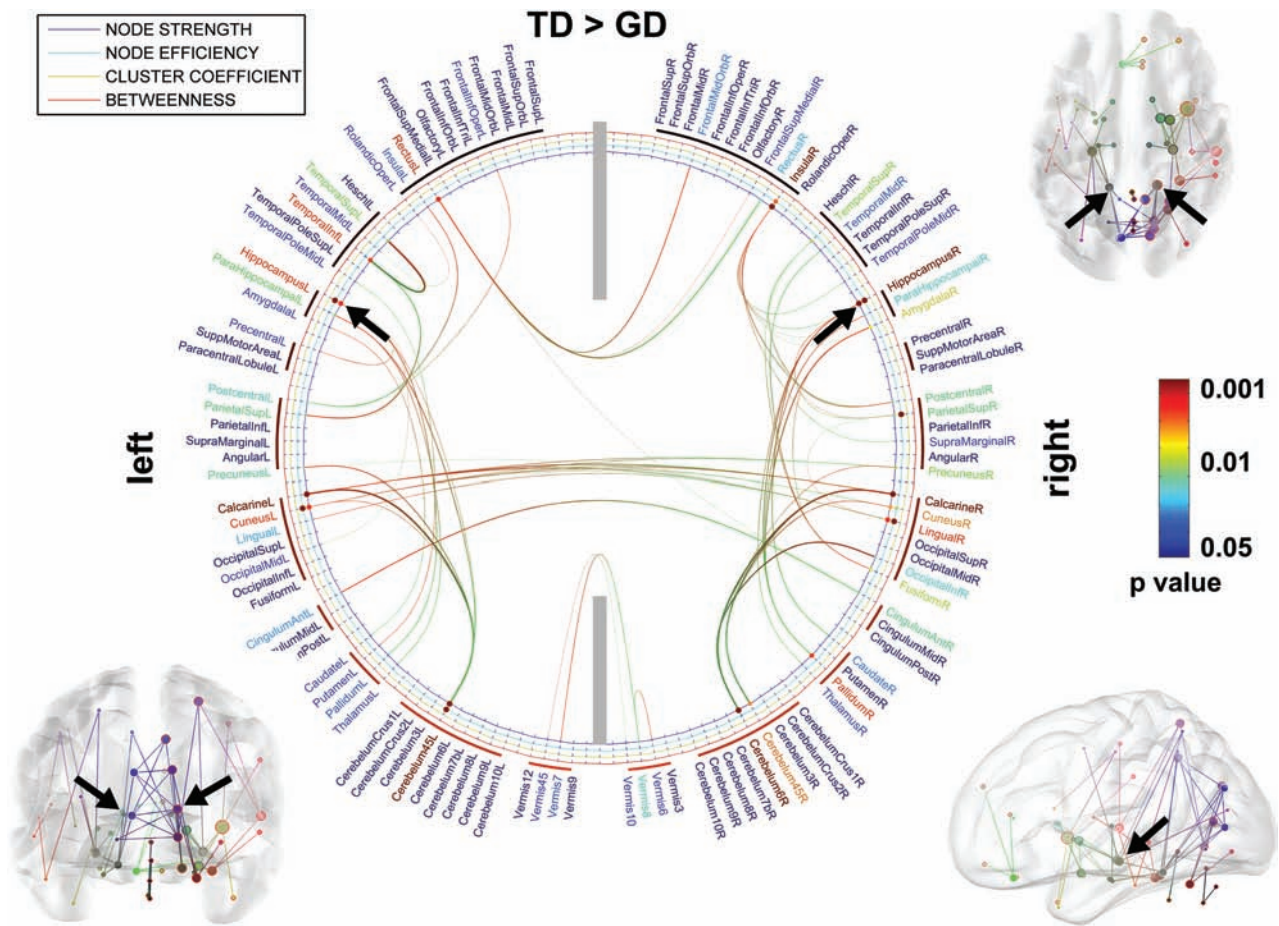


FIG 1. ROIs showing significantly altered network metrics in the group comparison of TD > GD. In the 2D connectogram, the color of anatomic label scales the *P* value of group difference in the AAL template. Similarly, the color of each circle represents the *P* value of individual metrics. The 3D connectogram shows individual pair-wise pathways having significant group differences in nodal strength (ie, the greater radius of the sphere, the greater the group difference). In both 2D and 3D connectograms, *block arrows* indicate the hippocampal network whose nodal properties are significantly reduced in GD compared with TD.

left cerebellum 4, 5 ($F > 13.89$, $P < .002$), right superior parietal ($F > 6.51$, $P < .02$), right insular ($F > 13.93$, $P < .003$), right calcarine ($F = 14.82$, $P < .001$), right cuneus ($F = 7.92$, $P = .008$), right lingual ($F = 14.01$, $P < .005$), right fusiform ($F = 6.49$, $P = .02$), and right cerebellum 4, 5, 6 ($F > 7.81$, $P < .01$). Compared with other regions such as the calcarine, cuneus, and cerebellum, the hippocampus (marked by black arrows) has more short paths to adjacent neighbors, including the parahippocampus, caudate, putamen, thalamus, and pallidum, suggesting its higher modular connectivity to detect sparse axonal connections in the GD group.

Figure 2 presents the comparison of the TD and SD groups. Compared with the SD group, the TD group shows increased pair-wise connectivity ($P < .05$), resulting in significantly increased node strength, efficiency, and/or clustering coefficient in the bilateral superior temporal ($F > 14.91$, $P < .001$), bilateral midtemporal pole ($F = 6.32$, $P < .01$), bilateral insular ($F > 6.35$, $P < .01$), bilateral midfrontal ($F > 6.29$, $P < .01$), bilateral calcarine ($F > 14.89$, $P < .001$), bilateral inferior orbitofrontal ($F > 6.26$, $P < .01$), bilateral inferior temporal ($F > 5.01$, $P < .03$), left rectus ($F > 6.20$, $P < .01$), left superior temporal ($F > 11.23$, $P < .005$), left cuneus ($F > 11.14$, $P < .005$), left anterior cingulum ($F > 10.13$, $P < .008$), left amygdala ($F = 5.73$, $P = .02$), left pallidum ($F = 5.71$, $P = .02$), left cerebellum 4, 5 ($F > 11.21$, $P < .005$), right midorbitofrontal ($F > 10.62$, $P < .006$), right inferior frontal triangularis ($F > 5.12$, $P < .03$), right superior temporal pole ($F > 15.24$, $P < .001$), right rolandic operculum ($F > 5.62$, $P = .02$), right postcentral ($F = 10.67$, $P = .006$), right superior parietal ($F > 6.28$, $P < .01$), right supramarginal ($F > 5.81$, $P < .02$), right precuneus ($F > 15.11$, $P < .001$), right calcarine ($F > 15.10$, $P < .001$), right cuneus ($F = 5.89$, $P = .02$), right inferior occipital ($F = 5.85$, $P = .02$), right anterior cingulum ($F = 10.66$, $P = .006$), right midcingulum ($F > 11.01$, $P < .005$), and right cerebellum 4, 5, 6 ($F > 5.78$, $P < .02$). A frontotemporal language network having increased axonal connections at the left midfrontal and left superior temporal gyrus was apparently distinctive in this comparison (indicated by black arrows).

In the comparison of the SD and GD groups (Fig 3), we found that compared with the GD group, the SD group had increased node strength, efficiency, and/or cluster coefficient in both hemispheres, hippocampus ($F > 6.26$, $P < .02$), parahippocampal ($F = 6.25$, $P < .02$), superior frontal ($F > 10.23$, $P < .004$), midfrontal ($F > 6.29$, $P < .02$), inferior frontal triangularis ($F > 6.26$, $P < .02$), superior medial frontal ($F > 6.28$, $P < .02$), insular ($F > 6.38$, $P < .02$), superior temporal ($F > 5.01$, $P < .03$), midtemporal ($F > 6.26$, $P < .02$), inferior temporal ($F > 6.29$, $P < .02$), caudate/putamen/pallidum/

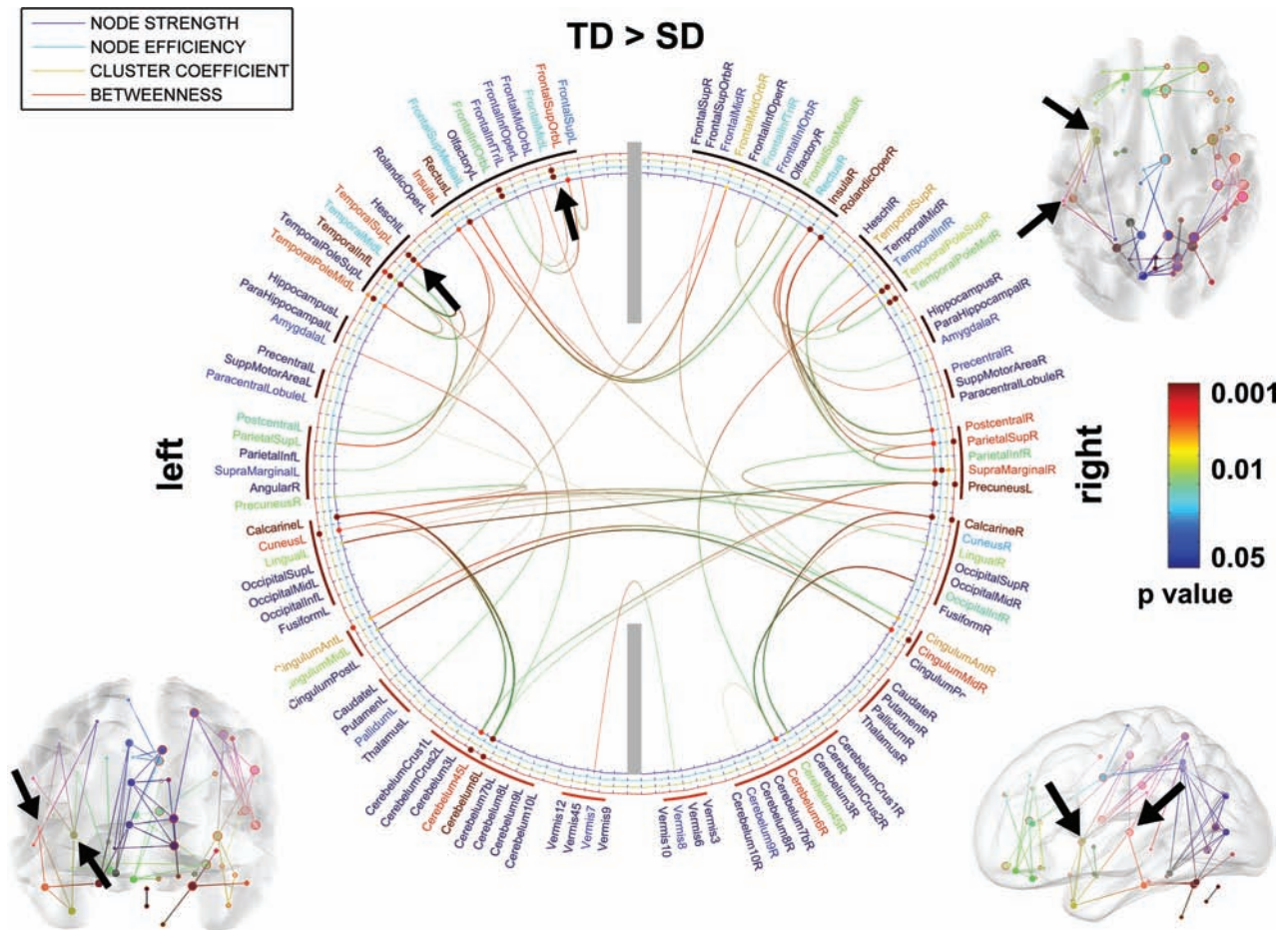


FIG 2. ROIs showing significantly altered network metrics in the group comparison of TD > SD. In the 2D connectogram, the color of anatomic label scales the *P* value of group difference in the AAL template. Similarly, the color of each circle represents the *P* value of individual metrics. The 3D connectogram shows individual pair-wise pathways having significant group differences in nodal strength (ie, the greater the radius of the sphere, the greater the group difference). In both 2D and 3D connectograms, *block arrows* indicate the frontotemporal language network in which nodal properties are significantly reduced in SD compared with TD.

thalamus ($F > 6.89$, $P < .01$), anterior and midcingulum ($F > 6.91$, $P < .01$), precentral/inferior parietal/supramarginal/angular ($F > 6.25$, $P < .02$), precuneus ($F > 14.99$, $P < .001$), calcarine and cuneus ($F > 15.21$, $P < .001$), lingual ($F > 9.67$, $P < .005$), fusiform ($F = 9.69$, $P = .005$), cerebellum crus 1, 2 ($F > 6.27$, $P < .02$), and cerebellum 6 and 8 ($F > 6.28$, $P < .02$). Sparser local connections are apparent in the bilateral hippocampal networks of the GD group but are more severe at the right hippocampus as indicated by black arrows.

No significant differences were observed at $P < .05$ for other group contrasts such as GD > TD, SD > TD, and GD > SD.

In Figs 1 and 2, we found that compared with the TD group, both the SD and GD groups showed significantly reduced inter-/intra-hemispheric connections in the calcarine gyrus, lingual gyrus, rectal gyrus, superior frontal gyrus, and cerebellum, resulting in significantly impaired axonal efficiency (both global and local efficiency) in long- and short-range whole-brain connections ($P < .001$, Fig 4). The Network Based Statistic toolbox could replicate our findings at a small number of permutations (≤ 500), which reflects the lower power of the nonparametric permutation test.

The subsequent support vector machine analysis by using

leave-one-out cross-validation revealed that the nodal strengths of 3 regions, bilateral hippocampi, left frontal language (mid-/superior frontal gyrus and insular), and left temporal language (superior temporal gyrus), have significant group differences between SD and GD ($P < .01$, Fig 5) and achieved a high accuracy of $>83\% \pm 4\%$ to discriminate GD from SD (Table). The other 3 measures, including nodal efficiency, clustering coefficient, and betweenness, had relatively lower statistical significance compared with the nodal strength.

DISCUSSION

In the present study, we found that global and local efficiency were significantly reduced in GD and SD. However, the nodal strengths of cognitive/language networks are differentially reduced between children with SD and those with GD. The GD group showed abnormal connectivity centered around the bilateral hippocampal network, whereas the left frontotemporal network was abnormal in the SD group. These abnormalities may represent the neuro-cognitive and behavioral features commonly identified in these children and allow subjects with SD to be distinguished from those with GD on the basis of objective parameters at a very young age when differentiation between these 2 conditions is usually

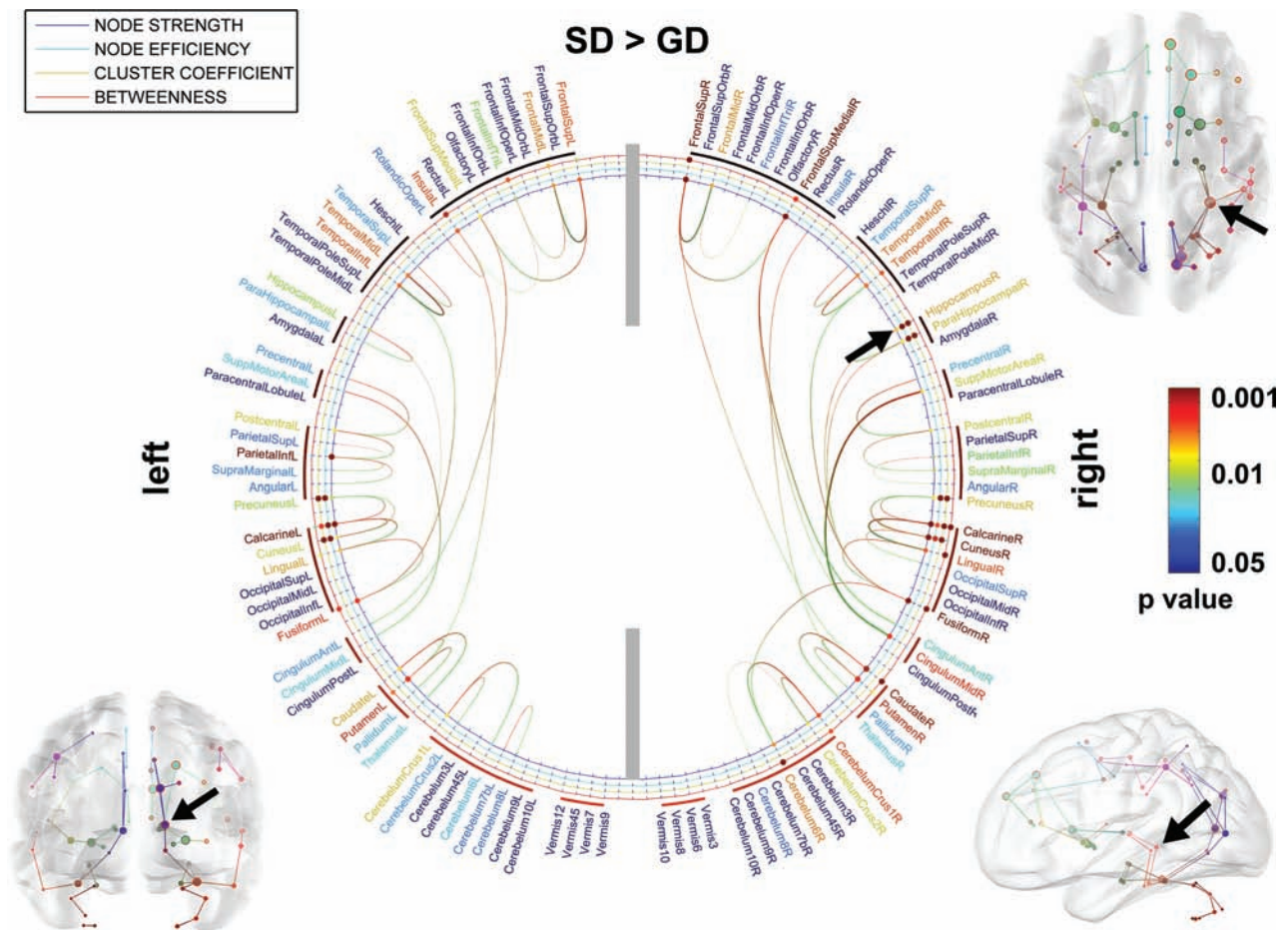


FIG 3. ROIs showing significantly altered network metrics in the group comparison of SD > GD. In the 2D connectogram, the color of anatomic label scales the *P* value of the group difference in the AAL template. Similarly, the color of each circle represents the *P* value of individual metrics. The 3D connectogram shows individual pair-wise pathways having significant group differences in nodal strength (ie, the greater the radius of the sphere, the greater the group difference). In both 2D and 3D connectograms, *block arrows* indicate the right hippocampus whose nodal properties are significantly reduced in GD compared with SD.

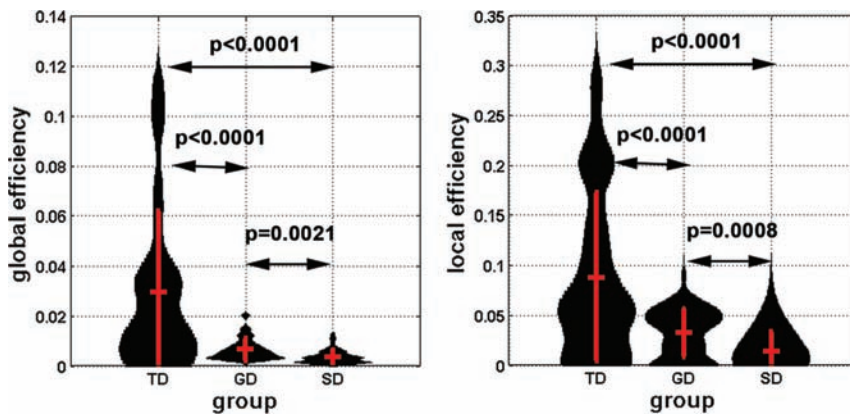


FIG 4. Global and local efficiency of the whole-brain network was obtained from individual subjects and is presented in the violin plots. Group mean and 1 SD are represented by *red vertical lines*. The *black curve* of each violin indicates the probabilistic attenuation function of the measure. To avoid the effect of arbitrary thresholding, we calculated the values of efficiencies at 3 discrete thresholds (5, 7, 10) of pair-wise connectivity scores of individual subjects to minimize the potential confounding across subjects.

difficult in the clinical setting. Furthermore, the present approach may encourage translation of advanced DTI techniques (ICA+BSM tractography effective for short-acquisition-time DTI) to clinical practice in the pediatric population, in which

currently available approaches are sub-optimal for whole-brain connectome analysis.

The anatomic basis of IQ, a measure defining the severity of GD, has been previously studied by neuroimaging techniques. On the basis of a review of 37 functional neuroimaging studies, Jung and Haier¹⁷ proposed a parietal-frontal integration theory of intelligence. However, other studies have noted that the volume of subcortical structures such as the hippocampus and cerebellum correlate with IQ.^{18,19} Such a cortical-versus-subcortical (ie, hippocampal and cerebellar) dichotomy has long been established for neurocognitive conditions such as aphasia and dementia in adults.²²⁻²⁴ Results of the present study are consistent with the notion that both cortical and subcortical connectivity abnormalities reported in the above studies may account for unrecognized distinctions within the GD and SD groups. Thus, the present study provides preliminary evidence to support the

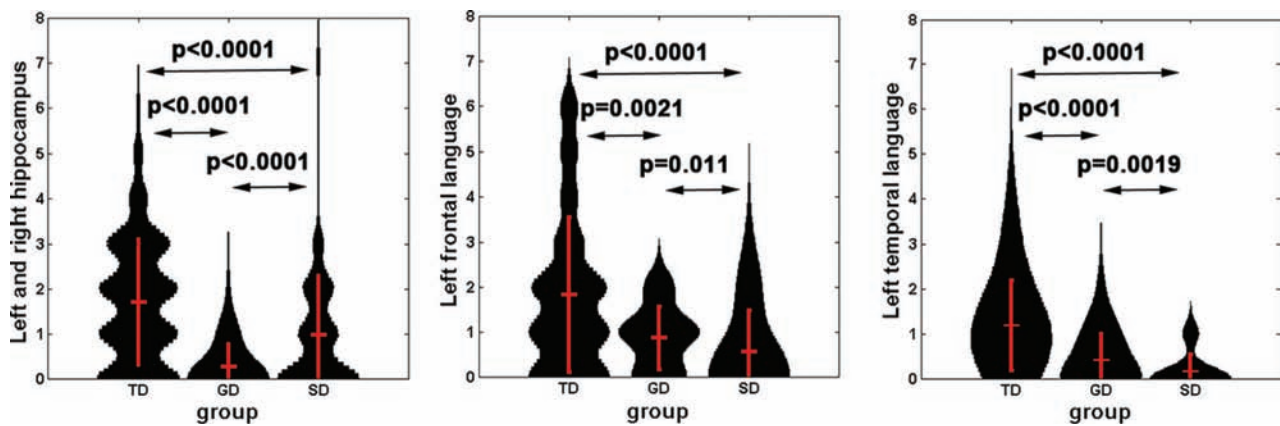


FIG 5. Violin plots show the probability attenuation functions of nodal strengths (black) measured from bilateral hippocampus (*left*), left frontal language region (mid-/superior frontal gyrus/insular, *middle*), and left temporal language region (superior temporal gyrus, *right*) of each group. To estimate the probability attenuation function of individual groups, we calculated the values of nodal strength by applying 3 discrete thresholds (5, 7, 10) to the single connectivity matrix. *Vertical red lines* show mean \pm 1 SD of each function.

Results of differentiation between GD and SD groups using SVM with nodal strength^a

Network	Accuracy	Sensitivity	Specificity	P Value
Hippocampal	89 (4)	96 (5)	74 (15)	.02
Frontal language	83 (4)	93 (6)	71 (16)	.04
Temporal language	88 (5)	94 (5)	77 (14)	.02

Note:—SVM indicates support vector machine.

^a The mean (SD) of accuracy, sensitivity, and specificity were reported in percentages. The *P* value indicates the probability of the permutation in that the accuracy of the permuted label is higher than the one obtained for the real label.

existence of cortical/subcortical subgroups of GD and SD. Future studies with both task-based functional imaging and meta-analysis are required to further validate this notion with a larger sample size.

It has also been observed that whole-brain, gray matter, and white matter volumes correlate with IQ.²⁵ In particular, volumes of different white matter tracts, a measure proportional to some of the network metrics used in the present study, were found to have high heritability.²⁶ Given such high heritability of tract volumes for IQ, it seems likely that a focused effort to identify the genetic variants responsible for low IQ in GD, by using connectivity measures such as endophenotypes, is likely to be successful. In fact, such an effort could identify mutations in 2 axon guidance genes (*EN2* and *MIDI1*) in patients with GD.²⁷ Our future studies will expand on this theme by using the network abnormalities as endophenotypes to identify the underlying genetic mechanisms driving the white matter abnormalities. By combining connectome and genetic techniques (eg, whole exome sequencing), we may be able to more comprehensively define the origin of abnormal cognitive/language networks in children with GD and SD.

The present study was limited by a small sample size and low spatial resolution to parcellate a small number of discrete regions in the whole brain. Due to the small sample size, most false discovery rate–corrected ANOVA *P* values reported in this study were statistically significant (ie, *P* < .05) only at the level of cortical lobar and subcortical regions. Further research needs to evaluate potential associations between axonal connectivity and network property at higher spatial resolutions and larger sample sizes to improve the statistical power of between-group comparison and also verify the reproducibility.^{28,29} Although the above limitations exist, our preliminary results suggest that the abnormali-

ties of network properties reported at the bilateral hippocampi and the left frontal-temporal language network may underlie the presence of sparse connections in both cognitive and language systems. Most important, our findings also reveal differential associations between distinct structural connectivities and specific behavioral problems that are suggestive of distinct neural substrates in children with GD and SD.

Despite the group-level differences found in this study, more studies with larger samples sizes are required before connectome data can be used in individual diagnosis. Especially, current neuropsychological tests are less reliable in younger children than in older children though they are still primarily used as the clinical standard. The impact of young age may not completely invalidate the tests but may increase the noise level in group classification. This possibility could, in turn, potentially inflate the statistical significance of the group differences reported in this study. Future studies that can evaluate these children with follow-up neuropsychological assessment (when they are more reliable) will be able to validate the results of the present study. Furthermore, a combinatorial model integrating all the abnormalities found in this study, including temporal pole (semantic memory), calcarine/fusiform/cuneus (visual perception), putamen/caudate (motor skill), and insular (social emotion) can be used as the starting basis to make individual diagnosis feasible.

CONCLUSIONS

By combining ICA + BSM tractography with whole-brain connectome analysis to differentiate subjects with GD and SD from healthy controls, the present study found that nodal strengths of cognitive/language networks are differentially reduced between children with SD and those with GD. The results of the present study promise a new, refined imaging tool to better examine the subgroups of developmental disorders at a very young age and evaluate their anatomic substrates *in vivo*.

Disclosures: Jeong-Won Jeong—RELATED: Grant: National Institutes of Health National Institute of Neurological Disorders and Stroke 1R01NS089659 (Principal Investigator). * Senthil Sundaram—UNRELATED: Grants/Grants Pending: National Institutes of Health. * Comments: supported by a National Institute of Child Health and Human Development grant 1R01HD059817 (2009–2014), “Diffusion Tensor Imaging Biomarker in Developmental Delay.” *Money paid to the institution.

REFERENCES

1. Shevell MI, Ashwal S, Donley D, et al; Quality Standards Subcommittee of the American Academy of Neurology, Practice Committee of the Child Neurology Society. **Practice parameter: evaluation of the child with global developmental delay—report of the Quality Standards Subcommittee of the American Academy of Neurology and the Practice Committee of the Child Neurology Society.** *Neurology* 2003;60:367–80 CrossRef Medline
2. Burden V, Stott CM, Forge J, et al. **The Cambridge Language and Speech Project (CLASP), I: detection of language difficulties at 36 to 39 months.** *Dev Med Child Neurol* 1996;38:613–31 Medline
3. Nelson HD, Nygren P, Walker M, et al. **Screening for speech and language delay in preschool children: systematic evidence review for the US Preventive Services Task Force.** *Pediatrics* 2006;117:e298–319 CrossRef Medline
4. Bashir AS, Scavuzzo A. **Children with language disorders: natural history and academic success.** *J Learn Disabil* 1992;25:53–65; discussion 66–70 CrossRef Medline
5. Downing JE, Perino DM. **Functional versus standardized assessment procedures: implications for educational programming.** *Ment Retard* 1992;30:289–95 Medline
6. Sattler JM. *Assessment of Children: Cognitive Applications.* 4th ed. Vol 1. San Diego: Jerome M. Sattler; 2001
7. Sundaram SK, Sivaswamy L, Makki MI, et al. **Absence of arcuate fasciculus in children with global developmental delay of unknown etiology: a diffusion tensor imaging study.** *J Pediatr* 2008;152:250–55 CrossRef Medline
8. Jeong JW, Sundaram SK, Kumar A, et al. **Aberrant diffusion and geometric properties in left arcuate fasciculus of developmentally delayed children: a diffusion tensor imaging study.** *AJNR Am J Neuroradiol* 2011;32:323–30 CrossRef Medline
9. Wilson BJ, Sundaram SK, Huq AH, et al. **Abnormal language pathway in children with Angelman syndrome.** *Pediatr Neurol* 2011;44:350–56 CrossRef Medline
10. Tiwari VN, Jeong JW, Wilson BJ, et al. **Relationship between aberrant brain connectivity and clinical features in Angelman syndrome: a new method using tract based spatial statistics of DTI color-coded orientation maps.** *Neuroimage* 2012;59:349–55 CrossRef Medline
11. Nagae LM, Zarnow DM, Blaskey L, et al. **Elevated mean diffusivity in the left hemisphere superior longitudinal fasciculus in autism spectrum disorders increases with more profound language impairment.** *AJNR Am J Neuroradiol* 2012;33:1720–25 CrossRef Medline
12. Peters SU, Kaufmann WE, Bacino CA, et al. **Alterations in white matter pathways in Angelman syndrome.** *Dev Med Child Neurol* 2011;53:361–67 CrossRef Medline
13. Catani M, Mesulam MM, Jakobsen E, et al. **A novel frontal pathway underlies verbal fluency in primary progressive aphasia.** *Brain* 2013;136(pt 8):2619–28 CrossRef Medline
14. Jeong JW, Asano E, Yeh FC, et al. **Independent component analysis tractography combined with ball and stick model to isolate intra-voxel crossing fibers of the corticospinal tracts in clinical diffusion MRI.** *Mag Reson Med* 2013;70:441–53 CrossRef Medline
15. Jeong JW, Asano E, Brown EC, et al. **Automatic detection of primary motor areas using diffusion MRI tractography: comparison with functional MRI and electrical stimulation mapping.** *Epilepsia* 2013;54:1381–90 CrossRef Medline
16. Jeong JW, Asano E, Juhász C, et al. **Localization of specific language pathways using diffusion-weighted imaging tractography for pre-surgical planning of children with intractable epilepsy.** *Epilepsia* 2015;56:49–57 CrossRef Medline
17. Jung RE, Haier RJ. **The Parieto-Frontal Integration Theory (P-FIT) of intelligence: converging neuroimaging evidence.** *Behav Brain Sci* 2007;30:135–54; discussion 154–87 CrossRef Medline
18. Haier RJ, Karama S, Leyba L, et al. **MRI assessment of cortical thickness and functional activity changes in adolescent girls following three months of practice on a visual-spatial task.** *BMC Res Notes* 2009;2:174 CrossRef Medline
19. Frangou S, Chitins X, Williams SC. **Mapping IQ and gray matter density in healthy young people.** *Neuroimage* 2004;23:800–05 CrossRef Medline
20. Benjamini Y, Hochberg Y. **Controlling the false discovery rate: a practical and powerful approach to multiple testing.** *Journal of the Royal Statistical Society. Series B (Methodological)* 1995;57:289–300
21. Fan RE, Chang KW, Hsieh CJ, et al. **LIBLINEAR: a library for large linear classification.** *J Mach Learn Res* 2008;9:1871–74
22. Cappa SF, Cavallotti G, Guidotti M, et al. **Subcortical aphasia: two clinical-CT scan correlation studies.** *Cortex* 1983;19:227–41 CrossRef Medline
23. Huber SJ, Shuttleworth EC, Paulson GW, et al. **Cortical vs subcortical dementia: neuropsychological differences.** *Arch Neurol* 1986;43:392–94 CrossRef Medline
24. Kirk A, Kertesz A. **Cortical and subcortical aphasias compared.** *Aphasiology* 1994;8:65–82 CrossRef
25. Posthuma D, De Geus EJ, Baaré WF, et al. **The association between brain volume and intelligence is of genetic origin.** *Nat Neurosci* 2002;5:83–84 CrossRef Medline
26. Hulshoff Pol HE, Schnack HG, Posthuma D, et al. **Genetic contributions to human brain morphology and intelligence.** *J Neurosci* 2006;26:10235–42 CrossRef Medline
27. Sundaram S, Huq AH, Hsia T, et al. **Exome sequencing and diffusion tensor imaging in developmental disabilities.** *Pediatr Res* 2014;75:443–47 CrossRef Medline
28. Zalesky A, Fornito A, Harding IH, et al. **Whole-brain networks: does the choice of nodes matter?** *Neuroimage* 2010;50:970–83 CrossRef Medline
29. Ge B, Tian Y, Hu X, et al. **Construction of multi-scale consistent brain networks: methods and applications.** *PLoS One* 2015;10:e0118175 CrossRef Medline

Relationship between M100 Auditory Evoked Response and Auditory Radiation Microstructure in 16p11.2 Deletion and Duplication Carriers

J.I. Berman, D. Chudnovskaya, L. Blaskey, E. Kuschner, P. Mukherjee, R. Buckner, S. Nagarajan, W.K. Chung, E.H. Sherr, and T.P.L. Roberts



ABSTRACT

BACKGROUND AND PURPOSE: Deletion and duplication of chromosome 16p11.2 (*BP4–BP5*) have been associated with developmental disorders such as autism spectrum disorders, and deletion subjects exhibit a large (20-ms) delay of the auditory evoked cortical response as measured by magnetoencephalography (M100 latency). The purpose of this study was to use a multimodal approach to test whether changes in white matter microstructure are associated with delayed M100 latency.

MATERIALS AND METHODS: Thirty pediatric deletion carriers, 9 duplication carriers, and 39 control children were studied with both magnetoencephalography and diffusion MR imaging. The M100 latency and auditory system DTI measures were compared between groups and tested for correlation.

RESULTS: In controls, white matter diffusivity significantly correlated with the speed of the M100 response. However, the relationship between structure and function appeared uncoupled in 16p11.2 copy number variation carriers. The alterations to auditory system white matter microstructure in the 16p11.2 deletion only partially accounted for the 20-ms M100 delay. Although both duplication and deletion groups exhibit abnormal white matter microstructure, only the deletion group has delayed M100 latency.

CONCLUSIONS: These results indicate that gene dosage impacts factors other than white matter microstructure, which modulate conduction velocity.

ABBREVIATIONS: ASD = autism spectrum disorder; CNV = copy number variation; FA = fractional anisotropy; HARDI = high angular resolution diffusion imaging; IQ = intelligence quotient; MD = mean diffusivity; MEG = magnetoencephalography; RD = radial diffusivity; VIP = Variation in Individuals Project

Recent studies have begun to investigate brain imaging and behavioral phenotypes in genetically defined cohorts as a way to provide better insight into etiologically heterogeneous neuropsychiatric diagnoses such as autism spectrum disorder (ASD).^{1–9} Deletion or duplication of the ≈600 kilobase segment of chromosome 16p11.2 (bounded by *BP4–BP5*) has been associated with neurodevelopmental disorders, including language impairment,

mild-to-moderate intellectual disability, schizophrenia, increased body mass index, epilepsy, and ASD.^{2–9} ASD is present in approximately 25% of individuals with a 16p11.2 deletion, and approximately 1% of all individuals in some cohorts with ASD have a 16p11.2 copy number variation (CNV).⁸

Prior studies have identified abnormal brain phenotypes associated with the 16p11.2 deletion and duplication. Increased brain size among the deletion carriers and decreased brain size among the duplication carriers were detected with structural MR imaging.¹⁰ Abnormal white matter microstructure, including increased fractional anisotropy (FA) and axial diffusivity, was observed throughout the major pathways of the cerebrum of children with 16p11.2 deletion.^{11,12} The magnetoencephalography (MEG)-measured auditory evoked cortical response latency (M100) was delayed about 20 ms in children with 16p11.2 deletion compared with matched controls, but not in children with

Received July 28, 2015; accepted after revision November 16.

From the Department of Radiology (J.I.B., D.C., L.B., E.K., T.P.L.R.), Children's Hospital of Philadelphia, Philadelphia, Pennsylvania; Department of Radiology (J.I.B., T.P.L.R.), Perelman School of Medicine, University of Pennsylvania, Philadelphia, Pennsylvania; Departments of Radiology (P.M.) and Neurology (E.H.S.), University of California, San Francisco School of Medicine, San Francisco, California; Department of Psychology (R.B.), Harvard University, Cambridge, Massachusetts; and Departments of Pediatrics and Medicine (S.N., W.K.C.), Columbia University Medical Center, New York, New York.

Paper previously presented in part at: Annual Meeting and Exhibition of the International Society for Magnetic Resonance in Medicine, May 30–June 5, 2015; Toronto, Ontario, Canada.

This work was supported by a grant from the Simons Foundation (SFARI 216074 and 251203) and is submitted on behalf of the Simons Variation in Individuals Project (Simons VIP) investigators. This work was supported in part by K01MH096091 and the Children's Hospital of Philadelphia/University of Pennsylvania Intellectual and Developmental Disabilities Research Center grant U54 HD086984.

Please address correspondence to Jeffrey I. Berman, MD, Children's Hospital of Philadelphia, Department of Radiology, 34th and Civic Center Blvd, Philadelphia, PA 19104; e-mail: bermanj@email.chop.edu

Indicates open access to non-subscribers at www.ajnr.org

<http://dx.doi.org/10.3174/ajnr.A4687>

16p11.2 duplication.¹³ The purpose of this study was to determine the role of abnormal thalamocortical white matter microstructure in modulating the profoundly delayed M100 auditory evoked response.

Abnormal structure and function of the auditory system and superior temporal gyrus have previously been associated with ASD, motivating this study of 16p11.2 CNV.^{14,15} Diffusion MR imaging is sensitive to white matter architecture, and high angular resolution diffusion imaging (HARDI) fiber tractography is used to delineate the 3D position of the auditory radiation bilaterally.¹⁶ The MEG-derived M100 evoked field component is generated by neurons in the superior temporal gyrus in response to an auditory stimulus. The latency of the M100 provides a measure of white matter conduction and synaptic transmission speed integrated from the ear to the cortex as well as corticocortical processing in primary and association auditory cortices. This study combined MEG and diffusion MR imaging in a group of subjects with a defined genetic etiology. We hypothesized that the relationship between structure and function is altered in children with 16p11.2 deletion and duplication.

MATERIALS AND METHODS

Participants

Deletion carriers were recruited through the Simons Variation in Individuals Project (VIP, <https://clinicaltrials.gov/ct2/show/NCT01238250>) Connect Web site (<https://www.simonsvipconnect.org/>).¹ The 16p11.2 deletion participants were identified by clinical chromosome microarrays and included individuals with the same recurrent ~600-kb deletion (chr16:29, 652,990–30,199,351; hg19) without other known genetic diagnoses or pathogenic CNVs. Age-matched neurotypical participants had a chromosome microarray to rule out abnormal CNVs at the 16p11.2 locus or elsewhere in the genome. Exclusion criteria included the inability to speak English fluently, drug use, or significant structural abnormalities on MR imaging. Any control subject with a potential clinical finding on MR imaging was excluded. Any deletion or duplication carrier with a clinical finding on MR imaging unrelated to 16p11.2 or an overt structural anomaly such as agenesis of the corpus callosum or polymicrogyria was also excluded. All children in the typically developing control group had no neurologic or genetic disorder and no evidence of current or past psychiatric diagnosis as measured by a parent report of *Diagnostic and Statistical Manual of Mental Disorders*, 4th ed, symptoms on a structured diagnostic interview, the *Diagnostic Interview Schedule for Children*, Version IV.

Participants were administered psychological and diagnostic measures by experienced and licensed child psychologists. Cognitive and language measures used for the current analyses included the *Clinical Evaluation of Language Fundamentals*, 4th ed, as a measure of basic language functioning, and the *Differential Ability Scales*, *Special Nonverbal Composite*, 2nd ed, as a measure of nonverbal intellectual functioning.^{17,18} *Clinical Diagnostic and Statistical Manual of Mental Disorders*, Text Revision, 4th ed, diagnoses were obtained by using all information gathered during the evaluation. Autism diagnostic measures included the *Autism Diagnostic Observation Schedule* and the *Autism Diagnostic Interview*, Revised.^{19,20}

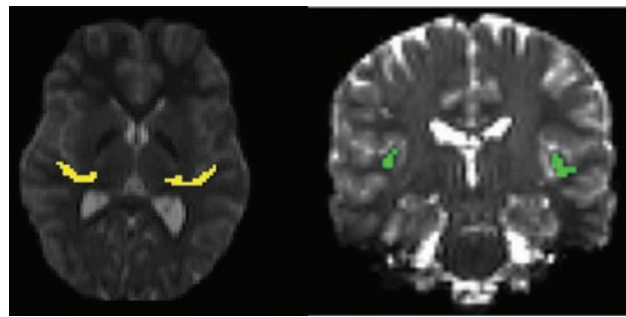


FIG 1. ROIs for diffusion MR imaging measures are shown. *Left:* Axial section through the auditory radiation, as defined by HARDI tractography. *Right:* Coronal section through the transverse gyrus (Heschl's gyrus) ROI as defined by the white matter parcellation performed by FreeSurfer.

MR Imaging

Imaging was performed at either the Children's Hospital of Philadelphia or the University of California with a 3T Tim Trio scanner (Siemens, Erlangen, Germany), a 32-channel radiofrequency head coil, and identical pulse sequences. The intersite equivalency of image data quality was confirmed before the study by scanning 5 subjects at both sites, and image quality was monitored during the study with phantom quality-assurance studies.²¹

The whole-brain DTI acquisition used 30 diffusion gradient directions at $b=1000$ s/mm², 1 $b=0$ s/mm² volume, TR/TE = 10 s/80 ms, voxel size = $2 \times 2 \times 2$ mm, and a 128×128 matrix. A separate whole-brain HARDI acquisition used 64 gradient directions at $b=3000$ s/mm², 2 $b=0$ s/mm² volumes, TR/TE = 13.9 s/119 ms, voxel size = $2 \times 2 \times 2$ mm, and a 128×128 matrix. Both diffusion acquisitions used a Stejskal-Tanner monopolar, spin-echo echo-planar sequence, a parallel acceleration factor of 2, and axial sections. Structural imaging was performed with a T1-weighted multiecho 3D magnetization-prepared rapid acquisition of gradient echo and $TE_{\text{minimum}} = 1.64$ ms, TR = 2530 ms, TI = 1200 ms, flip angle = 7°, and 1-mm isotropic resolution.²²

Probabilistic tractography by using the solid angle Q-ball imaging HARDI reconstruction was used to delineate the auditory radiation from the thalamus to the auditory cortex.^{16,23} Additional ROIs just in the transverse gyri (Heschl's gyrus) were defined from the FreeSurfer (<http://surfer.nmr.mgh.harvard.edu>) white matter parcellation (Fig 1).²⁴ The $b=1000$ s/mm² DTI data were used for all microstructural measures.

Magnetoencephalography

Data were acquired by using a similar 275-channel whole-head CTF magnetometer at either imaging site. The auditory stimulus consisted of passively presented tones of 200, 300, 500, and 1000 Hz of 300-ms duration (10-ms ramps) repeated 130 times each. The interstimulus interval varied randomly between 900 and 1100 ms. The M100 response in the left and right superior temporal gyrus was detected with a standard dipole source model that transforms the MEG sensor signals into source (brain) space. The details of the source modeling procedure have been previously described.¹³

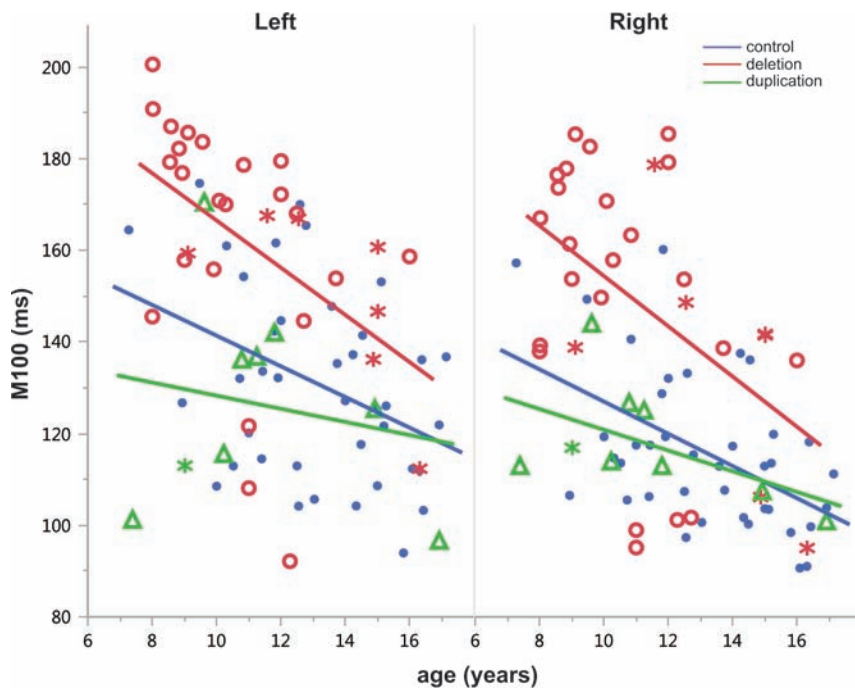


FIG 2. Developmental trajectory of M100 versus age for the left and right hemispheres. Left and right control and deletion regression lines significantly decrease with age ($P < .001$ each). There is no significant difference in slope between the groups. Individuals with an ASD diagnosis are indicated by an asterisk. The elevated M100 latency in the deletion group can be observed in both hemispheres.

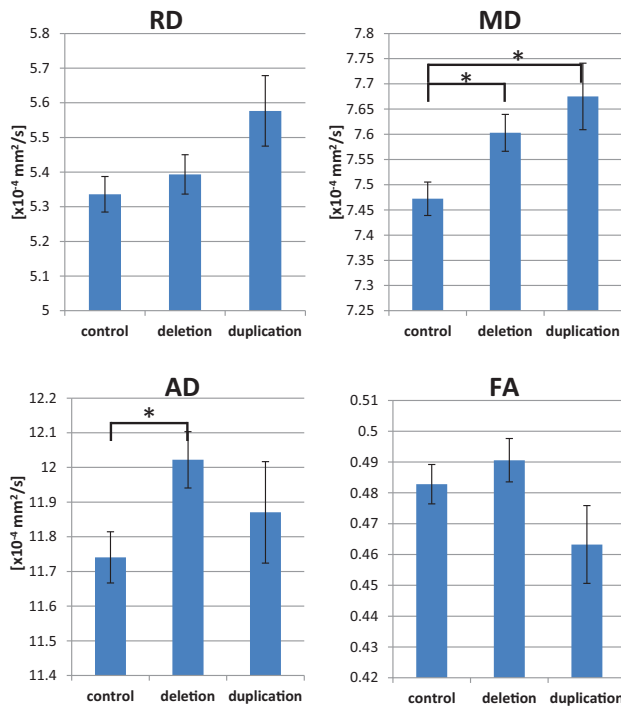


FIG 3. Group comparisons of auditory radiation DTI parameters are shown. The deletion group exhibits elevated AD, and both CNV groups have elevated MD. The asterisk indicates $P < .05$; AD, axial diffusivity.

Statistical Analysis

Statistical analysis was performed by using SPSS (Version 21; IBM, Armonk, New York) and JMP (Version 11; SAS Institute, Cary, North Carolina) with a threshold for significance at $P = .05$.

M100 latency varies by hemisphere and stimulus tone frequency²⁵; however, a single “effective” M100 for each subject’s left and right hemisphere was calculated with a linear mixed-model. The model contains fixed effects of hemisphere, stimulus frequency, group, imaging site, and age and a random effect of subject. Fitted values from the model were used to predict M100 values for subjects with partially missing observations.

For analysis of M100 and DTI group differences, a linear regression was performed with effects of group, age, hemisphere, imaging site, and nonverbal intelligence quotient (IQ). The Dunnnett method for multiple comparisons was used to compare deletion and duplication carrier groups with the control group. For multimodal analysis, multivariable linear regression was performed with M100 as the dependent variable and the effects of DTI parameter, group, hemisphere, nonverbal IQ, and imaging site. The interaction between DTI parameter and group was added to the

model to test for group differences in the regression slope. Data were segmented by group and hemisphere for additional analyses.

RESULTS

Population

This study included 78 children imaged at either Children’s Hospital of Philadelphia ($n = 34$) or the University of California ($n = 44$). Thirty pediatric deletion carriers, 9 duplication carriers, and 39 typically developing children were included. The mean age of deletion carriers was 11.2 ± 2.5 years (range, 8–16 years) with 17 males and 13 females. The mean age of duplication carriers was 11.3 ± 3 years (range, 7–16 years) with 6 males and 3 females. The mean age of control children was 13.2 ± 2.4 (range, 7–17) with 24 males and 15 females. There was a significant difference in chronologic age between the control and deletion groups ($P = .006$; Tukey honest significance test) but no significant difference in age between control and duplication groups or between deletion and duplication groups ($P = .13$, $P = .99$, respectively). Age was included as a covariate in the group comparisons of DTI metrics and M100 to account for the differences in age. There was no significant group difference in the sex ratio ($P = .85$; Fisher exact test). MEG data from some of these individuals has been independently reported in Jenkins et al.¹³ Diffusion MR imaging findings from a subset of these subjects have been reported in Berman et al.¹²

Mean nonverbal IQ of the control group (mean, 107.6 ± 13.1) was significantly higher than that in the deletion group (mean, 91.7 ± 15.5) and the duplication group (mean, 81.4 ± 12.1) ($P < .001$, each Tukey honest significance test). Nonverbal IQ was not significantly different between duplication and deletion groups

($P = .14$). Seven deletion carriers and 1 duplication carrier met the diagnostic criteria for ASD.

M100 Latency

As previously reported,¹³ the deletion group exhibited significantly prolonged M100 latencies with a group difference of 20.6 ms ($P < .001$). There was no group difference between duplication and control M100 latencies. M100 latency was significantly longer in the left hemisphere by approximately 6.6 ms ($P < .001$). M100 was observed to decrease with age at a rate of about 4 ms per year ($P < .001$). When analyzed separately by hemisphere and group, M100 significantly decreased in the left and right hemispheres of the control and deletion groups ($P < .001$ each, Fig 2). There was no significant group difference in the rate of M100 maturation. Imaging site and nonverbal IQ were not significant predictors of M100 latency.

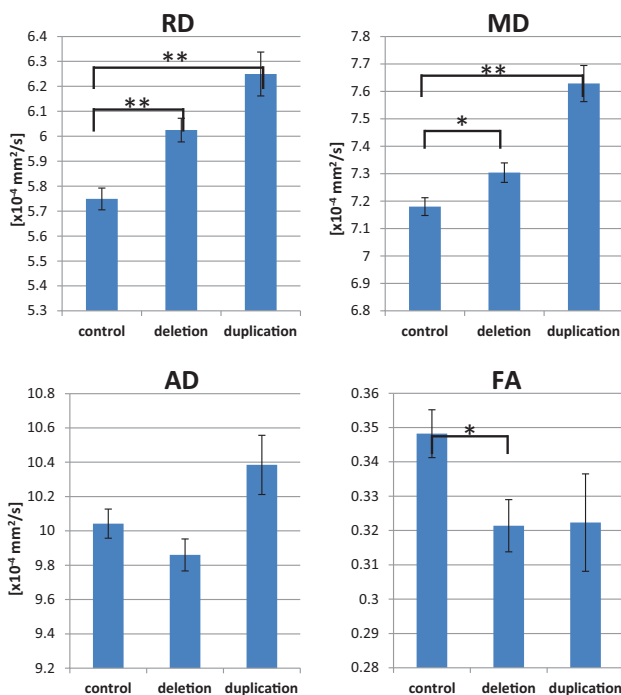


FIG 4. Group comparisons of Heschl's gyrus DTI parameters are shown. The deletion group exhibits elevated RD and MD and decreased FA. The duplication group exhibits higher MD and RD along with a trend toward decreased FA. The asterisk indicates $P < .05$; double asterisks, $P < .001$; AD, axial diffusivity.

Correlation of DTI with M100 within groups^a

	Auditory Radiation			Heschl's Gyrus		
	Control	Deletion	Duplication	Control	Deletion	Duplication
MD	16.4 $P = .044^b$	14.7 $P = .3$	1.1 $P = .9$	29.9 $P < .001^b$	1.2 $P = .9$	24.7 $P = .2$
FA	-67.4 $P = .15$	73.2 $P = .3$	-43 $P = .7$	-78.3 $P = .063$	-111 $P = .2$	-75.2 $P = .4$
RD	10.6 $P = .048^b$	1.3 $P = .9$	2.3 $P = .9$	21.7 $P < .001^b$	12.8 $P = .3$	17.4 $P = .2$
AD	0.6 $P = .9$	11.7 $P = .11$	-1.8 $P = .8$	2.4 $P = .5$	-4.9 $P = .4$	1.9 $P = .8$

Note:—AD indicates axial diffusivity.

^aRegression coefficients by group are shown with P values. Coefficients indicate the number of milliseconds per variable unit. MD, RD, and AD have units of $\times 10^{-4} \text{ mm}^2/\text{s}$.

^bSignificant.

DTI Metrics

As previously reported, the auditory radiation of the deletion group had abnormally high mean diffusivity (MD) ($P = .027$), which was primarily driven by an increase in axial diffusivity ($P = .033$, Fig 3). The duplication group had elevated auditory radiation mean diffusivity ($P = .021$), which was driven by trends of higher radial diffusivity (RD) and axial diffusivity.

Within Heschl's gyrus, the deletion group exhibited significantly elevated MD and RD ($P = .033$, $P < .001$, respectively) along with significantly decreased FA ($P = .031$, Fig 4). The duplication group exhibited higher Heschl's gyrus MD and RD ($P < .001$ each) and a trend toward decreased FA. Decreasing MD with age was observed in the left and right hemispheres of the control and deletion groups ($P < .05$ each).

Multimodal Analysis

Overall across groups, there was a significant main effect of auditory radiation MD ($P = .048$) and Heschl's gyrus FA ($P = .023$), MD ($P = .011$), and RD ($P < .001$) on M100 latency (with elevated MD or RD and decreased FA predicting longer latencies). Interactions between DTI parameters and group were not significant. Post hoc analysis within groups of relationships between auditory system white matter microstructure and M100 latency is shown in the Table. In controls, M100 latency was positively correlated with both MD and RD in the auditory radiation and Heschl's gyrus ROI. A trend toward an inverse correlation of Heschl's gyrus FA and M100 was observed in controls ($P = .063$). No significant correlations between DTI parameters and M100 latency were observed among the deletion or duplication groups.

Correlations between DTI parameters and M100 latency were separately examined in the left and right hemispheres for each group. The deletion and duplication groups exhibited no significant correlations with M100 in either the right or left hemispheres. Left hemispheric DTI parameters were not significant predictors of M100 in controls. In controls, right hemisphere microstructure and M100 latency were more strongly coupled than in the left hemisphere. Right hemisphere MD and RD were significantly correlated with M100 latency in both the auditory radiation and transverse gyrus of controls ($P < .05$, Figs 5 and 6). Although the correlations between DTI parameters and M100 were not significant in the right hemisphere of 16p11.2 deletion carriers, the regression slopes were not significantly different between groups. The slopes describing the relationship between

right hemisphere control auditory radiation MD and RD with M100 were observed to be similar to those in the deletion group (Figs 5 and 6). Deletion and duplication carriers with an ASD diagnosis are indicated in Figs 5 and 6. The small subsets of deletion or duplication carriers with an ASD diagnosis were not overtly different from those without an ASD diagnosis.

DISCUSSION

In controls, the degree of white matter myelination, axonal density, and integrity as measured with DTI were ob-

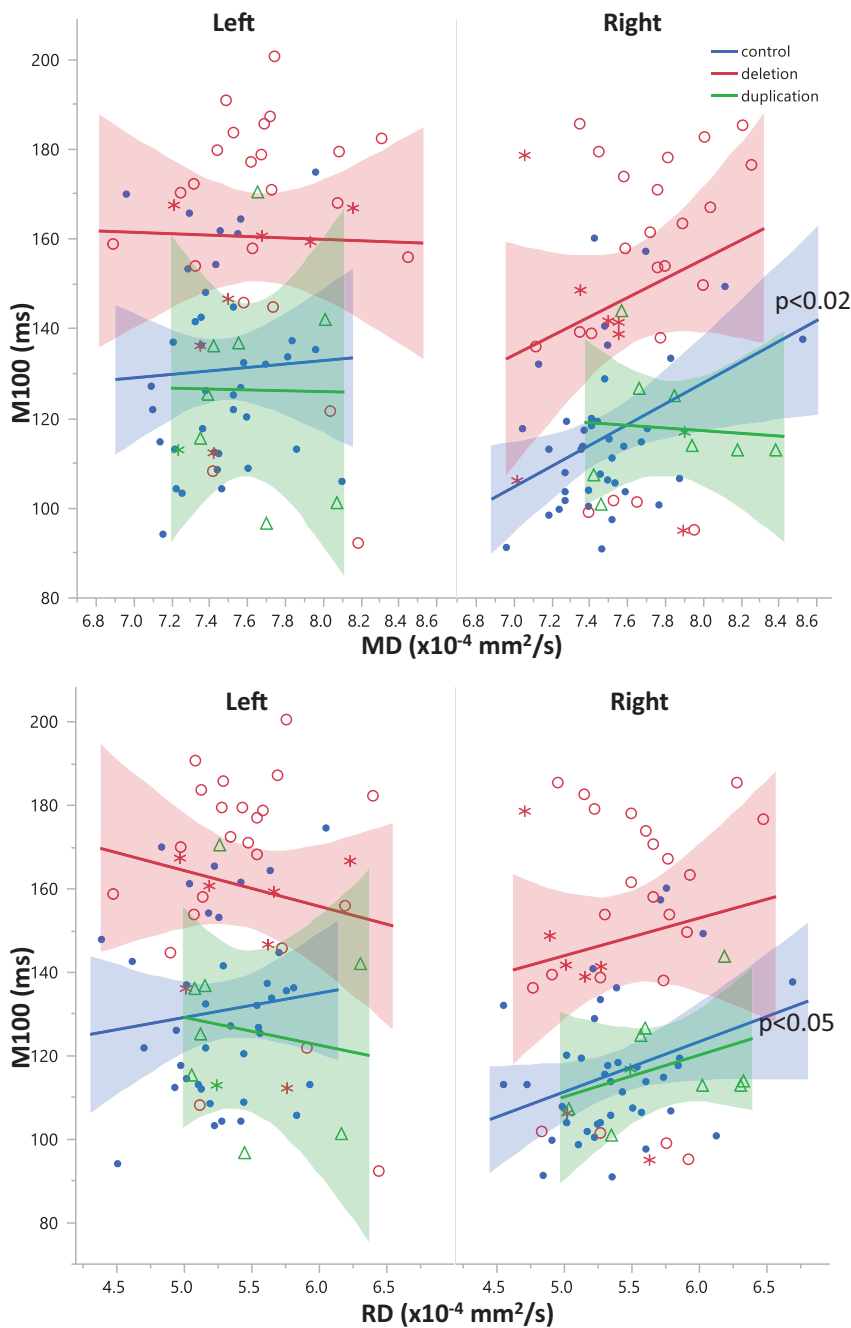


FIG 5. Relationships between diffusivity and M100 are shown for left and right auditory radiations. While overall there is a significant main effect ($P < .05$) of MD on M100 latency, post hoc analysis within groups reveals that this is only significantly resolved for right hemisphere control MD and RD ($P = .017$ and $P = .049$, respectively). Control subjects are blue, subjects with deletion are red, and subjects with duplication are green. Subjects with deletion and duplication with an ASD diagnosis are indicated by asterisks.

served to significantly modulate the speed of the M100 response. The relationship between structure and function appears uncoupled in 16p11.2 CNV carriers; however, the slope of the relationship still appears similar to that of controls. Both duplication and deletion groups exhibited white matter microstructural abnormalities, but M100 latency was delayed only in the deletion group. These results indicate that gene dosage impacts white matter microstructure and other factors that modulate conduction velocity. A limitation of the current study is the small number of subjects

with ASD; however, no overt trends differentiating 16p11.2 CNV subjects with and without ASD diagnosis were observed.

In addition to the previously reported large (20-ms) M100 latency delay in the deletion group, we additionally report a significant maturational decrease of the M100 of control and deletion groups.¹³ The duplication group also exhibited shortening of the M100 latency with age, but the relationship did not reach significance because of the small study population. Both deletion and duplication groups exhibited abnormal patterns of diffusivity in the thalamocortical white matter. Because of the relatively low number of subjects with duplication, it is difficult to determine whether thalamocortical white matter is more severely altered in deletion or duplication carriers. The unusual increase in axial diffusivity of the thalamocortical white matter is consistent with prior work using Tract-Based Spatial Statistics to examine white matter in 16p11.2 deletion.¹¹ Most interesting, the 16p11.2 duplication group has normal or possibly shorter M100 latency in the presence of microstructural abnormalities.

Overall, there was a significant association between microstructural parameters (MD and RD) and M100 latency, with elevated diffusivity predicting longer latency. However, within-group analyses indicated that the relationship is significant only in the control group and only in the right hemisphere. A prior study similarly observed a degraded relationship between the MEG 50-ms auditory evoked response and FA in children with ASD.¹⁴ We report that the M100 versus MD and RD slopes in controls were not significantly different from the slopes in 16p11.2 CNVs. The similarity of the structure-function slope between controls and deletion carriers indicates that white matter still

modulates M100 latency, though it has a diminished role. The degraded relationship between structure and function in 16p11.2 CNV and the difference in regression intercepts, despite similar slopes, indicate the influence of factors not accounted for by DTI measurements alone.

This study determined that the alterations to auditory system white matter structure are insufficient to completely explain the large delay in M100 latency in deletion carriers. Given the MD-to-M100 slope measured in this study, a $0.8 \times 10^{-4} \text{ mm}^2/\text{s}$ in-

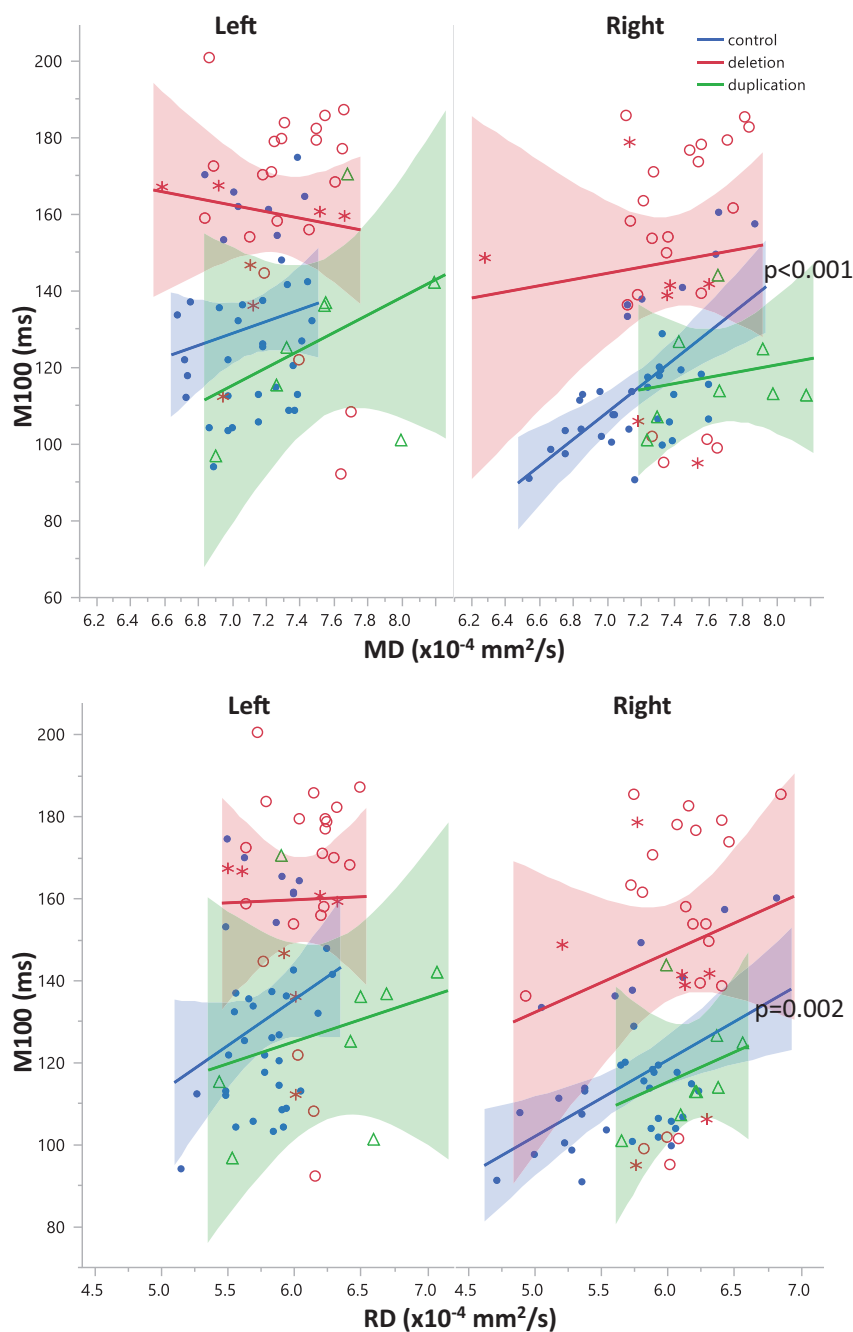


FIG 6. Relationships between diffusivity and M100 are shown for the left and right Heschl's gyri. While overall, there is a significant main effect of MD ($P < .02$) and RD ($P < .001$) on M100 latency, post hoc analysis within groups reveals that this is only significantly resolved for right hemisphere control MD and RD ($P < .001$, $P = .002$, respectively). Control subjects are blue, subjects with deletion are red, and subjects with duplication are green. Subjects with deletion and duplication with an ASD diagnosis are indicated by *asterisks*.

crease of right hemisphere auditory radiation MD would be necessary for an M100 increase of approximately 20 ms. The $0.1 \times 10^{-4} \text{ mm}^2/\text{s}$ elevation of MD accounts for only a 2.5-ms increase in M100, which is far short of the 20-ms delay observed in deletion carriers.

Both deletion and duplication groups have abnormal auditory system white matter microstructure; however, only the deletion group exhibited an M100 latency delay. Conduction velocity in the duplication group may indeed be facilitated given the small decrease

in M100 latency observed in a prior study and repeated in the current study.¹³ These results strongly indicate that factors other than auditory radiation white matter integrity contribute to elongated M100 latency in deletion carriers and normal, or even possibly faster than typical, M100 latency in duplication carriers.

The entire auditory system is necessary for producing or eliciting a cortical response. The M100 integrates travel time through the cochlear nerve, brain stem, midbrain, thalamus, auditory radiation, and auditory cortex. Examination of factors other than auditory radiation white matter that modulate signal transmission velocity is warranted. Abnormal synapse development or neurotransmitter concentrations can introduce synaptic delays and abnormal patterns of action-potential generation.^{26,27} MR spectroscopy may be sensitive to changes in neurotransmitter levels. The organization of local networks within the auditory cortex could also affect the speed of the corticocortical looping, which is required for an evoked response. The quality of local corticocortical connectivity can be examined with MEG metrics such as phase amplitude coupling.²⁸ Advanced diffusion MR imaging techniques that can discriminate crossing fibers may also be useful for examining the architecture of different cortical layers.²⁹ One or more of these factors may be responsible for uncoupling structure from function in deletion and duplication carriers and delaying the M100 response in deletion carriers.

In controls, right hemisphere microstructure and M100 were more strongly and significantly correlated than in the left hemisphere. This result has been observed previously and possibly results from the hemispheric functional specialization of the superior temporal gyrus.³⁰ In addition to auditory processing, the left superior temporal gyrus contains language networks. Thus, left hemisphere microstructural measures may reflect a mixture of auditory and language fibers, while the right hemisphere measures may primarily contain auditory fibers. Thus, right hemisphere auditory radiation diffusivity may be a proxy for diffusivity within all auditory system white matter.

CONCLUSIONS

White matter integrity is necessary but not sufficient for normal latency of the auditory evoked response. In carriers of the 16p11.2

CNV, auditory radiation MD and RD were not strong modulators of M100 latency. The increased variance in the structure-function relationship indicates the influence of other factors that modulate electrophysiology. The pronounced M100 latency delay in 16p11.2 deletion carriers could only be partially explained by degraded white matter integrity. Compensatory mechanisms apparently overcome the abnormal white matter microstructure in 16p11.2 duplication carriers to produce a normal (or possibly shorter) M100 latency. These results provide insight into the link among genetics, brain structure, function, and traits supporting neuropsychiatric disorders.

ACKNOWLEDGMENTS

We are grateful to all of the participating families and the Simons VIP Consortium. We appreciate obtaining access to phenotypic data on the SFARI Base. Approved researchers can obtain the Simons VIP population dataset by contacting SFARI. We are grateful to Thorsten Feiweier, PhD, from Siemens for providing the 511C diffusion work-in-progress package.

Disclosures: Lisa Blaskey—RELATED: Grant: Simons Foundation.* Emily Kuschner—RELATED: Grant: Simons Foundation.* Pratik Mukherjee—RELATED: Grant: Simons Foundation*; Support for Travel to Meetings for the Study or Other Purposes: Simons Foundation.* Randy Buckner—RELATED: Grant: Simons Foundation.* Comments: A not-for-profit grant from the Simons Foundation supported portions of this work; Consultancy: Pfizer. Comments: paid consultant for Pfizer in the domain of neuroscience. Srikantan Nagarajan—RELATED: Grant: Simons Foundation.* Wendy K. Chung—RELATED: Grant: Simons Foundation.* Elliott H. Sherr—RELATED: Grant: Simons Foundation.* Comments: This work is part of a larger project, called Simons VIP, that is studying the biology of the chromosomal region, 16p11.2; Support for Travel to Meetings for the Study or Other Purposes: Simons Foundation.* Timothy P.L. Roberts—RELATED: Grant: Simons Foundation*; UNRELATED: Consultancy: Prism Clinical Imaging, Guerbet, Johnson & Johnson. *Money paid to the institution.

REFERENCES

1. The Simons VIP Consortium. **Simons Variation in Individuals Project (Simons VIP): a genetics-first approach to studying autism spectrum and related neurodevelopmental disorders.** *Neuron* 2012; 73:1063–67 CrossRef Medline
2. Weiss LA, Shen Y, Korn JM, et al. **Association between microdeletion and microduplication at 16p11.2 and autism.** *N Engl J Med* 2008;358:667–75 CrossRef Medline
3. Bochukova EG, Huang N, Keogh J, et al. **Large, rare chromosomal deletions associated with severe early-onset obesity.** *Nature* 2010; 463:666–70 CrossRef Medline
4. Jacquemont S, Reymond A, Zufferey F, et al. **Mirror extreme BMI phenotypes associated with gene dosage at the chromosome 16p11.2 locus.** *Nature* 2011;478:97–102 CrossRef Medline
5. Fernandez BA, Roberts W, Chung B, et al. **Phenotypic spectrum associated with de novo and inherited deletions and duplications at 16p11.2 in individuals ascertained for diagnosis of autism spectrum disorder.** *J Med Genet* 2010;47:195–203 CrossRef Medline
6. Rosenfeld JA, Coppinger J, Bejjani BA, et al. **Speech delays and behavioral problems are the predominant features in individuals with developmental delays and 16p11.2 microdeletions and microduplications.** *J Neurodev Disord* 2010;2:26–38 CrossRef Medline
7. Hanson E, Bernier R, Porche K, et al; Simons Variation in Individuals Project Consortium. **The cognitive and behavioral phenotype of the 16p11.2 deletion in a clinically ascertained population.** *Biol Psychiatry* 2015;77:785–93 CrossRef Medline
8. Zufferey F, Sherr EH, Beckmann ND, et al; Simons VIP Consortium, 16p11.2 European Consortium. **A 600 kb deletion syndrome at 16p11.2 leads to energy imbalance and neuropsychiatric disorders.** *J Med Genet* 2012;49:660–68 CrossRef Medline
9. Hanson E, Nasir RH, Fong A, et al; 16p11.2 Study Group Clinicians. **Cognitive and behavioral characterization of 16p11.2 deletion syndrome.** *J Dev Behav Pediatr* 2010;31:649–57 CrossRef Medline
10. Qureshi AY, Mueller S, Snyder AZ, et al; Simons VIP Consortium. **Opposing brain differences in 16p11.2 deletion and duplication carriers.** *J Neurosci* 2014;34:11199–211 CrossRef Medline
11. Owen JP, Chang YS, Pojman NJ, et al; Simons VIP Consortium. **Aberrant white matter microstructure in children with 16p11.2 deletions.** *J Neurosci* 2014;34:6214–23 CrossRef Medline
12. Berman JI, Chudnovskaya D, Blaskey L, et al. **Abnormal auditory and language pathways in children with 16p11.2 deletion.** *Neuroimage Clin* 2015;9:50–57 CrossRef Medline
13. Jenkins J, Chow V, Blaskey L, et al. **Auditory evoked M100 response latency is delayed in children with 16p11.2 deletion but not 16p11.2 duplication.** *Cereb Cortex* 2015 Feb 11. [Epub ahead of print] CrossRef Medline
14. Roberts TP, Lanza MR, Dell J, et al. **Maturational differences in thalamocortical white matter microstructure and auditory evoked response latencies in autism spectrum disorders.** *Brain Res* 2013; 1537:79–85 CrossRef Medline
15. Lange N, DuBray MB, Lee JE, et al. **Atypical diffusion tensor hemispheric asymmetry in autism.** *Autism Res* 2010;3:350–58 CrossRef Medline
16. Berman J, Lanza M, Blaskey L, et al. **High angular resolution diffusion imaging probabilistic tractography of the auditory radiation.** *AJNR Am J Neuroradiol* 2013;34:1573–78 CrossRef Medline
17. Semel EM, Wiig EH, Secord W. *Clinical Evaluation of Language Fundamentals (CELF-4).* San Antonio: The Psychological Corporation; 2003
18. Elliott CD. *Differential Ability Scales.* 2nd ed. San Antonio: Pearson; 2007
19. Lord C, Risi S, Lambrecht L, et al. **The autism diagnostic observation schedule-generic: a standard measure of social and communication deficits associated with the spectrum of autism.** *J Autism Dev Disord* 2000;30:205–23 CrossRef Medline
20. Rutter M, Bailey A, Lord C. *Social Communication Questionnaire (SCQ).* Los Angeles: Western Psychological Services; 2003
21. Owen JP, Ziv E, Bukshpun P, et al. **Test-retest reliability of computational network measurements derived from the structural connectome of the human brain.** *Brain Connect* 2013;3:160–76 CrossRef Medline
22. van der Kouwe AJ, Benner T, Salat DH, et al. **Brain morphometry with multiecho MPAGE.** *Neuroimage* 2008;40:559–69 CrossRef Medline
23. Berman JI, Chung S, Mukherjee P, et al. **Probabilistic streamline q-ball tractography using the residual bootstrap.** *Neuroimage* 2008; 39:215–22 CrossRef Medline
24. Fischl B, Sereno MI, Tootell RB, et al. **High-resolution intersubject averaging and a coordinate system for the cortical surface.** *Hum Brain Mapp* 1999;8:272–84 Medline
25. Roberts TP, Ferrari P, Stufflebeam SM, et al. **Latency of the auditory evoked neuromagnetic field components: stimulus dependence and insights toward perception.** *J Clin Neurophysiol* 2000;17:114–29 CrossRef Medline
26. Taschenberger H, von Gersdorff H. **Fine-tuning an auditory synapse for speed and fidelity: developmental changes in presynaptic waveform, EPSC kinetics, and synaptic plasticity.** *J Neurosci* 2000;20: 9162–73 Medline
27. Gaetz W, Bloy L, Wang DJ, et al. **GABA estimation in the brains of children on the autism spectrum: measurement precision and regional cortical variation.** *Neuroimage* 2014;86:1–9 CrossRef Medline
28. Canolty RT, Knight RT. **The functional role of cross-frequency coupling.** *Trends Cogn Sci* 2010;14:506–15 CrossRef Medline
29. Aggarwal M, Nauen DW, Troncoso JC, et al. **Probing region-specific microstructure of human cortical areas using high angular and spatial resolution diffusion MRI.** *Neuroimage* 2015;105:198–207 CrossRef Medline
30. Roberts TP, Khan SY, Blaskey L, et al. **Developmental correlation of diffusion anisotropy with auditory-evoked response.** *Neuroreport* 2009;20:1586–91 CrossRef Medline

Differentiating Pediatric Rhabdomyosarcoma and Langerhans Cell Histiocytosis of the Temporal Bone by Imaging Appearance

K.M. Chevallier, R.H. Wiggins, N.A. Quinn, and R.K. Gurgel

ABSTRACT

BACKGROUND AND PURPOSE: Rhabdomyosarcoma and Langerhans cell histiocytosis are malignant lesions that can affect the skull base with similar radiographic characteristics on CT and MR imaging. We hypothesized that location within the temporal bone determined radiographically can provide useful adjunctive information in differentiating these distinct neoplasms.

MATERIALS AND METHODS: We identified patients with Langerhans cell histiocytosis and rhabdomyosarcoma by using an imaging data base and International Classification of Diseases, Ninth Revision codes at a tertiary care academic medical center. Cross-sectional images were reviewed by a neurotologist and neuroradiologist, who evaluated the location of the lesions and scored each subsite—middle ear, mastoid, petrous apex, retrosigmoid/posterior fossa—on a scale of 0 (no involvement), 1 (partial), or 2 (complete involvement).

RESULTS: We identified 12 patients representing 14 cases of Langerhans cell histiocytosis, and 9 patients representing 9 cases of rhabdomyosarcoma. For patients with Langerhans cell histiocytosis, mastoid involvement was rated 23/28 (82%) compared with 6/18 (33%) with rhabdomyosarcoma ($P = .001$). Langerhans cell histiocytosis was present in only the anterior portion of the temporal bone (petrous apex and middle ear) in 1 case (7.1%) and in the anterior portion of the temporal bone only in 5/9 (55%) cases of rhabdomyosarcoma ($P = .018$). The cortical bone was more commonly involved in Langerhans cell histiocytosis, 11/28 (39%) of cases compared with 2/18 (11%) cases in rhabdomyosarcoma ($P < .05$).

CONCLUSIONS: These results indicate that lesions involving only the anterior portion of the temporal bone (petrous apex and middle ear) are more likely to be rhabdomyosarcoma. Lesions involving the mastoid are more likely to be Langerhans cell histiocytosis. This difference in primary location may be helpful in predicting the pathology of these lesions on the basis of imaging.

ABBREVIATIONS: LCH = Langerhans cell histiocytosis; RMS = rhabdomyosarcoma

Rhabdomyosarcoma (RMS) and Langerhans cell histiocytosis (LCH) are both rare but potentially fatal neoplasms of the pediatric population. These diseases are distinct pathologically: RMS is a soft-tissue sarcoma arising from mesenchymal cells of the middle ear or skeletal muscle,¹ while LCH tumors arise from the abnormal proliferation of Langerhans cells (ie, dendritic cells).²

Both lesions are commonly found in the head and neck region,

30%–70% in RMS³ and 60% in LCH.⁴ Less frequently, the temporal bone is involved, with only 8%–10% of cases of RMS of the head and neck³ and 19%–25% of LCH cases in this location.⁴ The initial presentation for both diseases is variable and can range from a palpable periauricular mass or external auricular canal polyps to nonspecific symptoms such as hearing loss, otalgia, or otorrhea.^{3,4} Some patients may be completely asymptomatic.⁵ Because these diseases can easily mimic benign processes, the diagnoses of RMS and LCH are usually only considered after imaging reveals a skull base or temporal bone lesion. However, the imaging characteristics of these tumors are similar on both CT and MR imaging.

Much of the current literature focuses exclusively on either RMS or LCH. The objective of our study was to compare radiologic data from patients with both RMS and LCH to determine characteristics that may aid clinicians in differentiating these 2 pathologies. To our knowledge, this is the first study to compare the imaging characteristics of these lesions. We hypothesized that

Received August 21, 2015; accepted after revision November 30.

From the Division of Otolaryngology, Head and Neck Surgery (K.M.C., R.H.W., N.Q., R.K.G.), University of Utah, Salt Lake City, Utah; and Department of Radiology (R.H.W.), University of Utah Hospital, Salt Lake City, Utah.

Paper previously presented at: American Society for Pediatric Otolaryngology Poster Session at the Combined Otolaryngology Spring Meeting, May 14–18, 2014; Las Vegas, Nevada.

Please address correspondence to Keely Chevallier, MD, Division of Otolaryngology, 50 N Medical Dr, 3C120, Salt Lake City, UT 84132; e-mail: keely.chevallier@hsc.utah.edu

<http://dx.doi.org/10.3174/ajnr.A4676>

these lesions would have distinct characteristics on cross-sectional imaging, which will aid in making the proper diagnosis. Understanding the likely pathology before an operation is undertaken will help with surgical planning. Previously held wisdom suggested that RMS lesions would arise from muscle and be most likely to affect the middle ear, given the presence of the tensor tympani and stapedius muscles in the middle ear. LCH lesions would be most likely to arise from the marrow space and therefore more commonly affect the mastoid. We designed a single blinded review of cross-sectional imaging studies in pathologically confirmed cases to determine the most common site in the temporal bone for each lesion and the type of tissue most likely affected.

MATERIALS AND METHODS

To find cases of LCH and RMS affecting the temporal bone, we used billing data to find all International Classification of Diseases, Ninth Revision codes involving benign or malignant lesions of the temporal bone, skull, and bone, and we cross-referenced these data with patients seen in our otolaryngology clinics. Charts were reviewed retrospectively. Each chart was reviewed to establish a tissue diagnosis of LCH or RMS and to ensure that cross-sectional images were available for review. Both MR imaging and CT studies were in our inclusion criteria, depending on the technique available for each patient. We also used a radiology data base of temporal bone lesions to search for additional cases of known RMS or LCH for which images were available for review.

Demographic information was collected along with the presenting signs and symptoms for each case. Sample images representative of the lesions or the entire scan were reviewed independently by both a neuroradiologist and neurotologist. The reviewers were blinded to the pathology of the lesion.

A subsite and tissue type classification was created to describe the location of the lesion within the temporal bone and the type of tissue from which it appeared to arise. The temporal bone subsites included the petrous apex, middle ear, mastoid, and retrosigmoid/posterior cranial fossa. The petrous apex and middle ear were defined as the anterior temporal bone, and the mastoid and retrosigmoid/posterior cranial fossa were defined as the posterior temporal bone. Each reviewer was asked to identify the involved sites within the temporal bone and classify the degree of involvement on a scale of 0 (no involvement), 1 (partial involvement), or 2 (complete involvement). Subsites that appeared affected but were not at the center of the lesion were graded as 0.5.

Second, the type of tissue involved by the lesion was defined as being pneumatized bone, cortical bone, or the marrow space. The involvement of each type of tissue was again rated as 0 (no involvement), 1 (partial involvement), or 2 (complete involvement). Last, the reviewers were asked to rate otic capsule erosion as being present or absent.

Subsite, tissue type, and otic capsule erosion scores were compared with a χ^2 test if possible, but the low number of cases also required the use of a Fisher exact test. Two-tailed *P* values < .05 were statistically significant.

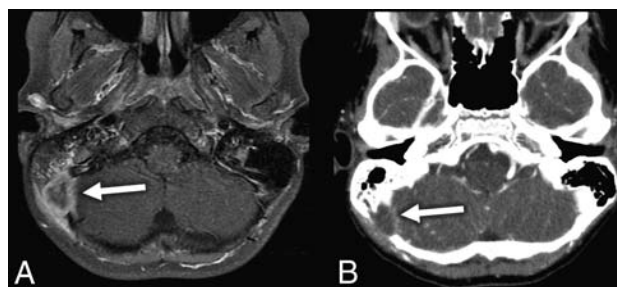


FIG 1. A, Axial T1 postcontrast fat-saturation MR image through the temporal bone demonstrates a peripherally enhancing posterior fossa or retrosigmoid LCH lesion (arrow). B, Axial standard algorithm postcontrast correlating CT scan demonstrates the same LCH lesion (arrow) with osseous destructive changes.

RESULTS

Our review of the records and the imaging data base identified 14 cases of LCH in 12 patients, with 2 patients having bilateral lesions, and 9 cases of RMS in 9 patients.

LCH Cases

Patients with LCH had an average age of 7.25 years and a male/female ratio of 1.4:1. Most patients (11/12) presented with otologic symptoms, and 1 patient presented with only constitutional symptoms. The most common otologic symptom was swelling or a periauricular mass (8/12). CT was the only imaging available in 8 of these cases, 1 had MR imaging only, and 3 additional cases had both MR imaging and CT performed.

The total for temporal bone subsite scores was 28 (14 cases with a possible total of 2 points each). The mastoid was the most commonly involved region with a score of 23/28 (82%), followed by middle ear involvement with a score of 13.5/28 (48%). The other sites were involved less commonly: retrosigmoid/posterior fossa involvement was 6/28 (21%) (Fig 1), and petrous apex involvement was 3/28 (10%). Disease was confined entirely to the anterior region in 1/14 ears and to the posterior region in 4/14 ears, with the remaining 9/14 cases having involvement in both the anterior and posterior temporal bone.

With respect to the tissue type at the center of the lesion, pneumatized bone was the most common area involved with a score of 24/28 (85%), the cortical bone was 11/28 (39%), and marrow space involvement was 3/28 (10%). There was otic capsule erosion in 3 of 14 ears.

RMS Cases

Patients with RMS had an average age of 4.93 years with a male/female ratio of 2.5:1. Most patients (8/9) presented with otologic symptoms, and only 1 patient presented with exclusively neurologic symptoms. The most common symptom was pain in 3/9 patients. Two patients presented with a mass, 2 patients presented with infectious symptoms, and 2 patients presented with facial palsy. CT was the only imaging available in 3 of these patients, 2 patients had MR imaging only, and 4 additional patients had both MR imaging and CT performed.

The total for subsite scores for RMS was 18 (9 cases with a possible total of 2 points each). Middle ear involvement was most common with a subsite score of 9.5/18 (52%). Mastoid involvement was 6/18 (33%), petrous apex involvement was 6/18

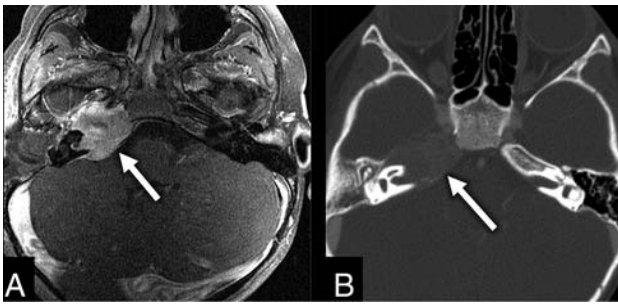


FIG 2. A, Axial fat-saturated postcontrast T1 MR image through the temporal bone shows a heterogeneous avidly enhancing lesion within the right petrous apex (arrow) found to be an RMS. B, Axial postcontrast correlating CT image in a bone window shows the same lesion (arrow) with expansile changes to the right petrous apex.

Temporal bone subsite scores for LCH and RMS lesions and associated P values

Subsite	LCH	RMS	P Value
Middle ear	48%	53%	.67
Mastoid	82%	33%	.001
Petrous apex	11%	33%	.12
Retrosigmoid/posterior cranial fossa	21%	0%	.07

(33%) (Fig 2), and retrosigmoid/posterior fossa involvement was 0/18 (0%). Disease was confined entirely to the anterior region of the temporal bone in 5/9 patients. The lesion involved only the posterior temporal bone in just 1/9 patients. The remaining 3 patients had involvement of the anterior and posterior temporal bone.

The most commonly involved area was in pneumatized bone in 11/18 (61%) scores, followed by marrow space involvement with a score of 6/18 (33%) and, least commonly, cortical bone with 2/18 (11%). There was otic capsule erosion in 2 of 9 ears.

Using a χ^2 analysis, we noted a statistically significant difference with respect to the involvement of the mastoid in LCH, 82%, and in RMS, 33%, ($P = .001$). The involvement of the remaining subsites was not significantly different between RMS and LCH. Please see the Table for the remaining subsite scores and associated P values. With the Fisher exact test, our data showed that confinement to the anterior region exclusively was significantly more likely in patients with RMS, 56%, versus 7.1% with LCH ($P = .018$).

Interrater reliability as measured by a weighted κ was moderate for the middle ear location, good for the mastoid and retrosigmoid/posterior cranial fossa locations, and very good for the petrous apex location ($P < .05$ for all comparisons).

Additionally, we found a significant difference in the rate of the cortical bone involvement, with LCH being more common in 39% of cases compared with 11% in RMS ($P = .05$). For the type of bone involved, interrater reliability was very good for pneumatized bone and marrow space ($P < .05$), but the reliability for cortical bone involvement did not reach statistical significance ($P = .09$). Thus, the involvement of cortical bone was not considered statistically significant. The data did not indicate significant differences in the type of bone involved, erosion of the otic capsule, or the presence of bilateral lesions.

DISCUSSION

Patients with RMS and LCH of the temporal bone frequently initially present with nonspecific symptoms. Both of these lesions occur most commonly in the pediatric population, which also has a high rate of benign ear disease, making the early diagnosis of a neoplastic process more difficult, yet critical in these complex cases.

Langerhans Cell Histiocytosis

LCH represents a spectrum of diseases from isolated lesions (eosinophilic granulomas) to multifocal disease (Hand-Schüller-Christian disease) and last to widespread disease with multiorgan involvement (Letterer-Siwe disease). The reported incidence of LCH involvement of the temporal bone varies widely from 13% to 40% of cases. Lesions tend to involve the marrow space and can arise from the diploic bone of the cranial vault.⁶ Lesions should be definitively diagnosed by histology demonstrating a proliferation of Langerhans cells and staining positive for S100 and CD1a on immunohistochemistry.⁴

Presentation of temporal bone involvement of LCH is most often with nonspecific otologic signs and symptoms, which could be mistaken for chronic otitis media or other infectious processes. According to published series, the most common presentations are a periauricular mass or otitis media. There is a slight male predominance of LCH cases of the temporal bone in the literature.^{4,7}

Consistent with the findings reported in this study, the series of Fernández-Latorre et al⁸ of LCH cases demonstrated 14 total cases with 2 patients having bilateral lesions. In their series, the site-specific frequency was 12 cases involving the mastoid, 9 involving the middle ear, and 2 cases involving the petrous apex. Similar to our series, several lesions involved multiple temporal bone subsites. Additionally, the series had 2 cases of otic capsule erosion. In another review of head and neck LCH, there was temporal bone involvement in the mastoid in 4 of 5 cases and in the petrous bone in 1 of 5 cases.⁷ Another case series noted “rare” otic capsule involvement.⁴ Treatment for LCH varies on the basis of the severity of the disease and includes surgical excision, chemotherapy, radiation, and intratumoral steroids. Given the relatively benign nature of isolated LCH lesions, some authors have argued that the therapy should not be worse than the disease.⁹

Rhabdomyosarcoma

RMS is a rare disease of the pediatric temporal bone. There are 4 distinct pathologic types of RMS: embryonal (most common in head and neck¹⁰), alveolar, pleomorphic, and botryoid. Tumors can arise from striated muscle or from undifferentiated mesenchymal cells. Desmin and muscle-specific actin stains are helpful in identifying RMS lesions. In 2 series, presentation was at approximately 4 years of age.¹⁰ Notably, there are no reported cases of bilateral temporal bone RMS, in contrast to reports of bilateral temporal bone LCH. There is a slight male predominance in RMS patients.¹⁰

The presentation of RMS is most commonly mistaken for benign ear disease, resulting in a reported delay in diagnosis ranging from 4 to 78 weeks.¹⁰ Chronic otitis media, polyps of the external auricular canal, and retroauricular masses are all common pre-

sentations.^{3,10} Other series showed a much higher prevalence of neurologic signs, including a series in which 9 of 14 patients presented with facial nerve palsies.¹⁰

Among patients with RMS lesions of the temporal bone, 50% had lesions that were localized to a specific temporal bone subsite, and the remaining 50% had extratemporal extension ($n = 6$).³ The staging system for RMS classifies a T1 lesion as being limited to 1 subsite of the temporal bone (mastoid, middle ear, or petrous apex).¹¹ The middle ear is considered an unfavorable subsite for RMS staging.¹² RMS cases affecting the bilateral temporal bones have not been reported, to our knowledge. Cases of RMS in the temporal bone have poorer prognosis than RMS of the orbit and the extratemporal head and neck.³

It has been reported that the most common site affected by RMS is the mastoid (57%), followed by the middle ear (43%), petrous apex (35%), and posterior fossa (14%), while 50% of cases affected multiple temporal bone subsites.¹⁰ A series published by Sbeity et al³ demonstrated RMS involvement of the middle ear in 50% of lesions, the mastoid in 50%, and the petrous apex in 17%. In a case reported by Viswanatha,¹³ the RMS lesion affected both the middle ear and mastoid. The role of surgery in treating RMS cases is variable, depending on the series. If the lesion can be completely excised, the prognosis improves regardless of the subsite. Most patients will be treated with chemotherapy, and 5-year survival rates vary from 66%³ to 90% in patients with resectable tumors.¹⁴

Imaging in LCH and RMS

In patients who ultimately are diagnosed with either RMS or LCH, imaging is often performed when initial treatments for otitis media and cholesteatoma fail. Each lesion has some imaging features that overlap with the imaging features of cholesteatoma and middle ear effusion. There are findings that help to differentiate these lesions on imaging.

On CT, RMS usually demonstrates a homogeneous lesion with mild contrast enhancement. On MR imaging, it has intermediate signal intensity on T1 and T2 sequences with significant enhancement with contrast. From the series of Sbeity et al,³ 1 case was localized to the mastoid; 1, to the middle ear; and 1, to the petrous bone.³ Because RMS does not arise from the bone, bony erosion is considered a poor prognostic sign and indicates a T3 lesion.¹¹

In the 1984 review of Coutté et al,¹⁵ CT findings could not distinguish cholesteatoma and LCH in children who presented with acute otitis media. Most series reported LCH lesions as being lytic or destructive.^{16–18} There was frequently an associated soft-tissue attenuation or a soft-tissue mass, and the otic capsule was usually spared.⁶ Lesions can have beveled edges because the LCH lesion seems to affect the inner and outer tables asymmetrically. Button sequestrum is a finding associated with lytic changes surrounding an area of apparently normal bone,¹⁹ though this process may not be appreciable in the 3D contours of the temporal bone.

MR imaging sequences show nonspecific changes consistent with inflammation and bone marrow involvement. MR imaging can better demonstrate intracranial extension and associated soft-tissue involvement, as well as distinguish these lesions from cholesteatoma. The MR imaging features of a cholesteatoma will in-

clude isointensity on T1, with slight hyperintensity compared with brain on T2, and no enhancement of the lesion. The lack of enhancement along with restricted diffusion in cholesteatoma cases is the critical imaging feature to differentiate LCH from cholesteatoma and demonstrates the improved soft-tissue evaluation of MR imaging over CT.

In our case series, only 2 of our 21 patients had a suspicion of an RMS or LCH before cross-sectional imaging. Cross-sectional imaging of these patients can suggest the underlying pathology of the lesion when the subsites of involvement are carefully evaluated. In all cases, a tissue diagnosis was made histologically. To our knowledge, this is the first series to compare imaging findings between these 2 uncommon pediatric temporal bone lesions. Lesions involving the mastoid subsite are significantly more likely to be LCH than RMS. Lesions involving the anterior portion of the temporal bone, including the petrous apex and middle ear, are more likely to be RMS.

The scope of this study was limited by its retrospective nature and the heterogeneity of imaging modalities available. Consequently, analysis of certain other features such as the presence of hemorrhage, necrosis, stalk thickening, or extratemporal involvement or comparison of ADC values could not be performed. Evaluating these other imaging characteristics could be helpful in the differentiation of these lesions for future research.

CONCLUSIONS

Rhabdomyosarcoma and Langerhans cell histiocytosis are both rare lesions of the pediatric temporal bone. Diagnosis usually occurs when patients fail standard treatment of suspected infectious causes or develop masses of the ear or temporal bone and imaging is undertaken. The imaging characteristics for these lesions are similar; however, the location of the lesion can be helpful in making a correct diagnosis. Our results indicate that the subsite of temporal bone involvement and the anterior or posterior nature of the lesion on imaging suggest the pathology of the lesion and allow better treatment planning before tissue diagnosis. LCH more frequently involves the mastoid, and RMS is typically confined to only the anterior temporal bone compared with LCH.

REFERENCES

1. Zhang X, Ma K, Wang J, et al. **A prospective evaluation for the combined helical tomotherapy and chemotherapy in pediatric patients with unresectable rhabdomyosarcoma of the temporal bone.** *Cell Biochem Biophys* 2014;70:103–08 CrossRef Medline
2. Martini A, Aimoni C, Trevisani C, et al. **Langerhans' cell histiocytosis: report of a case with temporal localization.** *Int J Pediatr Otorhinolaryngol* 2000;55:51–56 CrossRef Medline
3. Sbeity S, Abella A, Arcand P, et al. **Temporal bone rhabdomyosarcoma in children.** *Int J Pediatr Otorhinolaryngol* 2007;71:807–14 CrossRef Medline
4. Saliba I, Sidani K, El Fata F, et al. **Langerhans' cell histiocytosis of the temporal bone in children.** *Int J Pediatr Otorhinolaryngol* 2008;72:775–86 CrossRef Medline
5. Yildirim-Baylan M, Cureoglu S, Paparella MM. **Langerhans' cell histiocytosis of the temporal bone.** *Otol Neurotol* 2012;33:e15–16 CrossRef Medline
6. Azouz EM, Saigal G, Rodriguez MM, et al. **Langerhans' cell histiocytosis: pathology, imaging and treatment of skeletal involvement.** *Pediatr Radiol* 2005;35:103–15 CrossRef Medline

7. Anonsen CK, Donaldson SS. **Langerhans' cell histiocytosis of the head and neck.** *Laryngoscope* 1987;97:537–42 Medline
8. Fernández-Latorre F, Menor-Serrano F, Alonso-Charterina S, et al. **Langerhans' cell histiocytosis of the temporal bone in pediatric patients: imaging and follow-up.** *AJR Am J Roentgenol* 2000;174:217–21 CrossRef Medline
9. Boston M, Derkay CS. **Langerhans' cell histiocytosis of the temporal bone and skull base.** *Am J Otolaryngol* 2002;23:246–48 CrossRef Medline
10. Durve DV, Kanegaonkar RG, Albert D, et al. **Paediatric rhabdomyosarcoma of the ear and temporal bone.** *Clin Otolaryngol Allied Sci* 2004;29:32–37 CrossRef Medline
11. Donaldson CS, Castro JR, Wilbur JR, et al. **Rhabdomyosarcoma of the head and neck in children: combination treatment by surgery, irradiation, and chemotherapy.** *Cancer* 1973;31:26–36 Medline
12. Lawrence W Jr, Anderson JR, Gehan EA, et al. **Pretreatment TNM staging of childhood rhabdomyosarcoma: a report of the Intergroup Rhabdomyosarcoma Study Group.** *Cancer* 1997;80:1165–70 Medline
13. Viswanatha B. **Embryonal rhabdomyosarcoma of the temporal bone.** *Ear Nose Throat J* 2007;86:218–22 Medline
14. Baker KS, Anderson JR, Link MP, et al. **Benefit of intensified therapy for patients with local or regional embryonal rhabdomyosarcoma: results from the Intergroup Rhabdomyosarcoma Study IV.** *J Clin Oncol* 2000;18:2427–34 Medline
15. Coutté A, Brahe Pedersen C, Bartholdy N, et al. **Histiocytosis X; recurrent otitis media as a presenting symptoms in children with special reference to cholesteatoma.** *Clin Otolaryngol Allied Sci* 1984;9:111–14 CrossRef Medline
16. Hadjigeorgi C, Parpounas C, Zarmakoupis, et al. **Eosinophilic granuloma of the temporal bone: radiological approach in the pediatric patient.** *Pediatr Radiol* 1990;20:546–49 CrossRef Medline
17. Neilan RE, Kutz JW Jr. **Langerhans cell histiocytosis of the temporal bone.** *Otol Neurotol* 2012;33:e31–32 CrossRef Medline
18. Nelson BL. **Langerhans cell histiocytosis of the temporal bone.** *Head Neck Pathol* 2008;2:97–98 CrossRef Medline
19. Stull MA, Kransdorf MJ, Devaney KO. **Langerhans cell histiocytosis of bone.** *Radiographics* 1992;12:801–23 CrossRef Medline

T1-Weighted Dynamic Contrast-Enhanced MRI Is a Noninvasive Marker of Epidermal Growth Factor Receptor VIII Status in Cancer Stem Cell–Derived Experimental Glioblastomas

We read with great interest the article by Arevalo-Perez et al,¹ describing the potential value of T1-weighted dynamic contrast-enhanced MR imaging (DCE-MR imaging) as a biomarker for epidermal growth factor receptor variant III (EGFRvIII) mutation in patients with glioblastoma (GBM). In this retrospective study, the authors showed that EGFRvIII-positive tumors, compared with GBMs lacking the mutation, presented with a statistically significant increase in perfusion values of the contrast transfer coefficient (K^{trans}) and plasma volume (Vp). We agree with the authors' findings, and we also share some of their concerns; as the authors clearly stated in their discussion, both the genetic test performed on the tumor samples and the biopsy location may have induced some bias in their results. Specifically, the genetic test did not account for other mutations on the *EGFR* gene, which may also correlate to altered perfusion values; and the lack of the precise stereotactic biopsy localization may have confounded the assessment of EGFRvIII status. Furthermore, in this retrospective work, the possible presence of other concomitant mutations of genes regulating the tumor vascularization was not ruled out and might have contributed to the increased permeability of tumors positive for EGFRvIII.

To substantiate their findings, we tested the authors' hypothesis on a preclinical rat model of cancer stem cell (CSC)-derived GBM. CSCs were isolated by the neurosphere assay from a primary GBM tissue specimen, which was negative for the EGFRvIII mutation. CSCs were transduced with a lentiviral vector, coding for either the green fluorescent protein (GFP) or EGFRvIII under a constitutive promoter, according to our previously published protocol.² EGFRvIII messenger RNA and protein expression was confirmed by real-time polymerase chain reaction and Western blot, respectively. Five $\times 10^5$ transduced GBM CSCs were then injected into the left striatum of Rowett Nude rats; 3 rats were injected with GFP-transduced CSCs, whereas 4 rats were injected with the EGFRvIII-transduced CSCs.

MR imaging was performed on a small animal–dedicated 7T scanner (30/70 BioSpec; Bruker, Ettlingen, Germany) 35 days after CSC injection. The protocol included DCE-MR imaging during injection of gadobutrol (Gadavist; Bayer Schering Pharma, Berlin, Germany) performed by using a dynamic gradient-echo T1-weighted sequence (TR/TE = 67/3 ms, flip angle = 30°, matrix = 170 \times 170,

in-plane voxel size = 0.21 mm², section thickness = 0.75 mm). Eighty dynamic scans were obtained. DCE-MR imaging was preceded by a saturation recovery sequence for T1 mapping and followed by a contrast-enhanced T1 sequence for anatomic reference. DCE-MR imaging data were processed by using the software nordicICE (NordicNeuroLab, Bergen, Norway). Maps of pharmacokinetic parameters, Vp and K^{trans} , were calculated after deconvolution with an averaged arterial input function. Quantitative values were then obtained from both the region of maximal abnormality (hotspots) and histogram analysis. Volumes of interest were drawn on contrast T1-weighted images, previously coregistered to the DCE-MR imaging parametric maps. Values from both hotspots and histogram analysis were then normalized by using the ratio of tumor to normal white matter by placing ROIs on the contralateral healthy hemisphere, consistent with the analysis performed in our reference study.¹

As shown in Fig 1, our results confirm the observations by Arevalo-Perez et al¹: in fact, EGFRvIII-transduced CSC-derived tumors presented as very large lesions with heterogeneous contrast enhancement and a marked increase in tumor volume compared with the control GFP-transduced CSC-derived lesions. The mean volume for GFP-transduced CSC-derived lesions was 77.96 mm³ (range, 41.48–131.96 mm³), whereas for EGFRvIII-transduced CSC-derived tumors, the mean volume was 279.35 mm³ (246.82–331.35 mm³). Moreover, the latter tumors displayed markedly increased mean values of both normalized K^{trans} and Vp in the hotspot analysis, respectively 38.41 (range, 15.2–64.4) and 18.51 (9.2–26.7), compared with mean values of 6.77 (5.8–7.5) and 4.88 (2.6–7.5) for the control group. Histogram analysis in EGFRvIII-transduced CSC-derived tumors also showed an increase of the mean 75th and 90th percentile values for both K^{trans} and Vp. In EGFRvIII-transduced CSC-derived tumors, the mean normalized (relative) values were, respectively, 4.91 (range, 3.1–10.5), 5.22 (3.2–12.1) (75th), and 4.73 (2.5–10.9) (90th) for K^{trans} and 3.05 (2.8–4.9), 2.4 (2.2–4.2), and 2.43 (2.1–4.4) for Vp. For GFP-transduced CSC-derived lesions, the normalized values for K^{trans} were 1.91 (1.2–3.4), 3.42 (1.2–3.4), and 3.13 (1.4–3.3) and they were 2.68 (3.0–4.1), 2.12 (2.7–3.4), and 2.05 (1.7–3.1) for Vp. Immunofluorescence analysis of tumors confirmed an increase of vascularization in the brains transplanted with the EGFRvIII-transduced CSCs.

In conclusion, our findings, showing that the constitutive ex-

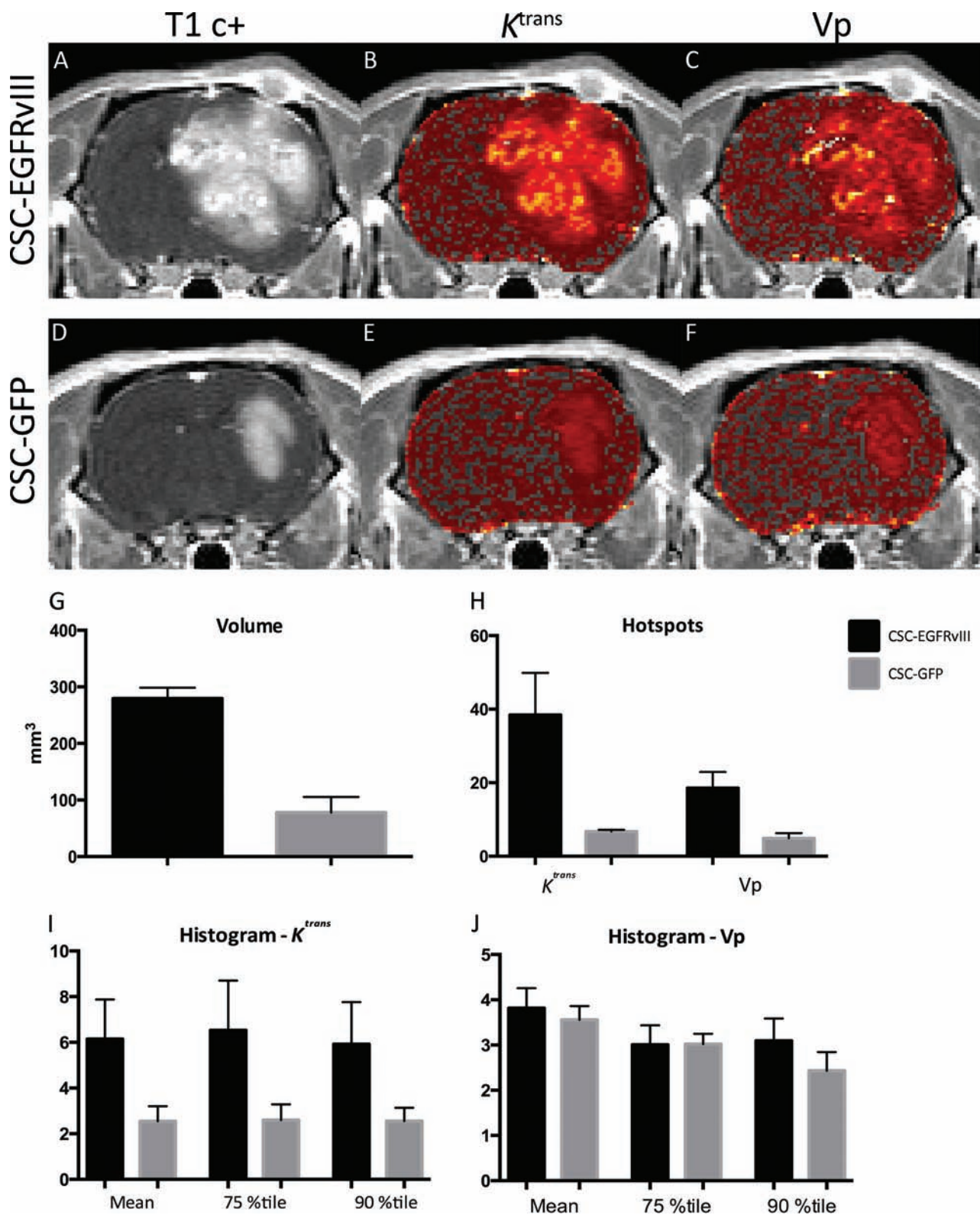


FIG 1. Representative postcontrast T1 and DCE-MR imaging parametric maps from EGFRvIII-transduced CSC-derived lesions (A–C) and control GFP-transduced CSC-derived lesions (D–F). Axial contrast T1-weighted images (A and D) demonstrate a larger and more heterogeneously enhancing lesion in EGFRvIII-transduced CSC-derived tumors. Corresponding K^{trans} and Vp maps reveal increased leakiness (B) and increased perfusion (C) in EGFRvIII-transduced CSC-derived lesions with respect to control lesions, which show little increase in K^{trans} (E) or Vp (F). Each parametric map is displayed by using the same thresholds for both cell lines (range: K^{trans} , 0–0.04 minutes⁻¹; range: Vp, 0–4). G–J. Bar graphs show the mean and standard error for volume (G), hotspots (H), histogram normalized (relative) K^{trans} (I), and normalized Vp (J) values in CSC-EGFRvIII (black bars) and CSC-GFP (gray bars) cell lines.

pression of EGFRvIII in a human CSC line can determine a significant increase in tumor perfusion parameters in experimental GBM, strongly support the hypothesis formulated by Arevalo-Perez et al.¹ Thus, the increase of permeability metrics may truly reflect the EGFRvIII status.

Disclosures: Marcello Cadioli—UNRELATED: Employment: Philips Healthcare. Rossella Galli—UNRELATED: Grants/Grants Pending: Associazione Italiana per la Ricerca sul Cancro (AIRC) Foundation,* Comments: grant support from the Italian charitable foundation supporting cancer research. *Money paid to the institution.

REFERENCES

1. Arevalo-Perez J, Thomas AA, Kaley T, et al. **T1-weighted dynamic contrast-enhanced MRI as a noninvasive biomarker of epidermal growth factor receptor vIII status.** *AJNR Am J Neuroradiol* 2015;36:2256–61 CrossRef Medline
2. Mazzoleni S, Politi LS, Pala M, et al. **Epidermal growth factor receptor expression identifies functionally and molecularly distinct tumor-initiating cells in human glioblastoma multiforme and is required for gliomagenesis.** *Cancer Res* 2010;70:7500–13 CrossRef Medline

 **L.S. Politi**

Neuroimaging Research, Hematology/Oncology Division
Boston Children's Hospital/Dana Farber Cancer Institute
Boston, Massachusetts
Radiology Department
University of Massachusetts Medical School
Worcester, Massachusetts

Neuroradiology Unit and CERMAC

Vita-Salute San Raffaele University and IRCCS San Raffaele Scientific Institute
Milan, Italy

 **G. Brugnara**

 **A. Castellano**

 **M. Cadioli**

 **L. Altabella**

Neuroradiology Unit and CERMAC

Vita-Salute San Raffaele University and IRCCS San Raffaele Scientific Institute
Milan, Italy

 **M. Peviani**

Neuroimaging Research, Hematology/Oncology Division

Boston Children's Hospital/Dana Farber Cancer Institute

Boston, Massachusetts

Neuroradiology Unit and CERMAC

Vita-Salute San Raffaele University and IRCCS San Raffaele Scientific Institute
Milan, Italy

 **S. Mazzoleni**

Neural Stem Cell Biology Unit, Division of Regenerative Medicine, Stem Cells and
Gene Therapy

IRCCS San Raffaele Scientific Institute

Milan, Italy

 **A. Falini**

Neuroradiology Unit and CERMAC

Vita-Salute San Raffaele University and IRCCS San Raffaele Scientific Institute
Milan, Italy

 **R. Galli**

Neural Stem Cell Biology Unit, Division of Regenerative Medicine, Stem Cells and
Gene Therapy

IRCCS San Raffaele Scientific Institute,

Milan, Italy

Regarding “Cerebral Angiography for Evaluation of Patients with CT Angiogram-Negative Subarachnoid Hemorrhage: An 11-Year Experience”

We would like to thank Heit et al¹ for their study “Cerebral Angiography for Evaluation of Patients with CT Angiogram-Negative Subarachnoid Hemorrhage: An 11-Year Experience” on the utility of digital subtraction angiography in patients with negative findings on CT angiography and subarachnoid hemorrhage. This is a laudable effort in addressing an issue with great heterogeneity in literature. However, we would like to raise a few questions regarding the article.

First, the statement that all patients with negative findings on CTA should be considered for DSA should be viewed with caution, especially for patients with perimesencephalic hemorrhage (pSAH). The authors reported that 2 aneurysms and 1 case of vasculitis were identified on DSA as causes of pSAH, which were initially missed on CTA. Heit et al¹ stated in the “Materials and Methods” section that if an aneurysm was identified by DSA after negative findings on CTA, the CTA was reviewed retrospectively. However, the results of that review were not available in the article. It would be helpful to know the number of cases with positive findings that could be retrospectively seen on CTA with the hindsight of the DSA results. On the other hand, in our own review of the literature, we found very few and questionable cases of pSAH in which imaging was of utility after initial negative findings on CTA.²

The authors quoted Delgado Almandoz et al³ to support the utility of follow-up DSA after negative findings on CTA because 1 aneurysm was detected on follow-up. On careful review of that article, in particular Fig 3B (the initial DSA that supposedly missed the 2-mm left superior cerebellar artery branch aneurysm), the aneurysm can be identified when correlated with subsequent DSA (Fig 3D), but the image quality was different, likely due to technical differences.² It would thus be more helpful to review the cases of missed aneurysms responsible for pSAH reported by Heit et al¹ and see whether they could be identified on the initial study in retrospect. On the basis of a literature review, Westerlaan et al⁴ found that 27% (19 of 71) of false-negative ruptured intracranial aneurysms could be detected at CTA retrospectively.

In the cases with pSAH caused by vasculitis or reversible cerebral vasoconstriction syndrome (RCVS), it would be unusual for RCVS to present with pSAH. Most of RCVS SAH tends to be convexity sulcal SAH.⁵ Vasospasm, although rare with pSAH, can also occur. The information about whether the 1 patient with SAH diagnosed as RCVS met the diagnostic criteria of SAH would be helpful.

Of further interest are the 16 patients with xanthochromia whose initial CTAs and subsequent DSAs had negative findings. Some publications have recommended the possible use of CTA to replace lumbar puncture in patients with thunderclap headache, and many institutions have used these papers to justify increased use of CTA for this indication.⁶ The absence of angiographic findings in the current study raises questions about that assumption.⁷

The authors’ recommendation that all patients with an initial CTA negative for pSAH should continue to undergo DSA needs further evidence and support. The current literature does not strongly support it, and this recommendation needs to be assessed in terms of its cost-effectiveness.⁸

REFERENCES

1. Heit JJ, Pastena GT, Nogueira RG, et al. **Cerebral angiography for evaluation of patients with CT angiogram-negative subarachnoid hemorrhage: an 11-year experience.** *AJNR Am J Neuroradiol* 2016; 37:297–304 CrossRef Medline
2. Kalra VB, Wu X, Matouk CC, et al. **Use of follow-up imaging in isolated perimesencephalic subarachnoid hemorrhage: a meta-analysis.** *Stroke* 2015;46:401–06 CrossRef Medline
3. Delgado Almandoz JE, Jagadeesan BD, Refai D, et al. **Diagnostic yield of repeat catheter angiography in patients with catheter and computed tomography angiography negative subarachnoid hemorrhage.** *Neurosurgery* 2012;70:1135–42 CrossRef Medline
4. Westerlaan HE, van Dijk JM, van Dijk MJ, et al. **Intracranial aneurysms in patients with subarachnoid hemorrhage: CT angiography as a primary examination tool for diagnosis—systematic review and meta-analysis.** *Radiology* 2011;258:134–45 CrossRef Medline
5. Miller TR, Shivashankar R, Mossa-Basha M, et al. **Reversible cerebral vasoconstriction syndrome, Part 1: epidemiology, pathogenesis, and clinical course.** *AJNR Am J Neuroradiol* 2015;36:1392–99 CrossRef Medline

6. McCormack RF, Hutson A. **Can computed tomography angiography of the brain replace lumbar puncture in the evaluation of acute-onset headache after a negative noncontrast cranial computed tomography scan?** *Acad Emerg Med* 2010;17:444–51 CrossRef Medline
7. Malhotra A, Wu X, Kalra VB, et al. **Cost-effectiveness analysis of follow-up strategies for thunderclap headache patients with negative non-contrast CT.** *Acad Emerg Med* 2016;23:243–50 CrossRef Medline
8. Kalra VB, Wu X, Forman HP, et al. **Cost-effectiveness of angiographic imaging in isolated perimesencephalic subarachnoid hemorrhage.** *Stroke* 2014;45:3576–82 CrossRef Medline

● X. Wu

● V.B. Kalra

● H.P. Forman

Department of Diagnostic Radiology

● C.C. Matouk

Department of Neurology and Neurosurgery

● G. Mongelluzzo

● R. Liu

● A. Malhotra

Department of Diagnostic Radiology

Yale School of Medicine

New Haven, Connecticut

REPLY:

We thank Dr Wu and colleagues for their comments regarding our recent article “Cerebral Angiography for Evaluation of Patients with CT Angiogram-Negative Subarachnoid Hemorrhage: An 11-Year Experience.”¹ We agree that there remains much heterogeneity in the literature regarding CTA-negative subarachnoid hemorrhage, which leads to complicated management decisions that necessarily compare the financial cost of repeat imaging with the risk of missing a ruptured cerebral aneurysm.

In response to the first question raised by our colleagues, a retrospective review of the CTA studies in patients with perimesencephalic SAH (pSAH) due to rupture of an aneurysm did not reveal the culprit aneurysms. The vessel irregularity in the patient with pSAH due to vasculitis or vasculopathy was not convincingly detectable on the original CTA. This patient presented with a headache 8 days after delivering a baby, which might suggest a diagnosis of reversible cerebral vasoconstriction syndrome, but further clinical follow-up was not available. Thus, our results do suggest that DSA is helpful in cases of CTA-negative pSAH. We would argue that the referenced data by Westerlaan et al,² in which ruptured aneurysms were missed by CTA and identified in 27% of cases on re-review, should lead to additional caution regarding the reliability of CTA. Missed aneurysms may be found retrospectively, but to our knowledge, no study compares the sensitivity of a secondary and independent review of a CTA with negative findings with a digital subtraction angiogram. Such a study would certainly be of interest to undertake.

The authors' article questioning the cost-effectiveness of digital subtraction angiography for evaluation of pSAH was well-written and compelling.³ However, we find it challenging to calculate accurately the cost of missing a cerebral aneurysm in a patient who subsequently has a second SAH and is left with a poor clinical outcome. Rupture of a missed aneurysm in a single young patient would be expected to incur millions of dollars in health care costs if that patient survives and is left with a large disability, as occurs in one-third of patients with rupture of a cerebral aneurysm.⁴ There is variability in the literature in determining the yield of diagnostic cerebral angiography in patients with CTA-negative SAH also makes cost-effectiveness analyses difficult.

We disagree with the publications that suggest that CTA should replace a lumbar puncture in patients with the sudden

onset of a severe headache. Cerebral aneurysms very rarely cause headaches in the absence of subarachnoid hemorrhage. A patient with a severe headache and a noncontrast head CT that does not demonstrate evidence of SAH should always undergo lumbar puncture. If the lumbar puncture is positive for xanthochromia, cerebral vessel imaging should be performed to identify a treatable cause of the SAH. Performing a CTA before a lumbar puncture would lead to a large number of incidentally identified unruptured aneurysms, and a lumbar puncture would still be required to determine whether the identified aneurysms should be treated acutely. This strategy would be expected to lead to increased costs due to additional imaging follow-up of these incidentally identified aneurysms and likely overtreatment of small cerebral aneurysms.

Last, we are all informed by our personal biases, values, and experiences as physicians. As interventional neuroradiologists who care for patients with ruptured aneurysms, we are very cognizant of the risk of re-rupture of a cerebral aneurysm, which is almost always a devastating or fatal event. Although perimesencephalic hemorrhage is very unlikely to be secondary to a ruptured cerebral aneurysm, we continue to believe that the minimal risk of diagnostic cerebral angiography (<0.2% at the authors' institutions) outweighs the risk of missing a ruptured aneurysm by not performing the criterion standard examination.

REFERENCES

1. Heit JJ, Pastena GT, Nogueira RG, et al. **Cerebral angiography for evaluation of patients with CT angiogram-negative subarachnoid hemorrhage: an 11-year experience.** *AJNR Am J Neuroradiol* 2016; 37:297–304 CrossRef Medline
2. Westerlaan HE, van Dijk JM, van Dijk MJ, et al. **Intracranial aneurysms in patients with subarachnoid hemorrhage: CT angiography as a primary examination tool for diagnosis—systematic review and meta-analysis.** *Radiology* 2011;258:134–45 CrossRef Medline
3. Kalra VB, Wu X, Forman HP, et al. **Cost-effectiveness of angiographic imaging in isolated perimesencephalic subarachnoid hemorrhage.** *Stroke* 2014;45:3576–82 CrossRef Medline
4. Al-Shahi R, White PM, Davenport RJ, et al. **Subarachnoid haemorrhage.** *BMJ* 2006;333:235–40 CrossRef Medline

JJ. Heit

Department of Interventional Neuroradiology
Stanford University Medical Center
Stanford, California

J.D. Rabinov

Department of Interventional Neuroradiology
Massachusetts General Hospital
Boston, Massachusetts

<http://dx.doi.org/10.3174/ajnr.A4802>